TRAVEL TIME TOMOGRAPHIC STUDIES OF SEISMIC STRUCTURES AROUND SUBDUCTED LITHOSPHERIC SLABS

Thesis by

Hua-wei Zhou

In Partial Fulfillment of the Requirements

for the Degree of

Doctor of Philosophy

California Institute of Technology

Pasadena, California

1990

(Submitted August 4, 1989)

Acknowledgements

My stay at Caltech has been a joyful and exciting experience. I deeply appreciate the encouragement, help and friendship of the faculty, students and the staff at the Seismo Lab and the Division.

I owe a great deal to Professors Rob Clayton, Don Anderson, Hiroo Kanamori, Brad Hager, Clarence Allen, Don Helmberger and Toshiro Tanimoto. Their support, patience and advice enabled me to complete my work at the Lab. My thesis advisor, Dr. Clayton, introduced me to tomographic imaging. Dr. Anderson inspired me on the significance of mantle seismic velocities in understanding the Earth. My interest in the seismic structure of subducted slabs began in discussions with Rob and Don.

I have always sought comments and inspiration from Don, Rob, Brad, Hiroo, and many other individuals. I thank all of my fellow students and friends, especially Robert Comer, Tom Hearn, Eugene Humphreys, Steve Grand, Michael Gurnis, John Vidale, John Louie, Richard Stead, Mark Richards, Jiajun Zhang, Robert Svendsen, Janice Regan, Ronan Le Bras, Luciana Astiz, Patricia Scott, Ann Mori, Vicki Lefevre, Hitoshi Kawasaku, Renata Dmowska, Christof Stork, Harold Magistrale, Oli Gudmundsson, Huw Davies, Phyllis Ho-Liu, Walter Kiefer, Robert Graves and Lorraine Hwang.

I'd also like to thank many faculty members at Cal State Long Beach who encouraged me to come to Caltech. I'm extremely grateful to the Li Foundation in New York, whose fellowship allowed me to start graduate study.

Abstract

The nature of the subducted lithospheric slab is investigated seismologically by tomographic inversions of ISC residual travel times. The slab, in which nearly all deep earthquakes occur, is fast in the seismic images because it is much cooler than the ambient mantle. High resolution three-dimensional P and S wave models in the NW Pacific are obtained using regional data, while inversion for the SW Pacific slabs includes teleseismic arrivals. Resolution and noise estimations show the models are generally well-resolved.

The slab anomalies in these models, as inferred from the seismicity, are generally coherent in the upper mantle and become contorted and decrease in amplitude with depth. Fast slabs are surrounded by slow regions shallower than 350 km depth. Slab fingering, including segmentation and spreading, is indicated near the bottom of the upper mantle. The fast anomalies associated with the Japan, Izu-Bonin, Mariana and Kermadec subduction zones tend to flatten to sub-horizontal at depth, while downward spreading may occur under parts of the Mariana and Kuril arcs. The Tonga slab appears to end around 550 km depth, but is underlain by a fast band at 750-1000 km depths.

The NW Pacific model combined with the Clayton-Comer mantle model predicts many observed residual sphere patterns. The predictions indicate that the near-source anomalies affect the residual spheres less than the teleseismic contributions. The teleseismic contributions may be removed either by using a mantle model, or using teleseismic station averages of

residuals from only regional events. The slab-like fast bands in the corrected residual spheres are are consistent with seismicity trends under the Mariana, Izu-Bonin and Japan trenches, but are inconsistent for the Kuril events.

The comparison of the tomographic models with earthquake focal mechanisms shows that deep compression axes and fast velocity slab anomalies are in consistent alignment, even when the slab is contorted or flattened. Abnormal stress patterns are seen at major junctions of the arcs. The depth boundary between tension and compression in the central parts of these arcs appears to depend on the dip and topology of the slab.

Table of Contents

Acknowledgements ii
Abstract iii

General Introduction 1

Chapter 1: A Tomographic Inverse Method: A Reconnaissance Survey of Major Seismic Slab Structures with ISC PP-Wave Travel Times

Abstract 7
1.1 Introduction 7
1.2 The Tomographic Inverse Method 10
1.3 Ray Tracing 17
1.4 Data Reduction 21
1.4.1 Data selection 24
1.4.2 Standard corrections and statics interpretation of PP waves 26
1.4.3 Bounce point corrections 34
1.5 Resolution Estimation 38
1.6 Error Estimation 45
1.7 Images of PP-Wave Structures 53
1.8 Summary 71
References to General Introduction and Chapter 1 73

Chapter 2: Tomographic Inversion in the Northwest Pacific: Detailed P and S Wave Slab Structures

Abstract 77
2.1 Introduction 77
2.2 Data and Method 80
2.2.1 Uncertainty in source locations 82
2.2.2 Data corrections 86
2.2.3 Inversion method 91
2.3 Estimation of Resolution by the Impulse Tests 94
2.4 Estimation of Error and Error Propagation 103
2.5 P and S Wave Images 111
2.6 Discussion 160
2.7 Conclusions 169
References to Chapter 2 171

Chapter 3: Tomographic Inversions in the Southwest Pacific: Regional P-Wave Structures from Primarily Teleseismic Data

Abstract 175
3.1 Introduction 176
3.2 Data and Corrections 180
3.3 Iterative Source Relocation and Inversion 192
3.4 Estimations of Noise Level and Resolution 201
3.5 Results 210
3.6 Discussion 231
3.7 Conclusions 236
References to Chapter 3 238

Chapter 4: Prediction of Observations from the Inverse Results: Modeling Focal Residual Spheres and Geoid

Abstract 241
4.1 Introduction 242
4.2 Data and Corrections 246
4.3 Modeling of Residual Spheres 258
4.4 A Test for Deep Mantle Velocity Heterogeneity 295
4.5 Method of Fitting for Slab-like Fast Bands 302
4.6 Results of Fitting for Slab-like Fast Bands 305
4.7 Modeling of Regional Geoid 320
4.8 Discussion 325
4.9 Conclusions 335
References to Chapter 4 337

Chapter 5: Seismic Stress in the Slab as Inferred from Focal Mechanisms

Abstract 339
5.1 Introduction 339
5.2 Earthquake Stress Axes 341
5.2.1 Earthquake focal mechanisms 342
5.2.2 Compilation of the data 343
5.3 Seismic Stress in Slabs 365
5.3.1 Determining the down-dip stress regime 365
5.3.2 Observations of down-dip stress in slabs 368
5.4 Comparison with Seismic Morphology of Deep Slabs 373
5.5 Discussion 386
5.6 Conclusions 390
References to Chapter 5 392

General Introduction

Seismic subduction zones have been central to seismic and tectonic studies since more than 90% of the earthquakes in the world occur within these zones. These earthquakes are thought to be a consequence of subduction of the lithosphere into the Earth's interior. According to Utsu [1971], Wadati was the first to show clear evidence for the existence of deep-focus earthquakes in the earth [Wadati, 1928], and he prepared a catalog of deep and intermediate earthquakes in and near Japan. In fact, Wadati [1935, Figure 4] gave the first iso-depth seismicity contour around Japan to a depth of 400-450 km, which depicts exactly the morphology of subduction zone in the region. Among important early documents, Gutenberg and Richter related seismicity with many geological features [1954]. Through cross-arc vertical cross sections, Benioff displayed the typical narrow slab-like seismicity patterns beneath many major trenches, including Tonga-Kermadec and South America [1948], Kurile-Kamchatka, Sunda, Central America, Aleutian, New Hebrides and Philippine [1954]. These seismicity zones are now called Wadati-Benioff zones, representing the trace of lithosphere penetrating the upper mantle.

Over the past two decades, the kinematic theory of plate tectonics has evolved to studies of dynamic movements in the earth's interior. One of the strongest evidences for such movements is the migration of the lithosphere in the form of a mosaic of plates at the surface. In particular, the oceanic lithosphere is found to originate along the mid-ocean ridges and spreads out. It

eventually subducts at a convergent margin with another plate, usually a continental continental plate, forming subduction zones (Figure 0.1). The descending lithospheric material is referred as a subducted lithospheric slab.

It is well known that the descending oceanic lithosphere has anomalously high-Q and high-velocity to a depth of at least several hundred kilometers beneath the arc, sandwiched by two low-Q, low-velocity zones in the upper mantle [e.g., Utsu, 1971]. The seismic structure of the slab is directly related to its morphology and the physical state, hence holds the key to the understanding of the dynamics of the earth's interior. A tremendous amount of geophysical studies, such as those on plate consumption, mantle convection, origin of island arc systems and structural discontinuities in the mantle, have pinned down to the fate of the subducted slab at depth.

Early studies on subduction zones were based on their seismicity. Later on, in a study on focal mechanisms of subduction zone earthquakes Isacks and Molnar [1971] concluded that the down-dip (along the direction of subduction) stress within a subducting slab is extensive or mixed at shallow to intermediate depths, and becomes primarily compressive at depths below about 350 km. Deep subduction zones below 350 km are also marked with one of the two distributional peaks of earthquakes with depth, contrasting to the other peak which includes all the bending events in the shallow region [Vassiliou *et al.*, 1984]. Due to the extinction of seismicity of a reliable focal depth below about 680 km [Stark and Frohlich, 1985], and the possible existence of aseismic subducting slabs, geophysical observables other than seismicity are needed. As pointed out by Toksöz *et al.* [1971], seismic travel

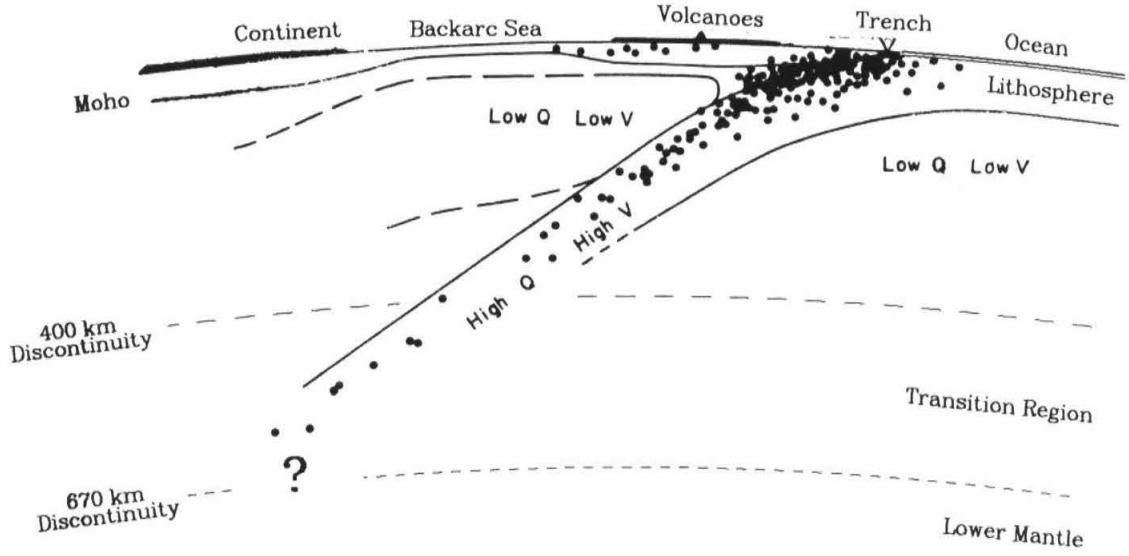

Figure 0.1 A cartoon cross section of possible seismic structure of the subducted slab [modified from Utsu, 1971]. Solid circles represent earthquake foci. The question mark at the lower left corner indicates the unknown nature of the deep slab.

times and amplitudes are the most informative for subduction zone study.

This thesis focuses on the seismic structures of subduction zones. The major approach is to apply a tomographic (slice-picturing) inverse method on ISC (International Seismological Centre) residual travel time data. Figure 0.2 shows all events deeper than 300 km that occurred from 1964 to 1982 reported by the ISC catalog, illustrating two profound subduction regions under investigation in this thesis, the northwest Pacific (NWP) and southwest Pacific (SWP). This thesis attempts to resolve the complete three-dimensional seismic structure of a slab, which is the most distinctive three-dimensional velocity anomalies in the mantle. Although the seismic structure of the earth is predominately depth-dependent (over 98% of travel times can be explained by an one-dimensional velocity model), the three-dimensional velocity variations are the most exciting part, since they are likely to provide clues to our understanding of the dynamics of the earth.

A tomographic inverse transforms the travel time residuals into a three dimensional image of slowness (reciprocal of seismic velocity) anomalies. In contrast to any modeling approach which nonuniquely fits the data with given models, an inverse is in the process of "data $\Rightarrow$ image $\Rightarrow$ model." Thus, the data is uniquely transformed (inverted) into an image in the first stage, and the image can be interpreted, though nonuniquely, in the second stage. This is analogous to reflection seismology, where data are imaged into seismic profiles and followed by geological interpretations. Furthermore, either the image or the interpretation can be used later to predict the observations.

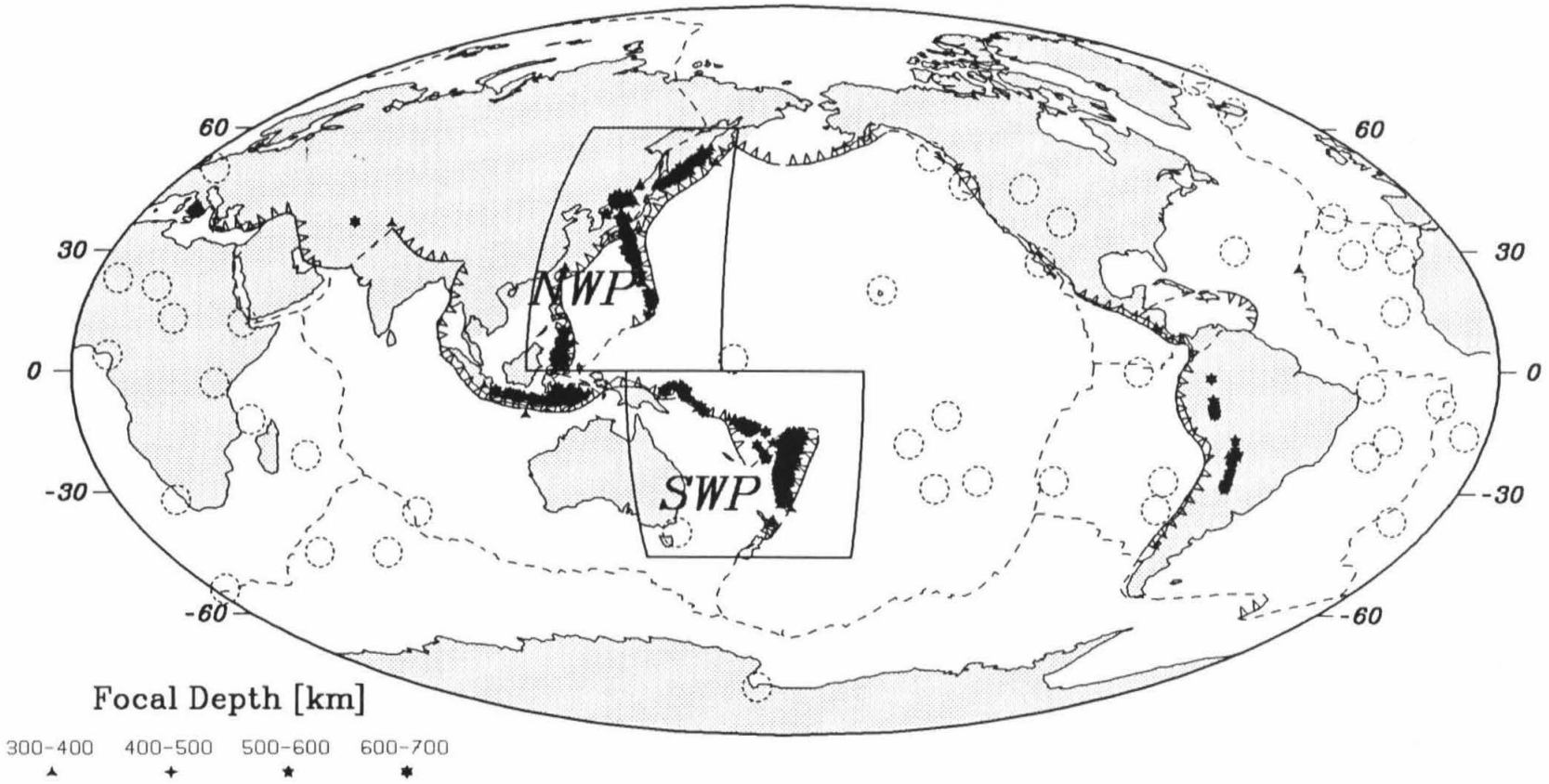

Figure 0.2 Global distribution of deep earthquakes. Stars represent events deeper than 300 km in ISC catalog (1964-1982). Dashed circles are hot spots. Plate boundaries are dashed, and trenches that are underlaid by subduction zones are plotted as open barbed lines. Regions under extensive investigations are the northwest Pacific (NWP) and southwest Pacific (SWP) in boxes.

In Chapter 1 an iterative tomographic inverse method and resolution and error error estimations are introduced and applied to ISC PP wave travel time residuals, in a reconnaissance survey on compressional velocity structures of major subduction zones in the world.

In Chapter 2 the compressional and shear velocity structures of the northwest Pacific subduction zones are obtained using primarily regional rays. The region possesses perhaps the best quality ISC data in the world, and an interpreted slab model for the region depicts the morphology of the subducted lithosphere.

In Chapter 3 the compressional velocity structures surrounding subduction zones in the southwest Pacific are derived from inversions using primarily teleseismic data. An epicenter relocation is attempted during the iterations of inversions.

In contrast to the previous chapters, Chapter 4 describes some predictions from the inverted velocity images, primarily the modeling of travel time residual spheres in the northwest Pacific.

Chapter 5 analyzes the state of stress in the subduction zones as inferred from seismic focal mechanisms in the northwest Pacific and Tonga-Kermadec region.

CHAPTER 1

A TOMOGRAPHIC INVERSE METHOD:
a reconnaissance survey of major seismic slab structures with ISC PP wave travel times

Abstract

An SIRT tomographic inverse method is discussed with particular application to the ISC PP wave data set. Details of data reduction, inversion, and estimations for resolution and error are presented. Despite the relatively high noise level and poor ray coverage of the PP wave data, some useful information is yielded on tectonic patterns. The images of PP waves, with coverage over some regions that is uncovered by P waves, indicate that most subduction zones are associated with relatively fast velocity anomalies.

1.1 Introduction

The morphology and physical state of subducted lithosphere is one of the key focal points in modern earth sciences. Nearly all intermediate and deep-focus earthquakes occur in association with subducting lithospheric slabs, forming seismic Wadati-Benioff zones. It is thought that the subducted lithospheric plate, or slab, is the most distinctive velocity anomalies in the mantle, because it is about 800 ° C cooler than the ambient mantle to at least 700 km depth (e.g., Toksöz *et al.*, 1973; Anderson, 1987). Previous studies in Japan and other regions have shown that the subducting slabs have

anomalously high seismic velocity and low attenuation to a depth of at least several hundred kilometers, and are sandwiched between low velocity and high attenuation zones [e.g., Utsu, 1971; Isacks and Barazangi, 1977; Hirahara, 1981]. Investigation of the morphology of the velocities around Wadati-Benioff zones and associated anomalies in three-dimension may provide new insights about the subduction process.

To resolve subduction zone velocities, the approach taken here is to apply simple ray theory to a large number but quite noisy travel time data taken from the ISC catalog. Perhaps the most promising approach is a tomographic inversion. The advantages of the inversion are laid out in the following. The inversion uses crossing rays to isolate locations of mantle heterogeneities; it is thus particularly suitable for large data sets. When the reference one-dimensional velocity model is reasonable, the travel time problem is linear, hence the inversion is guaranteed to converge to the global minimum. In addition, the deep seismicity not only provides a good ray coverage over a subduction zone, but also functions as the best guide for locating the subducting slab. The seismic energy radiated from a deep source will not be complicated by triplication caused by shallower velocity discontinuities. As concluded by Nolet [1985] in probing the applicability of three types of methods commonly used in seismicity tomography, regions of deep seismicity could be the only places where one can hope to sufficiently resolve the upper mantle.

There have been several regional upper mantle least-squares type inversions around some subduction zones, involving simultaneous source

relocations, such as that in Japan [Hirahara, 1977; Hirahara and Mikumo, 1980], southwest Japan [Hirahara, 1981], Izu-Bonin Trench [Roecker, 1985] and central Aleutians [Spencer and Engdahl, 1983; Engdahl and Gubbins, 1987]. Overall, the lateral structure along the strike of subducted lithospheric slab has not received much attention until recently [Isacks and Barazangi, 1977; Giardini and Woodhouse, 1984; Burbach and Frohlich, 1986]. The aim of this thesis is to invert tomographically a large amount of residual travel times for three-dimensional seismic structures around some deep Wadati-Benioff zones, from the surface down to at least the bottom of the upper mantle.

Adopted from a medical imaging technique [e.g., Jaffe, 1982], the term "tomography" has been widely used now in geophysics for almost any kind of structural inversion. In this thesis, however, this term is referred specifically to the reconstruction algorithms which linearize the problem by dividing a model into a mosaic of resolution blocks or cells. There are other ways to parameterize the model [e.g., Tarantola and Nercessian, 1984]. Since a three-dimensional subduction zone structure involves a model space which is often too large to be handled with a direct least-squares type inversion, we take an iterative back projection approach which was initiated by Clayton and Comer [1983]. This approach enables inverting a large data set, and has been applied to a wide range of model scales, from global [Clayton and Comer, 1983; Zhou and Clayton, 1985; Davies and Clayton, 1986] to regional [Grand, 1987; Humphreys *et al.*, 1984; Humphreys and Clayton, 1988; Zhou and Clayton, 1987] and crustal [Hearn and Clayton, 1986ab; Walck and Clayton, 1987] structures. A three-dimensional structure can be resolved to a desired

resolution level by this method as long as the data is sufficient and the ray theory holds valid.

In this chapter, a reconnaissance survey of compressional velocity structures of major subduction zones in the world is carried out with a tomographic inversion of ISC PP wave travel time data. Slabs are the major, but not the only, subjects of interest. Other mantle structures are inferred from the images as well. As the first attempt to use secondary phases in residual time tomography, we take PP waves because of their superior spatial coverage for shallow regions compared to P waves. In fact, a set of PP wave picks usually has more diverse takeoff angles at the source than that of the corresponding P wave data, yielding a better chance to cover a subduction zone. The disadvantage of using PP waves is that the data are often more limited in quantity and poorer in quality in comparison with the direct P arrivals.

1.2 The Tomographic Inverse Method

The iterative back projection scheme initiated by Clayton and Comer [1983] is an SIRT (Simultaneous Iterative Reconstruction Technique) reconstruction inverse. As summarized by Radcliff and Balanis [1979], there are three types of reconstruction algorithms used in medical CT (Computed Tomography) scanning, namely, BPT (Back Projection Technique), ART (Algebraic Reconstruction Technique) and SIRT. ART was introduced by

Gordon *et al.* [1970], and later was modified to SIRT by Gilbert [1972]. The early application of SIRT to geophysical problems was on cross-borehole seismic tomography [Dines and Lytle, 1979].

Since the earth's velocity structure is predominately a function of depth, our three-dimensional inversion is generally done for slowness perturbations with respect to a laterally homogeneous reference velocity model. Hence, the data used are residual travel times between observed times and predictions from the one-dimensional reference model. The Jeffreys-Bullen (JB) earth velocity model [Jeffreys and Bullen, 1948] is employed as the reference model in this thesis, since our data base is the ISC residual travel times which are relative to the JB tables. The choice of the reference models actually has little effect on the inversion because all the models among our choices do not vary very much from one another, and the slowness field resolved is in respect to the reference model. As a matter of fact, other models, such as the PREM (Preliminary Reference Earth Model) [Dziewonski and Anderson, 1981] and Herrin's model [Herrin, 1968], are comparable to the JB model in terms of ray paths; i.e., the ray paths are generally unchanged with respect to the basic resolution blocks when switching the reference models, or laterally perturbing the slowness up to about ten percent (about the possible maximum lateral slowness perturbations). The stability of a data ray path is due to the fixed locations of seismic source and receiver, and Fermat's principle.

A vector $\Delta \mathbf{t}$ is used to represent residual travel time data for M rays connecting earthquake sources and seismic stations. The velocity structure is approximated by a model mosaic of N blocks of constant slowness (the

reciprocal of wave velocity) perturbation. Assuming that the velocity perturbations are small and ignoring caustics, the forward travel time problem can generally be linearized [e.g., Aki *et al.*, 1977] into

$$\Delta \mathbf{t}_{M\times 1} = \mathbf{L}_{M\times N}\Delta \mathbf{s}_{N\times 1}, \tag{1.1}$$

where $\mathbf{L}_{M\times N}$ is a matrix which contains the path length of each ray traversed through each block, and the vector $\Delta\mathbf{s}$ denotes the slowness perturbations of all blocks. Note, the elements of L which are not traversed by a ray are set to zero. At the n-th iteration the recursive SIRT back projection formula by Comer and Clayton [unpublished manuscript, 1984] is

$$\Delta \mathbf{s}^{(n)} = \mathbf{L}^{B}\Delta \mathbf{t} + (\mathbf{I} - \mathbf{L}^{B}\mathbf{L})\Delta \mathbf{s}^{(n-1)}. \tag{1.2}$$

where $\mathbf{L}^{B} = \mathbf{S}\mathbf{L}^{T}\mathbf{D}$, $\mathbf{S} = \mathrm{diag}(\frac{1}{\mu+L_i^M})_{N\times N}$ and $\mathbf{D} = \mathrm{diag}(\frac{1}{L_k^N})_{M\times M}$. μ is a damping parameter, $L_i^M = \sum_{j=1}^{M} l_{ji}$ is the sum of all path lengths through the i-th block, and $L_k^N = \sum_{j=1}^{N} l_{kj}$ is the entire path length of the k-th ray.

In the beginning $\Delta\mathbf{s}^{(0)} = 0$. During each iteration the delays of all rays that pass through a block are accumulated and averaged with respect to their path lengths to update the slowness perturbation of that block. If a block is intersected by less than a certain number of rays (e.g., we set five rays for PP waves), it is removed by setting its slowness perturbation to zero. A generalized scheme of SIRT inverse will have the same formula as equation (1.2), often multiplied by a normalization factor in front of its right-hand-side, but $\mathbf{L}^{B}$ will be defined as the complex conjugate transpose of **L**.

To adopt a method by Olson [1987] for accelerating the convergence of inversion, a modification on the matrix $\mathbf{S}$ is necessary. From equation (1.2) Comer and Clayton have shown

$$\Delta \mathbf{s}^{(n)} = \mathbf{L}^B \sum_{m=0}^{n-1} (\mathbf{I} - \mathbf{L}\mathbf{L}^B)^m \Delta \mathbf{t}. \tag{1.3}$$

Now since

$$\sum_{m=0}^{n-1} (\mathbf{I} - \mathbf{A})^m \mathbf{A} = \sum_{k=0}^{n-1} C_n^{k+1} (-\mathbf{A})^k \mathbf{A} = \mathbf{I} - (\mathbf{I} - \mathbf{A})^n$$

we have

$$\Delta \mathbf{s}^{(n)} = \mathbf{L}^B \sum_{m=0}^{n-1} (\mathbf{I} - \mathbf{L}\mathbf{L}^B)^m \mathbf{L} \Delta \mathbf{s} = \left[\mathbf{I} - (\mathbf{I} - \mathbf{L}^B\mathbf{L})^n\right] \Delta \mathbf{s}. \tag{1.4}$$

Hence, $\mathbf{I} - (\mathbf{I} - \mathbf{L}^B\mathbf{L})^n$ is the conventional resolution matrix, the mapping matrix between the inverted solution and the real solution.

It is now clear that the convergence of this type of iterative inversion depends on whether or not all the eigenvalues of $(\mathbf{I} - \mathbf{L}^B\mathbf{L})$ matrix exceed unity in absolute values. Following Comer and Clayton, we denoted $\mathbf{D}^{1/2}\mathbf{L}\mathbf{S}^{1/2} = \mathbf{U}\Sigma\mathbf{V}^T$, where $\mathbf{U}_{M\times M}$ and $\mathbf{V}_{N\times N}$ are orthogonal matrices, and $\Sigma = \mathrm{diag}(\sigma_1, \sigma_2, \ldots, \sigma_{\min(M,N)})_{M\times N}$. Since

$$\begin{aligned}(\mathbf{I} - \mathbf{L}^B\mathbf{L}) &= \mathbf{S}^{1/2}(\mathbf{I} - (\mathbf{D}^{1/2}\mathbf{L}\mathbf{S}^{1/2})^T(\mathbf{D}^{1/2}\mathbf{L}\mathbf{S}^{1/2}))\mathbf{S}^{-1/2} \\ &= \mathbf{S}^{1/2}\mathbf{V}(\mathbf{I} - \Sigma^T\Sigma)\mathbf{V}^T\mathbf{S}^{-1/2},\end{aligned}$$

we have

$$(\mathbf{I} - \mathbf{L}^B\mathbf{L})^n = \mathbf{S}^{1/2}\mathbf{V}(\mathbf{I} - \Sigma^T\Sigma)^n\mathbf{V}^T\mathbf{S}^{-1/2} \tag{1.5}$$

where $(\mathbf{I} - \Sigma^T\Sigma) = \mathrm{diag}(1-\sigma^2_1, 1-\sigma^2_2, \ldots, 1-\sigma^2_{\min(M,N)}, 1, \ldots, 1)_{N\times N}$. Hence, the

convergence of this type of SIRT inversion requires that $|1-\sigma^2_i| < 1$, or $\sigma^2_i < 2$ as a necessary and sufficient condition.

Comer and Clayton [unpublished manuscript, 1984] have proved $\sigma_{max} \leq 1$ for a positive μ. To accelerate the convergence, we like to find the lower bound of μ under the condition that $\sigma_{max} \leq 2$, i.e., $||\mathbf{D}^{1/2}\mathbf{L}\mathbf{S}^{1/2}\mathbf{x}||^2 < 2||\mathbf{x}||^2$ holds for all $\mathbf{x}$, where $||\ ||$ denotes the second norm. In fact,

$$||\mathbf{D}^{1/2}\mathbf{L}\mathbf{S}^{1/2}\mathbf{x}||^2 = \sum_k \left[\sum_i l_{ki}(\mu+L_i^M)^{-1/2}x_i\right]^2 / L_k^N$$

$$\leq \sum_k (\sum_i l_{ki}) \sum_i \frac{l_{ki}x_i^2}{\mu+L_i^M} / L_k^N$$

$$= \sum_k \sum_i \frac{l_{ki}x_i^2}{\mu+L_i^M}$$

$$= \sum_i \frac{L_i^M}{\mu+L_i^M} x_i^2$$

$$< 2||\mathbf{x}||^2 = \sum_i x_i^2.$$

Therefore, so long as

$$\mu > -L_i^M/2 \tag{1.6}$$

we will always have $\sigma_{max} < 2$.

Under the condition in equation (1.6), one likes to have most of the eigenvalues σ_i, or their mean, as close to unity as possible. The smaller the denominator of each element in the $\mathbf{S}$ matrix, the larger the value of the

corresponding σ_i. Thus, if one takes the lower bound $L_i^M/2$ as shown in equation (1.6) and denotes n_i as the number of nonzero diagonal elements of **L** matrix, then

$$\begin{aligned}
\text{mean}\,(\sigma_i) &= \frac{1}{n_i}\text{trace}\,(\mathbf{D}^{1/2}\mathbf{L}\mathbf{S}^{1/2}) \\
&= \frac{1}{n_i}\sum_{i}^{\min(M,N)}\frac{l_{ii}/L_i^N}{\mu+L_i^M} \\
&< \frac{1}{n_i}\sum_{i}^{\min(M,N)}\frac{l_{ii}/L_i^N}{L_i^M/2} \\
&< \frac{2}{\min(L_i^M)}\frac{1}{n_i}\sum_{i}^{\min(M,N)} l_{ii}/L_i^N \\
&< \frac{2}{\min(L_i^M)}. \qquad (1.7)
\end{aligned}$$

Equation (1.7) implys that most of σ_i are much less than 1, and to enlarge these values one has to enlarge the elements of the diagonal matrix **S**. Nevertheless, even if one uses the largest elements possible by having the lower bound of equation (1.6), the mean of σ_is is still less than 1 in cases that $\min(L_i^M) > 2$. As a matter of fact, once we put a lower limit on the number of rays passing through every block, it is almost always true that $\min(L_i^M) > 2$. Hence, one should try to use values of the damping constant as close to their lower bound as allowable. From equation (1.6) we may modify the **S** matrix of our inverse equation (1.2) in the form of

$$\mathbf{S} = \frac{2}{1+\alpha\,\theta^{(n)}}\text{diag}\left(\frac{1}{L_i^M}\right)_{N\times N} \qquad (1.8)$$

where α is a positive real number and $\theta^{(n)}$ is the zero-th root of the Chebyshev polynomial for n-th iteration as described by Olson [1987]. The product $\alpha\ \theta^{(n)}$ is a variable damping factor which is set to place more weight on blocks with more ray coverage, and to damp over-shoot oscillations during iterations. The larger the value of α the larger the damping will be. In the inversions performed in this thesis α is fixed at 1.0. During one inversion $\theta^{(n)}$ goes from unity to zero monotonicly to accelerate the convergence of the inversion.

There is no quantitative way to decide the optimal number of iterations. In fact, a trade-off between resolution and error is well known for inversion on a linear system [Backus and Gilbert, 1967]. Both resolution and error will increase with increase of iteration numbers, although the rate of convergence can be accelerated. More iterations will increase the effect of smaller and smaller eigenvalues, and thus the amplitude of the solution will increase unrealisticly in such kind of numerical calculations. For instance, solution from 15 iterations and 100 iterations will have very similar patterns while the latter has higher magnitude. Therefore, we believe the large patterns of the image more than their magnitude. Practically, we decide the number of iterations based on the behavior of the solution. Following Tanimoto and Anderson [1985] we can plot the relation between the number of iterations and the solution value of every block. There is usually a boundary between solutions of most blocks that converge and a remaining number of blocks that have not yet converged. The second group of blocks have eigenvalues that are too small to be inverted within practical number of iterations and computer limitations. Since solutions of most blocks have converged farely well after several tens of

iterations, we choose to have thirty iterations for PP wave data. The corresponding variance reduction is near 32% during the inversion.

1.3 Ray Tracing

Ray tracing is an important step in the inversion procedure, since it connects the travel times with velocity anomalies. In an ideal case, we would like to use a three-dimensional ray tracer and calibrate both residuals and ray paths during an inversion. One of the early three-dimensional ray tracing techniques [Jacob, 1970] is designed particularly for the slab effect. There are two common types of three-dimensional ray tracing, shooting methods [Julian, 1970] and bending methods [Wesson, 1971]. There are also many hybrid versions [e.g., Julian and Gubbins, 1977; Pereyra *et al.*, 1980; Thurber and Ellsworth 1980]. Currently, however, it is impractical for us to adopt the three-dimensional ray tracing with the large data sets and the computing facilities. However, since the earth's velocity structure is predominately layered, ray tracers based on two-dimensional (assuming ray paths stay in the vertical plane through source and receiver) and even one-dimensional velocity models are applicable when the block size is sufficiently large. In this and the next chapters, as a first-order attempt, a ray tracer based on a one-dimensional velocity model is used and the ray paths are assumed to be fixed through inversion. The fixed ray path assumption may not produce large errors because it is a two-point problem rather than a shooting problem. Given less than about ten percent of slowness perturbations, the fixed source

and receiver locations do not allow much variation of the ray paths.

The ray tracer used in this thesis is based on a classic approximation due to Mohorovicic (p.122, Bullen [1953]). Within the i-th layer, the velocity v is approximated by

$$v = a_i r^{b_i} \tag{1.9}$$

where r is the distance to the center of the earth and a_i and b_i are two constants of the layer. This approximation allows analytic solutions of the ray integral equations for both travel time t and distance Δ. For calculating ray path length l, a fifth-order unweighted Gaussian integration scheme is utilized. The requirement for the accuracy of ray path length l is not as high as that for t and Δ because in the end it is only used as a weighting function for the solution. Because the block grid used for inversion is predefined, the ray tracing based on (1.9) allows velocity discontinuities between layers.

There are many other types of numerical ray tracing techniques for layered velocity structures. However, those using a piece-wise linear approximation often require too many layers, and those using a spline function approximation [Cerveny, 1980; Cerveny and Jansky, 1983] require several orders of continuity across the layer interfaces, will exclude zeroth and first order discontinuities in the velocity model.

In our ray tracing calculations, the ray parameter p (the horizontal slowness) is kept as the fundamental variable. The ray tracer is capable of producing all body phases with a very high precision. As an example, the synthetic travel time chart in Figure 1.1 is produced by this ray tracer.

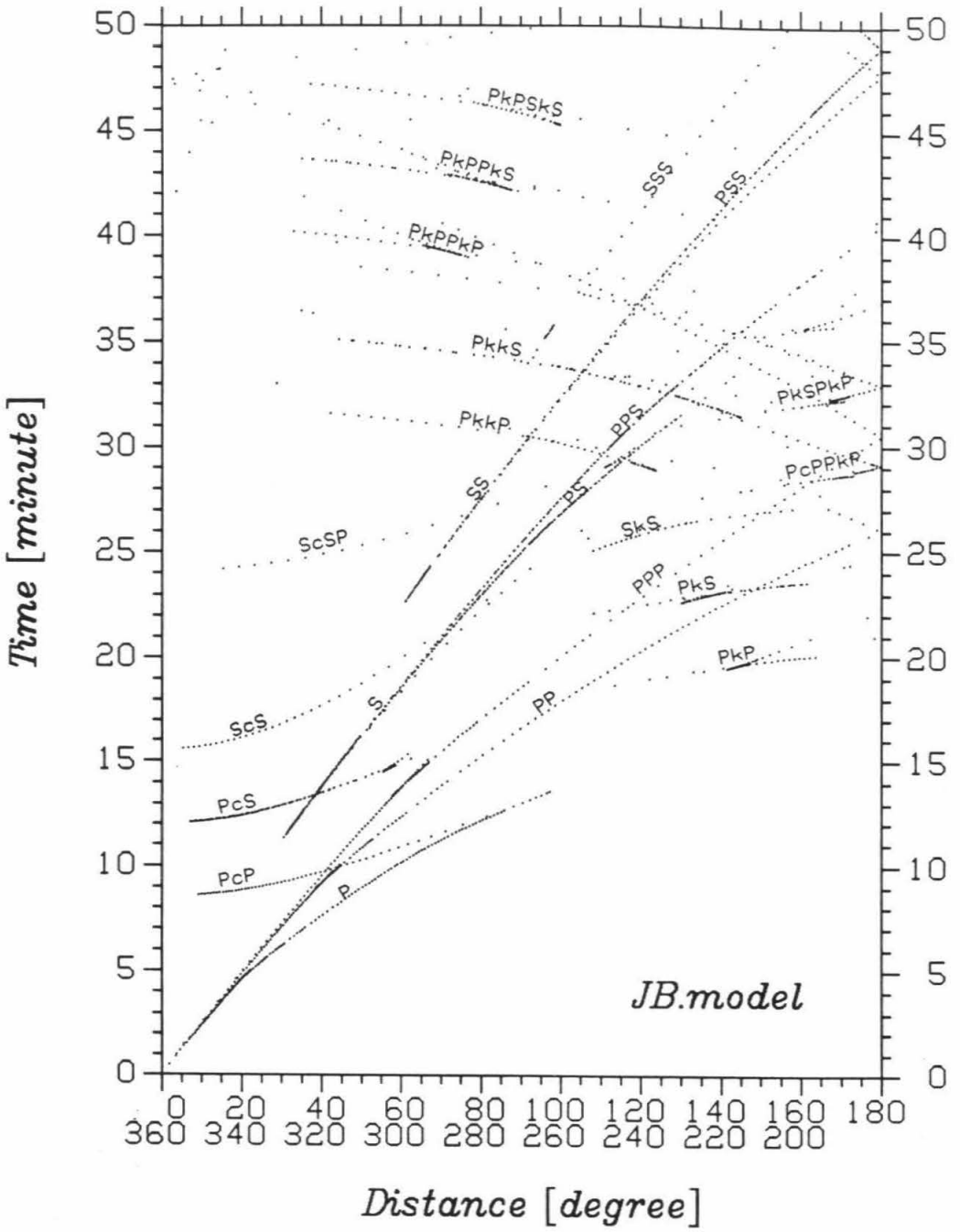

Figure 1.1 A theoretical travel time chart. This chart is calculated for a surface source and the JB P wave velocity model. Major body phases are labeled.

During the inverse calculation a major portion of computer time is devoted to the generation of the L matrix which contains the path lengths of all passing rays in each block. In such a calculation, the intersection points of each ray with block interfaces are located first, based on the assumption that a ray stays on the vertical plane containing the source and the receiver. Consequently, ray path length, travel time and distance are accurately calculated.

When tracing many seismic rays in a one-dimensional (laterally homogeneous) earth model, the reference ray technique such as that by Comer [1984] may be adopted. We constructed a reference ray table using the fact that all seismic stations are generally located at the surface of the earth. From a surface source, a series of rays in a given one-dimensional velocity structure can be found of source-receiver distances started from zero and incremented by a small $\delta\Delta$. Each row of our reference ray table contains parameters for one ray. The first column contains the ray parameters, and the rest of the columns contain the depths of all rays at each distance, which is also incremented by $\delta\Delta$. In using this reference ray table, we first locate the column which has a distance nearest to the given source-receiver distance, and then search through the column to obtain the ray with a depth nearest to the given focal depth. A very close approximation of the given ray is thus yielded, represented by the ray parameter p of the row. If a better approximation is desired, one can either trace further from the approximated ray or make a finer reference ray table.

1.4 Data Reduction

Data sets for ray theory tomographic inverse, such as the commonly used ISC data, are usually very large. As one example, Figure 1.2 displays all ISC travel time picks in the year 1982, with total of 480,507 picks. The ISC (International Seismological Centre) routinely processes and catalogs worldwide earthquakes that are also monitored by more than two dozen regional scientific agencies, such as JMA (Japan Meteorological Agency). The ISC data contains epicentral estimates and arrival times of various phases (most are body waves) at over 3,000 stations. It is undoubtedly the single largest seismological data set currently available. Of course, there is noise existed in the ISC data, although there has not been any quantitative estimate about it (A very recent estimate by Gudmundsson *et al.* [1989] of the random noise level in the teleseismic ISC P wave data is about 1/3).

The key issue to using the ISC data is to properly assess the signal to noise ratio in the data, hence to extract the reliable information. We like to determine whether secondary phases, such as the PP waves, can provide clues to the velocity structure of the mantle. Our emphases in data reduction are on estimations of noise level and resolution power. We will take the data set of ISC PP waves as an example to demonstrate the data reduction. The statistical properties (mean and standard deviation) at each stage of the reduction are presented in Table 1.1. In the next section the data reduction steps are described in detail.

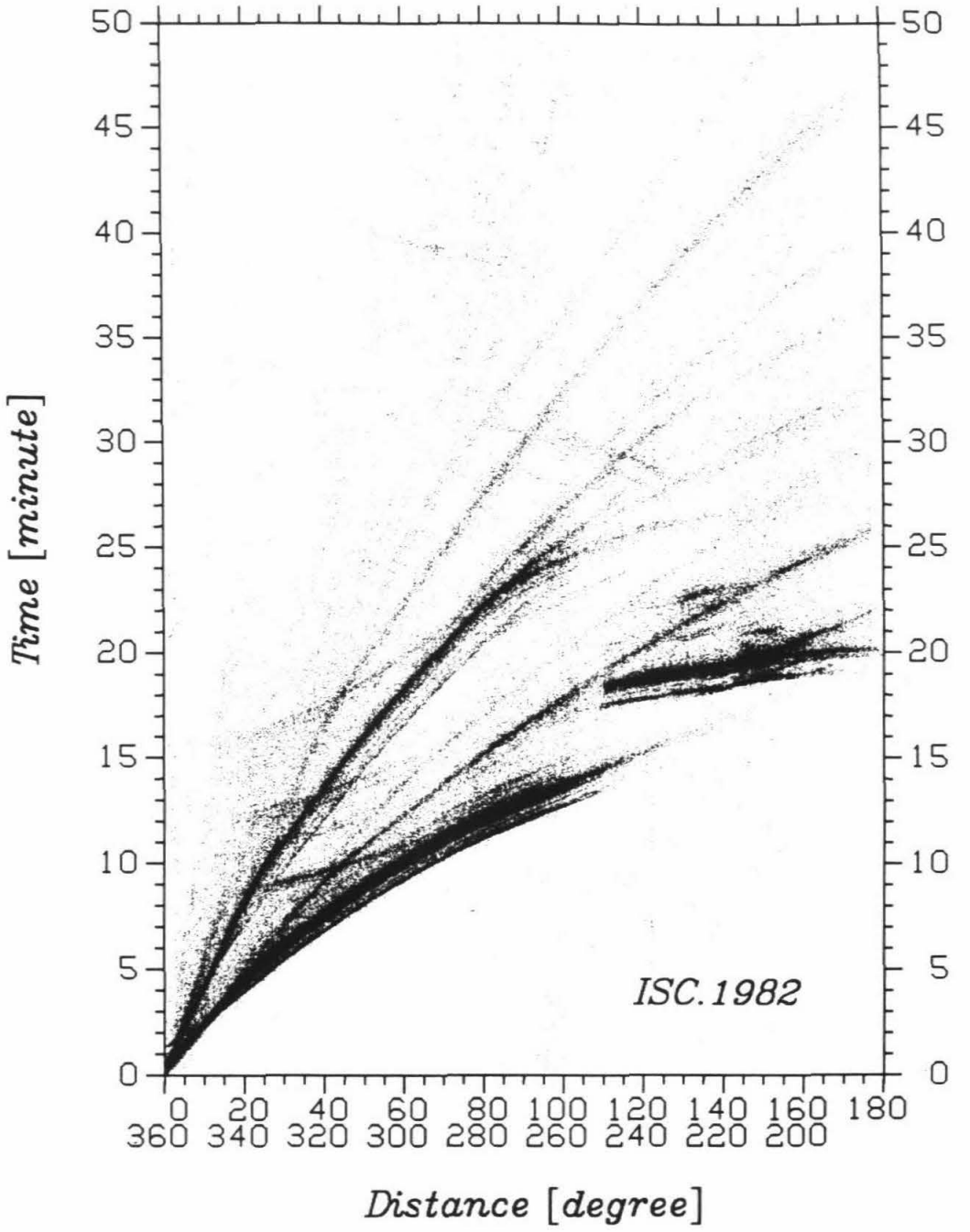

Figure 1.2 ISC travel time chart of 1982. See Figure 1.1 to identify major body phases. Notice the effect of different focal depths, i.e., the widening of a single phase such as P, S and PkP waves.

Table 1.1 Correction statistics of ISC PP-wave data.

corrections	event	pick	mean [sec]	s.d. [sec]
original ISC PP wave data	15550	101817	-0.7126	6.377
$62^\circ < \Delta < 142^\circ$, $\|dt\| < 16$ sec & np>50	8322	69886	-0.3835	5.666
earth ellipticity	8322	69886	-0.3267	5.623
bounce point elevations & $\|dt\| < 12$ sec	8136	66241	-0.0680	4.736
grouping and sorting ev. ($2.5^\circ \times 2.5^\circ \times 50$ km), st. ($1.25^\circ \times 1.25^\circ$)	1631	35020	-0.2227	4.420
5 source-receiver static & $\|dt\| < 10$ sec	1613	33744	-0.0002	3.546
6 bounce point statics	1613	33744	-0.0127	3.231
1 more source-receiver statics & $\|dt\| < 10$ sec	1613	33741	-0.0118	3.226

1.4.1 Data selection

The size of the data set prevents us from making a direct check on every individual pick. However, some types of erratic picks can be removed systematically. For instance, we may choose a particular distance range to avoid triplications or possible contamination from other phases. A check on a travel time chart, such as that in Figure 1.1, is often helpful. As shown in Figure 1.3, the PP wave picks are selected within a window which ranges from 62° to 142° in distance and 16 sec from the theoretical times. The near distance boundary is set to avoid ambiguities of triplications that are caused by major discontinuities in the mantle, such as the cluster of picks around 40° distance. The far boundary is established to eliminate contaminations by PKS waves. This distance restriction results in a maximum bottoming depth around 2,000 km.

The boundaries for residual times are used to window out some obvious picking errors. A very large residual travel time is very likely to be erratic (mispicking phases, wrong tic-marks, wrong source association, *etc.*). As shown in Table 1.1, during the data correction stage the residual boundaries are gradually reduced from ±16 sec to ±10 sec. If a ray travels 1000 km through a 10% velocity anomaly in a medium with a 10 km/sec background velocity, the residual travel time is about 10 sec. This case is assumed to be the one with the maximum residual that could be caused by mantle heterogeneities, including cool slabs, continental roots, and hot plumes. On the other hand, the initial residual boundary is larger than 10 sec in order to take account of the correctable systematic trends in the raw data.

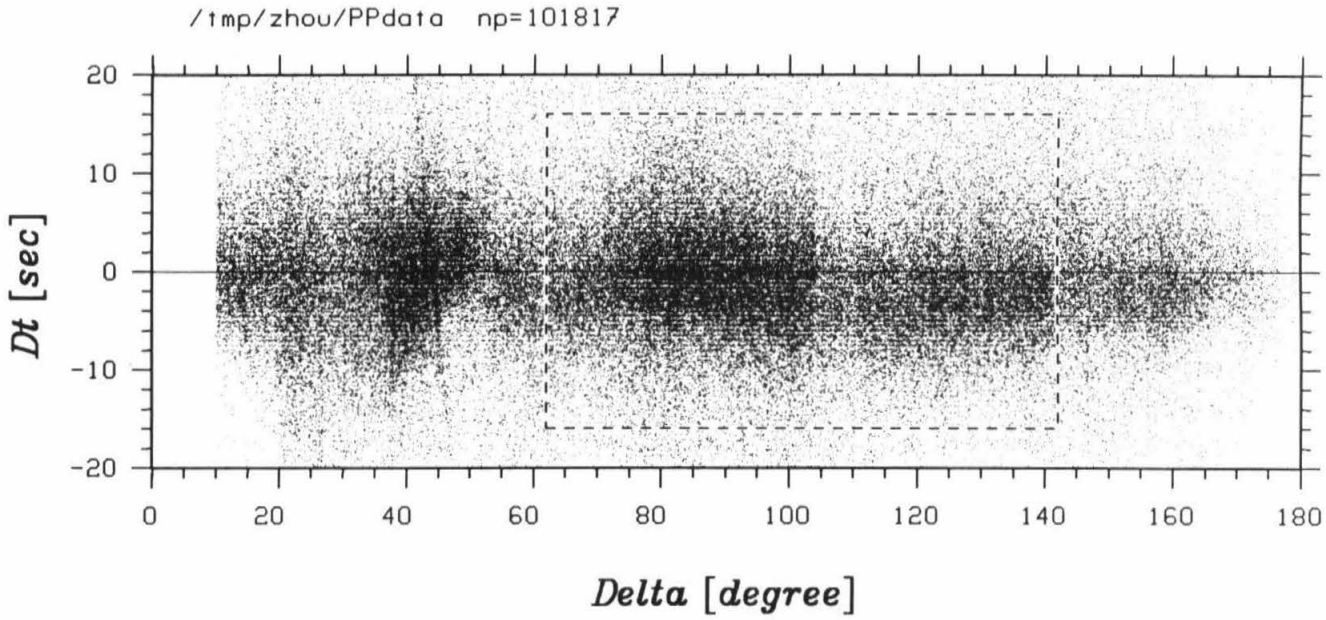

Figure 1.3 PP residual distribution over distance. The selected part of the PP waves fills in the dashed box of $62^\circ < \Delta < 142^\circ$ and $|dt| < 16$ sec. The triplication due to the 650 km discontinuity is shown as the cluster of arrivals around 40°. Arrivals to the right of the dashed box may contain some PKS waves (see Figure 1.2).

Finally, a lower bound for the quality of the event, in terms of source location and receiver density, is needed. It is commonly a choice between the minimum magnitude of events or the minimum total number of picks for each event. Small magnitude earthquakes or poorly picked ones tend to have more severe errors in source location and origin times. They are also more likely to contain wrong residual travel times. We have found that the total number of picks is a more reliable criterion than the magnitude. A large number of picks usually implies not only a relatively high magnitude, but also a good coverage of receivers. Total number of picks, therefore, has more direct influence on the quality of the residuals. For PP waves, every event used has more than 50 picks. Nearly 70,000 picks remain after the above selections.

1.4.2 Standard corrections and statics interpretation of PP waves

Any correction to the data has to be absolutely necessary because we would like to keep the modification of the data to a minimum. Most corrections are designed to treat a particular problem and therefore are not standard. For instance, in Chapter 3 we will make corrections for velocity variations outside the modeled region since most picks used in those cases are teleseismic and the distribution of ray paths is extremely uneven. A source relocation correction will also be discussed then. Furthermore, a correction for the elevation of the bounce points of secondary phases, such as PP waves, will be covered in the next section.

One of the few standard corrections is for the earth's ellipticity. Although the ellipticity term is small, usually less than 0.5 sec in travel time,

it is systematic and hence can be mapped into the solutions. In this thesis, an Earth ellipticity correction term obtained from an approximation method due to Dziewonski and Gilbert [1976] is removed from the data.

A data set for a tomographic inversion is almost always very biased in ray coverage. A summary ray technique which combines rays of the same source and receiver areas will improve the bias to some extent, hence is mentioned here as one of the standard corrections. We usually use a summary block which is of smaller size than the inversion block. Rays possessing the same source and receiver summary blocks belong to the same summary ray bundle. A median, rather than an average, of residual travel times of each bundle of rays is taken as the residual, since a median is less effected by error residuals that are sparse but of large amplitudes. In addition, we sometimes take smaller receiver summary blocks than source summary blocks because the receivers are more accurately located. The shortcomings of the summary ray technique include its subjectivity in the size of the summary block and in the assignment of the new source and receiver locations. When the block size is large, the source and receiver locations of summary ray get quite arbitrary.

Recently, Gudmundsson *et al.* [1989] proposed that by binning rays into groups of same source and station blocks, the average variance of ray groups at the smallest bin block size represents the variance of random noise, while the average variance at the largest bin block size approximates total data variance. This brings us to two interesting and important extensions of the summary ray technique for evaluating the noise level and improving data quality without using summary rays. The method of noise evaluation will be

discussed in Section 1.6. The method of quality improvement is carried out by eliminating residuals that deviate much from the medium of residuals of the same source and station areas. This "grouping and sorting" process is usually quite efficient. Of course, the size of the source and station areas and the threshold of deviation depend on the data and can be decided through experiments. Smaller area size and narrow deviation threshold result in better data quality, but poorer ray coverage, a typical trade-off between error and resolution. The size is usually a fraction of the inverse block size. The grouping and sorting process greatly reduces the high-frequency noise (see Figure 1.11), although it also cuts off a considerable portion of the data. The process reduces the number of PP wave picks by a half (Table 1.1), and the ray coverage by about 20%.

Another standard correction is for heterogeneities near source and stations, namely, statics. A statics term represents the average residual travel time at a joint point of seismic rays, thus containing the variations of lateral slowness in the shallow regions. The statics need to be removed from the data, especially for lower mantle inversions. The major reason for the removal is that most teleseismic rays have small take-off angles (see Figure 1.7). This tends to spread the upper mantle anomalies down in depth. Because the source and station statics are related by the seismic rays, our source-receiver statics calculation is done iteratively, i.e., a removal of average residuals for all sources, followed by a removal of average residuals for all stations, and then another cycle of removals for sources and stations, *etc.* The bounce point statics for PP waves in this study are averaged over a small area, as discussed

in the next subsection. Some useful tectonic information can be drawn from the statics components, especially that of stations, which have accurate locations. Statics maps of events or bounce points, on the other hand, are less reliable due to uncertainty of their locations.

The statics maps of stations, events and bounce points for PP waves are shown in Figure 1.4. The slow and fast regions on these maps are usually distinct, showing the effect of different tectonic provinces. The highly covered regions in these maps show similar patterns. There are also differences. For instance, patterns around China and Hawaii are different in the statics maps of stations (Figure 1.4a) and of events (Figure 1.4b). The stations, all on the surface, are of known locations; hence, the station statics are of less noise. On the other hand, the events bear more noise due to mislocation. Therefore, the differences in the statics are probably due to patterns at different depths and noise, which includes source mislocations. We attempt to interpret features in these maps in comparison and contrast with results from some of the earlier studies. The P wave station statics map by Hager and Clayton [1989] is produced by the same method as the one used here. The composite residual travel time maps by Dziewonski [1984], and the anomalous regions from Tanimoto and Anderson [1985] from surface wave data are compared as different types of studies. The maps of PP statics are generally consistent with the earlier studies in most of the regions that have been mentioned by these earlier workers. In particular, the maps correlate well with the station statics of P waves in the slow and fast regions, except that the magnitude of PP statics are larger than those of P result in many parts of the world. The

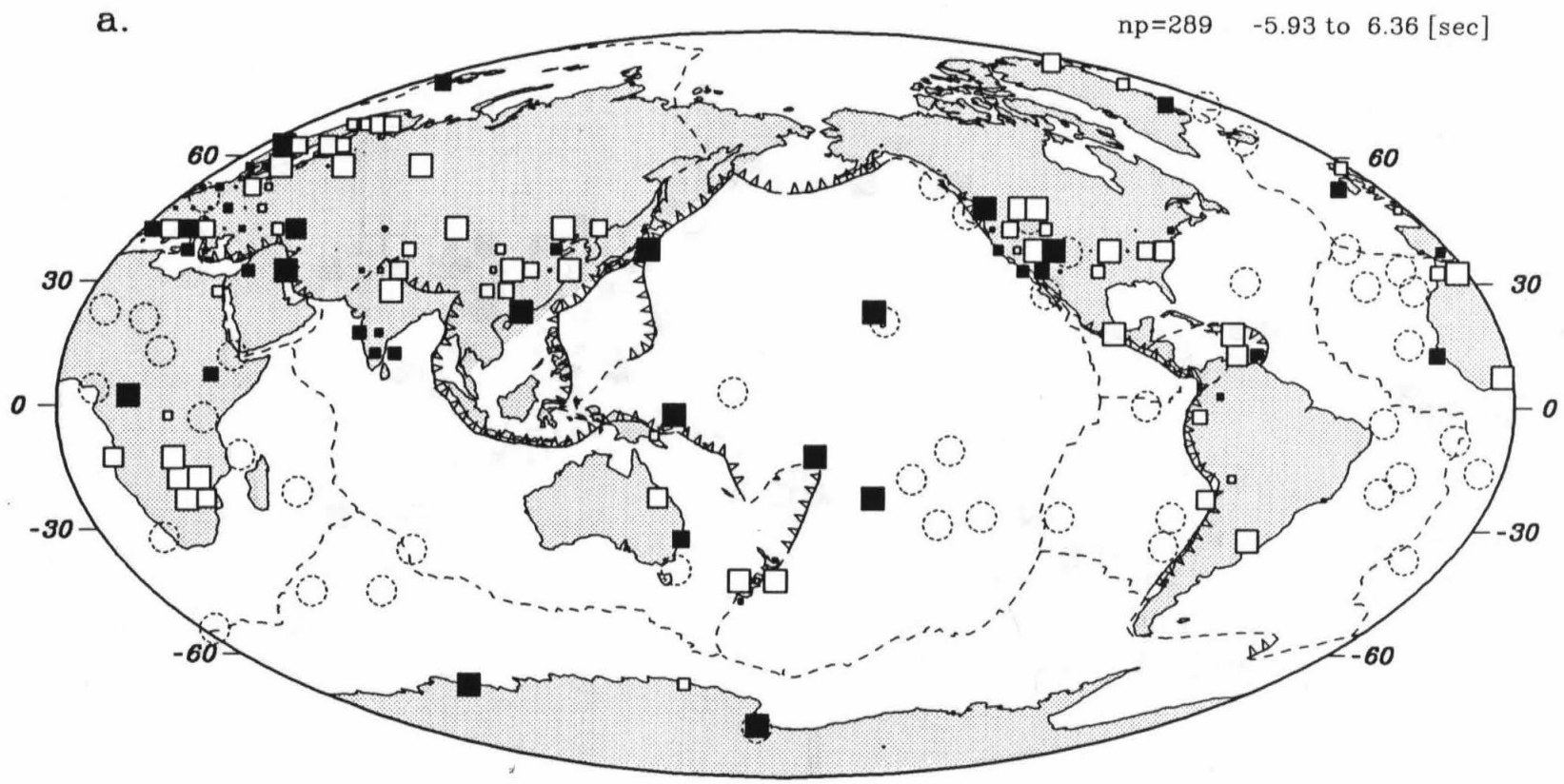

Figure 1.4 Statics maps. a. PP wave station statics; b. PP wave source statics; and c. PP wave bounce point statics. Plotting conventions are identical to Figure 0.2. White and black boxes are fast (negative) and slow (positive) statics, respectively. The size of the boxes is proportional to the magnitude of the statics term, and reaches to the maximum when the absolute value of a statics residual is greater than 2.0 sec.

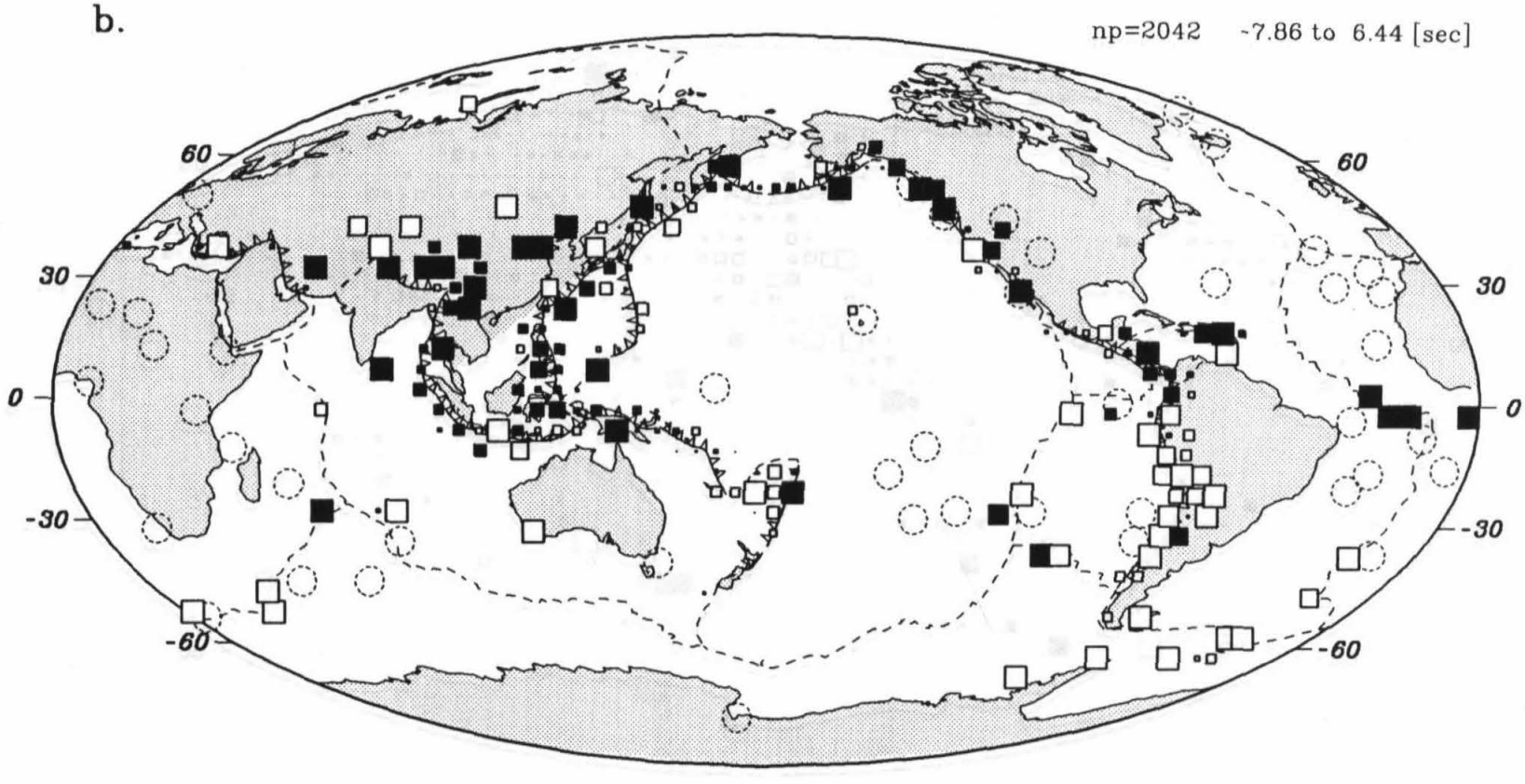

Figure 1.4 (continued)

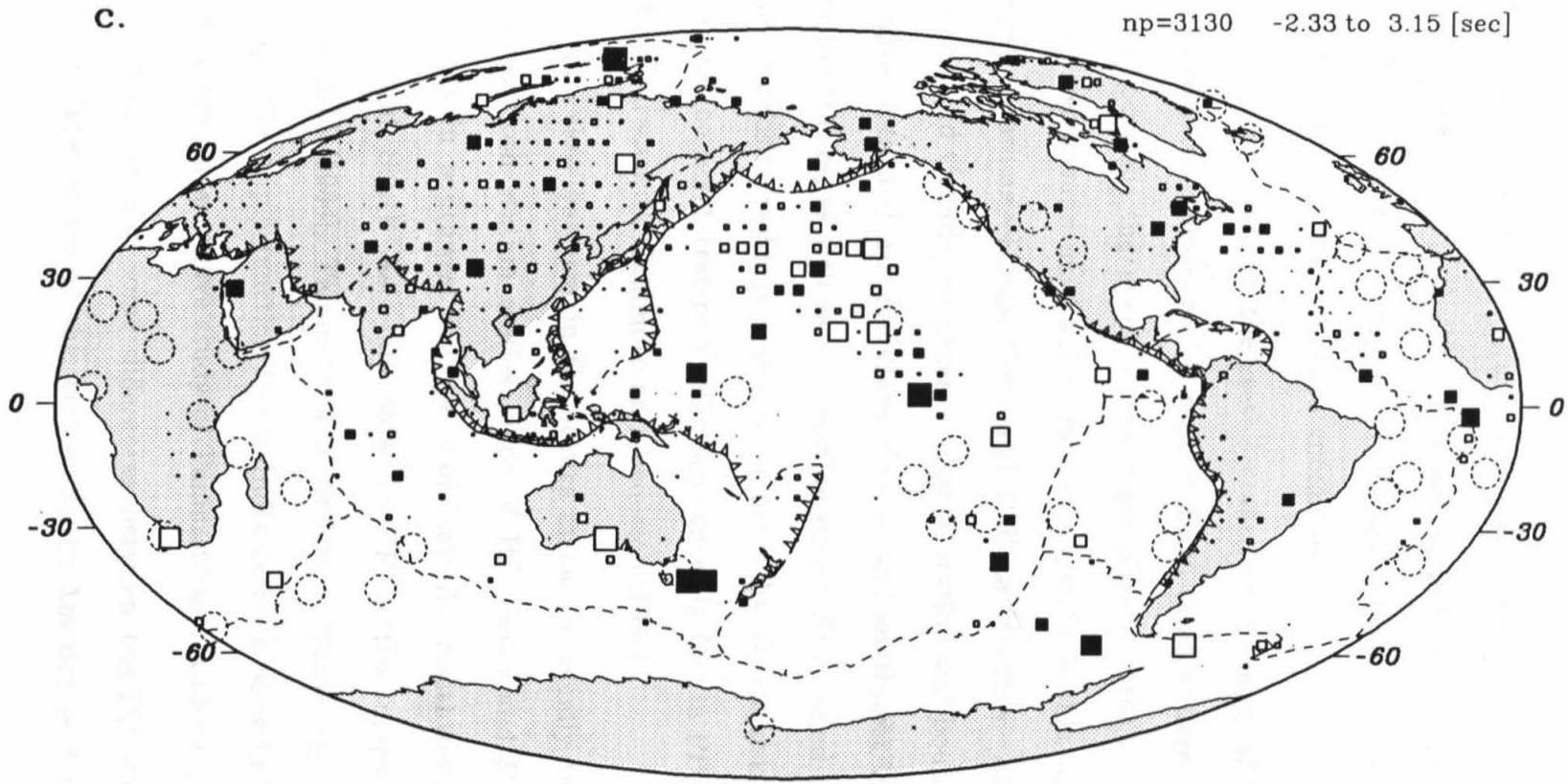

Figure 1.4 (continued)

large amplitude of PP wave results is probably due to the fact that PP waves are exposed to more shallow structures than P waves are. Finally, the shallow mantle is more heterogeneous [Gudmundsson *et al.*, 1989], with short wavelength but high amplitude anomalies.

The fast areas in the statics maps include most of the subduction zones and many tectonically stable regions. Even though there are probably errors in event location, the event statics map (Figure 1.4b) displays prominent fast signatures around most subduction zones, such as that underneath the Kurile, Japan, Mariana, Tonga, Peru and Chilean trenches. Shield regions such as Siberia and Canada are generally fast in station and bounce point statics maps (Figure 1.4a and c). Northern Europe and southwest Africa are fast in PP station statics, as well as in P station statics [Hager and Clayton, 1989] and in the composite residual travel time maps by Dziewonski [1984]. Old oceans such as the northwestern Pacific are generally fast in PP bounce point statics, which agrees with Tanimoto and Anderson [1985].

The slow patterns in the statics maps are usually the tectonically active regions. Both station statics maps of PP waves and P waves display slow residuals in southwest Europe and Hawaii. Southwestern North America, Tibet and South Asia are slow in PP statics maps and in studies by Dziewonski [1984], Tanimoto and Anderson [1985], and Hager and Clayton [1989]. The triple junction in the India ocean is slow in the PP event statics and by the surface wave study of Tanimoto and Anderson [1985].

There are also some differences between the PP statics and the earlier studies. The Andes on the west of South America is dominantly fast by PP

event statics, but it is not as fast in P station statics, although the same region is generally fast in the residual maps by Dziewonski [1984]. East Asia is mostly slow in P station statics map while it is mixed with fast and slow in the PP statics results.

The patterns along the mid-ocean ridge (MOR) are mixed in the PP event statics map. Many of the variations are perhaps due to noise. However, velocity perturbations underneath MOR could vary a lot from region to region. The upwellings beneath the MOR are hot and therefore may be of slow velocity. The slow MOR of the Atlantic ocean and fast MOR of the India ocean perhaps suggest that the former is younger and more active than the latter.

1.4.3 Bounce point corrections

One distinguishing feature of secondary phases, such as the PP waves, is the $\pi/2$ phase shift associated with each bounce. The bounce points benefit, by extending the coverage over the upper mantle, but they require an extra correction. The residual travel times of PP waves and other secondary phases that were reported by ISC have not been corrected for the effects of elevation and the velocity structures surrounding the bounce points. In this study of PP waves, a linear regression correction for the elevation effect of bounce points is applied. This correction and the bounce point statics calculation largely remove the influence of the local shallow velocity structure. The elevations of bounce points are based on a world bathymetric and elevation data ($1^\circ \times 1^\circ$ sample size) from the National Geophysical Data Center of NOAA.

The elevation of a PP wave bounce point can affect the travel time by as much as several seconds. In order to examine this effect, the residual travel times are plotted against elevations of bounce points for the PP wave data in Figure 1.5. There is a clear correlation between the residuals and the elevations. This correlation is also an evidence that the PP wave data is not totally noise, implying that there is systematic information which is worthwhile to be explored.

Due to the differences between the crustal velocity structure of deep ocean, shallow sea, planes and mountainous regions, and referring to the variation of mean residuals relative to the elevation of the bounce points as shown in the lower half of the figure, the data was divided into six portions according to the elevations of the bounce points. Their depth ranges are as follows: (1) deep ocean, elevation below -3.2 km; (2) mid-ocean and continental slope, -3.2 to -1.2 km; (3) shallow sea, -1.2 km to sea level; (4) flat land areas, sea level to 1.5 km; (5) mountains, 1.5 to 3.2 km; and (6) high mountainous regions, above 3.2 km. A linear regression equation is then derived from the data corresponding to each depth range. The slope of each regression line and average of residuals within each range decrease monotonically from deep ocean to high mountains, reflecting the thickening of the crust across this elevation spectrum.

Notice that in the first range of bounce point elevation in Figure 1.5, the distribution center of the data points deviates more from the zero residual line than the linear regression line does. This is because we originally placed equal residual bounds on both positive and negative sides in selecting data.

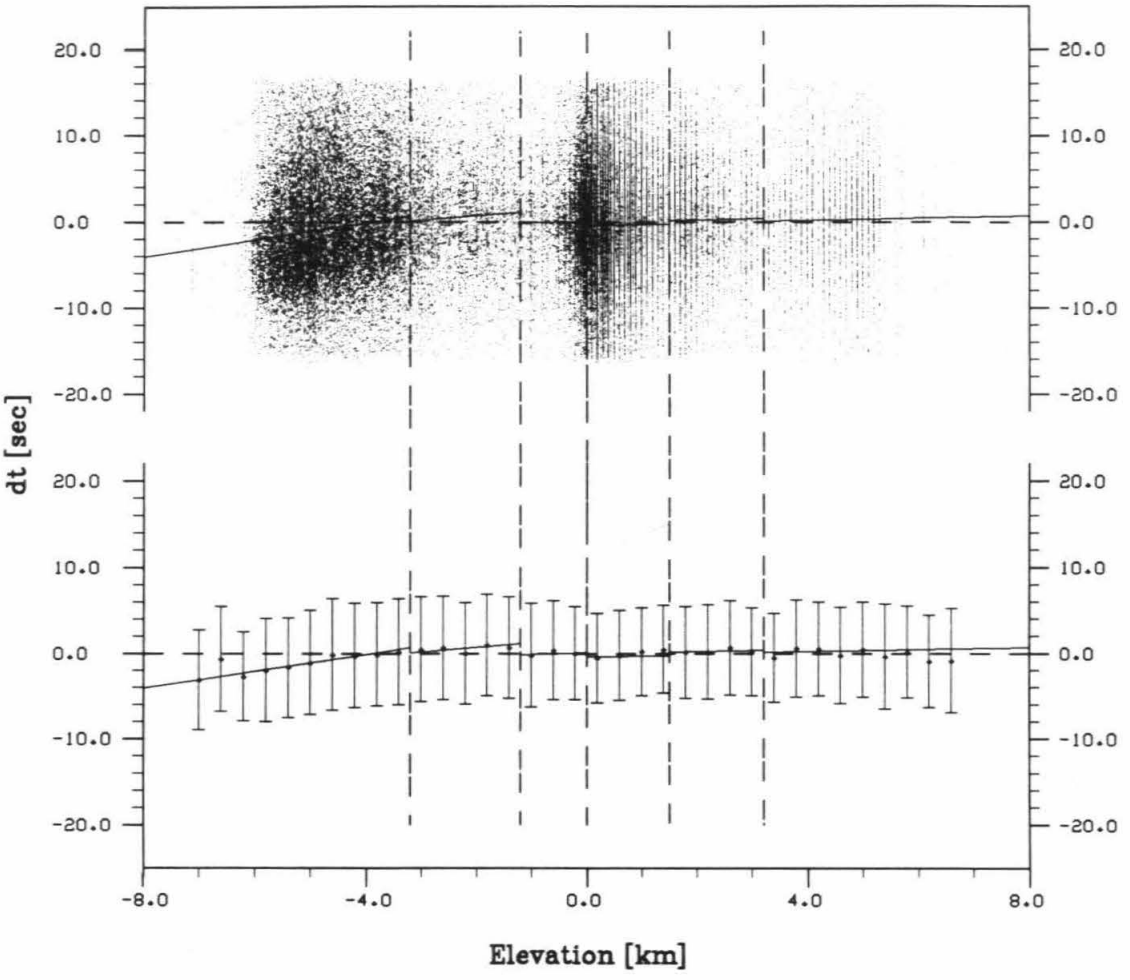

Figure 1.5 PP wave residual times vs. bounce point elevations. Each point in the top plot is an ISC PP wave pick. The bottom plot indicates the mean and standard deviations of residuals in each elevation interval of 400 m. The vertical dashed lines divide data into six elevation ranges. The straight line across each range is a linear regression of the data, indicating the effect of bounce point elevations which is used to correct.

Therefore, all corrections should be applied gradually (a little at a time) to the data to minimize this initial bias. For example, the correction for effect of the bounce point elevation is done iteratively with regard to the regression line within each range. The upper and lower bounds on the residuals are reduced gradually from ± 16 sec to ± 12 sec during the iterations.

The existence of bounce points also affect the statics calculation. We have to consider these effects because the statics are the variation of slowness in the shallow region of the earth and the rays near the bounce points traverse through the shallow structure. Since the locations of most of the bounce points are spatially scattered, it is not feasible to apply the conventional statics calculation by averaging rays at a common location. We have to average the statics over each $1^\circ \times 1^\circ$ area when there are more than 5 bounce points within it; this is called bounce point statics calculation. Because this calculation also affects the residuals of the sources and receivers, we also take source and receiver points as bounce points in the calculation.

The iterations of statics calculations are terminated when the statics contribution from each iteration is about the same level as that of the previous one. After a few trial-and-error experiments, we decided to run three iterations of regular source and receiver statics calculation, then three iterations of the bounce point statics, followed by two more source and receiver statics calculations.

1.5 Resolution Estimation

The resolution of the inversion depends on the coverage of the data rays, i.e., the number of passing rays and the distribution of their directions in each block. Most tomographic inverse problems are "mixed-determined" [Menke, 1984]. The number of independent parameters, or "over-determined" blocks, is fixed once the ray geometry is given. Hence, the size of inversion block is an important consideration. We usually choose the block size by inspecting the residual variance over a range of block sizes (e.g., Figure 1.11). Of course, the block size has to be much larger than the wavelength of the data waves, to allow the use of ray theory. In addition, we keep the block size large enough so that most of the rays will pass through less than three to four dozen blocks, to reduce the error in ray path computation. In the inversion we discard blocks of less than certain number of passing rays, because those blocks are more likely to be "under-determined."

The inversion of PP wave data was done on a grid (Figure 1.6) which is identical to that used previously in a P wave study [Clayton and Comer, 1983; Hager and Clayton 1989]. The blocks are of almost equal volume, with each block about $5^\circ \times 5^\circ$ horizontally on the earth's surface and 100 km in thickness. The azimuthal and vertical distributions of PP wave rays are shown in Figures 1.6 and 1.7. The coverage is quite good in most parts of the northern hemisphere and along most subduction zones. Some oceanic regions, such as the Atlantic ocean, seas around South Asia and a north-trending zone in the middle of Pacific ocean, are well covered. Along the vertical direction,

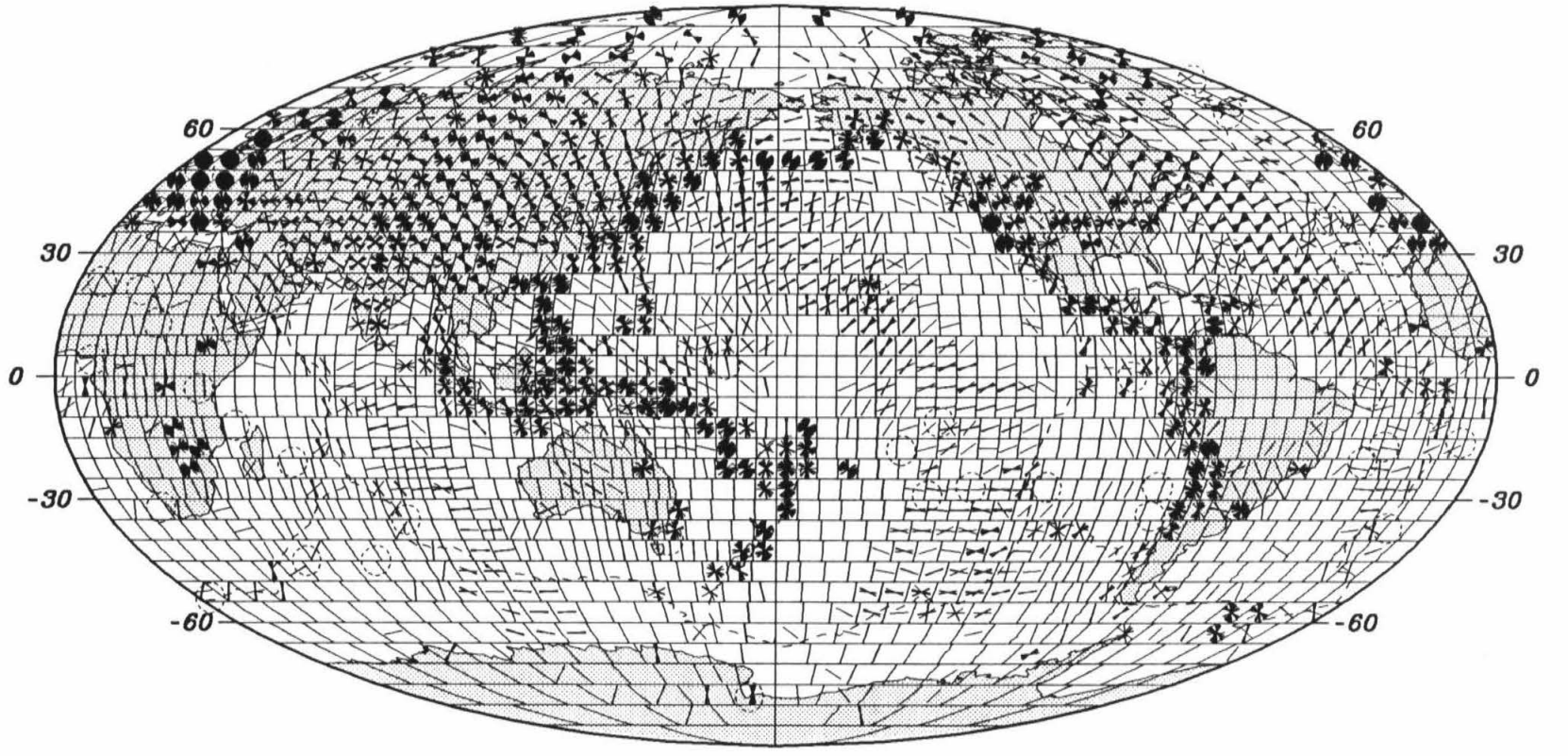

Figure 1.6 Azimuthal distribution of PP rays on the surface. This panel shows a map view of the framework of blocks used in this study. Each block has a dimension of approximately $5^\circ \times 5^\circ$ laterally near the equator and 100 km over depth. The bounce points of each PP ray used in the inversion are drawn across the block centers in the direction of the ray azimuth.

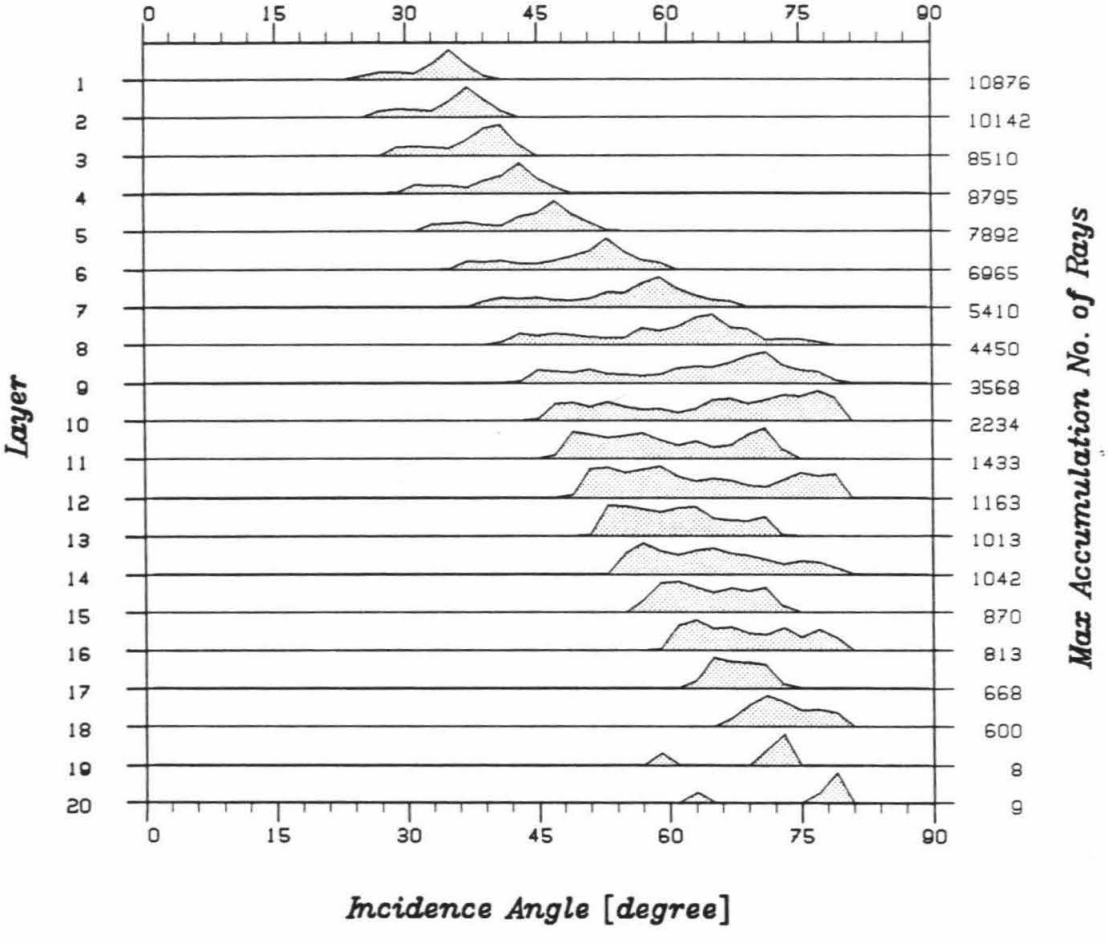

Figure 1.7 Distribution of ray incidence angles at each depth layer. The distribution curve at each layer is normalized by the layer's maximum, indicated on the right. The incidence angle varies most widely from layers 8 to 12, at depths from 700 to 1200 km.

the coverage within each layer is over 65% from surface down to 1300 km, and decreases to below 50% at 1700 km and to null near 2000 km.

From equation (1.4), the conventional resolution matrix at the n-th iteration is

$$\mathbf{R}^{(n)} = \mathbf{I} - (\mathbf{I} - \mathbf{L}^{B}\mathbf{L})^{n}, \tag{1.10a}$$

or

$$\mathbf{I} - \mathbf{R}^{(n)} = (\mathbf{I} - \mathbf{L}^{B}\mathbf{L})^{n}. \tag{1.10b}$$

This estimate for the resolution is for the linear system only, and ignores the non-linear (ray path perturbation) part of the problem. Tests by Christof Stork (1988) have shown that the linear resolution is reasonable for velocity variation under 10%.

The iterative nature of the method prevents a direct calculation of the resolution matrix. Evaluation of the resolution matrix for the entire parameter space by equation (1.10) is also impractical because of its size. Another approach is to compute, based on a given synthetic model of slowness field, the residual travel times for all data ray paths. These residuals are subsequently inverted to give a new slowness field. The comparison between the given and the inverted slowness fields provides a direct check on the resolution.

In practice, the resolution of the inversion has two aspects. The first is how well can the inversion recover the true amplitude of the anomaly for each block. The second is how much each block is coupled with its neighbors, that is, to what extent are the anomalies spread over adjacent blocks. The coupling

aspect, which has often not received much attention, is generally more critical than the first aspect because it could causes artifacts. The only practical way to estimate the resolution for the tomographic system is the "impulse" test, which will be addressed in detail in Section 2.3.

Since the intent of this chapter is to take a very crude reconnaissance survey over major subduction zones in the world with ISC PP wave data, we have only tried a few simple tests to gain an understanding of the resolution. In each test, residual travel times for data rays are calculated based on a synthetic slowness model. The result of the subsequent inversion is compared with the given model. More extensive resolution and noise analysis for the inverted results are given in Chapter 2 and Chapter 3 where detailed seismic structures of subduction zones are studied.

The synthetic model of the first resolution test has a slowness perturbation of 1.0 for all small boxes in the slices of Figure 1.8, and zero elsewhere. This test is actually based on the idea of "impulse tests," although it is not performed on each individual block. As displayed in the figure, the results after 30 iterations indicate that the model slowness field is imaged quite well, both in terms of locations and magnitudes when there is sufficient ray coverage. When the locations of the test zones are changed, the results are similar to the example given here.

The model for the second resolution test is an homogeneous slowness field. As shown in Figure 1.9, most blocks result in slowness values very close to the given one, after ten iterations. It turns out that as long as the model value is nonzero, the convergence of the inversion is not sensitive to the magnitude of

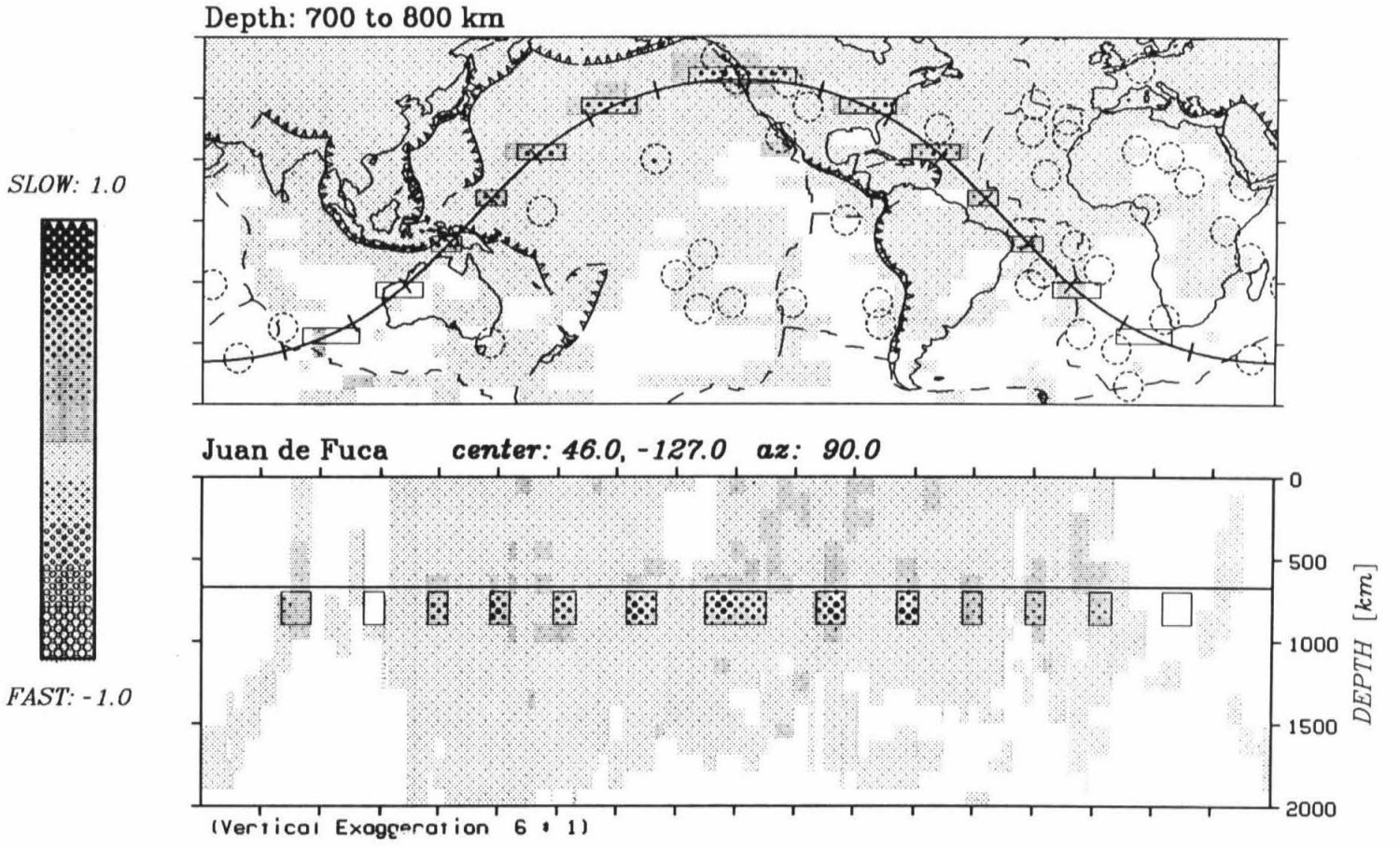

Figure 1.8 A resolution test. The top is a horizontal slice at depth 700-800 km, and the bottom is a vertical slice across the Juan de Fuca subduction zone. The heavy curve in the top panel is the trace of the vertical slice. Travel time residual for each PP ray is generated on a synthetic model with slowness perturbations in the small boxes. As shown, the subsequent inversion recovers the synthetic model well.

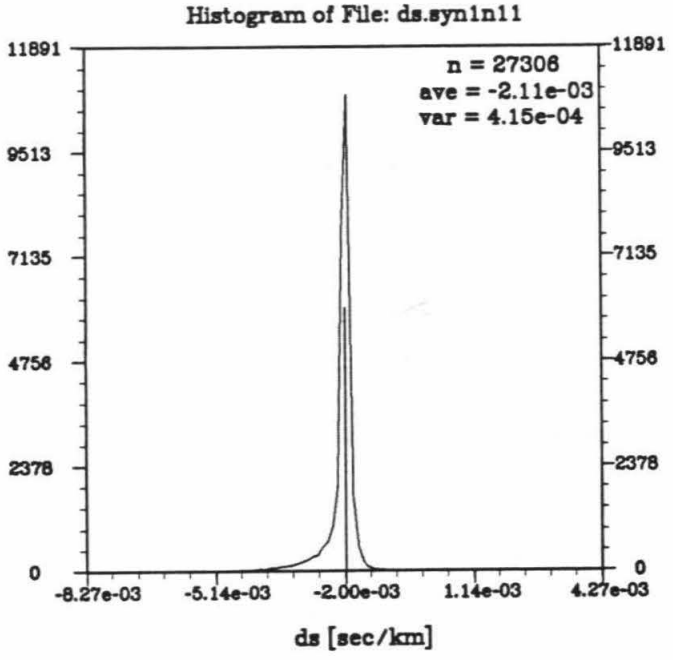

Figure 1.9 Histogram of the second resolution test. This plot is for a synthetic resolution test similar to that shown in Figure 1.8, except that the slowness model is homogeneous with a value of -2.0×10^{-3} sec/km for all blocks. This histogram displays the cumulative number of blocks over the resulting slowness value after 11 iterations. Notice that the block number is sharply peaked at the given homogeneous slowness value, as indicated by the vertical bar. Those blocks that have values far from the given are poorly- or unresolved blocks, usually located near the edge of the covered region.

the given model. Moreover, the poorly resolved blocks are usually located near the edges of the covered regions. Compared with the interior blocks, the edge blocks are poorer in azimuthal ray coverage and the inverse iterations are much less effective on them.

1.6 Error Estimation

The first question in addressing the error is whether the PP data is really informative. We think the answer is positive. The best proof of this is perhaps the correlation between the residual times and the elevation of the bounce points (Figure 1.5). Since the locations and elevations of bounce points are random, there would not be such a clear correlation if the data were just random. We have tried to reduce noise in the residuals by means of sortings, elevation corrections and statics removals. The data reduction procedures and the nature of SIRT inversion in terms of averaging cross-rays generally help to extract the systematic information from the data.

The error of the inversion depends on both the noise level in the raw data and the propagation of noise through the inversion. The noise includes errors in residual travel times and in the set-up of the inversion (such as error in assuming that the ray paths are fixed through the iterations). The propagation of noise is related to the ray distribution. In this section we examine the effect of the inversion process on the noise level.

The arrival times for each phase are dependent on the waveform. A survey over hundreds of randomly selected waveform records, in comparison with the ISC readings, suggests that the pickings for phases such as P, S and PP are reasonable in most cases. The $\pi/2$ phase shift of a PP wave relative to a P wave apparently does not effect the PP picks in a systematic manner. To pursue this further, we have compared the observation with synthetically generated waveforms from the onset time to several minutes after the PP wave train. An example of this comparison is shown in Figure 1.10, where waveforms from some shallow events which were studied by Nakanishi and Kanamori [1984] are examined. The focal mechanisms and other source parameters used are those given by Nakanishi and Kanamori. Notice that shallow events are the most difficult ones for picking the correct PP arrival times; hence, the estimate in this case represents a conservative one. The differential times between each pair of synthetic and ISC reported PP arrivals are listed in Table 1.2. This type of check suggests that ISC data set has generally picked the corrected "wiggles" of PP waves. However, it is apparently very difficult to assign the PP wave arrival time to the precision of a fraction of a second from these long-period body wave records. The error in PP wave pickings could be as high as several seconds; this will place serious restrictions on the attempted inversion.

Our next attempt is to detect any bias in the ISC PP wave arrivals. The distribution of the ISC PP wave residuals is between normal and double-exponential, although the kurtosis value obtained indicates the data is more normal-distribution-like. The picking error for PP arrival time is expected to

Figure 1.10 A comparison of observed and synthetic PP waveforms. The focal mechanisms on the left are taken from Nakanishi and Kanamori [1984]. The observed waveforms cover from onset P arrivals to after PP arrivals, while the synthetics below are for PP arrivals only, except the third trace for the Kurile event. Solid vertical bars indicate the synthetic PP arrival times, and the dashed bars indicate the PP arrival times picked by ISC.

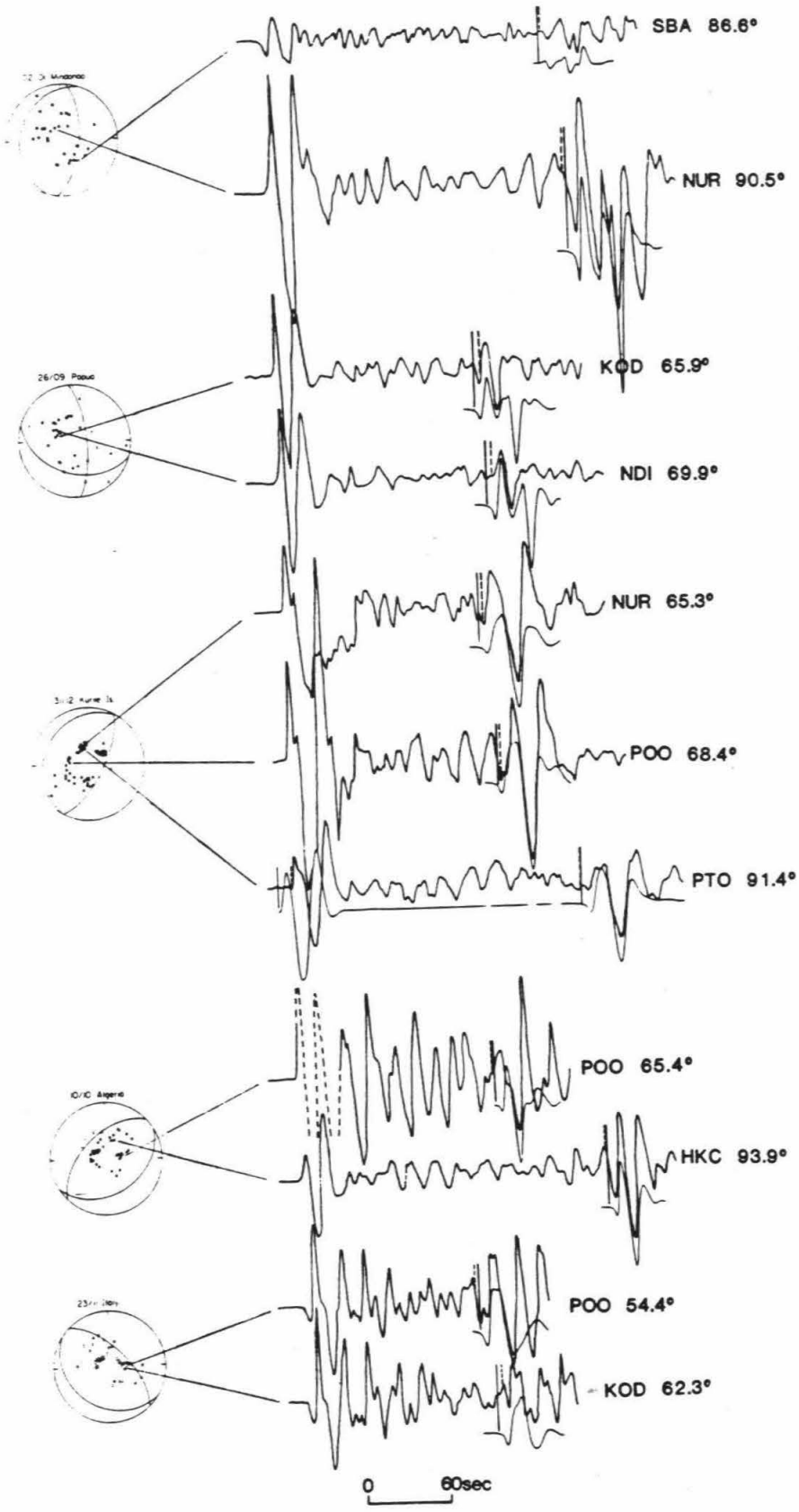
SBA 86.6°
NUR 90.5°
KOD 65.9°
NDI 69.9°
NUR 65.3°
POO 68.4°
PTO 91.4°
POO 65.4°
HKC 93.9°
POO 54.4°
KOD 62.3°
0
60sec

Table 1.2 Comparison of observed and synthetic PP arrivals of five shallow events in 1980.

Date	Region	Depth km	M_b	Faulting	Station	Distance degree	dt_{PP}† sec
Jan. 2	Mindanao	63	6.0	Reverse	SBA	86.6	-1.6
					NUR	90.5	2.3
Sep. 26	Papua	33	5.9	Strike-slip	KOD	65.9	-4.7
					NDI	69.9	-4.0
Dec. 31	Kurile Is.	33	6.1	Reverse	NUR	65.3	-3.0
					POO	68.4	-2.3
					PTO	91.4	0.4
Oct. 10	Algeria	10	6.5	Reverse	POO	65.4	1.3
					HKC	93.9	1.2
Nov. 23	Italy	10	6.0	Normal	POO	54.4	2.7
					KOD	62.3	-3.7

†: This is the differential time of the synthetic minus the observed PP arrivals.

be larger than that of P waves due to interference from coda of early arrivals before PP waves. We have conducted a noise level study on 19,023 pairs of P and PP arrival times. For these samples the standard deviation, which is caused by both the noise and the slowness heterogeneities, is 2.84 sec for P waves and 4.25 sec for PP waves. The higher deviation of PP waves may be caused by a higher noise level of PP waves as well as the fact that PP waves experience more shallow heterogeneities than the corresponding P waves. It is found that there is no difference between the observed average of time delays from P to PP waves and the theoretical average of delays, thus indicating an unbiased body of PP wave samples.

The above studies did not detect systematic error in the PP wave pickings, such as the suggested mispickings that could be caused by precursors and phase shift. However, many of the errors in waveform picking and data editing are larger than 10 seconds and hence will be windowed out during the data corrections. In particular, the summary ray sorting functions as a double check on each ray used, and thus significantly improves the data quality.

In Section 1.4.2 we mentioned when binning rays into groups of same source and station blocks, the average group variance for a very small bin block size approximates the variance of the random noise, while the average variance at the largest bin block size represents the total data variance [Gudmundsson *et al.*, 1989]. The relationships of average group variances and bin block sizes of PP data at different processing stages are displayed in Figure 1.11. The efficiency of each correction is judged by its reduction of the average variances at small block sizes. For instance, the grouping and sorting

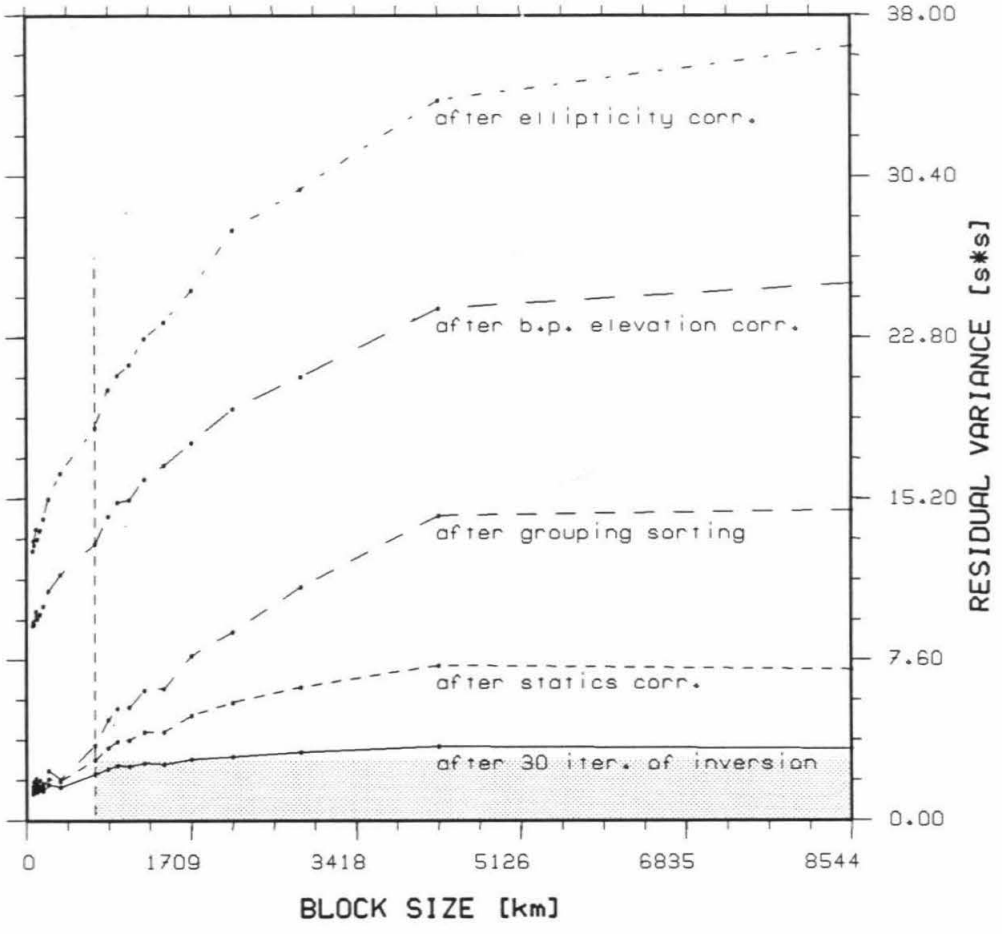

Figure 1.11 Variance reduction plot. The vertical axis shows the average group variance of residuals with same source and receiver areas, and the horizontal axis denotes the bin area size. The vertical dashed line at the left indicates the block size for inversion. The top of the shadowed zone is at the variance of data just before inversion at the inversion block size, representing the noise level in the data. The average variances at large bin sizes represent systematic variations, while the variances at small bin sizes represent random noise. Note that the sorting considerably reduces the noise level, and the inversion has absorbed a large portion of the long-wavelength variations of travel time residuals.

process considerably improves the data quality, since it largely reduces the high frequency noise with little effect on the long-wavelength variations, which are assumed to relate to mantle heterogeneities. On the other hand, the statics terms and the inverted image contain much of the long-wavelength variations which are usually the informative part of the data.

If the inversion were perfect, the lowest curve in Figure 1.11 would be a flat line along the top of the shadowed area, which represents the variance level before the inversion at bin block size equal to the inversion block size. Predicatably, the actual curve after inversion shows aliasing of some high frequency noise into the image, although the curve is quite flat. The change of the average group variance at a given block size during the inversion, denoted by $\Delta \mathbf{V}$, represents the portion of residual travel times being transformed into the image at the corresponding wavelength. As a result, the random noise level in the image can be estimated as

$$\left(\text{Random Noise Level}\right)_{\text{image}} = \left\{ \frac{\Delta \mathbf{V} \text{ at the Inverse Block Size}}{\Delta \mathbf{V} \text{ at the Largest Block Size}} \right\}^{1/2} \quad (1.11)$$

The estimations of random noise levels are nearly 42% for the PP wave image. One can further compute the model covariance matrix by a numerical method which is used by Davies and Clayton [1987], to evaluate the noise propagation. A large number of inversions are performed using data ray paths. The residual travel times used, however, are randomly generated from a distribution similar to that of the data but with the variance of random noise which is estimated above. Subsequently, the variance of slowness perturbations at each block due to noise in the data is obtained through many

inversions.

The resolution and error estimations discussed above suggest that the reliability of the PP wave images is marginal. We have more confidence on long-wavelength patterns than the high frequency features. There are several ad hoc ways to recognize reliable anomalies. For instance, if the data are sufficient, one may divide the data into portions, such as two halves, to run separate inversions. The similar features resolved from separated data sets are more likely to be realistic.

1.7 Images of PP Wave Structures

The application of the tomographic inverse to image the ISC PP wave residual times is intended as a reconnaissance survey of major seismic slab structures. We should keep in mind that the PP image contains a high level of noise (nearly one half as inferred in last section). The short-wavelength patterns and the magnitude of the image are not very reliable. Nevertheless, we would like to look over the image while regarding it as unrealistic in many aspects. Among the interesting features that we will attempt to see are, first, are there fast velocity anomalies associated with major subduction zones? Second, since the inverse solutions are not limited to subduction zones, what kind of velocity structures are associated with other tectonic elements, such as regions beneath continents and mid-ocean ridges? Third, to infer the size and magnitude scales of the compressional velocity anomalies in the upper mantle

and top half of the lower mantle. Finally, we also have interest in the coverage of PP wave image in comparison with the P wave's, since much higher quality PP wave travel time or waveform data may be used in the future to study regions not covered by direct P waves.

First we will examine the general features of the images of PP waves. Figure 1.12 shows two typical horizontal slices of the image, at depth ranges 300-400 km and 800-900 km, respectively. The slowness anomalies are contoured, with an interval of one half percent. Note that the image has fairly good coverage in the Pacific ocean at these depth ranges. A similar image of ISC P waves [Clayton and Comer, 1983] has much less coverage in the Pacific and the southern hemisphere at depth 300-400 km, and in the central Pacific at depth 800-900 km. At the 300-400 km depth range of the image, the subduction regions, such as under the Aleutian, Kurile, Japan, Izu-Bonin, Ryukyu, Java, Peru and Chilean trenches, are generally fast and of short wavelengths. Regions underneath the continental shields, such as the Eurasia, India and North America shields, are of long wavelength, and fast or neutral at 300-400 km depth and mixed at 800-900 km depth. These are the longest wave-length anomalies in the horizontal slices. Regions below oceans, on the other hand, are generally slow or mixed and of short wavelength.

The PP wave image is similar to the P result in some large scale patterns. For instance, the layered averages of PP wave image are slightly slow from surface down to 900 km and slightly fast from 900 km to 1900 km. P wave image shows very similar trends, which probably indicate that the compressional velocity of the JB model is slightly too fast in the the upper

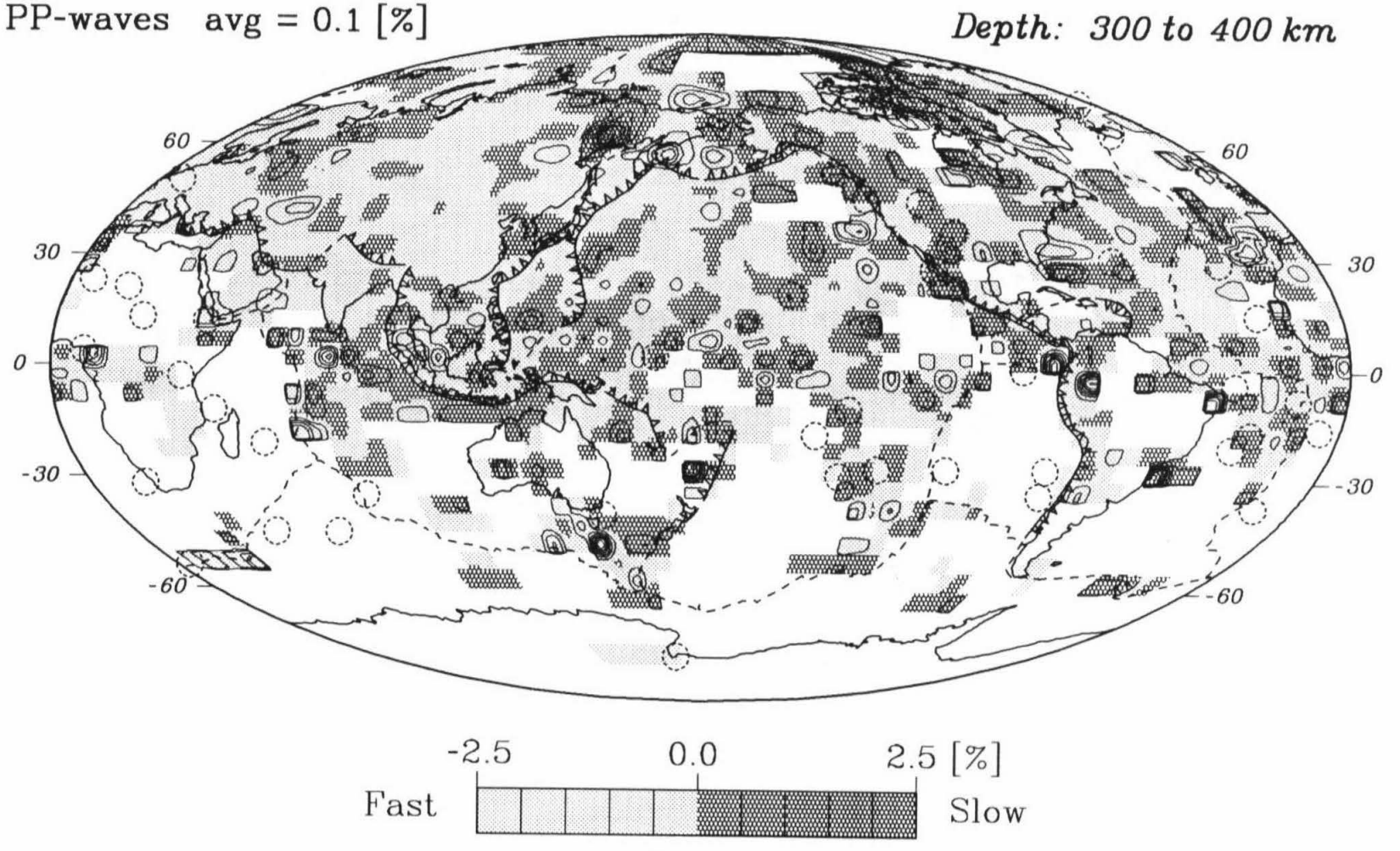

Figure 1.12 Examples of horizontal slices of the unsmoothed image of PP-waves. The image of PP wave perturbations at depth ranges 300-400 km and 800-900 km are shown. Map plotting conventions are identical to Figure 0.2. The contour interval is 0.5% and blank areas are uncovered.

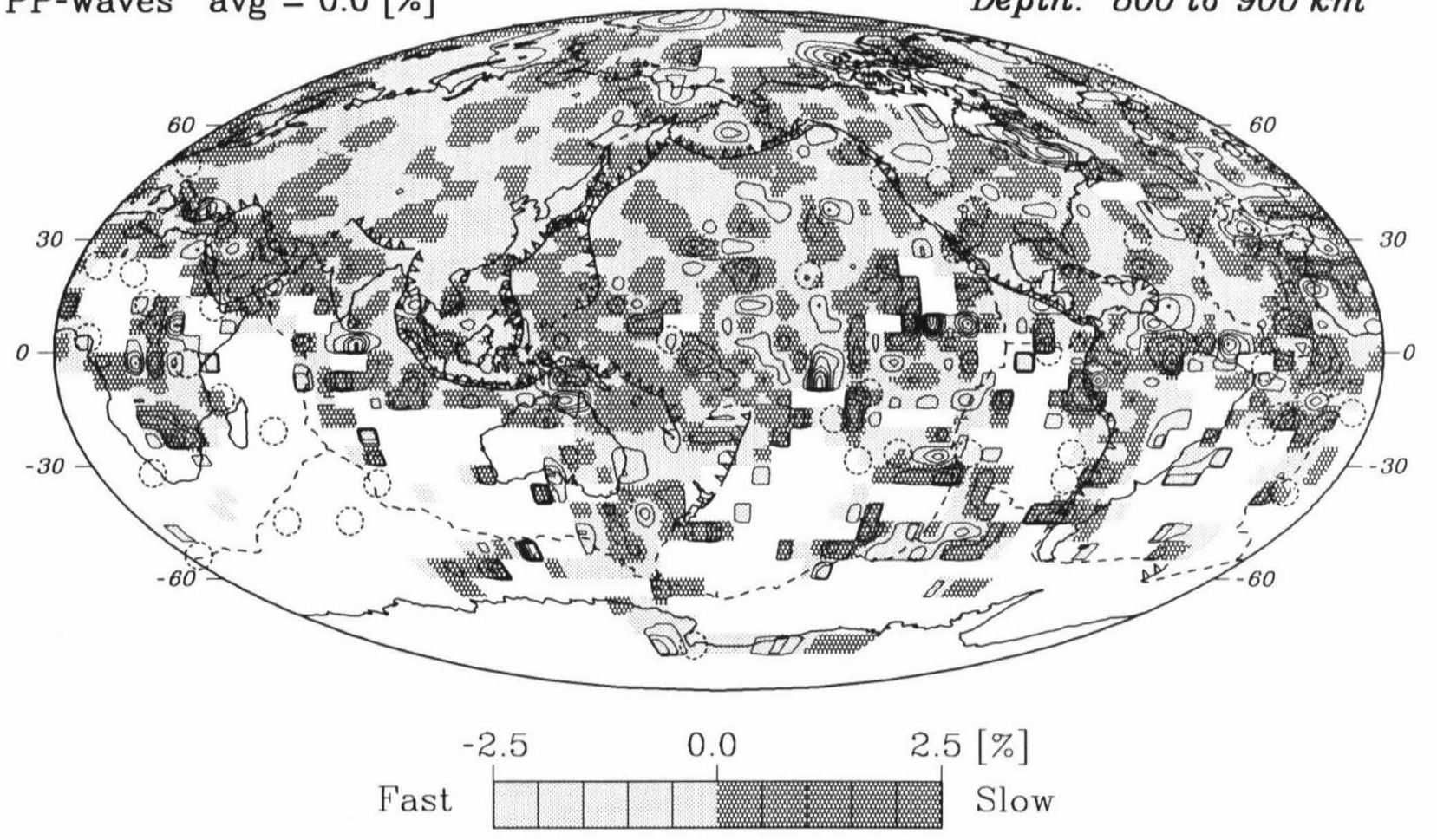

Figure 1.12 (continued)

mantle and top of the lower mantle, and too slow in the upper half of the lower mantle. On the other hand, the anomalies in the images are not completely relative to the JB model, because many of the data corrections could have changed the average character of the residuals. Both P and PP images show that most continental shields are underlaid by long-wavelength and low magnitude variations. Subduction zones are generally associated with fast anomalies. Mid-ocean ridges are underlaid with many slow features in the upper mantle. Many large features extend deep into the lower mantle. Some correlation exists between the PP wave image and the shear wave study by Grand [1987] in North America. The upper mantle under western North America is generally slow while eastern North America is generally fast.

By a least-squares method, we have fitted the image at all depth ranges with spherical harmonics. Figure 1.13 shows fitting results from degree 1 to 15 at depth ranges 300-400 km and 800-900 km. The fitting is satisfactory in general, since the power spectra, as given in Figure 1.14, are reduced towards the highest frequency. In fact, the expansions shown in Figure 1.13 are quite similar to the corresponding slices in Figure 1.12. At the 300-400 depth range most subduction regions are relatively fast in the expansions. At the 800-900 depth range the heterogeneities are of longer wavelengths. The average of the image is slow at 800-900 depth, indicating that the JB reference model is probably too fast in the top of the lower mantle.

According to Figure 1.14, except the top two layers, there is not much power for all layers at degrees larger than 12, or smaller than about 30° in lateral dimension. The maximum power ranges from degree 2 to degree 8, and

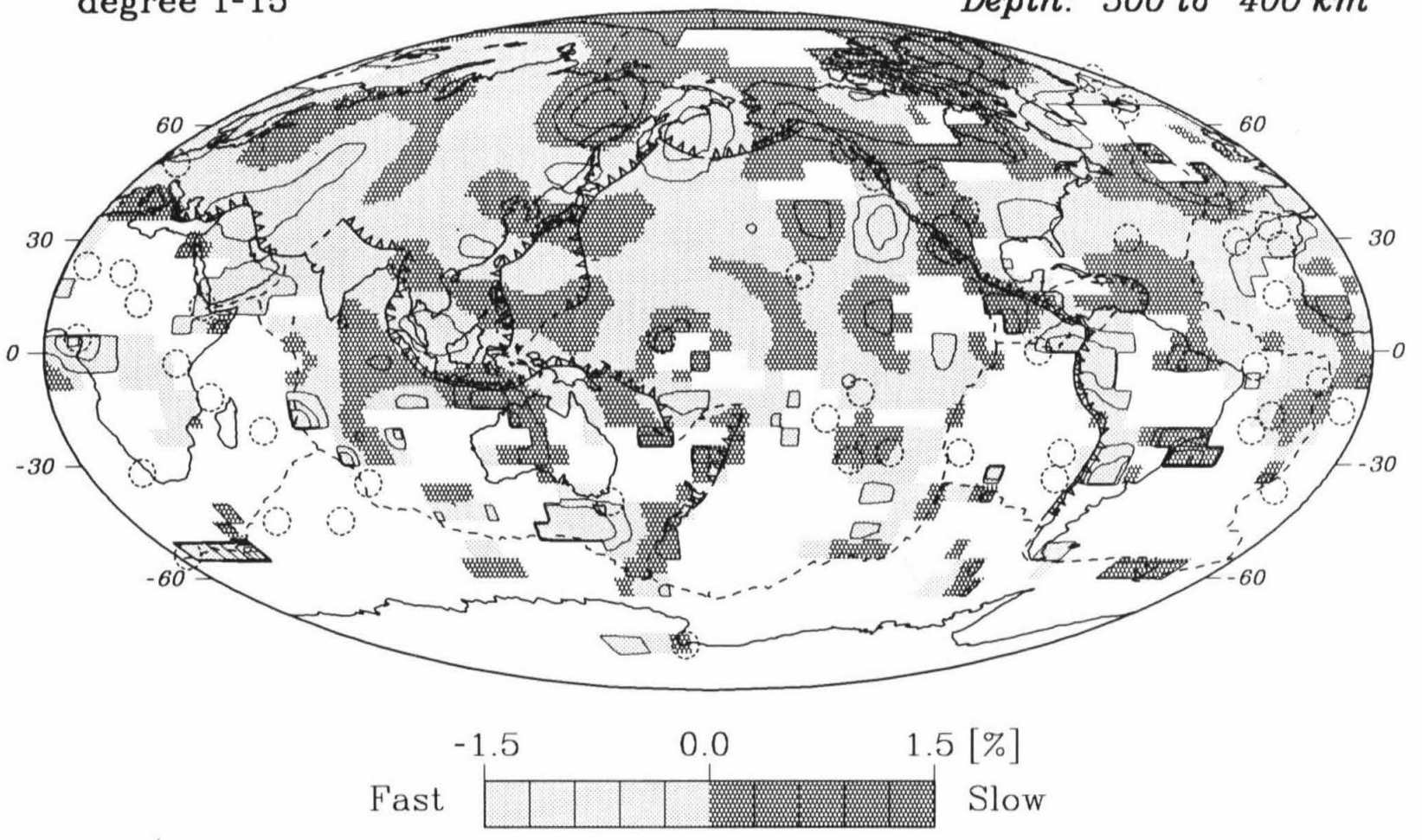

Figure 1.13 Spherical harmonic expansion of the images in Figure 1.12. The expansion is from degree 1 to 15. The contour interval is 0.3%. Note that the anomalies at 800-900 km layer are of longer wavelength in comparison with that at 300-400 km.

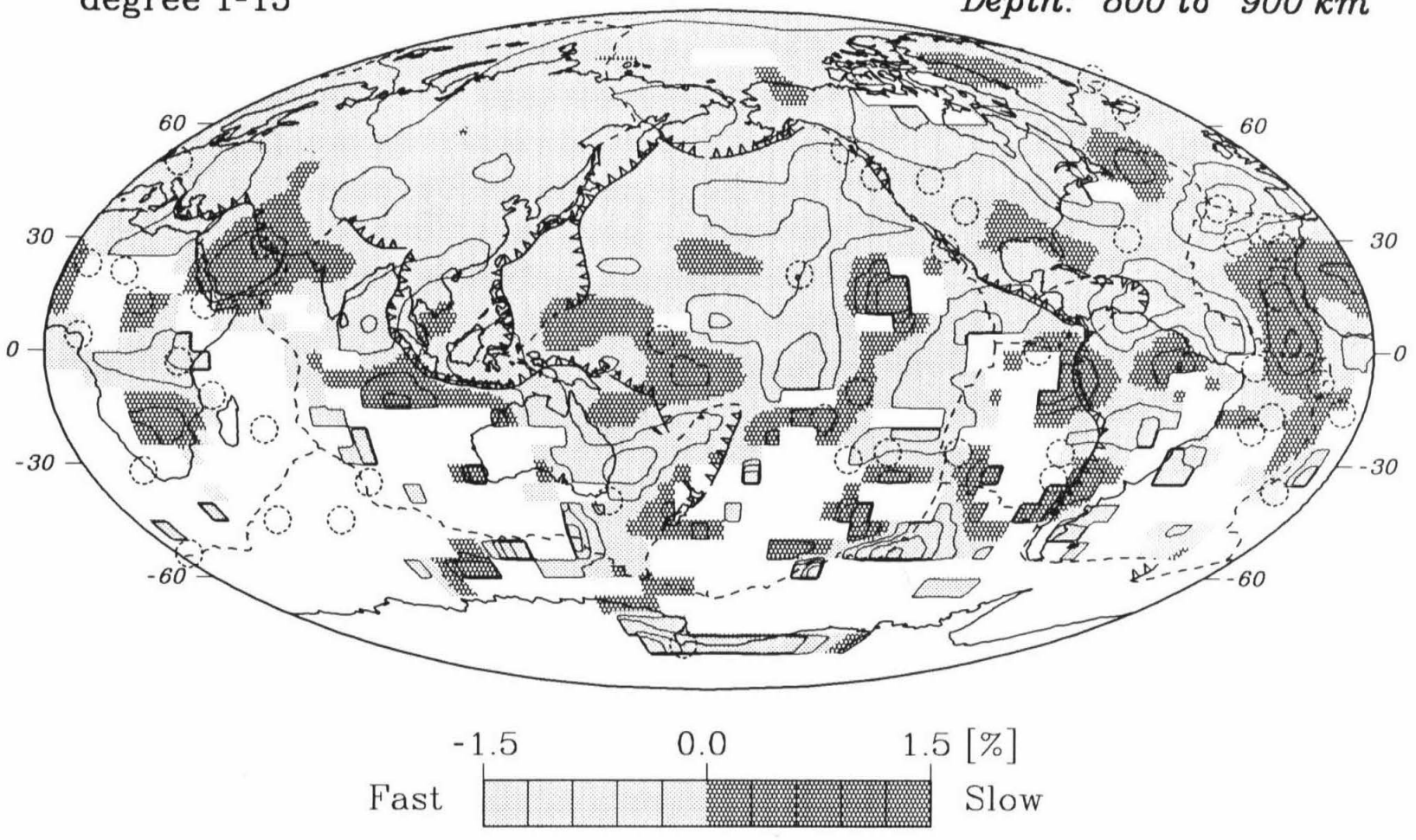

Figure 1.13 (continued)

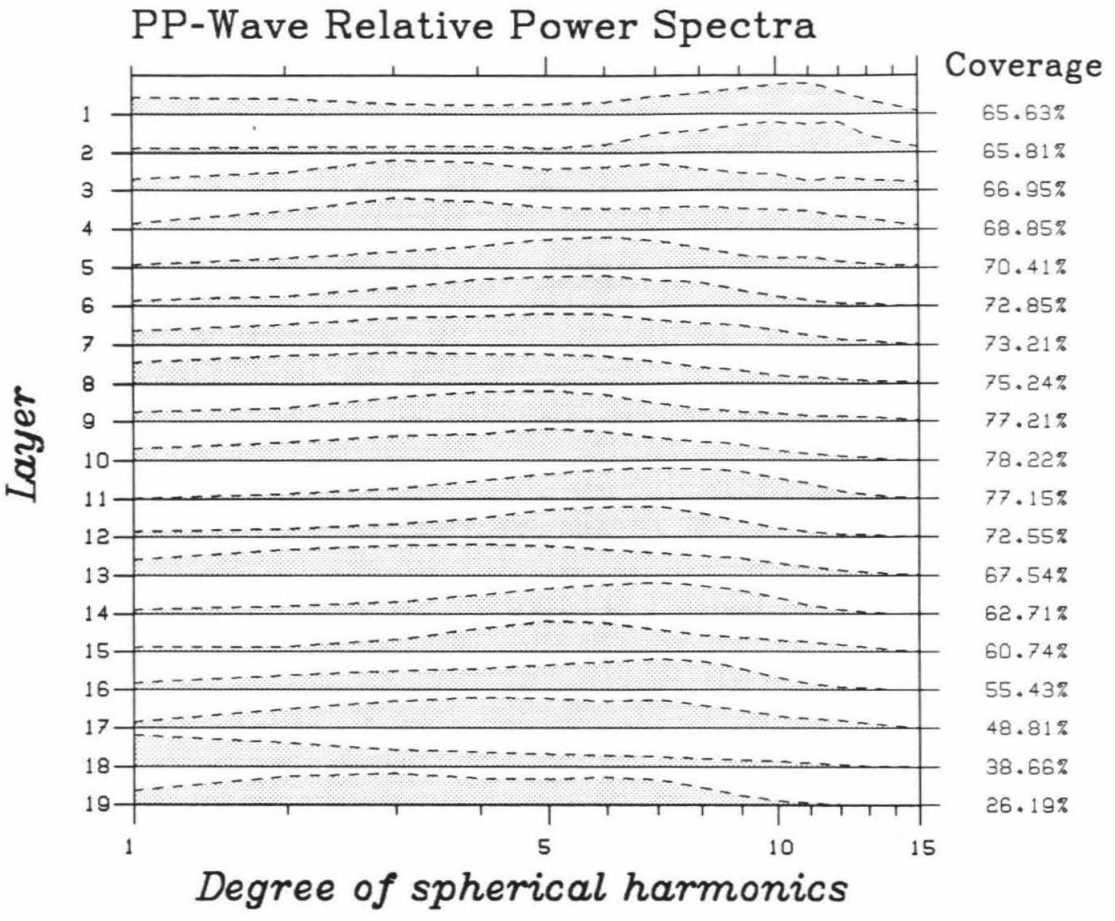

Figure 1.14 Relative power spectra of the PP wave image. Each shaded area is the power spectrum from spherical harmonic expansion of the image at each layer (starting from the surface). The power at each layer is normalized relative to the maximum of the layer. The coverage of the image at each layer is shown to the right. The power at each layer, except the top four, is dominated by degrees less than 12.

it seems to shift to lower degrees at deeper layers in our solution which covers about 2/3 of each layer of the upper mantle and top half of the lower mantle. Similar studies on P waves have shown that the power spectra from degrees 1 to 12 are essentially white for all lower mantle depths [Hager and Clayton, 1989], and the integrated lower mantle power peaks at degree 2 [Richards, 1986]. If the above observations are true in general, they suggest that the wavelength of mantle heterogeneities is increasing with depth in the upper mantle and most part of the lower mantle. This is in agreement with the study by Gudmundsson *et al.* [1989].

To carry out the reconnaissance survey, we have sliced the PP image according to subduction zone orientations from previous studies, mainly following Uyeda and Kanamori [1979]. The survey results are listed in Table 1.3. Several example slices are illustrated in Figure 1.15. Regions around the subduction zones are usually associated with fast anomalies, although they are of low amplitude (often a fraction of a percent).

It is clearly very subjective in assigning the range of the notable fast anomalies associated with subduction zones, as in Table 1.3. There are certainly many elongated fast anomalies in the image which do not associate with subduction zones at all. The values given in the table are selected through examining the image in terms of earthquake foci, resolution, and the stability of the image anomalies. The observations are of the quite lower order due to low resolution (large block size and low ray coverage) and high noise. This is the motivation for more detailed surveys over several dozen vertical slices in the hope of gaining a general feeling about the seismic structures

Table 1.3 Parameters of Benioff-Wadati Zones (modified from Uyeda and Kanamori [1979])

Arc	Position of Plate Boundary °	Strike of Section °	Maximum Depth† km	Dip °	References
Scotia	58°S, 24°W	EW	200 (200)	70	Frankel and McCann [1979]
South Chile	40°S, 72°W	N100°E	160 (200)	30	Isacks and Barazangi [1977]
Central Chile	30°S, 70°W	N100°E	200 (?)	11	Isacks and Barazangi [1977]
North Chile	20°S, 70°W	N70°E	300 (?)	30	Isacks and Barazangi [1977]
Peru	10°S, 78°W	N60°E	220 (300)	8	Isacks and Barazangi [1977]
Middle America	12°N, 87°W	N45°E	280 (400)	65	Dewey and Algermissen [1974]
Lesser Antilles	15°N, 60°W	EW	250 (300)	65	McCann and Sykes [1984]
Juan de Fuca	46°N, 127°W	EW	600 (700)	65	Rasmussen *et al.* [1987]
Alaska	59.5°N, 150°W	N73°W	150 (200)	55	Lahr [1975]
Aleutians	51°N, 177°W	N10°W	300 (600)	65	Engdahl and Gubbins [1987]
Kuriles	45°N, 153°E	N40°W	650 (900)	50	Engdahl *et al.* [1977]
NE Japan	40°N, 144°E	EW	600 (?)	40	Ishida [1970]
Ryukyu	24°N, 126°E	N30°W	300 (400)	45	Katsumata and Sykes [1969]
Philippine	5°N, 128°E	EW	600 (?)	55	Hamilton [1974]
Izu-Bonin	30°N, 143°E	N100°W	560 (700)	45	Shiono *et al.* [1980]
Marianas	18°N, 148°E	EW	700 (800)	90	Katsumata and Sykes [1969]
Tonga	21°S, 173°W	N70°W	650 (?)	53	Giardini and Woodhouse [1984]
Kermadec	33°S, 178°W	N70°W	600 (?)	65	Giardini and Woodhouse [1984]
New Zealand	40.5°S, 177°E	N48°W	350 (600)	67	Ansell and Smith [1975]
New Hebrides	17°S, 167°E	N70°E	300, 530 (300)	70	Isacks and Barazangi [1977], Dubois [1971]
New Britain	6°S, 147°E	N40°W	200, 600 (200)	65	Isacks and Molnar [1971]
Solomons	6°S, 154°E	N40°E	550, 150 (500)	70	Isacks and Molnar [1971]
Andaman	12°N, 92°E	EW	100 (400)	50	Eguchi *et al.* [1979]
Sumatra	5°S, 100°E	N60°E	200 (300)	30	Fitch [1970]
Java	10°S, 113°E	NS	300, 600 (300)	55	Fitch [1970]
Banda Sea	7°S, 130°E	N30°W	400 (500)	55	Fitch [1970]

† Maximum depth: The value in front of parentheses is of the Benioff-Wadati zone from the references. The value in parentheses is an estimate of the fast PP wave slowness anomalies associated with the subduction zone. All estimates are multiples of 100 km, the thickness of the resolution blocks used.

Figure 1.15 Vertical slices of the unsmoothed image of PP waves across subduction zones. Several examples of great circle slices passing normally through subduction zones at the center are shown. The numbers at the top give the central location of the slice, the azimuth of the great circle, and the dip and possible depth of the subduction zone. The map in the top panel of each plot is a projection of the world along the great circle slice, which is indicated by the heavy straight line. The dashed circles denote hot spots, dashed lines mark plate boundaries, and open barbed lines indicate subduction zones. The middle panel shows a slice with no vertical exaggeration. The bottom slice has a vertical exaggeration around 6. The open circles in each slice indicate fast regions, while dark circles indicate slow regions. The mean of anomalies at each layer has been removed. The location of the subduction zone below 100 km, as inferred from previous studies (Table 1.3), is marked with a short heavy line. The line is sometimes extended with dots to indicate fast regions just below the subduction zone.

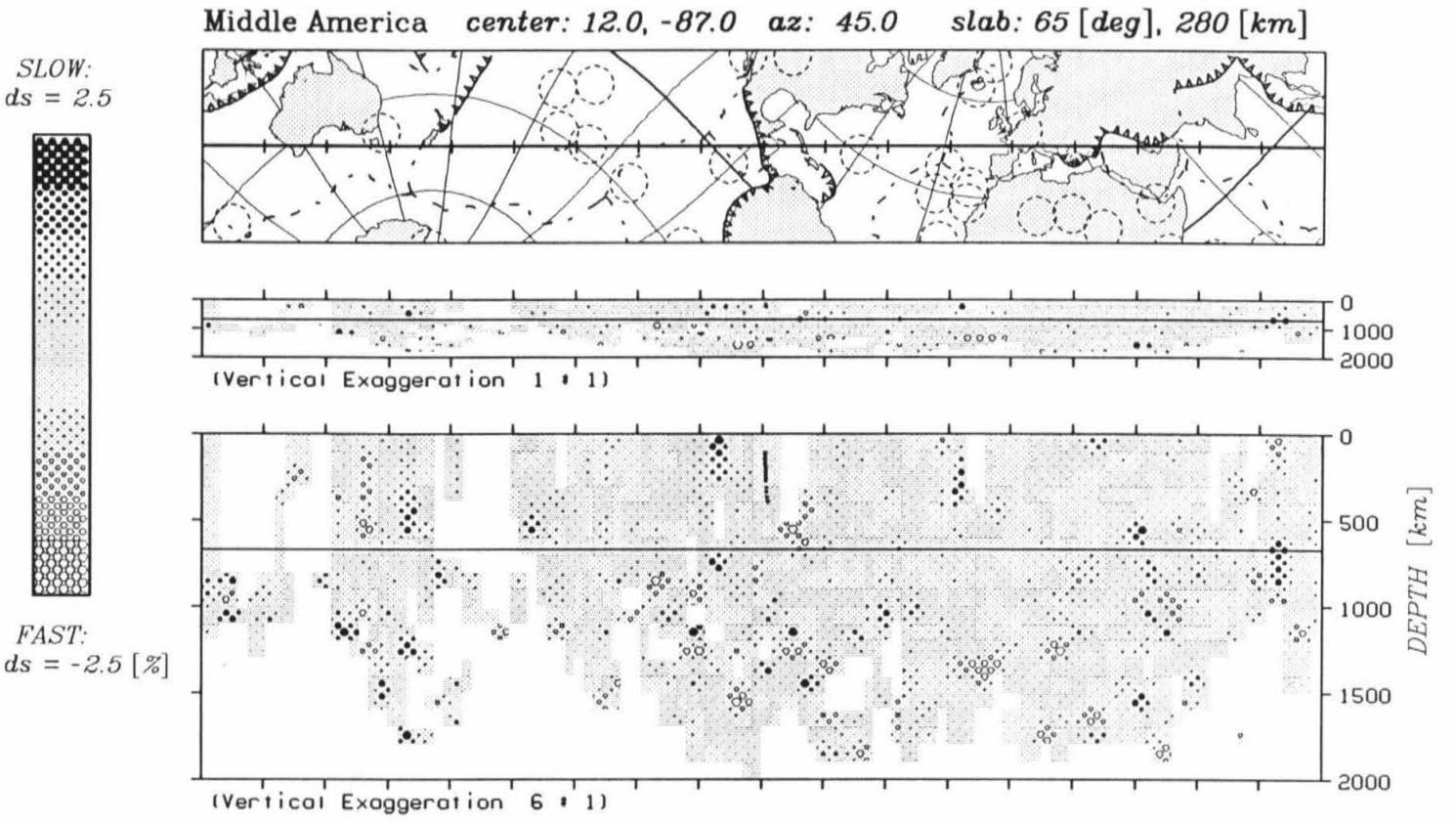

Figure 1.15 (continued)

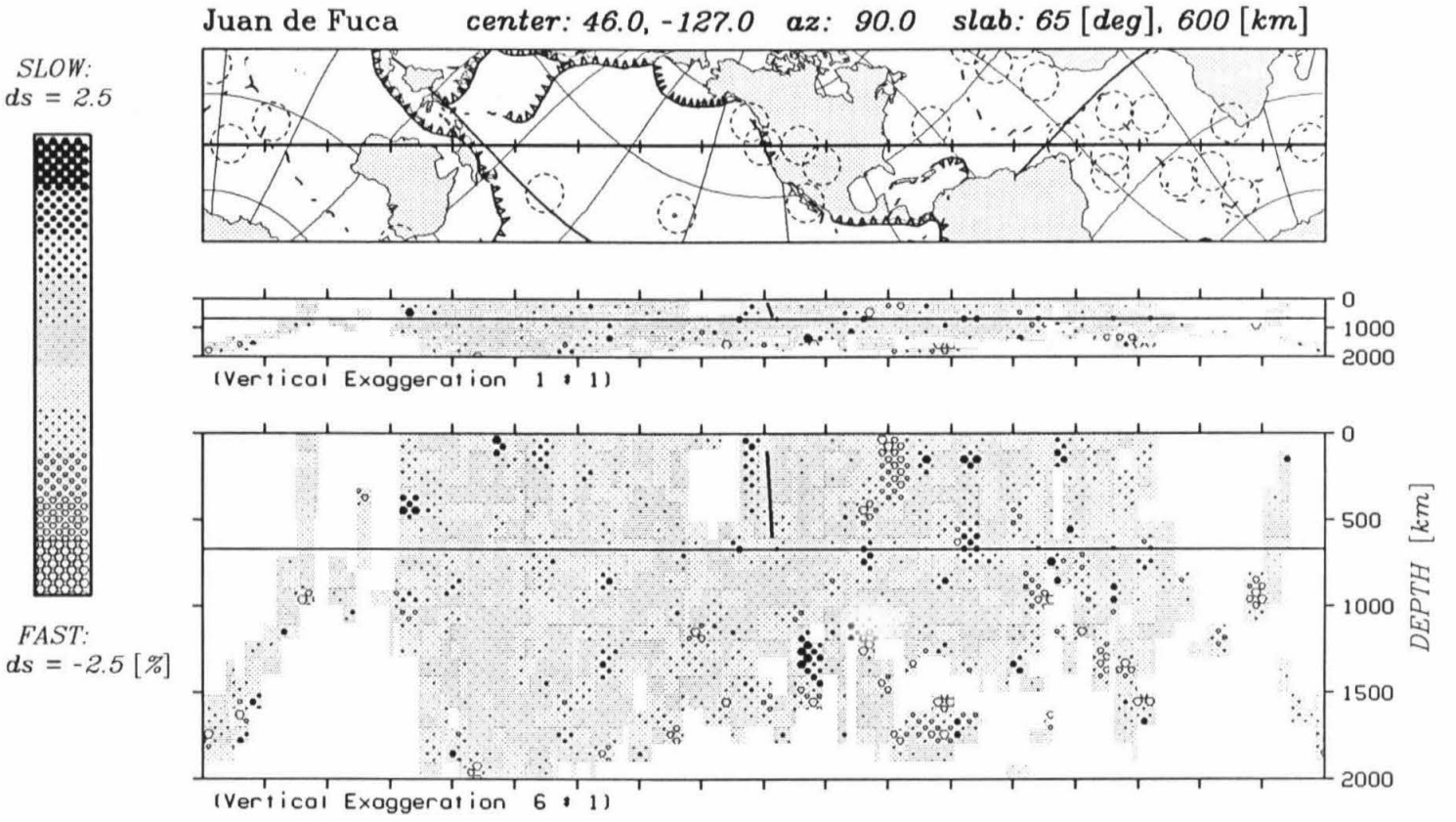

Figure 1.15 (continued)

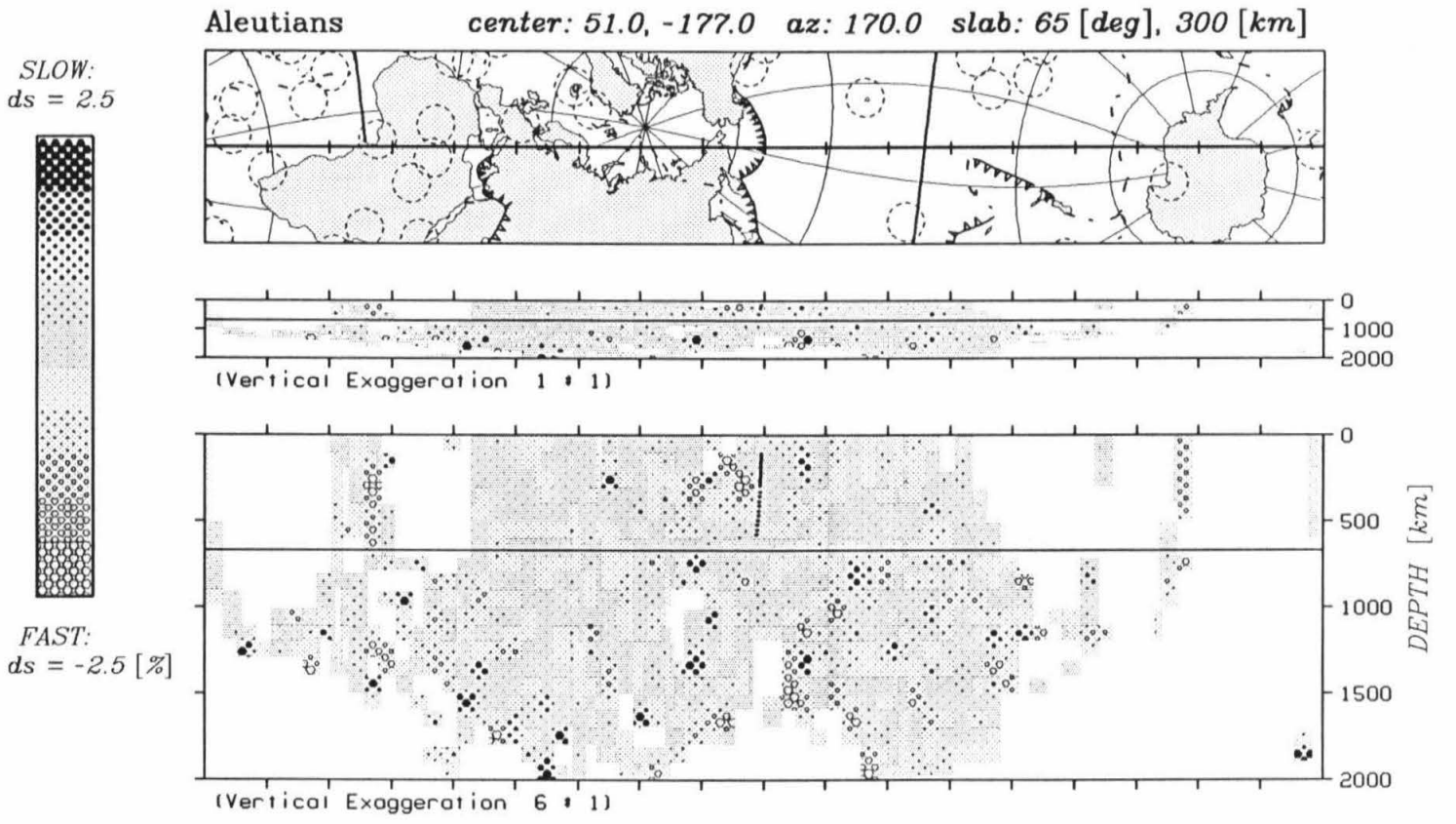

Figure 1.15 (continued)

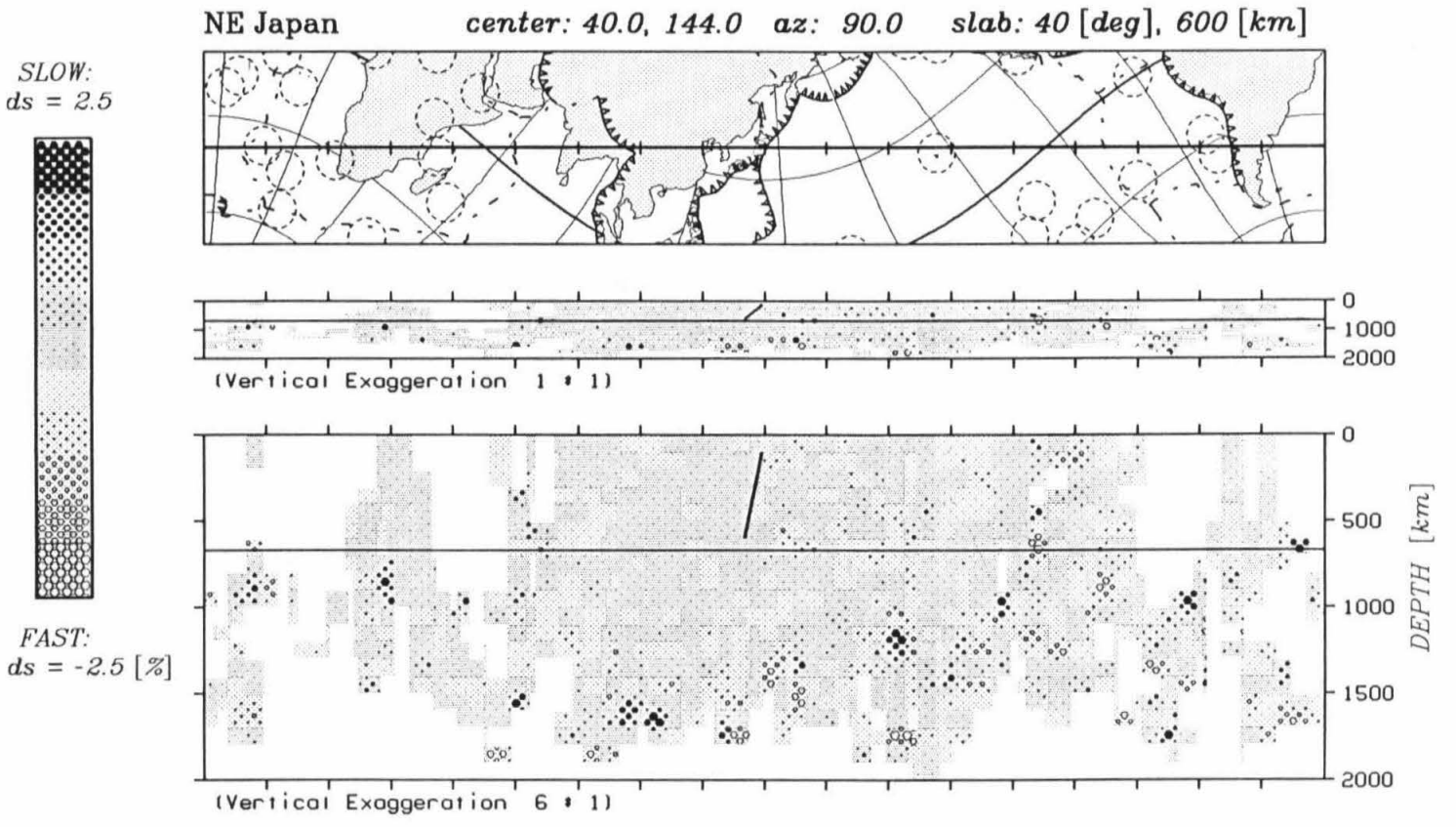

Figure 1.15 (continued)

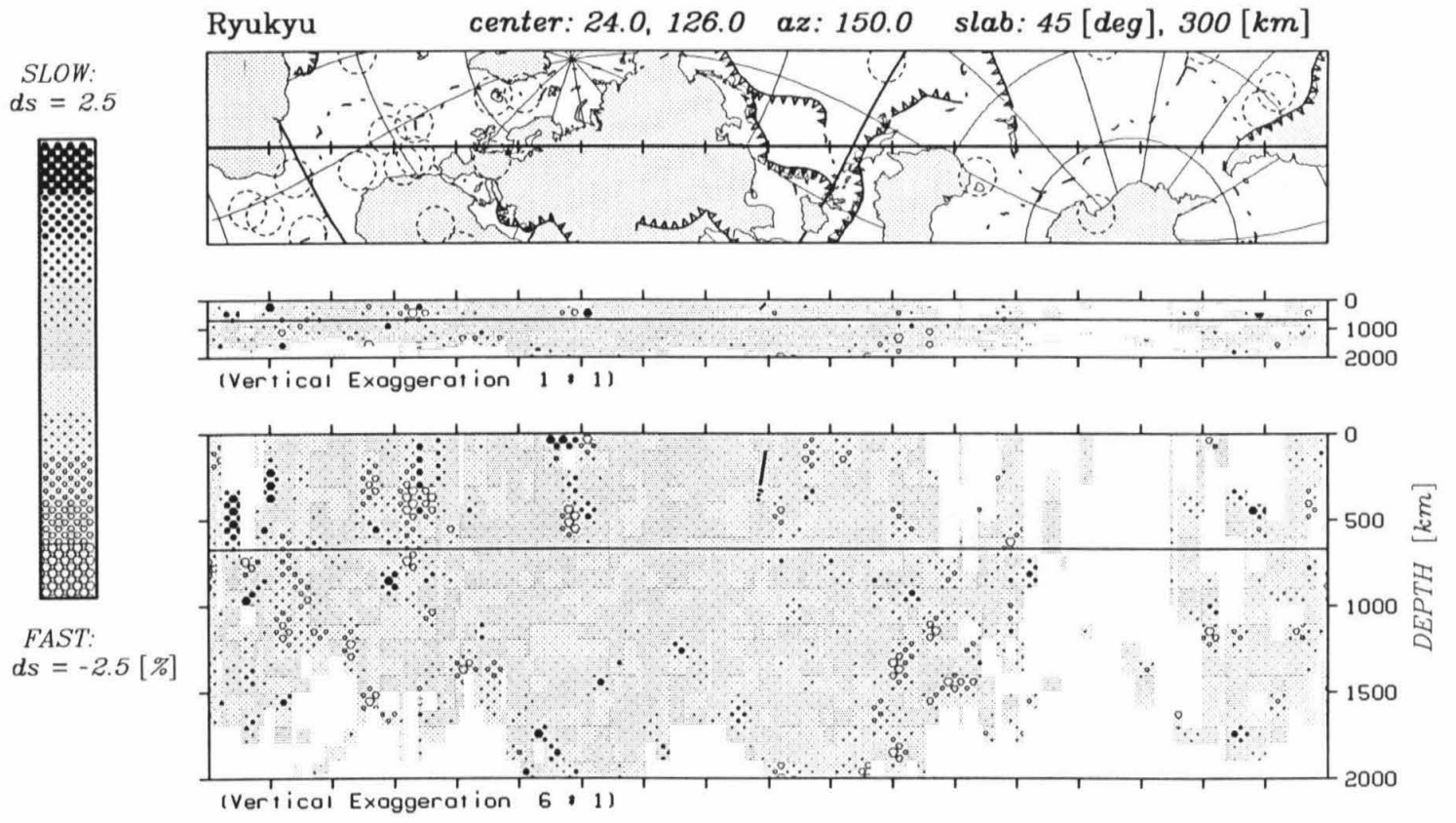

Figure 1.15 (continued)

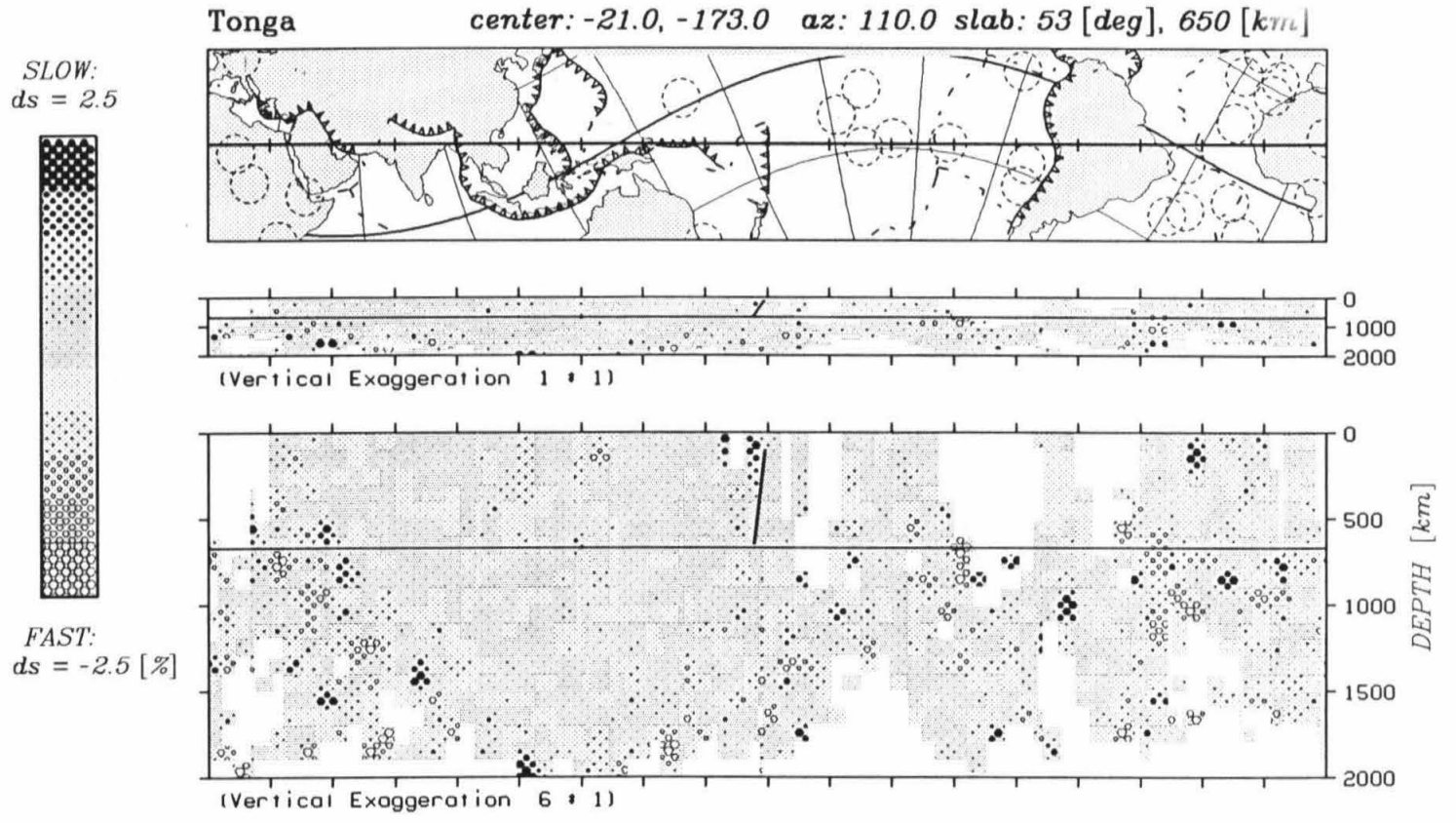

Figure 1.15 (continued)

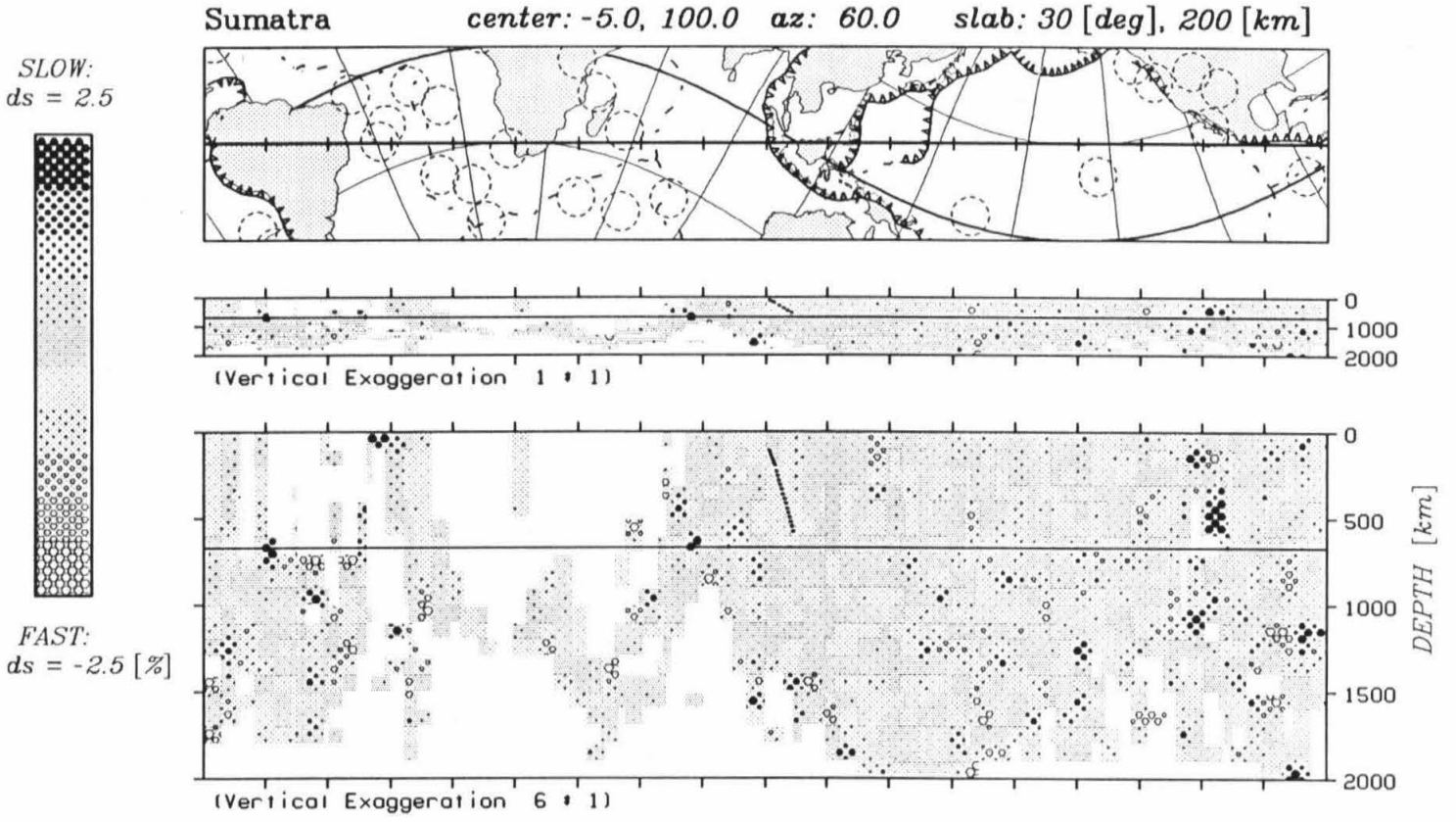

Figure 1.15 (continued)

around subduction zones. Mostly as coincidences, the maximum depths of the notable fast slabs in Table 1.3 are comparable to the subduction zone depths given by previous investigators.

As shown in Figure 1.15, the slice across Middle America indicates that the fast slab anomaly reaches to about 400 km depth, and there is a distinctive slow anomaly under the Azores near the triple junction of the plate boundaries in the North Atlantic. Underneath the Juan de Fuca trench, there is a fast slab-like anomaly that reaches to a depth of 600 km, comparable to that suggested by Rasmussen and Humphreys [1988]. The slice also shows that western North America is generally slow while eastern North America is generally fast in the upper mantle. A notable slab reaches to 500-600 km depth under the Aleutians and 500 km under NE Japan. The fast slab under the Ryukyu trench may reach to 400 km depth. Under the Tonga trench, Giardini and Woodhouse [1984] have suggested that the slab reaches to a 650 km depth. The anomalies in our image are fast and slab-like around the slab location, and the fast anomalies spread below 600 km. Finally, the slice across the Summatra trench shows broad fast bands to around 600 km in depth.

1.8 Summary

An SIRT tomographic inverse has been introduced in this chapter. Some aspects of the data reduction procedures, which probably possess more significance toward the resulting image than the inverse method does, are

discussed. In particular, the statics maps, which are produced as corrections for near source and station heterogeneities, show fast and slow velocity perturbations in general agreement with the known tectonic settings. We also described several practical ways in evaluating resolution and error of the inverse system. The resolution is estimated through some synthetic tests, while the noise levels in the data and the image are estimated by a summary ray technique.

The application of the inverse to the ISC PP wave data yield some useful clues about the heterogeneous velocity structures in the upper mantle and the top half of the lower mantle, although the reliability of the image is regarded as marginal. In this depth range the PP wave image, with nearly 1/2 of noise, shows a general increase in wavelength and decrease in magnitude of heterogeneities with depth. The image indicates that there are fast anomalies associated with most subduction zones. The depth extent of these notable fast slab-like anomalies is in general agreement with previous studies.

References to General Introduction and Chapter 1

Aki, K., A. Christoffersson, and E. S. Husebye, Determination of the three-dimensional seismic structure of the lithosphere, *J. Geophys. Res.*, **82**, 277-296, 1977.

Anderson, Don L., Thermally induced phase changes, lateral heterogeneity of the mantle, continental roots and deep slab anomalies, *J. Geophys. Res.*, **92**, 13968-13980, 1987.

Backus, G., and F. Gilbert, Numerical applications of a formalism for geophysical inverse problems, *Geophys. J. R. astr. Soc.*, **13**, 247-276, 1967.

Benioff, H., Seismic evidence for the fault origin of oceanic deeps, *Bull. Geol. Soc. Am.*, **60**, 1837-1856, 1949.

Benioff, H., Orogenesis and deep crustal structure — additional evidence from seismology, *Bull. Geol. Soc. Am.*, **65**, 385-400, 1954.

Bullen, K. E., An introduction to the theory of seismology, 2nd ed., *Cambridge [Eng.] Univ. Press*, 1953.

Burbach, G. V., and C. Frohlich, Intermediate and deep seismicity and lateral structure of subducted lithosphere in the Circum-Pacific region, *Rev. of Geophys.*, **24**, 833-874, 1986.

Cerveny, V., A new approximation of the velocity-depth distribution and its application to the computation of seismic wave fields, *Studia geoph. et geod.*, **24**, 17-27, 1980.

Cerveny, V., and J. Jansky, Ray amplitudes of seismic body waves in inhomogeneous radially symmetric media, *Studia geoph. et geod.*, **27**, 9-18, 1983.

Clayton, R.W., and R.P. Comer, A tomographic analysis of mantle heterogeneities from body wave travel times, *Eos Trans. AGU*, **64**, 776, 1983.

Comer, R. P., Rapid seismic ray tracing in a spherically symmetric earth via interpolation of rays, *Bull. Seism. Soc. Am.*, **74**, 479-492, 1984.

Comer, R. P., and R. W. Clayton, Reconstruction of mantle heterogeneity by iterative back projection of travel times: 1. Theory and reliability, *unpublished manuscript*, 1984.

Davies, J. H., and R. W. Clayton, Lower mantle S-wave tomography, *Eos Trans. AGU*, **67**, 1099, 1986.

Davies, J. H., and R. W. Clayton, Error analysis of a shear wave mantle tomographic inversion, *Eos Trans. AGU*, **68**, 1376, 1987.

Dines, K. A., and R. J. Lytle, Computerized geophysical tomography, *Proc. IEEE*, **67**, 1065-1073, 1979.

Dziewonski, A. M., Mapping the lower mantle: determination of lateral heterogeneity in P velocity up to degree and order 6, *J. Geophys. Res.*, **89**, 5929-5952, 1984.

Dziewonski, A. M., and Don L. Anderson, Preliminary reference earth model,

Phys. Earth Planet. Inter., **25**, 297-356, 1981.

Dziewonski, A. M., and F. Gilbert, The effects of small, aspherical perturbations on travel times and a re-examination of the corrections for ellipticity, *Geophys. J. R. astr. Soc.*, **44**, 7-17, 1976.

Engdahl, E. R., and D. Gubbins, Simultaneous travel-time inversion for earthquake location and subduction zone structure in the central Aleutian Islands, *J. Geophys. Res.*, **92**, 13855-13862, 1987.

Giardini, D., and J. H. Woodhouse, Deep seismicity and modes of deformation in Tonga subduction zone, *Nature*, **307**, 505-509, 1984.

Gilbert, P., Iterative methods for the reconstruction of three-dimensional objects from projections, *J. Theor. Biol.*, **36**, 105-117, 1972.

Gordon, R., R. Bender, and G. T. Herman, Algebraic reconstruction techniques (ART) for three-dimensional electron microscopy and X-ray photography, *J. Theor. Biol.*, **29**, 471-481, 1970.

Grand, S. P., Tomographic inversion for shear velocity beneath the North American plate, *J. Geophys. Res.*, **92**, 14065-14090, 1987.

Gudmundsson, O., J. H. Davies, and R. W. Clayton, Stochastic analysis of global travel time data: mantle heterogeneity and random errors in the ISC data, *submitted to Geophys. J.*, 1989.

Gutenberg, B., and C. F. Richter, *Seismicity of the Earth*, 2nd ed., Princeton Univ. Press, Princeton, New Jersey, 1954.

Hager, B. H., and R. W. Clayton, Constraints on the structure of mantle convection using seismic observations, flow models, and the geoid, in W. R. Peltier, ed., *Mantle Convection*, Gordon & Breach, in press, 1989.

Hearn, T. M., and R. W. Clayton, Lateral velocity variations in southern California: 1. Results for the upper crust from Pg-waves, *Bull. Seism. Soc. Am.*, **76**, 511-520, 1986a.

Hearn, T. M., and R. W. Clayton, Lateral velocity variations in southern California: 2. Results for the lower crust from Pn-waves, *Bull. Seism. Soc. Am.*, **76**, 495-509, 1986b.

Herrin, E., 1968 seismological tables for P phases, *Bull. Seism. Soc. Am.*, **58**, 1193-1241, 1968.

Hirahara, K., A large-scale three-dimensional seismic structure under the Japan islands and the Sea of Japan, *J. Phys. Earth*, **25**, 393-417, 1977.

Hirahara, K., Three-dimensional seismic structure beneath southwest Japan: The subducting Philippine Sea plate, *Tectonophys.*, **79**, 1-41, 1981.

Hirahara, K., and T. Mikumo, Three-dimensional seismic structure of subducting lithospheric plates under the Japan islands, *Phys. Earth Planet. Inter.*, **21**, 109-119, 1980.

Humphreys, E., and R. W. Clayton, Adaptation of back projection tomography to seismic travel time problems, *J. Geophys. Res.*, **93**, 1073-1085, 1988.

Humphreys, E., R. W. Clayton, and B. H. Hager, A tomographic image of mantle structure beneath southern California, *Geophys. Res. Lett.*, **11**, 625-627, 1984.

Isacks, B. L., and M. Barazangi, Geometry of Benioff zones, lateral segmentation and downwards bending of the subducted lithosphere, in *Island Arcs, Deep Sea Trenches and Back-Arc Basins*, Maurice Ewing Ser. **1**, edited by M. Talwani and W. C. Pitman III, 99-114, AGU, Washington, D.C., 1977.

Isacks, B., and P. Molnar, Distribution of stresses in the descending lithosphere from a global survey of focal mechanism solution of mantle earthquakes, *Rev. Geophys. Space Phys.*, **9**, 103-174, 1971.

Jacob, K. H., Three-dimensional seismic ray tracing in a laterally heterogeneous spherical earth, *J. Geophys. Res.*, **75**, 6675-6689, 1970.

Jaffe, C. C., Medical imaging, *Am. Sci.*, **70**, 576-585, 1982.

Jeffreys, H., and K. E. Bullen, Seismological tables, London, *British Asso. Adv. Sci.*, 50p, 1948.

Julian, B. R., Ray tracing in arbitrarily heterogeneous media, *Tech. Note, 1970-45*, Lincoln Laboratory, Mass. Inst. of Tech., Lexington, Mass., 1970.

Julian, B. R., and D. Gubbins, Three-dimensional seismic ray tracing, *J. Geophys.*, **43**, 95-113, 1977.

Menke, W., Geophysical data analysis: discrete inverse theory, *Academic Press*, New York, 1984.

Nakanishi, I., and K. Kanamori, Source mechanisms of twenty-six large, shallow earthquakes ($M_s \geq 6.5$) during 1980 from P-wave first motion and long-period Rayleigh wave data, *Bull. Seism. Soc. Am.*, **74**, 805-818, 1984.

Nolet, G., Solving or resolving inadequate and noisy tomographic systems, *J. Computational Phys.*, **61**, 463-482, 1985.

Olson, A. H., A Chebyshev condition for accelerating convergence of iterative tomographic methods — solving large least squares problems, *Phys. Earth Planet. Inter.*, **47**, 333-345, 1987.

Pereyra, V., W. H. K. Lee, and H. B. Keller, Solving two-point seismic ray tracing problems in a heterogeneous medium, *Bull. Seism. Soc. Am.*, **70**, 79-99, 1980.

Radcliff, R. D., and C. A. Balanis, Reconstruction algorithms for geophysical applications in noisy environments, *Proc. IEEE*, **67**, 1060-1064, 1979.

Rasmussen, J., and E. Humphreys, Tomographic image of the Juan De Fuca Plate beneath Washington and Western Oregon using teleseismic P-wave travel times, *Geophys. Res. Lett.*, **15**, 1417-1420, 1988.

Richards, M. A., Dynamical models for the earth's geoid, *Ph.D. thesis*, California Institute of Technology, 1986.

Roecker, S. W., Velocity structure in the Izu-Bonin seismic zone and the depth of the olivine-spinel phase transition in the slab, *J. Geophys. Res.*, **90**,

7771-7794, 1985.

Spencer, C. P., and E. R. Engdahl, A joint hypocenter location and velocity inversion technique applied to the central Aleutians, *Geophys. J. R. astr. Soc.*, **72**, 399-415, 1983.

Stark, P. B., and C. Frohlich, The depths of the deepest deep earthquakes, *J. Geophys. Res.*, **90**, 1859-1869, 1985.

Stork, C., Ray trace tomographic analysis of surface seismic reflection data, *Ph.D. thesis*, California Institute of Technology, 1988.

Tanimoto, T., and Don L. Anderson, Lateral heterogeneity and azimuthal anisotropy of the upper mantle: Love and Rayleigh waves 100-250 s, *J. Geophys. Res.*, **90**, 1842-1858, 1985.

Tarantola, A., and A. Nercessian, Three-dimensional inversion without blocks, *Geophys. J. R. astr. Soc.*, **76**, 299-306, 1984.

Thurber, C. H., and W. L. Ellsworth, Rapid solution of ray tracing problems in heterogeneous media, *Bull. Seism. Soc. Am.*, **70**, 1137-1148, 1980.

Toksöz, M. Nafi, J. W. Minear, and B. R. Julian, Temperature field and geophysical effects of a down-going slab, *J. Geophys. Res.*, **76**, 1113-1138, 1971.

Toksöz, M. Nafi, N. H. Sleep, and A. T. Smith, Evolution of the downgoing lithosphere and the mechanisms of deep focus earthquakes, *Geophys. J. R. astr. Soc.*, **35**, 285-310, 1973.

Utsu, T., Seismological evidence for anomalous structure of island arcs with special reference to the Japanese region, *Rev. Geophys. Space Phys.*, **9**, 839-890, 1971.

Uyeda, S., and H. Kanamori, Back-arc opening and the mode of subduction, *J. Geophys. Res.*, **84**, 1049-1061, 1979.

Vassiliou, M. S., B. H. Hager, and A. Raefsky, The distribution of earthquakes with depth and stress in subducting slabs, *J. Geodynamics*, **1**, 11-28, 1984.

Wadati, K., On the activity of deep-focus earthquakes in the Japan Island and neighbourhood, *Geophys. Mag., Tokyo*, **8**, 305-326, 1935.

Walck, M. C., and R. W. Clayton, P-wave velocity variations in the Coso region, California, derived from local earthquake travel times, *J. Geophys. Res.*, **92**, 393-406, 1987.

Wesson, R. L., Travel-time inversion for laterally inhomogeneous crustal velocity models, *Bull. Seism. Soc. Am.*, **61**, 729-746, 1971.

Zhou, H., and R. W. Clayton, Mantle velocities from PP-waves, *Eos Trans. AGU*, **66**, 975, 1985.

Zhou, H., and R. W. Clayton, Travel-time inversions for P and S velocities beneath the northwest edge of the Pacific: slab fingering? *Eos Trans. AGU*, **68**, p.1379, 1987.

CHAPTER 2

TOMOGRAPHIC INVERSION IN THE NORTHWEST PACIFIC:

detailed P and S wave slab structures

Abstract

Slab-like high P and S velocity anomalies around the Wadati-Benioff zone under island arcs of the northwest Pacific are resolved through travel-time tomographic inversions, with stations outside the modeled region excluded. Analyses of resolution and noise show that the images are generally well resolved. The images illustrate that slab anomalies are continuous along strike in most parts of the upper mantle of the region, and become contorted and generally broadened with depth. Near the bottom of the upper mantle, fingering of the slabs, including segmenting and spreading, is indicated. The fast anomalies associated with the Japan, Izu-Bonin and Mariana subduction zones tend to flatten to sub-horizontal at depth, while downward spreading may occur under parts of the Mariana and Kurile arcs. The fast anomalies below 700 km are not in the shape of a single coherent sheet. Slab fingering and intense deep seismicity are probably the consequence of the slab encountering a barrier of some form around the "670 km" *discontinuity.*

2.1 Introduction

In last chapter, the tomographic inversion method and its application to finding three-dimensional mantle velocities was introduced. While the high

noise level of PP data was discouraging, there was indication of fast anomalies associated with slabs. Travel times of direct arrivals such as P waves and S waves have a much lower noise level, but the ray coverage is so uneven for whole mantle studies that we simply don't have crossing-rays in many large regions. Consequently, a reasonable solution is to investigate regional structures using direct arrivals in region of good ray coverage. This strategy bridges the gap between local and global structural studies.

In this chapter, detailed compressional and shear velocity structures of the subduction zones under the island arcs of the Northwest Pacific are investigated. We take a tomographic inverse approach to transform the travel time residuals into three dimensional images of the slowness anomalies, and then interpret the images in terms of the seismic structures of the subduction zone. One of the primary reasons in choosing the Northwest Pacific region is that it possesses some of the deepest and most active subduction zones in the world (see Figure 0.2). The deep seismicity not only provides good ray coverage in the radial direction, but also produces travel times which have little or no contamination from velocity discontinuities, and has little ray path distortion when using a one-dimensional reference model. In addition, the earthquake locations are the best guide to the interpretation of the slab image, since it is generally assumed that these deep events are occurred in association with the descending lithospheric slab.

Previously, there were least-square type inversions in several areas in this region [e.g., Hirahara, 1977, 1981; and Hirahara and Mikumo, 1980] that resulted velocity structures with a fast signature for the subducting slab to a

depth of about 600 km. It is therefore quite promising to study the morphology of the subducting slab in this region using seismic observations. Particularly, there are very large amounts of P and S wave travel times in the ISC catalogs for the region, many for deep earthquakes that occurred along most parts of the major Northwest Pacific subduction zone. The concave nature of the trench towards the land and a large number of island stations improve the ray coverage for the subduction zone.

There are many tectonic components we would like to integrate into our interpretations. For example, the well-known increase in seismicity below 300 km is very distinctive in this region. This increase and the down-dip compressional mechanisms have been taken as evidence of stress build-up in the lower portion of the upper mantle [e.g., Isacks and Molnar, 1969, 1971; Vassiliou and Hager, 1988]. In Chapter 5 we will discuss the relationship between velocity anomalies and the principal stress axes of earthquakes.

We defined the segmentation and spreading of a deep slab as "fingering" [Zhou and Clayton, 1987; Zhou, 1988], which implies an independence in spreading direction of each fingered anomaly. The term is distinguished from "segmenting," which has been commonly used in subduction zone studies to describe fractures of a slab perpendicular to its strike at relatively shallow depth. For instance, Isacks and Barazangi [1977] have investigated lateral segmentation along many subducted plates and concluded that segmentation is one of the important factors enabling more uniform bending of the plate along each segment. Fingering of the slab-like fast anomaly is observed in the images resolved around the "670 km" discontinuity.

2.2 Data and Method

All the travel time residuals used are selected from the ISC catalog from 1964 to 1982. The raw data consists of 306,729 picks of P waves and 151,171 picks of S waves. In contrast to most previous inversions (e.g., Hirahara, 1981], stations outside our modeled region are excluded. The reason for this exclusion is good coverage provided by local stations. Had we included stations outside, we would have to do something to account for large regions with few crossing-rays. In the Southwest Pacific region in the next chapter we have included most teleseismic rays because regional stations provide insufficient coverage there. As shown in Figure 2.1, for the Northwest Pacific region we applied a smaller area window in selecting earthquakes than the window in selecting stations. All source locations are between 0 ° N to 60 ° N and 115 ° E to 164 ° E and station locations between 10 ° S to 72 ° N and 100 ° E to 180 ° E. Except for areas near the edge of the region where the ray paths are confined to narrow bundles, each ray path is almost entirely contained within the model. Blocks containing less than 5 rays are not included in the inversions. The exclusion of teleseismic rays means that at depth, say below 700 km, many ray paths are nearly horizontal. However, a coherent steep-dipping fast anomaly, if it exists in the modeled region, should be resolved by these rays because of the azimuthal crossings. As will be discussed in section 2.3, smearing along the ray path will be detected by the resolution tests.

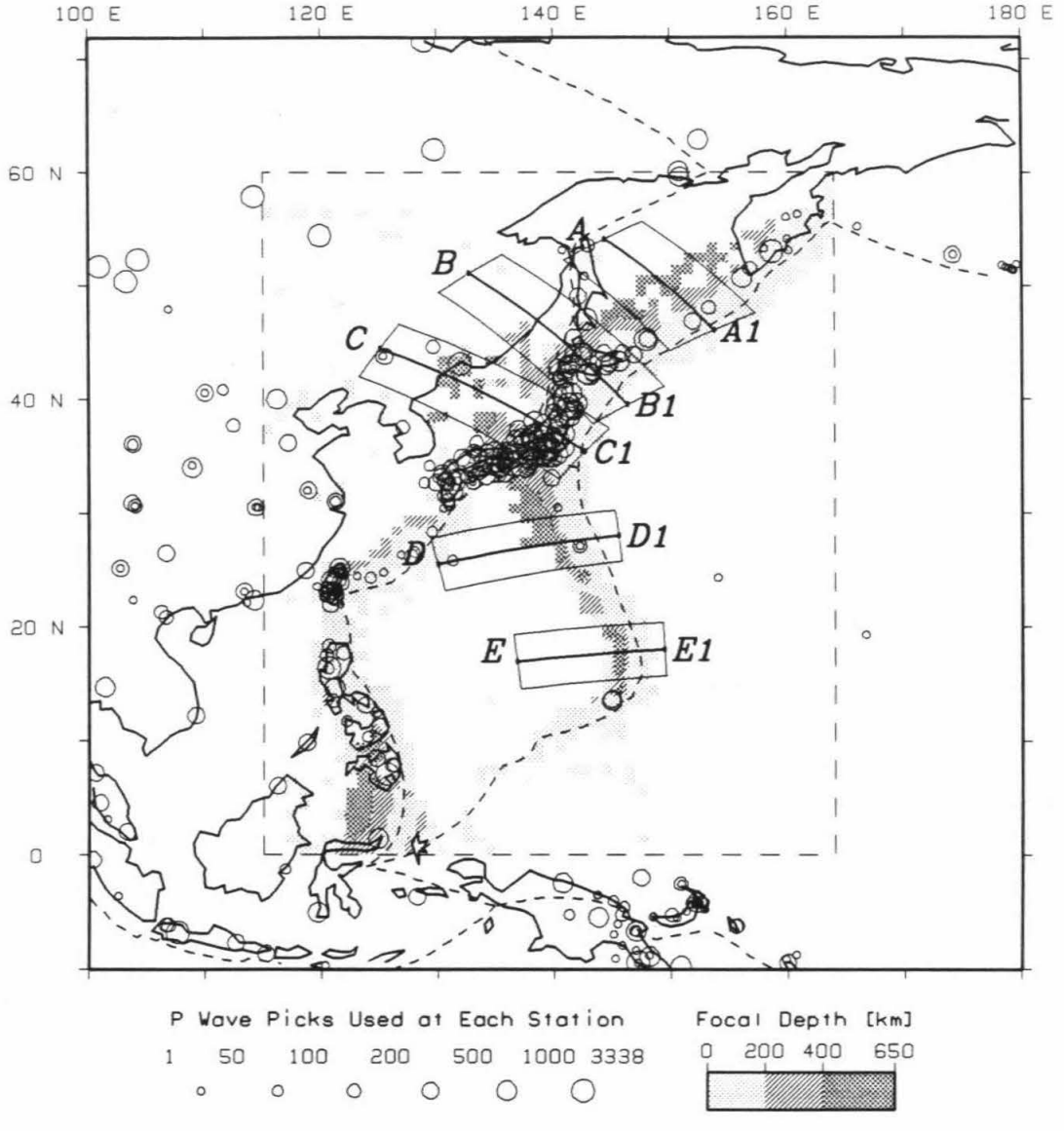

Figure 2.1. Index map around Island Arcs of the Northwest Pacific. The stations are circles, with their sizes indicating the number of P wave picks used. The events used are represented by the shaded areas located within the dashed box. The small boxes with labels "A" to "E" cover the locations of stacked vertical slices along the trench in Figures 2.16 and 2.17, and the solid lines in the middle show the locations of vertical slices in Figure 2.15.

2.2.1 Uncertainty in source locations

The uncertainty in source locations is of concern, because the velocity heterogeneity associated with a subduction zone can be quite large. The hypocenter uncertainty of teleseismically located events is usually less than 20 km [e.g., Spencer and Engdahl, 1983]. Barazangi and Isacks [1979] show that for earthquakes deeper than 50 km the location based on teleseismic data shows no substantial bias or distortion of the spatial distribution. This conclusion is supported by Nieman *et al.* [1984] with theoretical computations. The ISC earthquake locations, particularly for the deep events, are generally in good agreement with other more careful determinations (e.g., Hirahara, 1981; Giardini and Woodhouse, 1984; Engdahl and Gubbins, 1987; Bock, 1987). A comparison of focal depths determined by ISC vs. PDE (Preliminary Determination of Epicenters) by NEIS (National Earthquake Information Service) in Figure 2.2 indicates that the focal depth discrepancy between these agencies is usually less than 30 km for events deeper than 100 km. Note that the PDE has a fixed focal depth at 33 km for a series of events which assumably have relatively poor station coverage. In addition, there is no obvious decrease in the focal depth discrepancy by going to earthquakes of higher magnitude.

In the northwest Pacific region there are stations above most of the events which give good focal depth control. In the next chapter, we combined source relocation into the iterative velocity inversion in the Tonga region. The maximum source mislocation is found to be about 5 km for most intermediate and deep-focus events with station coverage comparable to those used for this

Figure 2.2. Example of discrepancy in focal depths. The two panels show focal depths given by PDE and ISC for some events in the 1977-1982 time period. Events in the top panel a) are of magnitude greater than 4.5, while events in the bottom panel b) are of magnitude greater than 5.5.

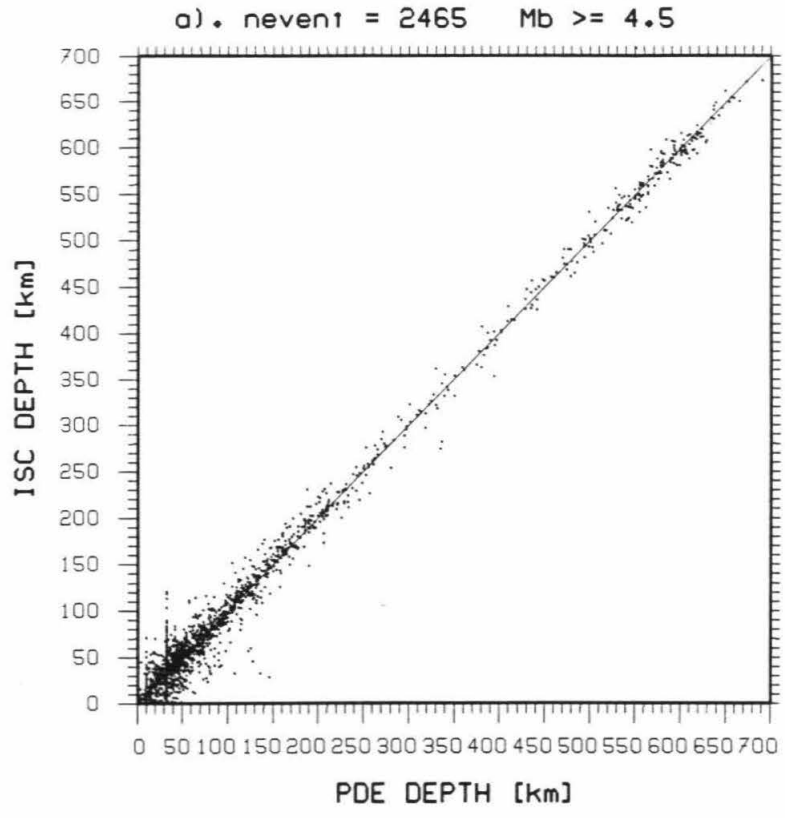
a). nevent = 2465 Mb >= 4.5
ISC DEPTH [km]
PDE DEPTH [km]
0 50 100 150 200 250 300 350 400 450 500 550 600 650 700

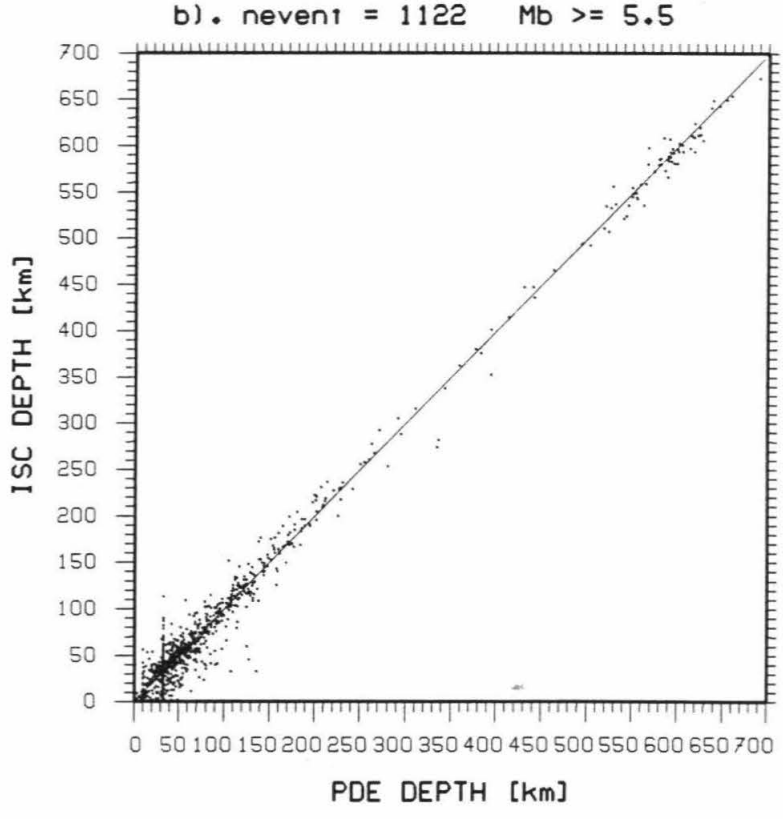
b). nevent = 1122 Mb >= 5.5
ISC DEPTH [km]
PDE DEPTH [km]
0 50 100 150 200 250 300 350 400 450 500 550 600 650 700

study. The two block sizes used in this study are $1^\circ \times 1^\circ \times 50$ km and $2^\circ \times 2^\circ \times 50$ km, which are much larger than average uncertainty in source locations.

One of the greatest difficulties in source relocation is that there is no a priori knowledge of the three-dimensional velocity structure. Previous slab inversions which involve source relocation generally invert for source locations and slab structures simultaneously [Hirahara, 1977, 1981; Hirahara and Mikumo, 1980; Spencer and Gubbins, 1980; Spencer and Engdahl, 1983; Roecker, 1985; and Engdahl and Gubbins, 1987]. We would like, in an ideal case, to invert the system iteratively and calibrate both travel time residuals and path lengths for source locations and perturbations of ray paths by a three dimensional ray tracer after each iteration. With a large data set, such as the one used in this study, however, it is currently impractical to do this.

As a first-order attempt, we use a ray tracer based on a one-dimensional velocity model and assume that the ray paths are fixed in order to make the computation feasible. Consequently, no source relocation is involved in this study since the original ISC location is also based on the one-dimensional JB velocity model. We attempted to select those events that are relatively well-located. First, we eliminated all events shallower than 60 km, since they usually have large location uncertainties. Secondly, each selected event has to be observed by more than 50 stations in the model region (the total number of stations used for source location is much greater), to ensure a wide aperture for source location. Thirdly, we iteratively removed average travel times, or statics, at stations and sources. The station statics represent near station

heterogeneities, while the removal of source statics tends to reduce the effect of depth mislocation. The fact that the P and S wave images from the current inversions correlate well in most parts of the upper mantle indicates that the effect of source mislocations is small, since the S wave data were not used in ISC hypocentral determinations.

2.2.2 Data corrections

The epicentral distance range of the data goes from nearly zero to about 75° (Figure 2.3), crossing the triplications of travel times caused by velocity discontinuities in the mantle. In order to avoid any artifacts that may be introduced by a cut-off of data over a certain distance range, we keep the picks across triplication ranges, and assume they are all first arrivals. This assumption is justified on the grounds of the lack of a distinctive pattern in the possible ranges of triplications.

The errors with source location are further reduced by data corrections. Some criteria have been imposed on data selection. Firstly, each event has to be observed by more than 50 stations in the region to insure a valid source location. Secondly, travel time residuals larger than 10 sec for P waves or 12 sec for S waves are discarded initially to avoid mispicks (erratic readings of tick marks or phase misidentification, *etc.*). Furthermore, we exclude rays with ratios of residual over path length greater than 12% of the reference slowness at their sources. This exclusion is designed to avoid erratic readings at short distances. A correction for the earth ellipticity is also done following Dziewonski and Gilbert [1967].

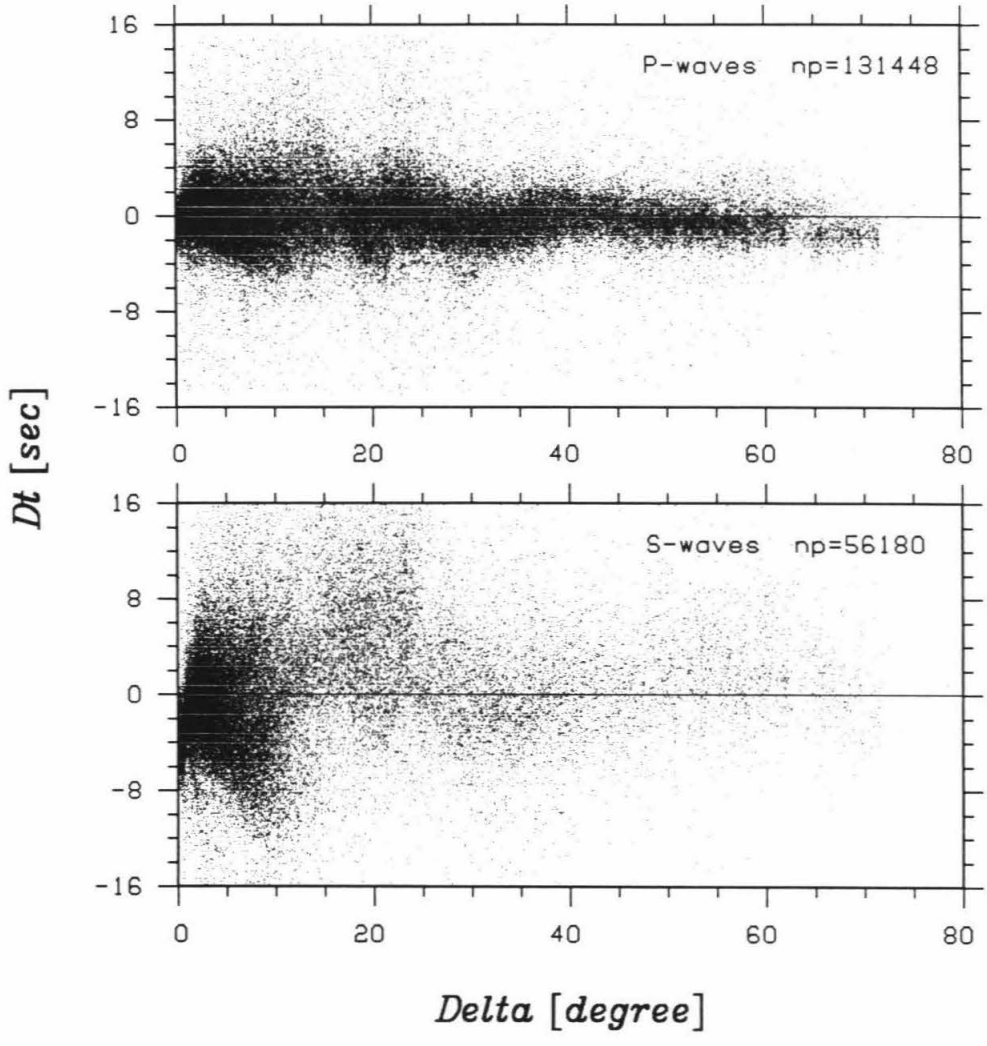

Figure 2.3. Plots of travel time residual vs. distance. The distance distribution of raw data for events of focal depth greater than 60 km. Most of the residuals which distance around the triplication regions are likely to be first arrivals.

In addition, we applied the grouping and sorting procedure, which is described in Section 1.4.2, to exclude picks in the P and S wave data that deviate significantly from the group mediums. The size of the source and station areas, and the threshold of deviation depend on the data. The smaller the size and narrower the deviation threshold, the better the data quality, but the poorer the ray coverage. The distributions of the data sets over epicentral distance and deviation from the group medium are shown in Figure 2.4. After some experiments, it was decided to take the group area size as $1^\circ \times 1^\circ \times 25$ km for both P waves and S waves. For the threshold of deviation, we first exclude all groups containing single rays. For P waves, picks were included with less than 1.2 second deviation in two-ray groups, less than 1.6 second in three-ray groups, and less than 2.0 second in groups with more than three rays. For S waves, the corresponding thresholds are 2.5, 3.2 and 4.0 seconds for groups with two rays, three rays and more than three rays, respectively.

This grouping and sorting process cuts off about 28% of P wave picks and about 32% of S wave picks. In return, the high-frequency noise in data is greatly reduced. In Section 2.5, images inverted with and without the grouping and sorting procedure are shown to illustrate its trade-off with the coverage. Estimations of resolution and noise level in Sections 2.3 and 2.4 are carried out on data sets with the sorting.

We have corrected for the local heterogeneity near stations and sources by iteratively removing the statics at stations and sources respectively, when the number of rays is more than eight. Even though this procedure eliminates the absolute calibration of anomalies, it is beneficial to remove event statics since

Figure 2.4. The plots show P waves (top) and S waves (bottom) travel time residuals, which are with respect to the group mediums and distributed over time and epicentral distance. The number at the peak of each plot indicates the maximum number of residuals. Residuals in the shaded areas are excluded during the grouping and sorting procedure.

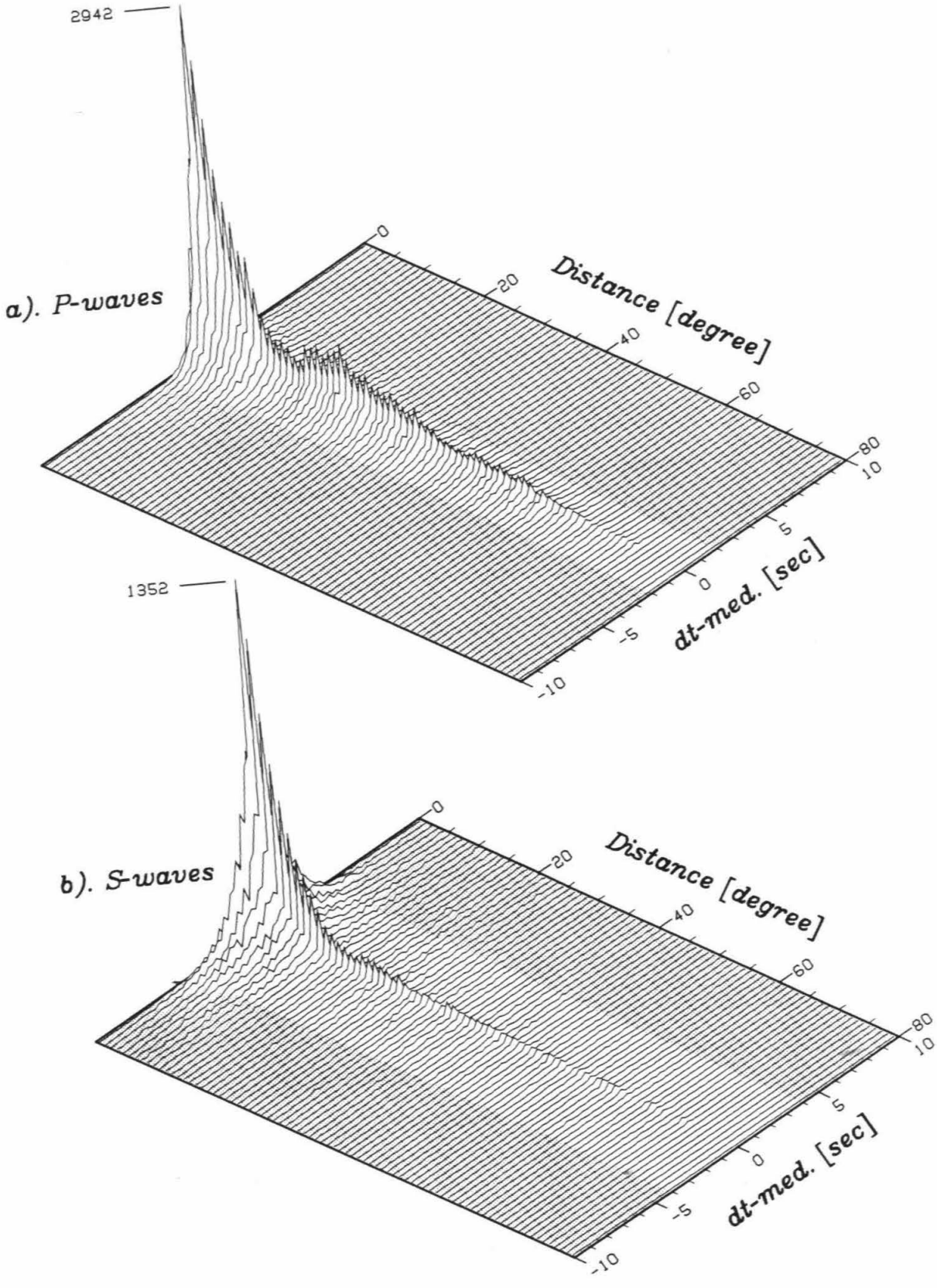
2942
a). P-waves
0
20
40
60
80
Distance [degree]
10
5
0
-5
-10
dt-med. [sec]
1352
b). S-waves
0
20
40
60
80
Distance [degree]
10
5
0
-5
-10
dt-med. [sec]

their removal enhances the contrast between the slab and its surroundings, and it will also eliminate systematic errors (e.g., focal depth errors) that are likely to contaminate the inverted results. As shown is Figure 2.5, the maps of station statics between P and S waves are generally similar and correspond well to surface tectonic patterns. The maps of event statics will be meaningful only when they are plotted at each depth range, to account for their vertical distribution.

2.2.3 Inversion method

An iterative inverse which is modified from the scheme by Comer and Clayton, as summarized by equation (1.8), is used. The model space is divided into resolution blocks of assumably constant velocity perturbations. Smaller block size means higher resolution power, but lower ray coverage and more model parameters. Since we do not know a priori the proper block size, we have performed inversions on two grids of different block sizes. The first grid has dimensions of $2^\circ \times 2^\circ \times 50$ km, while the second has dimensions of $1^\circ \times 1^\circ \times 50$ km. As shown later, these two grids resulted in velocity models very consistent with one another; hence, we consider the block sizes chosen to be adequate. As mentioned earlier, we assume all the ray paths are fixed in our computation. Because the problem is a two-point problem rather than a shooting problem, i.e., both the source and receiver for each ray are known and fixed, the fixed-path assumption probably holds true without large error, at least for the regional first arrivals and the block size used here.

Figure 2.5. Station statics. Dashed curves denote plate boundaries, and open barbed lines indicate trenches above subduction zones. The average travel times of the P waves (left panel) is generally similar to that of the S waves (right panel). The statics are fast along Kurile, Japan, Izu-Bonin trenches, and slow in the back arc regions. On the continental East Asia, P waves are fast while S waves are slow. China is slower than the Siberian Shield. The amplitude of the S wave statics is about double that of P wave statics.

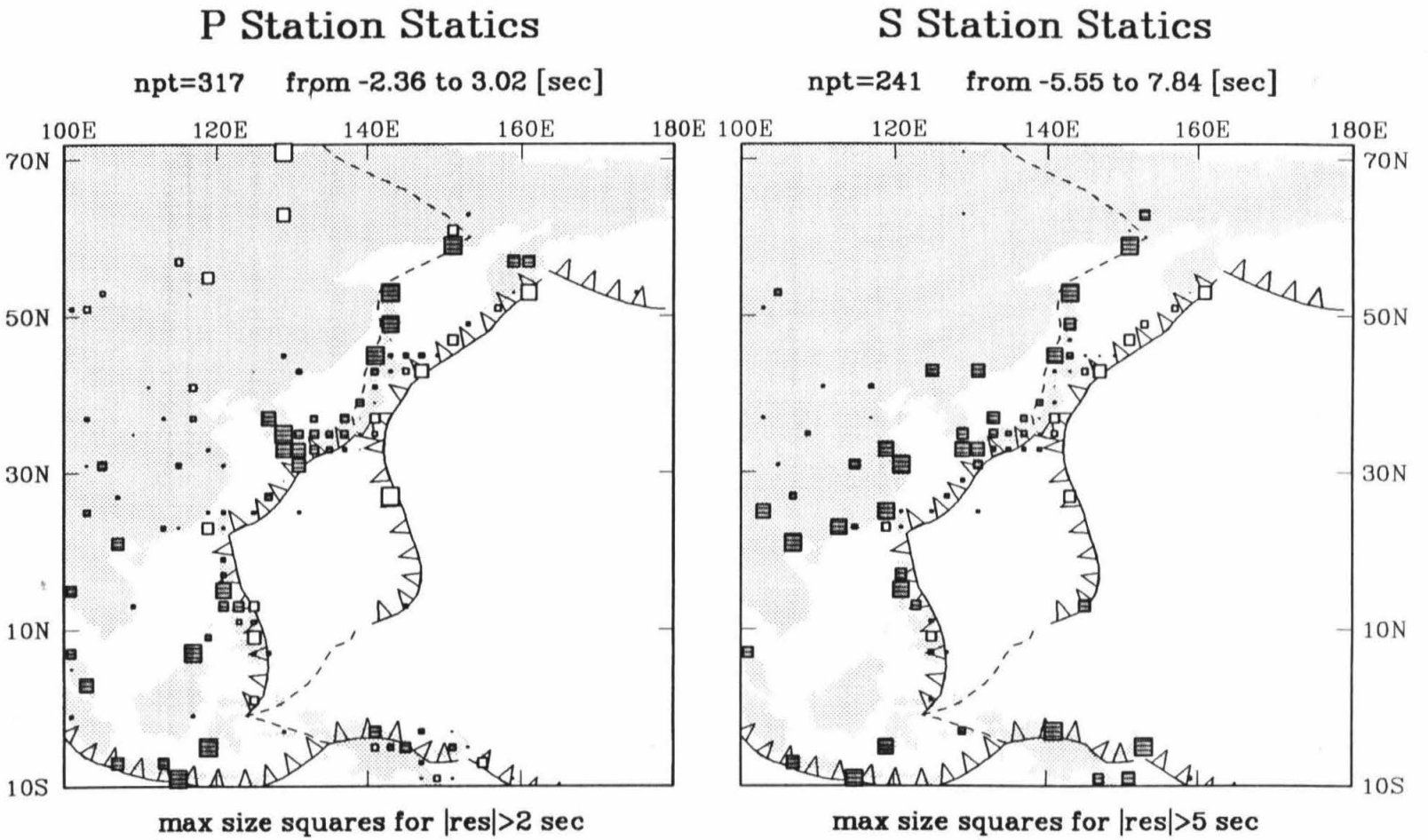
P Station Statics
npt=317 from -2.36 to 3.02 [sec]
S Station Statics
npt=241 from -5.55 to 7.84 [sec]
100E
120E
140E
160E
180E
70N
50N
30N
10N
10S
max size squares for |res|>2 sec
max size squares for |res|>5 sec
KEY: □ negative (fast); ■ positive (slow).

2.3 Estimation of Resolution by Impulse Tests

We have discussed the evaluation of resolution for the inverse problem in Section 1.5. In this section, we focus on the "impulse test," an approximate approach to computing the resolution matrix. The approach is based on the following test. A synthetic model is constructed with a slowness perturbation at the location of interest, such as in the subduction zone. The travel time residual of each data ray is then computed by ray tracing through the model, and is used in the subsequent inversions. Two examples of the comparison between the synthetic models and the corresponding solutions are shown in Figure 2.6. In the first case (Figure 2.6a), the high velocity model has a low dip angle, which is usually difficult to resolve with teleseismic rays alone. Our generally satisfactory resolution is due to the use of regional picks ($<25^\circ$) and deep earthquakes. The second model (Figure 2.6b) is under the central Izu-Bonin trench where seismicity bends to flatten around 550 km depth. This model has a rather unusual shape, combining a vertical high-velocity column (not a slab) which bends abruptly in the middle, and a vertical column which bends gradually in the middle. The inversion has properly recovered the shape of the model, but has underestimated the amplitudes in some places, particularly in the lower mantle. Generally, the resolution for patterns is sharp, but the resolution for amplitude is low at depth. Notice that the removal of layer mean velocities in the right panel of Figure 2.7b enhances the coherency of the pattern. This kind of removal was used for data images because we are mainly interested in the relative velocities.

Figure 2.6. Comparison of synthetic models with corresponding solutions. The left panels in a) and b) are the synthetic models. The middle and right panels in a) are the P and S wave solutions, respectively. Both the middle and right panels in b) are the P wave solution, and the right one has the mean layer velocities removed. The stars denote earthquake foci, and the slowness perturbations are contoured with an interval of 2%. The black areas are blocks with less than 5 passing rays, defined as uncovered. In the covered areas, the white areas are fast, cross-hatched areas are slow, and dotted areas are of less than one half of the contour interval, or 1.0%, of slowness perturbations. As shown, the patterns of the models are recovered well by the inversions, while the amplitudes are underestimated in some places.

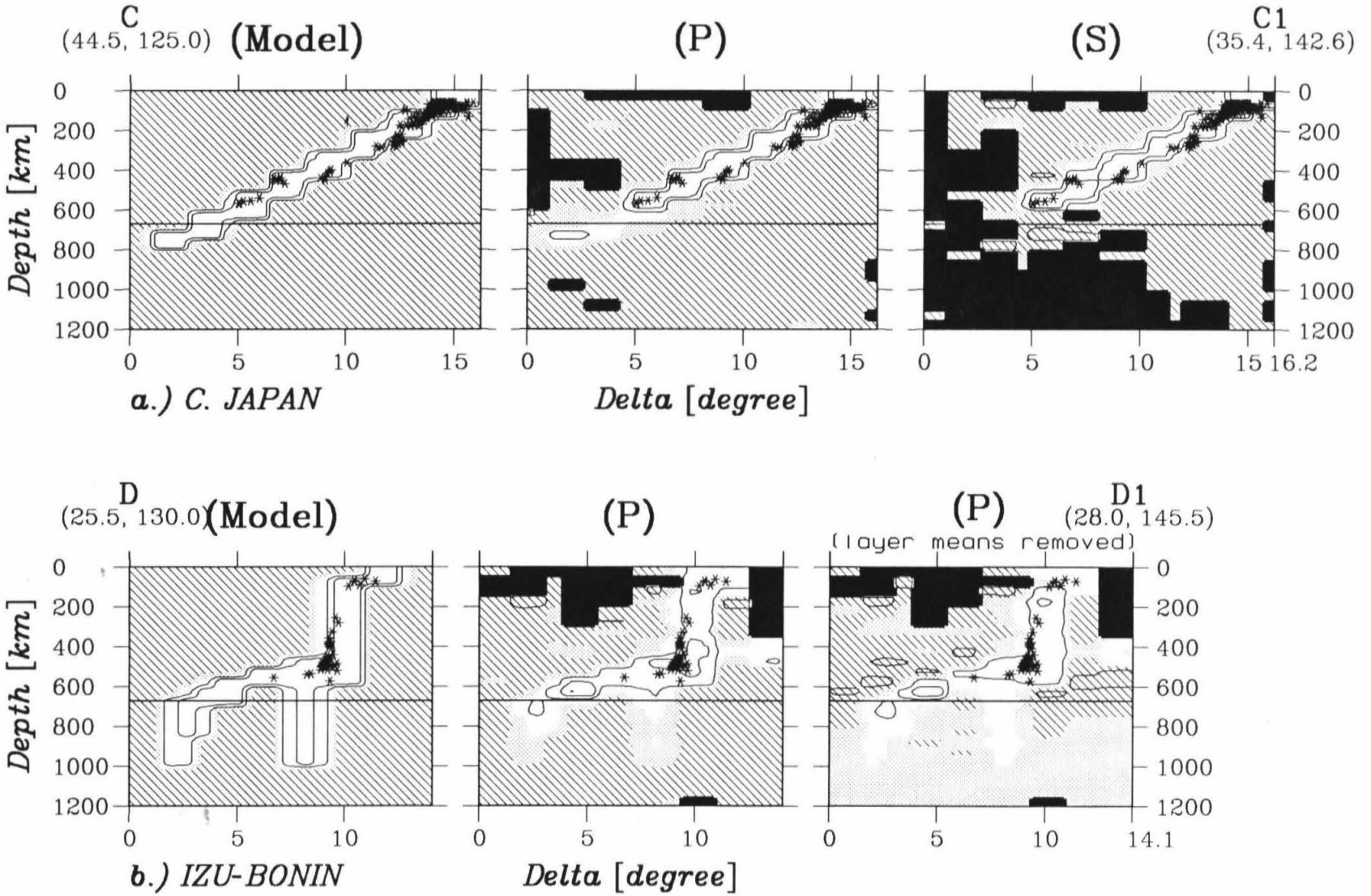
C
(44.5, 125.0) (Model)
(P)
(S)
C1
(35.4, 142.6)
Depth [km]
0
200
400
600
800
1000
1200
0
5
10
15
16.2
a.) C. JAPAN
Delta [degree]
D
(25.5, 130.0) (Model)
(P)
(P)
D1
(28.0, 145.5)
(layer means removed)
14.1
b.) IZU-BONIN
Delta [degree]

The idea behind the above test leads to our "impulse test" approximation. To "impulse test" the resolution for a particular block, we first construct a synthetic model with unity slowness perturbation at the block and zero elsewhere. The subsequent inversion using data ray paths and residual times generated from the synthetic model results in a column vector which corresponds to the block in the resolution matrix $\mathbf{R}^{(n)}{}_{N\times N}$. The conventional resolution vector for a block is the row vector in $\mathbf{R}^{(n)}{}_{N\times N}$. When $\mathbf{R}^{(n)}{}_{N\times N}$ is symmetric, i.e., when $\mathbf{S}$ is a constant multiplied with an unit matrix, the column vector yielded is the true resolution vector for the block. Even when $\mathbf{R}^{(n)}{}_{N\times N}$ is asymmetric, the diagonal element of the resolution matrix can always be obtained, which can partially indicate the resolution level.

A diagonal element of the resolution matrix provides information about the resolution for the corresponding block, because the sum of all elements of a resolution vector for a given block is unity. When the inverse problem is well resolved, the diagonal elements are large, while off-diagonal ones are small. One can also compare the values of the diagonal elements between different blocks to get an estimate of the relative resolving level. Furthermore, as mentioned by Aki and Richards [1980], the total sum of diagonal elements of a generalized inverse problem is equal to the number of independent model parameters that can be resolved.

The "impulse test" is useful to detect smearing in the image. The smearing will generally take place where rays travel in almost the same direction. The "impulse test" is also used to check the amplitude of the image. In addition, when the model space is large and the resolution is

expected sharp, one can perform many "impulse tests" simultaneously for well separated blocks. In this manner, we have conducted "impulse tests" for all model blocks in this study. As examples, horizontal slices of some "impulse tests" are shown in Figure 2.7. Note that the resolution vectors are generally concentrated over the impulsed blocks, even when the amplitude is of very low value in some cases. Poor resolution usually exist near the edge of the covered area. In general, the resolution of both compressional and shear velocities are quite sharp in most areas of interest. In particular, the resolution for patterns is uniformly satisfactory across the 670 km discontinuity, but the resolution for amplitudes decreases in the lower mantle.

Figure 2.7. Examples of the resolution "impulse tests." These are map views of some "impulse tests" for P and S waves on the $2^\circ \times 2^\circ \times 50$ km grid at depth 300-350 km, 600-650 km and 750-800 km. Heavy solid curves are coastal lines and plate boundaries. Open barbed lines denote trenches above subduction zones. Cross-hatched boxes are the impulsed blocks, blank areas are uncovered, and contour interval is 0.1. Each panel is the sum of the column vectors of resolution matrix for the impulsed blocks. Note that the pattern associated with each impulsed block is usually concentrated, even though the amplitude is low in many cases.

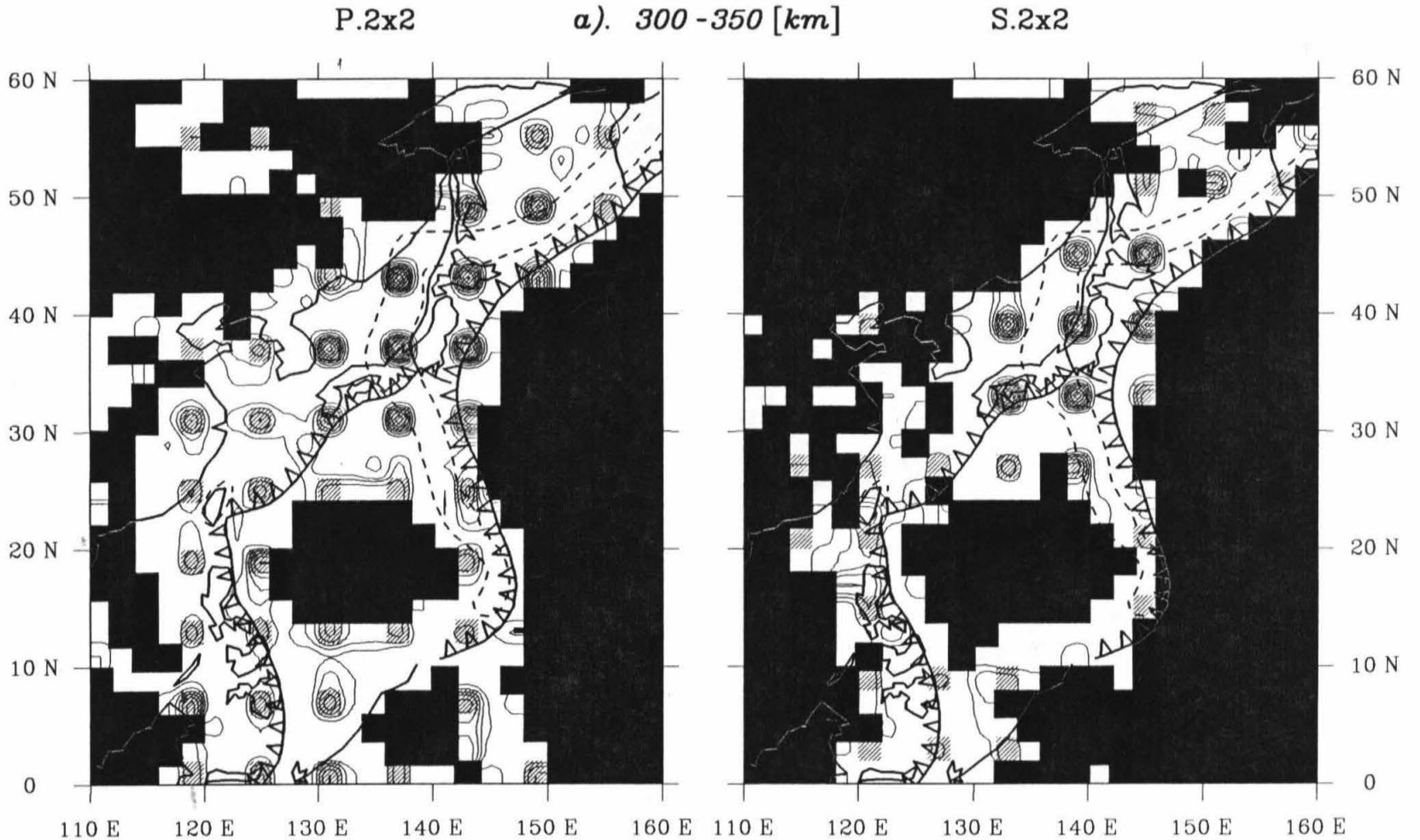
P.2x2
a). 300 - 350 [km]
S.2x2
60 N
50 N
40 N
30 N
20 N
10 N
0
110 E
120 E
130 E
140 E
150 E
160 E

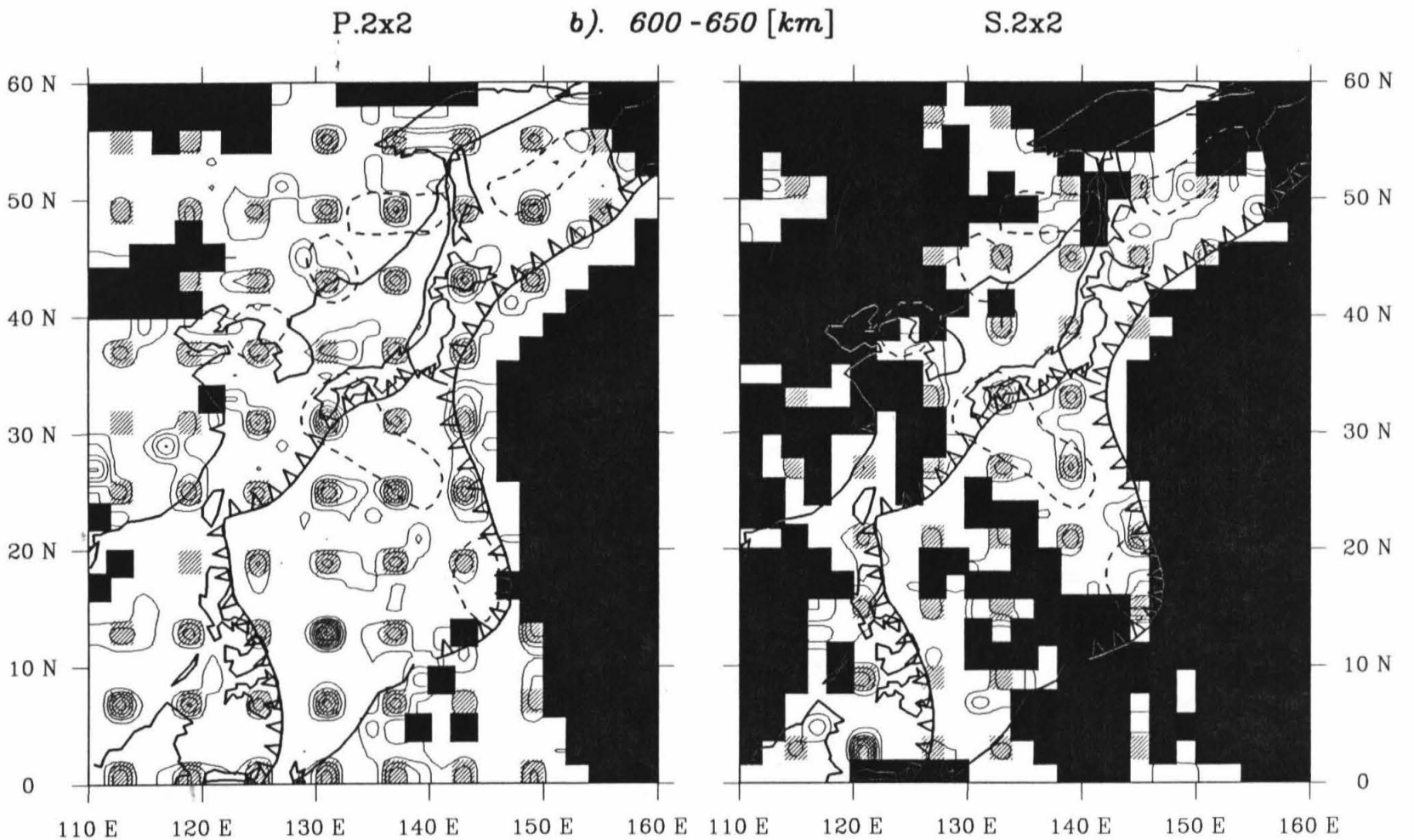
P.2x2
b). 600 - 650 [km]
S.2x2
60 N
50 N
40 N
30 N
20 N
10 N
0
110 E
120 E
130 E
140 E
150 E
160 E

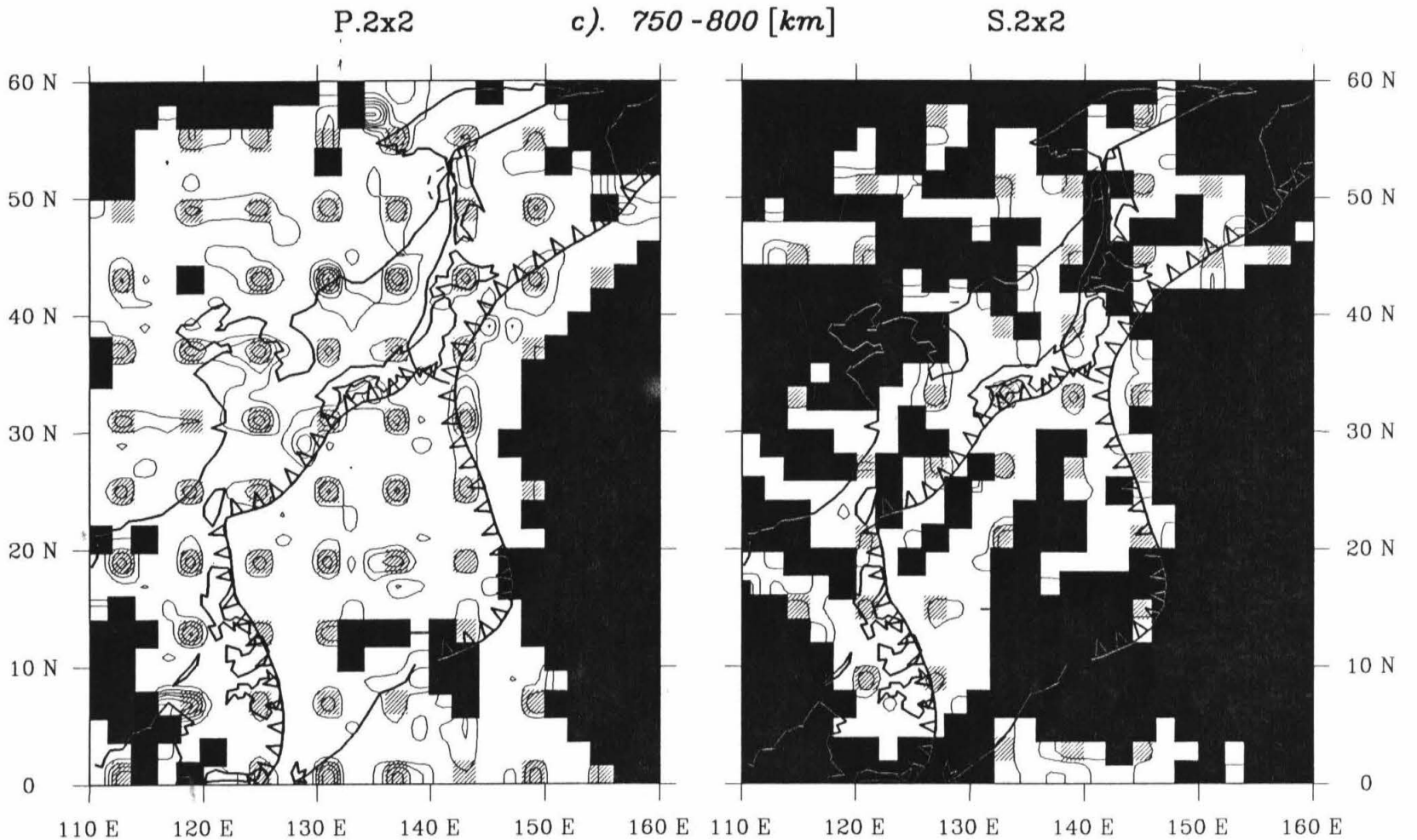
P.2x2
c). 750 -800 [km]
S.2x2
60 N
50 N
40 N
30 N
20 N
10 N
0
110 E
120 E
130 E
140 E
150 E
160 E

2.4 Estimation of Error and Error Propagation

The noise in the image comes from the data noise and the propagation of noise through the inversion. Following the discussion in Section 1.6, the effect of each data processing step, including corrections, sorting, and inversion, can be displayed by the relation between the block size and the average group variance. As shown in Figure 2.8, the efficiency of each correction is judged by its reduction of the average variances at small block sizes. For example, the grouping and sorting procedure considerably improves the data quality, because it largely reduces the high frequency noise of the data with little effect on the long-wavelength variations. On the other hand, the statics terms and the inverted image contain much of the long-wavelength variations, which are usually the informative part of the data relating to mantle heterogeneities. The number of inversion iterations is determined experimentally, by examining plots of the type shown in Figure 2.8. In the current study, 30 and 20 iterations, respectively, are used for inverting P and S wave data; while 50 iterations are used for data sets without the grouping and sorting.

According to equation (1.11), the random noise levels in the images are approximately 25% and 17% for P and S waves, respectively, at $2^\circ \times 2^\circ \times 50$ km grid, and 20% and 11% for P and S waves, respectively, at $1^\circ \times 1^\circ \times 50$ km grid. A finer grid is expected to result in lower noise level. The smaller values of S wave noise level in comparison with that of P wave are compensative to the much poorer S wave resolution. Based on these estimates of variance, we have computed the model covariance matrix following Davies

Figure 2.8. Relation between the average group variance and the grouping area size. The group variance is for a group of residuals for rays of the same source and station areas. The curves are for the P waves (top) and S waves (bottom) at different stages. The vertical dashed line at the left indicates the inverse block size of the $1^\circ \times 1^\circ \times 50$ km. The top of the shaded zone is at the variance of the data just before inversion at the inversion block size, representing the noise level. Note that the grouping and sorting procedure considerably reduces the noise level, and the inversion has absorbed a large portion of the long-wavelength variations of travel time residuals.

a). P-waves

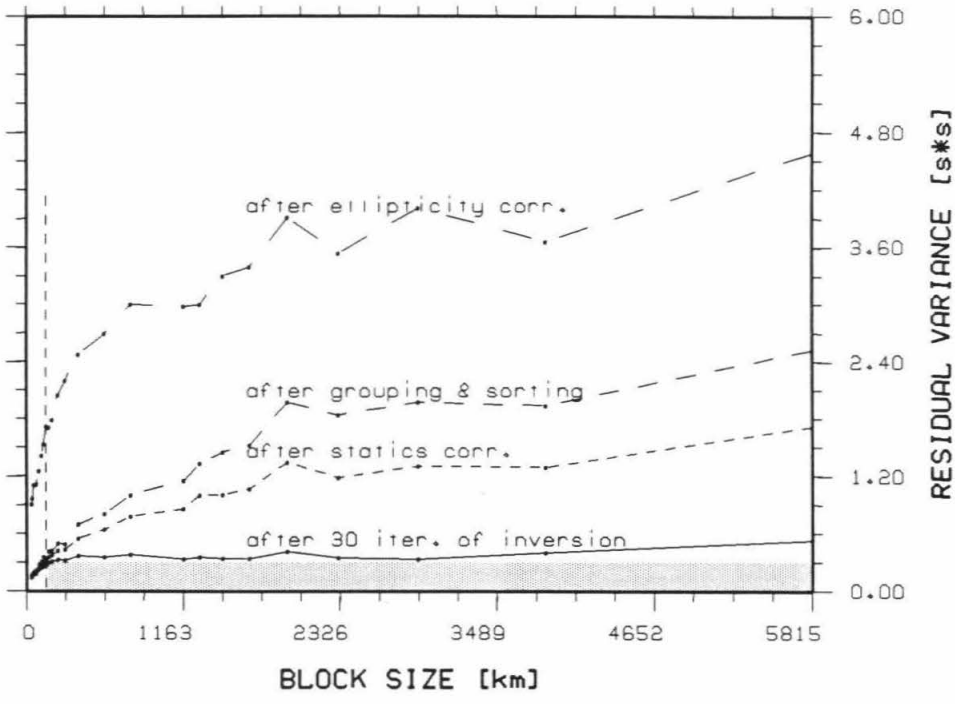

b). S-waves

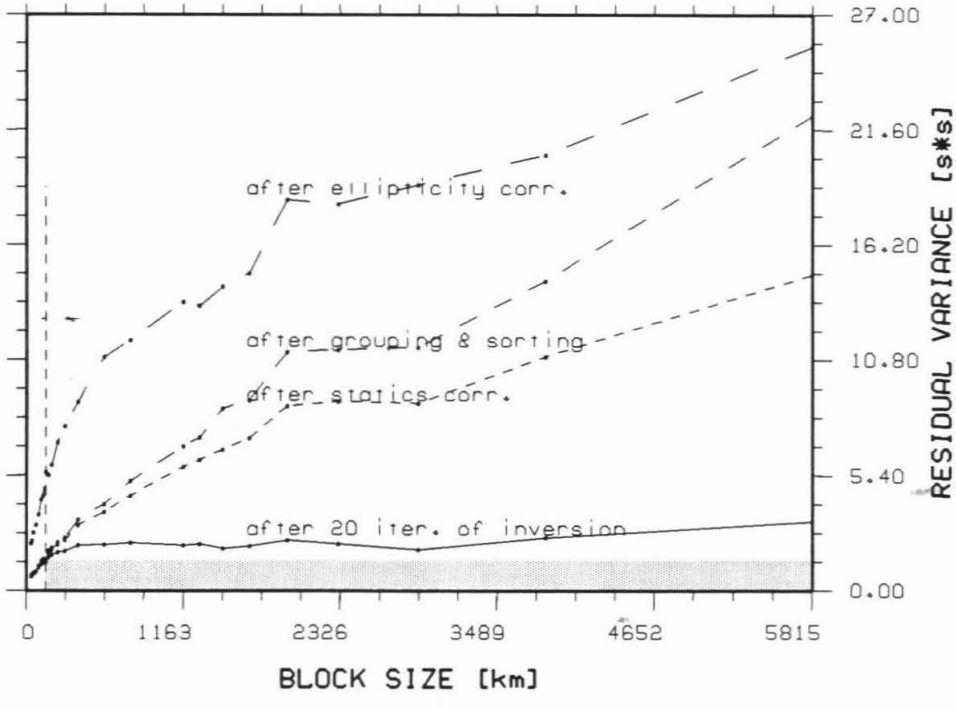

and Clayton [1987], to evaluate the noise propagation through the inversion. Basically, a large number of inversions are performed using the data ray paths but synthetic travel time residuals. The residuals are randomly generated from a distribution which is similar to the data distribution in shape, but with the variance obtained above. The inversions give large number of slowness perturbations for each model block. The variance of the perturbations for a block then represents the variance of model noise corresponding to noise in travel time residuals.

Figure 2.9 shows an example of a vertical slice of the P wave image of data in $2^\circ \times 2^\circ \times 50$ km grid, with cutoff of parts of the image that have slowness perturbations below the level of the propagated noise. As shown, most anomalous features in the figure, such as the slab-like fast features, stand above the noise level. On the other hand, of course, a real signal could have an amplitude below the noise level. The computation of the model covariance matrix suggests that most anomalies in our images are reliable, since they are from the long wavelength, or systematic, portion of the data.

Another issue is about the systematic error. We argue that such error in the data probably are sufficiently small because, firstly, all picks used are first arrivals within short to intermediate distances and all events have dense station coverage (Figure 2.1). Secondly, all earthquakes used have focal depth greater than 60 km, and therefore bear less influence from source mislocations, crustal effects and triplications. Thirdly, the corrections applied to the data, especially the grouping and sorting procedure, further ensure the data quality. Finally, the statics terms, which could also contain error with focal depth, are

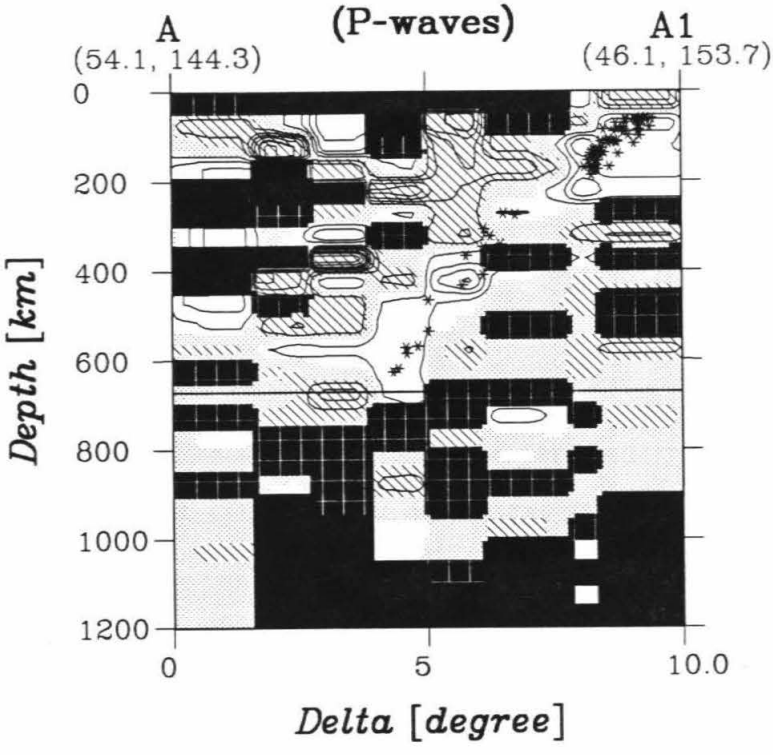

Figure 2.9. Vertical slices with cutoff from covariance matrix. This vertical slice, identical to that shown in Figure 2.15a, is of the P wave image under the Kurile trench. The plotting convention follows that used in Figure 2.6, and the contour interval is 1% now. Black areas with white cross lines denote blocks whose image amplitudes are below the noise level, which is estimated by computing the model covariance matrix.

removed iteratively for both stations and events.

We define the data variance reduction as

$$\sum_{j=1}^{M}(t_j - p_j)^2 \;/\; \sum_{j=1}^{M} t_j^2, \tag{2.1}$$

where t_j and p_j denote data and model prediction of travel time residuals, respectively, for the j-th ray. For the current work the data variance reductions, in the final inversion stage alone, are 58% and 59% for P and S waves, respectively, at $2^\circ \times 2^\circ \times 50$ km grid, and 48% and 51% for P and S waves, respectively, at $1^\circ \times 1^\circ \times 50$ km grid. The distributions of the remaining residuals after inversion are sharper and more Gaussian-like in comparison to that before inversions, indicating that much of the systematic information has been taken into the images. For instance, Figure 2.10 shows the residual histograms of data sets without application of the grouping and sorting procedure.

A smaller block size is expected to result in a higher variance reduction, because it means more model parameters. Of course, the values of variance reduction here merely show the relative fitting level of the inverted models. The efficiency of the inversion, however, is obscure from those values, because the presence of random noise has set an upper limit for any inversion technique. For this reason the group variance vs. area size graph shown in Figure 2.8 is a much better illustration of the efficiency of the inversions. A comparison of the variance curves in Figure 2.8 before and after the inversions indicates that the inverted models in this study have absorbed most of the long-wavelength and systematic components of the data.

Figure 2.10. These residual histograms are of P and S wave data without applying the grouping and sorting procedure. a) and e) are of raw data with ellipticity corrections; b) and f) are of data after other corrections and before final inversions; c) and g) are of data after inversions on $1^\circ \times 1^\circ \times 50$ km grid; and d) and h) are of data after inversions on $2^\circ \times 2^\circ \times 50$ km grid. On the upper right corner of each plot, the number of residuals and their average and standard deviation are printed. Notice that the inversions reduce the standard deviations of the residuals, and the distributions after inversions are narrower and more Gaussian-like.

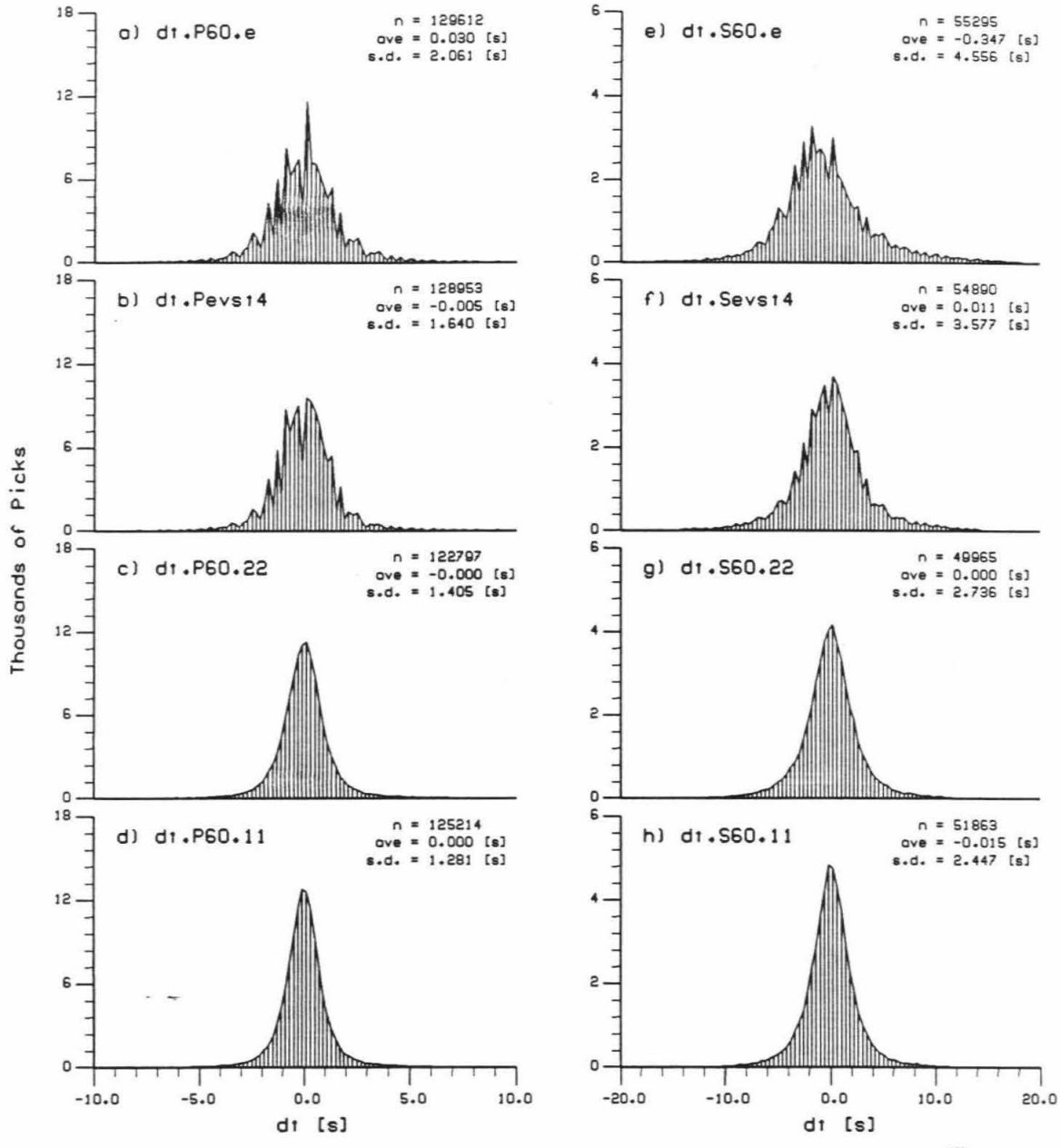
a) dt.P60.e
n = 129612
ave = 0.030 [s]
s.d. = 2.061 [s]
b) dt.Pevs14
n = 128953
ave = -0.005 [s]
s.d. = 1.640 [s]
c) dt.P60.22
n = 122797
ave = -0.000 [s]
s.d. = 1.405 [s]
d) dt.P60.11
n = 125214
ave = 0.000 [s]
s.d. = 1.281 [s]
e) dt.S60.e
n = 55295
ave = -0.347 [s]
s.d. = 4.556 [s]
f) dt.Sevs14
n = 54890
ave = 0.011 [s]
s.d. = 3.577 [s]
g) dt.S60.22
n = 49965
ave = 0.000 [s]
s.d. = 2.736 [s]
h) dt.S60.11
n = 51863
ave = -0.015 [s]
s.d. = 2.447 [s]
Thousands of Picks
dt [s]
dt [s]

2.5 P and S Wave Images

The P and S wave data, with or without the grouping and sorting procedure, are inverted on two different grids. Figure 2.11 shows several horizontal slices on the finer block grid, with data after the sorting. The model coverage decreases from the coarser to the finer block grids, and from data sets without the sorting to data sets with the sorting. In general, the P and S wave anomalies correlate well, as shown in Figures 2.12 and 2.13, respectively, for the images without and with the sorting. The resolution at several depth ranges are inferred from results of the impulse tests shown in Figure 2.7.

There are fast compressional and shear wave anomalies in the image associated with the descending lithosphere inferred from seismicity. Slab anomalies are generally continuous along strike in most parts of the upper mantle, and are often sandwiched by large amplitude slow anomalies on the arc and trench sides in the top several hundred kilometer depth range. P and S velocities correlate well over most of the upper mantle, but are less similar in the lower mantle, probably at least partially due to a decrease of resolution with depth. Anderson [1987b] pointed out that at relative low pressure and high temperature, shear velocity anomalies are expected to be similar to compressional velocity anomalies, since the temperature effect on both the bulk modulus and rigidity is very volume dependent. At high pressure, variations of seismic velocities are smaller and they are due primarily to changes in the rigidity.

Figure 2.11. Horizontal slices of the images on the $1^\circ \times 1^\circ \times 50$ km grid. Slice a) is of the S wave image at 200-250 km depth. Slices b), c) and d) are of the P wave image at 200-250 km, 400-450 km and 600-650 km, respectively. The legend convention is the same as that used in Figures 2.6 and 2.7. The average velocity variation of each layer, given at the top, has been removed. Our interpreted fast slab model at this depth range is indicated in heavy dashed lines, while the entire interpretation down to 800 km depth is pictured in Figure 2.14. Patterns in the P and S wave images generally correlate well. The fast slab-like anomalies associated with the subduction zone and slow anomalies on both sides of slabs are shown.

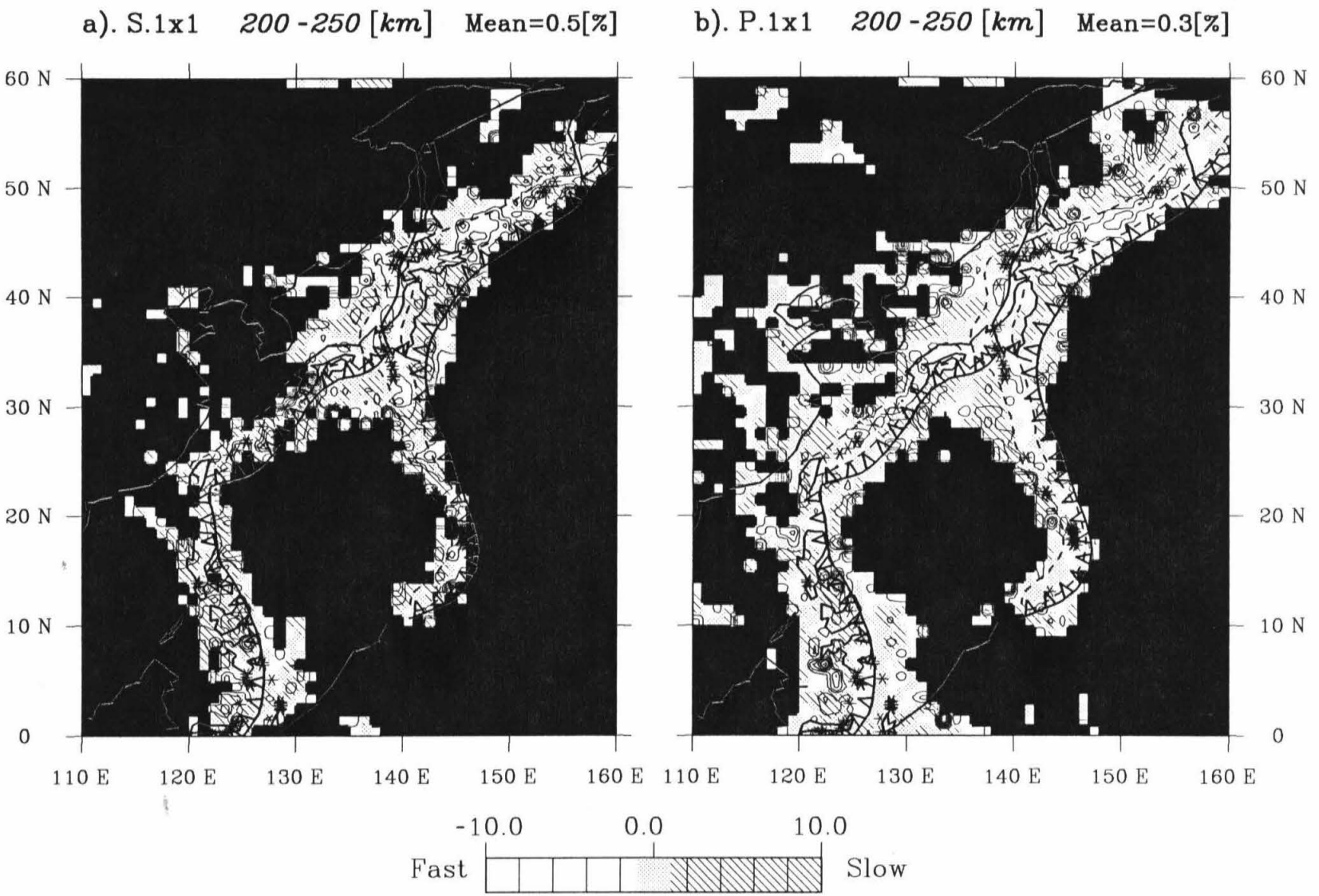
a). S.1x1 200 -250 [km] Mean=0.5[%]
b). P.1x1 200 -250 [km] Mean=0.3[%]
60 N
50 N
40 N
30 N
20 N
10 N
0
110 E
120 E
130 E
140 E
150 E
160 E
-10.0
0.0
10.0
Fast
Slow

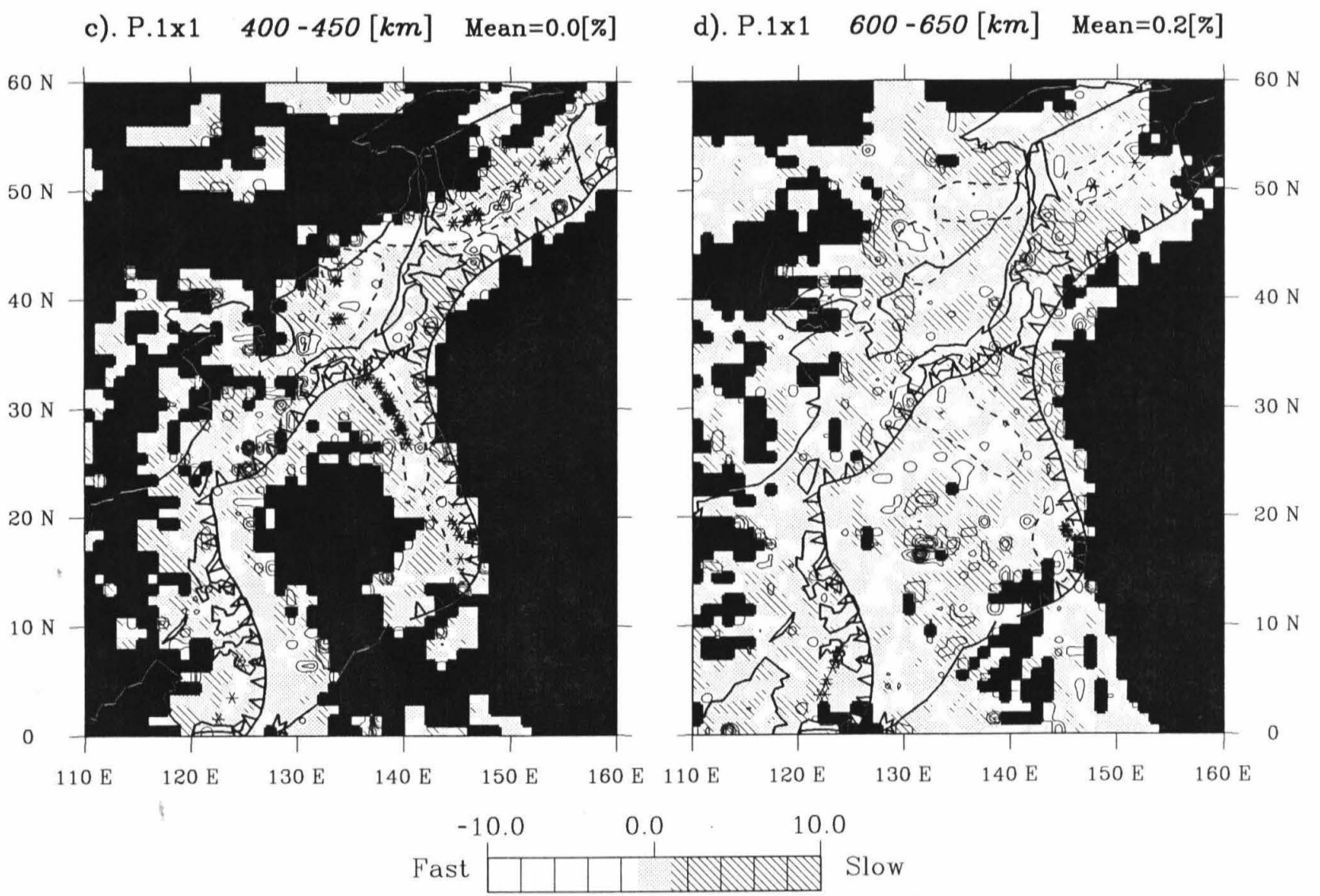
c). P.1x1 400 -450 [km] Mean=0.0[%]
d). P.1x1 600 -650 [km] Mean=0.2[%]
60 N
50 N
40 N
30 N
20 N
10 N
0
110 E
120 E
130 E
140 E
150 E
160 E
-10.0
0.0
10.0
Fast
Slow

Figure 2.12. Horizontal slices of the images on the $2^\circ \times 2^\circ \times 50$ km grid without grouping and sorting. The P (left) and S (right) wave images at each depth range are shown. The plotting convention is identical to that used in Figure 2.11. The anomalous features, especially these which are associated with subduction zones, are somewhat correlated between adjacent panels above 650 km. However, the correlation between adjacent panels becomes much poor below a depth around 650 to 700 km, even though the resolution for patterns is more or less uniform across this depth.

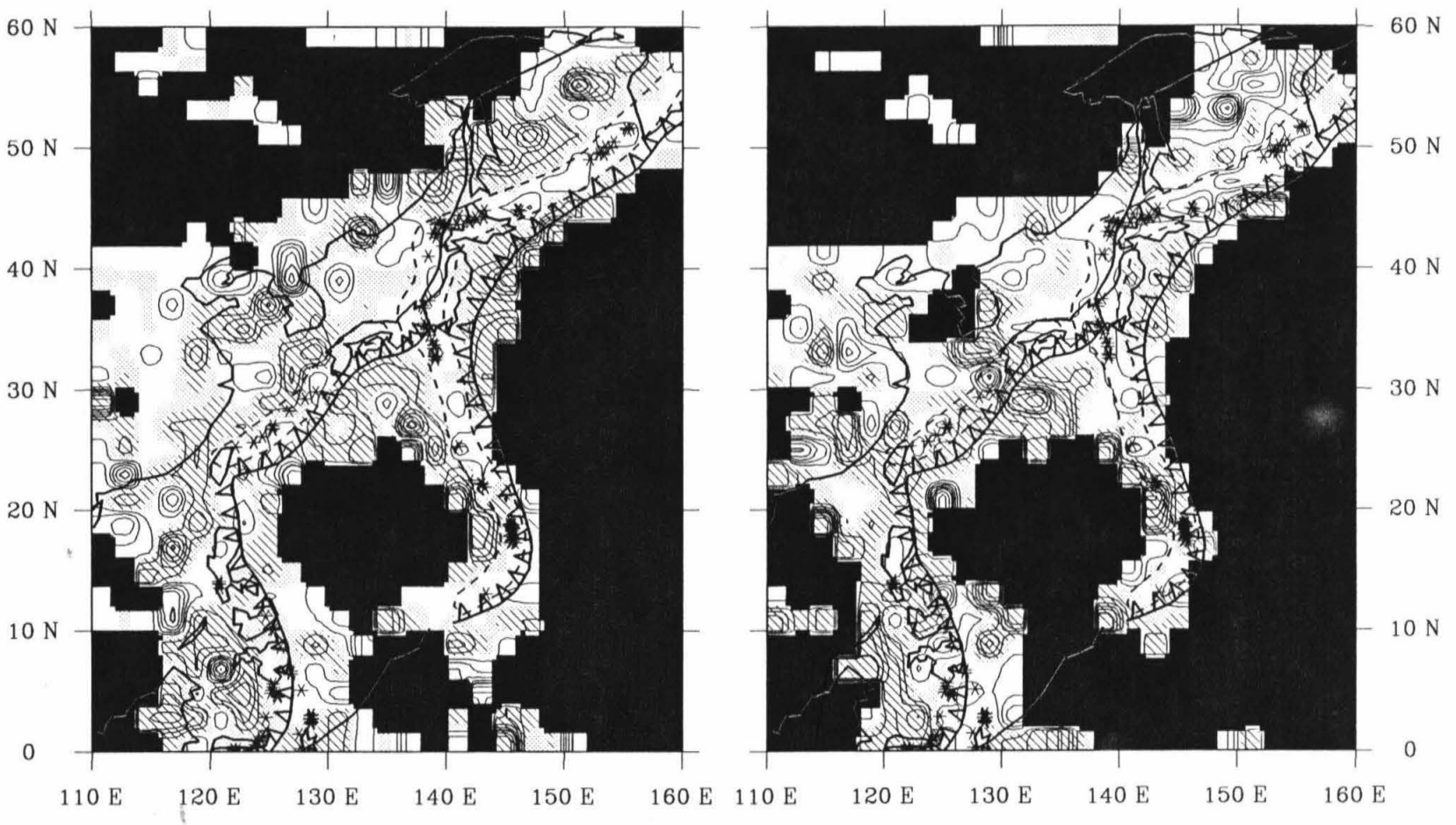
P.2x2 Mean=0.6[%]
200 -250 [km]
S.2x2 Mean=1.5[%]
60 N
50 N
40 N
30 N
20 N
10 N
0
110 E
120 E
130 E
140 E
150 E
160 E

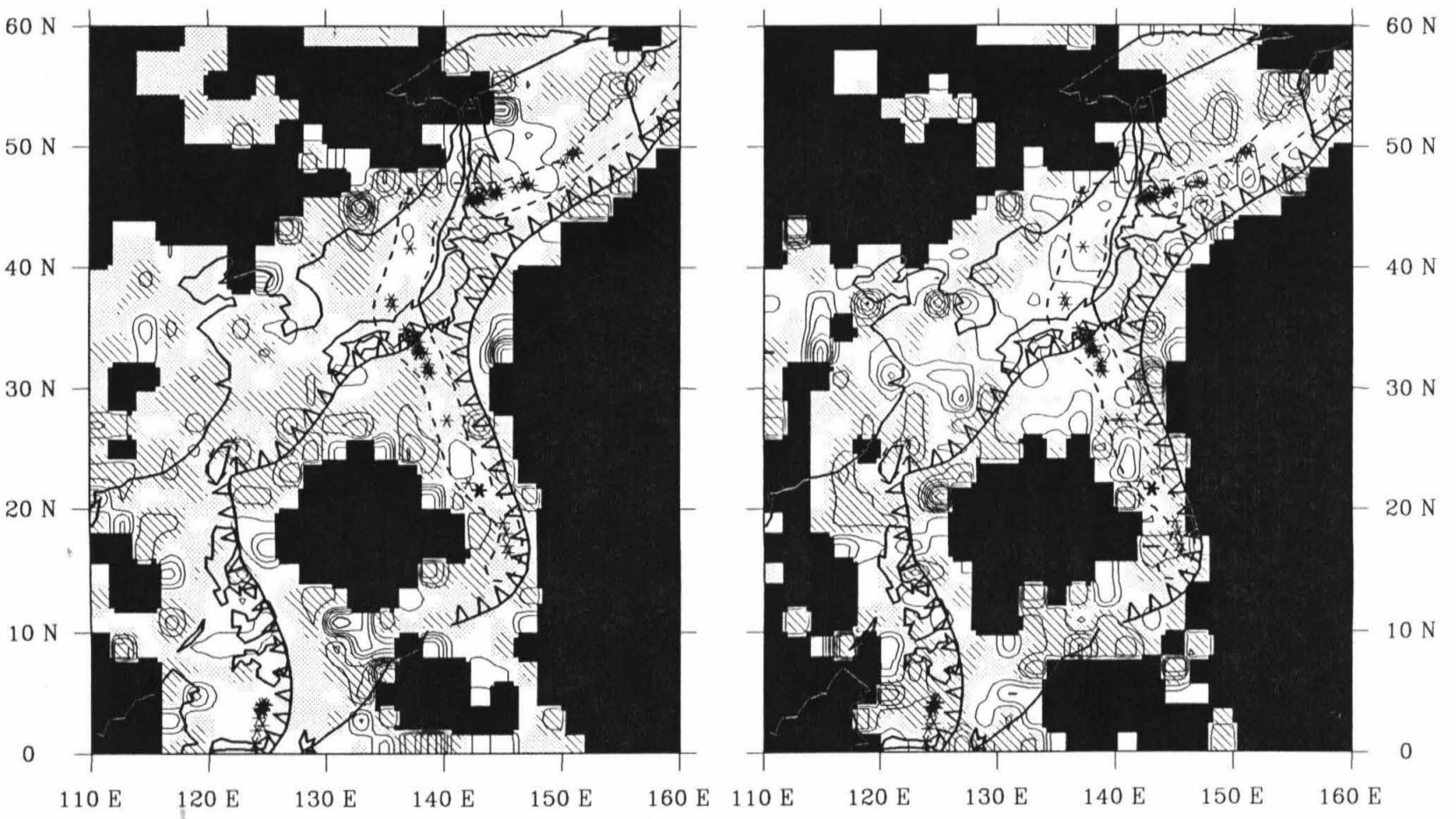
P.2x2 Mean=-0.1[%]
300 -350 [km]
S.2x2 Mean=0.6[%]
60 N
50 N
40 N
30 N
20 N
10 N
0
110 E
120 E
130 E
140 E
150 E
160 E

P.2x2 Mean=-0.0[%]
400 - 450 [km]
S.2x2 Mean=0.4[%]
60 N
50 N
40 N
30 N
20 N
10 N
0
110 E
120 E
130 E
140 E
150 E
160 E

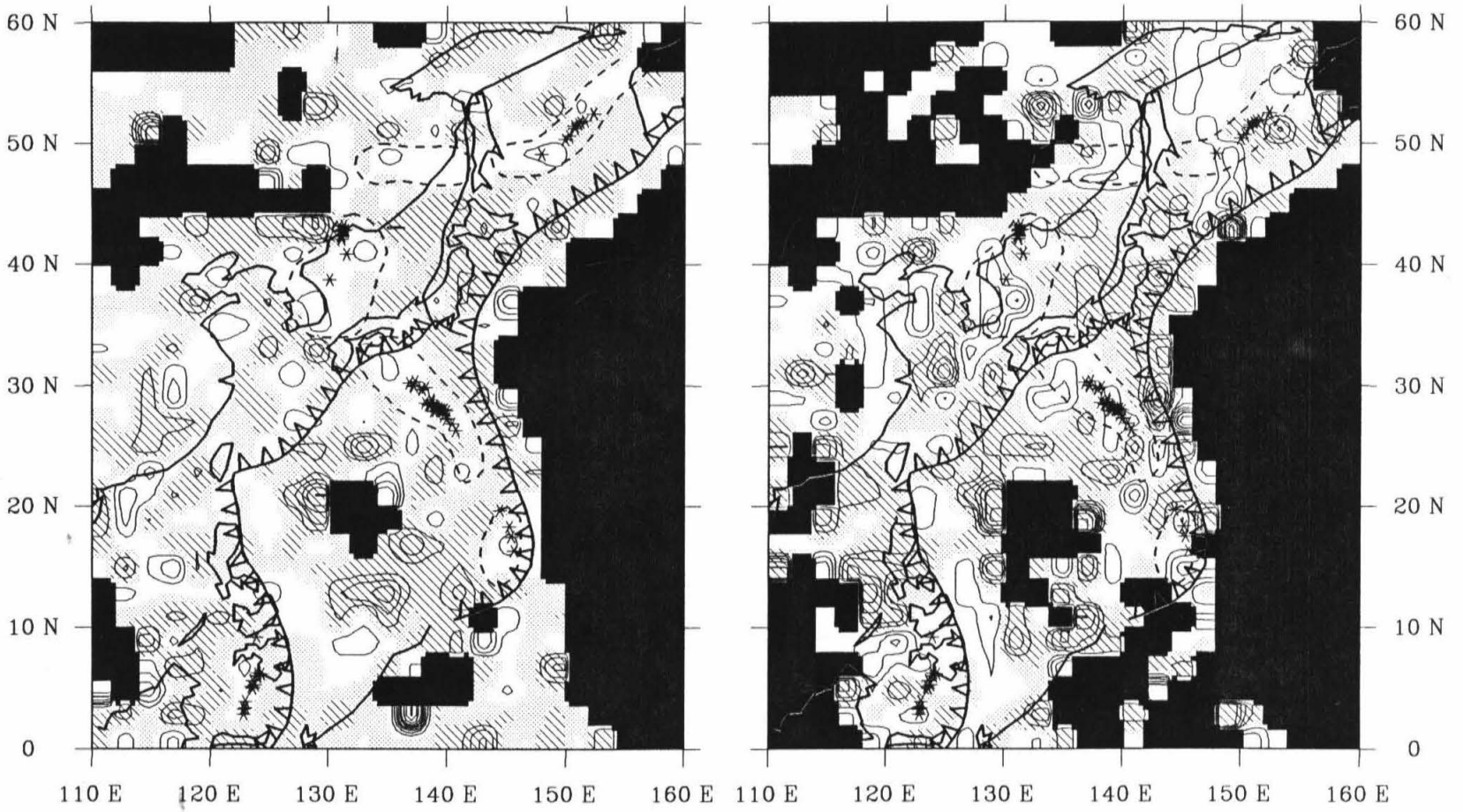
P.2x2 Mean=0.2[%]
500 -550 [km]
S.2x2 Mean=1.1[%]
60 N
50 N
40 N
30 N
20 N
10 N
0
110 E
120 E
130 E
140 E
150 E
160 E

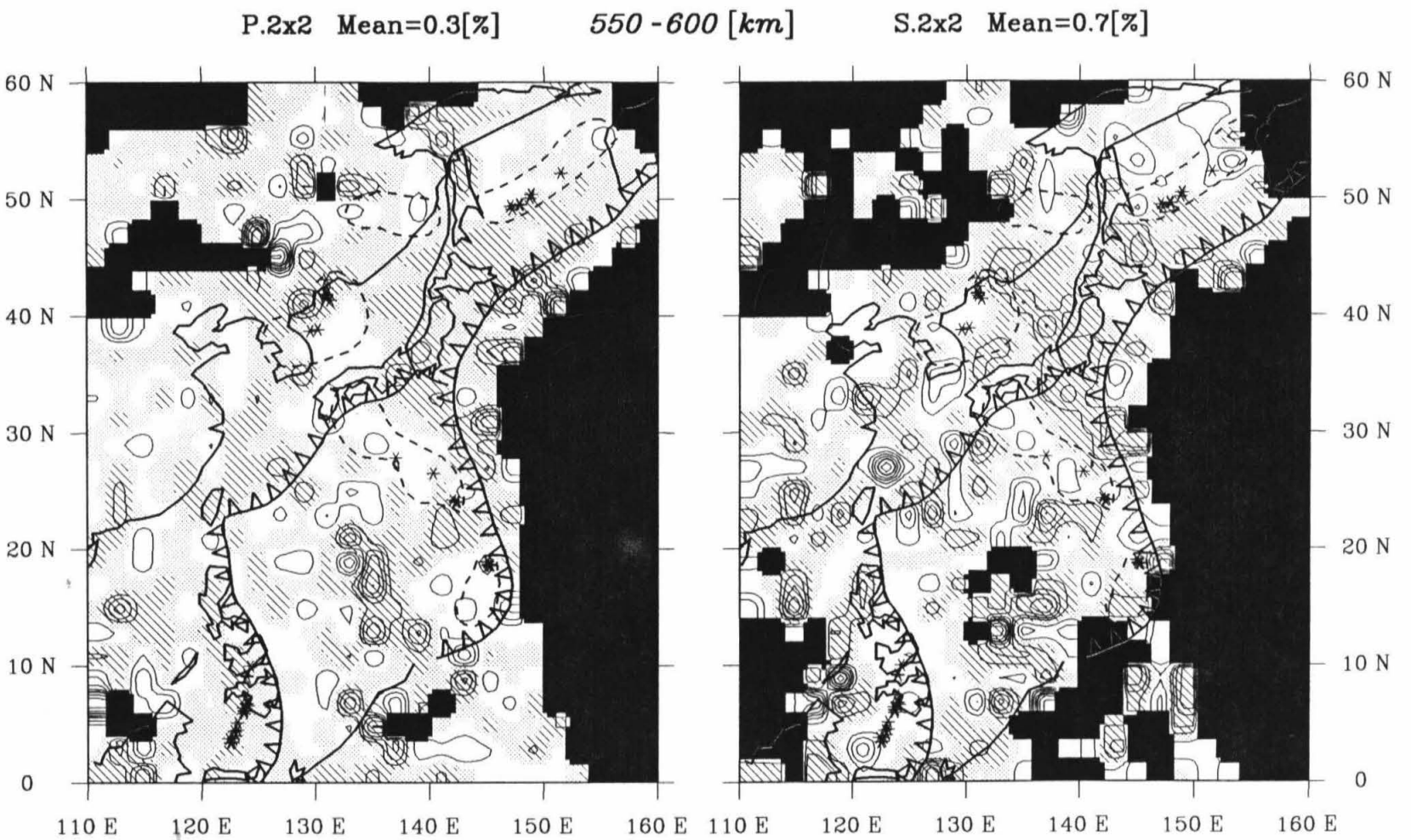
P.2x2 Mean=0.3[%]
550 -600 [km]
S.2x2 Mean=0.7[%]
60 N
50 N
40 N
30 N
20 N
10 N
0
110 E
120 E
130 E
140 E
150 E
160 E

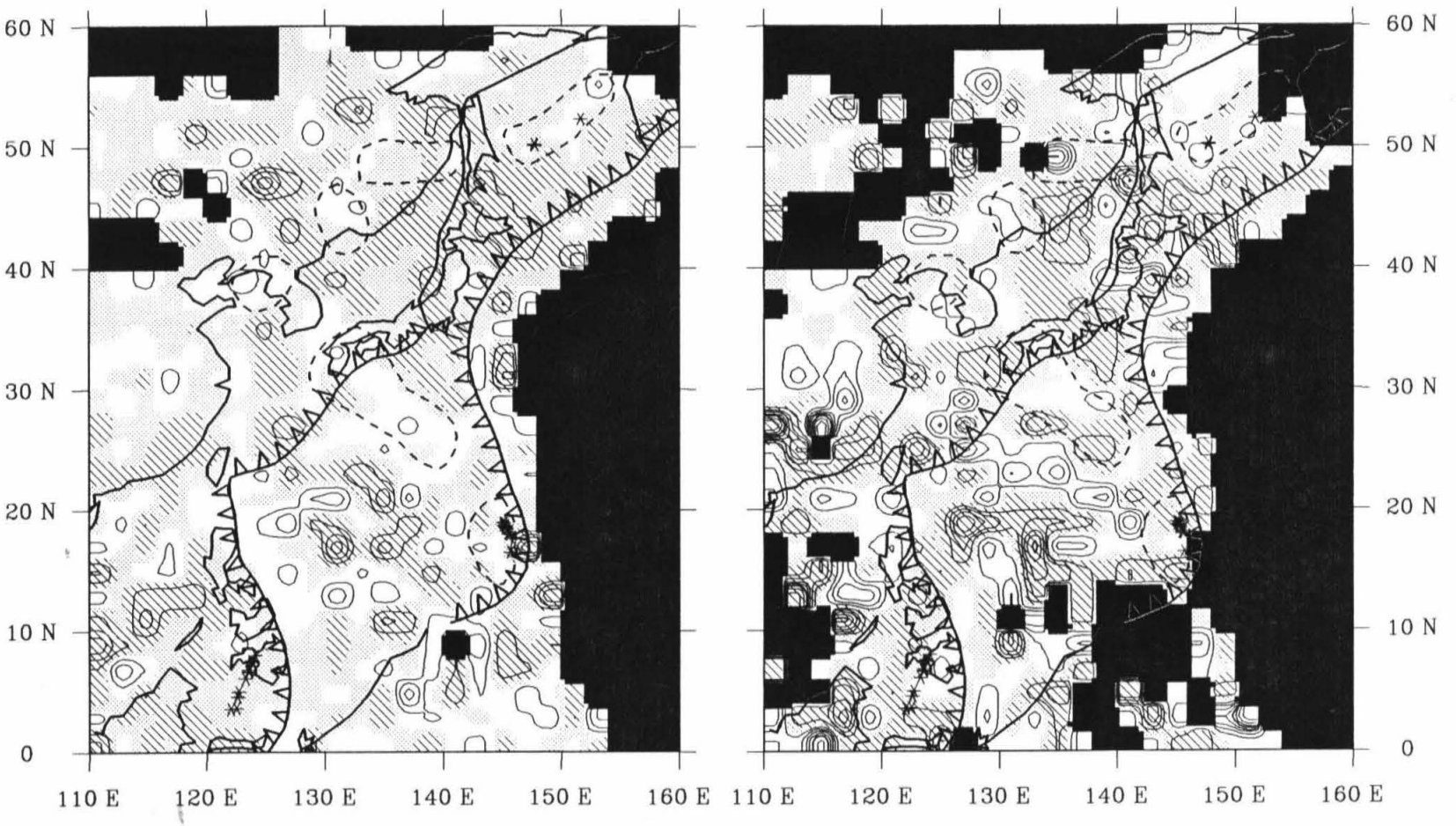
P.2x2 Mean=0.3[%]
600 - 650 [km]
S.2x2 Mean=0.4[%]
60 N
50 N
40 N
30 N
20 N
10 N
0
110 E
120 E
130 E
140 E
150 E
160 E

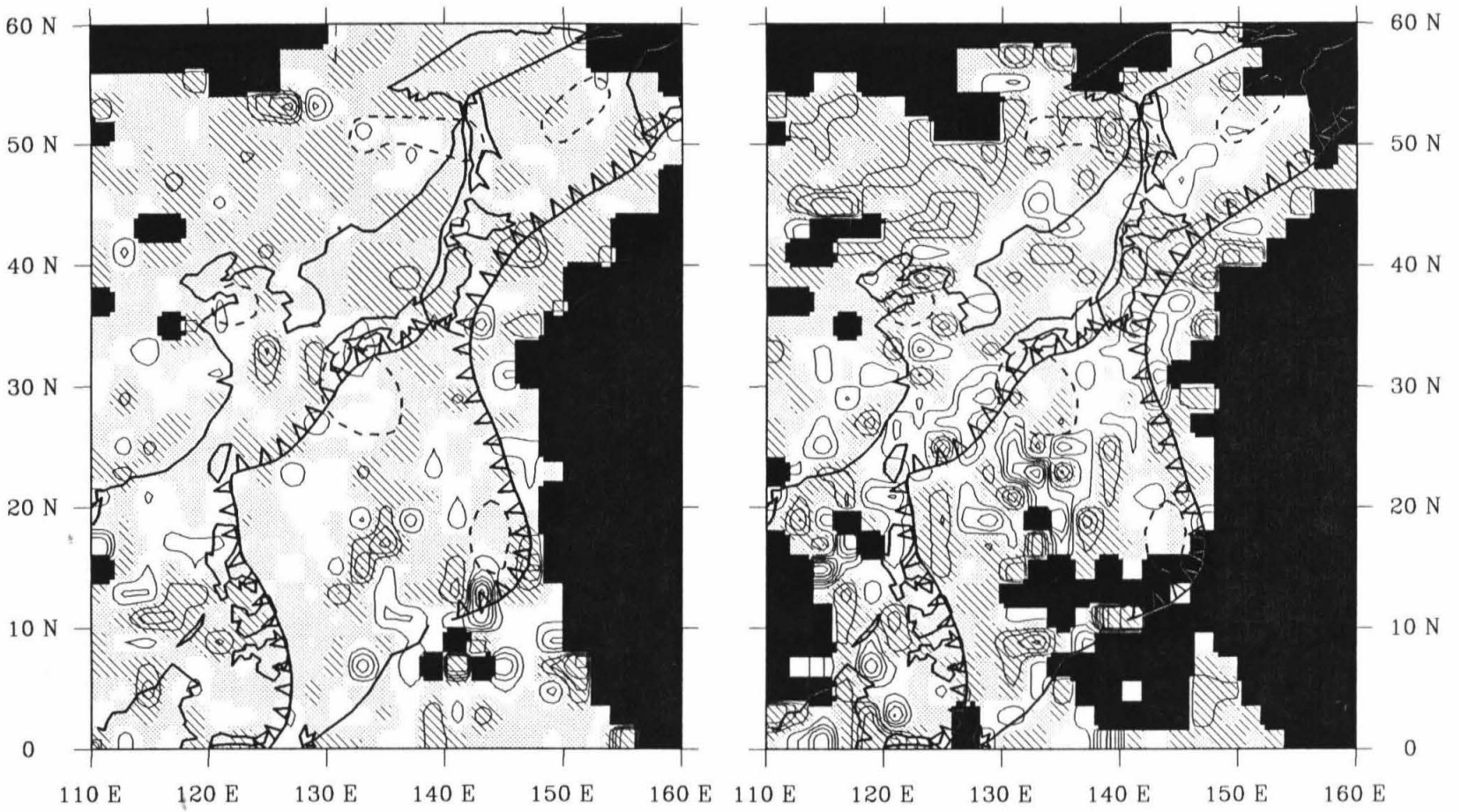
P.2x2 Mean=-0.0[%]
650 - 700 [km]
S.2x2 Mean=-0.6[%]
60 N
50 N
40 N
30 N
20 N
10 N
0
110 E
120 E
130 E
140 E
150 E
160 E

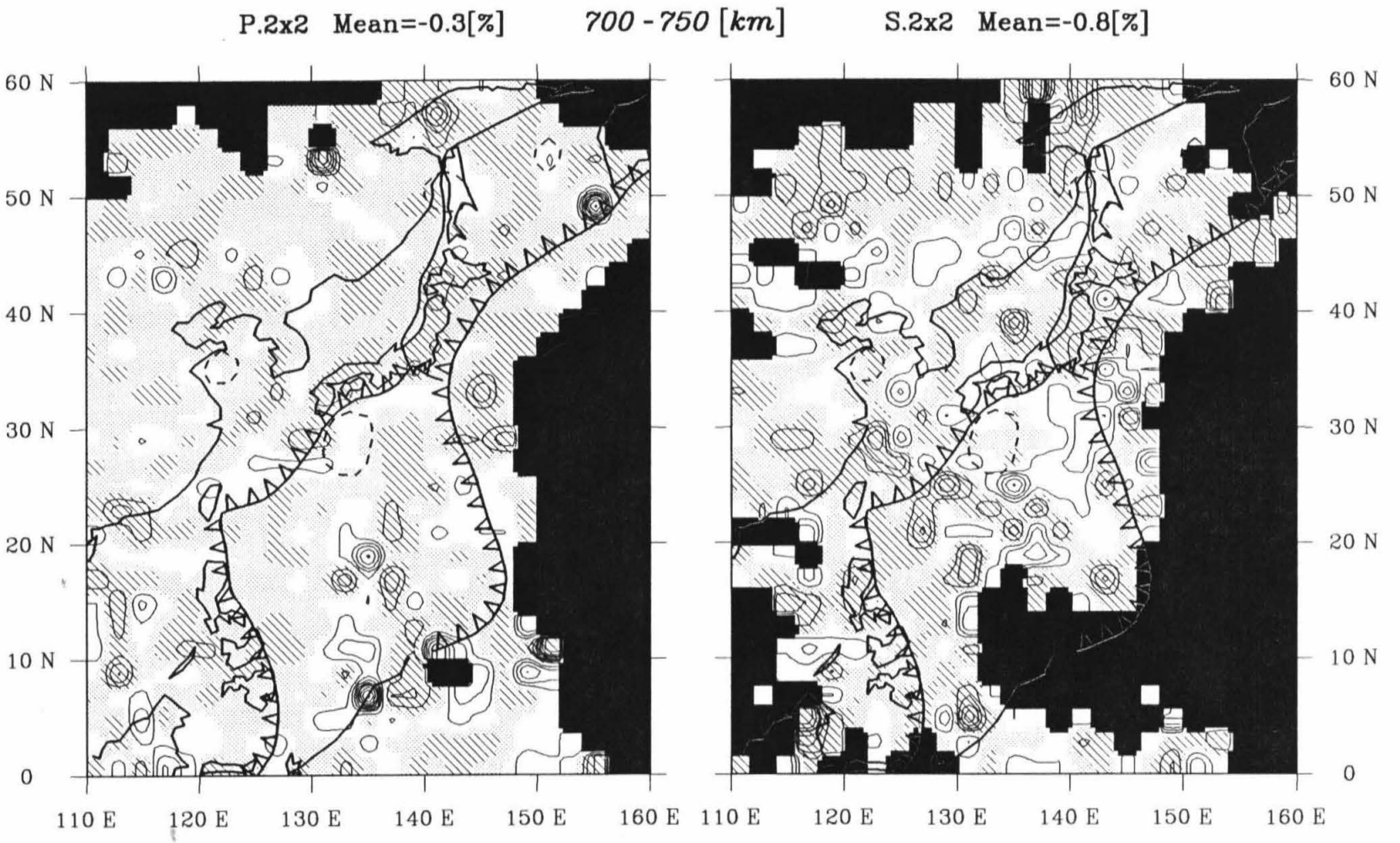
P.2x2 Mean=-0.3[%]
700 - 750 [km]
S.2x2 Mean=-0.8[%]
60 N
50 N
40 N
30 N
20 N
10 N
0
110 E
120 E
130 E
140 E
150 E
160 E

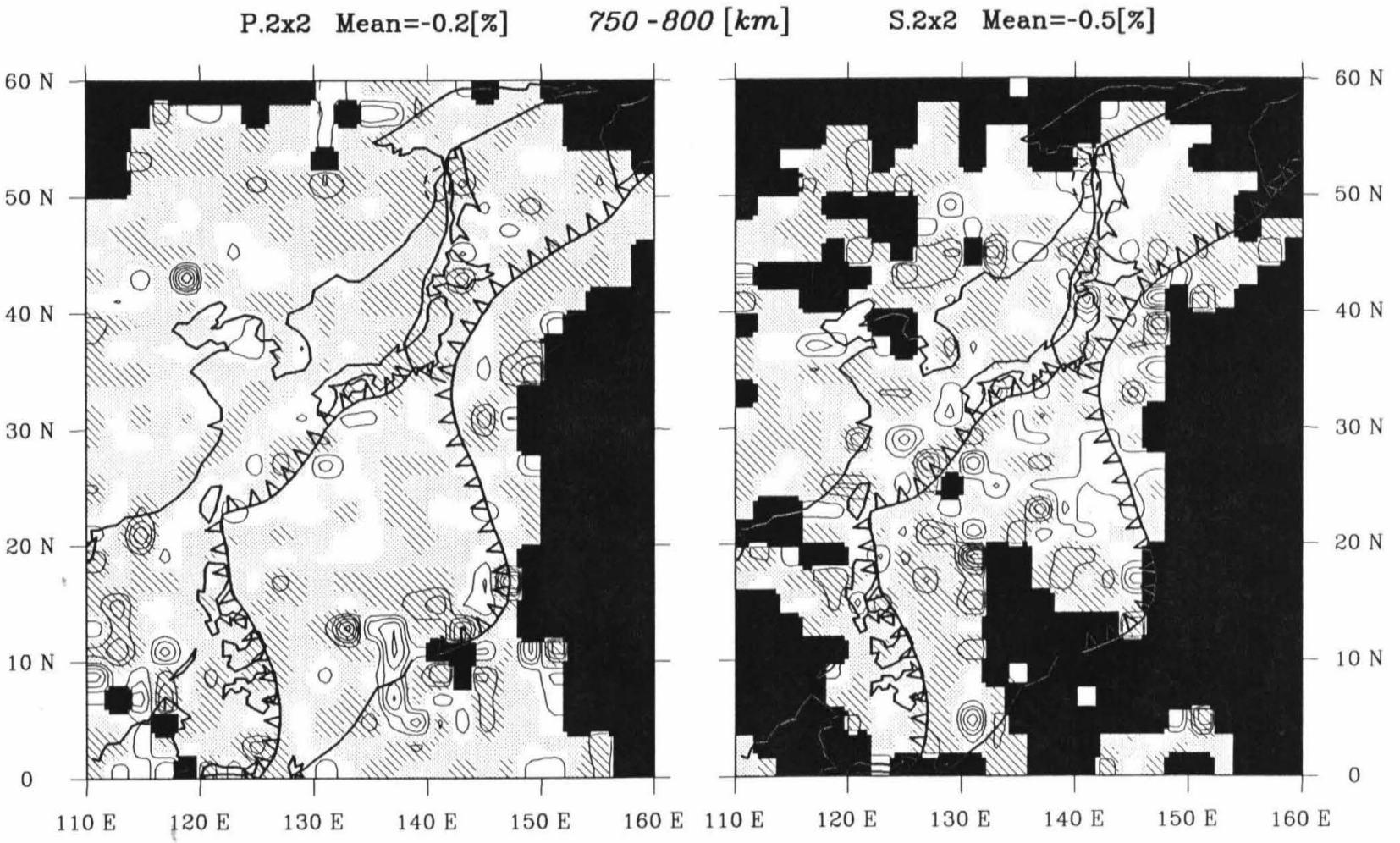
P.2x2 Mean=-0.2[%]
750 -800 [km]
S.2x2 Mean=-0.5[%]
60 N
50 N
40 N
30 N
20 N
10 N
0
110 E
120 E
130 E
140 E
150 E
160 E

Figure 2.13. Horizontal slices of the images on the $2^\circ \times 2^\circ \times 50$ km grid with grouping and sorting. See Figure 2.12 for interpretation. Slices in this figure show the more reliable anomalies in the slices in Figure 2.12. Notice that the patterns in the images at 200-250 km, 400-450 km and 600-650 km depth ranges correlate well to the patterns on $1^\circ \times 1^\circ \times 50$ km grid in Figure 2.11.

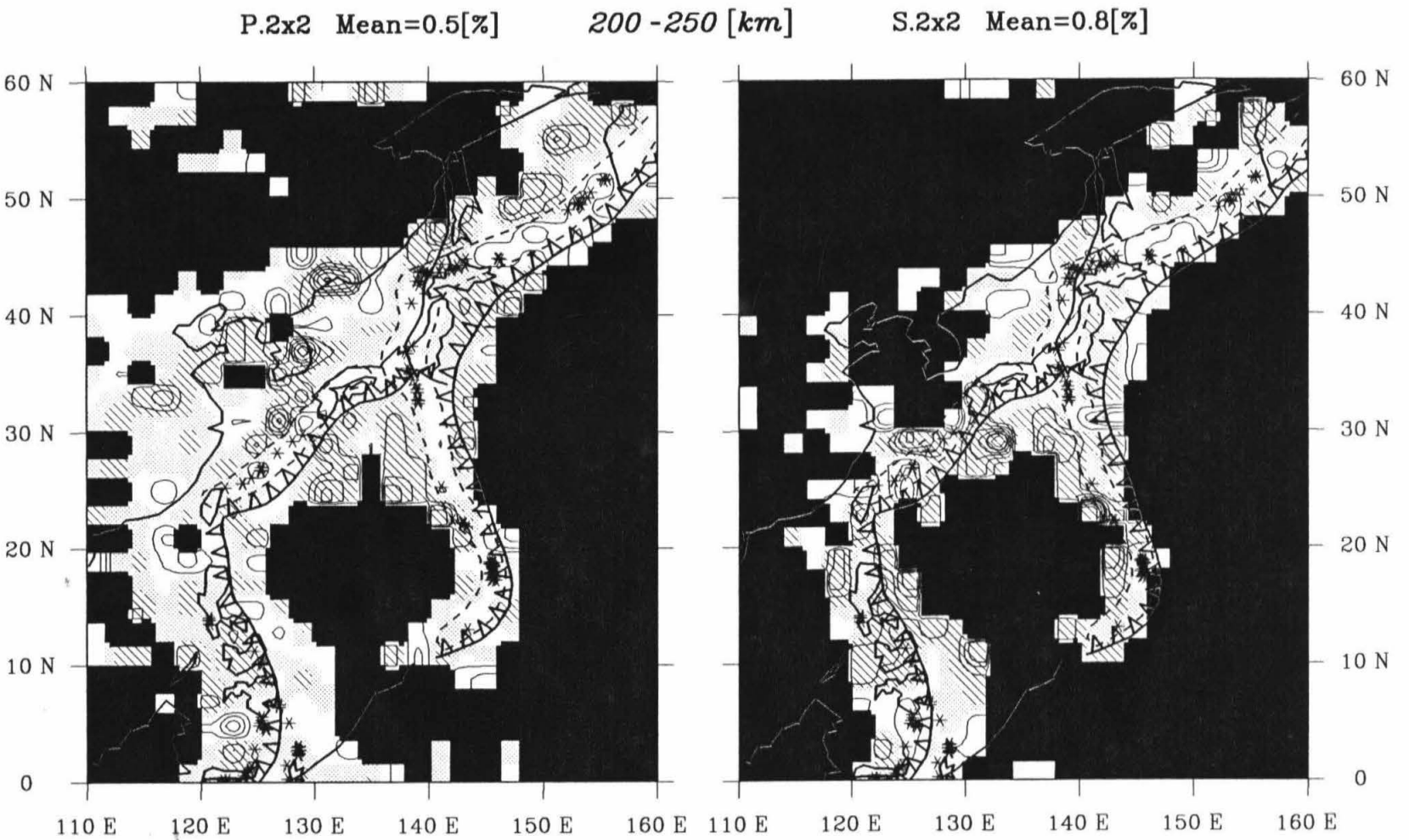
P.2x2 Mean=0.5[%]
200 -250 [km]
S.2x2 Mean=0.8[%]
60 N
50 N
40 N
30 N
20 N
10 N
0
110 E
120 E
130 E
140 E
150 E
160 E

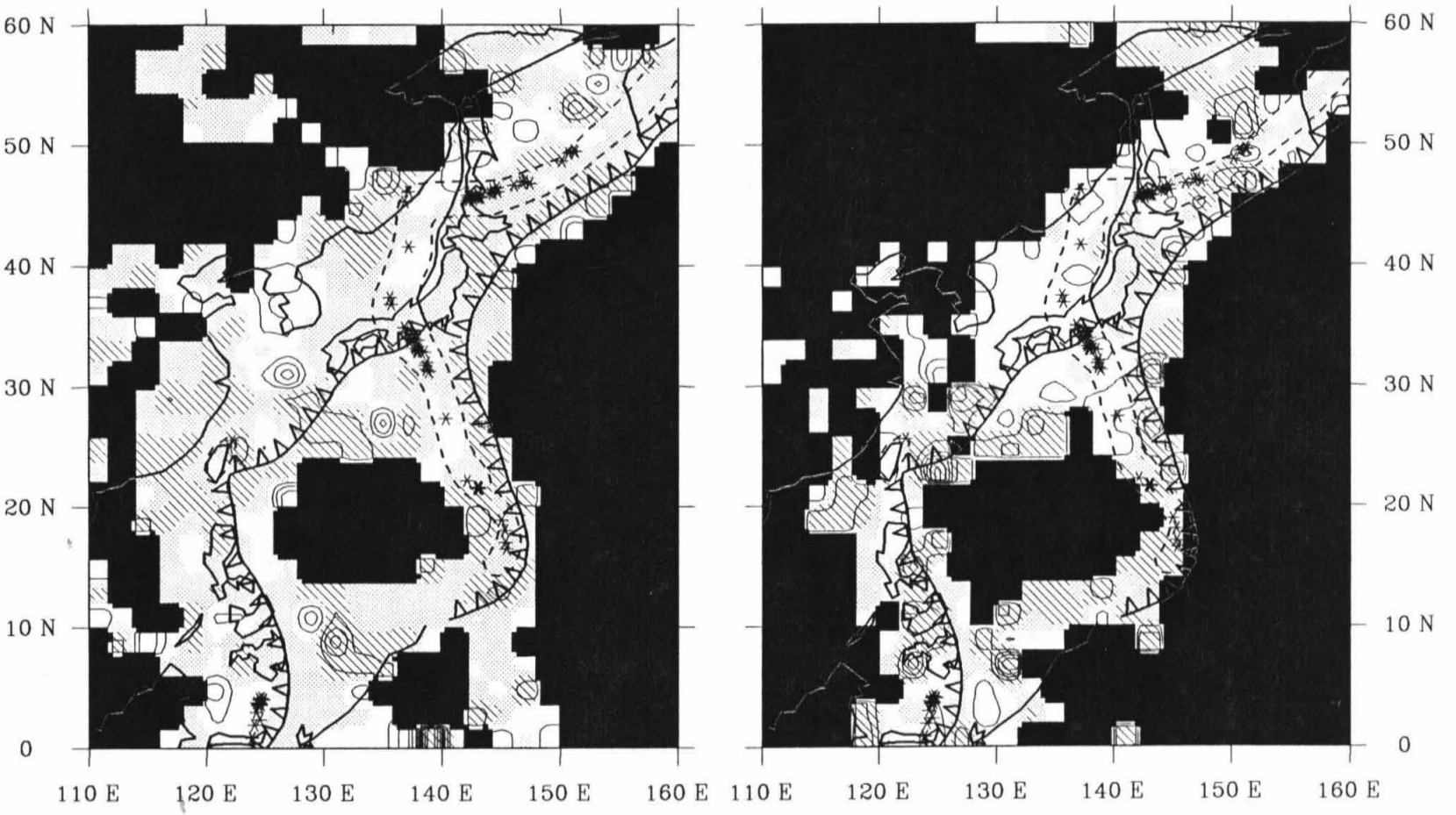
P.2x2 Mean=-0.1[%]
300 -350 [km]
S.2x2 Mean=0.7[%]
60 N
50 N
40 N
30 N
20 N
10 N
0
110 E
120 E
130 E
140 E
150 E
160 E

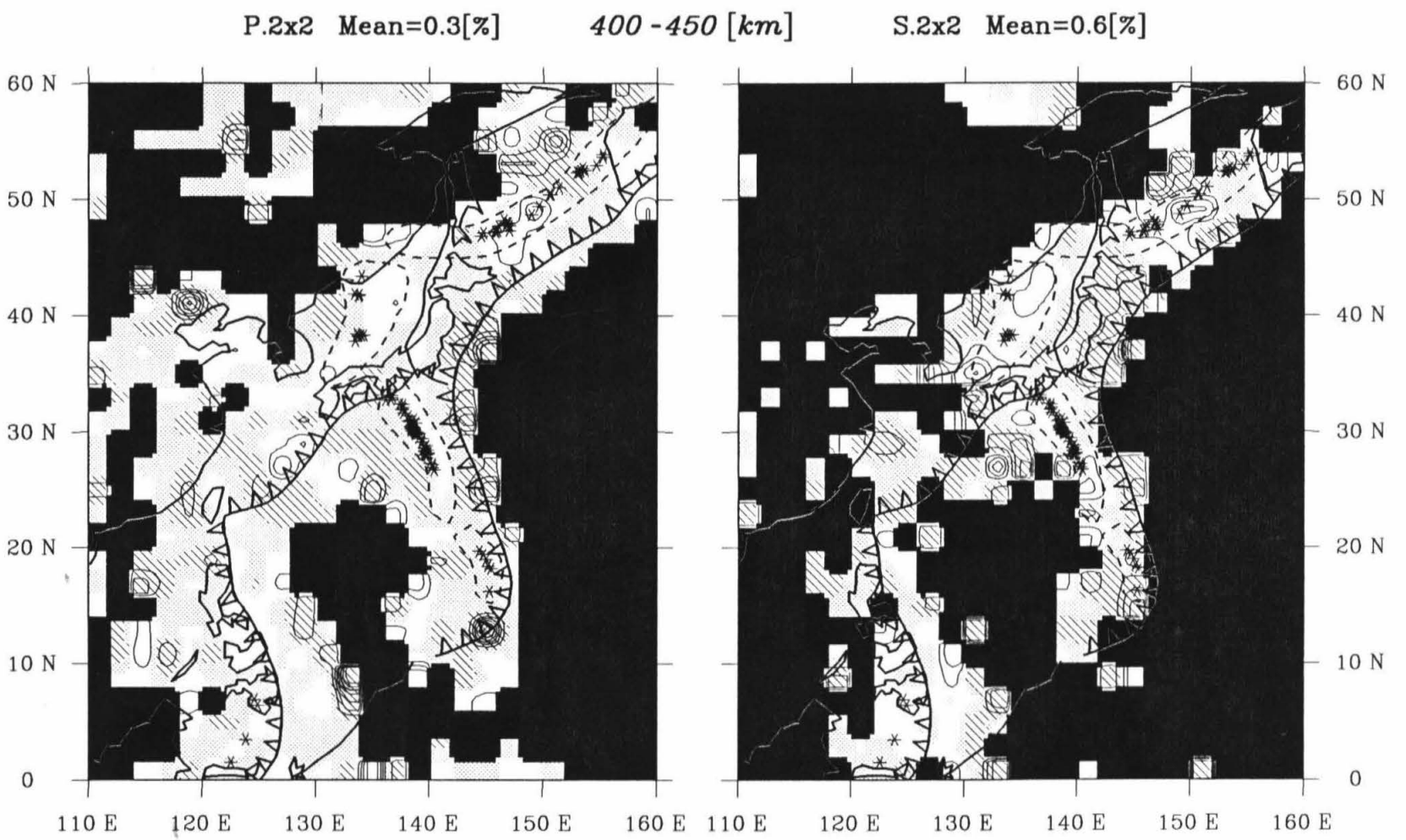
P.2x2 Mean=0.3[%]
400 -450 [km]
S.2x2 Mean=0.6[%]
60 N
50 N
40 N
30 N
20 N
10 N
0
110 E
120 E
130 E
140 E
150 E
160 E

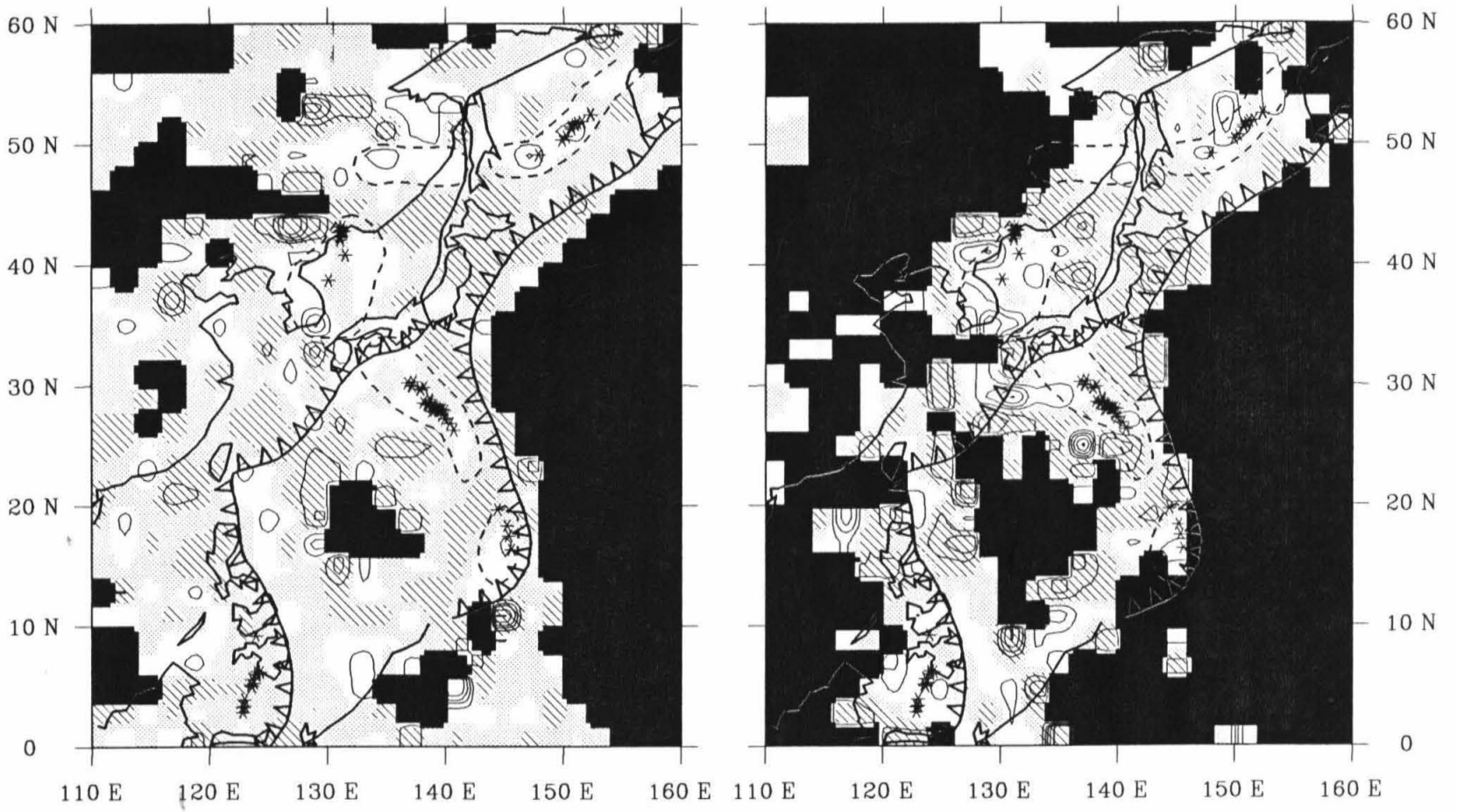
P.2x2 Mean=0.1[%]
500 -550 [km]
S.2x2 Mean=0.6[%]
60 N
50 N
40 N
30 N
20 N
10 N
0
110 E
120 E
130 E
140 E
150 E
160 E

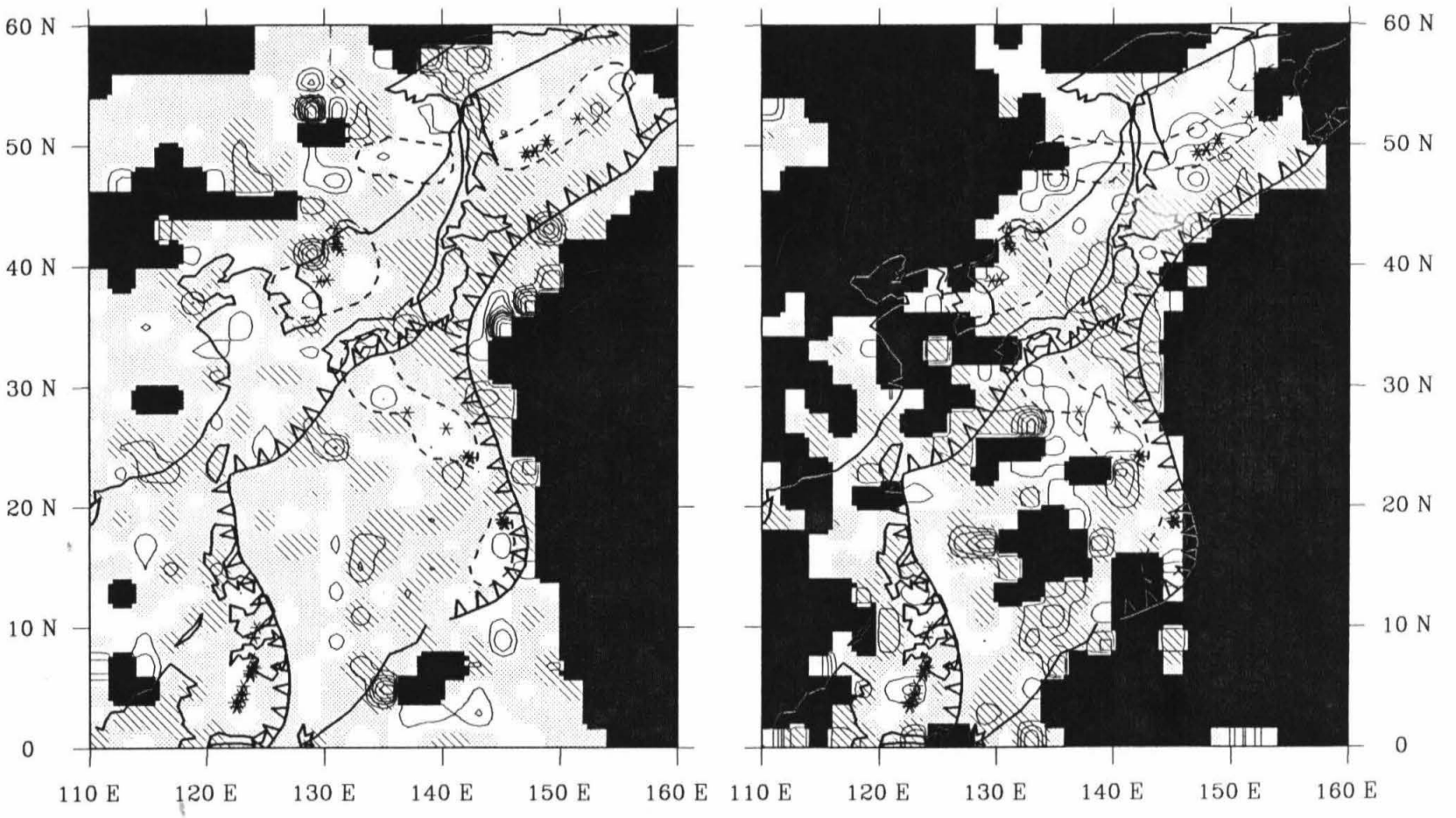
P.2x2 Mean=0.2[%]
550 -600 [km]
S.2x2 Mean=0.6[%]
60 N
50 N
40 N
30 N
20 N
10 N
0
110 E
120 E
130 E
140 E
150 E
160 E

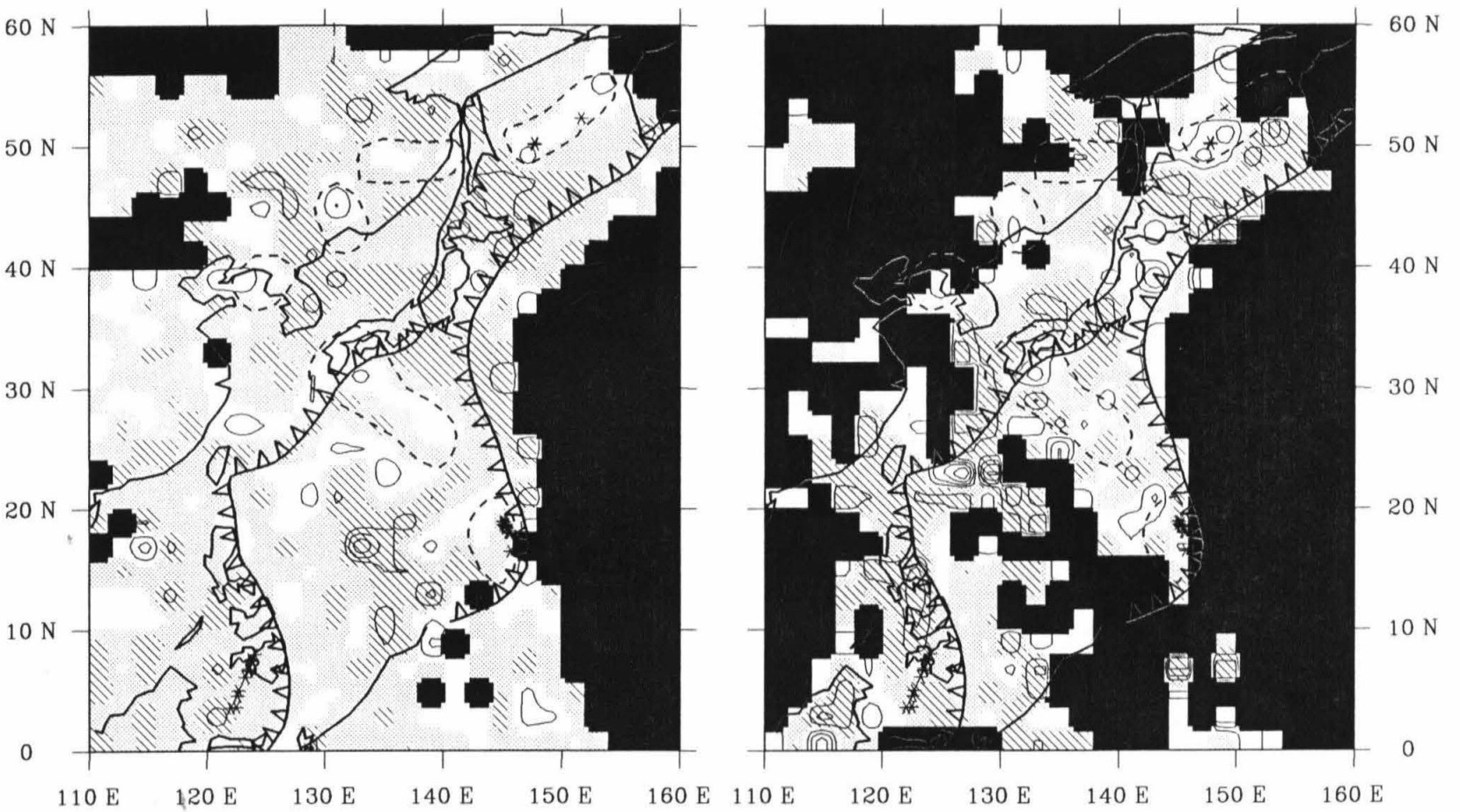
P.2x2 Mean=0.3[%]
600 - 650 [km]
S.2x2 Mean=0.2[%]
60 N
50 N
40 N
30 N
20 N
10 N
0
110 E
120 E
130 E
140 E
150 E
160 E

P.2x2 Mean=0.1[%]
650 - 700 [km]
S.2x2 Mean=-0.3[%]
60 N
50 N
40 N
30 N
20 N
10 N
0
110 E
120 E
130 E
140 E
150 E
160 E

P.2x2 Mean=-0.2[%]
700 - 750 [km]
S.2x2 Mean=-0.4[%]
60 N
50 N
40 N
30 N
20 N
10 N
0
110 E
120 E
130 E
140 E
150 E
160 E

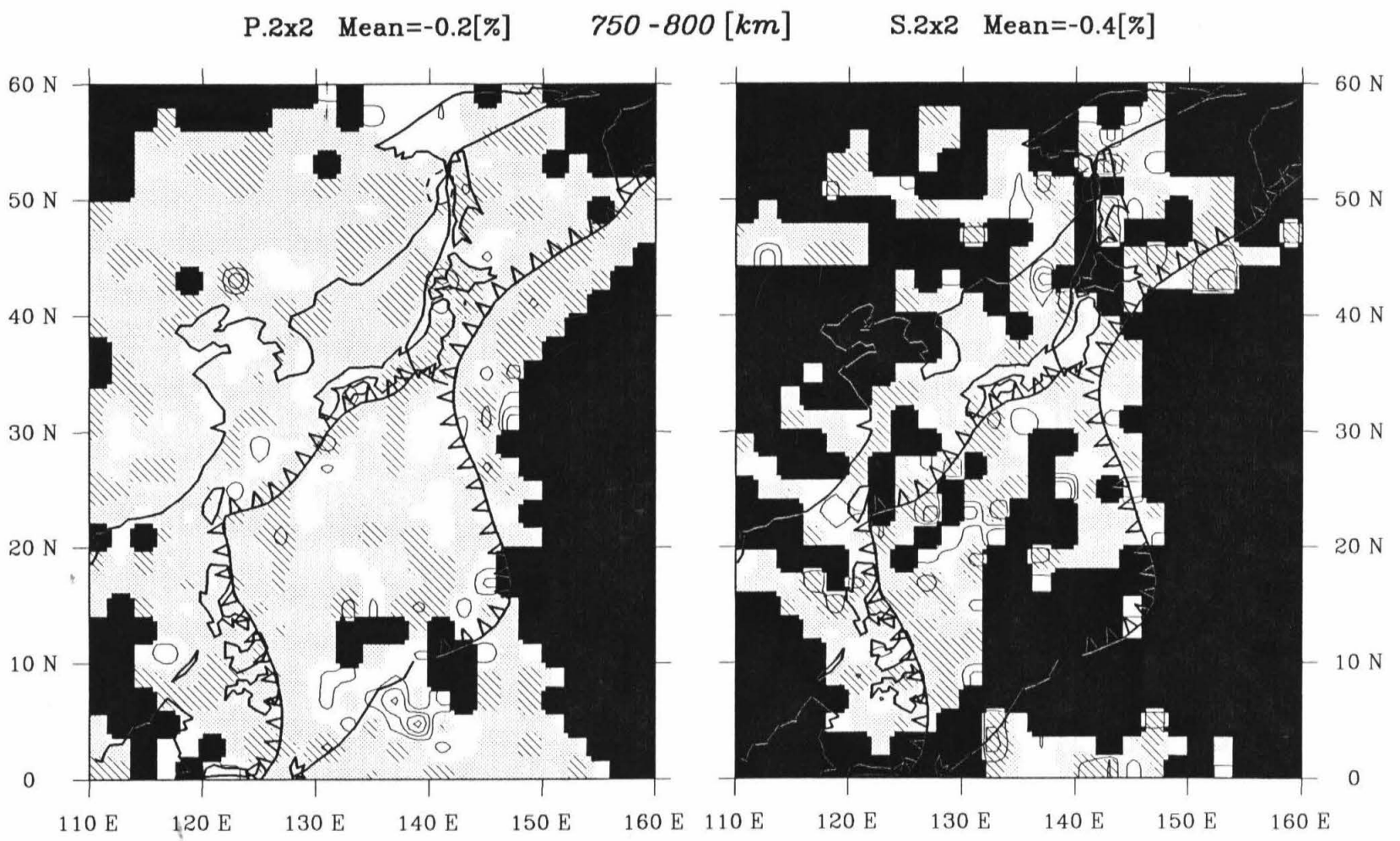
P.2x2 Mean=-0.2[%]
750 -800 [km]
S.2x2 Mean=-0.4[%]
60 N
50 N
40 N
30 N
20 N
10 N
0
110 E
120 E
130 E
140 E
150 E
160 E

Estimates of the average velocity variations of the slabs and of the ambient upper mantle, where the resolution for amplitude is reasonably good, are listed in Table 2.1. These values are with respect to the average velocity of each layer. The "ambient mantle" here is taken as the region outside of the most coherent fast anomalies that are associated with the Wadati-Benioff zones (the locus of the intermediate and deep focus earthquakes). Therefore, the estimates for the ambient mantle, particular for the top 300-400 km range, are possibly slower (more positive) than the real mantle average velocity, since those regions are heavily influenced by slow heterogeneities beneath the back-arc basins. The velocity contrast between slabs and their surrounding slow regions shows a large variation, as high as 7 to 8 percent in the shallow mantle. The relative amplitude of the shear wave anomalies, in a laterally averaged sense, is about one and a half times the amplitude of the compressional wave anomalies in percentage (i.e., $d \ln \mathbf{V_S} \approx 1.5\ d \ln \mathbf{V_P}$). The ratio is slightly lower than values estimated by some previous investigators, as described in Anderson [1987b]. The larger shear velocity variations shows that lateral variations in rigidity are more important to seismic velocity than lateral variations in bulk modulus.

A three-dimensional seismic slab model for the Northwest Pacific subduction zone, Figure 2.14, is interpreted from horizontal slices (map views) of the P and S wave images. Anomalies in horizontal slices are usually more recognizable than that in vertical slices (profiles), probably due to: a) layered images are more uniform in resolution; and b) curving and segmentation of the slab along its strike make rapidly varying patterns in vertical slices. The

Table 2.1 Estimated average amplitudes of slab related anomalies with respect to the average layer velocities.

Depth [km]	P-waves [%]		S-waves [%]	
	slab	ambient mantle	slab	ambient mantle
0 to 100	-2. to -4.	+2. to +3.5	-1. to -4.	2+ to +4.
100 to 200	-2. to -3.	+2. to +3.	-3. to -5.	+1. to +4.
200 to 300	-1. to -3.	+1.5 to +2.5	-1. to -4.	+1.5 to +3.
300 to 400	-0.5 to -4.	+1. to +2.	-2. to -3.	+2. to +3.
400 to 500	-1.5 to -3.	+1.5 to +2.5	-2. to -4.	+1.5 to +2.5
500 to 600	-1. to -2.	+1. to +2.	-0.5 to -2.	1.+ to +1.5
600 to 700	-0.5 to -2.	+0.5 to +1.5	-0.5 to -2.	+1. to +1.5

Figure 2.14. Interpreted model of slab anomalies. This figure illustrates two three-dimensional views of our interpretation model of the fast velocity anomalies associated with subducted lithosphere in the region, from surface down to 800 km depth. The model is interpreted based on correlated fast features in the P and S solutions in two different block grids, layer to layer comparisons, and seismicity. The model indicates the continuity of the fast slab in the upper portion of the upper mantle, and the complication of fingering and spreading of the slab in the transition region.

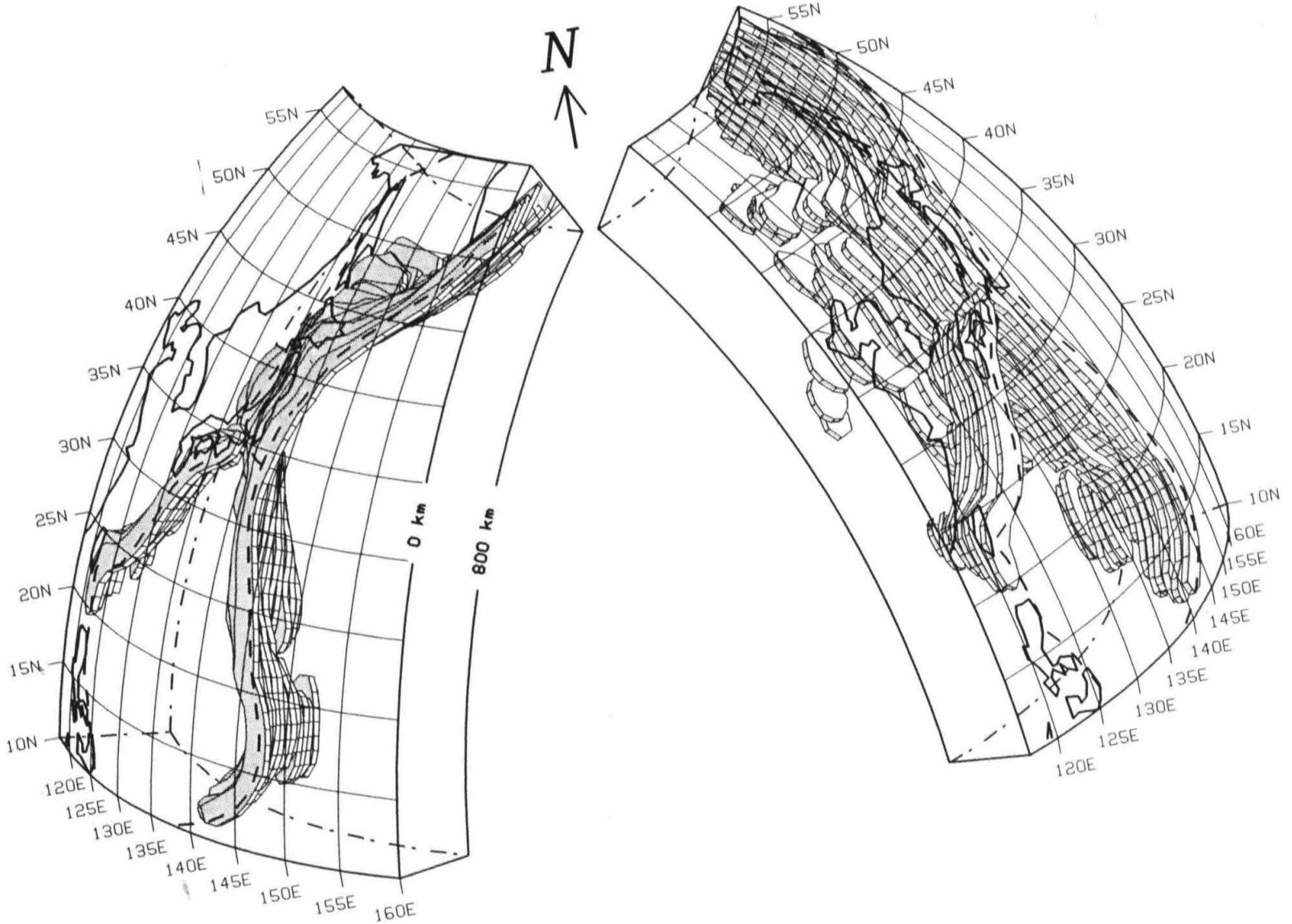
N
55N
50N
45N
40N
35N
30N
25N
20N
15N
10N
120E
125E
130E
135E
140E
145E
150E
155E
160E
0 km
800 km
55N
50N
45N
40N
35N
30N
25N
20N
15N
10N
60E
155E
150E
145E
140E
135E
130E
125E
120E

interpretation is based on correlated fast features in the P and S solutions in two different block grids, layer to layer comparisons, and the seismicity distribution. The interpretation assumes that the fast slab model is continuous in the down-dip direction in all places. Hence, in some vertical slices (e.g., Figure 2.15) the model is always continuous while fast anomalies along subduction zones are truncated by slow patches in some places. It is obvious that this slab model is merely one interpretation of the tomographic images. Even though it is arguable towards how to interpret these noise-bearing images, our intention is illustrating the images with their resolution and noise aspects as well as showing "our version" of slab interpretation.

The model covers the seismic slabs under the Kurile, Japan, Izu-Bonin, Mariana and Ryukyu arcs, from the surface down to 800 km depth. No interpretation is given for the Philippine arc since the data coverage is not adequate there. The interpretation is terminated at 800 km depth because both P and S velocity heterogeneities are of lower amplitude and more random appearance in the lower mantle compared with the upper mantle. This is especially true for S waves below 800 km. Laterally, the slab appears to buckle at several locations in the upper mantle, probably due to geometrical convergence similar to that proposed by Minamino and Fujii [1981]. There are apparently three major segmentations of the slab, as shown in horizontal slices in the depth range 400-450 km in Figures 2.12 and 2.13. These segmentations are under the junctions of the Kurile, Japan, Izu-Bonin and Mariana trenches, and all correlate with abrupt lateral changes in the Wadati-Benioff zone. The central portion of the Kurile slab anomaly is torn apart near the bottom of the

upper mantle.

To illustrate the vertical morphology of the slab, a series of vertical slices of the P wave image across the strike of subduction zones from the $2^\circ \times 2^\circ \times 50$ km grid are shown in Figure 2.15. These are paired with results of some "impulse tests" for resolution. The results of the "impulse tests" are used to judge the reliability of the image at various locations and, particularly, to detect any along-path smearing. Similarly, the seismic slab model for the region (Figure 2.14) is interpreted with reference to such "impulse tests." In order to display a more stable and representative anomalous pattern, we stacked parallel vertical slices of the P and S wave images in $1^\circ \times 1^\circ \times 50$ km grid. Figures 2.16 and 2.17, respectively, show the stacked slices of images for P and S wave data with and without the application of grouping and sorting. The locations of these stacked slices are shown as the small boxes in Figure 2.1.

In the cross sections, the fast slab-like anomalies which are associated with the seismicity subduction zone generally fold and definitely broaden with increase in depth. The thickness of the slab anomaly is about one to two hundred kilometers, which makes it thicker than the mechanical slab near surface. The thick slab anomaly could be due to the large block size used. On the other hand, the slab may be really thickening with depth. The slab anomalies reach to 650 km depth in most areas. Fingering of the slab, i.e., segmenting and spreading, is generally observed in the transition zone. Fast velocity anomalies in the form of single coherent sheets are not evident in the lower mantle of the region.

Figure 2.15. Vertical slices of the $2^\circ \times 2^\circ \times 50$ km grid. The surface locations of these slices are shown as the heavy solid curves in Figure 2.1. Each slice is paired with the result of the "impulse" resolution tests to the right. The plotting convention for the slowness follows that used in Figure 2.6, except the contour interval is now 1%. The heavy dashed lines indicate the cross section of the interpreted model shown in Figure 2.14, which is an interpretation of the coherent subduction zone related fast anomalies in the horizontal slices of the images. The plotting convention for the "impulse" tests follows that used in Figure 2.7. The depth of 670 km is indicated with a solid line. The curvature of the earth is removed, and there is no vertical exaggeration. In all slices the fast slab anomalies around the Wadati-Benioff zone are clearly shown; they all broaden with depth, and probably reach to the bottom of the upper mantle. The resolution is generally sharp, except in some areas under the Kurile and Mariana trenches.

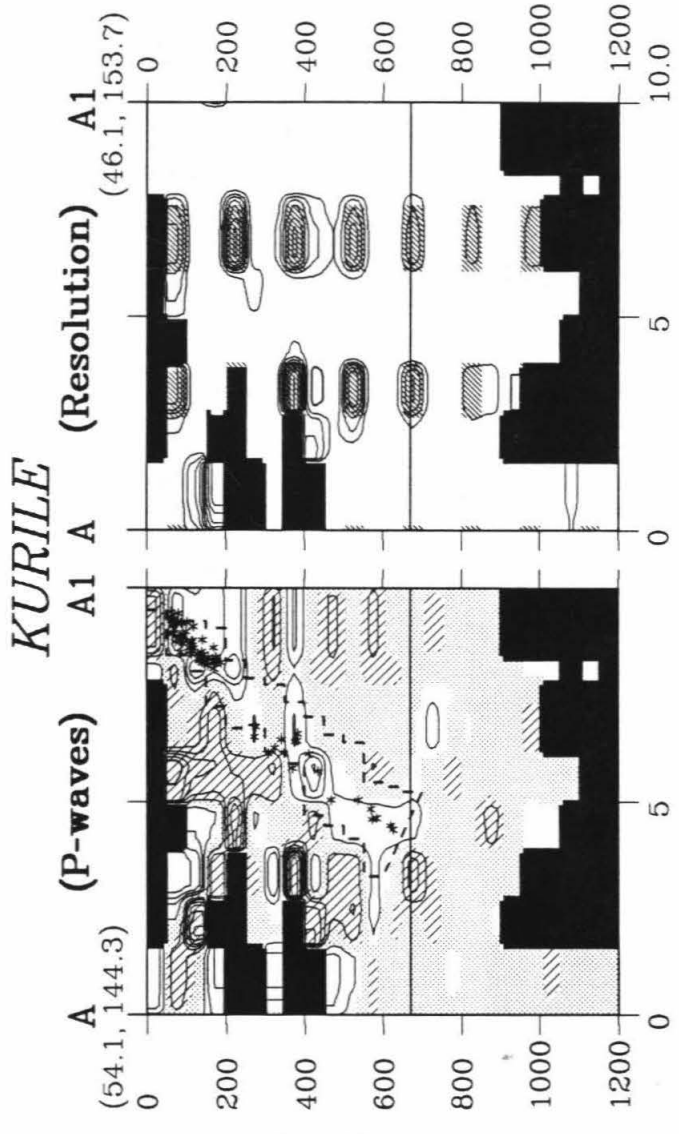
KURILE
A1 A
(P-waves)
(Resolution)
A
(54.1, 144.3)
A1
(46.1, 153.7)
Depth [km]
Delta [degree]
0
200
400
600
800
1000
1200
5
10.0

a).

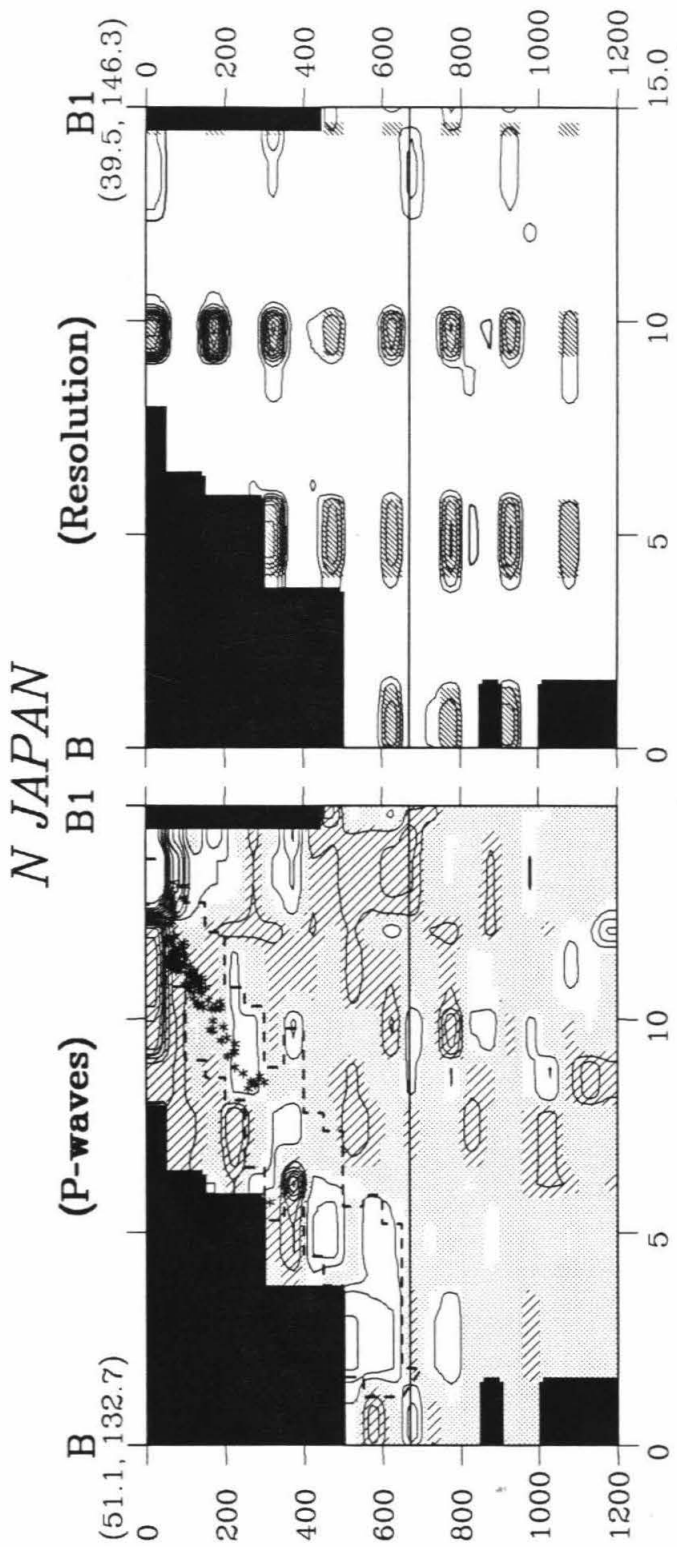
N JAPAN
(P-waves)
(Resolution)
B
(51.1, 132.7)
B1
B1
B
(39.5, 146.3)
Depth [km]
Delta [degree]
0
200
400
600
800
1000
1200
5
10
15.0

b).

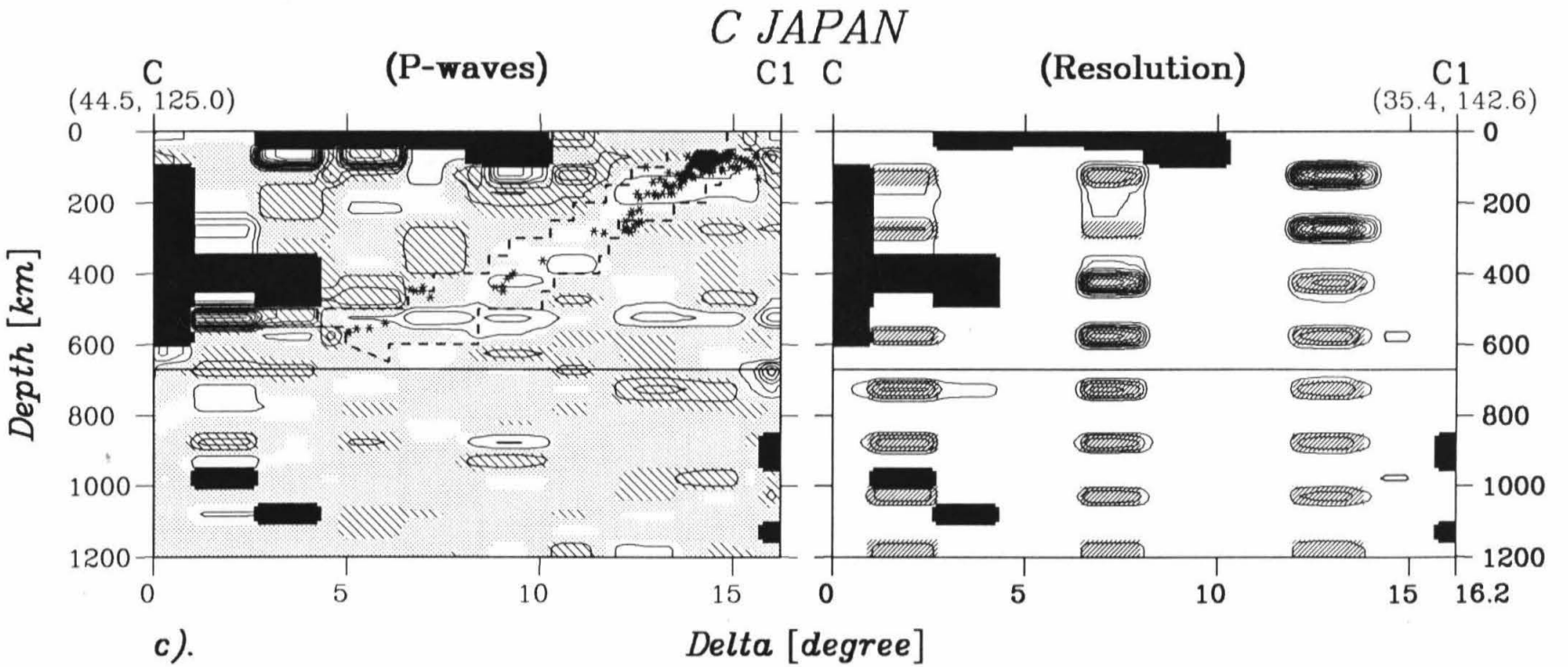
C JAPAN
C
(P-waves)
C1 C
(Resolution)
C1
(44.5, 125.0)
(35.4, 142.6)
Depth [km]
0
200
400
600
800
1000
1200
0
5
10
15
16.2
Delta [degree]

c).

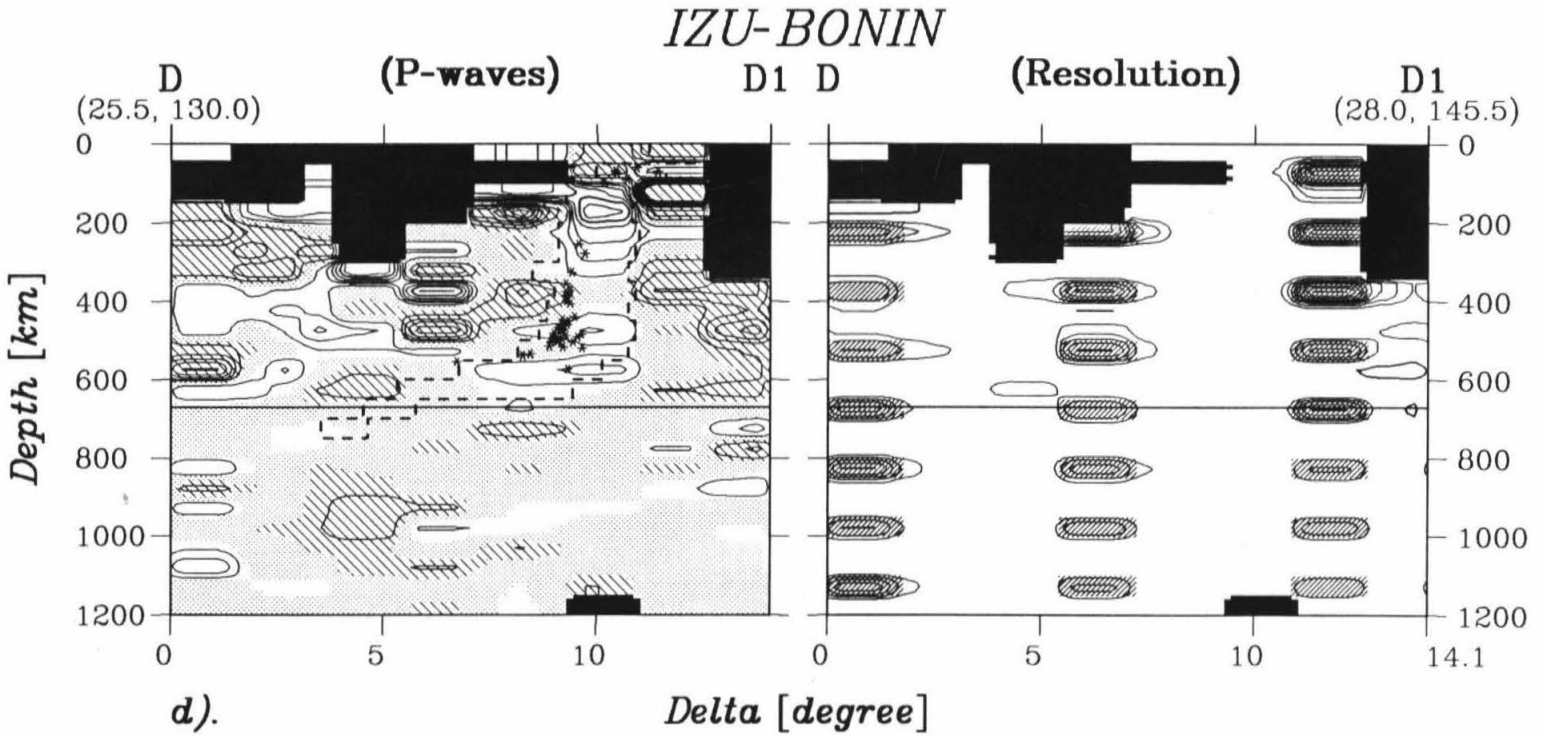
IZU-BONIN
D
(25.5, 130.0)
(P-waves)
D1
D
(Resolution)
D1
(28.0, 145.5)
Depth [km]
0
200
400
600
800
1000
1200
0
5
10
14.1
Delta [degree]

d).

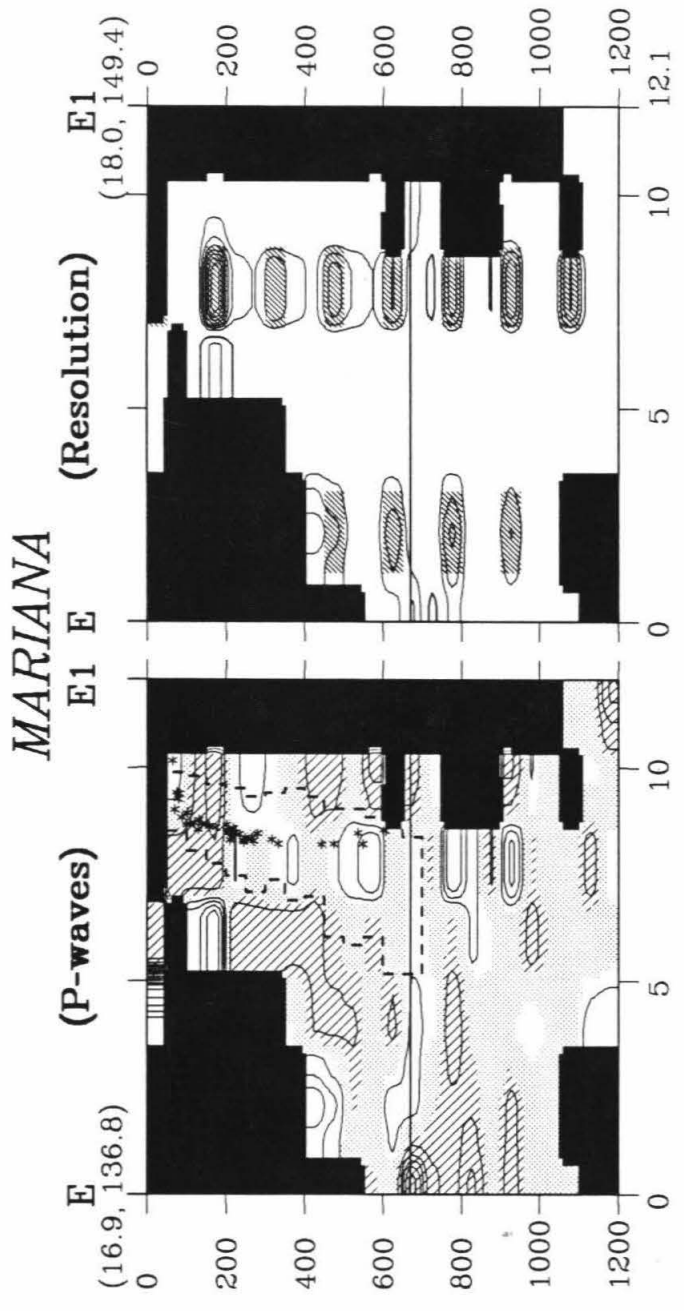
MARIANA
(P-waves)
(Resolution)
E
(16.9, 136.8)
E1
E
E1
(18.0, 149.4)
Depth [km]
Delta [degree]
0
200
400
600
800
1000
1200
5
10
12.1

e).

Figure 2.16. Stacked vertical slices of images from data sets without application of the grouping and sorting procedure. The images are in the $1^\circ \times 1^\circ \times 50$ km grid. The locations of these stacked slices are indicated as the small boxes in Figure 2.1. Each pair of slices are the P (top) and S (bottom) wave images, respectively. The plotting convention follows that used in Figure 2.6, except the contour interval is 1%.

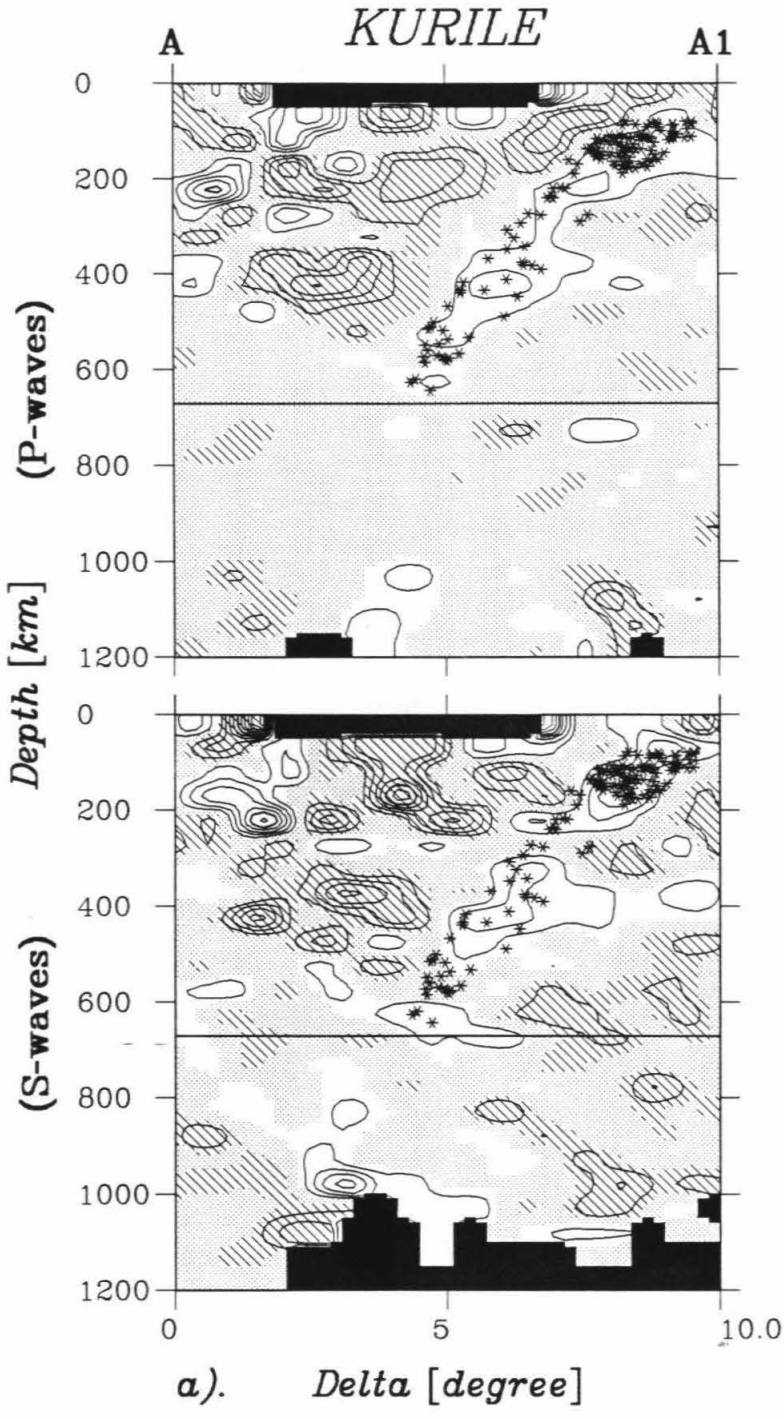
KURILE
A
A1
0
200
400
600
800
1000
1200
(P-waves)
Depth [km]
(S-waves)
0
5
10.0
a). Delta [degree]

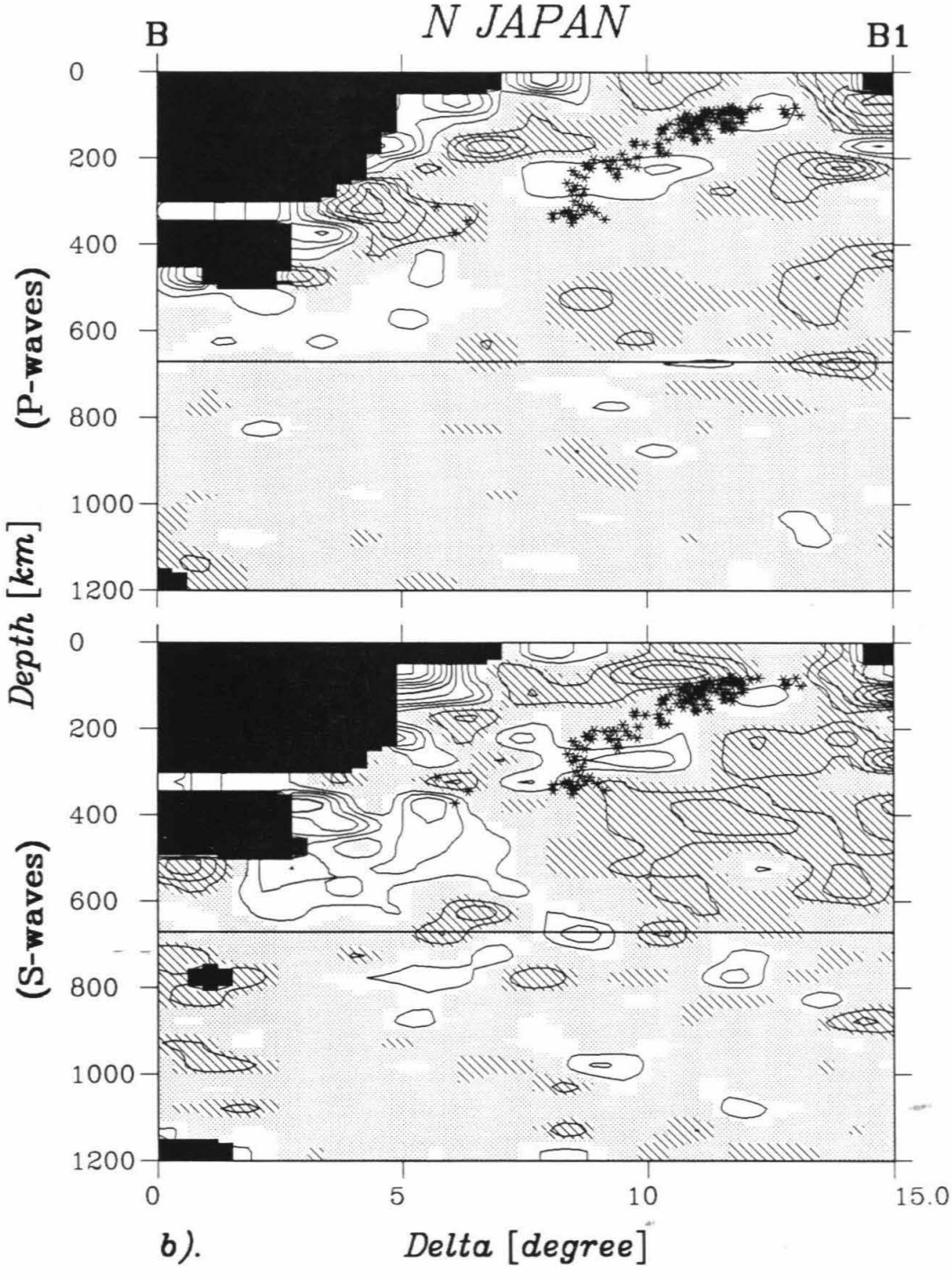
N JAPAN
B
B1
0
200
400
600
800
1000
1200
(P-waves)
Depth [km]
(S-waves)
0
5
10
15.0
Delta [degree]

b).

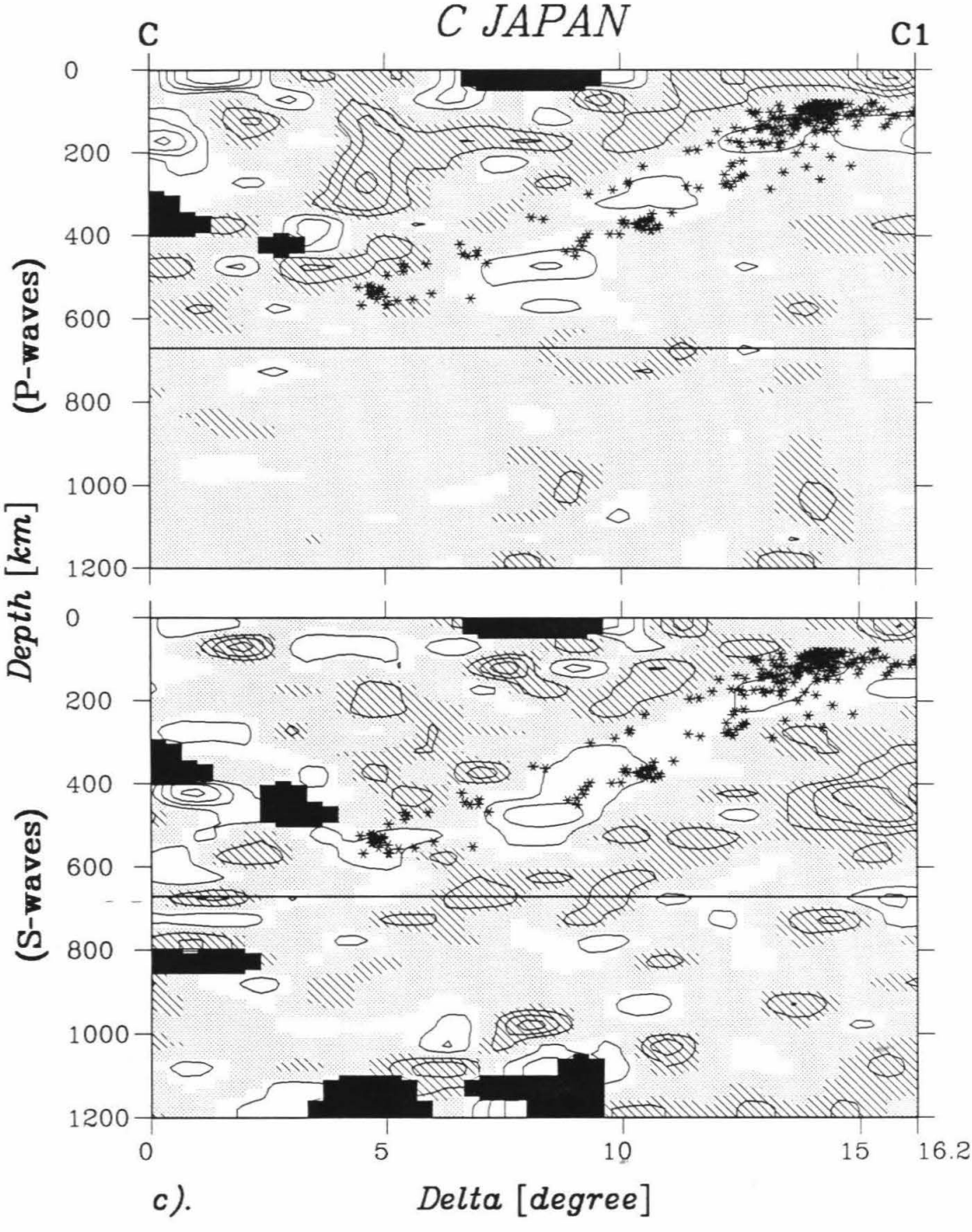
C JAPAN
C
C1
(P-waves)
(S-waves)
Depth [km]
0
200
400
600
800
1000
1200
0
5
10
15
16.2
Delta [degree]

c).

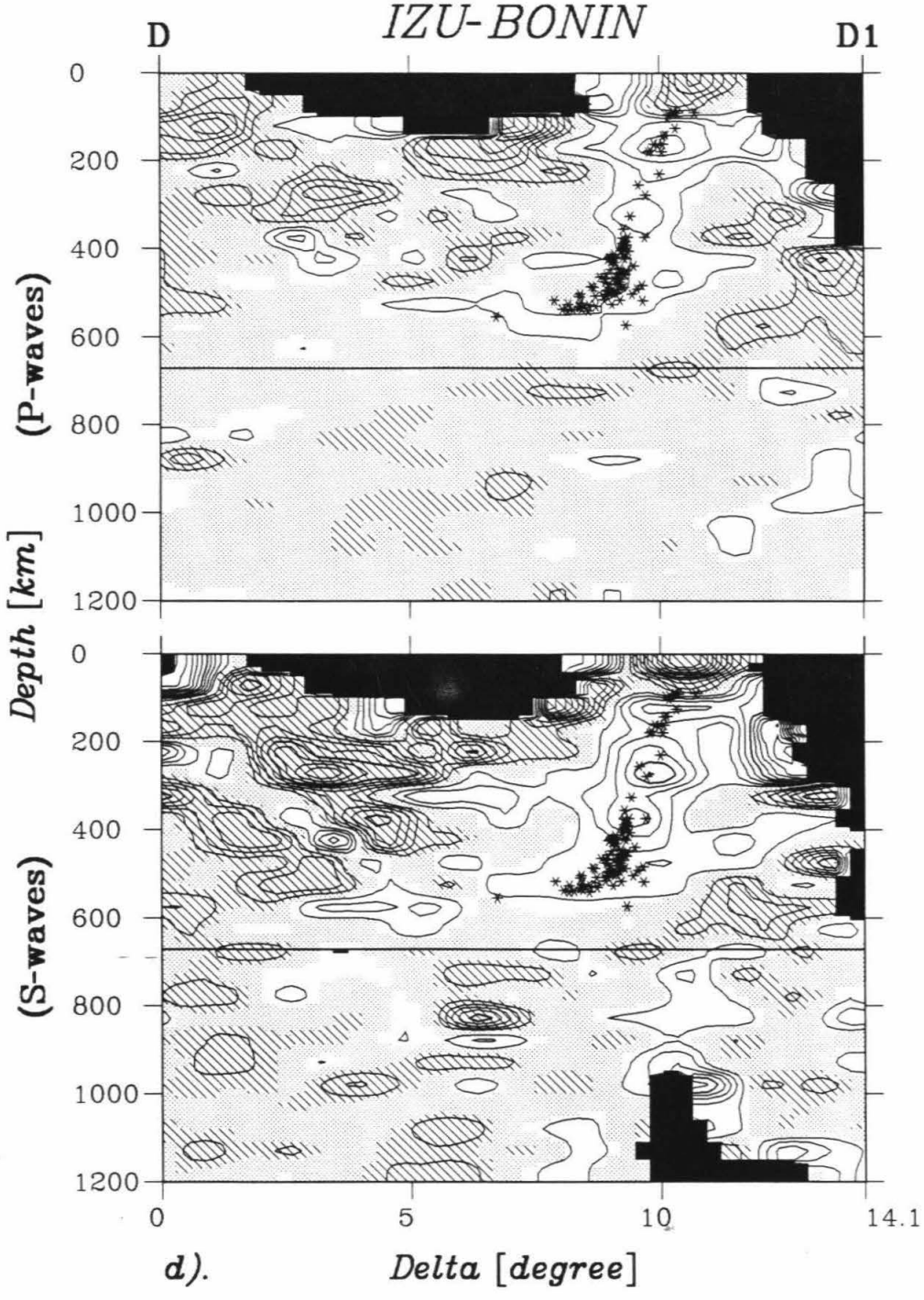
IZU-BONIN
D
D1
0
200
400
600
800
1000
1200
(P-waves)
Depth [km]
(S-waves)
0
5
10
14.1
Delta [degree]

d).

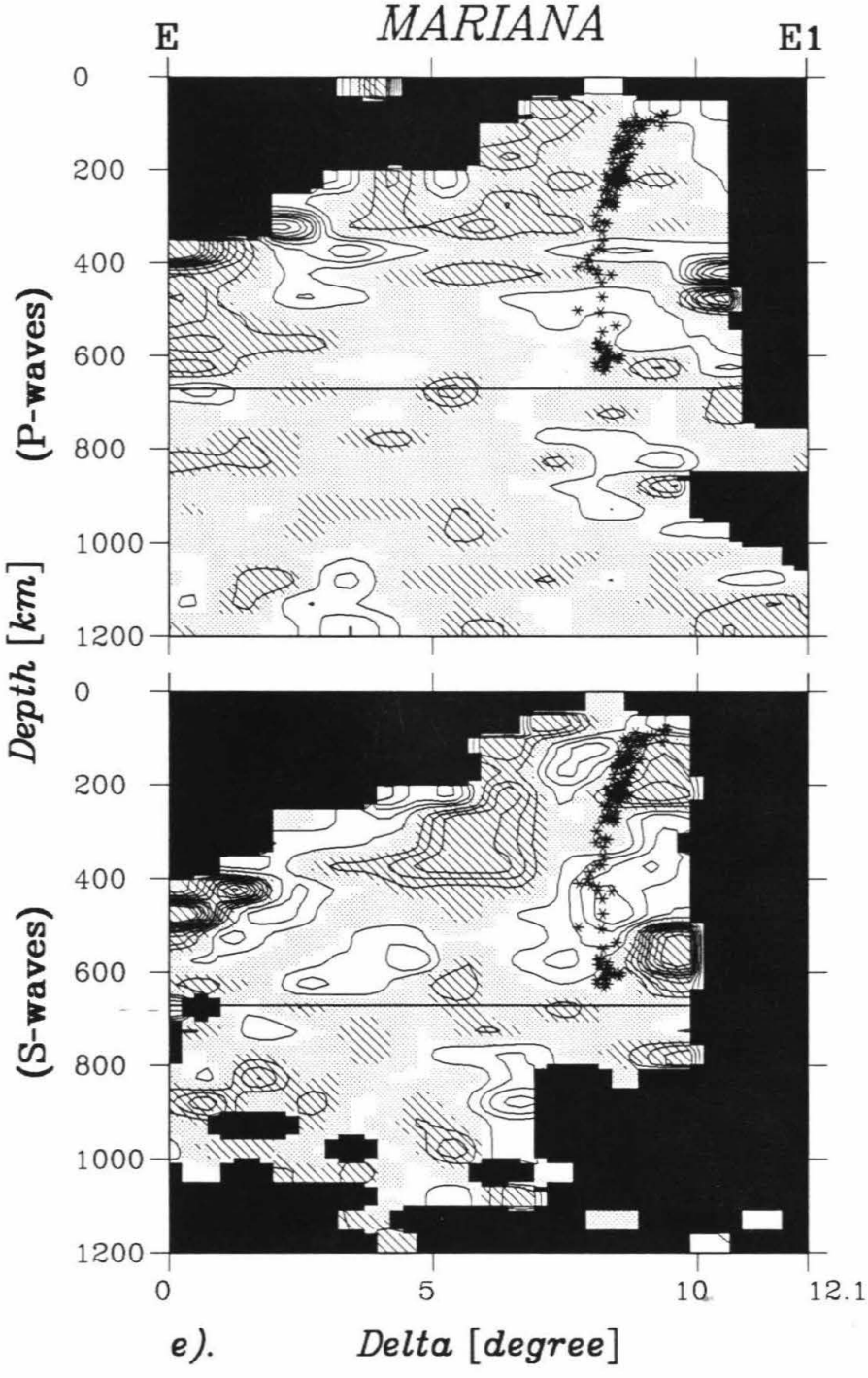
MARIANA
E
E1
(P-waves)
(S-waves)
Depth [km]
0
200
400
600
800
1000
1200
0
5
10
12.1
Delta [degree]

e).

Figure 2.17. Stacked vertical slices of images from data sets with the grouping and sorting procedure. See Figure 2.16 for explanation.

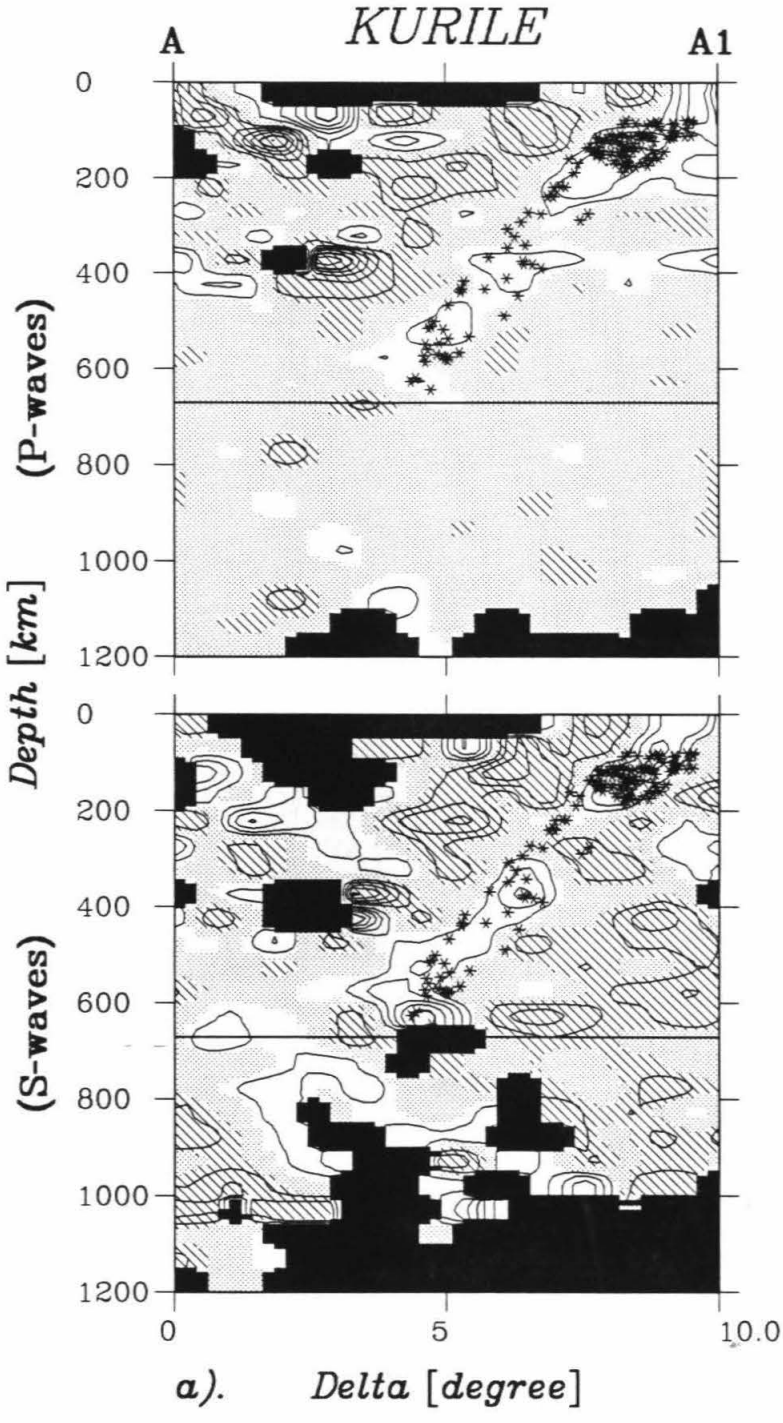
KURILE
A
A1
0
200
400
600
800
1000
1200
(P-waves)
Depth [km]
(S-waves)
0
5
10.0
a). Delta [degree]

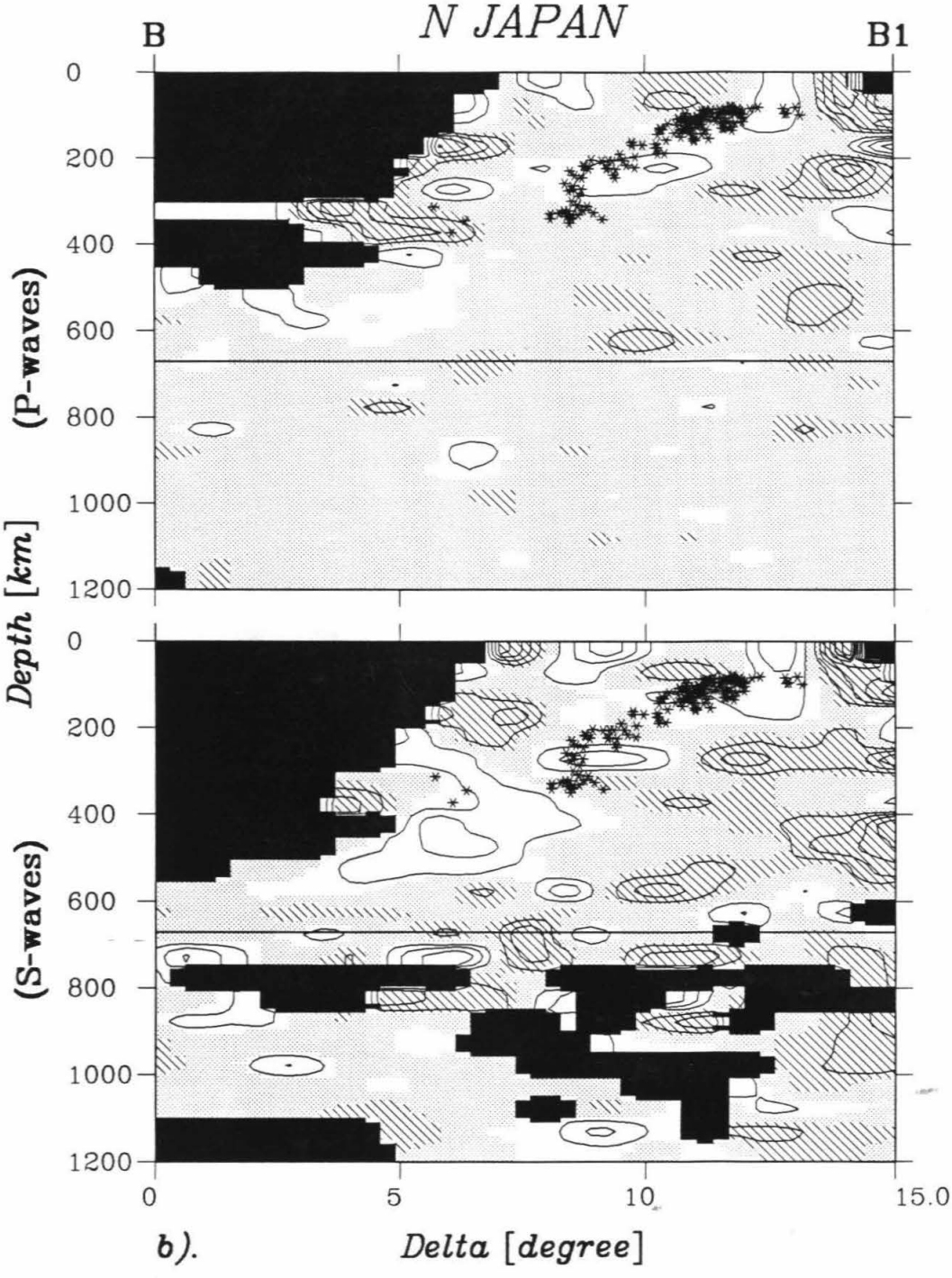
N JAPAN
B
B1
(P-waves)
(S-waves)
Depth [km]
0
200
400
600
800
1000
1200
0
5
10
15.0
Delta [degree]

b).

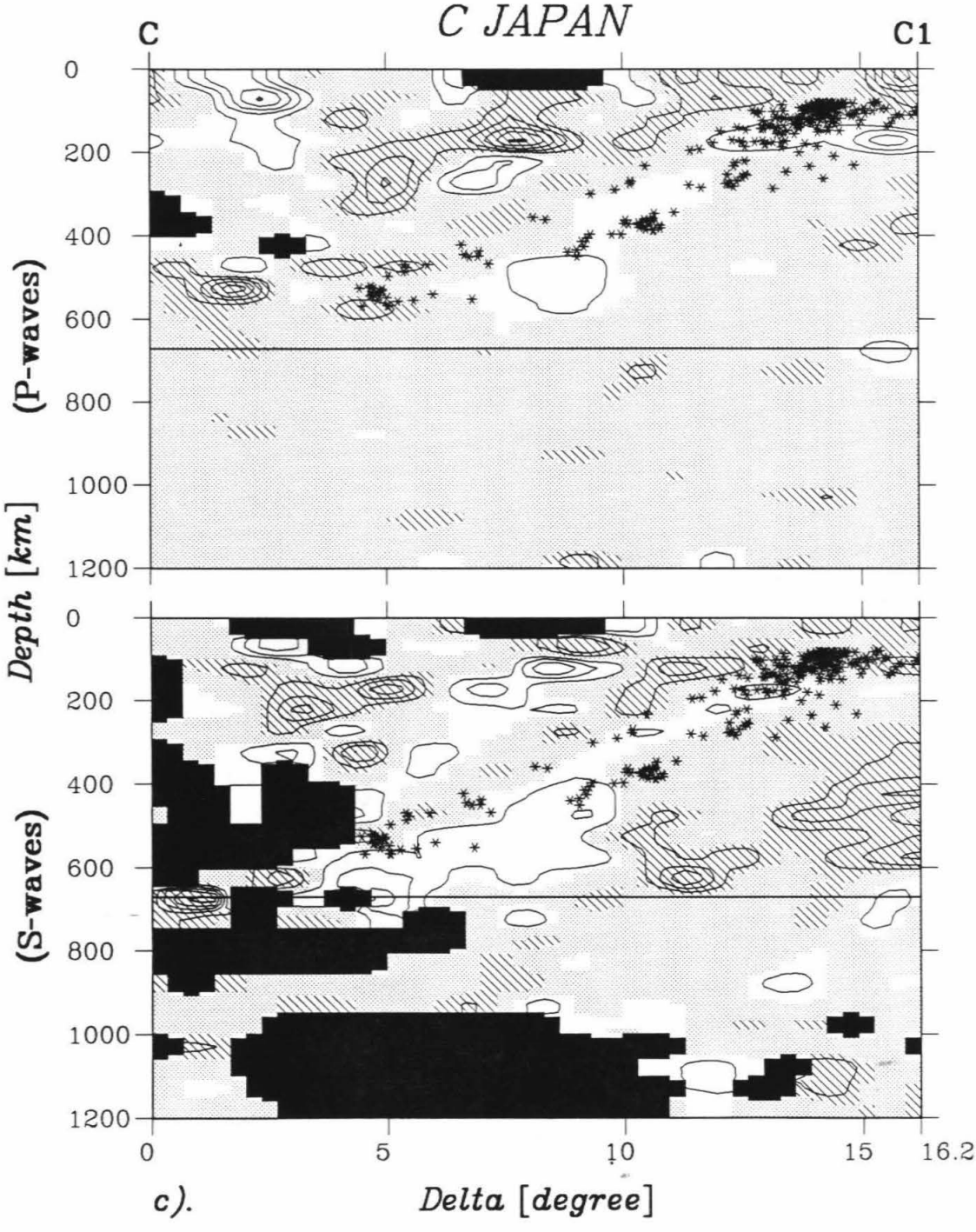
C JAPAN
C
C1
(P-waves)
(S-waves)
Depth [km]
0
200
400
600
800
1000
1200
0
5
10
15
16.2
Delta [degree]

c).

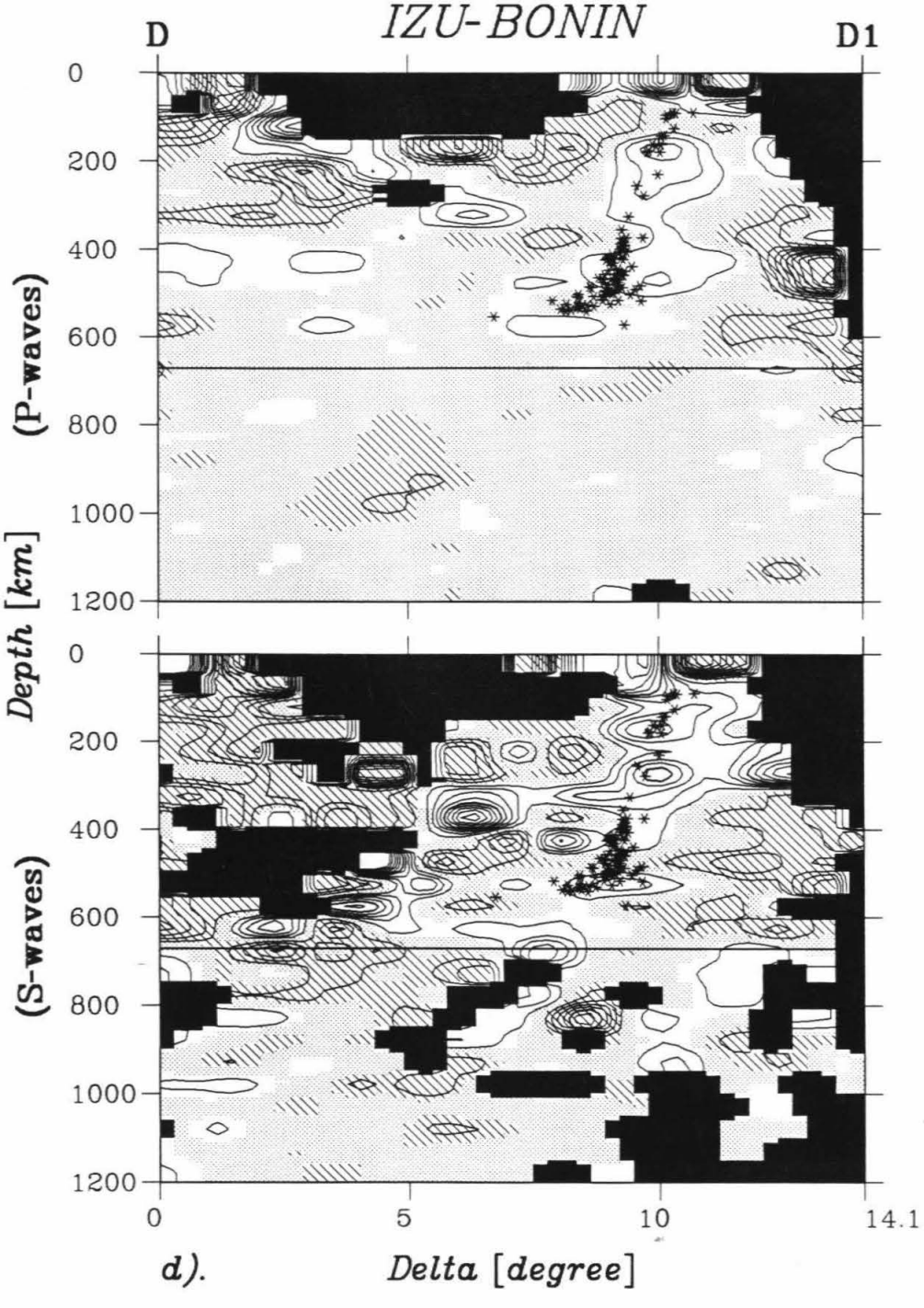
IZU-BONIN
D
D1
(P-waves)
(S-waves)
Depth [km]
0
200
400
600
800
1000
1200
0
5
10
14.1
Delta [degree]

d).

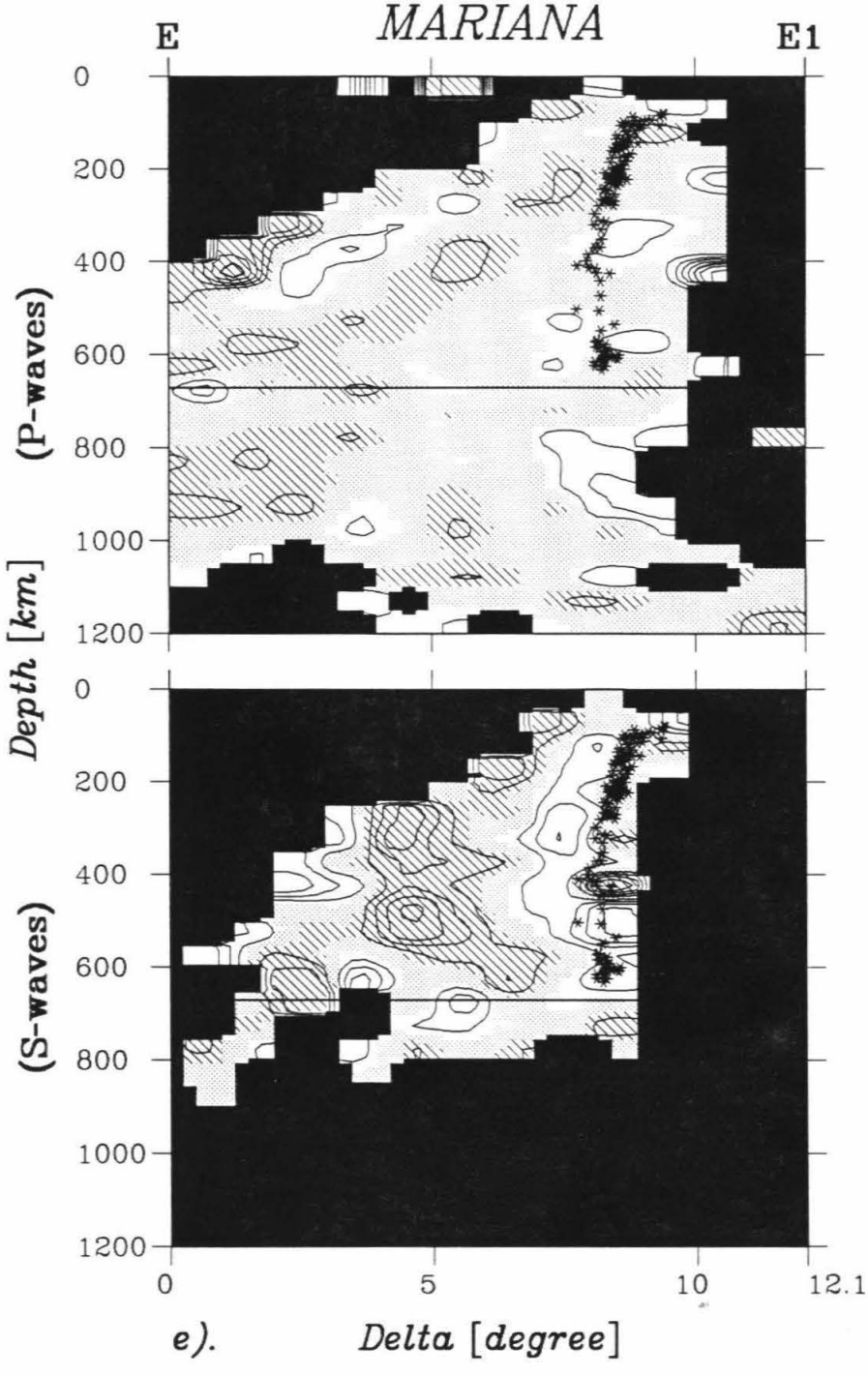
E
MARIANA
E1
0
200
400
600
800
1000
1200
(P-waves)
Depth [km]
(S-waves)
0
5
10
12.1
e).
Delta [degree]

Under the Kurile trench (slice A-A1), the fast slab-like anomalies appears folded, and fingering is seen around 600 km. A fast anomalous band at depth around 850 km in this region was seen in an inversion on data without the grouping and sorting procedure. However, this band is not so evident in the slices currently shown, based on the data after the grouping and sorting procedure. The resolution in this region is quite poor in the lower mantle (see the right panel of Figure 2.15a). The slab under Japan (slices B-B1 and C-C1) has more or less constant low dip angle, which flattens to sub-horizontal near the 670 discontinuity. Even though there are no earthquakes below 450 km along slice B-B1, a fast slab is seen extending to the upper mantle-lower mantle boundary. The resolution of the image is very sharp in the area under Japan. The subducted Pacific lithosphere is probably flowed underneath Japan into sub-horizontal under the edge of the continent Asia. Bending is apparent in both seismicity and the slab-like anomaly under the Izu-Bonin trench (slice D-D1) near the bottom of the upper mantle. The slab is steeply dipping above 400 km, but becomes sub-horizontal at depth somewhat below the deepest earthquakes. Finally, both the horizontal and downward spreading of the slab are indicated under the Mariana trench (E-E1), although the resolution is poor in parts of this region. Thickening and flattening of the slab are possible, and some fast anomalies are seen around 900-1000 km depth, in forms of horizontal layers which are separated by slow layers above and below.

Slow velocity anomalies on the arc and ocean sides of the slabs in the upper part of the upper mantle are clearly shown in the images. One of the

largest slow anomalies imaged is under the back-arc region of the northern Philippine plate, extending north to underneath the Sea of Japan (see the 200-250 km panels in Figures 2.11, 2.11 and 2.12, and vertical slices C-C1 and D-D1 in Figures 2.15, 2.16 and 2.16). This anomaly occurs from the near surface down to almost 300 km in depth, coincident with the anomalous absence of seismic activity in the same area below 70 km. Apart from deep subduction zones, shallow fast slab anomalies are also resolved under Luzon and Ryukyus, extending farther north, along the east edge of the Sea of Japan (Figures 2.11, 2.12 and 2.13). In the following discussion, however, we will concentrate on structures under the major subduction zones of the northwest Pacific.

2.6 Discussion

The depth extent of the subducted lithosphere is a critical but difficult problem. Although this study yields some high-resolution images of the fast slab-like anomaly, the question is still largely open, mainly due to the nonuniqueness in interpretation and decrease in the amplitude of resolution at depth. Penetration of the lithospheric slab into the lower mantle has been proposed previously for the region based on extensive residual sphere studies [Jordan, 1977; Creager and Jordan, 1984, 1986]. A deep anomaly has been found in the Kurile region from a waveform analysis [Silver and Chan, 1986]. Our study involves earthquakes in a large region, and utilizes rays from other

sources which traverse the mantle below the earthquakes. The inverse approach we use makes no assumptions about the form of the anomaly. Forward modeling is a logical check on the inversion results (e.g., Zhou *et al.*, 1988, as the Chapter 4 of this thesis), but it should be pointed out that since residual sphere studies have essentially zero resolution along the ray paths, the anomaly could generally be anywhere between the source and the receiver.

Our images indicate that fast slab-like anomalies appear to extend to below 670 km under parts of the Mariana trench, and possibly parts of the Kurile trench (Slice E-E1 and A-A1 in Figures 2.15, 2.16 and 2.17). The slab in other regions, however, tends to flatten to sub-horizontal around 600 km depth, in accordance with the flattening of seismicity. The difficulty in making a general interpretation of the slab is apparent in these figures. There are apparently many fast regions in the upper part of the lower mantle that are unrelated to Wadati-Benioff zones, and other regions where the deepest earthquakes are underlain by slow anomalies in the lower mantle. In many cases, because we don't know whether the 670 km discontinuity is elevated or depressed, we don't know if the velocity anomaly, or the inferred mechanic lithosphere, crosses the discontinuity.

According to Hager and Raefsky [1981], an accumulation of old slab would lead to a depression of the 670 km discontinuity by at least 25 km and would likely reach 150 km if the mantle is chemically layered. From this type of system to the whole mantle convection, the degree of depression is expected to be smaller. Observationally, a sharp 670 km discontinuity has previously been suggested based on precursors to P'P', denoted by P'670P' [e.g., Engdahl

and Flinn, 1969; Whitcomb and Anderson, 1970; Richards, 1972; Husebye *et al.*, 1977; and Nakanishi, 1988]. However, the P'670P' phases are not consistently observed and their erratic nature suggests extreme lateral heterogeneity in the 670 km discontinuity [Nakanishi, 1988; Wallace and Holt, 1988]. Barley *et al.* [1982] and Faber and Müller [1984] discussed converted phases and suggested that they are scattered from lateral heterogeneity around 650 km depth. Faber and Müller pointed out that a relatively smooth transition zone between the upper mantle and lower mantle below East Asia can explain the lack of precursor energy for events around Japan. Bock and Ha [1984] found a large S-P phase conversion depth ($\sim$ 700 km) under Tonga, which may result from a dynamical or thermal deformation of the 670 km discontinuity beneath the Tonga slab. In this study correlations between adjacent panels appear much poorer across a depth around 650 km (Figures 2.12 and 2.13). This suggests that if slabs do cross the 670 km discontinuity, they likely do not retain the form of a single coherent sheet, but exist in the form of either small fingers or very broad patches. But this is not consistent with the hypothesis of Creager and Jordan (1984, 1986).

Previous theoretical and experimental studies [e.g., Anderson, 1979, 1987a; Knittle *et al.*, 1986; Kincaid and Olson, 1987; Ringwood and Irifune, 1988] give varying results on the relative buoyancy of the slab near the upper mantle-lower mantle boundary. Consequently, the fingering of the slab, i.e., co-existence of the down-going and flattening of slab fingers during the evolution history of subduction, is possible. Anderson [1979, 1987a] points out that both peridotite and eclogite are less dense than the lower mantle and

slabs may therefore be unable to penetrate the boundary, although boundary deformation is possible. Fast regions in the lower mantle may be due to thermal coupling, i.e., cooling of the lower mantle by the slab. This adds an extra difficulty to interpreting deep slab morphology from tomographic images. Flattening of the slab could be the result of either chemical or viscous stratification. A deep extension of a fast anomaly could be the result of local penetration or thermal coupling. The images indicate that morphology of the slab in the transition region is apparently very complicated. The fates of the descending slab have been discussed in many studies [e.g., Davies, 1980; Vidale, 1987; and Gurnis and Hager, 1988]. It is therefore not adequate to extrapolate the general characteristics of the slab from observations in a few places only. For instance, even if the slab descends into the lower mantle under the Kurile trench, the calculation of the total downward flux across the boundary based on this result, would obviously be too large, since the high-velocity anomaly is not continuous across the boundary in many other places. Our study also shows that it is not appropriate to take the magnitude of the slab-related-anomaly from shallow and intermediate depth earthquakes and apply it to deep-focus earthquakes. More detailed studies of all subduction regions are needed to advance our understanding about the slab penetration issue.

Our study has illustrated many aspects of the vertical and lateral morphology of the slab. Along the strike of slab, our image solutions suggest that most slab anomalies under island arcs of the Northwest Pacific are continuous, but become quite contorted and broadened with depth. This

indicates that the descending lithosphere is initially quite coherent, but as suggested in our interpreted model in Figure 2.14, segmentation of the major northwest Pacific slab, which is under the Kurile, Japan, Izu-Bonin and Mariana arcs, takes place below 400 km depth. The segmentation may partially be a consequence of along-strike stretching due to differential flattening on different slab segments. In our interpreted slab model, the along-strike length of the major northwest Pacific slab between 13° N to 51° N increases about 15% from the surface to 400 km depth, ignoring truncations of the slab. This estimation can also be made simply from the lateral trace of seismicity at those depths. If along-strike stretching and across-strike broadening of the lithospheric slab really occurs, the descending velocity of the slab should decrease.

Contortion and flattening seem to be a general characteristic of the vertical morphology of the slab in the upper mantle. The slab probably thickens with depth, and is fingered and broadened to several times its near-surface thickness in the transition zone. This slab broadening phenomena, if real, is obviously not just a thermal conduction effect. Temperature induced phase changes [Anderson, 1987a], increase in viscosity with depth [Gurnis and Hager, 1988] and slab doubling [Giardini and Woodhouse, 1984] are large effects. Piling up of the slab material around the boundary is another hypothesis [Anderson, 1987a]. These effects seem to be in accord with the peak of deep seismicity below 350 km and the down-dip compressional stress regime of the slab as suggested by focal mechanisms of deep earthquakes [Isacks and Molnar, 1969, 1971].

In most cases, the resolved slab anomalies are associated with clusters of seismic activity. There are indications that the peaks of deep seismicity tend to spatially coincide with either flattening or fingering of the slab-related anomalies. Most shallow earthquakes occur near the top of the lithospheric slab [e.g., Engdahl and Gubbins, 1987] due to bending of the oceanic plate and breaking of interplate asperities [Lay and Kanamori, 1981]. From this study, however, we find that hypocentral locations in the lower half of the upper mantle sometimes lie nearer the central or even the bottom parts of the fast anomalies. Source location uncertainty does not affect this observation greatly since the fast slab anomalies are resolved with respect to the given source locations, and the location uncertainty is small for most events used. This means that the dips of Wadati-Benioff zones, as determined from earthquake locations, can differ from the slab dips inferred from the fast velocity anomalies. The shallow dips of the earthquakes, assumed to represent the slab, have been used to argue for whole mantle convection and deep slab penetration (e.g., Hager and O'Connell [1981]).

Our models support the hypothesis that the descending lithospheric slabs finger and spread above or near the upper mantle-lower mantle boundary. This, plus the peaks of deep seismicity, appears to be the consequence of the slab encountering a barrier of some form around the transition zone. This could be associated with an increase in viscosity [e.g., Hager, 1984; Hager *et al.*, 1985], a chemical or intrinsic density contrast or the loss of negative buoyancy of the slab [Anderson, 1979, 1984; Jeanloz and Thompson, 1983; Anderson and Bass, 1986].

The compressional and shear velocities obtained in this study agree well with some previous works in the northwest Pacific region. For instance, comparison with five cross sections from a regional least-squares inversion by Hirahara [1981] indicates good correlation exist with four of them, with the one under Kinki to Kii being the exception. Under the southern part of the Sea of Japan and central Honshu, a slow anomaly from the near surface to about 300 km depth was previously detected [Hirahara, 1977, 1981; Hirahara and Mikumo, 1980]. This is part of a large slow feature resolved in this study (Figures 2.11, 2.12, 2.16b and 2.16c). This feature extends to the Philippine plate and coincides with the absence of intermediate to deep earthquakes in parts of the region. These results are obtained from different inversion methods on different block grids, from similar data.

Recently, Kamiya *et al.* [1988] obtained tomographic images with a fast slab-like anomaly extending to 1200 km under Japan Their image correlates well with ours from the surface down to 600 km under Japan and Izu-Bonin [Zhou, 1988]. The lower mantle results differ, probably due to the difference in data. Kamiya *et al.* used ISC data from 1977 to 1983, and included teleseismic picks and shallow events. In contrast, we used ISC data from 1964 to 1982 and excluded teleseismic picks and events shallower than 60 km. The region with deep slab anomaly of Kamiya *et al.* below 950 km is not covered by our images. The block size of Kamiya *et al.* is finer than that of the small block grid of ours, thus their ray coverage is correspondingly lower than ours. Hence, their deep slab anomaly is entirely from teleseismic data, and therefore subject to along-path smearing. The deepest seismicity around 500-600 km

depth in the slice under Japan is on the edge of the model by Kamiya *et al.*, and shows a tendency of flattening to sub-horizontal from the fast slab anomalies at 400-600 km depth in both theirs and our models. A residual sphere study of this area [Zhou *et al.*, 1988] also gives a fast horizontal slab-like feature at the base of the mantle and show. Furthermore, the deep lower mantle contains large scale coherent structures which sometimes map into the residual sphere as steeply dipping slab-like structures.

In a recent survey of intermediate and deep seismicity in the Circum-Pacific region, Burbach and Frohlich [1986] have located four well constrained PSBs (Possible Segmentation Boundaries) along the Kurile, Japan, Izu-Bonin and Mariana trenches. They have also noticed the abnormal absence of deep seismic activity around two of their PSBs at the junctions of the Kurile and Japan trenches and Japan and Izu-Bonin trenches. Our images indicate segmentations of the slab anomalies along these PSBs within the upper mantle (Figures 2.12, 2.13 and 2.14). Previous investigators have suggested that the slab is buckled under the two junctions, and that there may be a hinge fault under the first one [Isacks and Molnar, 1971; Minamino and Fujii, 1981], and the slab is continuous to at least a few hundred kilometers depth under the second one [Aoki, 1974; Utsu, 1974; Hirahara, 1981]. P and S results in this study indicate that slab is buckled under both junctions and torn apart at about 400 km depth.

Kanamori [1971] proposed a model to interpret the opposite first motions between a great Tokachi-Oki earthquake (M_s~8.0) and its largest aftershocks (M_s~7.5) under the first junction. The model suggests that a tear exists along

the junction but the two segments are held together by lateral compression. Since the separation takes place with no detectable seismic activity, we are inclined to extend Kanamori's model in the following way. We suspect that the slab is indeed broken under the junction by a tear or a hinge fault near the surface, but the two segments are kept together in the shallow region by lateral compression from the convergent geometry of the slab there. Due to differential flattening of the slab in the deep portion of the upper mantle, the lateral compression gradually diminishes with increasing depth and the separation finally takes place aseismically.

The strong slow anomalies on the ocean side of the slab in the upper mantle, which are usually not as strong as the slow regions under back-arc basins, have not been discussed previously. One interpretation of the slow anomaly is that it is actually a representative of normal mantle at that depth. This interpretation will shift the anomaly amplitudes of slab and ambient mantle as listed in Table 1 to be more negative (fast). Both the P and S results show a slow background in the upper mantle, as indicated by layered means given for each panel in Figures 2.12 and 2.13, and cross sections in Figures 2.15, 2.16 and 2.17. This probably suggests that the JB model is too fast in the upper mantle. Nataf *et al.* [1984, 1986] also conclude that the shallow mantle in the vicinity of the Pacific subduction zones is slow for shear waves and the mantle below 300 km is fast. Some global studies of compressional waves [Clayton and Comer, 1983; Hager and Clayton, 1989; Zhou and Clayton, 1985] indicate that the JB model is, in general, too fast in the lower mantle above 900 km depth, too slow from 900 km to 1,100 km, and

then too fast again to about 1,900 km. The contour pattern of the slow anomalies under the back-arc basin near Honshu seems to support the wedge flow model [McKenzie, 1969; Toksöz and Hsui, 1978], the absence of intermediate and deep earthquakes and presence of volcanic activity from the island of Honshu to the northern Philippine Sea.

2.7 Conclusions

Images of three-dimensional P and S velocity structures under the island arcs of the northwest Pacific have been resolved by a tomographic inversion method. A grouping and sorting of rays with the same source and station areas considerably reduces the noise of the data. Analysis of resolution and noise show the images are generally well resolved. The resulting velocities substantially improve the fit of the data. There are strong high velocity anomalies associated with the Wadati-Benioff zone. Although earthquakes are generally embedded in fast regions, the dip of the Wadati-Benioff zone seismicity sometimes differs from the dip of the high velocity regions. The P and S results correlate well, especially in the upper mantle. Laterally, the amplitude of the shear anomalies is around one and a half times that of the compressional anomalies in percentage. The slab anomalies appear contorted and broadened with depth in most parts of the upper mantle, while fingering and spreading of the slab occurs in the transition zone. The slab usually flattens to sub-horizontal around the 670 km discontinuity, although

downward continuity of fast anomalies below this depth may occur under parts of the Mariana and Kurile arcs. The shallowly dipping slab under Japan may have slipped under the edge of the Asia continent. A three-dimensional interpretive slab model of the region has been constructed based on velocity images and seismicity. Our results support the hypothesis that the fingering and spreading of slab anomalies above or around the upper mantle-lower mantle boundary and their relation with deep seismic activity reflect the behavior of the descending lithosphere, and they are caused by the slab encountering a barrier of some form near that boundary. We cannot resolve whether the slab sometimes penetrates the boundary or the boundary is simply depressed underneath the subduction zone. If the slab does cross the boundary, however, it appears not to retain the form of a single coherent sheet.

References to Chapter 2

Aki, K., and P. G. Richards, *Quantitative Seismology Vol. 2*, W.H. Freeman, San Francisco, 1980.

Anderson, Don. L., Chemical stratification of the mantle, *J. Geophys. Res.*, **84**, 6297-6298, 1979.

Anderson, Don. L., Chemical inhomogeneity of mantle above 670 km transition, *Nature*, **307**, p.114, 1984.

Anderson, Don L., Thermally induced phase changes, lateral heterogeneity of the mantle, continental roots and deep slab anomalies, *J. Geophys. Res.*, **92**, 13968-13980, 1987a.

Anderson, Don L., A seismic equation of state, II. shear properties and thermodynamics of the lower mantle, *Phys. Earth Planet. Inter.*, **45**, 307-323, 1987b.

Anderson, Don L., and J. Bass, Transition region of the Earth's upper mantle, *Nature*, **320**, 321-328, 1986.

Aoki, H., Plate tectonics of arc-junction at central Japan, *J. Phys. Earth*, **22**, 141-161, 1974.

Barazangi, M., and B. Isacks, A comparison of the spatial distribution of mantle earthquakes determined from data produced by local and by teleseismic networks for the Japan and Aleutian arcs, *Bull. Seism. Soc. Am.*, **69**, 1763-1770, 1979.

Barley, B. J., J. A. Hudson, and A. Douglas, S to P scattering at the 650 km discontinuity, *Geophys. J. R. astr. Soc.*, *69*, 159-172, 1982.

Bock, G., P wave travel times from deep and intermediate-depth earthquakes to local seismic stations and the subducted slab of oceanic lithosphere beneath the Tonga island arc, *J. Geophys. Res.*, **92**, 13863-13877, 1987.

Bock, G., and J. Ha, Short-period S-P conversion in the mantle at a depth near 700 km, *Geophys. J. R. astr. Soc.*, *77*, 593-615, 1984.

Burbach, G. V., and C. Frohlich, Intermediate and deep seismicity and lateral structure of subducted lithosphere in the Circum-Pacific region, *Rev. of Geophys.*, **24**, 833-874, 1986.

Clayton, R. W. and R. P. Comer, A tomographic analysis of mantle heterogeneities from body wave travel times, *Eos Trans. AGU*, **64**, 776, 1983.

Comer, R. P., and R. W. Clayton, Reconstruction of mantle heterogeneity by iterative back projection of travel times: 1. Theory and reliability, *unpublished manuscript*, 1984.

Creager, K. C., and T. H. Jordan, Slab penetration into the lower mantle, *J. Geophys. Res.*, **89**, 3031-3049, 1984.

Creager, K. C., and T. H. Jordan, Slab penetration into the lower mantle

beneath the Mariana and other island arcs of the northwest Pacific, *J. Geophys. Res.*, **91**, 3573-3580, 1986.

Davies, G. F., Mechanics of subducted lithosphere, *J. Geophys. Res.*, **85**, 6304-6318, 1980.

Davies, J. H., and R. W. Clayton, Error analysis of a shear wave mantle tomographic inversion, *Eos Trans. AGU*, **68**, 1376, 1987.

Dziewonski, A. M., and F. Gilbert, The effects of small, aspherical perturbations on travel times and a re-examination of the corrections for ellipticity, *Geophys. J. R. astr. Soc.*, **44**, 7-17, 1976.

Engdahl, E. R., and E. A. Flinn, Seismic waves reflected from discontinuities within the earth's upper mantle, *Science*, *163*, 177-179, 1969.

Engdahl, E. R., and D. Gubbins, Simultaneous travel-time inversion for earthquake location and subduction zone structure in the central Aleutian Islands, *J. Geophys. Res.*, **92**, 13855-13862, 1987.

Faber, S., and G. Müller, Converted phases from the mantle transition zone observed at European stations, *J. Geophys.*, *54*, 183-194, 1984.

Giardini, D., and J. H. Woodhouse, Deep seismicity and modes of deformation in Tonga subduction zone, *Nature*, **307**, 505-509, 1984.

Giardini, D., and J. H. Woodhouse, Horizontal shear flow in the mantle beneath the Tonga arc, *Nature*, **319**, 551-555, 1986.

Gurnis, M., and B. H. Hager, Controls on the structure of subducted slabs and the viscosity of the lower mantle, *Nature*, **335**, 317-321, 1988.

Hager, B. H., Subducted slabs and the geoid: constraints on mantle rheology and flow, *J. Geophys. Res.*, **89**, 6003-6015, 1984.

Hager, B. H., and R. W. Clayton, Constraints on the structure of mantle convection using seismic observations, flow models, and the geoid, in W. R. Peltier, ed., *Mantle Convection*, Gordon & Breach, in press, 1989.

Hager, B. H., R. W. Clayton, M. A. Richards, R. P. Comer, and A. M. Dziewonski, Lower mantle heterogeneity, dynamic topography and the geoid, *Nature*, **313**, 541-545, 1985.

Hager, B. H., and R. J. O'Connell, A simple global model of plate dynamics and mantle convection, *J. Geophys. Res.*, *86*, 4843-4867, 1981.

Hager, B. H., and A. Raefsky, Deformation of seismic discontinuities and the scale of mantle convection, *Eos Trans. AGU*, *62*, 1074, 1981.

Hirahara, K., A large-scale three-dimensional seismic structure under the Japan islands and the Sea of Japan, *J. Phys. Earth*, **25**, 393-417, 1977.

Hirahara, K., Three-dimensional seismic structure beneath southwest Japan: The subducting Philippine Sea plate, *Tectonophys.*, **79**, 1-41, 1981.

Hirahara, K., and T. Mikumo, Three-dimensional seismic structure of subducting lithospheric plates under the Japan islands, *Phys. Earth Planet. Inter.*, **21**, 109-119, 1980.

Husebye, E. S., R. A. Haddon, and D. W. King, Precursors to P'P' and upper

mantle discontinuities, *J. Geophys.*, *43*, 535-543, 1977.

Isacks, B. L., and M. Barazangi, Geometry of Benioff zones, lateral segmentation and downwards bending of the subducted lithosphere, in *Island Arcs, Deep Sea Trenches and Back-Arc Basins*, Maurice Ewing Ser. **1**, edited by M. Talwani and W. C. Pitman III, 99-114, AGU, Washington, D.C., 1977.

Isacks, B., and P. Molnar, Mantle earthquake mechanisms and sinking of the lithosphere, *Nature*, **223**, 1121-1124, 1969.

Isacks, B., and P. Molnar, Distribution of stresses in the descending lithosphere from a global survey of focal mechanism solution of mantle earthquakes, *Rev. Geophys. Space Phys.*, **9**, 103-174, 1971.

Jeanloz, R., and A. B. Thompson, Phase transitions and mantle discontinuities, *Rev. Geophys. Space Phys.*, *21*, 51-74, 1983.

Jordan, T. H., Lithospheric slab penetration into the lower mantle beneath the Sea of Okhotsk, *J. Geophys.*, **43**, 473-496, 1977.

Kamiya, S., T. Miyatake, and K. Hirahara, How deep can we see the high velocity anomalies beneath the Japan Island? *Geophys. Res. Lett.*, **15**, 828-831, 1988.

Kanamori, H., Focal mechanism of the Tokachi-Oki earthquake of May 16, 1968: Contortion of the lithosphere at the junction of two trenches, *Tectonophys.*, **12**, 1-13, 1971.

Kincaid, C., and P. Olson, An experimental study of subduction and slab migration, *J. Geophys. Res.*, **92**, 13832-13840, 1987.

Knittle, E., R. Jeanloz, and G. L. Smith, Thermal expansion of silicate perovskite and stratification of the Earth' mantle, *Nature*, **319**, 214-216, 1986.

Lay, T., and H. Kanamori, An asperity model of large earthquake sequences, in *Earthquake Prediction*, edited by D. W. Simpson and P. G. Richards, 579-592, AGU, Washington, D. C., 1981.

McKenzie, D. P., Speculations on the consequences and causes of plate motions, *Geophys. J. R. astr. Soc.*, **18**, 1-32, 1969.

Minamino, T., and N. Fujii, The effect of the contorted "nose" of a subducting slab on the stress field in the continental lithosphere at an arc-arc junction, *Geophys. J. R. astr. Soc.*, **67**, 145-158, 1981.

Nakanishi, I., Reflections of P'P' from upper mantle discontinuities beneath the Mid-Atlantic Ridge, *Geophys. J.*, *93*, 335-346, 1988.

Nataf, H.-C., I. Nakanishi, and Don L. Anderson, Anisotropy and shear-velocity heterogeneities in the upper mantle, *Geophys. Res. Lett.*, **11**, 109-112, 1984.

Nataf, H.-C., I. Nakanishi, and Don L. Anderson, Measurements of mantle wave velocities and inversion for lateral heterogeneities and anisotropy, III, *J. Geophys. Res.*, **91**, 7261-7307, 1986.

Nieman, T. L., K. A. Wagner, and K. Fujita, Effects of subducting slabs on teleseismic hypocentral determinations — Theoretical calculations, *Eos Trans. AGU*, **65**, 234, 1984.

Richards, P. G., Seismic waves reflected from velocity gradient anomalies within the earth's upper mantle, *J. Geophys.*, *38*, 517-527, 1972.

Ringwood, A. E., and T. Irifune, Layered convection in a grossly homogeneous mantle, *Eos Trans. AGU*, **69**, 486, 1988.

Roecker, S. W., Velocity structure in the Izu-Bonin seismic zone and the depth of the olivine-spinel phase transition in the slab, *J. Geophys. Res.*, **90**, 7771-7794, 1985.

Silver, P. G., and W. W. Chan, Observations of body wave multipathing from broadband seismograms: evidence for lower mantle slab penetration beneath the Sea of Okhotsk, *J. Geophys. Res.*, **91**, 13787-13802, 1986.

Spencer, C. P., and E. R. Engdahl, A joint hypocenter location and velocity inversion technique applied to the central Aleutians, *Geophys. J. R. astr. Soc.*, **72**, 399-415, 1983.

Spencer, C. P., and D. Gubbins, Travel-time inversion for simultaneous earthquake location and velocity structure determination in laterally varying media, *Geophys. J. R. astr. Soc.*, **63**, 95-116, 1980.

Toksöz, M. Nafi, and A. T. Hsui, Numerical studies of back-arc convection and the formation of marginal basins, *Tectonophys.*, **50**, 177-196, 1978.

Utsu, T., Space-time pattern of large earthquakes occurring off the Pacific coast of the Japanese islands, *J. Phys. Earth*, **22**, 325-342, 1974.

Vassiliou, M. S., and B. H. Hager, Subduction zone earthquakes and stress in slabs, *PAGEOPH*, *128*, 547-624, 1988.

Vidale, J. E., Waveform effects of a high-velocity subducted slab, *Geophys. Res. Lett.*, **14**, 542-545, 1987.

Wallace, T. C., and W. E. Holt, The 670 km discontinuity and precursors to P'P': Implications for the sharpness of the boundary and its global extent, *Eos Trans. AGU*, *69*, 1333, 1988.

Whitcomb, J. H., and Don L. Anderson, Reflections of P'P' seismic waves from discontinuities in the mantle, *J. Geophys. Res.*, *75*, 5713-5728, 1970.

Zhou, H., How well can we resolve the deep seismic slab with seismic tomography? *Geophys. Res. Lett.*, **15**, 1425-1428, 1988.

Zhou, H., Don L. Anderson, and R. W. Clayton, Modeling of residual spheres for subduction zone earthquakes in the northwest Pacific, submitted to *J. Geophys. Res.*, 1988.

Zhou, H., and R. W. Clayton, Mantle velocities from PP-waves, *Eos Trans. AGU*, **66**, 975, 1985.

Zhou, H., and R. W. Clayton, Travel-time inversions for P and S velocities beneath the northwest edge of the Pacific: slab fingering? *Eos Trans. AGU*, **68**, p.1379, 1987.

CHAPTER 3

TOMOGRAPHIC INVERSIONS IN THE SOUTHWEST PACIFIC:

regional P wave structures from primarily teleseismic data

Abstract

A three-dimensional P wave velocity model around subduction zones in the southwest Pacific is obtained through tomographic inversions of ISC travel time residuals of deep and intermediate depth earthquakes. Corrections for mantle heterogeneities outside the model are performed. Ray paths inside the model are traced allowing two-dimensional velocity variations. The rays of similar source and receiver locations are combined into summary rays, and the hypocenters are relocated as part of the inversion iterations. The resulting images are interpreted in conjunction with resolution and error estimations.

Slab-like anomalies of several percent fast are seen around most subduction zones in the resolved model of block size $2^\circ \times 2^\circ \times 50$ *km and* $1^\circ \times 1^\circ \times 50$ *km. These slabs are generally continuous in places of high seismic activity, and decrease in amplitude with depth. The most coherent slab anomalies are beneath the Tonga, Kermadec and New Hebrides trenches, surrounded by large slow patches between the surface and 350 km depth. The fast slab beneath the Tonga arc appears to end around 550 km depth, but there is a fast band at 750-1000 km depths below the deepest Tongan earthquakes. The fast slab-like anomaly beneath the Kermadec arc tends to flatten to subhorizontal near the bottom of upper mantle, and it exists aseismically near New Zealand down to 500-550 km depth. No clear fast anomalies are seen around the flat lying deep seismicity beneath the North Fiji Basin. While this deep feature appears to be unrelated to the northern New Hebrides slab, its*

southward extension seems to connect with the southern New Hebrides slab. Interpretations in the lower mantle in many places, such as Kermadec and New Hebrides arcs, are hampered by the poor resolution.

3.1 Introduction

The southwest Pacific region, around the major subduction zones under the Tonga, Kermadec and New Hebrides trenches, possesses a very unique and spectacular tectonic environment (Figure 3.1). During the past 25 million years or so [Hilde *et al.*, 1976], the subduction zones in the region served as a margin between two major oceanic plates, the northwestly-moving Pacific Plate to the east and the northly-moving Indo-Australian Plate to the west. The difference in directions and velocities of the two plates is thought to be the primary cause of subduction of the Pacific Plate near the margin and rapid reconfiguration of the subduction zones.

As shown in Figure 0.2, the region has some of the most profound and deepest Wadati-Benioff zones in the world. These zones are characterized by a sharp cutoff near 670 km depth [Stark and Frohlich, 1985] and a large release of deep seismic energy and flattening and thickening of seismicity patterns in the deepest part [Richter, 1979; Giardini and Woodhouse, 1984]. These characteristics of the Wadati-Benioff zones are argued by the above authors as being consistent with the model that the slab fails to penetrate the 650 km discontinuity due to strong resistance. A possible lateral displacement of subducted lithospheric slabs has been suggested by Giardini and Woodhouse

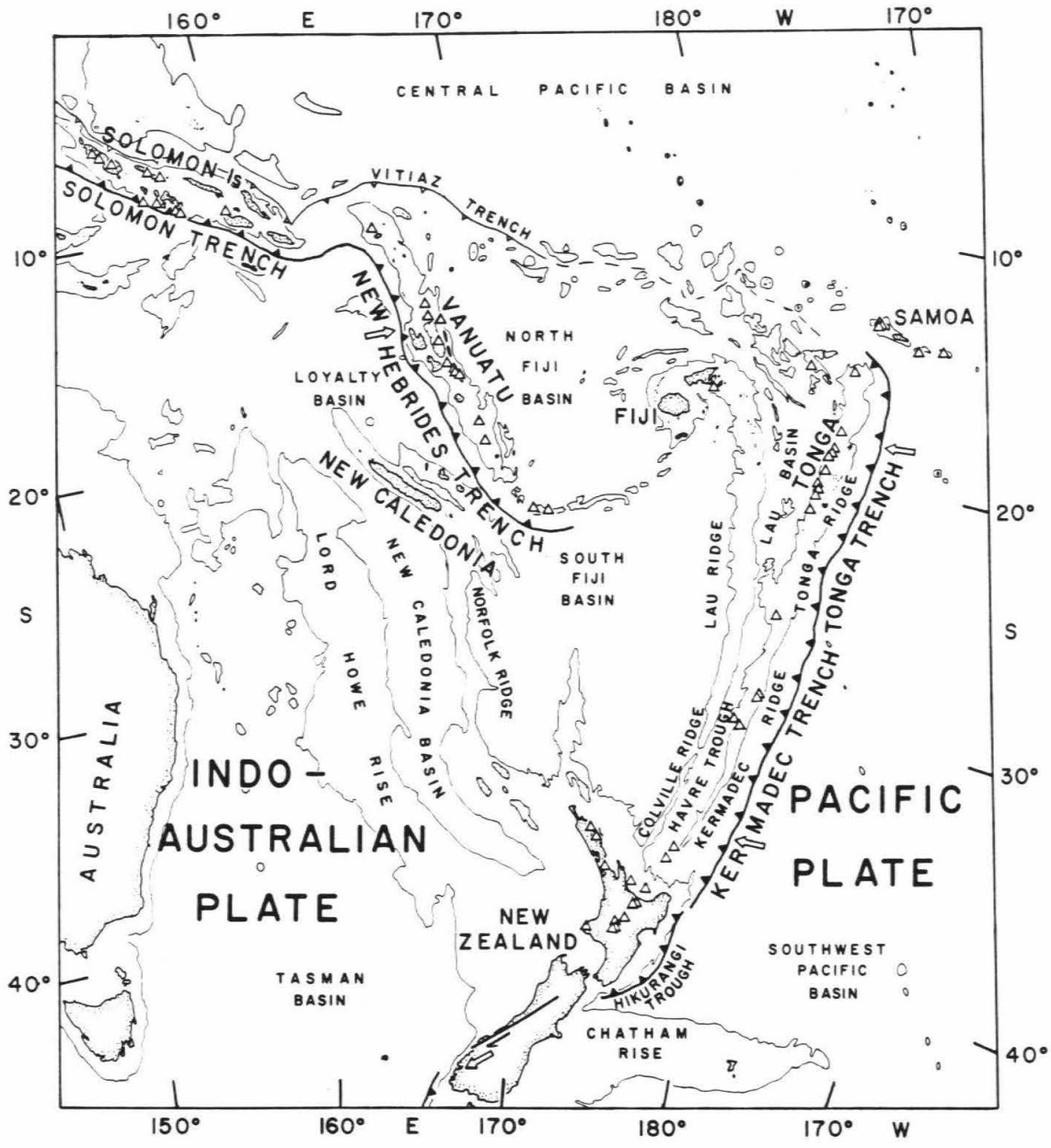

Figure 3.1. Tectonic and morphologic features of the southwest Pacific region (after Hamburger and Isacks, 1987). Open arrows indicate direction of relative plate convergence. Contour lines show 2-km isobath. Holocene volcanoes are indicated by open triangles. Solid and open barbed lines indicate active and relict convergent plate boundaries, respectively. Dashed lines indicate possible eastward extension of the Vitiaz Trench.

[1986], based on moment tensor focal mechanism solutions.

On the other hand, higher seismic velocities in subduction zones beneath the Tonga Trench relative to the surrounding mantle have been detected [Mitronovas and Isacks, 1971; Frohlich and Barazangi, 1980; and Ansell and Gubbins, 1986]. The anomalous fast arrivals of different body wave phases traveling close to the strike direction of subduction zones in the region convincingly indicate the existence of profound fast velocities around seismic zones. These early arrivals raise the possibility that fast slab-like regions associated with the subduction zone may extend below the deepest earthquakes [Frohlich and Barazangi, 1980; Huppert and Frohlich, 1981].

So far, the key problem concerning the fast slab-associated anomalies is not their existence, but how deep they extend. Travel time studies by Sondergeld *et al.* [1977], Bock [1981] and Ansell and Gubbins [1986] found no convincing evidence for velocity anomalies below the bottom of the upper mantle. On the other hand, 5-10% fast velocity anomalies below the deepest earthquakes have been suggested by Fitch [1975; 1977], Frohlich and Barazangi [1980] and Fischer *et al.* [1988] (also see an early report of this work [Zhou and Clayton, 1988]). The complex Cenozoic tectonics of the region [Hamburger and Isacks, 1987] resulted in very complex morphology of subduction zones. The strong contortions of the subducting plates, as indicated by seismicity [Giardini and Woodhouse, 1984], will certainly overcast on any interpretation in a travel time analysis [Bock, 1987].

A tomographic velocity inversion has the potential to determine the locations of large velocity heterogeneities, hence to reconcile different

interpretations based on seismicity, earthquake mechanism, and seismic travel time models. This is the primary motivation of this chapter, which is devoted to the processing and inversion of ISC P wave travel time residuals from the intermediate and deep earthquakes in the region to obtain a three-dimensional compressional velocity model. The observations of significant preferential patterns in travel times and attenuation [Bowman, 1988], plus the deep seismicity, make such an inversion plausible.

In the previous chapter, coherent fast velocity anomalies are obtained in association with the NW Pacific subduction zones in almost entire upper mantle. These fast slab-like anomalies appear to be contorted in many locations, and are fingering, i.e., thickening and flattening, near the bottom of the upper mantle. The current investigation, in the southwest Pacific, is an attempt to extend our understanding about the morphology of subducted slabs. There are some fundamental differences between these two regions. First, the Pacific plate is subducted under a continental plate in the northwest Pacific, while it is subducted under an oceanic plate in the southwest Pacific. Second, from an inversion point of view, only regional arrivals are used for the northwest Pacific inversion, while for the southwest Pacific region, the inversion has to rely largely on teleseismic rays.

Using teleseismic rays to invert local or regional velocity structures are not uncommon. In fact, since the earliest damped least squares tomographic inversions by Aki and Lee [1976], almost all large scale regional inversions are of this type. For example, there are regional inversions involving simultaneous source relocations in Japan [Hirahara, 1977; Hirahara and Mikumo, 1980; and

Kamiya *et al.*, 1988], southwest Japan [Hirahara, 1981], Izu-Bonin Trench [Roecker, 1985] and central Aleutians [Spencer and Engdahl, 1983; Engdahl and Gubbins, 1987]. One difficulty for such inversions is the correction for mantle heterogeneities outside of the model. Most of previous workers did not do the correction, while others have removed near receiver average travel time residuals, simply because there is no reliable mantle velocity model available. In fact, this is one of the major reasons to exclude the receivers outside the modeled region in Chapter 2. In this chapter, however, the correction is done by using other mantle models.

3.2 Data and Corrections

The ISC catalog has reported nearly 14,000 events occurring in the modeled region from 1964 to 1982 (Figure 3.2), with over 600,000 P wave picks. Most of the standard processings that was discussed in Sections 1.4.1 and 1.4.2 are applied to the data. First of all, the data is windowed to include 1) only those picks of focal depths greater than 80 km, 2) only events with a total number of P wave picks more than 50, and 3) epicentral distances between 0.5° and 94°. The selected data consists of 3,220 events with 201,745 P wave picks including teleseismic ones. The earth ellipticity term is then corrected from the data. The average residuals at stations (station statics) as reported by Clayton and Comer [1983] are removed. For stations not included by Clayton and Comer [1983], the average residual is removed if

Figure 3.2. Station distribution map for events used in the southwest Pacific. The stations are circles, with their sizes indicating the number of P wave picks utilized. The events used are expressed by the shaded areas in the boxed area, which is also shown in the next figure, representing the model region.

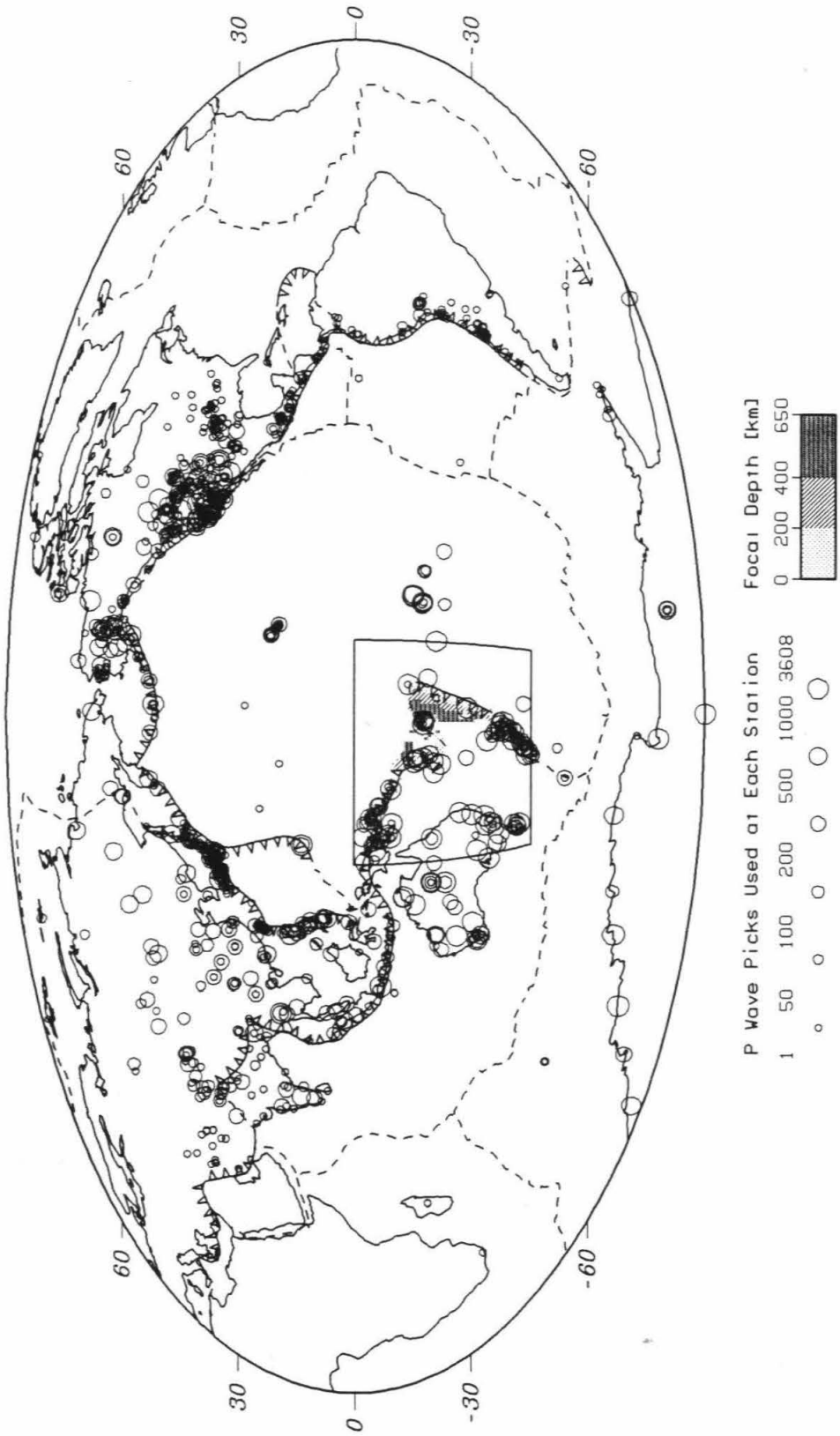
0
30
-30
60
-60
-90
P Wave Picks Used at Each Station
1 50 100 200 500 1000 3608
Focal Depth [km]
0 200 400 650

a station has reported more than eight events in the data set. The event statics are not removed here due to the use of source relocation which will be discussed in the next section.

The distribution of intermediate and deep earthquakes in the region is illustrated in Figure 3.3. Clearly, the major deep seismicity is concentrated under the Tonga Trench. Several bands of seismicity along the strike of the trench reflect the distortion or folding of the seismicity trend with depth. In other words, the local dip of the seismic slab is changing with depth, although on average the whole Wadati-Benioff zone has a steep dip. This seismicity pattern is also evident in cross sections by Giardini and Woodhouse [1984]. Another striking seismicity feature is the flattened trend of deep earthquakes (about 600-650 km) east in the northern New Hebrides Trench. This pattern is best seen through the stereoscopic views of this figure.

The teleseismic station distribution for events in this region is heavily clustered (Figure 3.2). To reduce this effect, and to exclude inconsistent picks, the data set is further stacked into summary rays of similar source and receiver areas, as discussed in Section 1.4.2, with the mediums of travel time residuals used as the resulting residual. The data distribution over epicentral distance and residual time, before and after the summary ray procedure, is plotted in Figure 3.4. Using of the summary ray procedure rather than the grouping and sorting procedure is mainly to allow source relocation. The azimuthal distribution of stations is one of the most significant factors governing the location of a hypocenter. Weighting the azimuthal distribution of stations during a relocation process is a non-trivial matter. The summary

Figure 3.3. Earthquake distribution in the southwest Pacific. Panel a) shows the original events selected before the summary ray procedure, and panel b) shows the summarized events. The lateral and depth distributions of events are best seen at the bottom illustration using a pair of stereoscopes. A-A1 to D-D1 shown in a) indicate the locations of cross section which are displayed later in Figure 3.9.

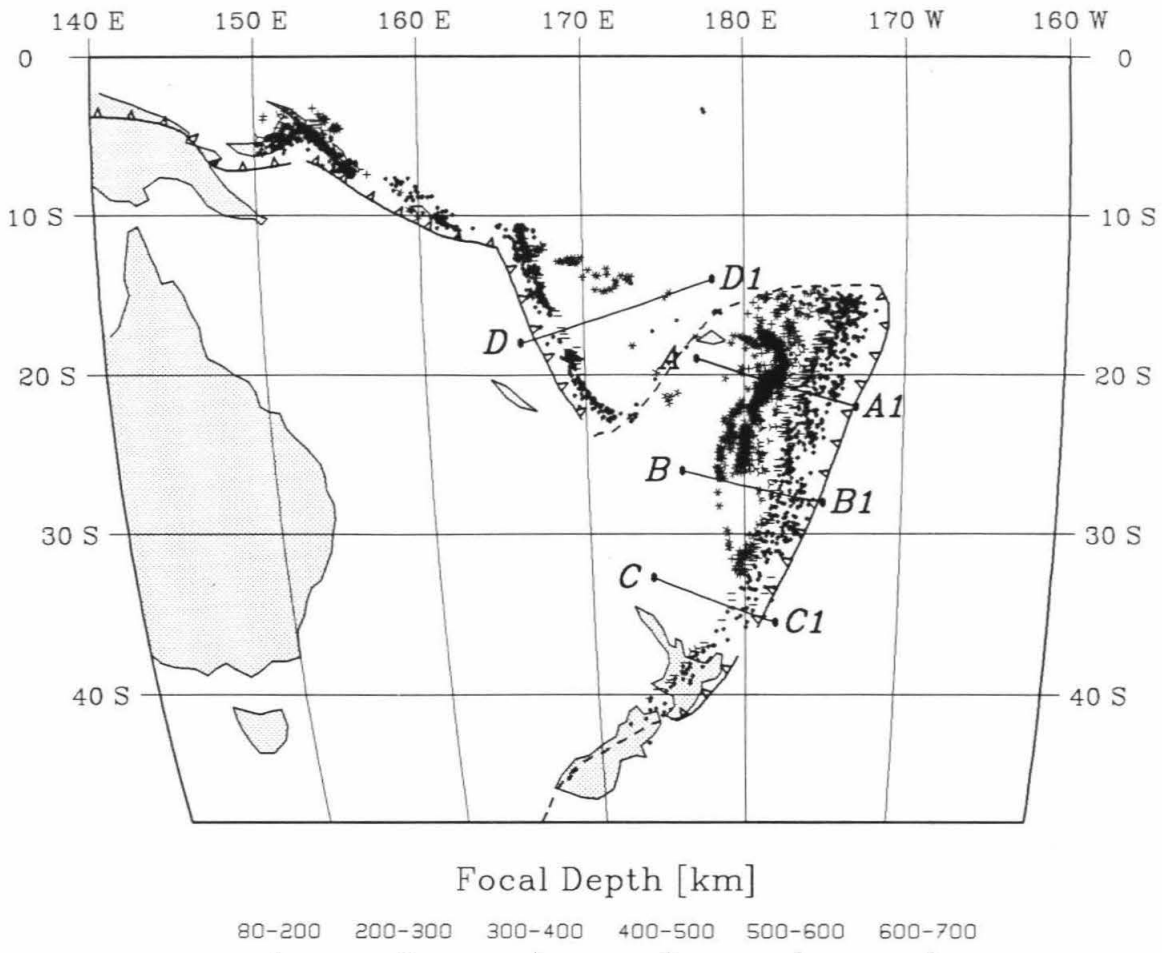
140 E
150 E
160 E
170 E
180 E
170 W
160 W
0
10 S
20 S
30 S
40 S
D1
D
A
A1
B
B1
C
C1
Focal Depth [km]
80-200
200-300
300-400
400-500
500-600
600-700

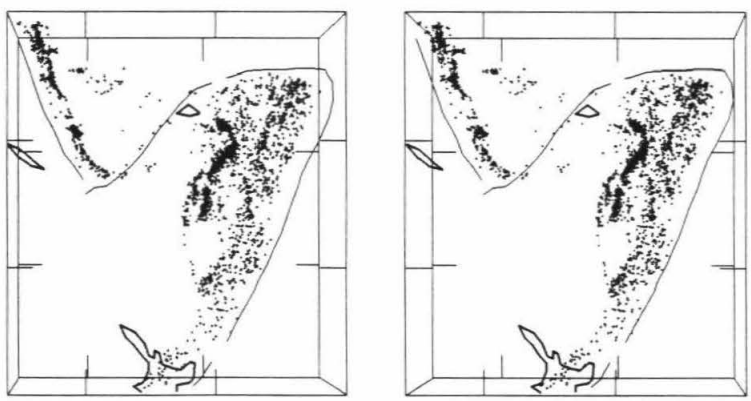

Figure 3.3 a).

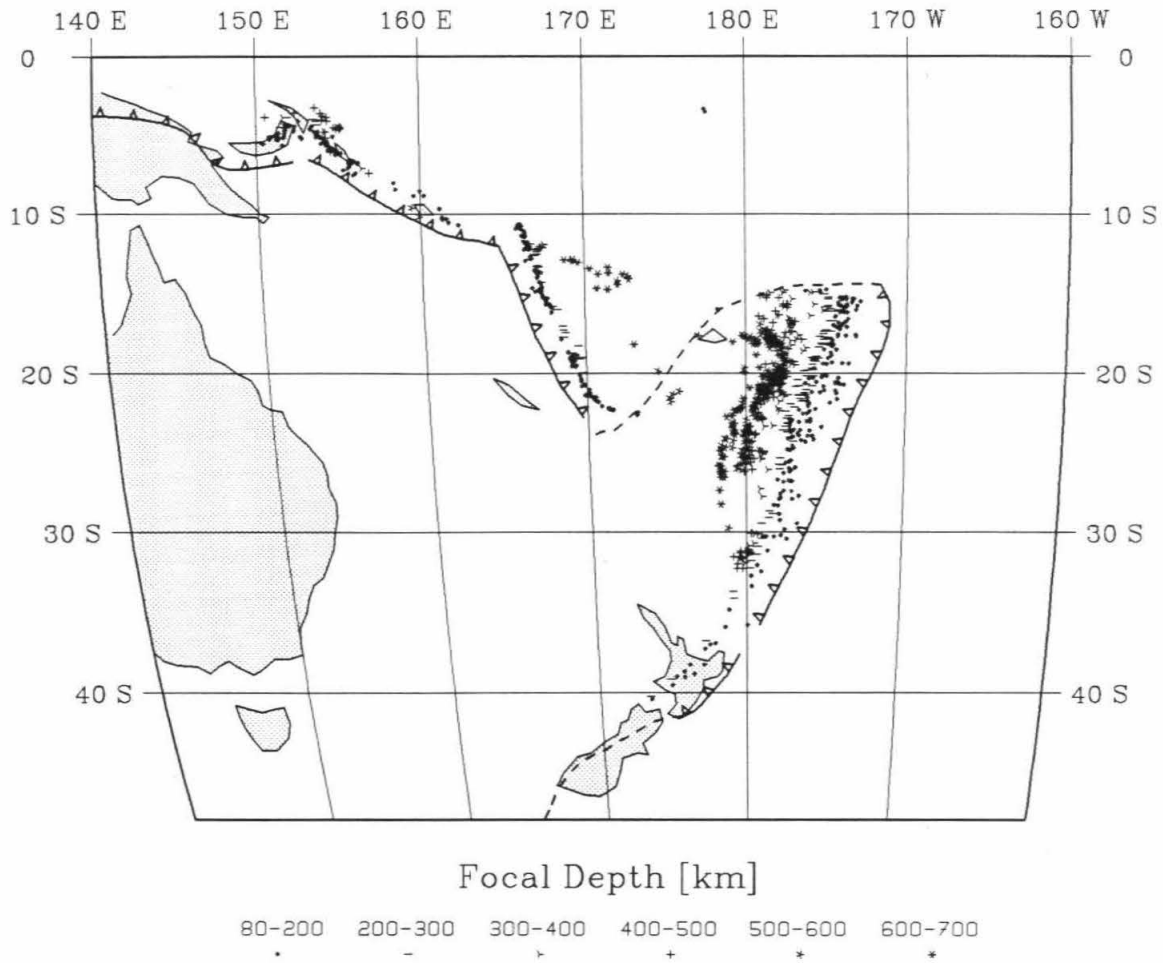
140 E
150 E
160 E
170 E
180 E
170 W
160 W
0
10 S
20 S
30 S
40 S
Focal Depth [km]
80-200
200-300
300-400
400-500
500-600
600-700

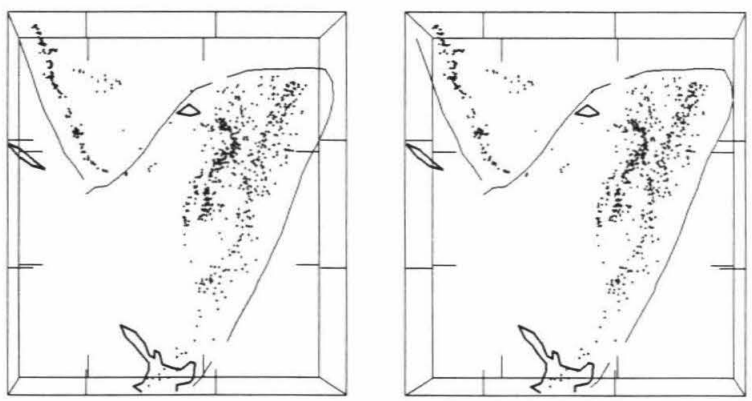

Figure 3.3 b).

Figure 3.4. Variation of residuals over epicentral distance. The plots show P wave data before (top) and after (bottom) the summary ray procedure. The travel time residuals are with respect to the group mediums and distributed over time and epicentral distance. The number at the peak of each plot indicates the maximum number of residuals.

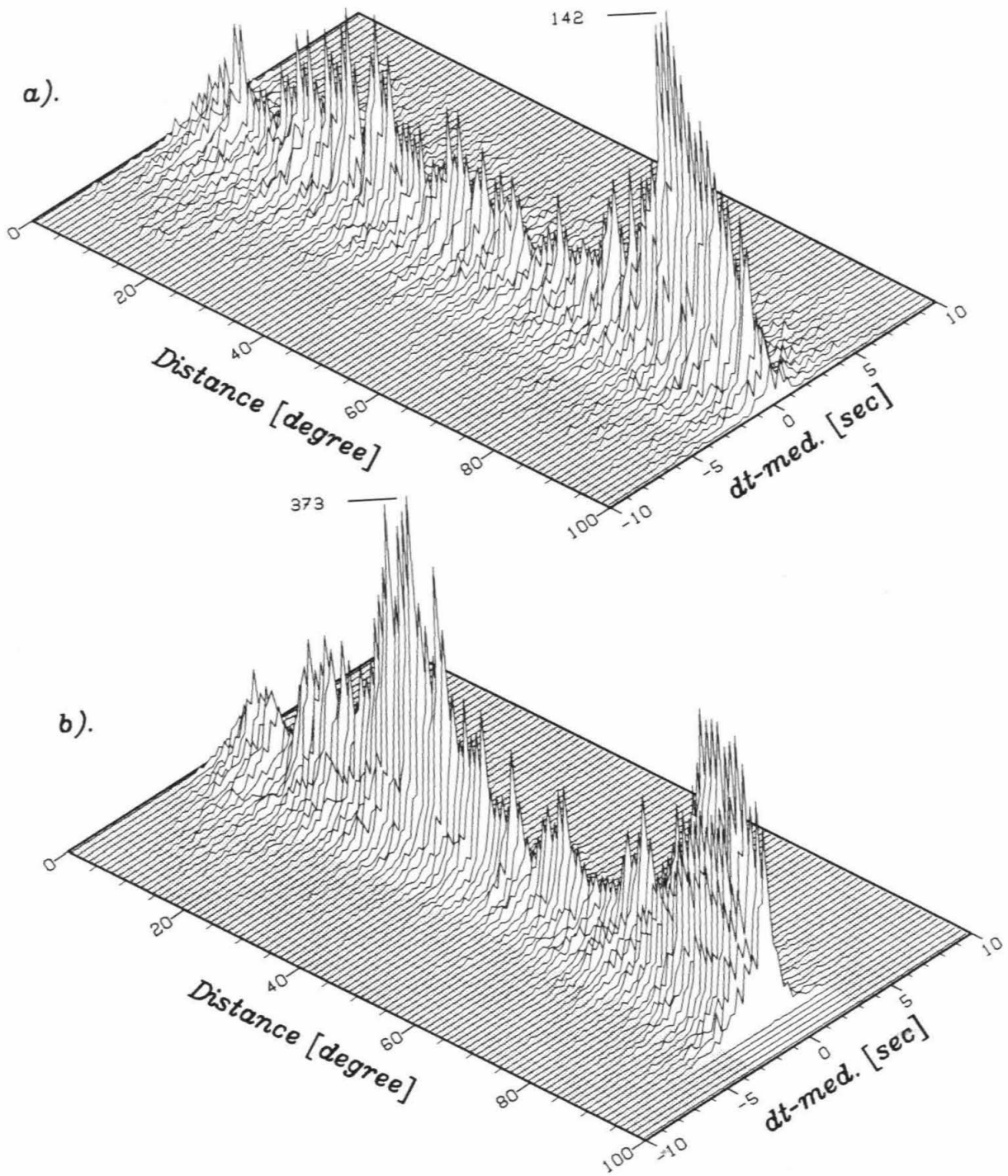
a).
142
0
20
40
60
80
100
Distance [degree]
10
5
0
-5
-10
dt-med. [sec]
b).
373
0
20
40
60
80
100
Distance [degree]
10
5
0
-5
-10
dt-med. [sec]

ray procedure which is utilized in this chapter tends to even out the station azimuthal distribution and therefore no further weighting is applied during the later relocation process. In addition, each summarized event has a much better station coverage which allows a better source relocation, and the number of summarized events (Figure 3.3b) is much less than the number of original events, resulting in much less computation time. The size of area over which rays are summed is $0.5^\circ \times 0.5^\circ \times 12$ km for events and stations inside the model region, and $5^\circ \times 5^\circ$ for stations outside the region. The original 3,220 events are reduced to 953 events (620 of them, or 65%, are summary events). The resulting summary ray data consists of 82,518 picks, or roughly 40% the original number of picks.

The exclusion of shallow events and use of the summary ray technique both attempt to improve the data quality. At the same time, however, the density of ray illumination for many inversion blocks is reduced. However, in the current study, the data set after all corrections still has good ray coverage for most of the interesting areas in the region. This is evident in Figure 3.5, which shows an example of the azimuthal distribution of ray paths at 500-550 km depth range.

The correction for mantle heterogeneities outside the model is very important for regional inversions that use teleseismic data. The contribution from these heterogeneities will be mapped into the regional model if the correction is not performed. In most previous studies, however, this correction is ignored, largely due to a lack of *a priori* knowledge about the mantle velocities outside the model. Removal of the receiver average travel time

Figure 3.5 Azimuthal distribution of data at 500-550 km depth. Each piercing point of a data ray through the 500-550 km layer is drawn across the center of the block it passes in the direction of the ray azimuth. Notice that the hit count and azimuth distribution are quite good around most of the subduction zones in the region. The ray paths shown are after the summary ray procedure; hence, many of the ray paths here are summarized ray paths.

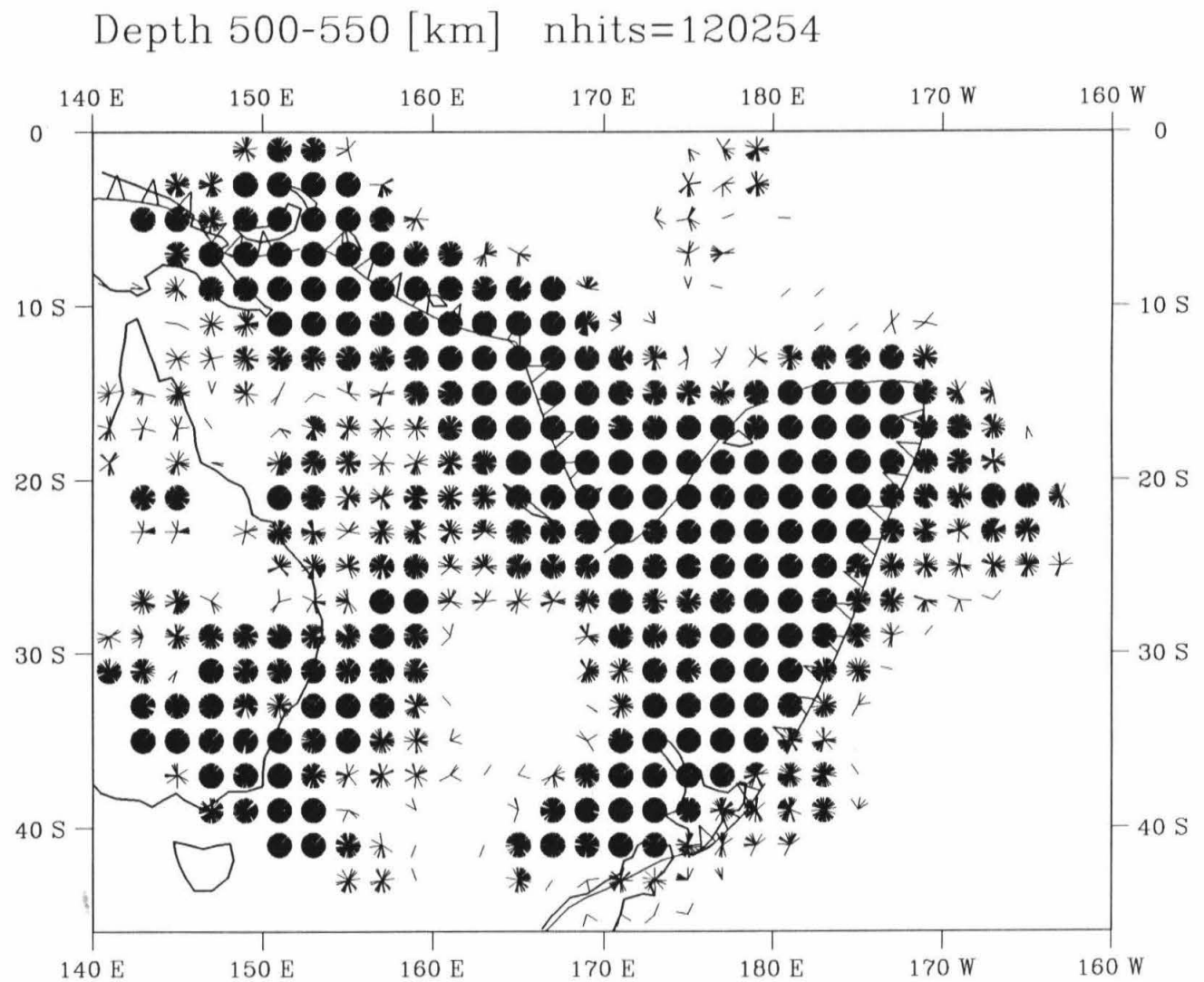
Depth 500-550 [km] nhits=120254
140 E
150 E
160 E
170 E
180 E
170 W
160 W
0
10 S
20 S
30 S
40 S

residuals is a common practice. For large scale regional inversions, however, the receiver residual averages contain only contributions from near receiver heterogeneities. Tests have shown that the lower mantle corrections are also significant.

In this chapter, velocities outside the modeled region are corrected using the Clayton-Comer lower mantle velocity model [Hager and Clayton, 1989] and the upper mantle P wave model of the northwest Pacific obtained in the previous chapter. Although these velocity models are different from the real earth in many aspects, it is my opinion that it is more reasonable to do corrections using these models than not do any corrections at all. The corrections are performed for summarized rays in order to reduce the computation, because ray tracing for each pick is involved. The data residuals after this correction have an average of -0.25 seconds and a standard deviation of 1.41 seconds.

3.3 Iterative Source Relocation and Inversion

In one of the earliest attempts of resolving three-dimensional velocity anomalies with travel times, Aki and Lee [1976] determined the source parameters and velocity structures simultaneously by a damped least squares method. Most of the slab inversions which involved source relocation have inverted for source locations and slab structures simultaneously [Hirahara, 1977, 1981; Hirahara and Mikumo, 1980; Spencer and Gubbins, 1980; Spencer

and Engdahl, 1983; Roecker, 1985; and Engdahl and Gubbins, 1987]. In this chapter, the source relocation and velocity inversion are performed as a sequence of iterations. The reasons not to take the two parts of inversion simultaneously are the following. First, no *a priori* information exists for weighting source relocation versus the velocity back-projection. Second, the iterative nature of the inversion process blends these two parts together, thus has the effect of a simultaneous inversion. Third, monitoring the relocation relative to the back-projection is important.

The basic algorithm for our inversion is the following loop, which will be iterated until the fitting variance convergences to an acceptable level:

i) updating the three-dimensional heterogeneous velocity model (the first one is spherically symmetric);

ii) relocating hypocenters with a standard least squares method;

iii) generating the L matrix of ray path lengths in all model blocks;

iv) inverting for a new velocity model with a small number of iterations (five iterations used here).

The relocation scheme used here is quite standard. First of all, we can linearize the source location problem for the j-th station as

$$dt_j = \delta t_j^{3D} + \delta t^\circ + (\frac{\partial t}{\partial \theta})_j \delta\theta + (\frac{\partial t}{\partial \phi})_j \delta\phi + (\frac{\partial t}{\partial h})_j \delta h \qquad (3.1)$$

where dt_j is the observed travel time residual, δt_j^{3D} is the contribution of travel time from the three-dimensional velocity perturbations, δt° is a correction for the event's origin time, and the rest terms are the corrections for the source location in terms of latitude θ, longitude ϕ and depth h. The

gradients of t in each of directions $(\frac{\partial t}{\partial \theta})_j$, $(\frac{\partial t}{\partial \phi})_j$ and $(\frac{\partial t}{\partial h})_j$ are fixed for each station (depending on epicentral distance, focal depth and the velocity structure). Hence, the equation (3.1) is a linear set of equations with four unknowns, $\delta t°$, $\delta\theta$, $\delta\phi$, and δh, for each source to be determined. For each event, we computed all the coefficients in the equation and then solved the equation by a simple least squares inversion. Due to the nonlinearity of the original problem, variance of the residuals is computed before and after each relocation inversion, a new location is accepted provided that it reduces the variance.

For generating the L matrix, a two-dimensional ray tracing is performed for regions inside the model, assuming that the ray paths stay in the great circle vertical slice, while a one-dimensional ray tracing is taken for regions outside. The two-dimensional ray tracer used is an approximated one based on Equation (1.9), as used in the one-dimensional ray tracer in the previous two chapters. In performing it, we first find the cross section two-dimensional velocities between the given source and station combination. We then treat the ray tracing as the one-dimensional problem which we encounted in the previous chapters, except when crossing vertical edges of blocks where Snell's law is used. This technique is similar to the one discussed by Langan *et al.* [1985], and can also be developed to treat three-dimensional cases.

After updating the L matrix, the same iterative inversion used in the previous two chapters is performed. Several such iterations are executed in each loop simply because ray tracing (generating the L matrix) is very expensive. The amplitudes of slowness for all blocks are kept within 10% of

the reference one-dimensional JB model. The three-dimensional regional model is subsequently updated, and readied for the next loop.

The importance of source relocation was well documented previously. For example, Spencer and Engdahl [1983] reported that high velocity slab could affect locally determined hypocentral locations, and therefore the wrong focal locations might affect the slab structure by an inversion. In Section 2.2.1, we have given a rather qualitative estimate to the uncertainty in source locations, based on previous investigations and comparisons of epicenters given by different agencies. The uncertainty for source location and depth is approximately 20-30 km. As shown in Figure 3.6, among 953 summarized events used in the inversion loops, 338 events, or a little over one third of the total, have been relocated. Although the maximum relocation distance, including lateral and depth components, is nearly 45 km, only 17 events were relocated by more than 20 km, and 80 by more than 10 km. For the inversion block size used, the source location uncertainty is generally too small to affect the inversion in a significant way.

The convergence of the inversion is illustrated by the distribution of residuals over epicentral distance as shown in Figure 3.7. Reduction of standard deviation of residuals is about 5% by the relocation process and about 28% by 30 velocity iterations on the $2^\circ \times 2^\circ \times 50$ km grid. The portion of residuals absorbed into the model (the middle panel) shows a more systematic pattern. The pattern of remaining residuals appears smoother, more symmetric and Gaussian-like. Based on this, we think that the inversion has done a reasonable job in accounting for the most systematic variations in the

Figure 3.6. Displays of relocated events. The top panel is a map view of over 300 relocated events, which is about one third of total events under the source relocation attempt. A dot is on an original hypocenter with a little tail pointing to the relocated hypocenter. The bottom pair of panels is a stereo display of the same suite of relocated events. The pair is best seen using an aerial photograph stereoscopes. The maximum relocation distance in three-dimension is nearly 45 km, while the depth component of it is 7.4 km. As shown, however, 95% of these relocated events have relocation distance less than 20 km.

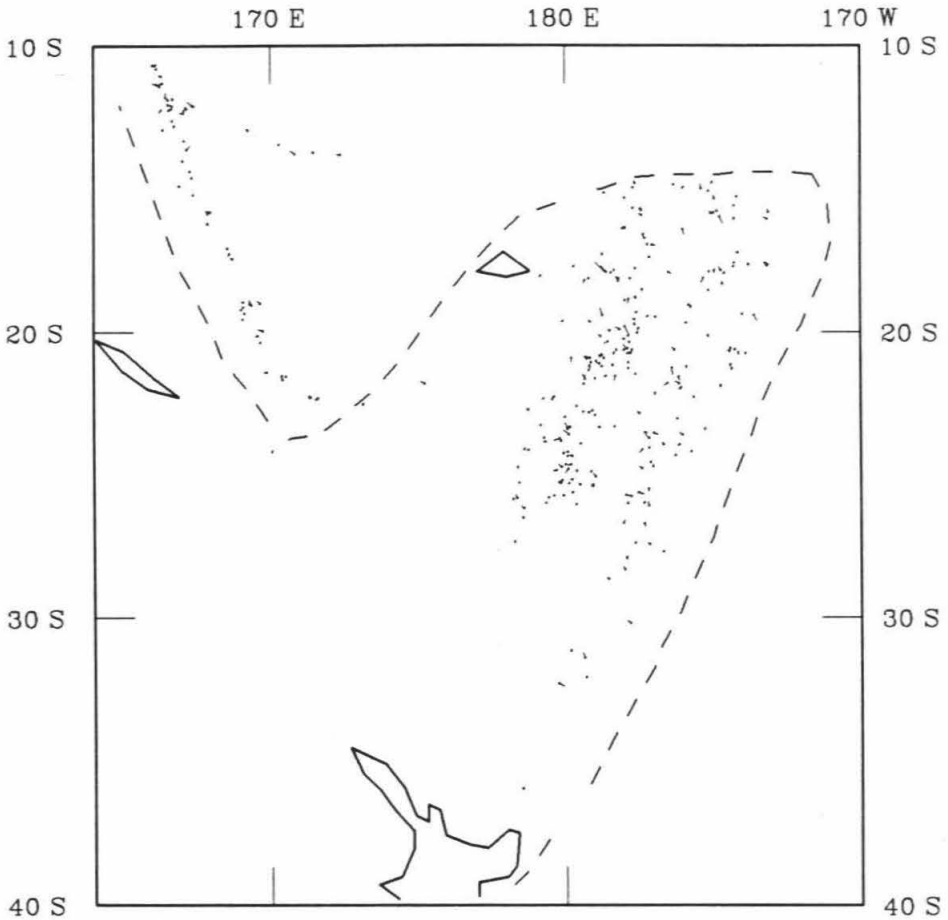
170 E
180 E
170 W
10 S
20 S
30 S
40 S

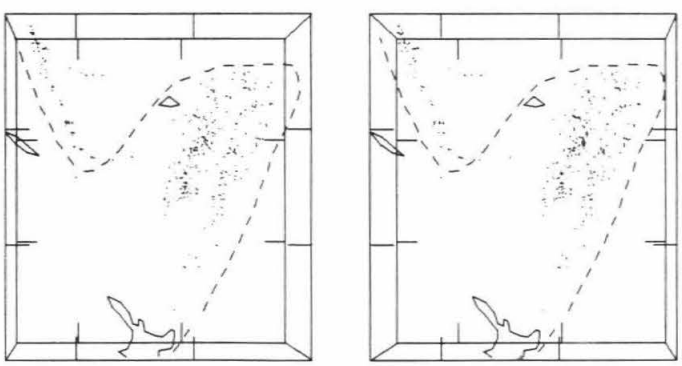

Figure 3.7. Epicentral distance distribution of data. The three panels shown as travel time residuals before the inversion (top), from the inverted image at $2^\circ \times 2^\circ \times 50$km block grid (middle), and the remaining (bottom). Hence, the top panel is a combination of the middle and bottom panels. Notice that the residual distribution is quite systematic in the inverted image, and is smooth and Gaussian-like in the remaining data after the inversion. The standard deviation of residuals in the inverted model is comparable to that in the remaining data.

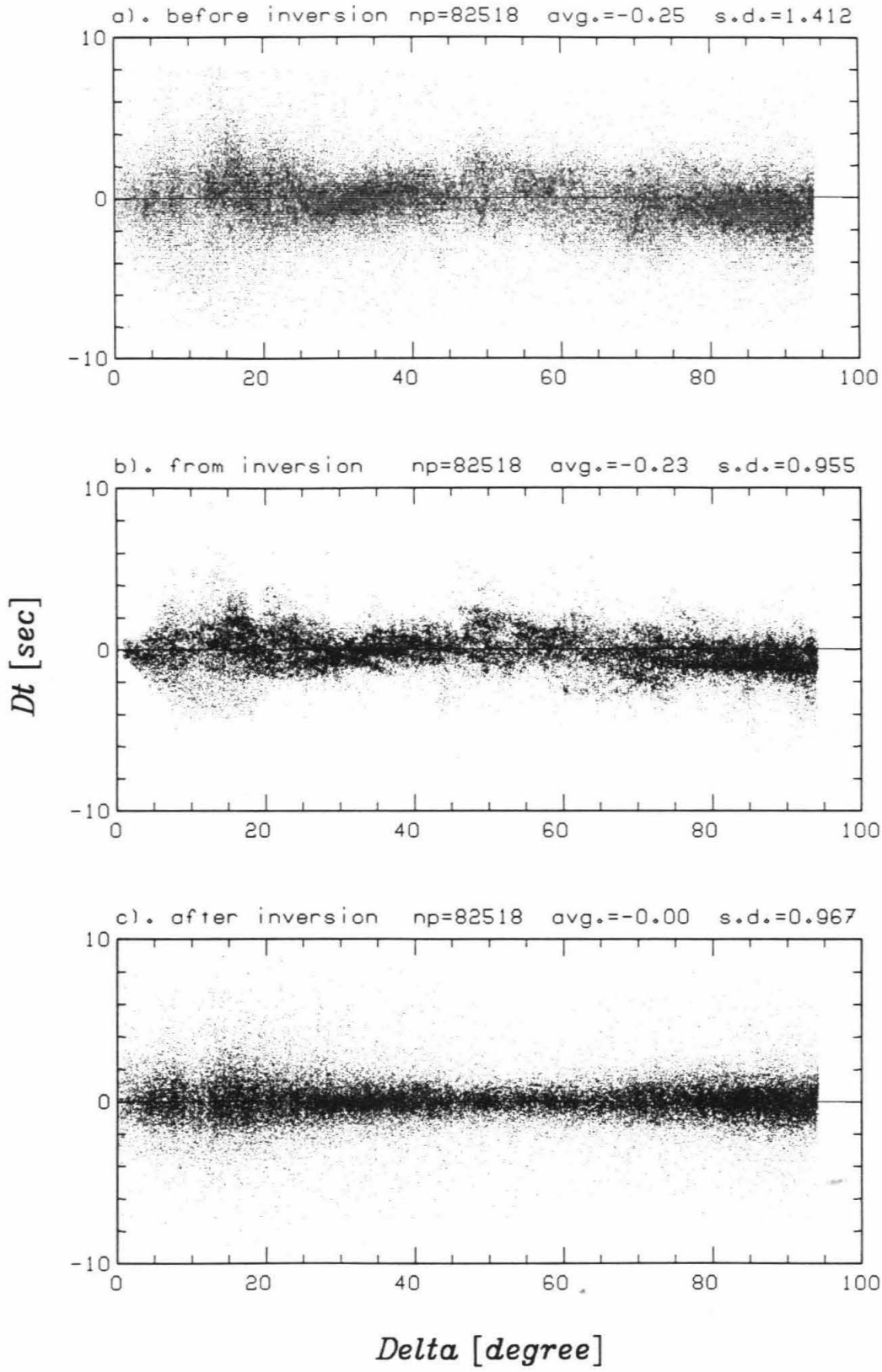
a). before inversion np=82518 avg.=-0.25 s.d.=1.412
b). from inversion np=82518 avg.=-0.23 s.d.=0.955
c). after inversion np=82518 avg.=-0.00 s.d.=0.967
10
0
-10
0
20
40
60
80
100
Dt [sec]
Delta [degree]

residual travel times. The reliability of these velocity variations is analyzed in terms of resolution and noise estimations in the next section.

As will be shown in the results section, the anomaly patterns in the $2^\circ \times 2^\circ \times 50$ km block grid, although quite stable, do not show clear fast slab-like features around earthquake foci in the deep part of the upper mantle. Beside the fact that the resolving power of the data is less than perfect, we think that the block size, particularly the lateral dimension of $2^\circ \times 2^\circ$, is too coarse to resolve the steeply dipping slab in the region. Consequently, we further inverted the residuals on a ($1^\circ \times 1^\circ \times 50$ km) block grid, starting from the three-dimensional velocities of the coarser grid. As a compromise between higher resolution and less computing time, this inversion is done in the same manner as that in the previous chapters, i.e., it involves no further adjustments in source relocation and ray paths.

During inversion of the finer block grid, the slowness amplitudes of all blocks were clamped to be of within 10% the JB model. This means that I assumed that the maximum amplitude of slowness perturbation from the one-dimensional reference model is 10%. Of course, an inversion from a finer block grid usually results in less stable and noiser images. A comparative analysis of anomalies from the coarse and fine grids can help to assess the reliability of the anomalies.

3.4 Estimations of Noise Level and Resolution

This section carries on in the same spirit as of Sections 1.5, 1.6, 2.3 and 2.4. We attempt to assess incoherent noise level in residual time data and its propagation through the inversion; and, for given data ray coverage and inverse block grids, to quantify the resolution power.

Figure 3.8 displays the average variance of groups of residuals of the same SW Pacific source areas and the same station areas, with respect to the size of these areas. The detailed data for this plot is listed in Table 3.1. The number of groups listed in the Table eventually decreases as the grouping areas get very small, because only groups containing more than two rays are counted. The average variances shown are very useful. For instance, at the smallest block size, roughly $23 \times 23 \times 12$ km^3, incoherent variance level in data before inversions is 0.3 s^2, which is about one sixth of the total data variance level. The incoherent variance before inversions is about 0.64 s^2 for the $2^\circ \times 2^\circ \times 50$ km block grid and 0.50 s^2 for $1^\circ \times 1^\circ \times 50$ km block grid, respectively.

The number of summary rays in this case is about 40% of the original. As shown in Figure 3.8, the variance level at large block sizes doesn't change very much before and after the procedure of summarizing rays. This again indicates the advantage of summarizing rays; namely, it keeps the ray coverage as well as the long wavelength character of the data while it reduces duplicating rays and hence beats down azimuthal bias caused by dense clusters of stations.

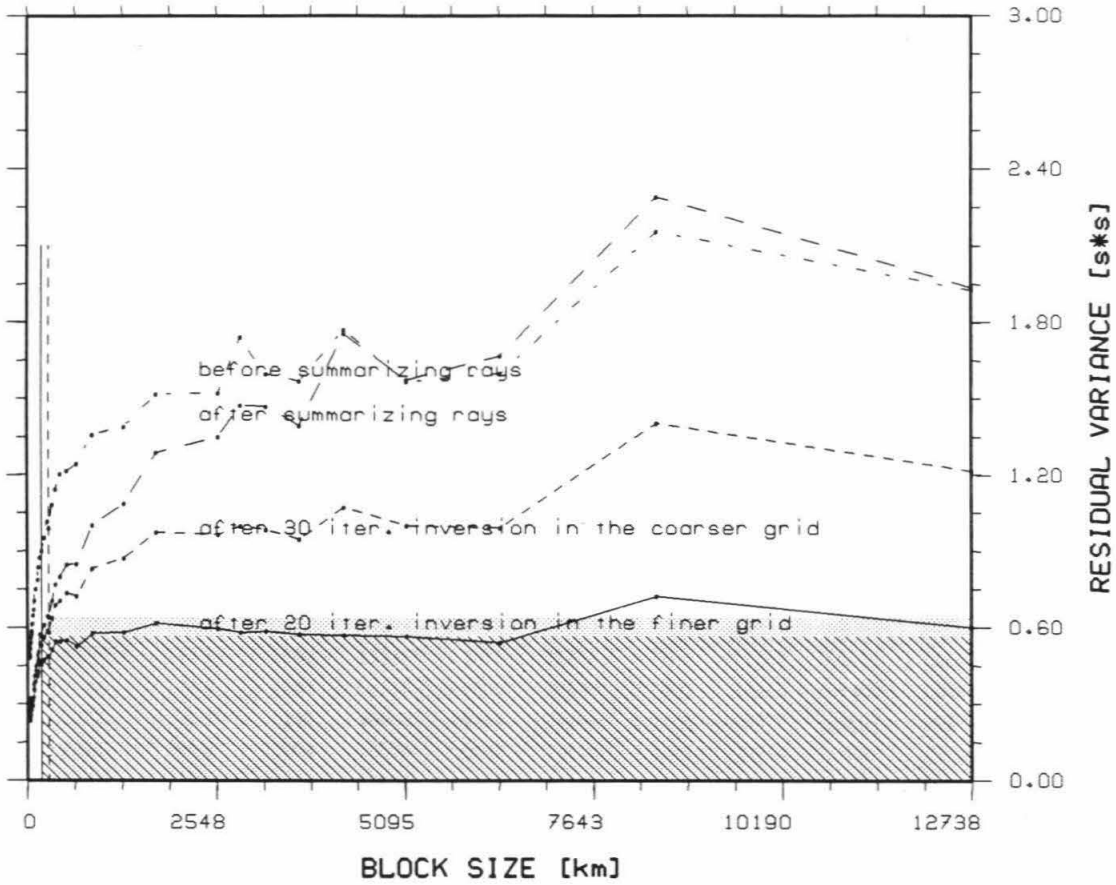

Figure 3.8. Relation between the average group variance and the grouping area size. This plot is similar to that shown in Figure 2.7. A group variance is for residual variance of a group of rays of same source and station areas. The curves are of the southwest Pacific P-wave data at different stages. The vertical solid and dashed lines, respectively, indicates the inverse block size of the $1^\circ \times 1^\circ \times 50$ km grid and $2^\circ \times 2^\circ \times 50$ km grid. The dotted and hatched shaded zones indicates the residual variance just before inversion at the coarser and finer inversion block sizes, respectively. Notice that the summary ray procedure reduces the noise level at short wavelengths. The inversions have absorbed a large portion of the long-wavelength variations of travel time residuals.

Table 3.1 Average Variance of Ray Groups.

dimension of grouping area			before summary rays		after summary rays		after coarser grid inverse		after finer grid inverse	
Δlateral (deg.)	Δdepth (km)	size (km)	n.g.	a.v. (s^2)	n.g.	a.v. (s^2)	n.g.	a.v. (s^2)	n.g.	a.v. (s^2)
90.000	500.0	12738	16	1.9269	16	1.9374	16	1.2142	16	0.6010
60.000	500.0	8500	63	2.1576	54	2.2913	54	1.4054	54	0.7233
45.000	500.0	6384	66	1.5994	58	1.6680	58	0.9908	58	0.5428
36.000	500.0	5116	172	1.5688	168	1.5751	168	1.0012	168	0.5658
30.000	500.0	4272	189	1.7712	168	1.7559	168	1.0741	168	0.5711
25.714	500.0	3671	266	1.5701	252	1.3928	251	0.9460	251	0.5734
22.500	500.0	3221	423	1.5965	384	1.4685	382	0.9833	382	0.5856
20.000	500.0	2872	438	1.7408	390	1.4738	388	1.0003	388	0.5816
18.000	333.3	2567	652	1.5204	610	1.3490	605	0.9638	605	0.5959
12.000	333.3	1729	1607	1.5174	1389	1.2871	1377	0.9749	1377	0.6196
9.000	250.0	1297	2994	1.3898	2564	1.0863	2539	0.8722	2539	0.5814
6.000	200.0	872	5643	1.3557	4464	1.0018	4420	0.8317	4420	0.5780
4.500	166.7	658	9177	1.2415	6749	0.8498	6698	0.7236	6698	0.5268
3.600	142.9	529	11922	1.2143	8309	0.8473	8175	0.7364	8175	0.5514
3.000	125.0	442	15274	1.2021	10212	0.7985	10111	0.7062	10111	0.5469
2.571	111.1	380	18248	1.1415	11478	0.7701	11287	0.6894	11287	0.5465
2.250	100.0	334	21816	1.0809	12526	0.7062	12415	0.6400	12415	0.5125
2.000	50.0	287	28068	0.9882	15844	0.6405	15577	0.5807	15577	0.4855
1.800	83.3	268	26620	1.0168	14110	0.6455	13914	0.5880	13914	0.4857
1.500	71.4	224	31033	0.9508	15439	0.6112	15242	0.5624	15242	0.4752
1.286	62.5	192	33323	0.8988	16659	0.5656	16489	0.5281	16489	0.4533
1.125	55.6	169	34940	0.8740	16641	0.5748	16284	0.5379	16284	0.4660
1.000	50.0	150	37580	0.8365	17091	0.5046	16886	0.4764	16886	0.4231
0.900	45.5	135	40190	0.7870	16443	0.4910	16124	0.4601	16124	0.4082
0.750	38.5	113	41483	0.7506	15650	0.4491	15182	0.4318	15182	0.3897
0.643	33.3	97	43445	0.7052	14143	0.4120	13880	0.3873	13880	0.3537
0.562	29.4	85	41925	0.6724	13070	0.3799	12661	0.3581	12661	0.3269
0.500	26.3	75	41952	0.6482	11478	0.3212	11211	0.3147	11211	0.2925
0.450	23.8	68	42875	0.6150	10737	0.3077	10105	0.3163	10105	0.2930
0.409	21.7	62	41314	0.5747	9084	0.3163	8517	0.3050	8517	0.2853
0.375	20.0	57	40082	0.5864	8252	0.3058	8227	0.2996	8227	0.2778
0.346	18.5	52	39647	0.5623	7191	0.2760	6792	0.2760	6792	0.2600
0.321	17.2	49	38562	0.5403	7006	0.3000	6743	0.3004	6743	0.2812
0.300	16.1	45	35843	0.5173	5043	0.2723	4832	0.2480	4832	0.2360
0.281	15.2	43	39104	0.5390	6222	0.3250	6014	0.2927	6014	0.2668
0.265	14.3	40	34363	0.5177	2745	0.2917	2555	0.2518	2555	0.2403
0.250	13.5	38	32735	0.4847	2424	0.2385	2146	0.2709	2146	0.2592
0.237	12.8	36	32046	0.4819	1847	0.2647	1636	0.2696	1636	0.2611
0.225	12.2	34	31127	0.4962	1313	0.3045	1096	0.2847	1096	0.2654

n.g. – number of groups; a.v. – average group variance.
Underlined variance values are used to estimate random noise level in inversed images.

The random noise level in the resulted velocity images, as estimated with equation 1.11, is about 29% at the coarser block grid and about 25% at the finer block grid. These estimates are slightly larger than that for the NW Pacific region in Chapter 2. Following equation 2.1, residual variance reduction, with respect to data before inversion, is 57% (see Figure 3.7) by inversions at the coarser block grid with source relocation, and is further reduced to 38% after the inversion at the finer block grid.

To estimate the resolution power of the data ray paths, "impulse tests" have been conducted for the two grid sizes. Even though most rays used are teleseismic, the impulse tests indicate that the resolution power, particularly for anomaly's pattern, is quite reasonable. Examples of these impulse tests are shown in the next section, paired with inversion images. A synthetic test, which is designed to assess the resolution power for the fast velocity slab structure of the region, was also done.

In the test a synthetic velocity model is created, and the corresponding residual travel times are generated for data ray paths. The synthetic model is a mimic of the large anomalous features observed in the real image, as shown in Figure 3.9. The surface traces of these vertical slices are given in Figure 3.3a. The test is aimed to answer specific questions such as these: Is the large fast patch below the deepest earthquakes in N. Tonga real? And is the lack of fast anomalies around earthquakes 500-700 km below Tonga due to poor resolution power there?

Details about the test results are discussed in Section 3.6. In general, the resolution in pattern is quite good around Wadati-Benioff zones in the region,

Figure 3.9. Examples of synthetic resolution tests. Shown in a suite of vertical slices for each region are inversed data image in the $1^\circ \times 1^\circ \times 50$ km grid (left), a synthetic slowness model (middle), and the corresponding solution (right) with data ray paths. The stars denote earthquake foci, and the slowness perturbations are contoured with an interval of 1%. The black areas are blocks with less than 5 passing rays, defined as uncovered. In the covered areas, the white areas are fast, cross-hatched areas are slow, and dotted areas are of less than one half of the contour interval, or 0.5%, of slowness perturbations.

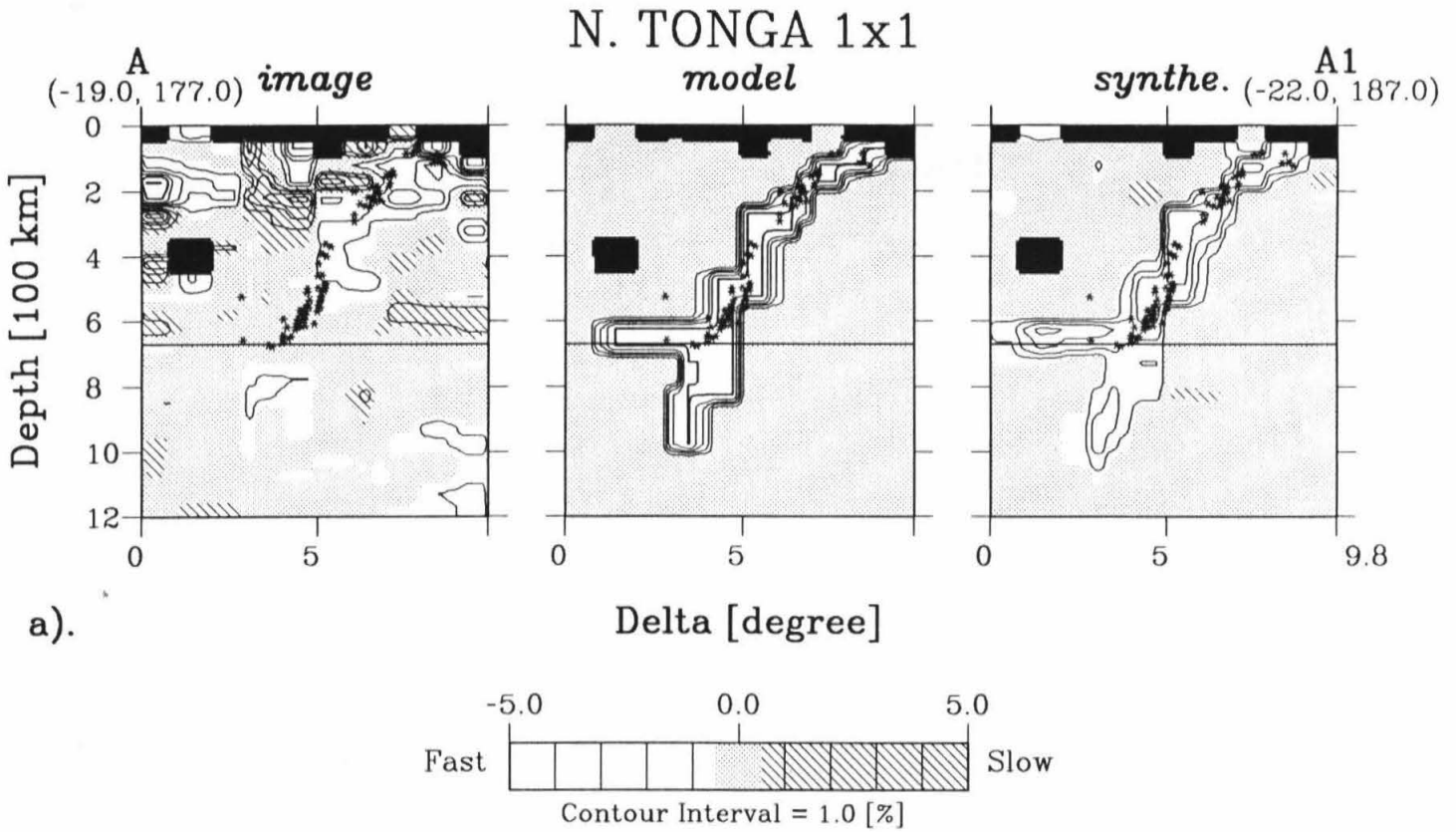
N. TONGA 1x1
A
(-19.0, 177.0)
image
model
synthe.
A1
(-22.0, 187.0)
Depth [100 km]
0
2
4
6
8
10
12
0
5
0
5
0
5
9.8
Delta [degree]
a).
-5.0
0.0
5.0
Fast
Slow
Contour Interval = 1.0 [%]

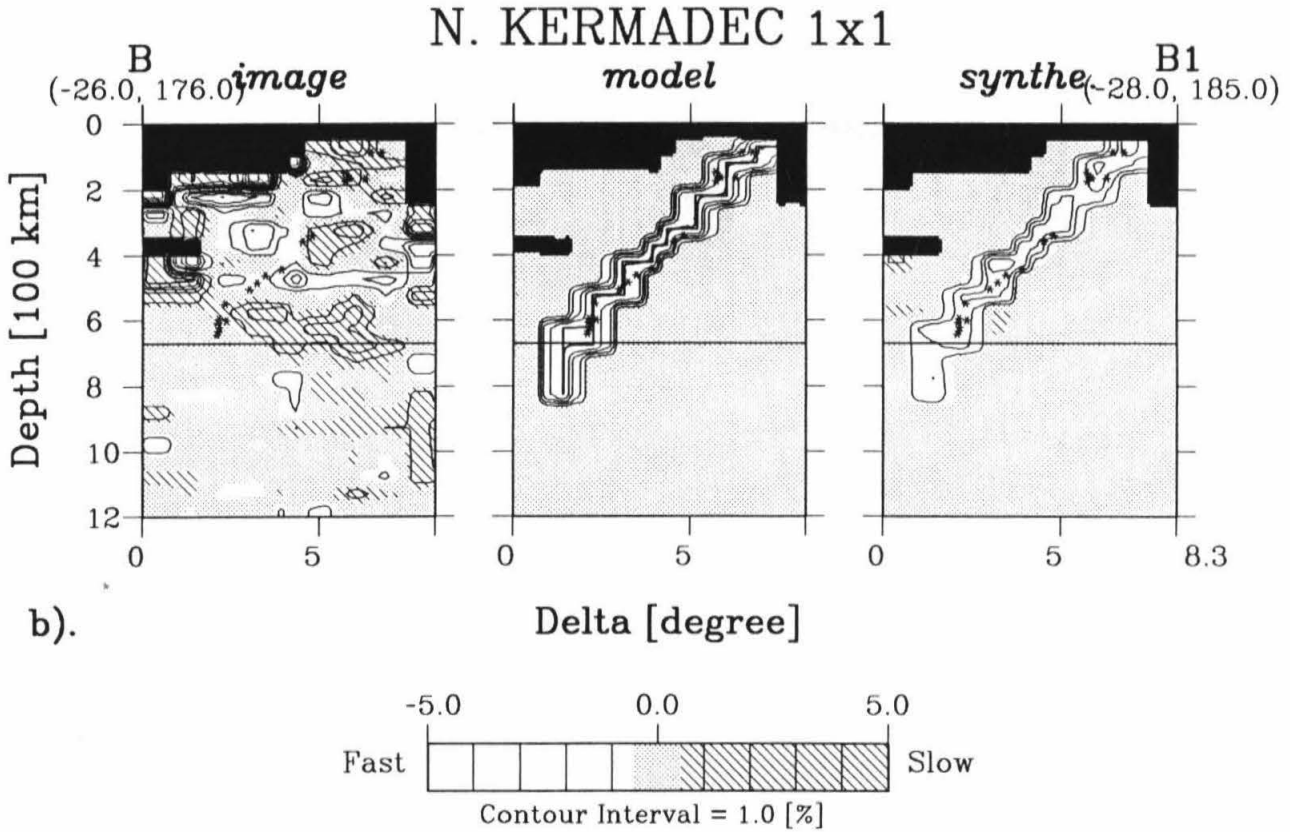
N. KERMADEC 1x1
B
(-26.0, 176.0)
image
model
synthe
B1
(-28.0, 185.0)
Depth [100 km]
0
2
4
6
8
10
12
0
5
0
5
0
5
8.3
Delta [degree]
b).
-5.0
0.0
5.0
Fast
Slow
Contour Interval = 1.0 [%]

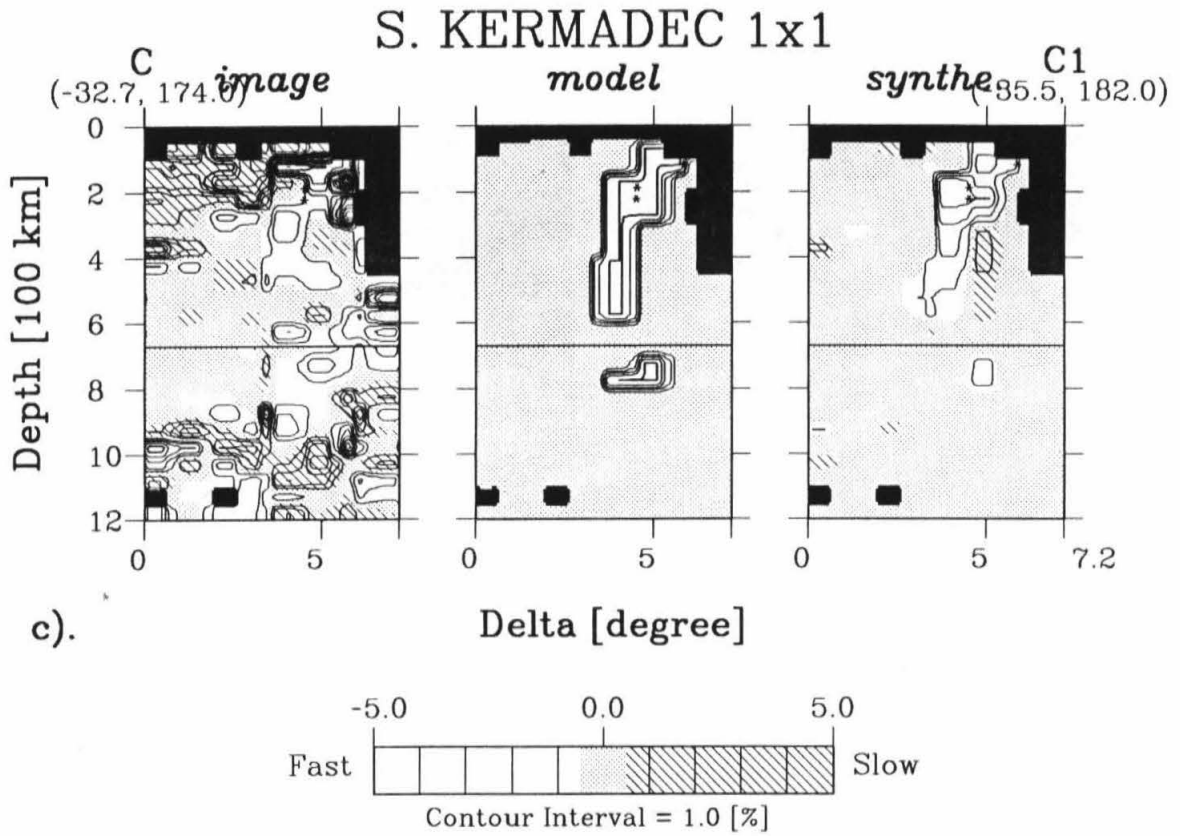
S. KERMADEC 1x1
C
(-32.7, 174.0)
image
model
synthe
C1
(-35.5, 182.0)
Depth [100 km]
0
2
4
6
8
10
12
0
5
0
5
0
5
7.2
Delta [degree]
c).
-5.0
0.0
5.0
Fast
Slow
Contour Interval = 1.0 [%]

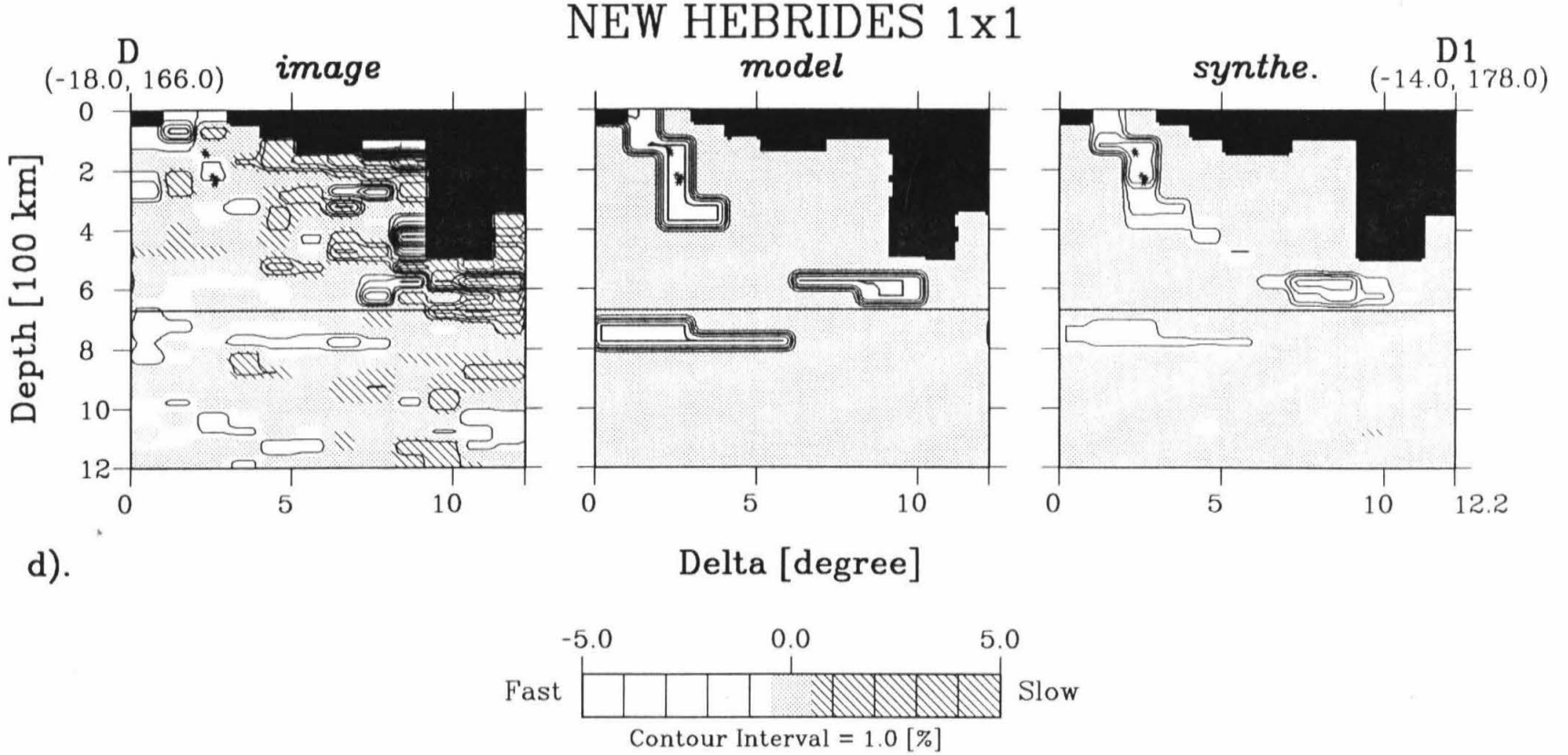
NEW HEBRIDES 1x1
D
(-18.0, 166.0)
image
model
synthe.
D1
(-14.0, 178.0)
Depth [100 km]
0
2
4
6
8
10
12
0
5
10
0
5
10
0
5
10
12.2
Delta [degree]
-5.0
0.0
5.0
Fast
Slow
Contour Interval = 1.0 [%]

d).

although there is along-path smearing in some localities, such as under the New Hebrides Trench (Figure 3.9d) at 400-500 km. The resolution of amplitude generally decreases with depth. For instance, the fast anomaly below the deepest Tongan earthquakes in the data image (left panel of Figure 3.9a) probably has a real amplitude twice that shown (about 3% instead of 1.5%), because the test results indicate a 50% decrease in the anomaly's amplitude at the location.

3.5 Results

Horizontal slices of the image and impulse resolution test results from the $2^\circ \times 2^\circ \times 50$ km grid are shown in Figure 3.10. Around most subduction zones in the region there are slab-like anomalies that are several percent fast in the upper mantle. The average perturbation velocity in each layer, which usually differs from zero, is not removed. In many places, although the slab anomaly is only slightly faster than the average velocity, it is much faster than the adjacent large slow regions.

The results of resolution tests are reasonable for most localities, but there is a decrease in amplitude resolution with depth. In addition, as we discussed previously, reliability of the image becomes very poor near the edge of the covered region. In general, most coherent anomalies in these images are reliable. Distortions of the fast slab-like anomalies sometimes may be due to the large block size. This is a major motivation for the further inversion with

Figure 3.10. Horizontal slices of the image and resolution tests on the $2^\circ \times 2^\circ \times 50$ km grid. At each 50 km depth range, from 100 km to 1000 km, each image slice at the left is paired with a result from an "impulse" resolution test. The legend convention for images is the same as that used in Figures 3.9, and convention for impulse tests follows that used for Figure 2.7.

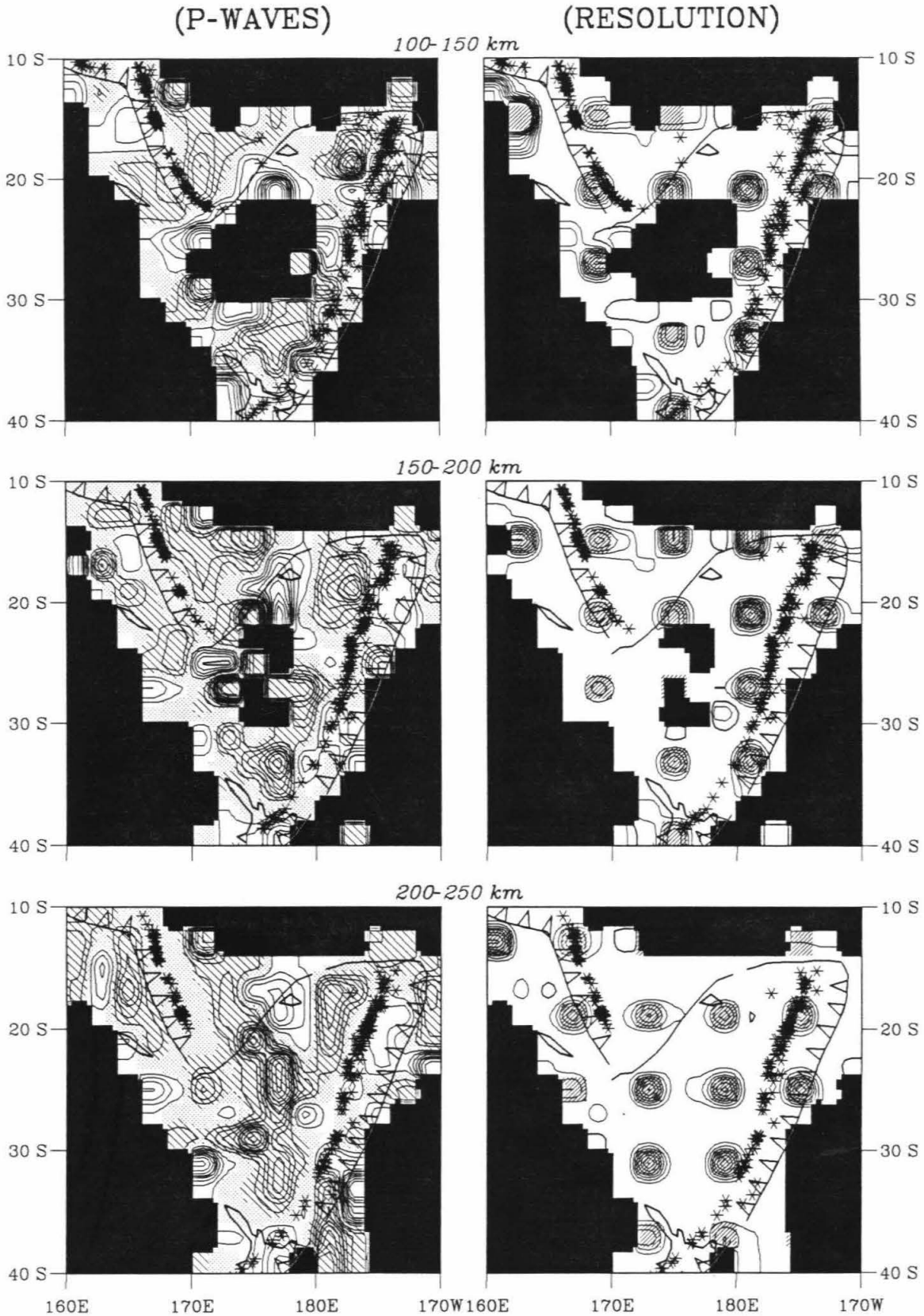
(P-WAVES)
(RESOLUTION)
100-150 km
150-200 km
200-250 km
10 S
20 S
30 S
40 S
160E
170E
180E
170W

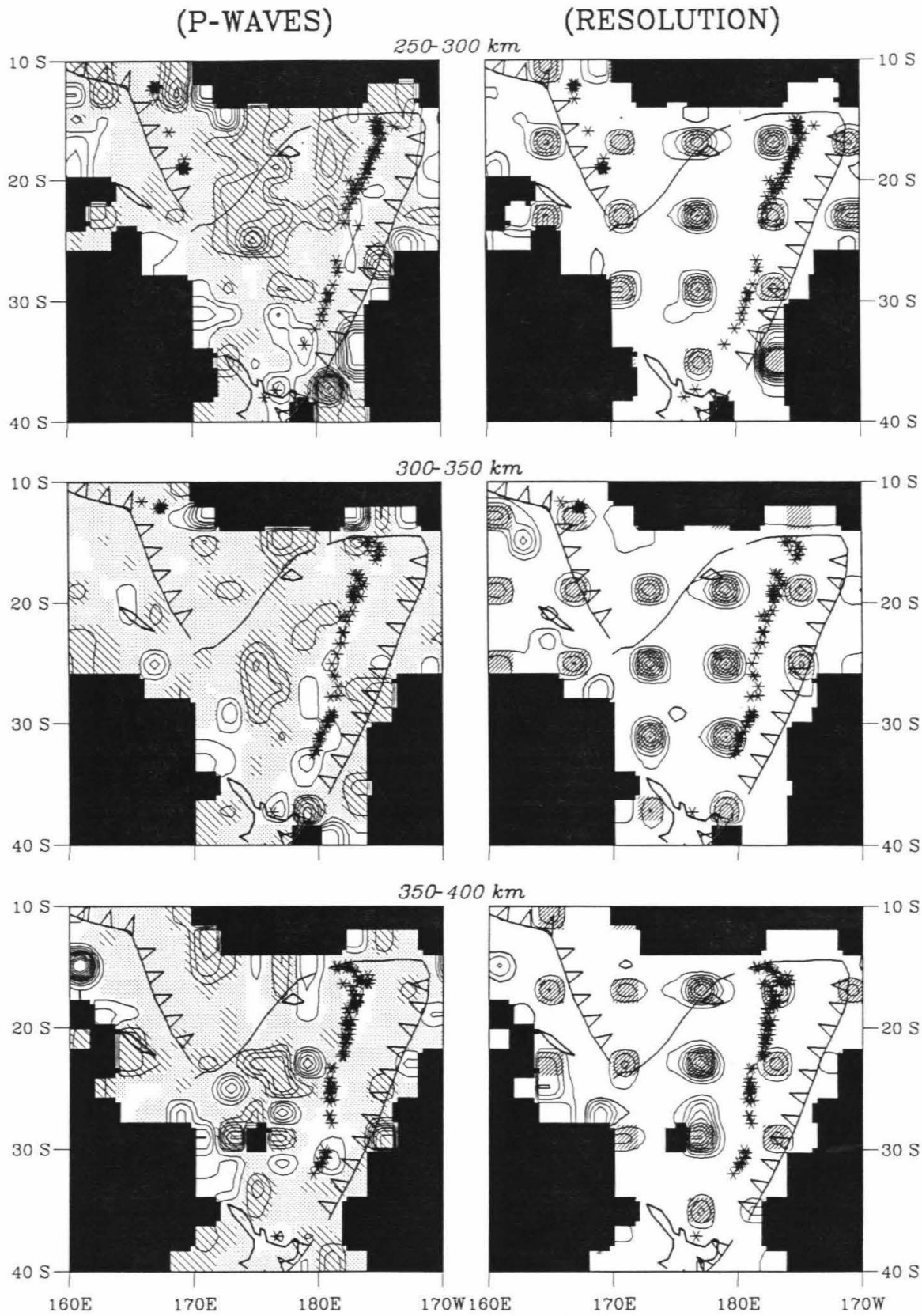

Figure 3.10 (continue)

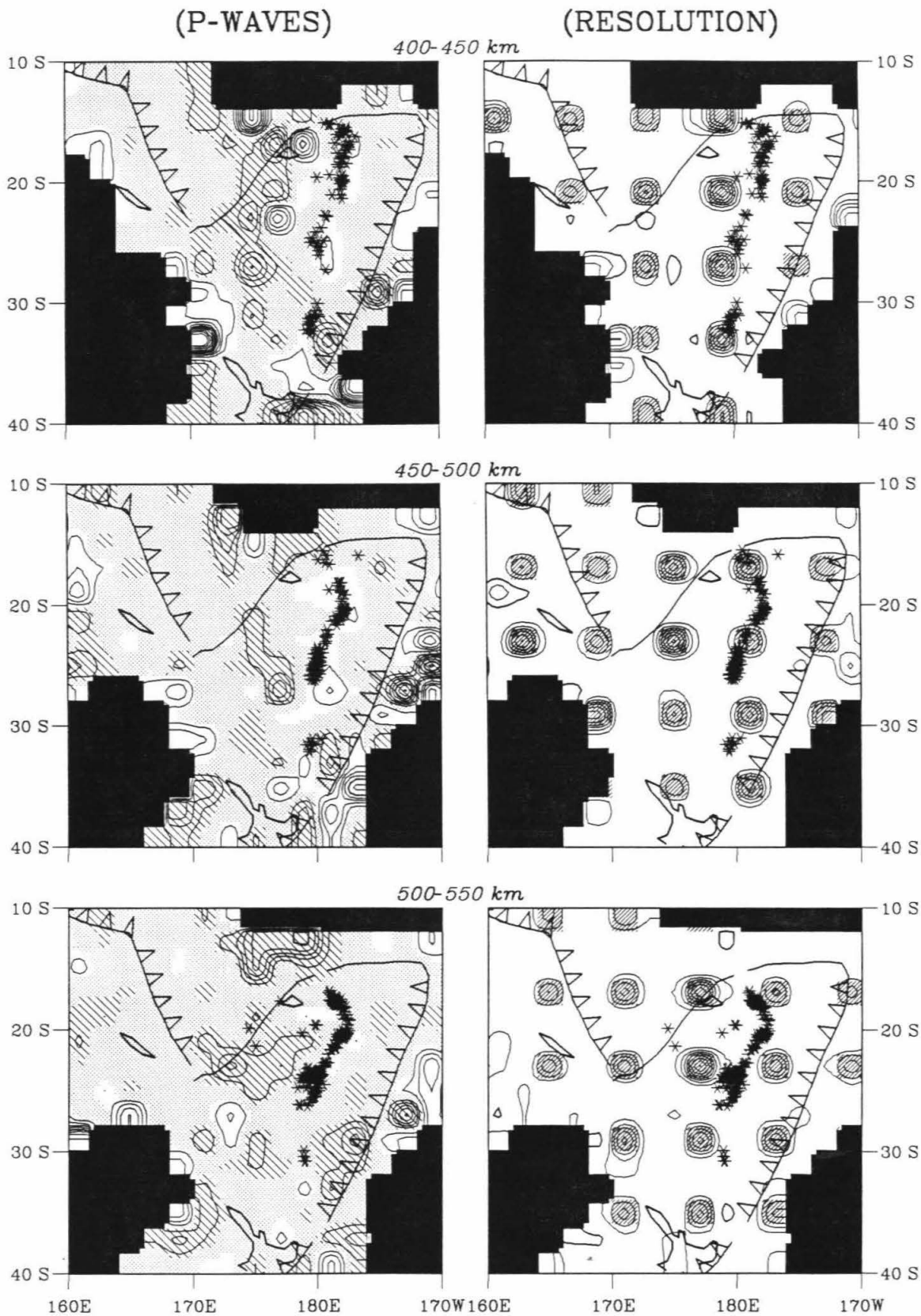

Figure 3.10 (continue)

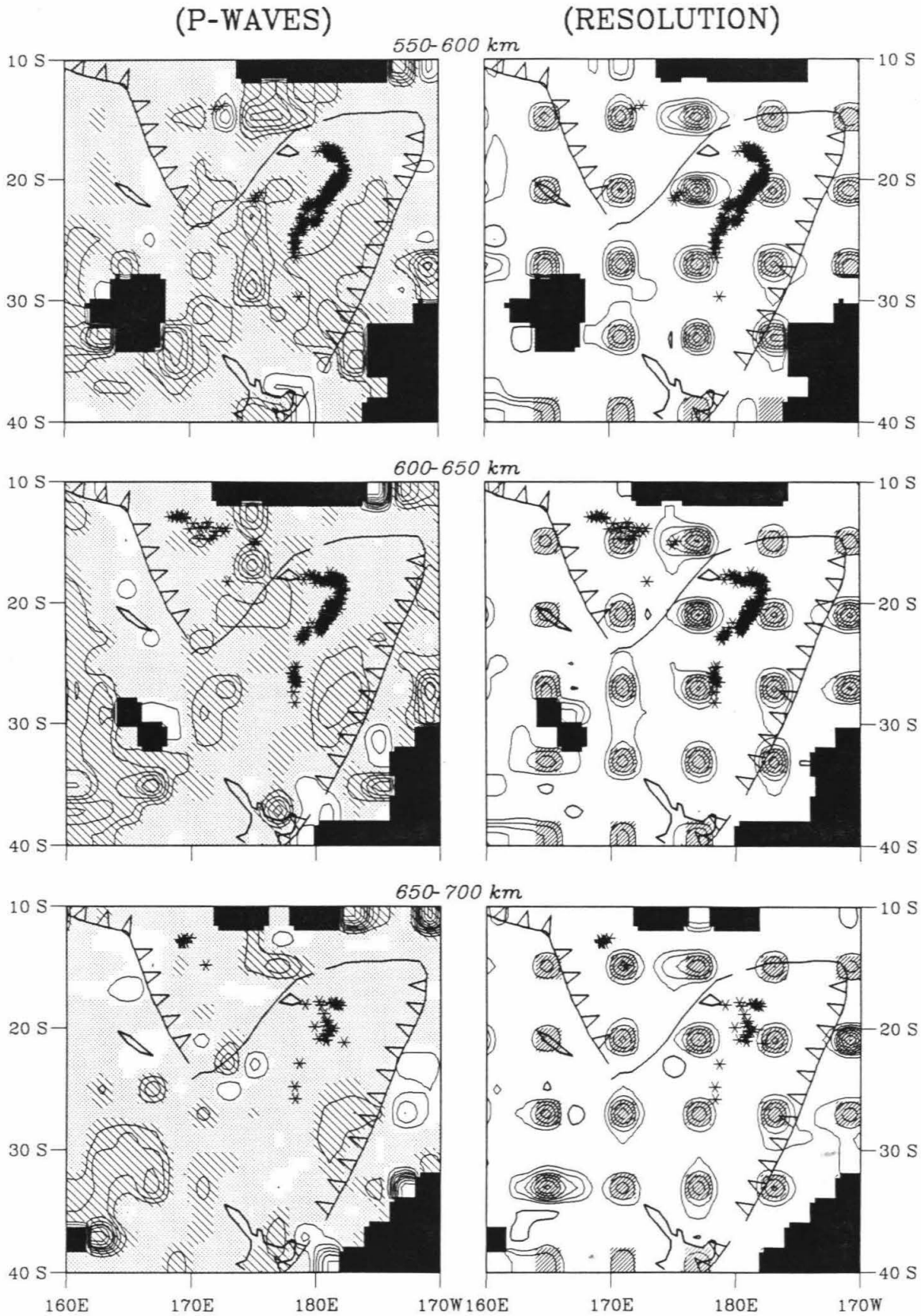

Figure 3.10 (continue)

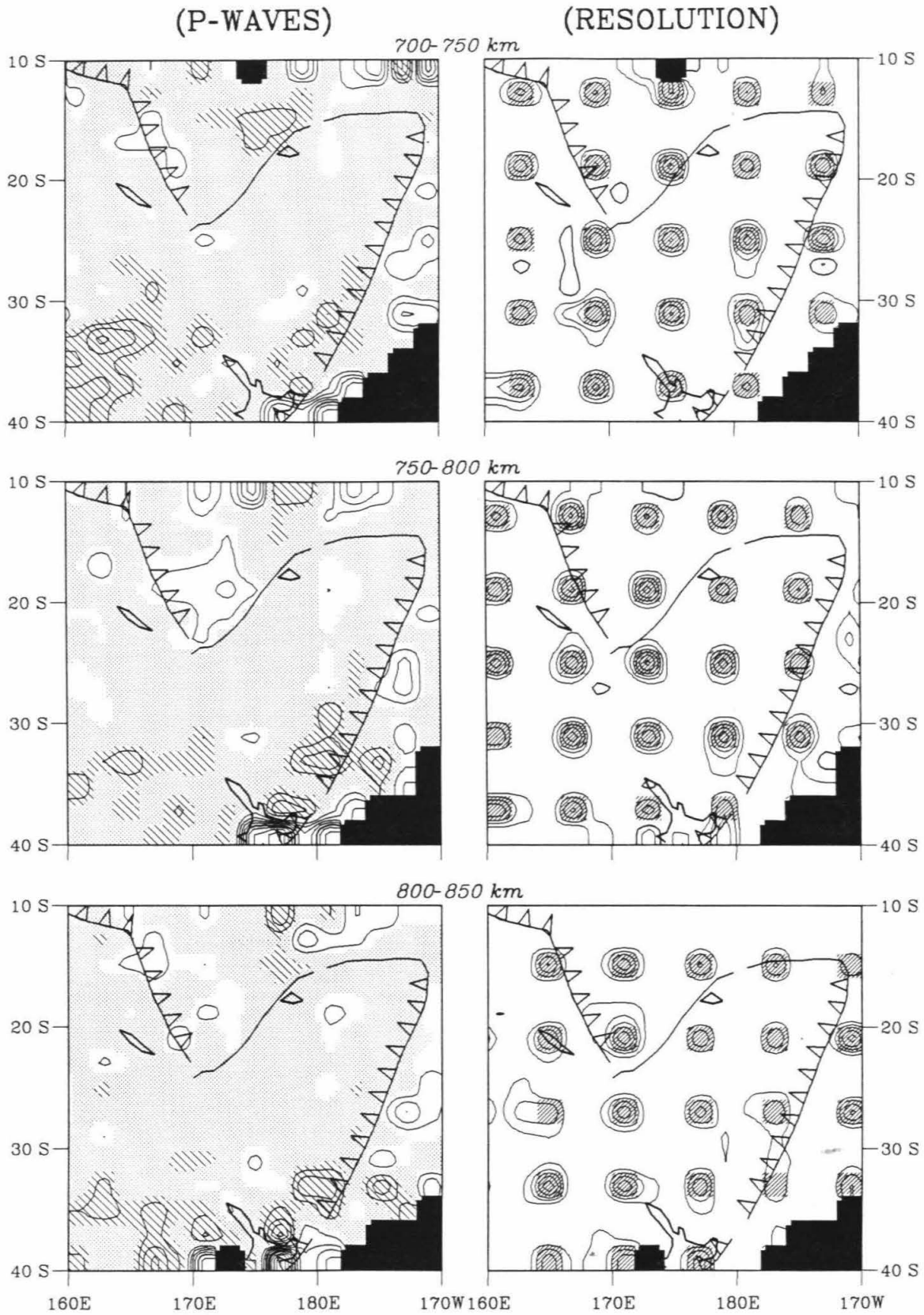

Figure 3.10 (continue)

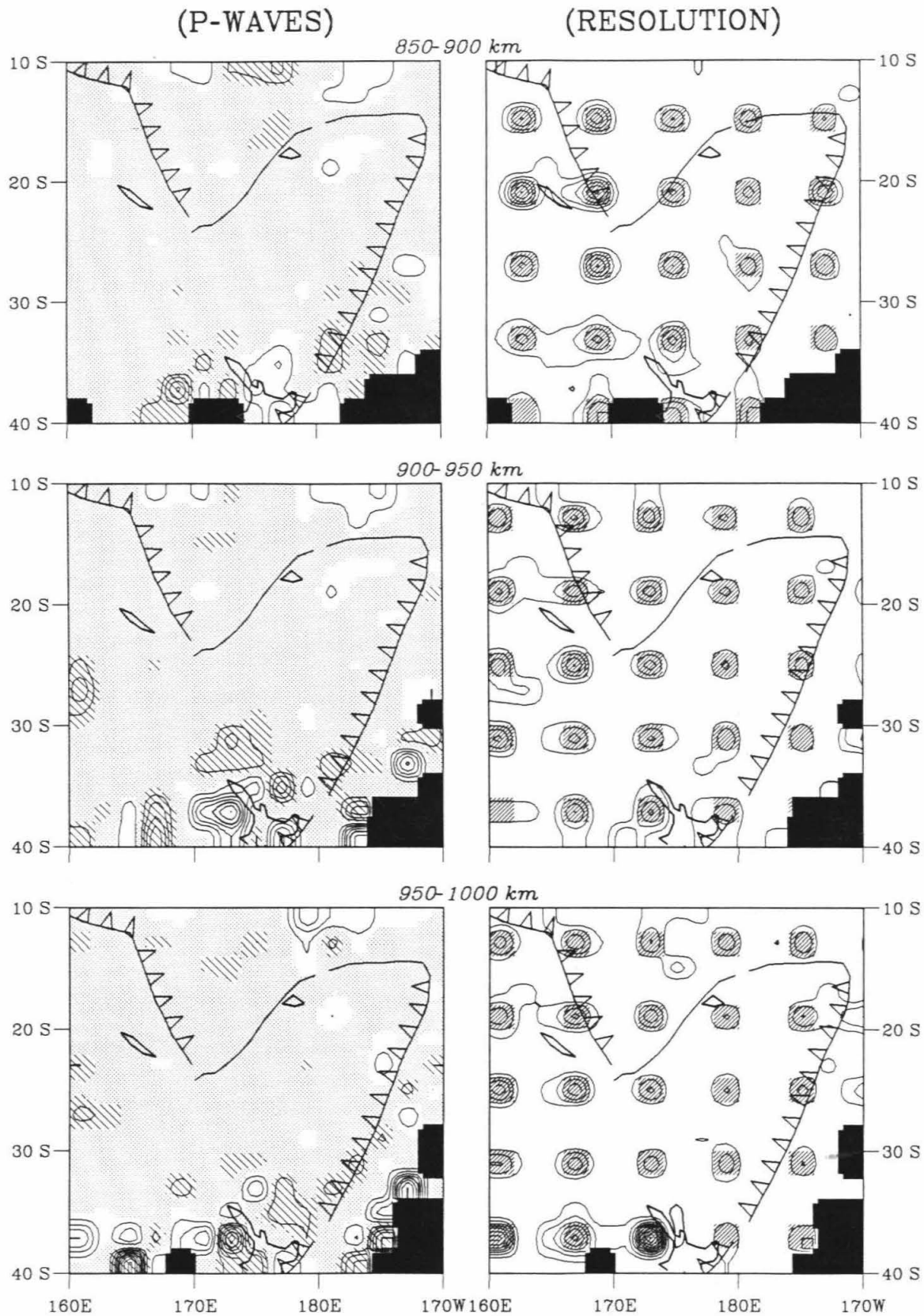

Figure 3.10 (continue)

the finer ($1^\circ \times 1^\circ \times 50$ km) block grid. In Figure 3.11, horizontal slices of images from the finer grid are shown. The earthquake foci displayed in Figures 3.10 and 3.11 are the original ISC events locations.

The anomalies shown in Figure 3.11 resemble those in the coarser block grid. As expected, the anomalies in the finer grid image have shorter scale-lengths and higher peak-amplitudes. The slab anomalies in images of both block grids are quite coherent in the upper mantle, and decrease in amplitude with depth. Interpretations for the lower mantle are somewhat hampered by the poor resolution at depth. Even after a correction for decreasing amplitude with depth, it seems still true that the amplitude of heterogeneities associated with seismic subduction zones in these images generally decreases with depth in most places.

The most coherent anomalous features in these horizontal images are the fast slab-like anomalies beneath the Tonga and Kermadec trenches, which coincides with the highest seismic activity, and large slow regions around seismic subduction zones. The large slow anomalies dominate the images above 300 km and seem to disappear below about 700 km depth. The fast anomaly around the Tonga Wadati-Benioff zone exists from the surface down to around 550 km, then disappears until it reappears at around 700-750 km and extends to near 1100 km.

A series of stacked cross sections of the image to a depth of 1200 km at the finer block grid under the Tonga, Kermadec and New Hebrides arcs are shown in Figure 3.13, where the most profound subduction zones in the southwest Pacific region exist. The locations of these stacked cross sections

Figure 3.11. Horizontal slices on the $1^\circ \times 1^\circ \times 50$ km grid. The legend convention follows that used in Figures 3.9. This slowness field was inverted starting at the solution at the coarser block grid (Figure 3.10). Panels from 100 km to 1300 km depth are shown.

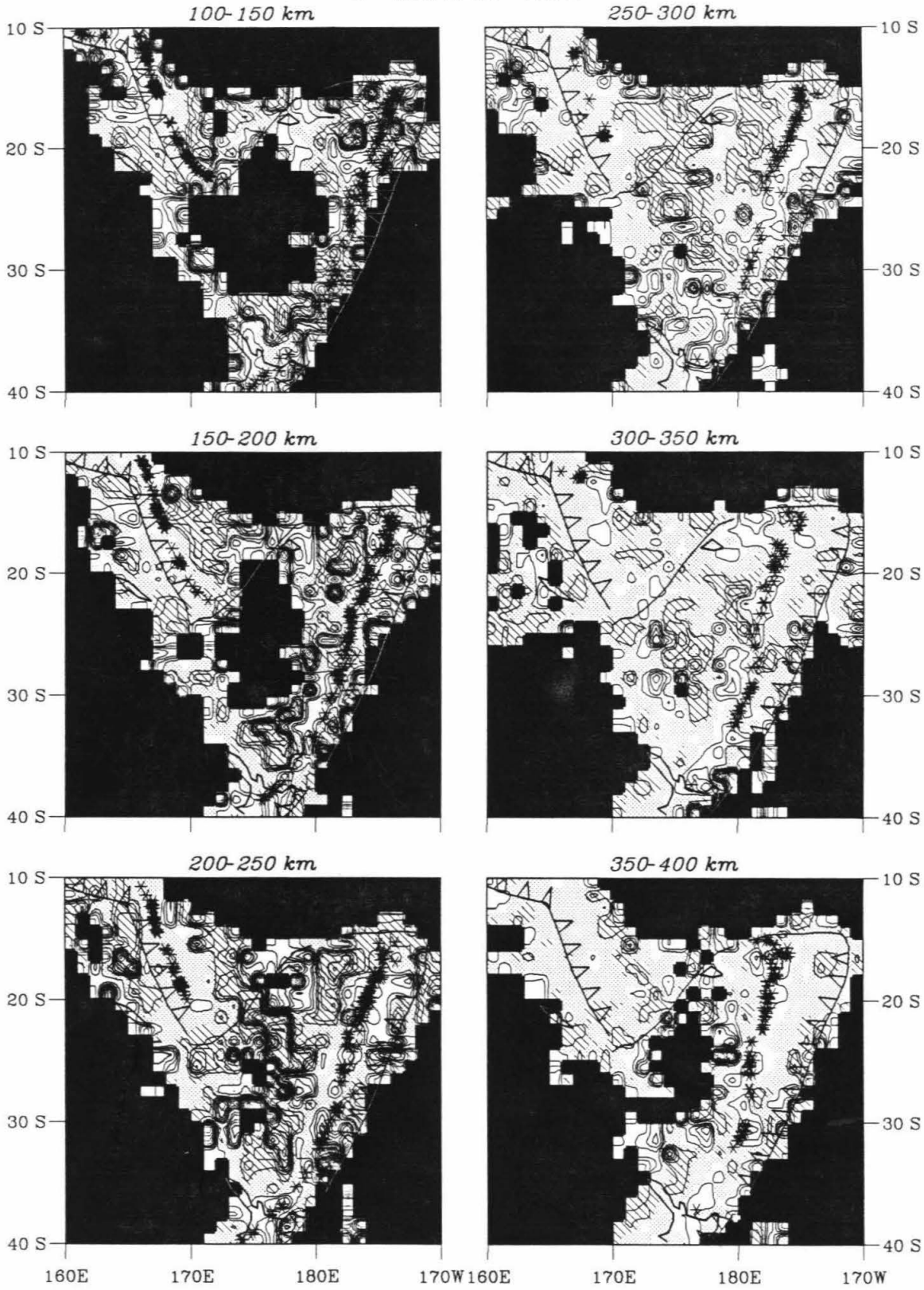
P-WAVES 1x1
100-150 km
250-300 km
150-200 km
300-350 km
200-250 km
350-400 km
10 S
20 S
30 S
40 S
160E
170E
180E
170W

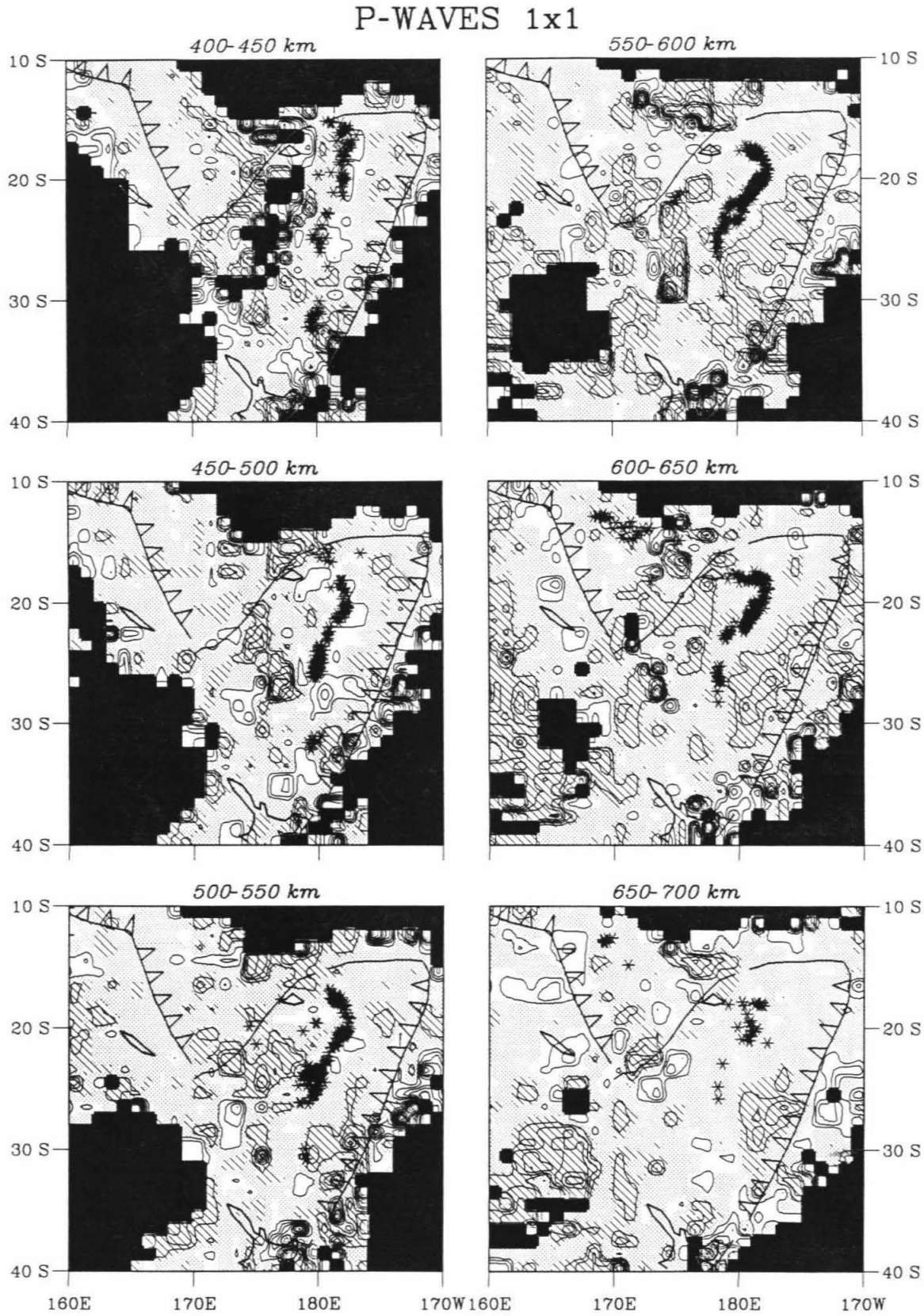

Figure 3.11 (continue)

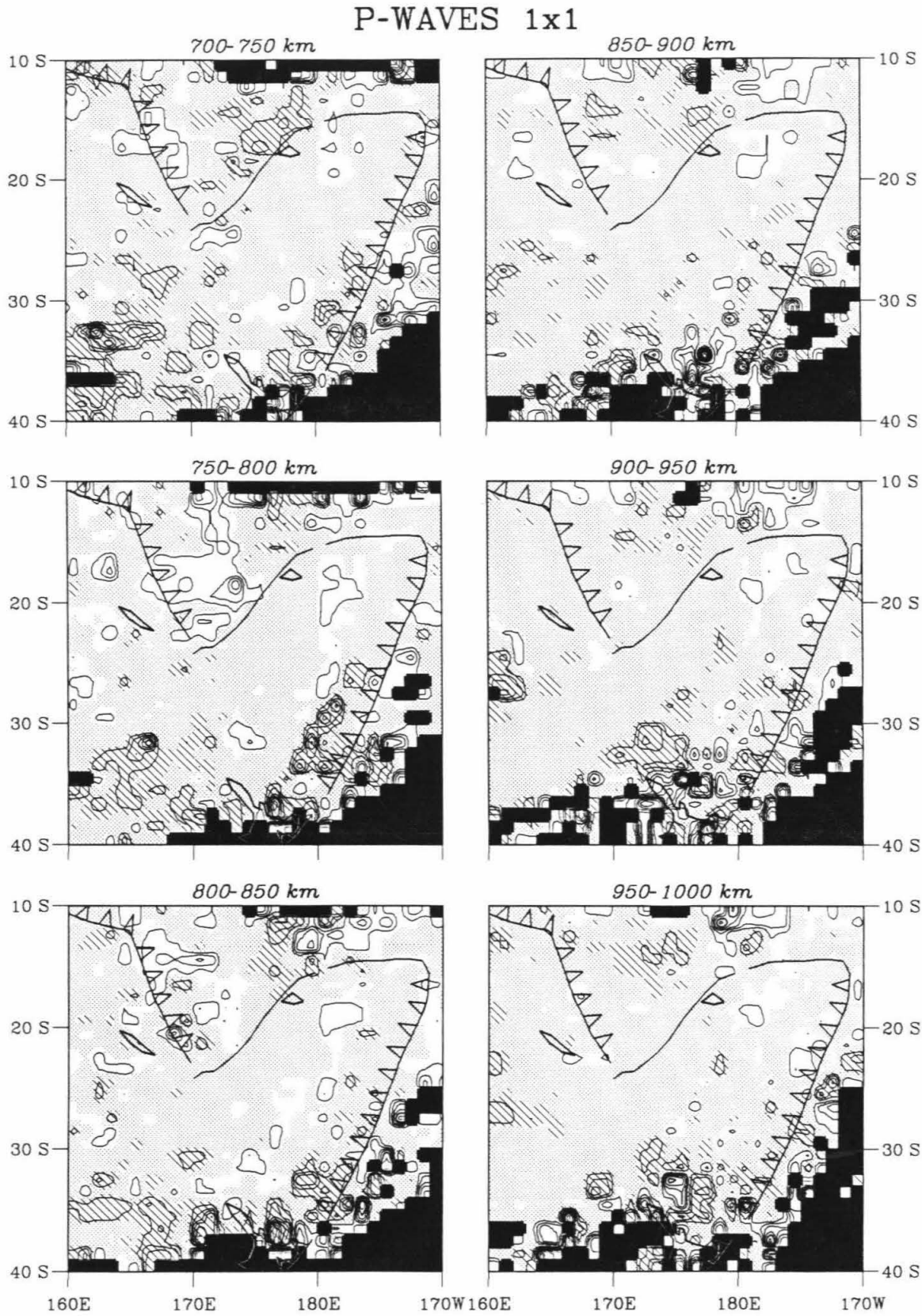

Figure 3.11 (continue)

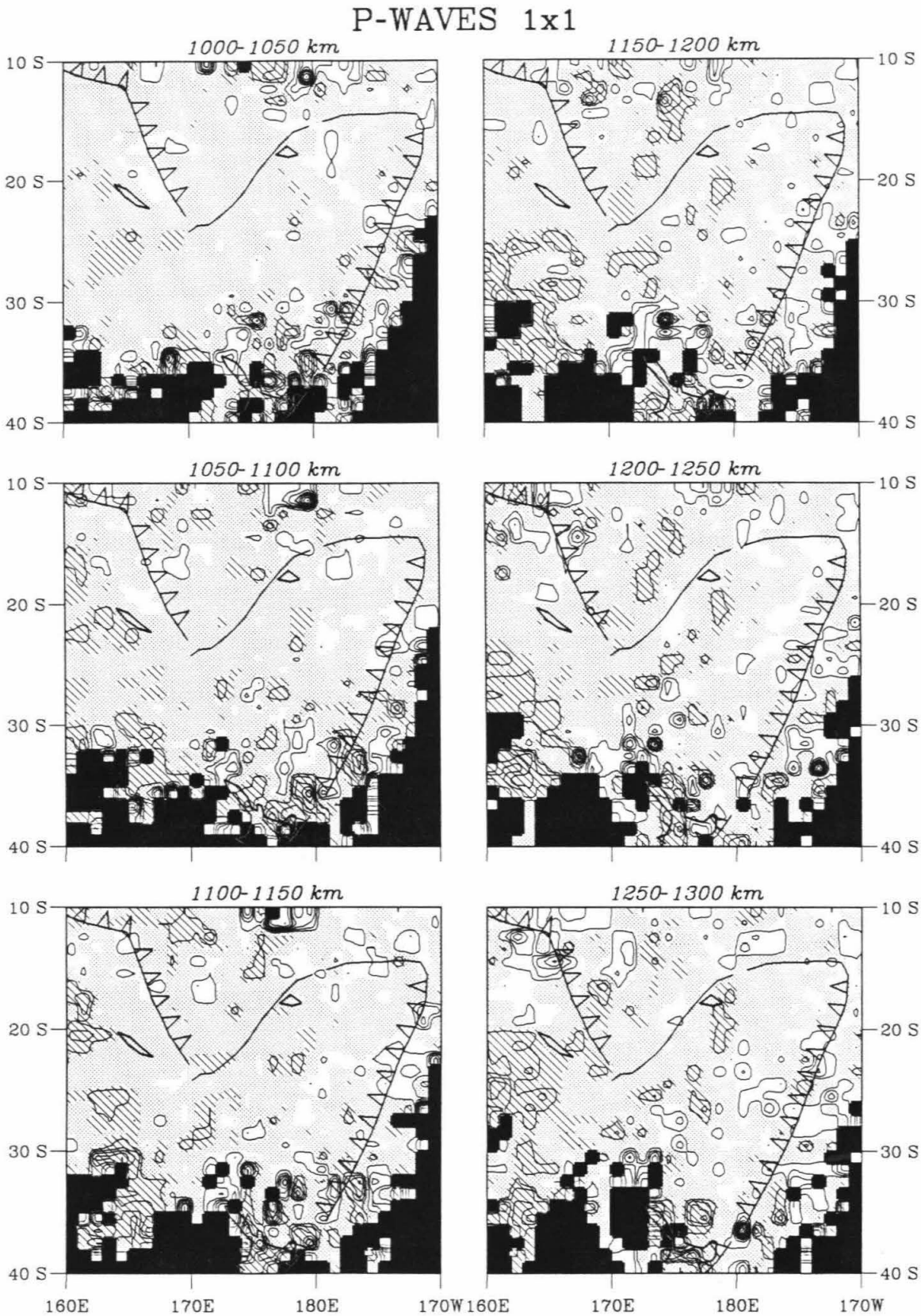

Figure 3.11 (continue)

are shown in Figure 3.12, with seismicity distribution of summarized events.

The fast anomalies around seismicity zones under the Tonga arc (Slices S2-S5) are seen from the surface down to about 500-600 km; they appear to be truncated around 500-700 km and are underlain by a fast band which is essentially horizontal, but appears to tilt slightly to the north in the depth range 750-1000 km. A resolution test shown in Figure 3.9 across A-A1 indicates that the truncation as well as the deep fast band are resolved. Their appearance provides a striking contrast to the geometry of the local Wadati-Benioff zone which is generally continuous in the upper mantle and seems to flatten to subhorizontal at its bottom around 650 km. More than 5% slow anomalies dominate the back-arc region of the Tonga arc from the surface down to about 300 km. There are also large slow anomalies, up to about 1% from the reference velocity, at depths below 300 km beneath the Wadati-Benioff zone.

Velocity anomalies beneath the Kermadec arc are more sporadic in appearance, due to relatively poor resolution. In the upper mantle, both the seismicity zones and the associated fast anomalies tend to flatten to subhorizontal around 600 km (Slices S7-S10). Just north to the North Island of New Zealand (Slice S11) a steeply dipping aseismic fast slab seems to extend to 500 km. It is also seen in map views such as the panels of 400-550 km depths in Figure 3.10. Figure 3.9c shows that the resolution at this location is acceptable in pattern to a depth of about 500 km. Resolution for the lower mantle in this area is fine for the northern part (Slices S7-S9), but very poor in the southern part (Slices S10 and S11). A fast feature in the northern part of

Figure 3.12. A series of boxes indicate the locations of the stacked cross sections S1 to S10 and H1 to H6 which will be shown in the next figure. Solid line A-A1, B-B1, C-C1 and D-D1 locate cross sections which have been shown previously in Figure 3.9. Foci of summarized events are indicated by stars.

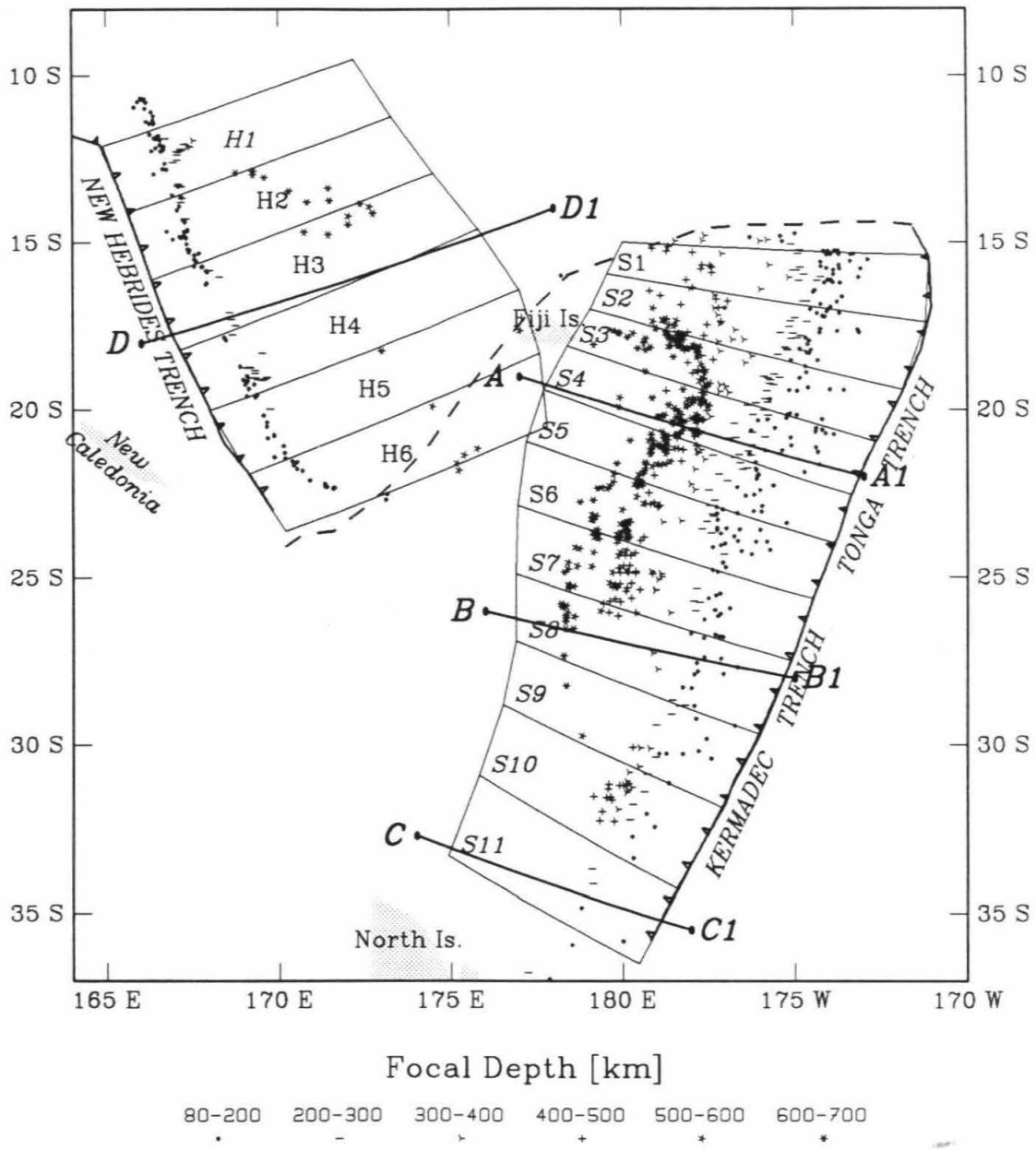
10 S
15 S
20 S
25 S
30 S
35 S
165 E
170 E
175 E
180 E
175 W
170 W
H1
H2
H3
H4
H5
H6
S1
S2
S3
S4
S5
S6
S7
S8
S9
S10
S11
D
D1
A
A1
B
B1
C
C1
NEW HEBRIDES TRENCH
TONGA TRENCH
KERMADEC TRENCH
New Caledonia
Fiji Is.
North Is.
Focal Depth [km]
80-200
200-300
300-400
400-500
500-600
600-700

Figure 3.13. Stacked cross sections of the image on the $1^\circ \times 1^\circ \times 50$ km grid. The legend convention follows that used in Figures 3.9.

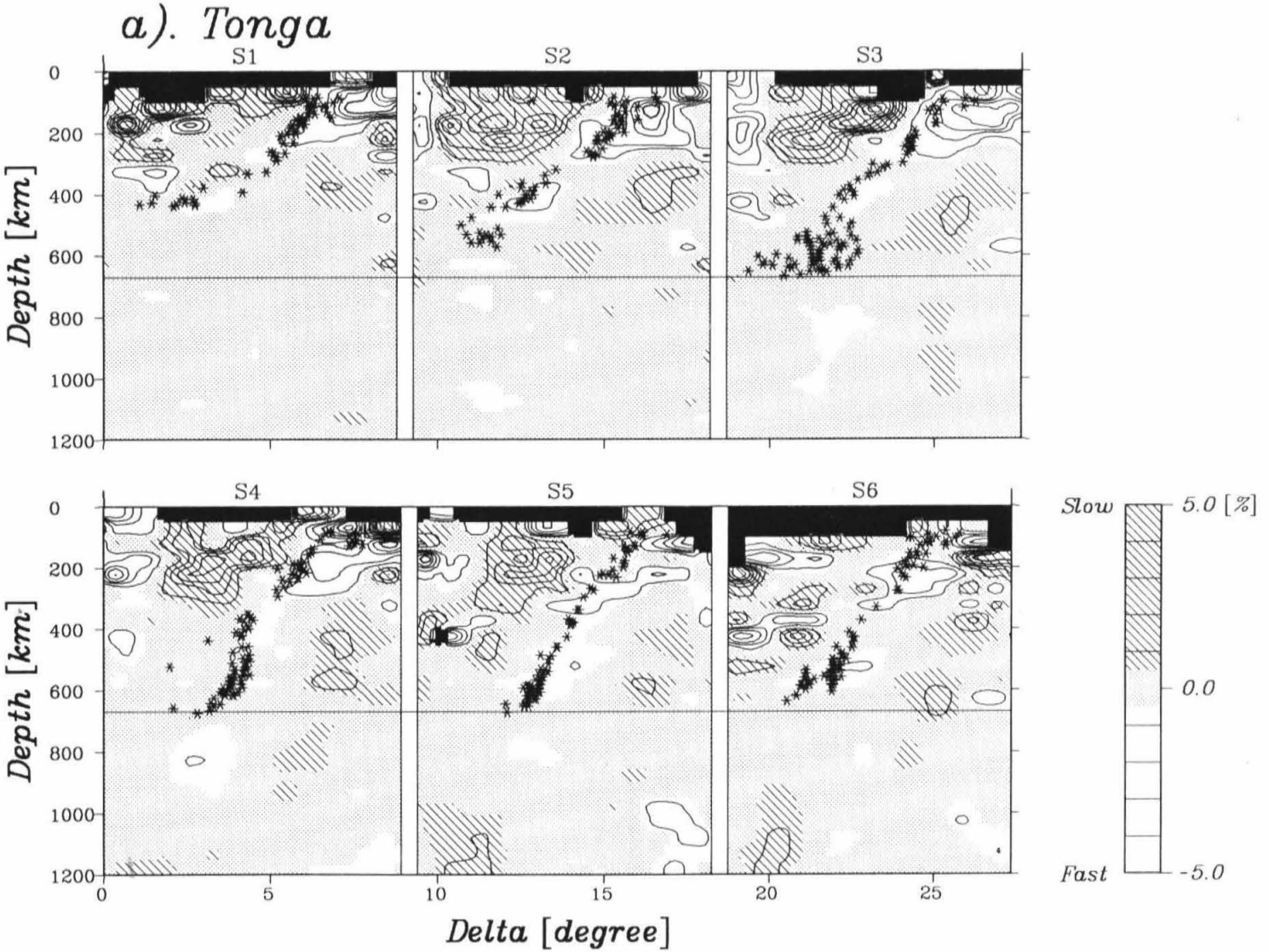
a). Tonga
S1
S2
S3
S4
S5
S6
Depth [km]
0
200
400
600
800
1000
1200
0
5
10
15
20
25
Delta [degree]
Slow
Fast
5.0 [%]
0.0
-5.0

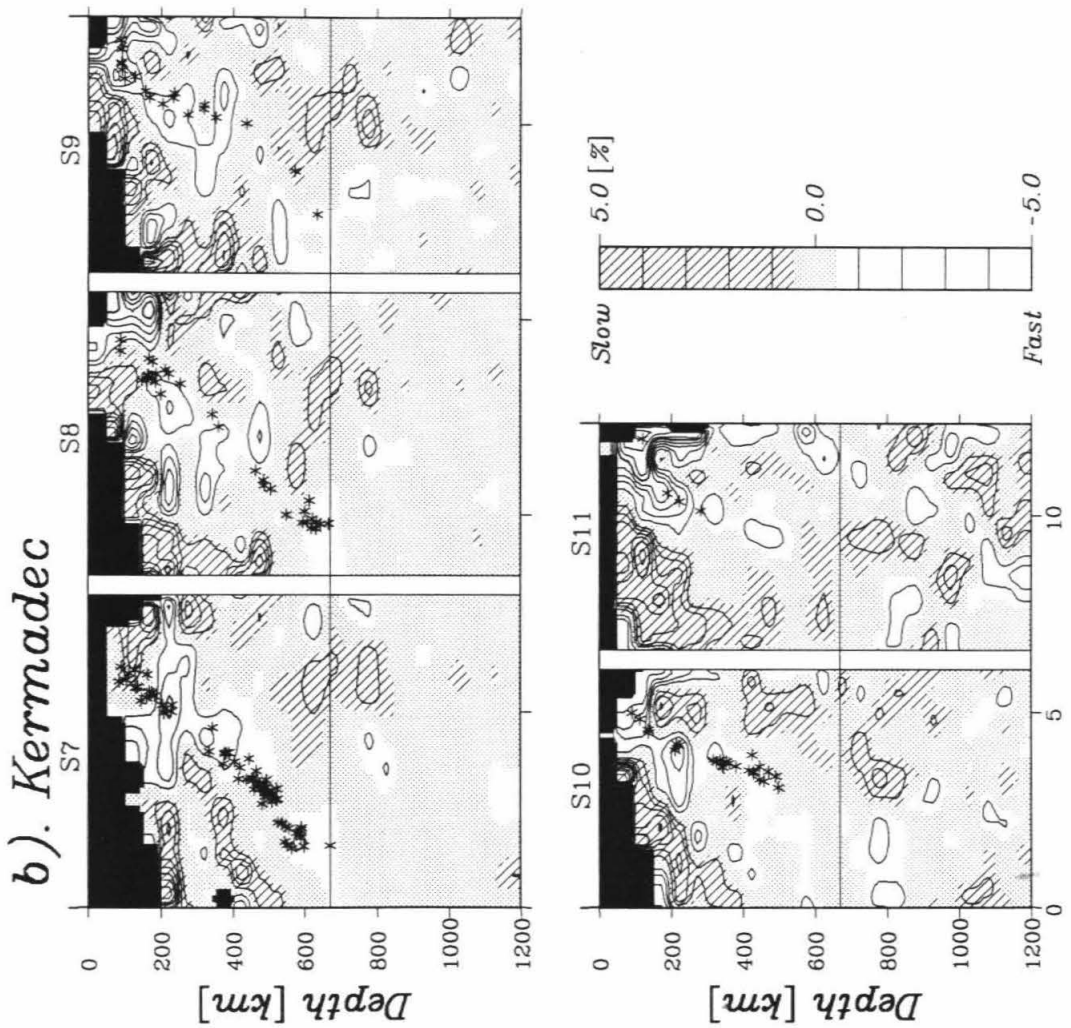
b). Kermadec
S7
S8
S9
S10
S11
Depth [km]
0
200
400
600
800
1000
1200
Slow
Fast
5.0 [%]
0.0
-5.0
0
5
10
Delta [degree]

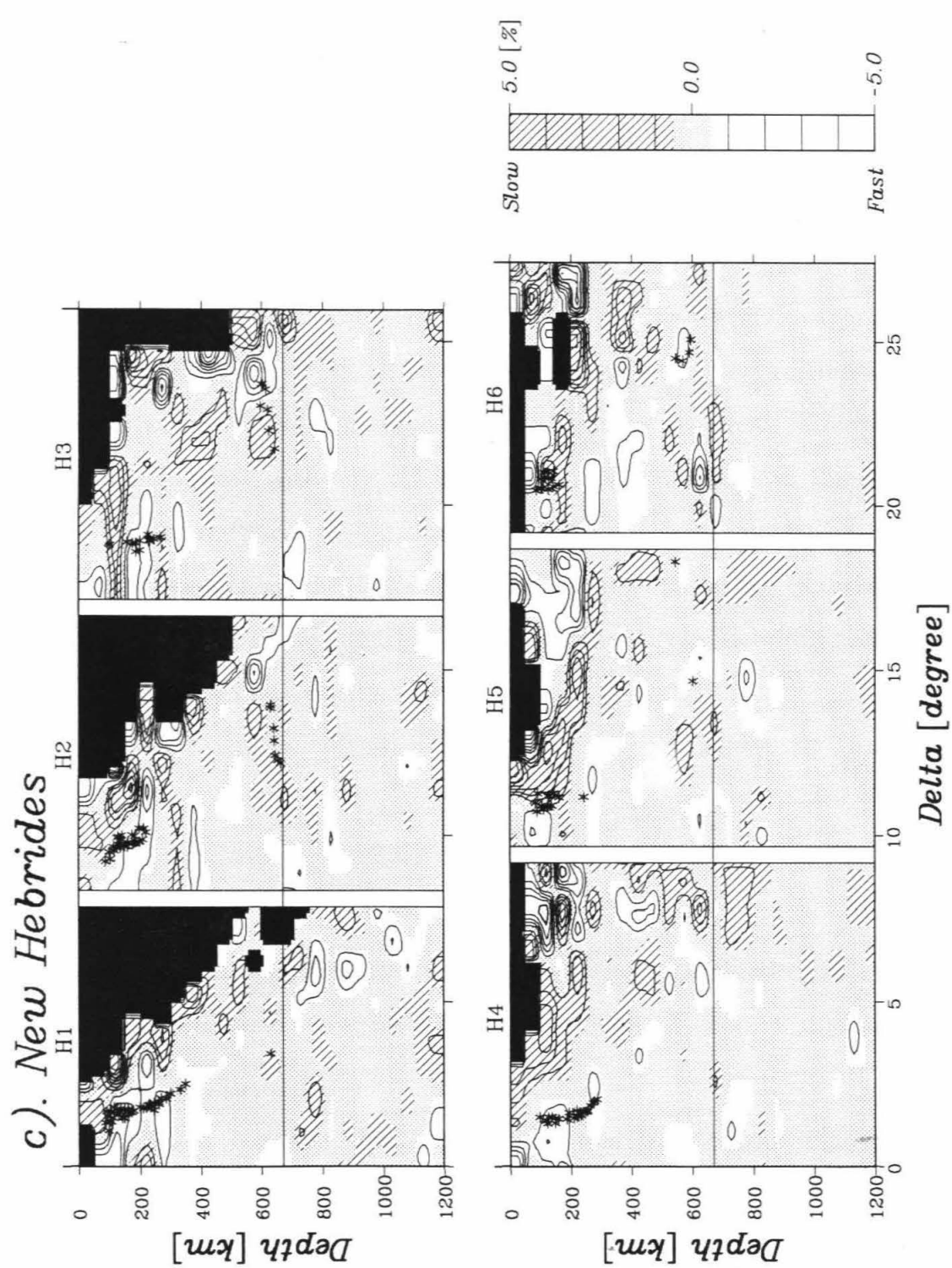
c). New Hebrides
H1
H2
H3
H4
H5
H6
Depth [km]
0
200
400
600
800
1000
1200
0
5
10
15
20
25
Delta [degree]
Slow
Fast
5.0 [%]
0.0
-5.0

the area at depth range of about 750-1000 km cannot be ruled out as an artifact. This feature appears to relate with the similar deep fast anomalous band under the Tonga arc as mentioned before, but it is not directly beneath the deepest earthquakes in the Kermadec subduction zone.

Wadati-Benioff zone beneath the New Hebrides arc ends at a depth of about 350 km at its northern part (Slice H1), and gets shallower at its southern end. There is a very intriguing deep seismicity feature in a horizontal planar form lying at a depth of 600-650 km beneath the North Fiji Basin (see Figures 3.1 and 3.3). A large part of this deep planar seismicity in Slices H1 to H3 doesn't associate with any coherent fast velocities. Beneath the southern New Hebrides arc (Slices H4-H6), however, there is a weak indication that the deep earthquakes near the bottom of the upper mantle lay in locally fast velocities which appear to connect with the southern New Hebrides subduction zone by a series of fast velocity anomalies.

3.6 Discussion

Coherent fast velocities are found around major subduction zones under Tonga, Kermadec and New Hebrides arcs. These are specifically discussed below.

A scenario for the deep fast velocities in Tonga. One striking feature in the real data image (Figure 3.9a) is the truncation of the fast velocities associated with the seismicity around 550-700 km depths and the

fast anomalies below the deepest earthquakes. This pattern is seen under most parts of the Tonga arc (see Figure 3.13a). The artificial velocity model shown in the middle panel of Figure 3.9a is designed in accordance with the real image, i.e., a fast slab-like anomalies which is a close mimic of the Wadati-Benioff zone, plus a deep-going fast band below the deepest earthquakes. The result of the synthetic inversion on the model in the right panel shows that the pattern of the model is mostly resolvable while the amplitude can be resolved to around 50%. The test indicates that the truncation as well as the deep fast band beneath the deepest earthquakes in the left image are consistent with the data.

Previous travel time analyses in this region have found quite contrary results. Although virtually all travel time studies for major subduction zones in the region agree that 5-10% higher velocity anomalies are presented in the top several hundred kilometers of the subducting plates, they disagree on the lower extent of the slab. The result in this study is that the region around the Tonga Wadati-Benioff zone is fast from the surface down to around 550 km, where it becomes "normal." This is consistent with the studies by Sondergeld *et al.* [1977], Bock [1981] and Ansell and Gubbins [1986]. Fitch [1977] obtained close-to-normal velocities between 500 and 580 km, but higher velocities below. The presence of a fast band below the deepest earthquakes between around 750-1000 km, is also consistent with studies by Frohlich and Barazangi [1980] and Fischer *et al.* [1988]. Of course, whether this fast band is the signature of a deep-penetrating slab cannot be determined from this kind of study.

An aseismic slab-like anomaly in the south Kermadec arc. Ansell and Gubbins [1986] suggested that anomalous P wave residuals from events in the Tonga-Kermadec subduction zone to New Zealand can be explained if the high velocity slab anomaly extends to a depth of 450 km in the region of the deep seismicity gap between 32 ° S - 36 ° S. The above explanation certainly agrees with the result in this study (cross sections C-C1 in Figure 3.9 and S11 in Figure 3.13) which shows the presence of an aseismic fast anomaly extending to about 500-550 km from the shallow seismicity slab. The resolution test along C-C1 (Figure 3.9c) confirms the consistence of the anomaly, but suggests very poor resolution below this depth, and hence the fast anomaly could extend even further down. In addition, the appearance of fast and slow anomalies below 600 km in the data images of this area are probably mostly artifacts due to poor resolution.

The deep flat seismicity zone beneath the North Fiji Basin. The striking flat lying deep seismicity feature in the 600-650 km depth range beneath the North Fiji Basin (Figure 3.3) appears to extend southeasterly to the Tonga Wadati-Benioff zone. The tectonic evolution history of the region [Chase, 1971; Hamburger and Isacks, 1987] suggests that this feature could be remnants of an ancient subducting slab along the New Hebrides arc or along the Vitiaz arc (Figure 3.1). The southward extension of the feature could be remnants of an ancient subducting slab along the New Hebrides arc and along the Hunter Fracture Zone or the Tonga arc. It is hoped that a detailed velocity structure around this region would offer new insights about the origin of the deep material.

The resolution test shown in Figure 3.9d suggests that a flat lying fast anomaly in the location, if it exists, is resolvable with the data ray paths. Areas in the lower mantle depths, however, are poorly resolvable. The flat lying deep earthquake cluster in cross sections H1-H3 (see Figures 3.12 and 3.13c) does not associate with any clear fast velocity anomalies. If this pattern is true and the earthquakes indeed occur in old slabs, then it implies that the velocity anomaly of the slab probably has diminished due to long-term thermal diffusion. The data images have unsatisfactory coverage beneath the Vitiaz arc. Because there is no obvious indication that the fast slab-like anomaly beneath the northern New Hebrides arc (slices H1-H3) extends down to beyond 400 km, it could be true that the deep material around the flat lying seismicity is originated in the Vitiaz Trench subduction zone [Hamburger and Isacks, 1987]. The images for the southern New Hebrides arc (slices H4-H6), however, show some fast velocity anomalies connecting the shallow Northern New Hebrides subduction zone with the deep seismicity beneath the Hunter Fracture Zone. Hence, these deep earthquakes likely occurred in old slab material originating from the southern New Hebrides Trench.

Slow anomalies around slabs. Large slow anomalies are found on both sides of fast slab subduction zones in the northwest Pacific (the previous chapter). This kind of slow patches is even more profound around subduction zones in the southwest Pacific. They dominate the back-arc as well as forearc regions from the surface down to about 300 km. Some are even deeper (Figure 3.13). As suggested near the end of Section 2.6, these slow anomalies may be partially caused by a negatively-biased reference velocity model due to the fact

that most deep and intermediate-depth earthquakes occur in fast velocity subducting lithospheres.

The slab penetration issue. Numerous seismic studies, including this one, have been conducted in subduction zones of the southwest Pacific and many other regions, with the ultimate goal of resolving the slab penetration issue. So far, however, quite controversial results have been found. This is due to the poor data quality both in terms of high noise and low ray coverage (especially crossing rays), but also to the speculative nature of the velocity interpretations. For example, a fast anomaly below the deepest earthquakes could be thermal coupling or the upper mantle and lower mantle boundary could be depressed below slabs.

It may be unreasonable to insist in the extreme cases that all slabs are either penetrating or trapped. Geochemical, petrological and experimental studies have been providing better and tighter constraints on the problem. Penetrating or trapping of the slab with respect to the upper mantle-lower mantle boundary is sensitive to the relative densities of slab, upper mantle, and lower mantle, as well as slab dip [Kincaid and Olson, 1987]. Both the density values given by geochemical and petrological studies and observed slab dip are varying, although the formers are roughly around the threshold. It therefore widens our interpretation of slabs to allow the intermediate situations between the two extremes.

The seismogenic part of the slab is usually quite thin at shallow depth (e.g., Ansell and Smith, 1975). At depth, particularly near the bottom of deep Wadati-Benioff zones (e.g., under the Tonga, Kermadec and Izu-Bonin arcs),

however, earthquake foci often occupy a much thicker range. The tectonic evolution history, such as that for the Western Pacific by Hilde *et al.* [1976] based on magnetic data, and the strong contortions of deep subducting plates in many places, such as indicated by seismicity beneath Tonga and Kermadec arcs [Giardini and Woodhouse, 1984], should certainly be used in any travel time analysis [Bock, 1987].

3.7 Conclusions

Over a quarter million P wave travel time residuals from ISC catalog, all of focal depth greater than 80 km, are used to derive a three-dimensional P wave velocity structure around subduction zones in the southwest Pacific. The tomographic inversion method used in the previous chapters is applied to summary rays of similar source and receiver locations. A two-dimensional ray tracing is utilized inside the model, and mantle heterogeneities outside the model are corrected with the Clayton-Comer lower mantle model. Among velocity anomalies which are consistent with the data under some resolution and error tests, coherent slab-like anomalies of several percent fast are present around most seismicity subduction zones, surrounded by large slow regions. The fast Tonga slab appears to end around 550 km depth, but is underlain by a fast band at 750-1000 km depths. The fast slab-like anomaly beneath the Kermadec arc tends to flatten to subhorizontal near the bottom of upper mantle, and it also appears to extend down to 500-550 km depth in the

seismicity gap near New Zealand. No clear fast anomalies are seen around the flat lying deep seismicity between 600-650 km depth underneath the North Fiji Basin, but some fast velocities which are associated with the southward extension of the deep seismicity seems to be connected with the southern New Hebrides slab.

References to Chapter 3

Aki, K., and W. H. K. Lee, Determination of three-dimensional velocity anomalies under a seismic array using first P arrival times from local earthquakes, 1. A homogeneous initial model, *J. Geophys. Res.*, **81**, 4381-4399, 1976.

Ansell, J. H., and D. Gubbins, Anomalous high-frequency wave propagation from the Tonga-Kermadec seismic zone to New Zealand, *Geophys. J. R. astr. Soc.*, **85**, 93-106, 1986.

Bock, G., The effect of the descending lithosphere beneath the Tonga island arc on P wave travel-time residuals at the Warramunga Seismic Array, *Phys. Earth Planet. Inter.*, **25**, 360-371, 1981.

Bock, G., P wave travel times from deep and intermediate-depth earthquakes to local seismic stations and the subducted slab of oceanic lithosphere beneath the Tonga island arc, *J. Geophys. Res.*, **92**, 13863-13877, 1987.

Bowman, J. R., Body wave attenuation in the Tonga subduction zone, *J. Geophys. Res.*, **93**, 2125-2139, 1988.

Chase, C., Tectonic history of the Fiji Plateau, *Geol. Soc. Amer. Bull.*, **82**, 3087-3109, 1971.

Clayton, R. W., and R. P. Comer, A tomographic analysis of mantle heterogeneities from body wave travel times, *Eos Trans. AGU*, **64**, 776, 1983.

Engdahl, E. R., and D. Gubbins, Simultaneous travel-time inversion for earthquake location and subduction zone structure in the central Aleutian Islands, *J. Geophys. Res.*, **92**, 13855-13862, 1987.

Fischer, K., T. H. Jordan, and K. C. Creager, Seismic constraints on the morphology of deep slabs, *J. Geophys. Res.*, **93**, 4773-4783, 1988.

Fitch, T. J., Compressional velocity in source regions of deep earthquakes: An application of the master earthquake technique, *Earth Planet. Sci. Lett.*, **26**, 156-166, 1975.

Fitch, T. J., In situ P wave velocities in deep earthquake zones of the SW Pacific: Evidence for a phase boundary between the upper and lower mantle, in *Island Arcs, Deep Sea Trenches and Back-Arc Basins*, Maurice Ewing Ser. **1**, edited by M. Talwani and W. C. Pitman III, 99-114, AGU, Washington, D.C., 1977.

Frohlich, C., and M. Barazangi, A regional study of mantle velocity variations beneath eastern Australia and the southwestern Pacific using short-period recording of P, S, PcP, ScP and ScS waves produced by Tongan deep earthquakes, *Phys. Earth Planet. Inter.*, **21**, 1-14, 1980.

Giardini, D., and J. H. Woodhouse, Deep seismicity and modes of deformation in Tonga subduction zone, *Nature*, **307**, 505-509, 1984.

Giardini, D., and J. H. Woodhouse, Horizontal shear flow in the mantle beneath the Tonga arc, *Nature*, **319**, 551-555, 1986.

Hager, B. H., and R. W. Clayton, Constraints on the structure of mantle convection using seismic observations, flow models, and the geoid, in W. R. Peltier, ed., *Mantle Convection*, Gordon & Breach, in press, 1989.

Hamburger, M.W., and B.L. Isacks, Deep earthquakes in the southwest Pacific: a tectonic interpretation, *J. Geophys. Res.*, **92**, 13841-13854, 1987.

Hilde, T. W. C., S. Uyeda, and L. Kroenke, Tectonic history of the Western Pacific, in *Geodynamics Progress and Prospects*, edited by C. L. Drake, 1-15, AGU, Washington, D.C., 1976.

Hirahara, K., A large-scale three-dimensional seismic structure under the Japan islands and the Sea of Japan, *J. Phys. Earth*, **25**, 393-417, 1977.

Hirahara, K., Three-dimensional seismic structure beneath southwest Japan: The subducting Philippine Sea plate, *Tectonophys.*, **79**, 1-41, 1981.

Hirahara, K., and T. Mikumo, Three-dimensional seismic structure of subducting lithospheric plates under the Japan islands, *Phys. Earth Planet. Inter.*, **21**, 109-119, 1980.

Huppert, L. N., and C. Frohlich, The P velocity within the Tonga Benioff zone determined from traced rays and observations, *J. Geophys. Res.*, **86**, 3771-3782, 1981.

Kamiya, S., T. Miyatake, and K. Hirahara, How deep can we see the high velocity anomalies beneath the Japan Island? *Geophys. Res. Lett.*, **15**, 828-831, 1988.

Kincaid, C., and P. Olson, An experimental study of subduction and slab migration, *J. Geophys. Res.*, **92**, 13832-13840, 1987.

Langan, R. T., I. Lerche, and R. T. Cutler, Tracing of rays through an heterogeneous media: an accurate and efficient procedure, *Geophysics*, **50**, 1456-1465, 1985.

Mitronovas, W., and B. L. Isacks, Seismic velocity anomalies in the upper mantle beneath the Tonga-Kermadec island arc, *J. Geophys. Res.*, **76**, 7154-7180, 1971.

Richter, F. M., Focal mechanisms and seismic energy release of deep and intermediate earthquakes in the Tonga-Kermadec region and their bearing on the depth extent of mantle flow, *J. Geophys. Res.*, **84**, 6783-6795, 1979.

Roecker, S. W., Velocity structure in the Izu-Bonin seismic zone and the depth of the olivine-spinel phase transition in the slab, *J. Geophys. Res.*, **90**, 7771-7794, 1985.

Sondergeld, C. H., B. L. Isacks, M. Barazangi, and S. Billington, A search for velocity anomalies near the deep portions of the inclined seismic zone of Tonga island arc, *Bull. Seism. Soc. Am.*, **67**, 537-541, 1977.

Spencer, C. P., and E. R. Engdahl, A joint hypocenter location and velocity inversion technique applied to the central Aleutians, *Geophys. J. R. astr.*

Soc., **72**, 399-415, 1983.

Spencer, C. P., and D. Gubbins, Travel-time inversion for simultaneous earthquake location and velocity structure determination in laterally varying media, *Geophys. J. R. astr. Soc.*, **63**, 95-116, 1980.

Stark, P. B., and C. Frohlich, The depths of the deepest deep earthquakes, *J. Geophys. Res.*, **90**, 1859-1869, 1985.

Zhou, H., and R. W. Clayton, P wave velocities around subduction zones in the southwest Pacific, *Eos Trans. AGU*, **69**, p.398, 1988.

CHAPTER 4

PREDICTION OF OBSERVATIONS FROM THE INVERSE RESULTS:

modeling focal residual spheres and geoid

Abstract

P wave travel time residual spheres for 145 subduction zone earthquakes along the northwest edge of the Pacific are analyzed in this chapter. They are compared with predictions from the regional velocity model of Chapter 2 and a global mantle velocity model by Clayton and Comer [1983]. The mantle models fit much of the residual sphere data and, to certain extent, suggest the location of mantle velocity heterogeneities responsible for various residual sphere patterns. For most deep events considered, the predicted fast slab-like residual sphere anomalies are caused by diffuse heterogeneities, mainly of deep lower mantle and receiver mantle origin. The region immediately below the deepest earthquakes, depths 650-1500 km, has an effect usually smaller than or comparable to the effect of other regions of the velocity models. Attributing the long wavelength anomalies of the residual sphere to near-source slab effects alone, or even primarily, is not always valid.

Two types of corrections for the teleseismic effects are suggested, either by using a well determined global mantle model or by removing teleseismic station averages of residuals from many local events. After eliminating the teleseismic effects, the dominate slab-like fast band in a residual sphere, if it exists, can be determined by seeking the best fitting low degree harmonics. The detectable fast bands in residual spheres are generally consistent and follow the seismicity trends under the Mariana, Izu-Bonin and Japan trenches, but are inconsistent and differ from the seismicity trend under the Kuril trench. The fast band for most deep events under

Japan is subhorizontal rather than near vertical, and the amplitude of the vertically dipping fast band of Mariana events decreases with depth.

A static computation of the gravitational potential from the upper mantle velocity models of Chapter 2, after converting into a density contrast through the seismic equation of state by Anderson [1967], shows patterns similar to the degree 6-9 components of the observed geoid.

4.1 Introduction

We now change our view point from the inversion, as done in the previous three chapters, to analyzing predictions from the inverse results, the three-dimensional velocity models (called images in previous chapters).

Most of this chapter is devoted to the study of residual spheres. The residual sphere [Davis and McKenzie, 1969] is the focal-sphere projection of travel time residuals of an earthquake and represents graphically the accumulated mantle heterogeneity traversed by all rays. Travel times of seismic waves from a deep focus earthquake are plotted on an imaginary sphere surrounding the earthquake. Each ray penetrates this sphere at a specific point, which depends on the azimuth and distance between the event and the station. In practice, the difference between the travel time of the ray and the travel time in a reference Earth model is plotted on a lower hemisphere projection. Thus, the steepest rays and those traveling to the most distant stations are plotted near the center of the hemisphere, and rays leaving the source horizontally are plotted on the boundary of the hemisphere.

The residual spheres of deep subduction zone earthquakes are particularly interesting since they have been used to study the depth of the subducting lithospheric slab. Previous studies on residual spheres of some subduction zone earthquakes [Jordan, 1977; Creager and Jordan, 1984 and 1986] have been used to argue for penetration of the lithospheric slab deep into the lower mantle, based on the assumptions that there are no long wavelength heterogeneities in the lower mantle. This means that low harmonic anomalies on the residual sphere are near source effects. The anomalies are further assumed to be due to thermal effects alone. The validity of these assumptions is critical to the conclusions advanced by these authors. These assumptions are tested in this chapter.

Deep focus earthquakes are generally assumed to be embedded in cold subducted slabs with high seismic velocities. High-velocity slabs act as anti-waveguides, causing seismic energy to defocus and to leave the slab. By contrast, seismic wave energy is trapped in low velocity channels, or waveguides, and can travel for large distances in the channel. It has been proposed that 1 to 2 second travel time anomalies from deep focus earthquakes are due to long distance propagation in high-velocity slabs (Creager and Jordan, 1984). Thus, a slab related velocity anomaly of 5% implies slab propagation paths of 200 to 400 km. Alternatively, the travel time anomaly may be accumulated in the deeper mantle since teleseismic rays spend most of their time there.

The travel times of seismic waves to teleseismic stations are of the order of 1000 seconds. Long wavelength velocity anomalies of only 0.5% can

therefore lead to travel time residuals of 5 seconds. Observed travel-time residuals of deep focus earthquakes, after smoothing, are of the order of 1 to 2 seconds. Seismic waves from deep focus earthquakes recorded at distant stations spend on the order of 2-4% of their travel time in the region where deep slab penetration has been hypothesized, i.e., the upper mantle and the top part of the lower mantle under the source. Since large scale coherent velocity anomalies of the order of 0.5% or larger in the lower mantle are available (e.g., Dziewonski *et al.*, 1977; Dziewonski, 1984; Hager *et al.*, 1985; Dziewonski and Woodhouse, 1987), it would seem to be difficult to extract evidence for deep slab penetration from teleseismic data. In particular, seismic rays from deep focus earthquakes are well spread out at lower mantle depths, especially if they are defocused near the origin by fast slab "anti-waveguides."

A major task of this chapter is to investigate the limitation of the residual sphere method in constraining the morphology of subducted slabs. I am primarily interested in the effect of the deep mantle on residual spheres. By "deep mantle" I mean the mantle between a depth of 1500 km at the source side of the seismic ray, to the surface at the receiver site. Thus, the part of the mantle where previous investigations have assumed a cold, fast slab is masked out. If the travel-time residuals for wave propagation in the deep mantle project onto the residual sphere as a fast band, or if they are of high amplitude, then it would be difficult to argue for a near-source deep slab structure in observed data.

Upper and middle mantle (650-1500 km) models are now available for many subduction zones so the accumulated travel-time anomaly, or residual,

for these parts of the mantle can be calculated. We can then compare observed residual spheres with the component, as well as total, of the computed residual spheres. In particular, I attempt to relate the location of mantle heterogeneities responsible for features in the observed residual spheres by analyzing predicted residual spheres based on three-dimensional mantle velocity models obtained from inversions of ISC (International Seismic Center) travel time delays. I used a global lower mantle model [Clayton and Comer, 1983; Hager and Clayton, 1989], and a regional model covering the upper mantle and upper half of the lower mantle around the northwest Pacific subduction zones (Chapter 2). These mantle models, although possibly unrealistic in some respects, may help to relate residual sphere anomalies to specific mantle heterogeneities. For instance, most lower mantle tomographic models exhibit a broad band of high velocities surrounding the Pacific, thus giving a fast band on residual spheres which has approximately the orientation of the seismic zone. This band is more than 5000 km broad, but projects onto the residual sphere as a narrow band that could be confused with, or dominate, a similar band caused by near source effects.

If the dominate slab-like fast band in the remaining residual sphere, after removing the teleseismic effects, are indeed caused by subducted slabs, the band can be determined by seeking the best fitting low degree harmonics. As discussed in the sixth section of this chapter, many fast bands detected in the observed residual spheres, particularly for intermediate depth events, show general agreement with seismicity trends and the regional upper mantle model.

4.2 Data and Corrections

The basic plan here is to calculate the contribution to the residual sphere from upper, middle and deep mantle models. Rather than just computing residual spheres at arbitrary locations and depths, the calculation is done at the hypocenters of the 145 best recorded NW Pacific earthquakes (Figure 4.1) in ISC catalogs between 1965 to 1982. Consequently, the model prediction can be compared with specific observed residual spheres. The 145 events used, listed in Table 4.1, include all events that have more than 240 P wave picks, plus the deepest Mariana event (event 3, ISC focal depth 624 km). These events occurred in the major subduction zones of the northwest Pacific from 17 ° N to 54 ° N, with focal depths greater than 120 km. The criteria to select these events are a) source-receiver distance is short enough (less than about 98 °) to avoid core interactions, and b) after corrections, including source relocation, the observed travel times differ by less than 6 seconds from the JB (Jeffreys-Bullen) model times. The station residual averages obtained by Clayton and Comer [1983] are removed to correct for near receiver shallow structure. The data are also corrected for Earth's ellipticity following Dziewonski and Gilbert [1976].

The predictions of the contributions to the residual spheres from different regions of the mantle velocity models depend on the reliability of the models utilized. The predicted residual spheres are very similar for nearby events. A source mislocation, however, changes the pattern and amplitude of the observed, or data, residual spheres. However, in terms of the residual sphere

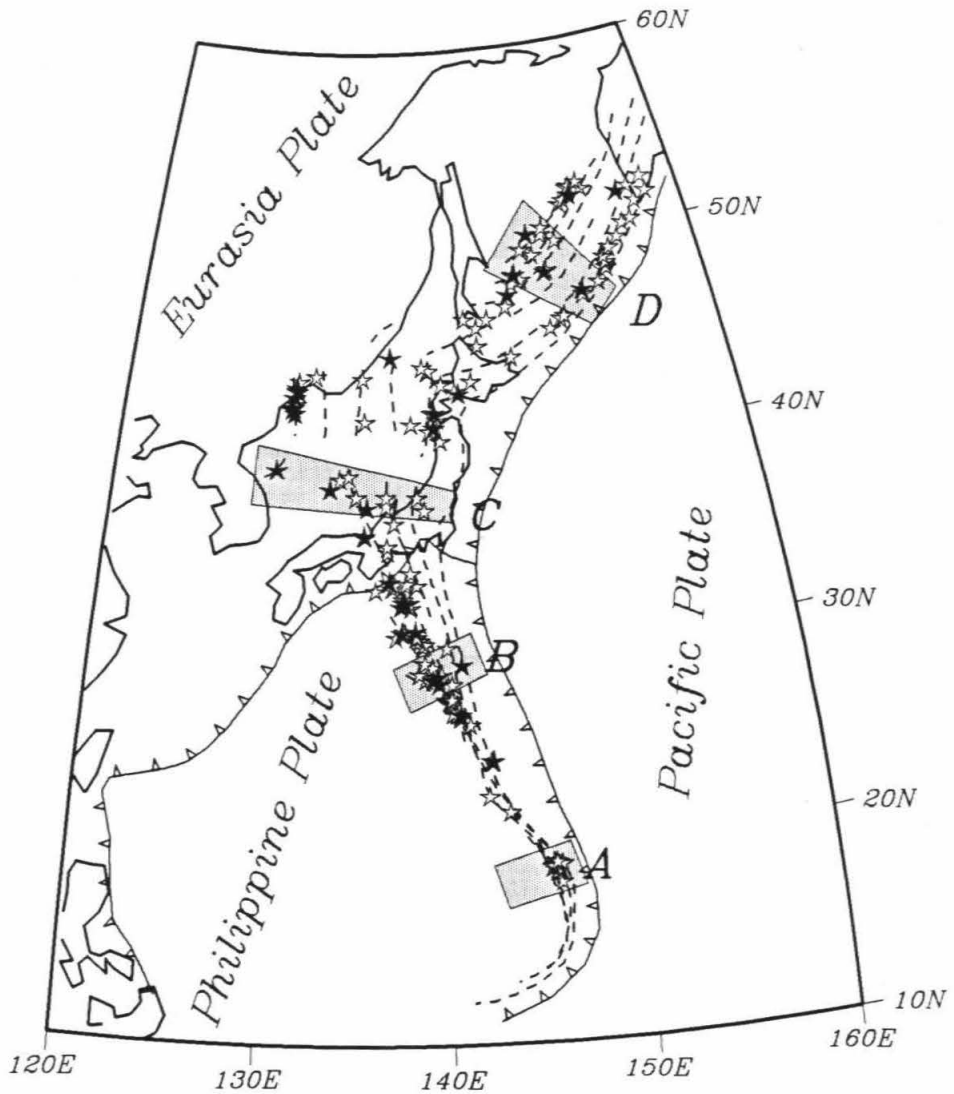

Figure 4.1. Index map. The northwest Pacific region shown here is the location of the regional velocity model which covers the upper mantle and upper half of the lower mantle. The major NW Pacific subduction zone is shown in dashed contours at 100 km depth intervals. Solid and open stars are earthquakes utilized in this study. All events with more than 400 P-wave arrivals, denoted by solid stars, are considered in a test shown in Figure 4.18. Events in four shaded areas, A, B, C, and D, are used in fitting for dominant fast bands.

Table 4.1 Source Parameters and Correlations Between Observed and Predicted Residual Spheres.

Event	Date	Time	Latitude °N	Longitude °E	Depth km	m_b	n†	Correlation Coefficients‡ R_w	R_u	R_m	R_d
1	1- 4-82	6 5: 2.2(-.4)	17.99(-.00)	145.64(-.02)	600(-8)	6.0	279	.24	.36	.26	.16
2	10-17-79	543: 2.8(-.3)	18.50(.02)	145.43(.04)	597(-3)	6.2	293	.24	.39	.18	.16
3	7- 3-72	119:27.2(-.1)	18.71(.01)	145.15(.06)	621(-3)	5.5	185	.10	.15	.18	.03
4	10-30-79	137: 6.7(.2)	18.78(.02)	145.21(.06)	583(-2)	5.2	234	.20	.45	.19	.05
5	5-24-77	1023:26.0(-.2)	18.80(.02)	145.53(.04)	230(-1)	5.5	270	.43	.39	.38	.34
6	1-25-74	2028:13.3(-.4)	18.90(.03)	145.69(.06)	143(-6)	5.6	241	.30	.33	.15	.12
7	5-13-79	626: 8.7(.3)	19.00(-.00)	145.44(.03)	257(2)	6.2	268	.37	.32	.21	.32
8	8-15-69	841:55.3(.5)	21.58(.01)	143.15(.05)	324(5)	5.9	222	.27	.04	.37	.28
9	2- 8-80	13 7:14.4(.0)	22.39(.02)	142.11(.04)	283(-1)	4.6	249	.35	.23	.27	.33
10	5-25-79	1815:41.0(-.2)	24.11(.02)	142.27(.01)	591(-2)	5.1	350	.39	.61	.39	.24
11	5-18-79	2018: 3.5(.0)	24.13(-.00)	142.41(.00)	599(1)	5.8	444	.43	.57	.31	.41
12	7- 7-75	1928:44.3(-.2)	25.97(.03)	141.24(.01)	139(-2)	5.5	293	.70	.72	.30	.38
13	10- 7-68	1920:20.8(.0)	26.31(.02)	140.71(.01)	520(2)	6.0	378	.31	.27	.02	.30
14	3-15-78	22 4:41.7(-.1)	26.46(.02)	140.77(.01)	278(0)	5.9	452	.51	.48	.17	.38
15	12-11-80	157:47.0(-.1)	26.51(.03)	140.53(-.04)	486(-5)	4.2	249	.32	.33	.21	.22
16	2-14-76	1050:23.9(-.1)	26.55(.02)	140.32(.01)	573(1)	5.4	368	.40	.59	.13	.25
17	9- 8-82	237:32.8(-.1)	26.99(.05)	140.26(-.02)	445(-5)	5.3	303	.44	.48	.26	.27
18	1-15-73	9 2:59.1(.0)	27.08(.03)	140.21(.00)	488(2)	5.5	348	.40	.42	.20	.24
19	5-16-74	20 0: 3.3(.2)	27.19(.05)	140.16(-.02)	490(1)	5.3	323	.37	.42	.25	.22
20	5-27-70	12 5: 8.1(-.2)	27.24(.02)	140.27(-.02)	405(-1)	6.0	371	.56	.56	.29	.39
21	11-13-72	811:49.4(.1)	27.95(.03)	140.12(-.01)	375(1)	5.5	244	.35	.39	.11	.22
22	4-16-80	650:14.7(.1)	28.00(.03)	140.34(-.02)	255(0)	4.2	352	.41	.52	-.09	.20
23	12-12-76	1 8:50.8(-.3)	28.06(.03)	139.64(-.03)	500(-2)	5.8	460	.31	.51	.23	.23
24	1-31-73	2055:54.0(-.2)	28.24(.03)	139.29(-.00)	507(-1)	5.9	414	.42	.50	.26	.38
25	1-17-80	921:55.0(-.2)	28.30(.01)	138.88(-.03)	520(-3)	4.2	309	.25	.57	.09	.18
26	5-13-77	1113:32.6(-.3)	28.44(.03)	139.57(-.02)	446(-2)	5.6	495	.35	.39	.14	.32
27	12-16-80	13 8:25.4(.1)	28.51(.03)	139.76(-.06)	399(-1)	4.5	301	.50	.54	.20	.37
28	12-29-77	1945:28.5(.0)	28.55(.04)	138.51(-.00)	541(0)	5.0	301	.28	.33	.10	.32
29	10-23-67	827: 7.2(-.1)	28.87(.00)	139.26(-.01)	477(2)	5.3	270	.35	.58	-.10	.23
30	12-11-79	1726:18.3(-.2)	28.97(.02)	140.93(-.01)	126(-1)	6.0	459	.52	.59	.02	.33
31	6-23-82	151:55.5(.0)	29.08(.04)	138.83(-.03)	483(-3)	5.1	335	.19	.44	.07	.11
32	12- 7-70	2135:21.6(-.3)	29.81(.02)	140.10(-.01)	182(-1)	6.0	398	.39	.52	-.06	.25
33	6-25-76	747:48.4(.0)	29.92(.03)	138.73(-.01)	456(1)	5.4	330	.29	.29	.07	.29
34	1-11-78	810:14.2(.0)	30.02(.06)	138.85(-.02)	428(-1)	5.1	249	.29	.35	.36	.15
35	8- 4-76	2321:45.4(.0)	30.23(.06)	138.61(-.03)	444(-1)	5.4	359	.18	.39	-.02	.13
36	6-12-82	6 2: 2.8(-.1)	30.36(.01)	138.36(.00)	459(1)	5.1	313	.32	.29	.31	.23
37	7-18-78	2158:19.2(.0)	30.39(.02)	137.26(-.01)	503(2)	4.5	256	.25	.42	-.08	.22
38	3- 4-71	028:38.1(-.2)	30.41(.01)	138.44(.00)	449(0)	5.5	314	.35	.35	.08	.37
39	4-20-77	20 4:29.2(-.1)	30.63(.03)	137.61(-.02)	493(-0)	5.5	438	.17	.28	.02	.15
40	3- 6-67	440:17.6(-.3)	30.62(-.02)	137.79(-.03)	488(2)	5.0	245	.21	.27	-.01	.15
41	5-31-81	842:18.6(.1)	30.70(.03)	137.70(-.03)	482(1)	4.3	344	.22	.34	.07	.15
42	11-29-74	22 5:23.2(-.3)	30.71(.01)	138.40(-.03)	428(-1)	6.0	421	.36	.23	.09	.41

43	6-26-75	952:20.2(.0)	31.85(.01)	138.11(-.03)	394(1)	5.3	307	.18	.45	.07	.02
44	3- 7-78	248:38.9(-.2)	31.94(.02)	137.60(-.02)	436(0)	6.4	487	.30	.15	.15	.32
45	8-12-75	1421: 5.7(-.2)	32.09(.03)	137.86(-.01)	399(-0)	5.5	444	.44	.33	.26	.45
46	10-30-71	1416:23.2(-.2)	32.09(.00)	137.77(-.03)	392(1)	5.5	338	.34	.35	.20	.33
47	3- 5-81	1859: 0.8(.1)	32.13(.02)	138.06(-.03)	361(1)	4.8	291	.35	.42	.20	.25
48	4-22-80	534:14.4(-.1)	32.14(.02)	137.69(-.02)	402(1)	5.8	504	.32	.29	.17	.30
49	3-10-66	426:21.1(-.2)	32.29(-.01)	137.70(-.01)	399(2)	5.3	251	.32	.35	.15	.27
50	10-12-79	655:35.7(-.1)	32.73(-.01)	136.11(-.04)	450(3)	4.2	255	.24	.20	.17	.28
51	6-24-74	19 1:40.7(-.1)	32.84(.02)	137.07(-.03)	402(1)	5.1	307	.31	.23	.25	.23
52	1- 6-81	1535:29.1(.1)	32.97(.03)	138.48(-.03)	310(1)	4.4	319	.35	.38	.28	.22
53	2-28-68	12 8: 1.6(-.2)	32.96(.01)	137.83(-.02)	349(1)	5.5	351	.22	.42	.06	.05
54	5-29-75	1544:45.2(-.1)	33.05(.02)	137.21(-.03)	386(1)	5.0	261	.22	.12	.13	.23
55	10-29-72	720:39.8(-.1)	33.07(.01)	137.91(-.04)	346(1)	5.3	288	.19	.23	.21	.03
56	2-22-74	036:54.3(-.3)	33.18(.01)	136.95(-.02)	391(0)	5.9	430	.28	.30	.11	.23
57	9-27-78	17 0:18.0(.1)	33.57(.03)	138.16(-.05)	296(-0)	5.0	287	.17	.19	.03	.16
58	11-10-70	026:22.0(-.2)	34.66(-.01)	136.85(-.01)	352(2)	5.1	278	.23	.27	.13	.17
59	8-25-81	656:24.3(.0)	34.94(.02)	136.82(-.03)	335(2)	5.0	250	.30	.29	.18	.23
60	8-13-67	20 6:52.1(-.2)	35.44(.01)	135.47(-.02)	369(2)	6.0	340	.13	.21	-.09	.12
61	3-31-80	732:32.3(-.1)	35.52(.03)	135.49(-.03)	364(1)	5.4	473	.29	.20	.22	.25
62	10- 8-78	19 9:22.2(.1)	36.09(.02)	137.25(-.03)	255(2)	4.5	338	.27	.46	.31	.02
63	12-29-76	1436:48.8(-.2)	36.73(.02)	139.10(-.04)	142(1)	5.3	369	.35	.40	.12	.30
64	2- 3-82	2042:45.2(-.1)	36.91(-.00)	135.67(-.02)	346(1)	5.3	454	.23	.32	.13	.20
65	8-29-70	143:12.2(-.1)	37.00(-.00)	136.81(-.00)	287(2)	5.1	272	.18	.33	.19	.07
66	9-21-71	843:31.9(-.0)	37.36(.02)	138.69(-.03)	188(2)	5.4	252	.28	.40	.14	.16
67	5-28-79	1439:35.0(.0)	37.42(.01)	136.81(-.04)	282(2)	5.0	320	.18	.36	.20	.04
68	6-21-80	2130:17.7(-.1)	37.43(.01)	134.98(-.02)	372(2)	5.0	333	.26	.27	.16	.17
69	1-18-80	2210:15.1(-.1)	37.87(.02)	133.41(-.02)	427(2)	5.4	463	.40	.21	.04	.51
70	3- 6-78	1511:38.2(-.1)	38.34(.02)	133.99(-.01)	416(2)	5.0	316	.25	.20	.13	.24
71	3-31-69	1925:26.7(-.3)	38.49(.00)	134.51(-.01)	397(0)	5.6	325	.21	.08	-.02	.28
72	6-29-75	1037:40.4(-.2)	38.79(.01)	130.10(.01)	550(1)	6.0	485	.45	.50	.30	.39
73	3-23-70	020:54.7(-.4)	40.18(.00)	140.30(-.01)	146(-1)	5.5	284	.28	.22	.13	.28
74	9- 5-73	030:53.8(-.1)	40.70(.02)	139.62(-.01)	194(1)	5.5	299	.13	.08	.12	.13
75	6- 9-80	20 6:35.1(.0)	40.87(.03)	139.95(-.02)	169(2)	5.6	413	.29	.26	.20	.28
76	6-10-71	1959:53.0(-.3)	41.08(-.01)	138.48(-.03)	234(1)	5.5	345	.31	.32	.16	.30
77	11-23-75	23 2: 8.2(.1)	41.28(.03)	140.16(-.04)	170(3)	5.3	253	.18	.18	.11	.22
78	10-21-78	236:10.1(-.1)	41.27(.01)	135.55(.01)	362(0)	5.0	281	.14	.22	.07	.06
79	2- 2-67	1624:39.7(.0)	41.60(.04)	139.83(-.01)	185(3)	5.3	259	.25	.25	.16	.22
80	7-28-81	17 0:57.6(-.1)	41.66(.01)	140.03(-.01)	181(1)	5.4	431	.38	.41	.24	.31
81	3- 9-77	1427:56.0(-.2)	41.69(.03)	131.05(.00)	559(3)	5.9	564	.31	.61	.33	.13
82	8-16-79	2131:24.6(-.3)	41.86(.01)	130.87(.01)	565(-1)	6.0	555	.39	.53	.35	.32
83	9-29-73	044: 0.2(-.1)	41.96(.03)	130.96(-.02)	571(4)	6.3	460	.38	.56	.35	.25
84	4-10-69	1454: 3.6(-.1)	42.12(.02)	131.06(-.00)	551(4)	5.1	248	.40	.42	.45	.26
85	9-10-73	743:32.0(-.3)	42.48(-.00)	131.01(-.04)	554(2)	5.8	446	.26	.49	.31	.12
86	11- 8-74	2123:22.1(-.1)	42.54(.01)	141.70(-.04)	127(1)	5.9	436	.34	.17	.15	.37
87	8-17-69	1154:55.0(-.1)	42.67(.03)	141.43(-.04)	135(2)	5.5	291	.40	.36	.25	.38
88	1-31-79	1236:24.0(-.2)	42.78(-.00)	131.20(-.00)	537(2)	4.8	432	.35	.36	.34	.20
89	4-11-76	13 3:36.6(-.2)	42.82(.02)	131.07(.02)	542(1)	5.0	250	.36	.40	.36	.23

90	11-27-81	1721:44.1(-.2)	42.95(.02)	131.19(.01)	526(2)	5.6	558	.42	.40	.43	.28
91	8-20-66	932:31.5(.0)	43.03(.05)	140.56(-.04)	165(3)	5.5	248	.34	.16	.23	.34
92	7- 4-67	2342:12.7(-.2)	43.12(.02)	142.55(-.03)	159(2)	5.5	303	.29	.24	.12	.24
93	12-25-79	336:52.0(-.3)	43.26(.03)	131.27(.02)	522(-2)	4.9	281	.37	.24	.35	.32
94	6-15-78	319: 8.9(-.1)	43.42(.02)	135.41(-.03)	369(4)	4.8	358	.32	.39	.08	.24
95	5- 6-73	1439:27.2(-.1)	43.55(.01)	132.35(-.01)	488(3)	5.1	316	.30	.40	.15	.19
96	2-28-66	2 2:12.7(-.2)	43.71(.02)	139.65(-.02)	220(2)	5.5	256	.28	.34	.12	.26
97	6-21-79	14 5:45.5(-.3)	43.77(.01)	139.75(-.00)	216(-1)	4.3	347	.41	.36	.34	.39
98	8- 6-75	2137:39.8(.0)	43.94(.04)	139.34(.01)	231(1)	5.5	305	.29	.28	.29	.29
99	10-25-65	2234:22.2(-.2)	44.21(-.00)	145.44(-.01)	160(1)	6.0	342	.39	.23	.25	.46
100	5-31-81	2359:34.0(-.3)	44.49(.00)	137.31(-.01)	288(1)	5.5	406	.39	.35	.12	.49
101	1-19-69	7 2: 7.4(-.5)	44.89(-.00)	143.21(.00)	237(-1)	6.3	397	.32	.18	.09	.37
102	4- 9-74	1311:23.5(-.1)	45.42(.04)	148.39(-.02)	160(1)	5.4	253	.23	.26	-.16	.25
103	7-14-82	1042:12.6(.0)	45.78(.05)	143.25(-.02)	314(3)	5.1	315	.17	.21	.21	.09
104	1-29-78	2 5: 1.3(-.1)	45.85(.01)	149.22(.02)	151(1)	5.0	271	.35	.35	.10	.35
105	3-29-76	1948:39.1(-.6)	45.97(.01)	149.50(-.00)	159(-4)	5.4	243	.34	.35	.18	.20
106	12-27-72	14 6: 7.2(-.2)	46.18(.01)	144.04(.01)	328(2)	5.1	324	.33	.32	.18	.31
107	12-18-69	1332: 4.0(.1)	46.25(.04)	142.44(-.01)	334(5)	5.9	352	.32	.16	.07	.39
108	11-11-75	425:32.1(-.2)	46.72(.00)	145.47(.01)	351(1)	5.4	313	.28	.48	.13	.18
109	6-13-73	020:52.2(-.6)	46.91(.01)	151.05(.00)	173(-2)	5.4	275	.28	.25	.03	.24
110	6-19-77	1147:23.5(-.4)	47.14(.02)	151.09(.01)	154(-1)	5.5	401	.32	.36	.06	.23
111	7-10-76	1137:13.9(-.1)	47.33(.03)	145.75(-.00)	404(3)	5.8	451	.21	.21	.26	.13
112	7-20-79	2120: 1.6(-.9)	47.40(.00)	152.35(.00)	129(-6)	4.2	241	.24	.21	.24	.17
113	12-11-80	2253:24.2(-.3)	47.82(.04)	146.08(.01)	436(-1)	5.0	252	.23	.04	-.04	.37
114	11-22-66	629:51.9(-.5)	48.00(-.00)	146.78(-.01)	441(-2)	5.5	277	.30	.27	.11	.23
115	3-25-72	056: 3.0(-.9)	48.03(-.00)	153.11(-.01)	119(-4)	5.8	304	.24	.42	.10	.08
116	12-22-80	2031:43.7(-.3)	48.21(.03)	146.23(-.00)	465(-0)	5.3	359	.22	.22	.11	.25
117	3- 3-71	2154: 8.9(-.8)	48.25(.02)	153.09(.02)	123(-4)	5.6	270	.21	.35	.04	.12
118	6-21-78	1110:38.3(-.4)	48.28(.01)	148.64(-.02)	379(-1)	5.8	506	.25	.14	.19	.26
119	2- 6-81	1647: 8.2(-.3)	48.29(.01)	146.39(.01)	490(0)	4.7	460	.23	.14	.11	.25
120	3-11-74	1137:30.8(-.8)	48.31(.01)	153.16(.00)	149(-5)	5.8	348	.31	.33	.16	.22
121	10-14-72	0 0:22.8(-.2)	48.35(.02)	148.77(.00)	375(-0)	5.5	262	.29	.29	.17	.23
122	12-20-77	850:37.9(-1.5)	48.59(.03)	153.07(.01)	141(-12)	5.6	328	.19	.28	.06	.05
123	3-22-72	1027:41.0(-1.1)	49.00(-.05)	153.61(.02)	128(-7)	6.1	349	.39	.34	.26	.22
124	1-29-82	0 2: 4.2(-.3)	49.17(.02)	147.88(.00)	532(-0)	5.0	337	.37	.44	.16	.18
125	12- 1-67	1357: 2.6(-.8)	49.48(.03)	154.41(.01)	139(-5)	5.9	308	.14	.13	.09	.07
126	8-21-72	623:48.0(-.6)	49.48(.01)	147.07(.00)	570(-4)	5.9	338	.20	.34	.14	.09
127	12-20-74	1638:55.0(-.3)	49.75(-.00)	149.75(.01)	411(-1)	5.0	263	.37	.44	.21	.27
128	5-12-77	2137:33.1(-.5)	50.10(-.01)	155.04(.01)	128(-2)	5.1	301	.24	.09	.31	.16
129	3- 6-72	1850:16.0(-.8)	50.15(.02)	148.79(-.01)	563(-7)	5.4	250	.30	.39	.18	.19
130	11-27-82	955:38.6(-.3)	50.23(.04)	147.75(-.01)	618(-1)	5.5	466	.29	.54	.11	.12
131	10-28-78	1630:17.8(-.7)	50.23(-.00)	155.73(.02)	133(-5)	4.6	244	.46	.37	.31	.29
132	7-28-73	20 6:35.0(-.4)	50.47(.03)	148.91(-.01)	583(-2)	5.5	312	.27	.38	.21	.12
133	1-25-79	21 3:20.4(-.5)	50.48(.02)	148.92(.01)	569(-4)	4.3	339	.23	.28	.14	.11
134	8- 8-82	614: 7.4(-2.0)	51.07(.03)	156.41(.00)	122(-17)	5.0	255	.36	.30	.30	.12
135	10-13-81	1553:55.4(-1.2)	51.44(-.00)	157.43(.02)	113(-9)	5.3	245	.27	.25	.12	.16

136	6-10-80	2313:23.7(-.4)	51.53(.02)	150.63(-.01)	545(-3)	4.5	306	.18	.34	.22	.07
137	1-29-71	2158: 2.3(-.9)	51.69(-.00)	150.99(.02)	508(-7)	6.0	356	.21	.27	.17	.09
138	9-21-77	21 1:43.5(-.9)	51.72(.02)	155.26(.03)	230(-6)	5.5	411	.23	.19	.23	.13
139	6-26-72	10 5:59.4(-.9)	51.88(.01)	156.14(.01)	187(-10)	5.4	288	.36	.42	.26	.17
140	12-21-75	1054:16.6(-.6)	51.93(.01)	151.56(-.01)	543(-3)	6.0	428	.33	.79	.21	.11
141	10-12-67	1253:45.4(-.5)	52.16(.01)	152.57(.00)	464(-2)	5.5	243	.33	.48	.24	.26
142	8-22-79	1828:53.1(-1.8)	52.23(.01)	157.35(.02)	116(-13)	5.0	348	.33	.44	.13	.18
143	9- 5-70	752:26.6(-.6)	52.27(-.01)	151.49(.00)	558(-2)	5.6	330	.31	.44	.14	.30
144	8-30-70	1746: 8.2(-.7)	52.36(.00)	151.64(-.00)	639(-4)	6.5	384	.11	.53	.23	.04
145	12-30-79	418:31.6(-.5)	52.53(.02)	152.30(.01)	527(-4)	4.8	338	.36	.38	.17	.29
avg.	—	—	—	—	—	—	336	.30	.34	.17	.23

Values in parentheses correspond to new source location values minus ISC values.

† n: number of receivers used.

‡ Correlation coefficient of non-zero residuals between unexpanded observed and predicted residual spheres:

R_w — predictions are from the whole mantle model;

R_u — predictions are from the upper mantle model;

R_m — predictions are from the middle mantle model;

R_d — predictions are from the deep mantle model.

data smoothed by spherical harmonics, a mislocation or an error in origin time show up in the l=1 and 2, and l=0 terms respectively (in a homogeneous Earth).

The source mislocation effect is of critical importance to recognizing a slab signature in observed residual spheres, but is less essential to determining the location of mantle heterogeneities responsible for a given residual sphere pattern. To facilitate a more reliable comparison between the predicted and observed residual spheres, however, all the events in this study are relocated. Based on the observed travel times and the JB reference model, a standard source relocation scheme is applied using the linearization formula

$$dt_j = \delta t^\circ + (\frac{\partial t}{\partial \theta})_j \delta\theta + (\frac{\partial t}{\partial \phi})_j \delta\phi + (\frac{\partial t}{\partial h})_j \delta h + \epsilon \qquad (4.1)$$

for the j-th station, where dt_j is the observed travel time minus theoretical travel time, δt° is a correction for the origin time, the next three terms are the corrections for the source location in terms of latitude θ, longitude ϕ and depth h, and ϵ is error term. The gradients of t in each direction $(\frac{\partial t}{\partial \theta})_j$, $(\frac{\partial t}{\partial \phi})_j$ and $(\frac{\partial t}{\partial h})_j$ is assumed to be linear, near the source, for each ray (depending on epicentral distance, focal depth and the velocity structure). Hence, the four unknowns δt°, $\delta\theta$, $\delta\phi$ and δh in the equation can be solved iteratively in a least square sense. Figure 4.2 provides one example showing the effect of source mislocation on a residual sphere by perturbing a relocated hypocenter 0.1° laterally and 10 km in depth. Notice that all perturbed hypocenters result in higher residual variances than that of the unperturbed, indicating that the

Figure 4.2. Effect of source mislocation on residual sphere anomalies. All residual spheres shown here are for observed residuals of event 7. The center one is at the relocated location, while the hypocenters of eight surrounding spheres are perturbed (+ and -) 0.1° laterally and 10 km in depth from the relocated location. On each residual sphere, crosses and circles denote late and early arrivals, respectively, and their sizes correspond to the magnitudes. The light dashed circle represents 90° (horizontal) take-off angle, and residuals inside and outside correspond to downgoing and upgoing rays, respectively. The circumference corresponds to rays that go vertically up. The heavy dashed curve indicates the slab orientation from seismicity. Notice that the standard deviation of residuals is a minimum at the relocated hypocenter, and most residual sphere features are robust with the given amount of hypocenter perturbations. For example, open circles tend to lie along the trend of the slab in all the residual spheres.

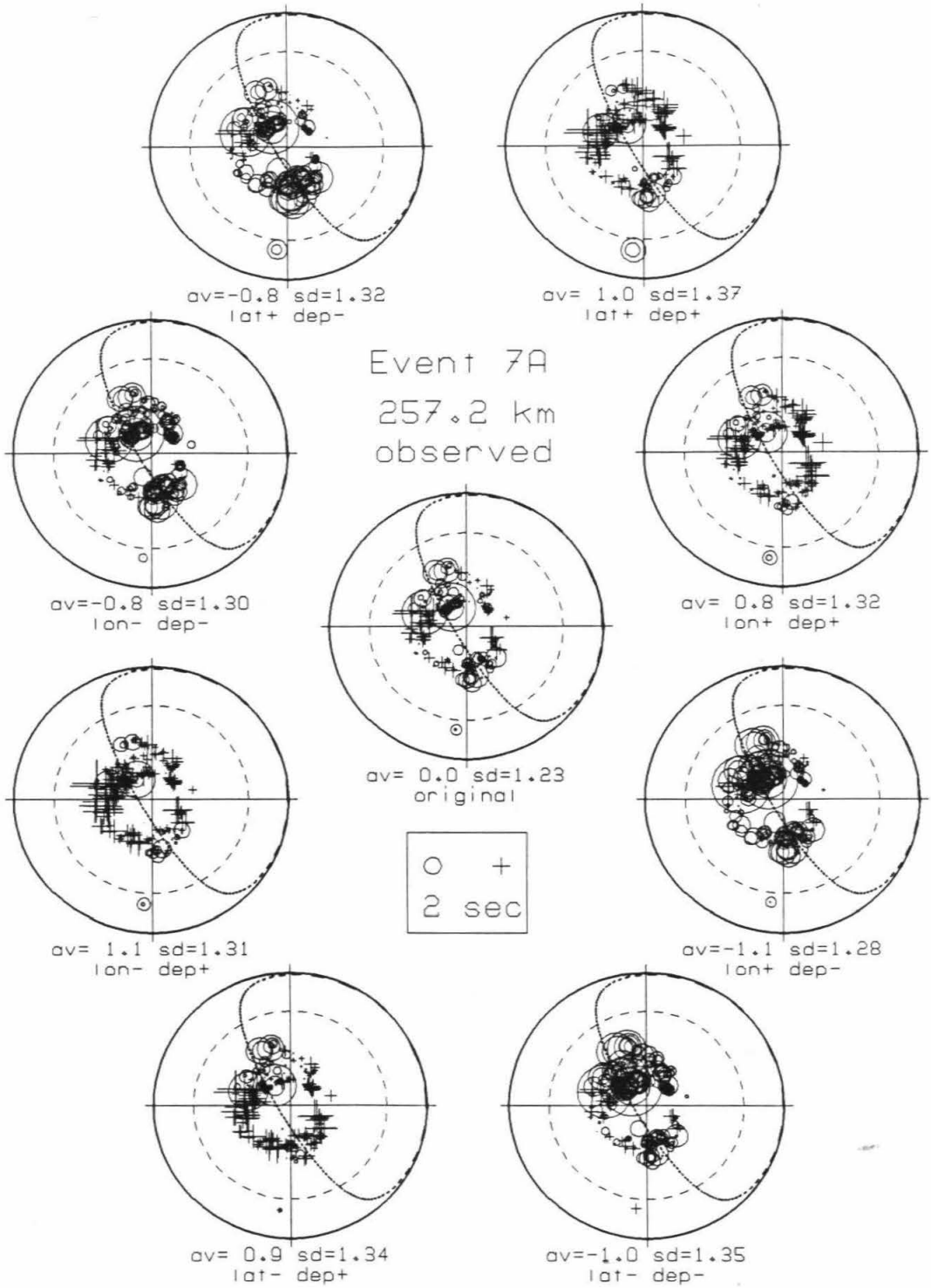
av=-0.8 sd=1.32
lat+ dep-
av= 1.0 sd=1.37
lat+ dep+
Event 7A
257.2 km
observed
av=-0.8 sd=1.30
lon- dep-
av= 0.8 sd=1.32
lon+ dep+
av= 0.0 sd=1.23
original
O +
2 sec
av= 1.1 sd=1.31
lon- dep+
av=-1.1 sd=1.28
lon+ dep-
av= 0.9 sd=1.34
lat- dep+
av=-1.0 sd=1.35
lat- dep-

hypocenter is relocated properly. The observed residual spheres of events 7, 83, 126, 137 and 142 (in Figures 4.5, 4.10, 4.14 4.16 and 4.17 shown later) are very similar to those of the same events in Creager and Jordan (1984, 1986), even though the data are corrected in different ways. Hence, I conclude that our differing conclusions are not due to different patterns in the data.

To compare the data and predictions at long wavelengths, the observed and predicted residual focal spheres are expanded in spherical harmonics, following the standard formula (e.g., equation C.12 in Stacey [1977])

$$\delta t(\theta,\phi) = \sum_{l=0}^{L} \sum_{m=0}^{l} \left(C_l^m \cos m\phi + S_l^m \sin m\phi \right) P_l^m(\cos\theta) \qquad (4.2)$$

where δt is a travel time residual which depends on θ and ϕ, the source take-off angle and source to receiver azimuth in spherical coordinates, with the source as origin. C_l^m and S_l^m are spherical harmonic coefficients of degree l and order m, and P_l^m are associated Legendre polynomials. The coefficients are obtained by a least squares fitting of the above equation. The expansion is essentially a low-pass filtering of the original residuals, similar to the smoothing technique by Creager and Jordan [1984].

The P wave velocity models utilized are obtained from iterative inversions of ISC travel time data. The first is a global mantle P wave velocity model of block size $5^\circ \times 5^\circ \times 100$ km [Clayton and Comer, 1983; Hager and Clayton, 1989], which is based on ISC travel time delays at epicentral distance greater than 25°. The second is a regional P wave velocity model of block size $2^\circ \times 2^\circ \times 50$ km [Zhou and Clayton, 1987, 1988], which is based on regional ISC travel time delays that cover the upper mantle and upper portion of the

lower mantle around the subduction zones of the northwest Pacific. Analyses of resolution and noise show that the images are generally resolved well [Zhou, 1988]. The top portion of the regional model contains coherent high-velocity heterogeneities associated with Wadati-Benioff seismicity zones. These fast velocities, interpreted as the signature of the subducted lithosphere, are slab-like in the shallow mantle but, in many places, tend to be contorted and flattened as they deepen.

A composite mantle velocity model was constructed by embedding the regional model into the global model, excluding regions in the global model that overlap with the regional model. Variants of the composite model are used to predict travel time residuals. The first variant is the entire composite model, or the whole mantle model. The second variant is the near source upper mantle model, the upper mantle portion ($<$650 km) of the regional model. The third variant includes the region between 650 to 1500 km beneath the source area, the range of interest for the deep slab penetration hypothesis. The fourth variant is the first variant (whole mantle model) minus the second (near source upper mantle) and third variants (near source middle mantle). This should be free of any effect caused by the subduction zones of the northwest Pacific, because at 1500 km depth the rays have spread out and narrow-slab-like features will not show up as coherent patterns affecting more than a few stations. I refer to the second, third and fourth variants as the upper mantle, middle mantle and deep mantle models respectively, and their combination, the first variant, as the whole mantle model. Notice that the "deep mantle" model actually also includes upper mantle and middle mantle

regions outside the area of the regional velocity model. These regions are traversed by the up-going legs of teleseismic rays. By examining predicted residual spheres from each model, the locations of the velocity heterogeneities that contribute to the calculated residual sphere anomalies are isolated in the models. The similar patterns in the observed and predicated residual spheres are then suggestive of the locations of real mantle heterogeneities. A shortcoming of the residual sphere method is that ordinarily there is no constraint on the locations and magnitudes of the anomalies. The deep slab penetration hypothesis, for example, is based on assumptions about both the location and the magnitude of the mantle anomaly that causes a given residual sphere anomaly.

The velocity models used differ considerably from the simple idealized slab models used in previous studies because they are based on tomographic images. Of course, these models contain noise due to data error, poor ray coverage and limited resolution of the inversion. I do not intend to discuss the derivation of the velocity models themselves, nor do I argue that they are well enough known to be removed from the data in order to discuss residual near source effects. At the very least, these models can be viewed as independently determined structures which introduce "noise" into residual spheres, complicating the use of this kind of data for near source studies of slab structure. On the other hand, if the velocity models predict the observed residual sphere data well, then the residual spheres lend credence to the velocity models. The residual sphere modeling process certainly provides a different view-point for evaluating three-dimensional velocity models.

4.3 Modeling of Residual Spheres

The main topic of this section is the comparison of observed residual focal spheres with those obtained by tracing rays through each of the four velocity models, and to determine the contribution to the residual sphere from the various mantle sources. The geometry of the computed ray paths is controlled by the JB model. From this point on, the figure captions are an important part of the text and much of the discussion is not repeated in the text.

Figure 4.3 illustrates the effect of heterogeneities at various mantle locations on the residual sphere patterns. It is a special projection (Figure 4.4) of the composite velocity model along a set of conical ray paths of a constant take-off angle (ray parameter). The average velocity of each layer (shell) has been removed. The large scale spatial variation of velocity is clearly evident. Note also the fast and slow anomalies in the middle lower mantle (Figure 4.3a) and in the bottom lower mantle (Figure 4.3b). Many anomalies are of large scale and far from the source region (the center of the map). The calculated residual sphere pattern can be directly related to certain mantle heterogeneities. A residual at a station located close to the dashed circle is generated by the heterogeneities, shown in the velocity map, along a straight line connecting the station with the center of the map (the source). Notice that the teleseismic arrivals from this Kuril event are affected by deep lower mantle velocity variations that are relatively fast along the strike direction of the Kuril trench. In fact, one of the reasons for showing the velocity maps of this event is that the regional velocity model has deep, probably slab-related,

Figure 4.3. Effect of mantle velocities on computed residual sphere of event 137. The large circle map, which shows coast lines and plate boundaries, is centered on event 137 in the Kuriles. The superimposed pattern is a projection (Figure 4.4) of the seismic velocity on a surface swept out by a cone of rays with a constant take-off angle (37° for 3a and 28° for 3b) from the source at the center. The rays are diving into the mantle in the inner part of the circle and are rising toward the surface in the outer part of the map. The surface of Earth is in grey, while the unsampled mantle regions are in black. The fast and slow regions are contoured and patterned (stipples are slow; whites are fast; and grey tones are within a quarter percent from layer means). The location of the regional model is outlined. The ray-surfacing points are indicated by a dashed circle in the two smaller circle plots on the top, the standard residual sphere on the left and the station location residual map on the right. The legend of the residual sphere follows that of Figure 4.2, except that the circumference here corresponds to take-off angle of 90°. The station location residual map has the same map orientation as that of the velocity map, but with computed travel time residual plotted at each station location. Opposite to the sense of distance for the station location residual map, the radial direction on the residual sphere is take-off angle. The ray bottoming depths are about 1,810 km for 3a and 2,550 km for 3b. Long wavelength velocity variations are visible in both plots. Note in 3a that velocities are generally fast in the NE quadrant and slow in southern directions. The velocity map is applicable only to stations located close to the ray-surfacing circle; i.e., the magnitude of travel time residual for such a station is an integral along a straight line connecting the origin and the station.

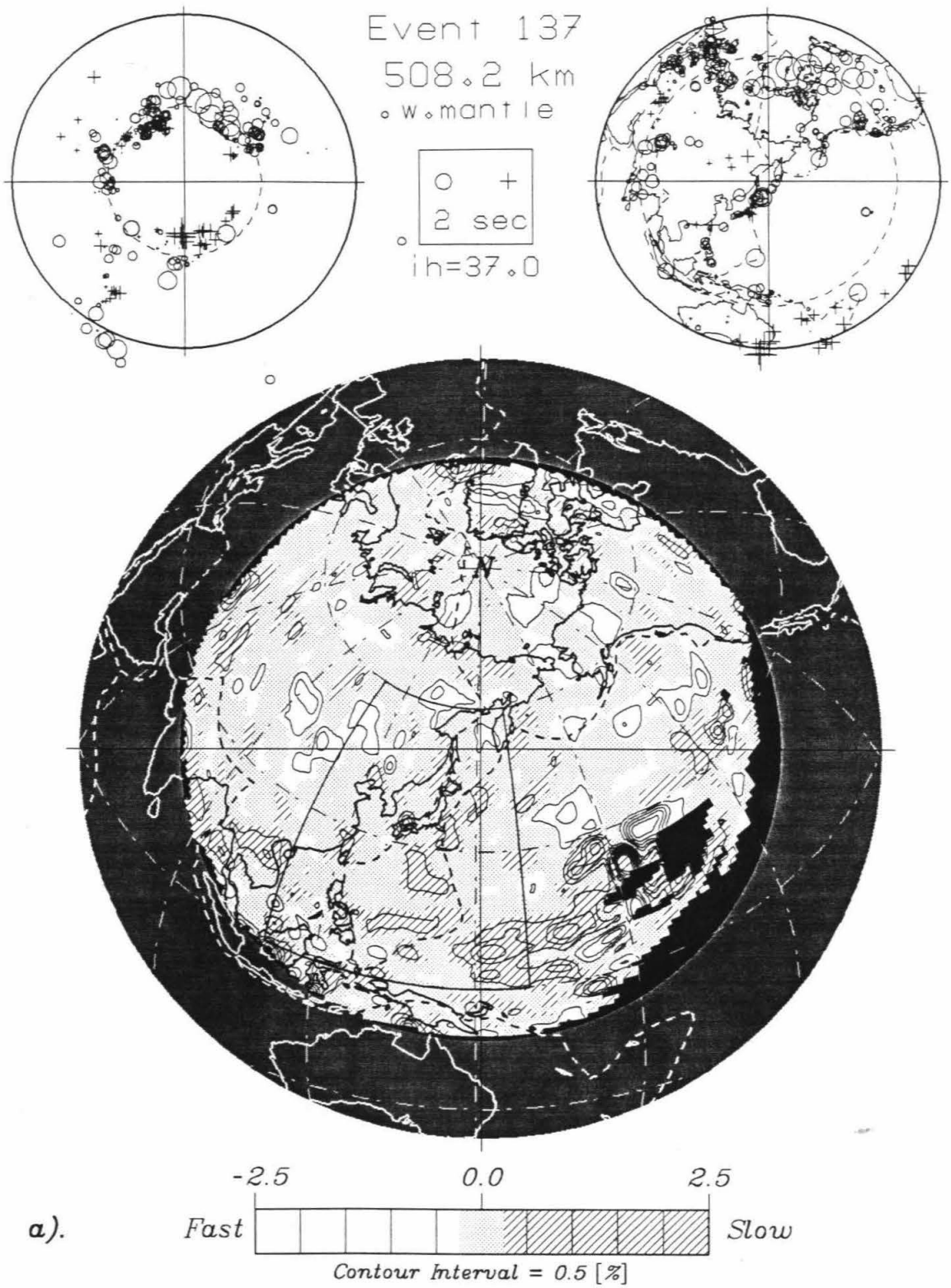
Event 137
508.2 km
w.mantle
O +
2 sec
ih=37.0
N
-2.5
0.0
2.5
Fast
Slow
Contour Interval = 0.5 [%]

a).

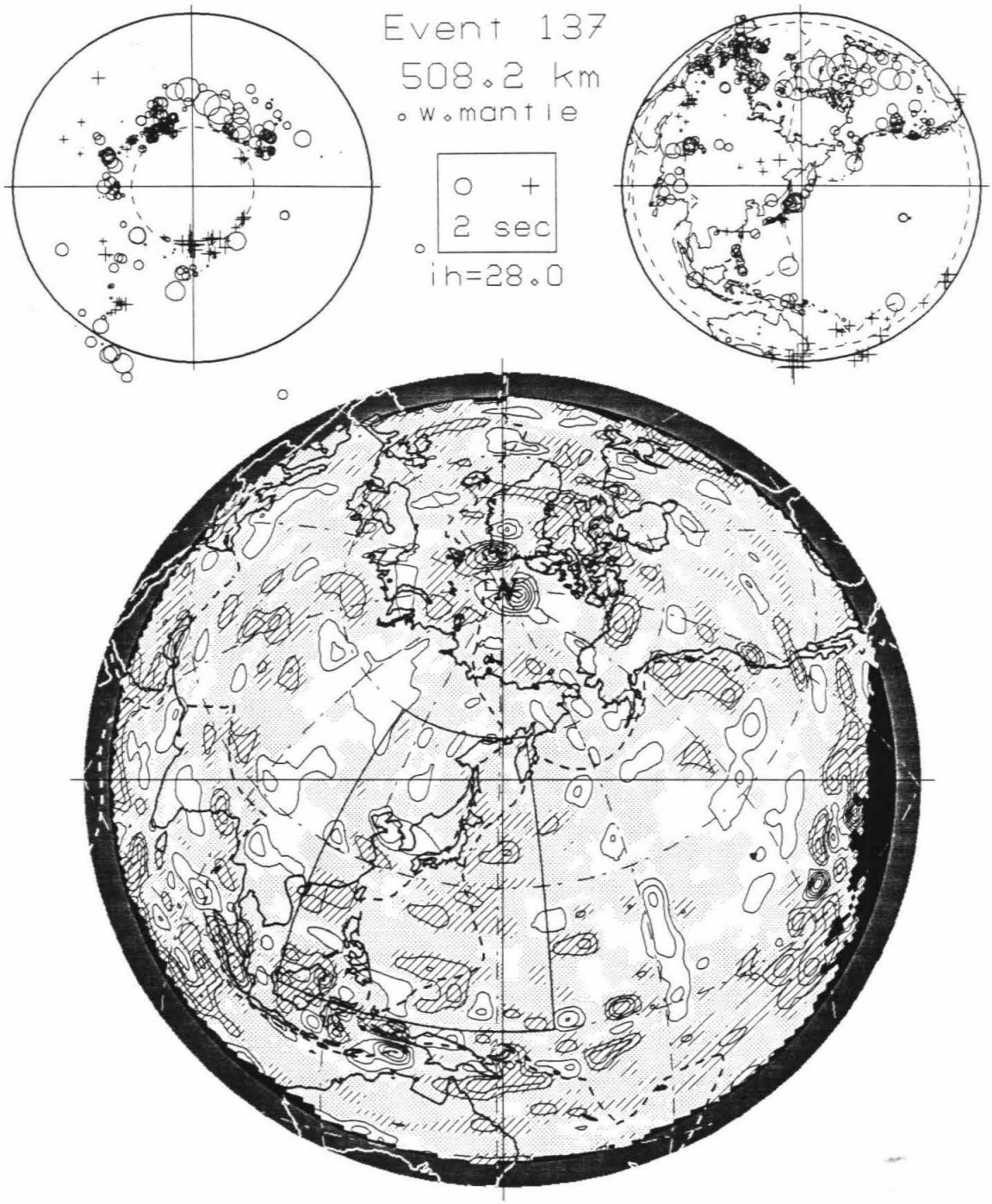
Event 137
508.2 km
w.mantle
2 sec
ih=28.0
-2.5
0.0
2.5
Fast
Slow
Contour Interval = 0.5 [%]

b).

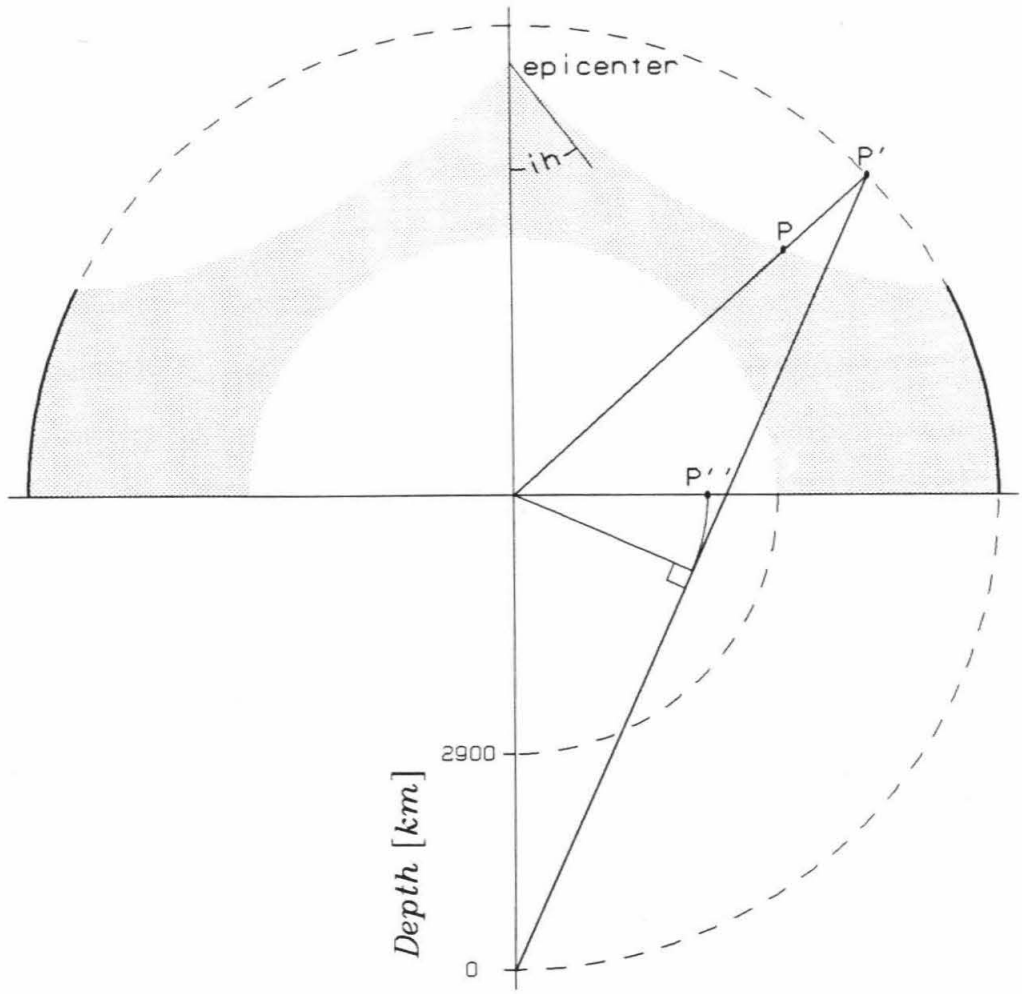

Figure 4.4. The projection of velocity map in Figure 4.3. This is a cross section view of the velocity map in Figure 4.3a. The mantle velocity anomaly at a point P, which is traversed by a ray at the constant take-off angle (ih) from the hypocenter, is taken to a surface point P' and then projected to a point P" on the velocity map. In this way, the mantle velocities that are traversed by a cone of rays of a given take-off angle are mapped. Note that the locations of the traversed points depend on the source location and the given take-off angle. The maps are equal-area projections.

fast "fingers" beneath the Kuril trench. These are the small fast features near the center of the maps. Even in this case, however, the contribution to the residual sphere from these fast slab-like features is less than from other fast regions which have no clear connection with the northwest Pacific subduction zone.

Lower mantle models from other studies, summarized in Dziewonski and Woodhouse [1987], also show a broad band of fast velocities from eastern North America to Southeast Asia, i.e., along strike of the Northwest Pacific subduction zones. The long wavelength velocity variations in the deep mantle mean that residual sphere travel time anomalies may accumulate rather than cancel. If lower mantle effects do not cancel, a basic premise of residual sphere interpretations concerning deep slab penetration is invalid.

For the purpose of probing deep slabs, previous residual sphere studies [e.g., Creager and Jordan, 1986] used narrow cones ($\pm 60^\circ$ take-off angles minus core phases) of downgoing rays. Shallow dipping structures or horizontal high-velocity slabs (e.g., see later discussion of event 83) would not be detected in these studies. Previous studies would interpret any large coherent structure in the deep mantle as a steeply dipping shallow structure. The focus of this chapter is on the comparison of the predicted and observed residual sphere patterns and identification of the responsible (model) mantle heterogeneities. Consequently, residuals from the entire focal sphere, except core phases, are included in the comparison. As expected, the upper residual sphere, which samples the slab above the earthquake, exhibits a slab-like pattern for most of the events in this study.

Some example residual spheres of the data and predictions, along with corresponding smoothed versions (spherical harmonic expansion of degrees 0 to 6) are shown in Figures 4.5 to 4.18. The correlation coefficient r between observed data and each prediction is also given in these figures. When a portion of a model contains gaps, i.e., regions that are poorly covered by crossing rays and regions exterior to the model, those rays that traverse entirely in gaps of a model are excluded from the correlation computation. The correlation coefficients for raw data residual spheres of each event (prior to spherical harmonic smoothing) are listed in Table 4.1. The correlation between the observed data and the whole mantle model predictions for all events exceed the 99% confidence level as determined from a Student's t test [e.g., O'Connell, 1971]. In general, the correlations will be much improved through the expansion, or through any other kind of smoothing. As described in detail in the figure captions, the observed and predicted residual spheres are similar in pattern and general characteristics, and both have long wavelength as well as short wavelength variations. Surprisingly, some of the short wavelength anomalies are caused by near-source heterogeneities. These are particularly evident as rapid changes in sign. See for example the computed residual spheres for the middle mantle for most events. For most residual spheres, the amplitudes of the predicted anomalies from the whole mantle model are about the same as the amplitudes of the observed anomalies.

Creager and Jordan (1984) showed that Sea of Okhotsk earthquakes deeper than 400 km are dominated by NE-SW trending troughs of negative anomalies (i.e., fast arrival times) having strikes and dips similar to the seismic

Figure 4.5. Residual spheres of event 7. The format of each residual focal sphere is the same as described in the caption of Figure 4.2. As indicated to the left, the top pair of residual spheres is the observed, followed (downwards) by four pairs of predictions from four mantle models. The left and right columns are the original version (station corrected data) and corresponding spherical harmonic expansion of degrees 0 to 6. The correlation coefficients r between each prediction and the observed, original or expanded, are also shown at the lower-left corner of each prediction. This event is the same as Creager and Jordan's [1986] Mariana event 2. My spherical harmonic expansions are similar to their filtered results. As these authors suggested, the observed residual spheres of this event (top row) exhibit a strong, consistent slab-like signature, as expected from its shallow depth. Note, however, that part of the slab-like signal is of upper mantle (plus signs away from the slab trend) and deep mantle origin (circles along the trend of the slab; plus signs away from the slab trend). Besides the upper and middle mantle predictions, the deep mantle also exhibits a similar pattern to the observed, i.e., early arrivals along strike and late arrivals in the ESE direction. Slab-like signature in the middle mantle prediction is quite weak (the velocity model has patches of fast heterogeneities around 650 to 800 km). The slow anomalies in the W direction of the upper mantle and the E direction of the deep mantle are largely responsible for the clear slab pattern in the whole mantle prediction.

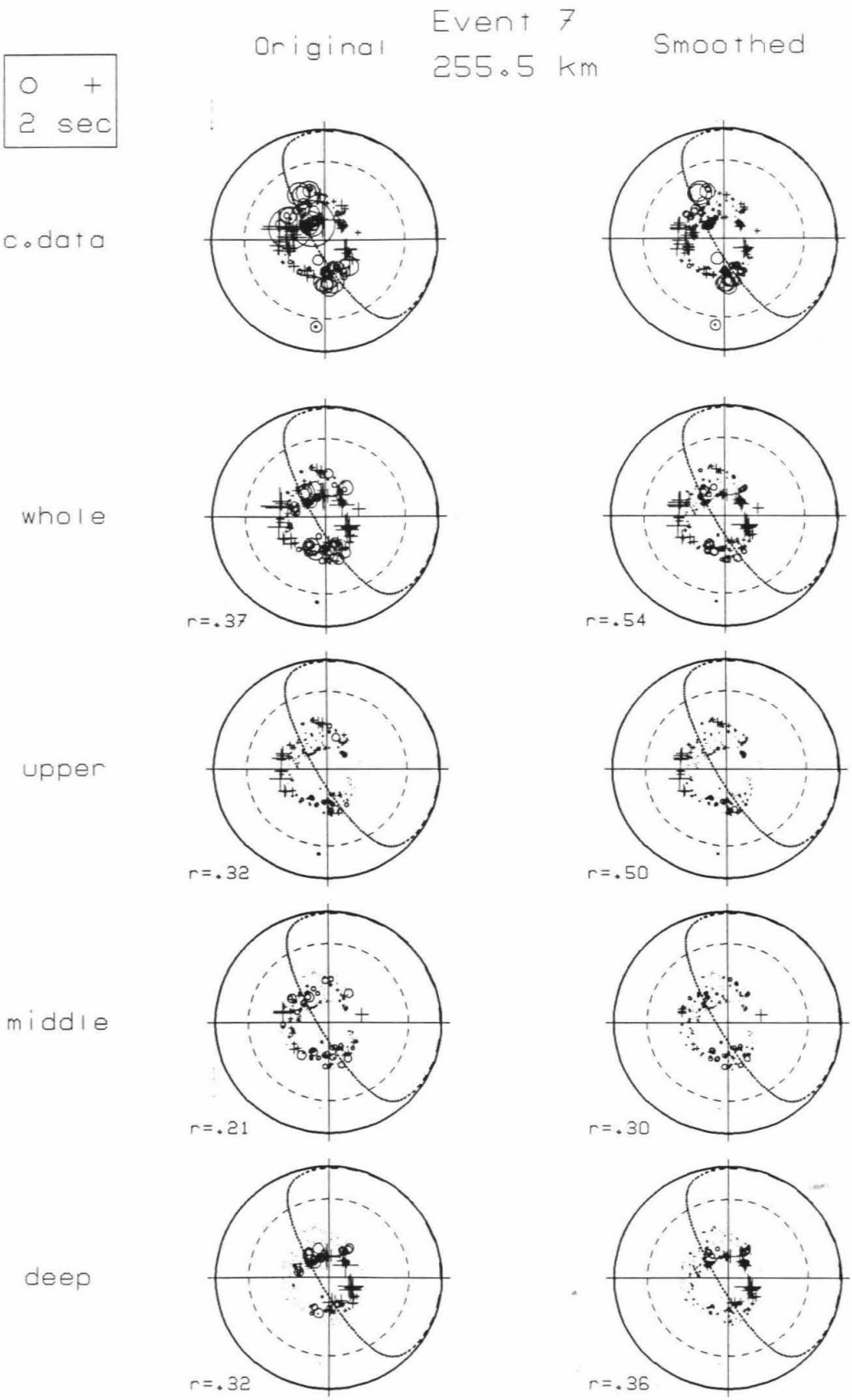
Original
Event 7
255.5 km
Smoothed
O +
2 sec
c.data
whole
r=.37
r=.54
upper
r=.32
r=.50
middle
r=.21
r=.30
deep
r=.32
r=.36

Figure 4.6. Residual spheres of event 14. Plotting conventions are identical to Figures 4.5. The event is relatively shallow and we expect to see the effect of the underlying slab. Indeed, there is a strong slab signature (fast velocity along the inferred strike direction of the slab) which is caused by a combination of the upper, middle and deep mantles. The slow patches in the west quadrant of the upper mantle and in the east quadrant of the deep mantle make the combination particularly slab-like. Although an underestimation of magnitude in the velocity models may reduce the contributions from the middle and deep mantle, the middle mantle contributes less than the deep mantle does.

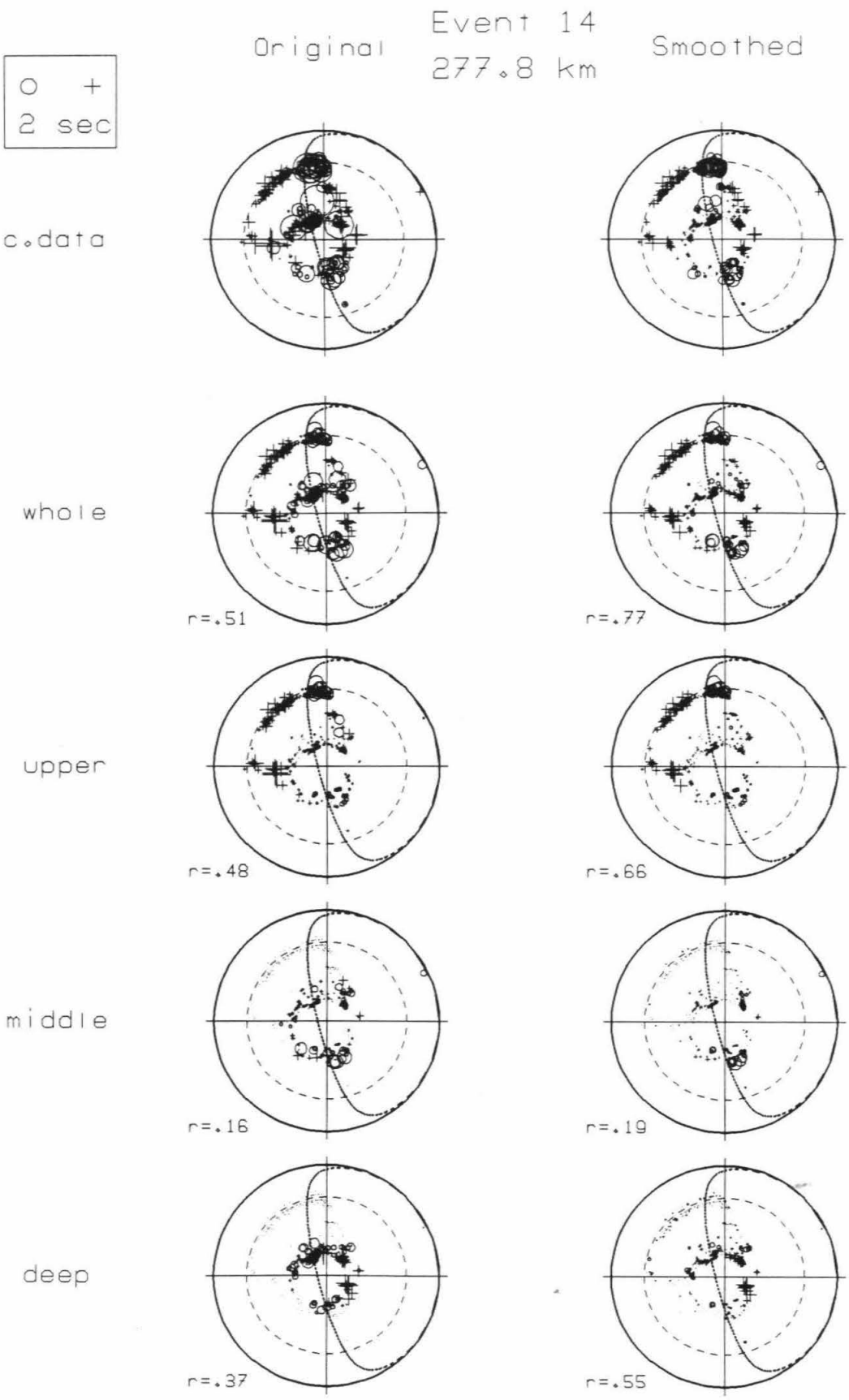
Original
Event 14
277.8 km
Smoothed
O +
2 sec
c.data
whole
r=.51
r=.77
upper
r=.48
r=.66
middle
r=.16
r=.19
deep
r=.37
r=.55

Figure 4.7. Residual spheres of event 30. Plotting conventions follows that of Figures 4.5. Comments for the last figure (Event 14) is also true here. The whole mantle model duplicates well the observed pattern and has a correlation coefficient of 0.76 in smoothed versions.

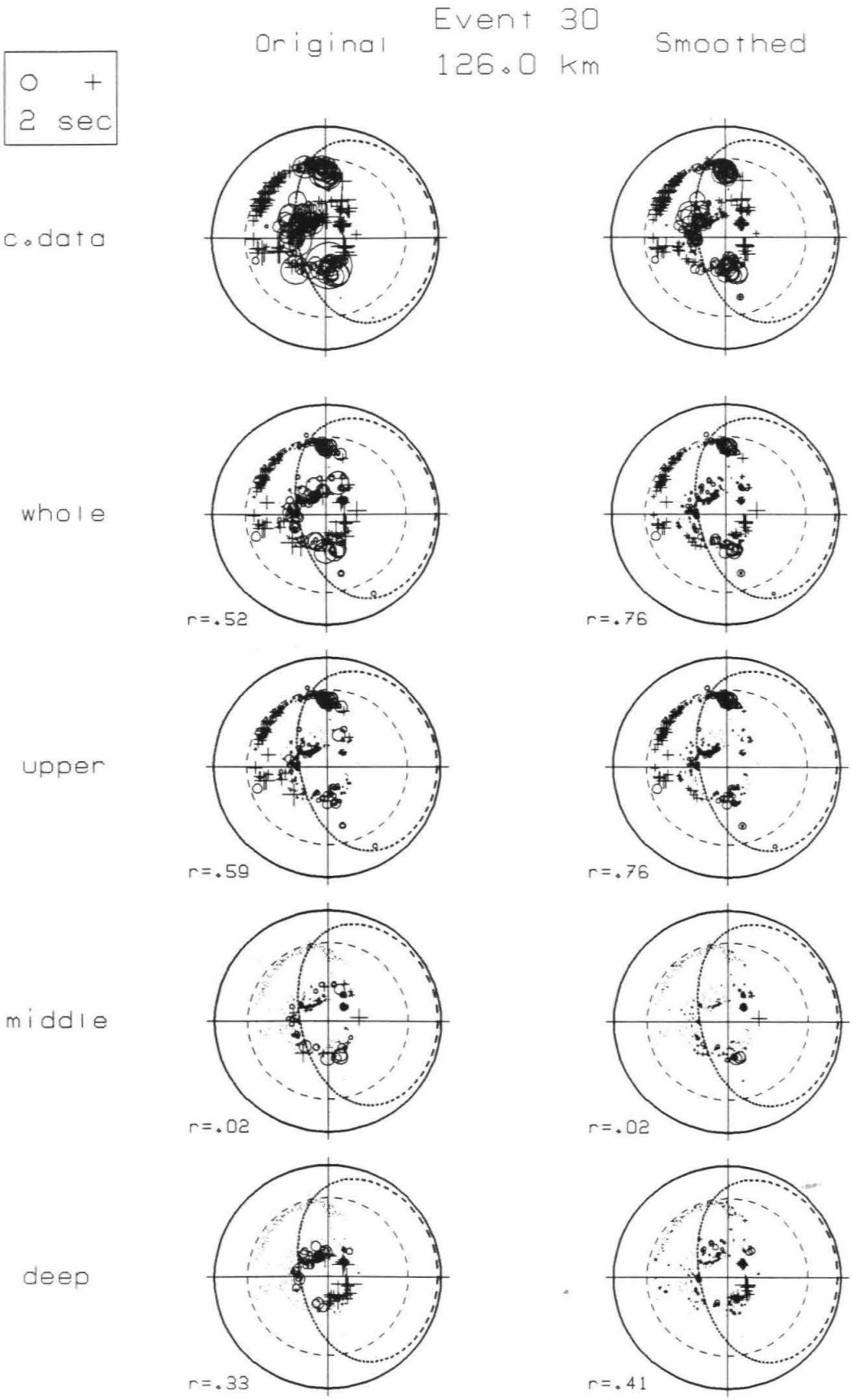
Original
Event 30
126.0 km
Smoothed
O +
2 sec
c.data
whole
r=.52
r=.76
upper
r=.59
r=.76
middle
r=.02
r=.02
deep
r=.33
r=.41

Figure 4.8. Residual spheres of event 38. Plotting conventions follows that of Figures 4.5. This is an example of a deep focus event that does not exhibit a clear slab-like signature. The pattern of arrivals near the center of the residual sphere is controlled by lower mantle effects while the pattern around the edge of the sphere is controlled by the mantle above 650 km. These patterns, however, do not follow slab seismicity trends. Note that the observed lower residual sphere data of this and the next two events actually show a fast residual "ring" in the lower focal spheres, indicating a fast subhorizontal layer lying beneath these earthquakes.

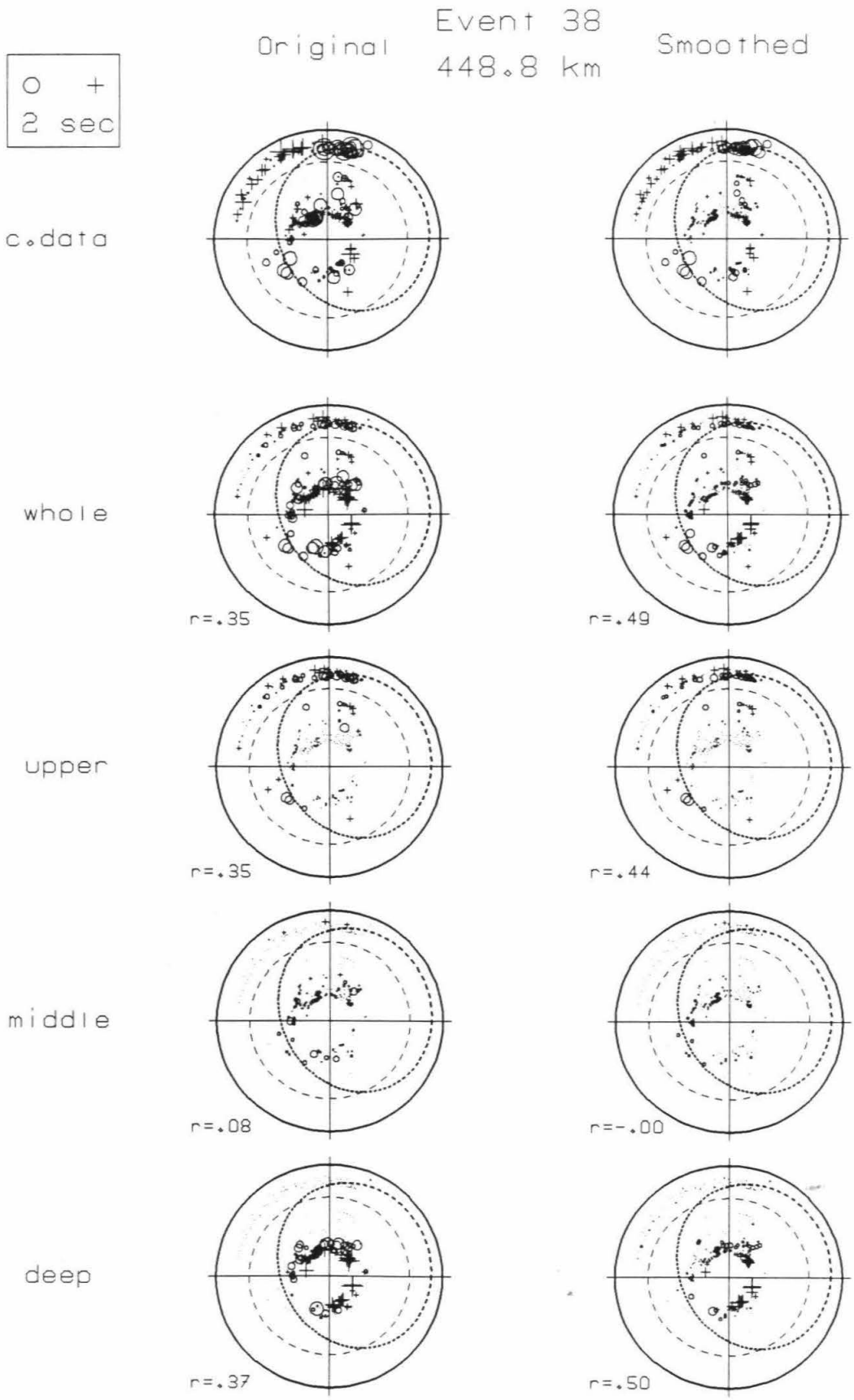
Event 38
448.8 km
Original
Smoothed
O +
2 sec
c.data
whole
r=.35
r=.49
upper
r=.35
r=.44
middle
r=.08
r=-.00
deep
r=.37
r=.50

Figure 4.9. Residual spheres of event 69. Plotting conventions follows that of Figures 4.5. Short wavelength variations appear in data and all predictions. No clear steeply dipping slab-like feature is found in either the data or the predictions for this event under central Japan.

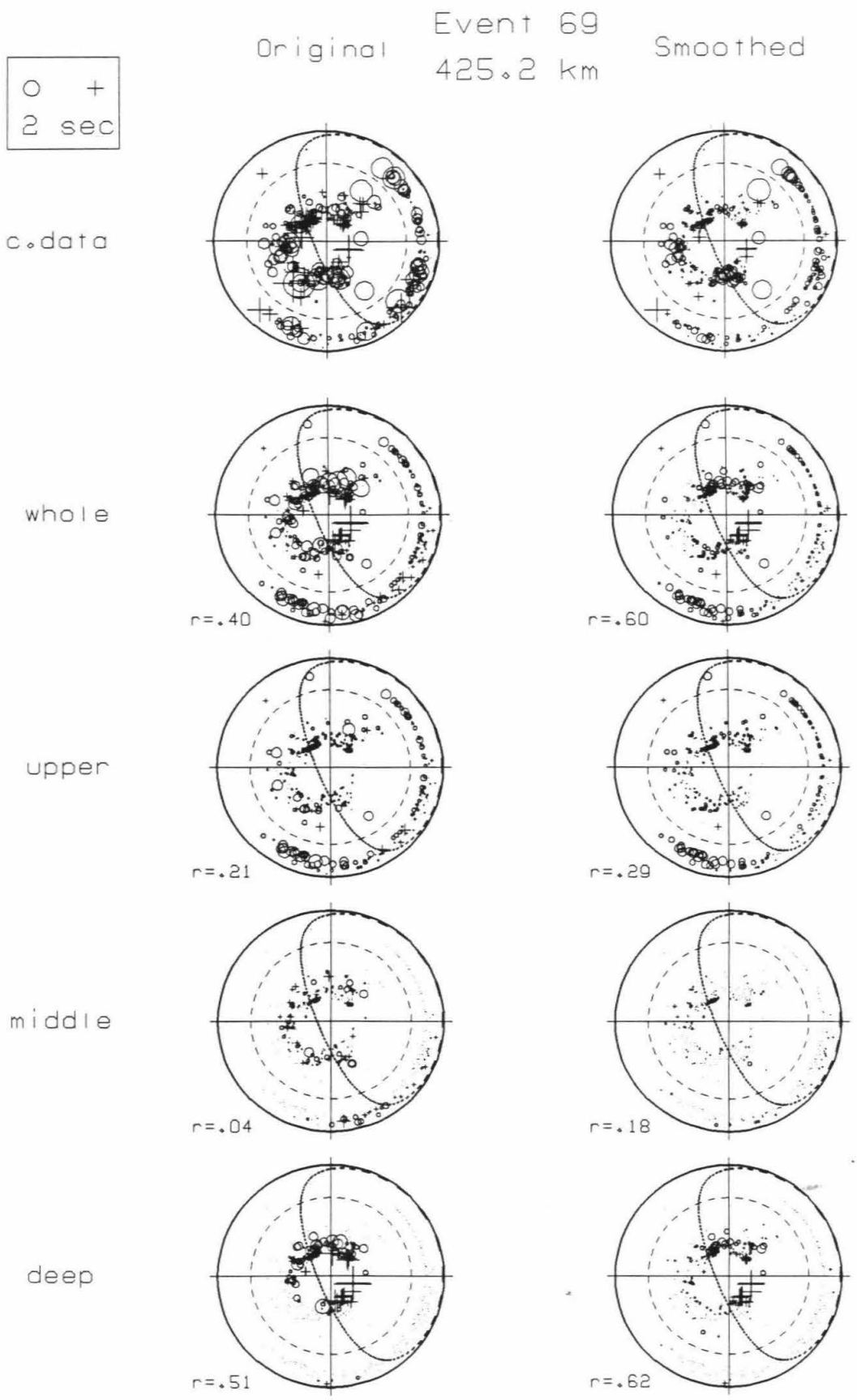
Event 69
425.2 km
Original
Smoothed
O +
2 sec
c.data
whole
upper
middle
deep
r=.40
r=.60
r=.21
r=.29
r=.04
r=.18
r=.51
r=.62

Figure 4.10. Residual spheres of event 83. Plotting conventions follows that of Figures 4.5. This is the same as Creager and Jordan [1986] event 8. There are fast anomalies of nearly equal magnitudes in all four quadrants of the middle mantle prediction, indicating that a subhorizontally lying fast anomaly exists and extends to about 800 km depth in this area. The generally fast N and NW quadrants and slow SE quadrant in the deep mantle prediction is more-or-less slab-like. On the other hand, the most dominate fast band in the observed residual sphere is subhorizontal. This was overlooked in the Creager and Jordan study because of their restriction to steeply dipping features.

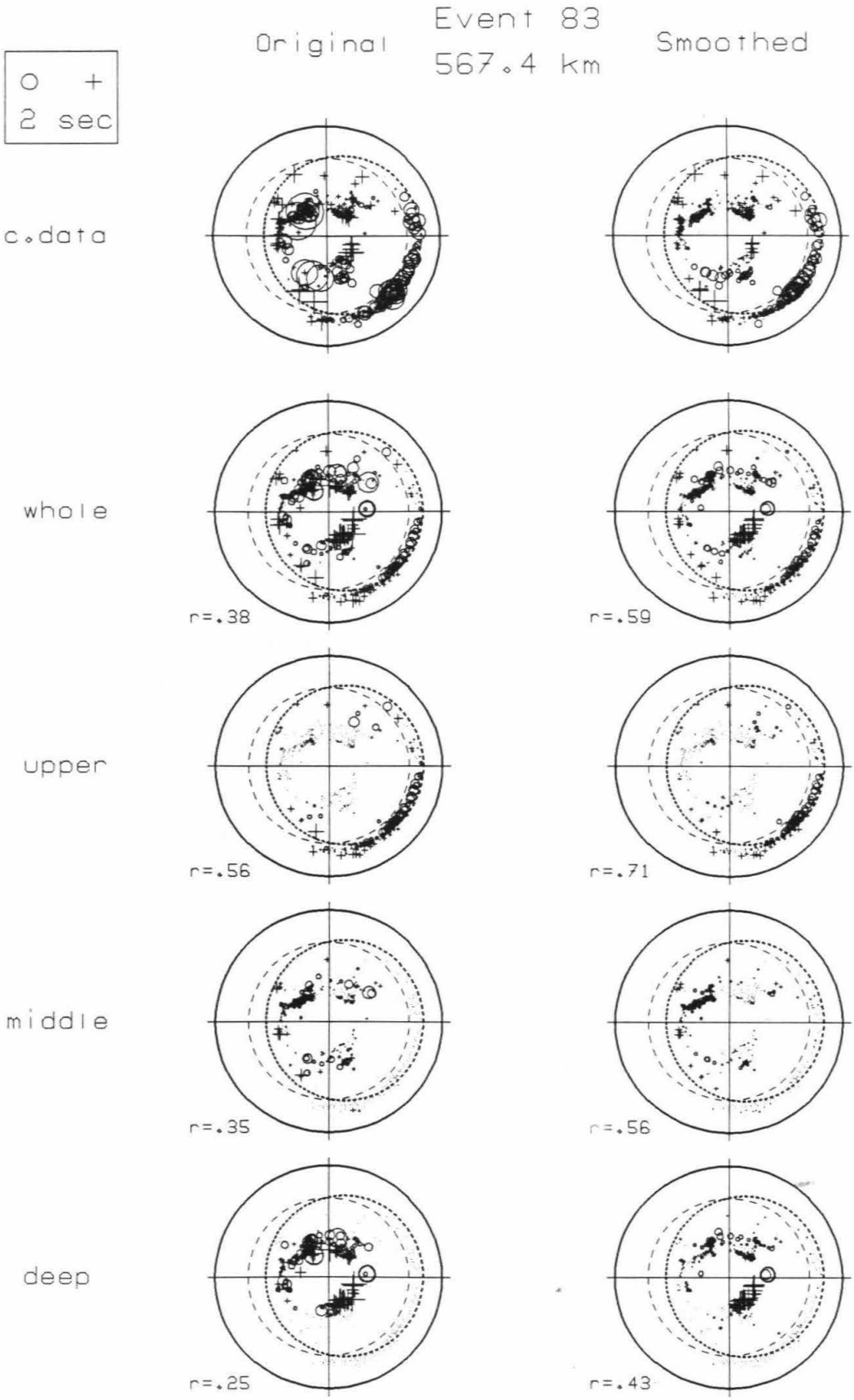
Event 83
567.4 km
Original
Smoothed
O +
2 sec
c.data
whole
r=.38
r=.59
upper
r=.56
r=.71
middle
r=.35
r=.56
deep
r=.25
r=.43

Figure 4.11. Residual spheres of event 106. Plotting conventions follows that of Figures 4.5. The event displays a band of fast residuals which is made up of separate contributions from the deep mantle and the upper mantle. The middle mantle, although slab-like, has very minor effect on the whole mantle pattern. The apparent slab-like signature in the whole mantle prediction is an artifact of this accidental alignment.

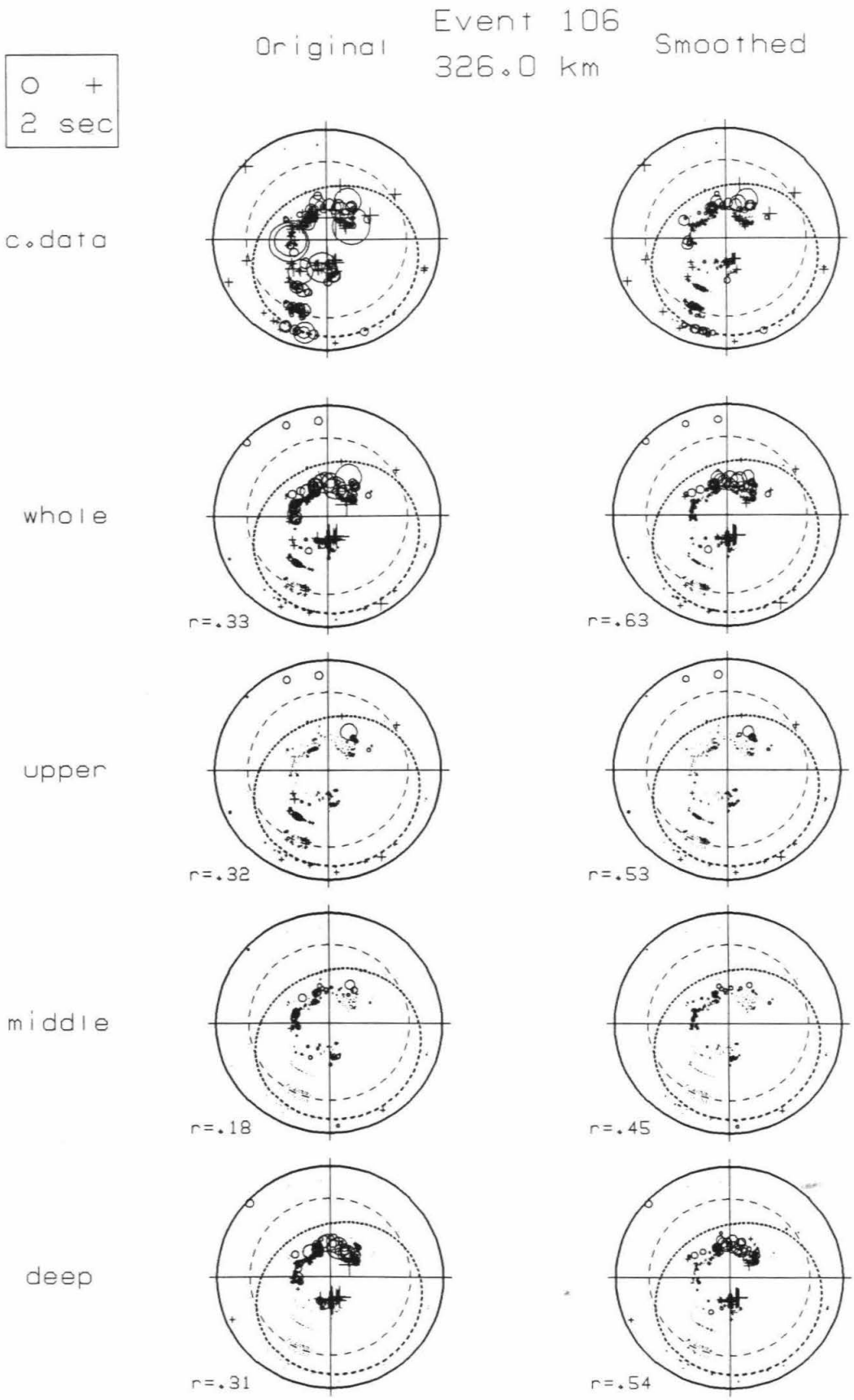
Event 106
326.0 km
Original
Smoothed
O +
2 sec
c.data
whole
upper
middle
deep
r=.33
r=.63
r=.32
r=.53
r=.18
r=.45
r=.31
r=.54

Figure 4.12. Residual spheres of event 119. Plotting conventions are identical to Figure 4.5. See comments for the last figure (Event 106).

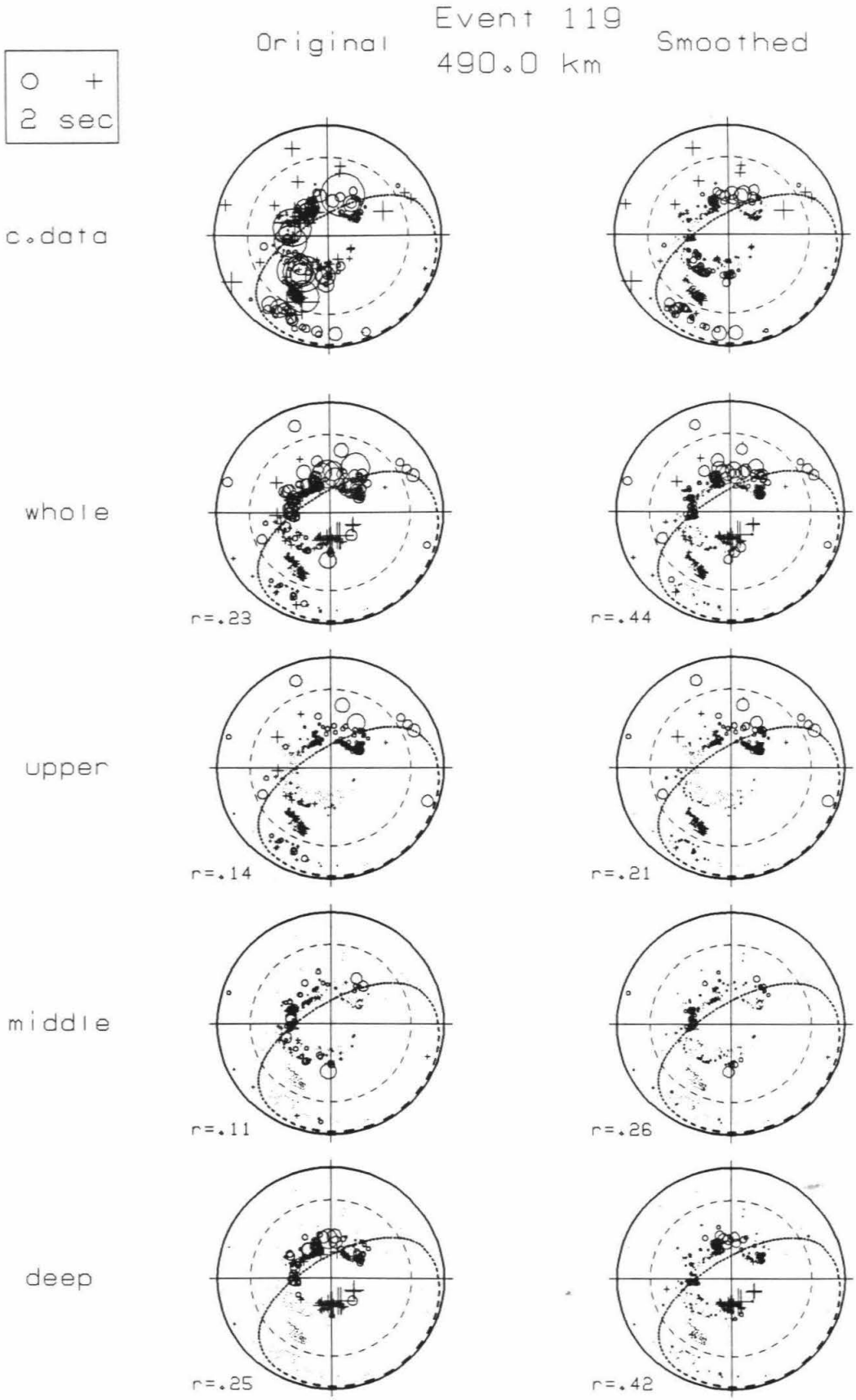
Event 119
490.0 km
Original
Smoothed
O +
2 sec
c.data
whole
upper
middle
deep
r=.23
r=.44
r=.14
r=.21
r=.11
r=.26
r=.25
r=.42

Figure 4.13. Residual spheres of event 124. Plotting conventions follows that of Figures 4.5. The event exhibits a pronounced slab-like signature with the expected trend in both data and whole mantle prediction. However, decomposition of the computed residuals into upper, middle and deep mantles shows that the fast velocities along the trend of the slab in the NE quadrant come from below 1500 km depth while the fast arrivals in the SSW and ENE directions come from above 650 km. The middle mantle contribution is relatively small.

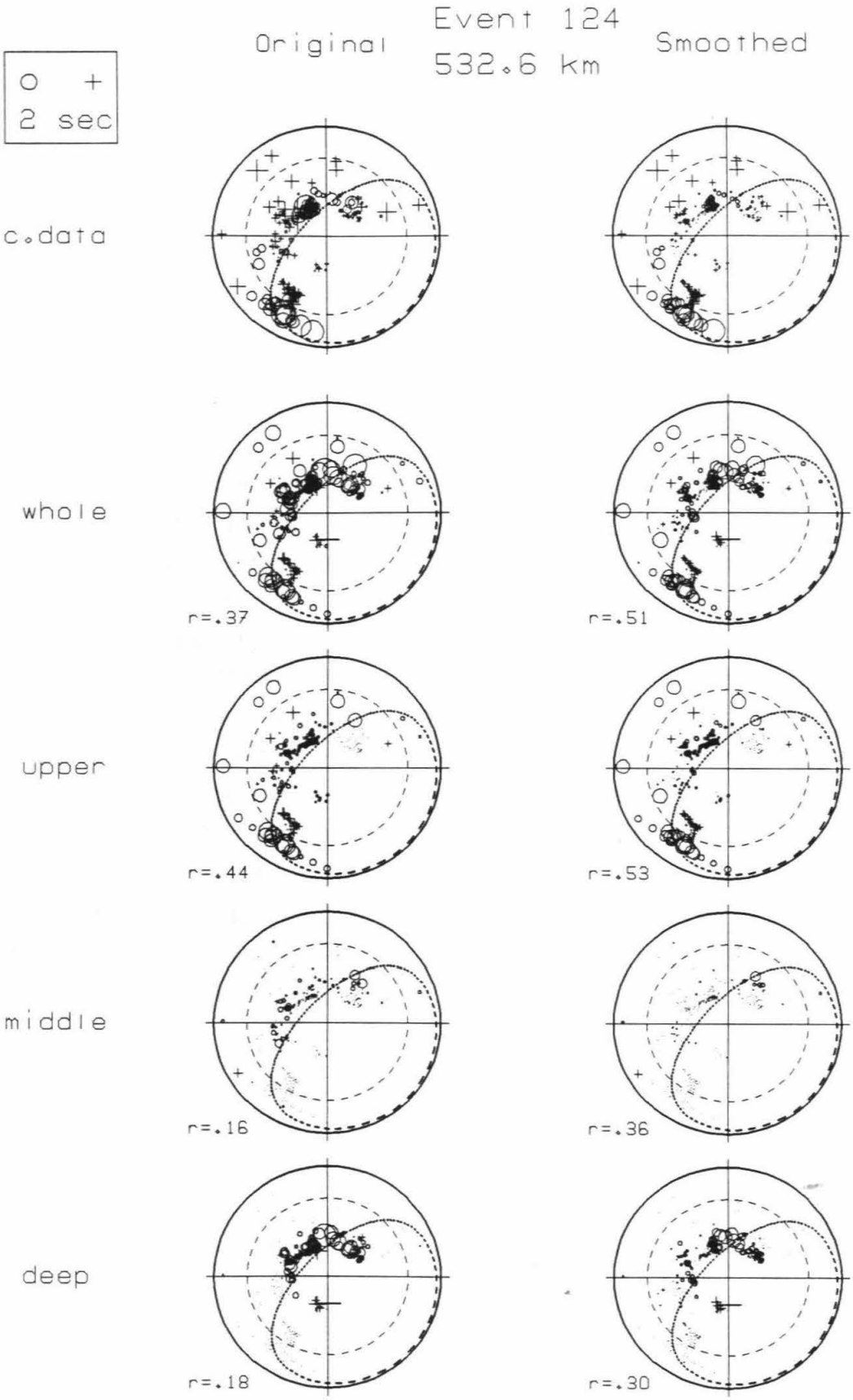
Event 124
532.6 km
Original
Smoothed
O +
2 sec
c.data
whole
upper
middle
deep
r=.37
r=.51
r=.44
r=.53
r=.16
r=.36
r=.18
r=.30

Figure 4.14. Residual spheres of event 126. Plotting conventions follows that of Figures 4.5. There is a strong slab-like signature with the appropriate orientation of the deep seismic zone. The integrated effect of the deep mantle accounts for the fast velocities in the northern quadrants and slow in the southern quadrants, while the mantle above 650 km gives slow in the NW quadrant and enhanced the fast slab-like trend in the whole mantle prediction. The middle mantle pattern is flat and has a minor role (much smaller amplitude contribution) on the whole mantle slab-like signature. This is the same as Creager and Jordan's [1984] Sea of Okhotsk event 6, one of the events used to infer slab penetration below 1000 km. My results show that a large part of the slab-like signal comes from below 1500 km, where the rays have spread away from the subduction zone.

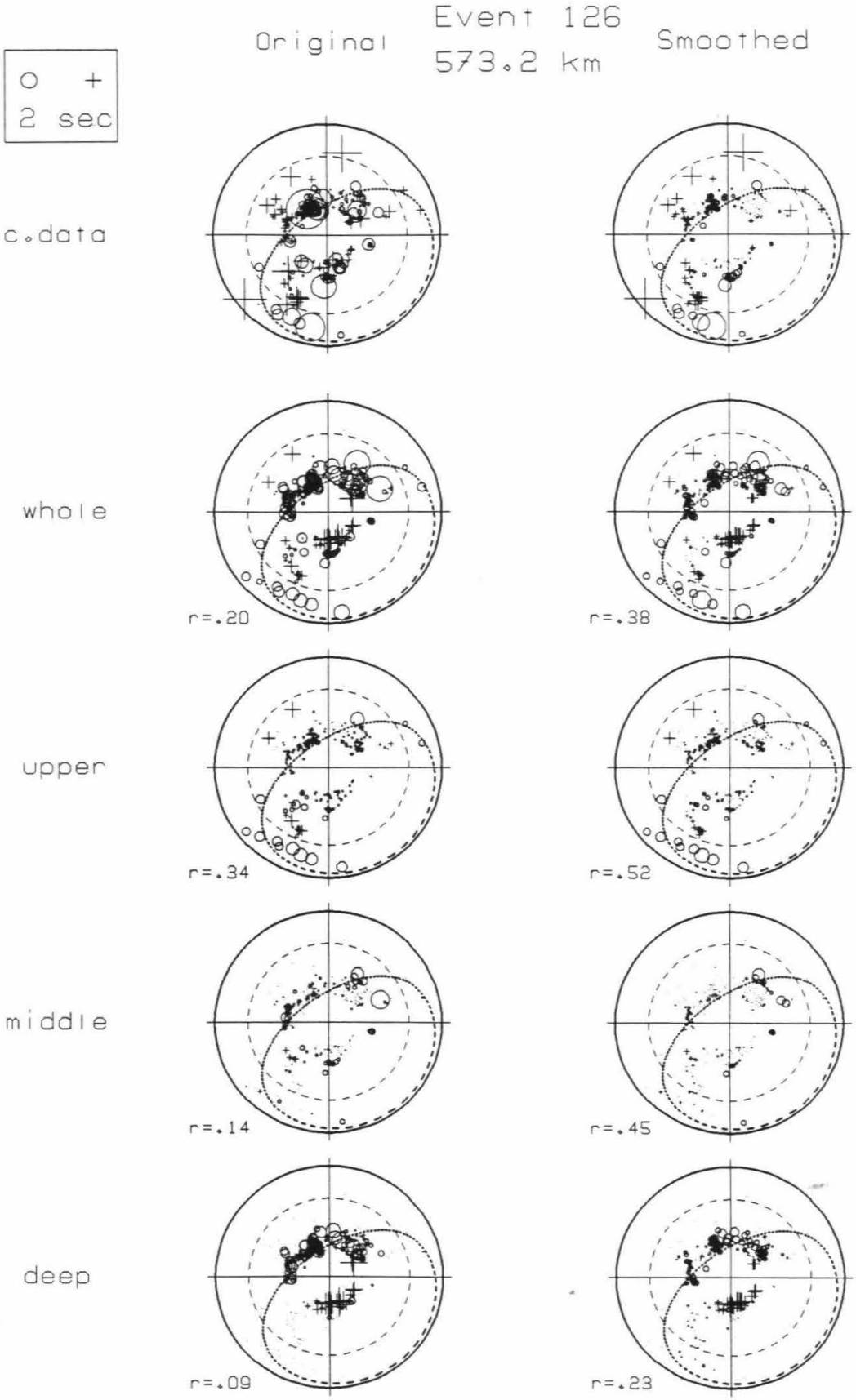
Original
Event 126
573.2 km
Smoothed
O +
2 sec
c.data
whole
r=.20
r=.38
upper
r=.34
r=.52
middle
r=.14
r=.45
deep
r=.09
r=.23

Figure 4.15. Residual spheres of event 130. Plotting conventions follows that of Figures 4.5. This has one of the clearest slab-like signature for a deep focus event. The decomposed residual spheres, however, suggest that the deep mantle, which is away from the Kuril subduction zone, has a much higher amplitude contribution than that of the middle mantle. The middle mantle residual sphere again has a diffuse look.

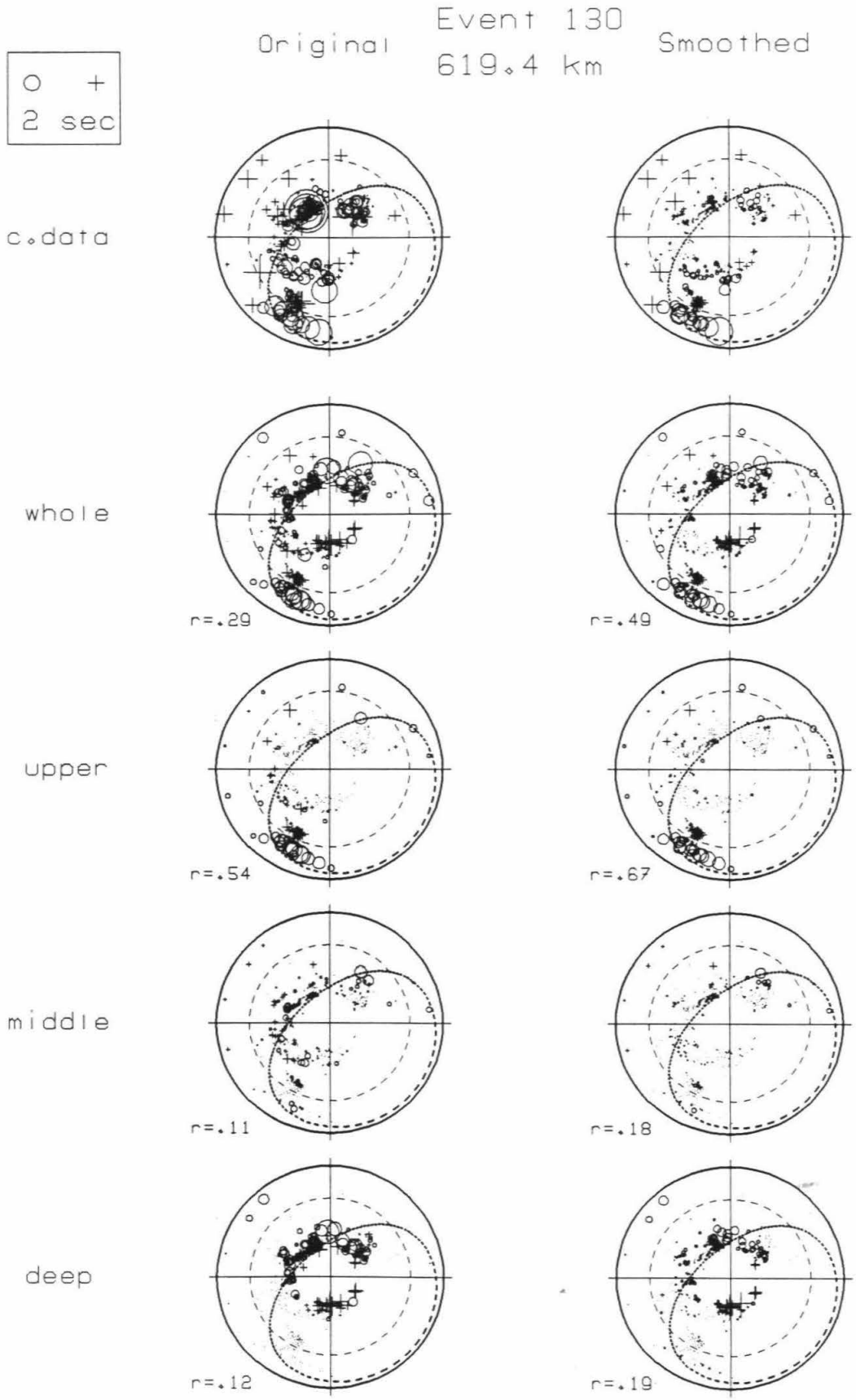
Event 130
619.4 km
Original
Smoothed
O +
2 sec
c.data
whole
upper
middle
deep
r=.29
r=.49
r=.54
r=.67
r=.11
r=.18
r=.12
r=.19

Figure 4.16. Residual spheres of event 137. Plotting conventions follows that of Figures 4.5. This is the same as Creager and Jordan [1986] event 6, and the comments made for event 126 (Figure 4.14) also apply here. The deep mantle, as usual, plays an important role in the whole mantle prediction, even though it alone has a poor correlation with the data. Many residual sphere anomalies are explained by the velocity maps in Figure 4.3.

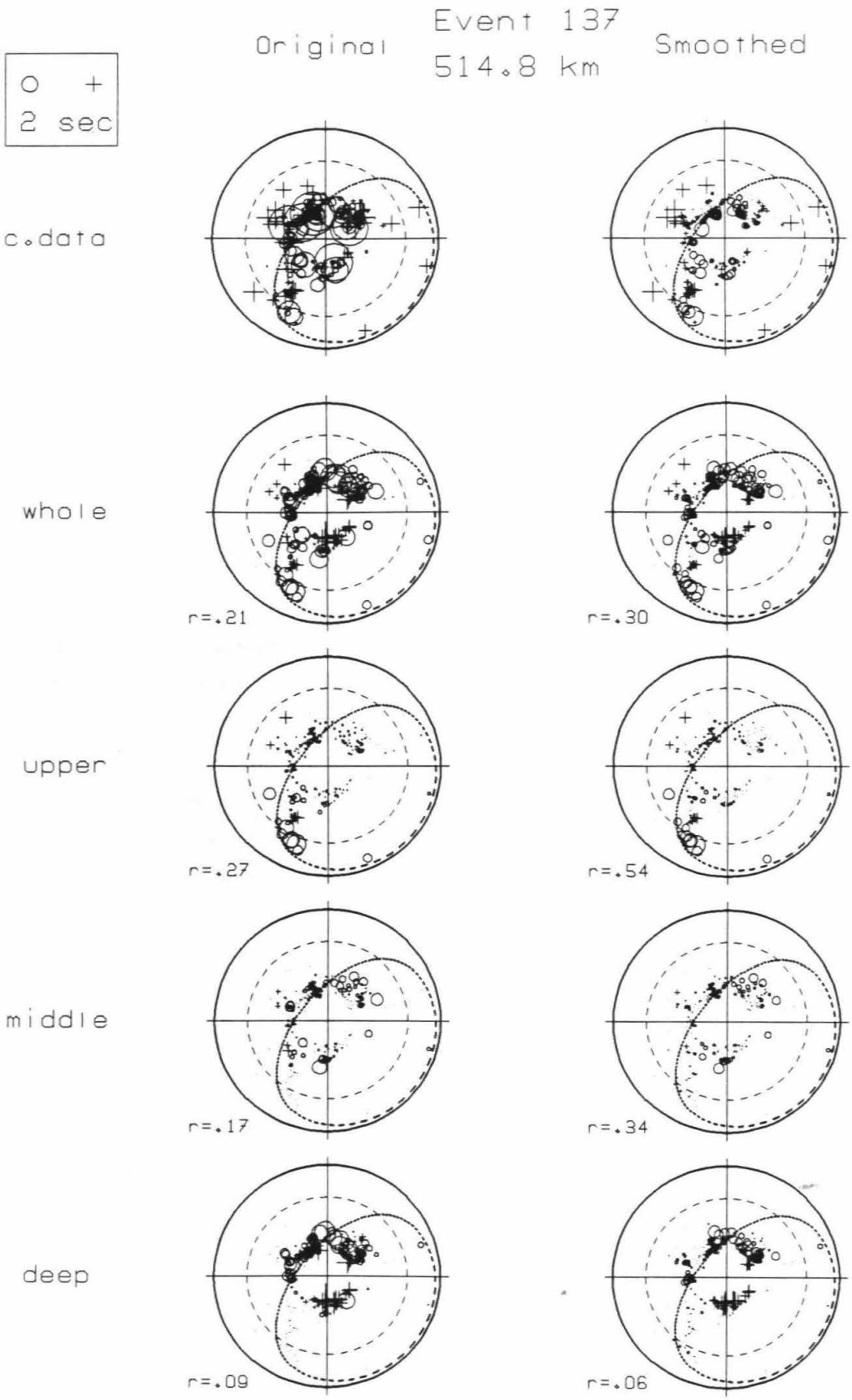
Event 137
514.8 km
Original
Smoothed
O +
2 sec
c.data
whole
upper
middle
deep
r=.21
r=.30
r=.27
r=.54
r=.17
r=.34
r=.09
r=.06

Figure 4.17. Residual spheres of event 142. Plotting conventions follows that of Figures 4.5. This is the same as event 5 in Creager and Jordan [1986]. In fact, the pattern shown in the middle part of the smoothed data (top right sphere) is very similar to that shown by these authors. The upper mantle plays a major role, as expected for this shallow event. The contribution from the middle mantle is smaller than that either from the upper mantle or from the deep mantle.

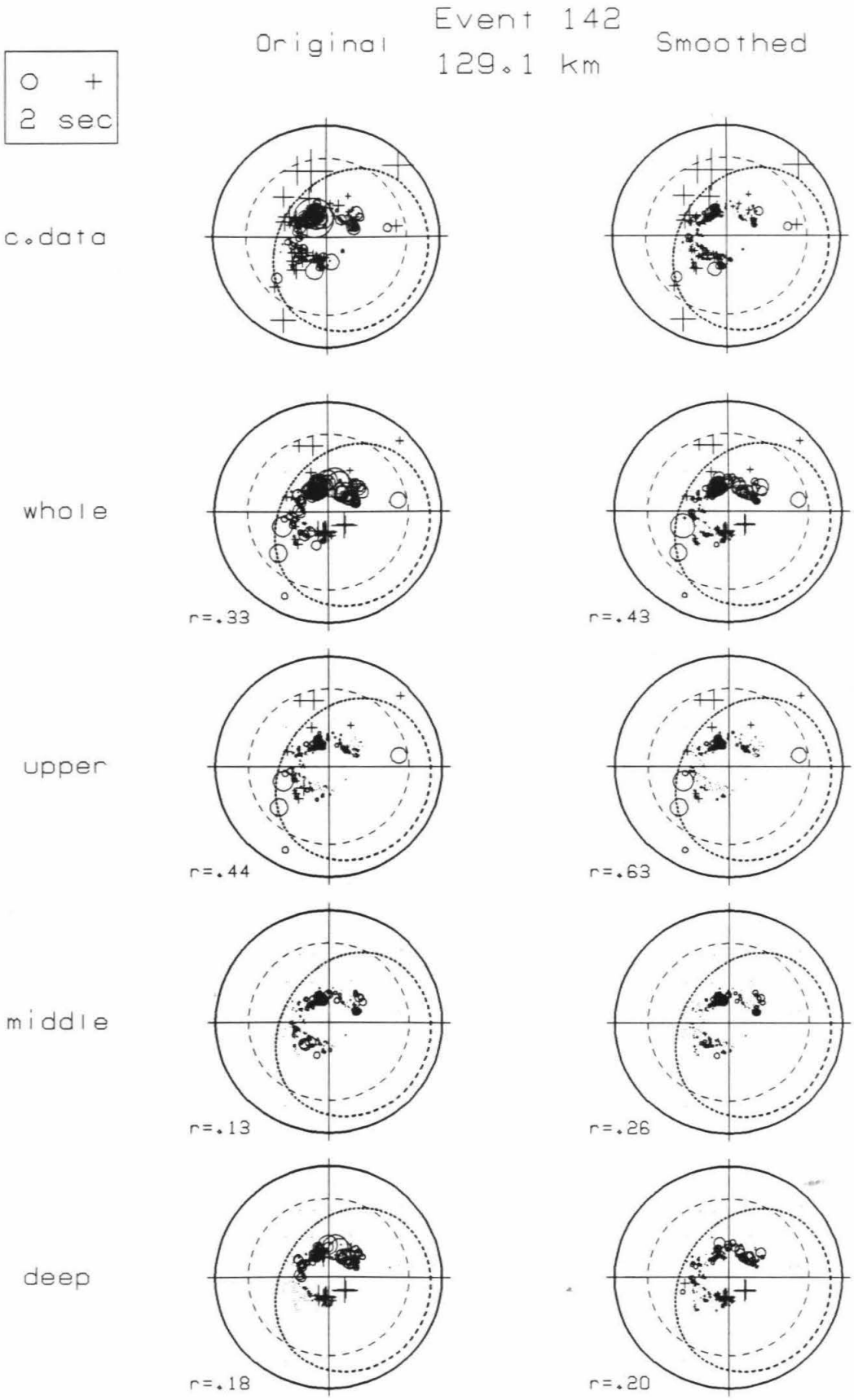
Event 142
129.1 km
Original
Smoothed
O +
2 sec
c.data
whole
upper
middle
deep
r=.33
r=.43
r=.44
r=.63
r=.13
r=.26
r=.18
r=.20

Figure 4.18. Residual spheres of event 145. Plotting conventions follows that of Figures 4.5. This event displays a discontinuous band of fast residuals, a northern clump and a SW clump. The former is mainly due to deep mantle propagation while the latter is primarily due to the mantle above 650 km. Together they combine with a rather flat middle mantle to give a slab-like anomaly. Note the importance of the slow clump in the southern quadrants of the deep mantle, in canceling the fast arrivals in the middle mantle away from the seismicity trend.

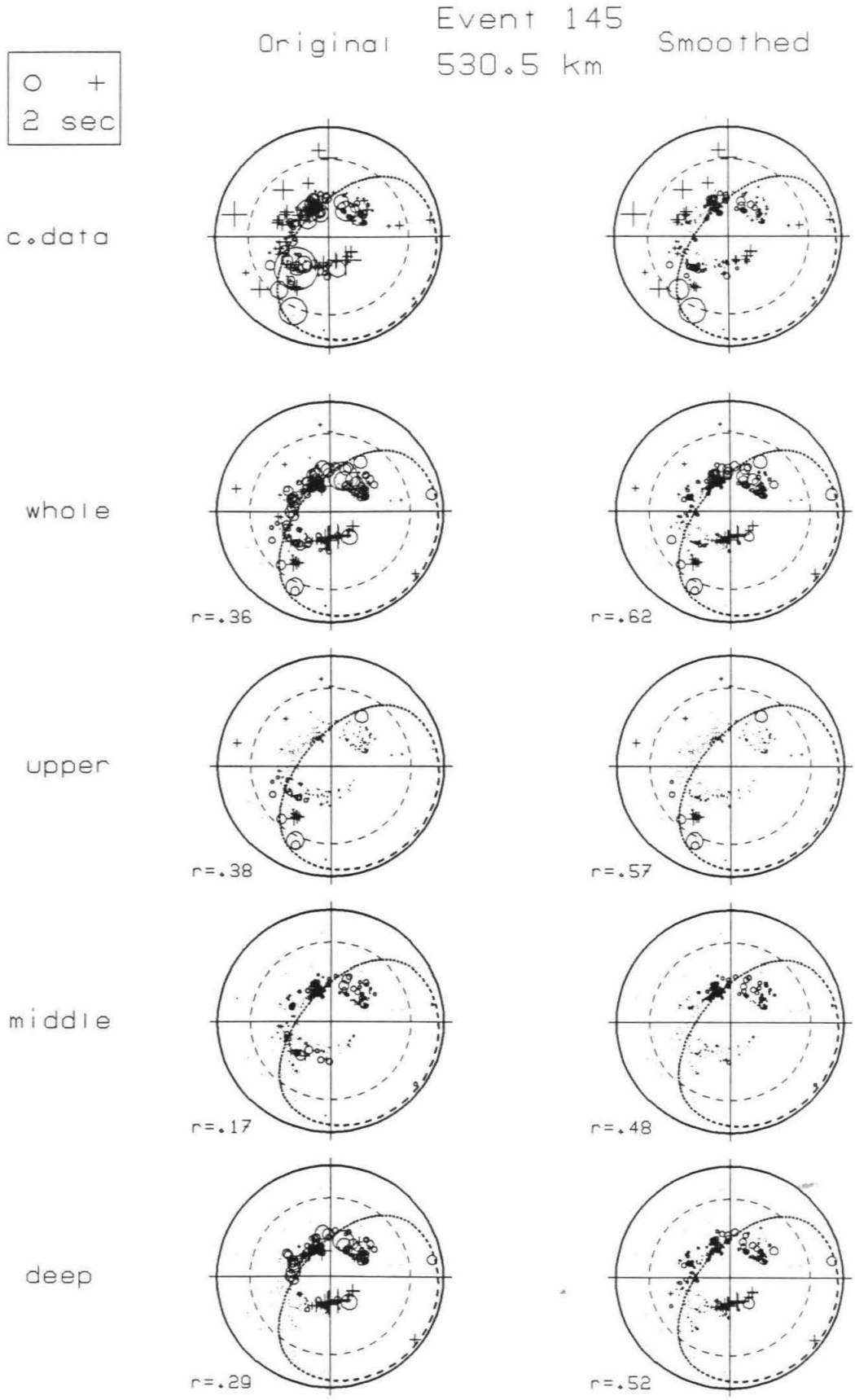
Event 145
530.5 km
Original
Smoothed
O +
2 sec
c.data
whole
r=.36
r=.62
upper
r=.38
r=.57
middle
r=.17
r=.48
deep
r=.29
r=.52

zone and having P wave anomalies of 1 to 2 seconds. Similar trends have been found in the present study. Creager and Jordan interpret their results in terms of slab penetration to depths of at least 900-1000 km, implying circulation of at least some upper mantle material into the deep mantle. I found, however, that independently derived lower mantle models, when projected onto the residual sphere, give similar fast bands caused primarily by heterogeneities exterior to that part of the mantle between 650 and 1500 km beneath the earthquakes. Examples of diffuse deep mantle structure having the trends of NW Pacific subduction zones are also evident in the study of Dziewonski and Woodhouse (1987).

Event 83 is the same as event 8 in Creager and Jordan (1986). Notice the similarity in residual sphere patterns for steep rays (near the center of plot) in the smoothed data and whole mantle prediction with the smoothed data presentation by Creager and Jordan. The main features here are fast arrivals to the NW and slow anomalies to the W, NE and SE. These features are also evident in the predictions of the "deep mantle" model (lower panel). Many of the other features of the data (top panel) are caused by variations in the upper mantle (middle panel). The mantle between 650 to 1500 km depth (on the down-going ray), however, predict a fast feature with nearly zero dip which has less amplitude and structure, in comparison with the deep mantle. It indicates flattening of the slab below about 571 km depth. The fast arrivals in the data which are unexplained by the upper and deep mantle models are not on the trend of the seismic zone and therefore provide little support for the slab penetration hypothesis.

Figure 4.14 shows results for event 126 in the Sea of Okhotsk. This is the same as event 6 in Creager and Jordan (1984) and event 7 in Creager and Jordan (1986), which they used as the main evidence for their deep slab penetration hypothesis. A cluster of fast arrivals along the seismicity trend in the N-NE directions is evident in both my smoothed version of deep mantle prediction and the plot by these authors. This suggests that the anomaly is due to a diffuse high velocity region in the deep mantle. In fact, the rays contributing to this band are widely spread out by the time they reach 1500 km depth.

Event 137 (Figure 4.16), a 508 km deep event in the Kuril region, is the same as Creager and Jordan (1986) event 6. This gives another opportunity to compare the different smoothing and event location procedures. This event is about 150 km above the normal boundary between the upper and lower mantles. The boundary, however, is possibly much deeper beneath cold slabs. The common features are a band of fast arrivals along but steeper than the trend of the seismic zone and slow arrivals to the NW, E and S. The total range of the data (in the region where coverage is common) is about 2-3 seconds. This is an important test because a serious error in event location would change the pattern and amplitude of observed residual spheres. Although they used different smoothing and location procedures the observations shown by Creager and Jordan (1986) generally agrees well with ours. They interpreted the patches of fast residuals as being due to a fast slab, beneath the event, indicating "slab penetration to depths exceeding 1000 km." These results, however, show that much of the residual is accumulated

by rays that have spread out into the deep lower mantle. The "deep" mantle (from 1500 km depth below the source to the receiver) contributes fast arrivals in the N-NE and SW directions and the upper and middle mantles contributes slow arrivals to the NW. Note that the upper mantle also gives some fine structures, e.g., a slow patch to the SW surrounded by fast patches. The middle mantle which is relevant to the deep slab penetration hypothesis, 650 to 1500 km depth interval beneath the source, contributes a minor part to the overall residual sphere prediction.

4.4 A Test for Deep Mantle Velocity Heterogeneity

We have arrived at an important conclusion in the previous section, i.e. the deep mantle alone, far below the postulated depth of slab penetration and deep enough so that the seismic ray bundles are spread far beyond the confines of narrow slabs, predicts residual spheres having the general patterns of observed residual sphere data for deep focus earthquakes. Of course, this result is based on the velocity models used. A very simple test is now designed, using only observed travel time residuals without any velocity models.

In this test, all events that were recorded by a large number (>400) of receivers are used. The 33 events thus selected, are well spread over the NW Pacific region (see solid stars in Figure 4.1) where the subduction zone is highly variable in strike and in dip. I then compute the average residual at

each teleseismic station that has picked up more than 16 of these events. The variability of the slab trend means more cancellation for the near source effects, hence relatively more power for deep mantle and receiver effects. In this procedure the rays from the various sources only sample similar mantle after they have traveled some distance from the source. The rays converge as they travel. The new station residual averages from the selected events represent a cumulative contribution from mantle regions far away from the source region, comparable to a true deep mantle model. Finally the mean location of the selected events is taken as a hypothetical hypocenter to construct a residual sphere (Figure 4.19a) using these new station residual averages.

If the deep mantle anomalies are unimportant or not coherent over large distances, the residual sphere produced in this test should have a very small amplitude and a random pattern. However, as we can see in Figure 4.19, this is not the case. The station residual averages are around 1 sec in magnitude (well above 2 sec peak-to-peak), and form very distinctive patterns which correlate with major tectonic features. The large fast averages at stations in New Guinea and Timor Islands are likely due to upper mantle effects of the major Sunda subduction zones. Large slow residual averages at the island stations of Marquesas, Tahiti and Cook Islands are probably due to deep slow mantle beneath the west Pacific. The Canadian, Australian and Baltic shields are fast. Western North America and central Asia are also very evident as slow anomalies. Variations of the event selection criteria for the above test do not change the result qualitatively. Remember that my previous data

Figure 4.19. A test of deep mantle and near-station velocities. Plotting conventions for this figure is similar to that for the top two small spheres in each panel of Figure 4.3. The circumference in residual sphere (a.) corresponds to take-off angle of 90°, the corresponding epicentral distance in the station location sphere (b.) is shown by a dashed circle near the center. The small solid stars in b. denote events used in this test, which is discussed in section 4.4.

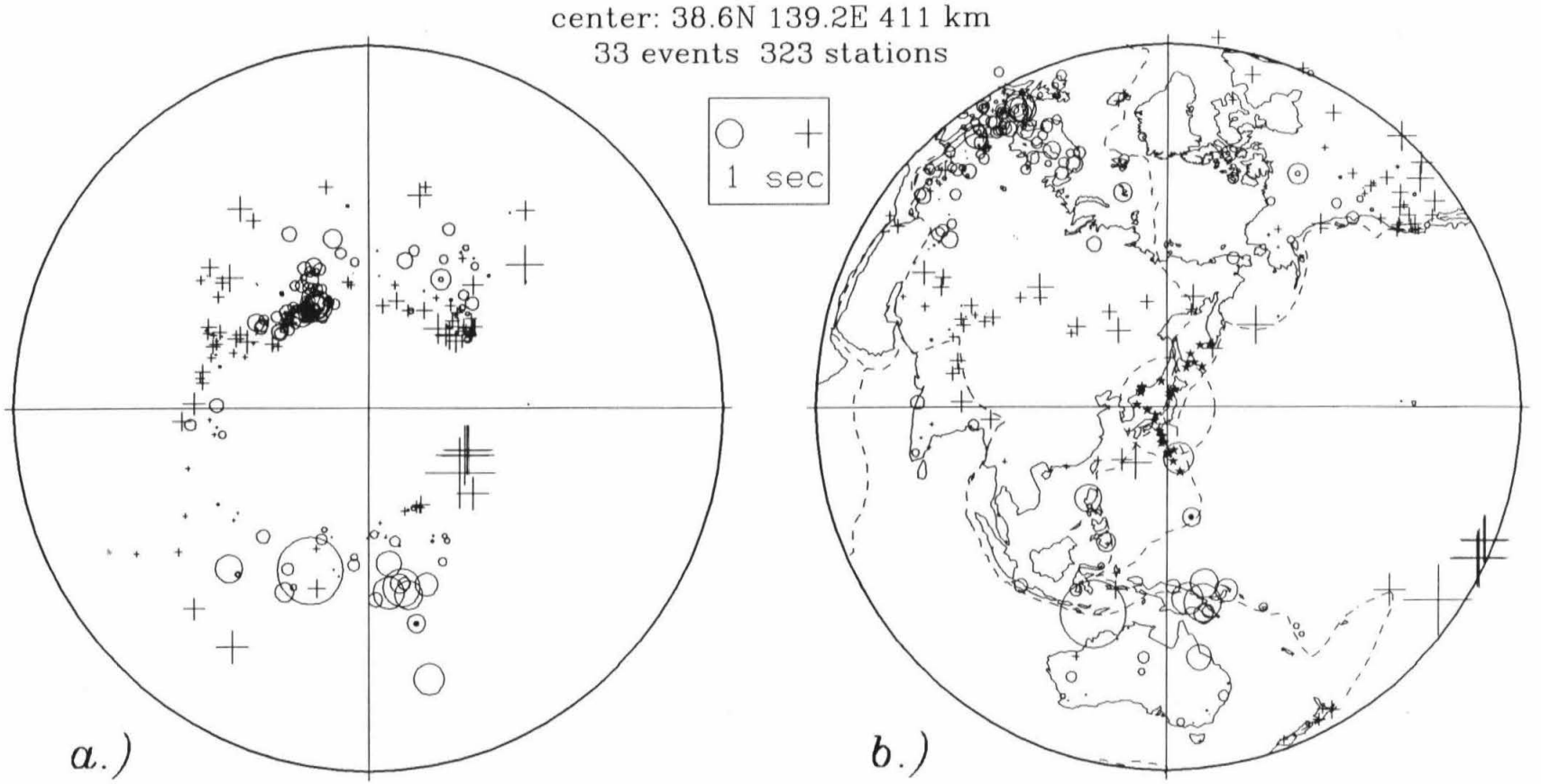
center: 38.6N 139.2E 411 km
33 events 323 stations
1 sec
a.)
b.)

corrections include a removal of the station residual averages of Clayton and Comer [1983] which are based on a global data base. The above result therefore suggests that a global average of residuals at a station may include only the effect of shallow heterogeneities beneath the station.

The test confirms the suggestion that there is a significant effect on the residual spheres by deep mantle anomalies and receiver effects. Furthermore, the pattern in Figure 4.19a is more-or-less "slab-like" with a north-south fast trend. This pattern is quite similar to the smoothed data by Creager and Jordan (1986) for their event 6, 7 and 8, as well as the smoothed data and lower mantle prediction of most events in this chapter (see Figures 4.6 to 4.11, 4.14, 4.15, 4.17 and 4.18). The long wavelength deep mantle heterogeneities plus very uneven and poor coverage of seismic stations make it very difficult to isolate near-source effects by residual sphere techniques.

To show the robustness of the teleseismic station averages, the averages were reconstructed using 94 events of focal depth greater than 300 km among the original 145 events (Figure 4.20). Each station average here uses at least 20 of the events, representing the teleseismic effect from the study region toward this station. The pattern of the station residual averages in this figure is essentially the same as that shown in Figure 4.19; hence, it is quite stable. The station averages shown in this figure are used in the next section as the teleseismic effects to be corrected.

If the deep mantle effect can somehow be removed, however, a residual sphere study may give the approximate orientation, but still not the depth extent, of near source fast velocities. In earlier studies a full lower hemisphere

Figure 4.20. station residual averages for the second type of correction. Plotting conventions for this figure follow that of the last figure. The box in the middle of station map (b.) indicates the study area shown in Figure 4.1. Each average is constructed at a station using more than 20 deep ($>$ 300 km) earthquakes in the study region, representing the teleseismic effect from the region toward the station.

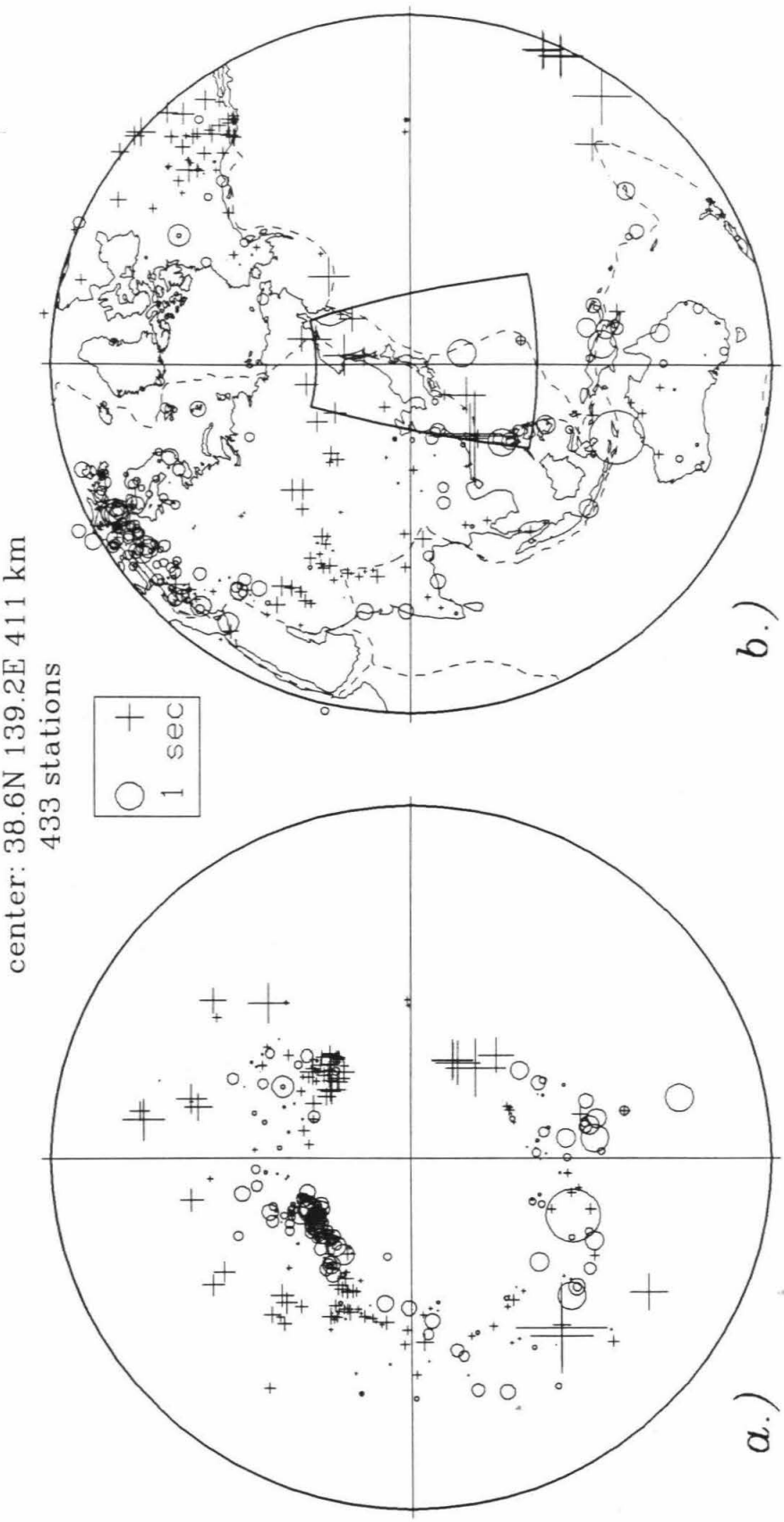
center: 38.6N 139.2E 411 km
433 stations
1 sec
a.)
b.)

was not used — a spherical cap defined by a cone of downgoing rays of less than 60° take-off angle (greater than about 25° in epicentral distance for an event of 550 km focal depth) has been commonly used. This eliminates the possibility of finding slabs which are confined to the upper mantle or slabs which are deflected to shallow dip by the 650 km discontinuity.

4.5 Method of Fitting for Slab-like Fast Bands

The cumulative travel time anomalies due to inhomogeneities in the deep mantle (greater than about 1500 km for downgoing rays) and receiver mantle (for upgoing teleseismic rays) are referred as the teleseismic effects, or teleseismic contributions. If the teleseismic effects on travel time residuals can somehow be isolated, then the question regarding the existence and nature of fast velocity trend near the subduction zone earthquakes can be reasked. This is the focus of the present and next sections, where a fitting technique is used to detect slab-like fast trend in observed residual spheres.

The fitting is applied after each of the two corrections suggested for removing the teleseismic effects, namely, a) using a reliable mantle velocity model; and b) removing teleseismic station statics that are constructed using the regional events. The first correction has been applied previously. For example, Creager and Jordan [1986] correct for the effects of the lower mantle model by Dziewonski [1984], but conclude that the correction is minor although it helps in the variance reduction. Dziewonski [1984] concludes,

however, that the spectrum for degrees 2 to 6 of his highly smoothed lower mantle model is flat; thus, the actual perturbations may be significantly larger. His method of smoothing and damping is expected to underestimate the total variation, particularly since he uses a minimum-norm inversion algorithm. The Clayton-Comer [1983] velocity model also have long wavelength components, but those are much larger in amplitude than in the Dziewonski model. In this chapter the Clayton-Comer model is used in the first type teleseismic correction. Precisely speaking, travel time anomalies by this model along all downgoing legs of rays from 1500 km depth down and entire upgoing legs of teleseismic rays are removed from the data.

The models obtained using seismic tomography usually suffer to some degree from poor resolution and noise; hence, this can result in misrepresentation of pattern and amplitude [Zhou, 1988]. To avoid use of velocity models, the second type of correction is proposed by removing teleseismic station residual averages which are constructed from only earthquakes in the study region. Station residual averages based on global earthquake database, however, only contain near station contributions, but not a large portion of the teleseismic effects. The station averages shown in Figure 4.20 are removed from the residual data as the second type of teleseismic correction in this study. A residual will be discarded if there is no station average available for it.

When a fast slab-like band exists in a residual sphere, the amplitude pattern has to possess a strong positive C_2^0 component in the appropriate reference frame. Therefore, the residual focal sphere data can be systematically

fitted with spherical harmonics of degree 0 to 2 to determine the best fitting slab orientation. To reduce the effect of slab distortion near the earthquakes, such as the possible slab kink around 650 km discontinuity for deep focus events, one may restrict the data to within a certain range of take-off angle. In this chapter seismic rays of take-off angle greater than 90° are excluded. In other words, all the rays used here take off downwards from the source.

The fitting for a C_2^0 component is equivalent to seeking a best fitting ellipsoid to the residual sphere data. In fact, the residual sphere data are fitted with a symmetric surface

$$\delta t(\theta) = C_0 + C_1 \cos\theta + C_2 \cos 2\theta \qquad (4.3)$$

where θ is the colatitude with respect to a symmetric axis normal to an assumed band orientation, and C_0, C_1 and C_2 are constants which are convertible to spherical harmonic coefficients. One could, of course, include higher degree terms as well.

Once a direction for the symmetric axis is given, the linear form of the above equation enables an unique determination of the three coefficients by a simple least squares inversion. The orientation of the best fitting symmetric axis can be determined quickly using the symmetric property of the fitting surface. In the first step we try the axis in all horizontal directions and find the best fitting horizontal direction. In the second step we try the axis in all directions on a vertical plane along the best fitting horizontal direction.

There could be two types of surfaces resulted from the above procedure. One has a positive C_2 and resembles a fast band residual sphere. The other

has a negative C_2 and resembles a slow band in the residual sphere. The best fitting orientation of the surface, which is assumed to be the one offering the highest correlation between the residual data and the fitted surface, represents the orientation of either a fast or a slow band in the residual sphere. Because the purpose is to determine the best fitting fast band, the fitting is restricted to only positive C_2. In some rare occasions, such as the fitting of event 64 in this study, fitting in all directions yields a negative C_2 term, indicating that the dominate trend in the residual sphere is a slow band in all directions. It was decided to use the orientation of the lowest correlation in this case.

4.6 Results of Fitting for Slab-like Fast Bands

The fitting method in the last section is applied to the residual sphere data, after each of the two types of teleseismic corrections, of 44 events that fall in the four shaded areas in Figure 4.1. To evaluate the fitting result, two aspects can be emphasized: a) the relative goodness of fit, or how much better is the best fitting orientation in comparison with all other orientations; and b) the orientation and amplitude of the best fitting band. The fitting goodness for most events studied, particularly the shallower ones, is very high. Figure 4.21 provides an example of the besting fitting fast bands for residual spheres of four Mariana earthquakes. The residual spheres of these events have been analyzed previously by Creager and Jordan [1986]. The predominant fast bands resulted by my fitting technique match the residual pattern well; they

Figure 4.21. Examples of fitting fast trend in observed residual spheres. The residuals used here are after the first type of teleseismic correction, that is, corrected for the deep mantle portion of the Clayton-Comer model. The four pairs of spheres are for four Mariana events in area A. The top sphere in each pair is the residual sphere with the best fitting second order surface, while the bottom sphere is the corresponding station map. Fitted surfaces in the unshaded region have positive C2 values, including all possible fast bands, while the shaded region corresponds to fitted surfaces with negative C2 values, including all slow bands. The "plus" sign indicates polar locations of the best fitting fast (or slow) band surfaces. The value of C2 term and the correlation coefficient of the fitting are indicated. Note the fitting method works fine for these events, and the amplitude of the bands, as indicated by the C2 value, is decreasing with depth.

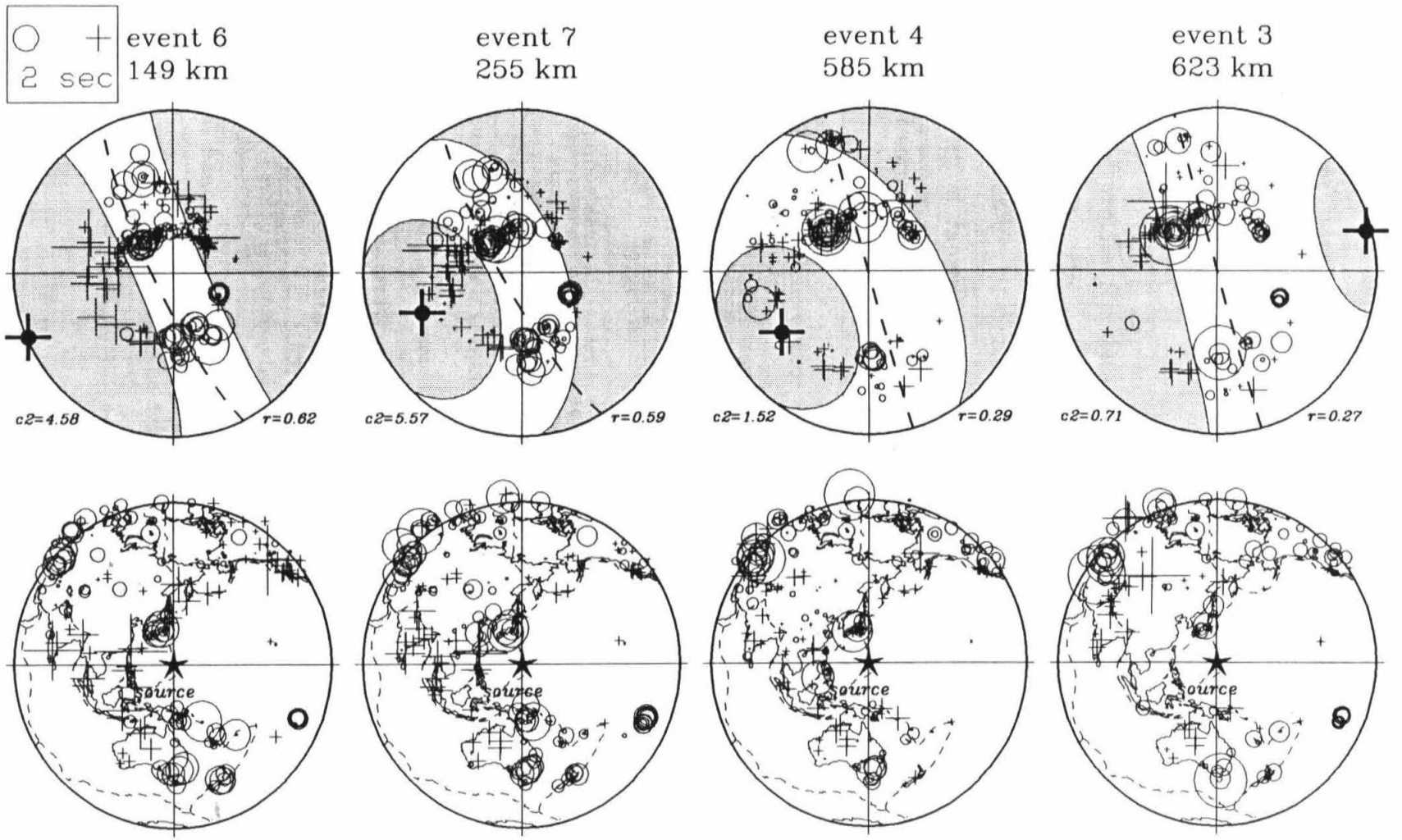
2 sec
event 6
149 km
event 7
255 km
event 4
585 km
event 3
623 km
c2=4.58
r=0.62
c2=5.57
r=0.59
c2=1.52
r=0.29
c2=0.71
r=0.27
source
source
source
source

also follow the seismicity trend for many events. The magnitude of the best fitting fast band, when it exists, is quantified by the value of the C_2 term. In this example, the magnitude of the fast bands in these four events decreases with depth.

The fitting results for data after the two teleseismic corrections are displayed area by area in Figure 4.22 to 4.25. The meaning of the fast band is discussed in the figure captions. The fittings for events in the Mariana, Izu-Bonin and Central Japan areas are generally good, and the results from the two types of corrections are similar. Fast slab-like bands are clearly visible for these events and generally agree with the seismicity trends. The amplitude of the fast bands and the correlation coefficient decreases with depth under the Mariana trench (Figure 4.22) where the slab descends near vertically, while no such decreasing trend is found under Japan (Figure 4.24) where the slab is shallowly dipping. In fact, the predominant fast band for most deep earthquakes under central Japan is subhorizontal.

After both teleseismic corrections, the detectable fast bands for events under the Izu-Bonin trench (Figure 4.23) are consistent with the seismic trend from the surface down to around 500 km, but the patterns have more difference for deeper events. The fitting is relatively poor for events between 300-500 km depth. A sharp flattening of fast slab at 500-550 km depth as found by Zhou (1988) is consistent with the above observation.

The fast bands detected in the data from the Kuril trench area are very inconsistent and different from the seismic trend. Recall that we do not limit ourselves to searching for only nearly vertical fast bands, i.e., bands near the

Figure 4.22. Fitting of fast bands for events in Area A: Mariana. This and the next three figures display the fitting of dominating fast bands in residual spheres in four areas. The spheres in each row are ordered from shallow to deep events. The top and bottom rows, respectively, are for data after the first type and the second type of teleseismic corrections. Each sphere displays the best fitting surface of the residuals like that shown in the top row of Figure 4.21. The two numbers below each sphere are the C2 value at the left and the correlation coefficient of the fitting at the right. The fitting graph above each sphere shows the residual (seconds) vs. colatitude (degrees) plot for the best fitting fast band surface with data (dots). Fittings for events in this area are generally good, and the results from the two types of corrections are similar. The fast bands resolved generally agree with the trends of seismicity, suggesting that fast regions may exist below earthquakes. The amplitude of the fast band (C2 term) and the correlation coefficient decrease from shallow to deep events.

MARIANA

Corr. 1

6 149 km

5 231 km

7 256 km

4 585 km

2 601 km

1 607 km

3 624 km

Corr. 2

Figure 4.23. Fitting of fast bands for events in Area B: Izu-Bonin. Plotting conventions are the same as Figure 4.22. Fittings for most events in this area are good, although it is relatively poor for events between 300-500 km depth, as indicated by the correlation coefficients. Similar fast bands exist in results from the two types of corrections for events shallower than 500 km, but the patterns have more difference for deeper events. The fast bands have similar orientations to the seismic trend above 500 km and generally dissimilar orientations below.

IZU-BONIN (α)

Corr. 1

30 126 km 32 183 km 22 254 km 21 374 km 27 400 km 26 448 km

Corr. 2

IZU-BONIN (b)

Corr. 1
Corr. 2
29 475 km
31 486 km
23 503 km
24 508 km
25 523 km
28 541 km
dr[s]
ih[o]
0.69
0.18
0.68
0.22
1.47
0.36
0.43
0.24
0.00
0.39
0.68
0.31
0.55
0.27
1.07
0.33
0.01
0.30
1.61
0.22
0.62
0.55
0.39
0.40

Figure 4.24. Fitting of fast bands for events in Area C: central Japan. Plotting conventions are the same as Figure 4.22. Fitting level is generally reasonable, but because the best fitting fast bands for most events are nearly horizontal, data coverage is quite poor. Fitting results after the two corrections resemble each other well. For event 64 fitting in all directions yield negative C2 term, indicating that the dominate trend in this residual sphere is a slow band in all directions. The orientation of the lowest fitting level is used in this case. The flat fast bands for most events generally agree with shallowly dipping seismicity trend.

C. JAPAN (a)

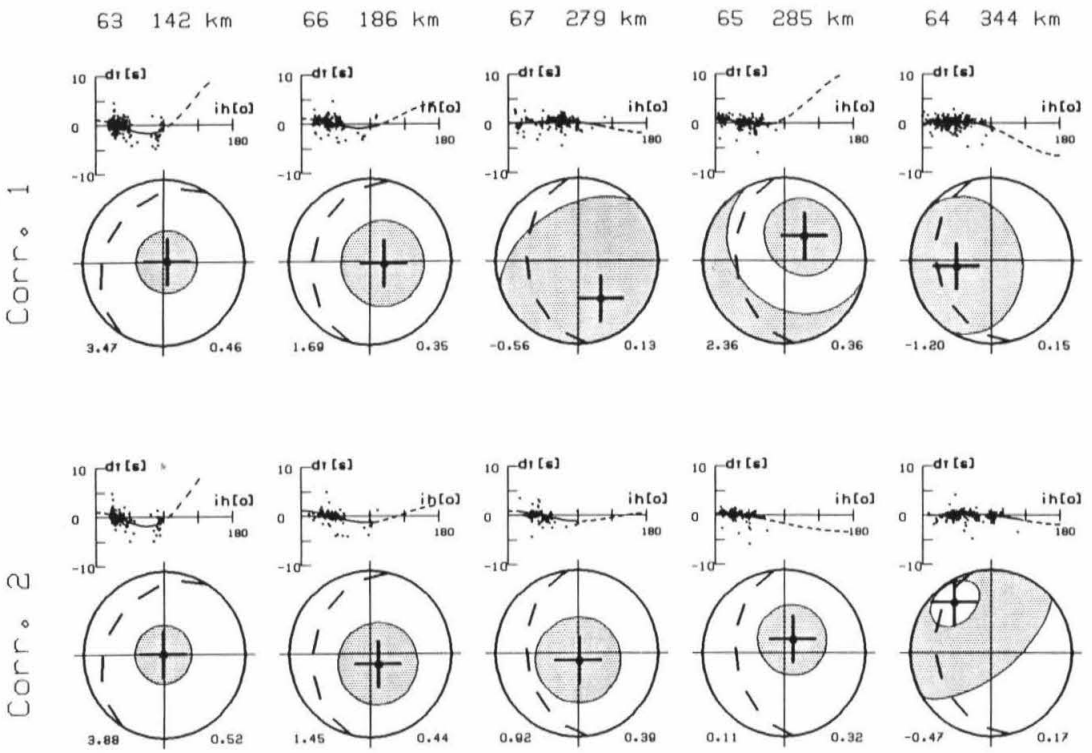
63 142 km
66 186 km
67 279 km
65 285 km
64 344 km
Corr. 1
Corr. 2
dt[s]
ih[o]
10
0
-10
180
3.47
0.46
1.69
0.35
-0.56
0.13
2.36
0.36
-1.20
0.15
3.88
0.52
1.45
0.44
0.92
0.39
0.11
0.32
-0.47
0.17

C. JAPAN (b)

Corr. 1
Corr. 2
68 370 km
71 397 km
70 414 km
69 425 km
72 549 km
dr[s]
ih[o]
0.77
0.34
9.65
0.31
2.55
0.45
1.90
0.39
0.01
0.40
2.35
0.38
20.05
0.34
0.07
0.31
3.78
0.32
0.64
0.23

Figure 4.25. Fitting of fast bands for events in Area D: Kuriles. Plotting conventions are the same as Figure 4.22. Fitting level in this area is also generally reasonable, but the orientation of the resulting fast bands is mixed. After the first teleseismic correction for Clayton-Comer deep mantle, results for events 121, 118, 127, 114, 129, 126 and 132 in depth range 375-585 km show fast bands along the trench direction, but have nearly vertical dip, and results are flat or variable for other events. After the second teleseismic correction, using teleseismic station averages of local events, fast bands for all five events deeper than 560 km are horizontally lying. Fast bands from almost all events differ from the seismic trend.

KURILE (a)

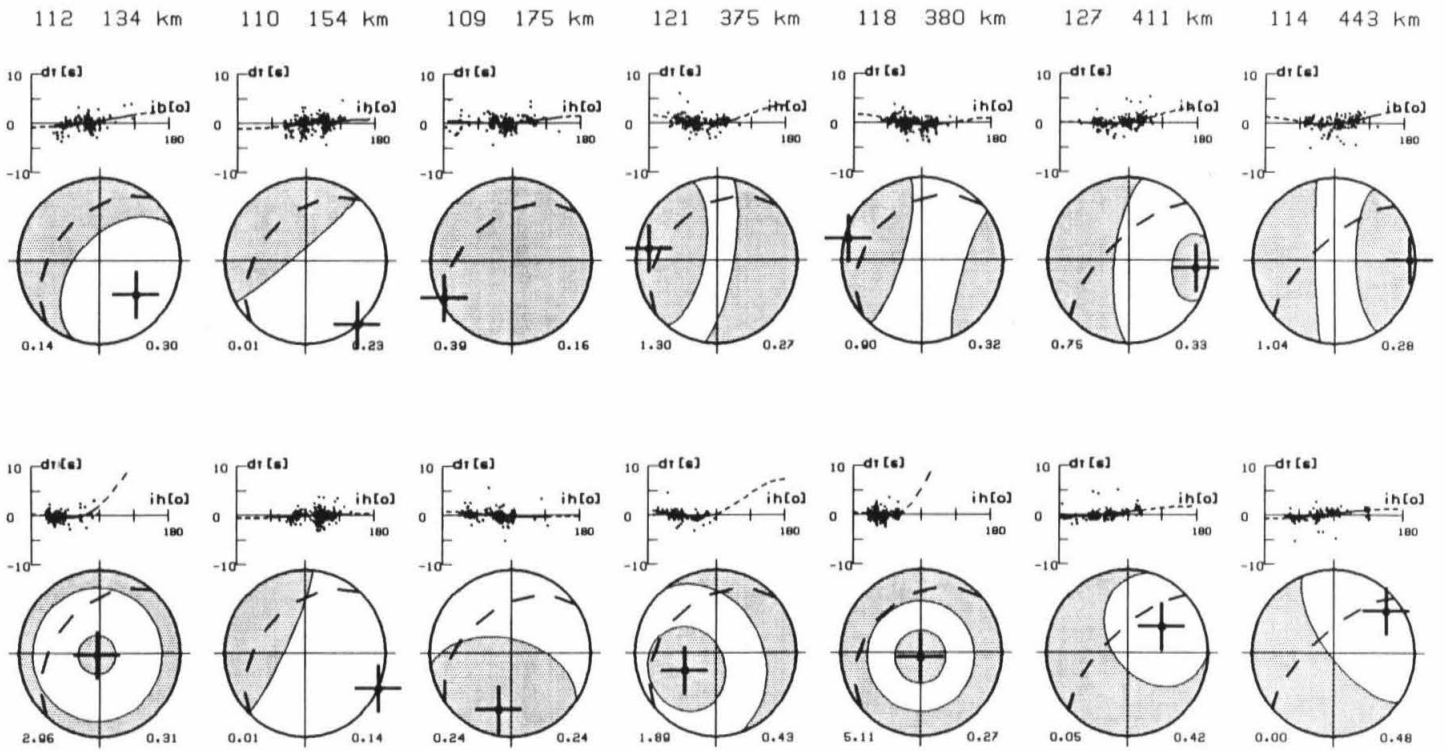
112 134 km
110 154 km
109 175 km
121 375 km
118 380 km
127 411 km
114 443 km
Corr. 1
Corr. 2
dt [s]
ib[o]
ih[o]
0.14 0.30
0.01 0.23
0.39 0.16
1.30 0.27
0.90 0.32
0.75 0.33
1.04 0.28
2.96 0.31
0.01 0.14
0.24 0.24
1.89 0.43
5.11 0.27
0.05 0.42
0.00 0.48

KURILE (b)

Corr. 1
Corr. 2
116 465 km
119 490 km
124 533 km
129 569 km
133 572 km
126 573 km
132 585 km
130 619 km
dr[s]
ih[o]

trend of the deep seismicity. Fitting level in this area is generally acceptable. After the first teleseismic correction for Clayton-Comer deep mantle, results for many events in depth range 375-585 km show fast bands along the trench direction but have nearly vertical dip, but results are flat or variable for other events. After the second teleseismic correction, using teleseismic station averages of local events, fast bands for five deepest events ($>$ 560 km) are all horizontally lying.

4.7 Modeling of Regional Geoid

This section is a minor part of the chapter, namely, the prediction of surface gravity anomalies from the inversed velocity models. The characteristic gravity anomalies over major subduction zones have long been recognized (e.g., Hatherton, 1969; Grow and Bowin, 1975) with a landward high (positive), although the total effect of a descending slab is thought to be too small to obtain a detailed configuration of the slab [Watts and Talwani, 1975]. On a global scale, Hager [1984] has recently fitted the long-wavelength geoid with a fluid mechanical model including cool subducting slabs. This type of modeling also provided a test on tomographically obtained three dimensional velocity models [Hager *et al.*, 1985].

The gravitational contribution of a large dynamic system such as the earth is not a trivial matter. The integrated effect sometimes is contrary to intuition, such as the apparent opposite sign of geoid due to deformation of

compositional boundaries [Hager *et al.*, 1985]. According to Hager [1984], the total geoid anomaly resulting from a given density contrast in a convecting earth is affected not only by the density contrast itself, but also by the mass anomalies associated with the flow-induced deformation of the upper surface and internal compositional boundaries. Hence, gravity anomalies, particularly their amplitude, cannot restrict detailed slab morphology. On the other hand, when we restrict ourselves to the upper mantle and concentrate on short wavelength features only, a comparison in pattern between the observations and a simple static computation of gross gravity due to the regional upper mantle velocity models is quite meaningful as a interesting test. The static computation, corresponding to the rigid-earth calculation by Hager [1984], is performed for the gravitational potential of the top 800 km of velocity structures of Chapter 2.

According to Anderson [1967], the density contrast with respect to the one-dimensional (lateral homogeneous) model can be expressed as

$$\delta\rho = \left[(\Phi_3/\Phi_1)^{0.323} - 1\right]\rho_1 \tag{4.4}$$

where the subscripts 1 and 3, respectively, denote the values in the reference one-dimensional model and the three-dimensional structures. ρ is density, and Φ is the seismic parameter, which is a function of compressional velocity V_P and shear velocity V_S

$$\Phi = V_P^2 - \frac{4}{3}V_S^2. \tag{4.5}$$

Using the above equations and density distribution in the PREM model [Dziewonski and Anderson, 1981], the upper mantle P and S wave velocity models are converted into a density contrast for the northwest Pacific region. Figure 4.26a shows the gravitational potential map from the upper mantle density contrast structure with a static computation [Zhou, 1984]. The computed pattern is compared with the spherical harmonic expansion of the observed geoid in degree 6 to 9 in Figure 4.26b, which best correlates the prediction according to Table 4.2.

Hager [1984] found that the degree 4-9 components of the observed long-wavelength geoid are highly correlated with those predicted by a density model for seismically active subducted slabs. It is not a surprise that the best correlated components in this regional modeling are of higher degrees. As shown in Figure 4.26, the computed pattern is very similar to the observed, with a broad high over the landward part of the Japan trench. The amplitude of the computed features is about five times that of the observed at degree 6-9 components. Nevertheless, the amplitude is a minor part of the comparison because, firstly, as being mentioned above, such a static calculation cannot handle the amplitude aspect. Secondly, much of the power in the observation are contained in components other than degree 6-9. Thirdly, the regional model makes the prediction more circular over the center of the region and therefore tends to bulge up features of size comparable to the region.

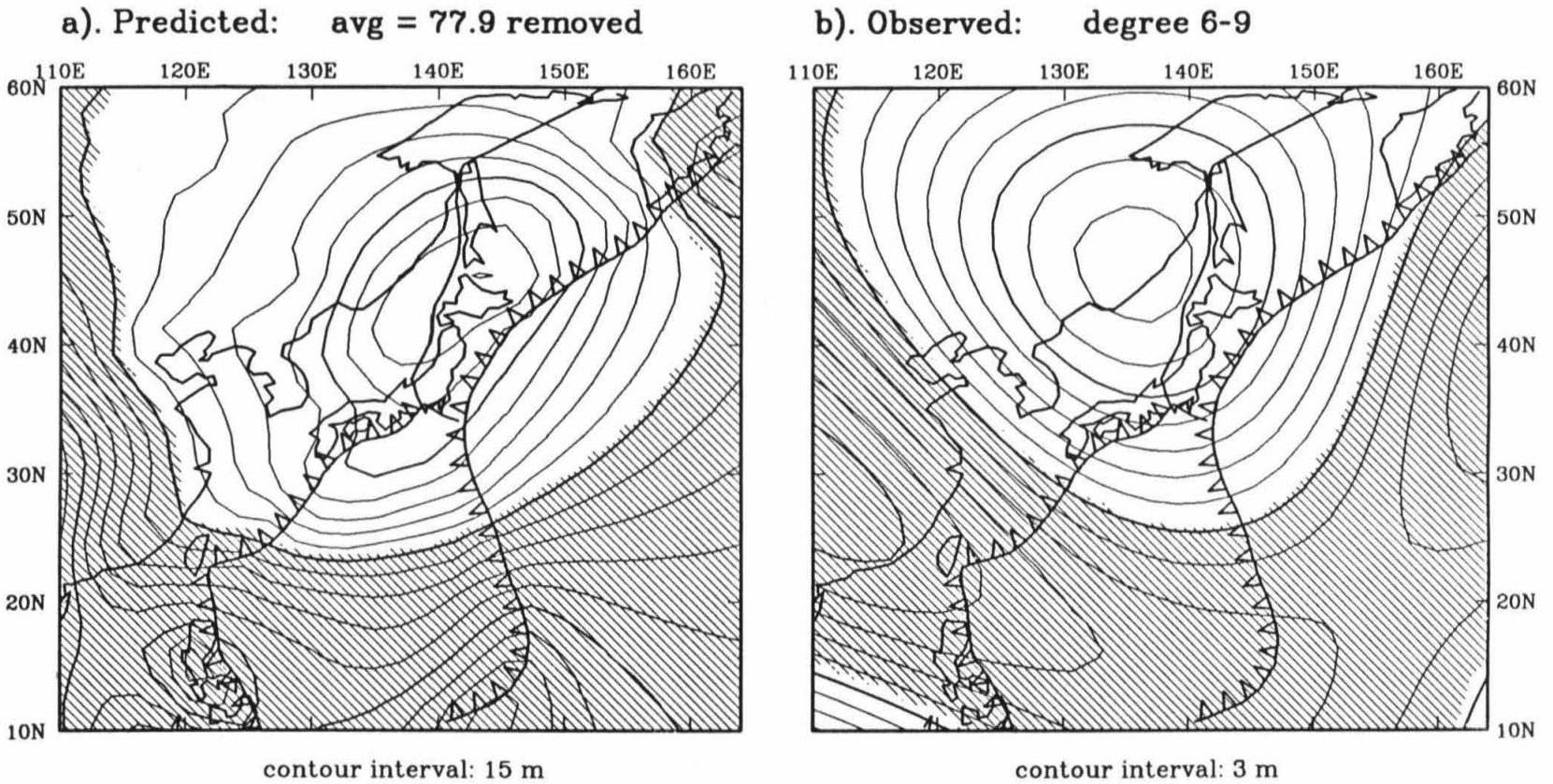

Figure 4.26. A comparison of the gravitational potential. a). computed gravitational potential based on the top 800 km of the P and S wave velocity models obtained in Chapter 2; b). the degree 6-9 components of the observed geoid.

Table 4.2 Correlation of predicted gravitational potential with the degree l_{min} - l_{max} components of the observed geoid.

l_{max}	l_{min} 4	5	6	7	8	9
5	-0.073					
6	0.012	0.156				
7	0.225	0.500	0.722			
8	0.347	0.635	0.754	0.681		
9	0.445	0.710	0.798	0.742	0.693	
10	0.401	0.666	0.770	0.734	0.643	0.401
11	0.409	0.657	0.753	0.720	0.609	0.394
12	0.407	0.663	0.764	0.724	0.622	0.383
13	0.406	0.658	0.750	0.707	0.587	0.347
14	0.399	0.651	0.748	0.710	0.589	0.339
15	0.396	0.643	0.741	0.701	0.571	0.319
16	0.397	0.641	0.741	0.703	0.571	0.323
17	0.400	0.645	0.743	0.706	0.576	0.333
18	0.401	0.648	0.747	0.708	0.580	0.340
19	0.402	0.647	0.746	0.707	0.579	0.342
20	0.400	0.644	0.744	0.707	0.578	0.340

4.8 Discussion

Earlier work on the fate of the subducting slab involved the analysis of residual sphere data alone [Jordan, 1977; Creager and Jordan, 1984, 1986]. Penetration of lithospheric slabs into the lower mantle was proposed. However, raw residual sphere data is extremely noisy, a fact not readily apparent from published data which is heavily smoothed. The interpretation of raw or smoothed residual spheres is not unique since the pattern can be caused by velocity heterogeneities other than subducted slabs. In fact, high-velocity trends on the residual sphere can be due to the following:

1. near source fast anomalies such as extensions of the slab or, in a layered mantle, thermal coupling between the upper and lower mantles
2. near source anisotropy, due to shear induced alignment of anisotropic crystals in the slab or in the mantle surrounding the slab
3. deformation of interfaces or phase-change boundaries
4. large scale coherent structures in the lower mantle which define bands when projected onto the focal sphere
5. large scale structures in the upper mantle beneath the recording stations.

Attempts are made to remove the latter effects (near-station effects) by removing station corrections from the data. However, results in the previous section indicate that a station correction term obtained from a global data base may include only the effect of shallow region beneath the station.

Residual spheres are computed using three-dimensional regional and global mantle velocity models and are compared with observations. The regional mantle model includes all major subduction zones of the northwest Pacific. The complexity of the upper mantle in this region yields complex residual spheres which exhibit rapid and short wavelength variations that can alias the smoothed results. Travel time residuals have been integrated through different portions of the mantle model in order to isolate the locations of major velocity heterogeneities causing slab-like residual sphere patterns. The following are some points to be addressed in more detail.

Inferred contribution from each portion of the mantle. Among the three portions of the whole mantle model (upper, middle, deep), the upper mantle portion, as expected, shows the strongest slab signature. But the upper mantle model alone generally underestimates the variation on the residual spheres, particularly for deep events.

The middle mantle, depths 650 km to 1500 km below the earthquakes, is the region important to the deep slab penetration hypothesis. The top portion of the middle mantle also includes part of the region where flattening and fingering of fast slab-like anomalies have been suggested [Zhou and Clayton, 1987, 1988]. Amplitude contribution (Figures 4.5 to 4.18) and correlation coefficients (Table 4.1) for the middle mantle model are low for most events, indicating that the middle mantle has the lowest contribution to the predicted residual sphere patterns in comparison with upper mantle and deep mantle models. The relatively smaller and more homogeneous residual accumulations

in the middle mantle model are often overwhelmed by the contributions from other portions of the mantle since they overlay the same area on a residual sphere. In fact, the middle mantle has lower amplitude anomalies and exhibits less coherency relative to the upper mantle, while the ray paths in the deep mantle are much longer and more widely separated relative to those in the middle mantle.

For most events presented, down-going rays from deep events are primarily perturbed from their normal travel times by the deep mantle (between a depth of 1500 km and the receivers) and are only secondarily affected by middle mantle heterogeneities. The deep mantle predictions of travel time anomalies are often similar to the patterns which would be caused by near source fast slab-like anomalies. This is due to the fact that the long wavelength heterogeneity of the deep mantle sometimes mimics a long slab when projected onto the residual sphere. The deep mantle model is characterized by low amplitude but long-wavelength seismic velocity anomalies. For example, most of the lower mantle between the northwestern Pacific and North America or Europe is fast, while paths to the Pacific, New Zealand and central Asia are slow or mixed (Figures 4.3 and 4.16). The anomalies are of small amplitude, but are spatially consistent over large areas, and therefore the delay time values accumulate to the level observed in residual sphere projection.

For deep mantle propagation from the Mariana source region (e.g., Figure 4.5), about 1 sec negative (fast) residuals accumulate in the NW (European) and SE (New Zealand, Eastern Australia) quadrants, while most easterly and

ESE directions (central Pacific) are slow. These anomalies combine to give a trend, as mapped on the focal sphere, approximately the same as the trend of the northern part of the Mariana arc. They are, however, unrelated to present subduction under the Mariana trench. Even though we know that there are some fast heterogeneities in the top portion of the middle mantle in this area, the fast band in the residual sphere is clearly exaggerated by the deep mantle contribution. In Northern Japan the data exhibit a continuous band of fast arrivals in the northern quadrants (northern Europe, Canada) extending from W to NE. This is due to the fast deep lower mantle encountered by rays going to these locations. For events in the Kuril-Kamchatka area, the deep mantle contributes mostly fast velocities in the northern quadrants and slow velocities to the south and southeast (New Zealand to the central Pacific), which is also evident in the velocity maps of Figure 4.3. The upper mantle contributes to the fast arrivals in the SW quadrant (India and southeast Asia), which combine with the deep mantle and, to a lesser extent, the middle mantle anomalies, to give the appearance of a continuous fast band having more-or-less the trend of the arc in this region.

Reliability of the mantle P wave models. A major finding in this chapter is that apparent slab-like patterns in residual spheres may be caused by diffuse mantle heterogeneities other than subducted slabs. The relative influence levels of slabs and other heterogeneities may vary at different locations. Although the above finding has been confirmed in section 4, it also quantitatively depends on the velocity model, particularly the regional model,

used. The reliability of the regional mantle model of Zhou and Clayton [1988] is discussed at great length in the original paper (also in Zhou [1988]). They calculated resolution and did tests on synthetic models and also derived similar P wave and S wave structures. The residual spheres that include rays of take-off angle greater than 90° (the upper hemisphere) provide an additional check on this model.

In most mantle velocity tomographic inversions, the amplitude of heterogeneities at depth is usually underestimated. For our modeling, the underestimation will primarily effect predictions from middle mantle and deep mantle models. In this sense, the ratio between residual sphere predictions from the middle mantle and deep mantle models will be less affected. In addition, the magnitude of the predicted residual spheres for most events in this chapter are comparable to that of the observed, indicating that the magnitude underestimation for the current study is perhaps not too serious.

The large fast heterogeneity pattern in the deep mantle model, taken from Clayton and Comer [1983], is also evident in the studies of Dziewonski [1984], Hager *et al.* [1985] and Dziewonski and Woodhouse [1987]. The origin of these large heterogeneities is unknown, but we can rule out the possibility that they are totally artifacts from the inversions because of the following: a) Similar patterns are not observed in the middle mantle model; b) crossing rays used in the construction of the deep mantle model are from many more sources and receivers than only those of the northwest Pacific subduction region; and c) the dominant fast trend in the pattern does not always agree with the strike of the northwest Pacific subduction zone, due to the

geometrical variation of the latter. Nevertheless, the pattern usually gives a long wavelength signature to residual spheres which has about the trend of the northwest Pacific subduction zones. It is not always appropriate, therefore, to attribute the long wavelength part of the residual sphere to near-source effects. Conventional smoothing of residual sphere data is not adequate to resolve the location of the mantle anomaly.

Items a) and b) above make it less likely that upper mantle or near source anomalies are severely projected into the lower mantle, a real danger if only earthquakes from the study region were used in the lower mantle tomography. Normal residual sphere analyses, in particular, have this defect, having no crossing rays to cancel out projected near source artifacts.

About Shear Waves. Tanimoto (1988) has recently derived an S wave structure for the whole mantle using SH body waves and long period Love waves. From a depth of 1600 km to the core-mantle boundary, the lower mantle is fast beneath most of the subduction zones of the western Pacific. Furthermore, great circle paths along strike of the NW Pacific subduction zones travel in faster than average velocity in the lower mantle and emerge through faster than average upper mantle under North America and SE Asia. The lateral variations are of the order of 0.5 to 1%. A similar pattern is found in the lower mantle shear velocity model displayed in Dziewonski and Woodhouse (1987). For lower mantle shear wave travel times of 500 seconds, this would give anomalies of 2.5 to 5 seconds. This is a large fraction of the variation actually observed on an S wave residual sphere (Jordan, 1977) and

which has been attributed to deep slab penetration.

Most of the power in the long-wavelength variation of the lower mantle is in harmonics of degree 1, 2 and 3 (Tanimoto, 1988). This long wavelength power maps onto the residual sphere as long wavelength anomalies. Thus, the basic assumption of the deep slab penetration hypothesis, namely, that long wavelength variations on the residual sphere are due to near source velocity anomalies, is false.

In the first S wave study of residual spheres in the Sea of Okhotsk area, Jordan (1977) noted that in the NW and SE quadrants the residuals are generally positive, whereas in the NE and SW quadrants the residuals are generally negative. "The broad spatial coherence of this pattern suggests the existence of velocity heterogeneity in the vicinity of the source." Precisely the same pattern is obtained in this region using the deep mantle model, even though the residual anomalies are integrated more than a thousand kilometers below the source. Additional negative residuals are picked up by rays traveling in the upper mantle toward the SW. The combination of the fast patches contributed by the deep mantle and the upper mantle gives the appearance of a single fast band which Jordan (1977) interpreted as a slab signature from the middle mantle region.

Previous Residual Sphere Modelings. There have been two previous attempts to compare residual spheres predicted by velocity models with actual residual sphere data (Dziewonski, 1984, Creager and Jordan, 1986). It is difficult to judge the reliability of a tomographically obtained velocity model,

and comparison with residual sphere data is one test of such models. In the above studies the general patterns are similar, but the lower mantle model L02.56 (from Dziewonski, 1984 in each case) predicts residual amplitude much smaller than observed. This is probably due to the damped minimum-norm procedure used to obtain the lower mantle model. This tends to minimize the perturbations. In order to help the reader judge the reliability of the residual sphere predictions, I have used a different lower mantle model [Clayton and Comer, 1983]. Some details of this model and the procedures used to derive it are in Hager and Clayton [1989]. In long wavelength characteristics, it is similar to L02.56 in pattern, but different in amplitude [Hager *et al.*, 1985]. Relatively short wavelength perturbations of the lower mantle, not included in the L02.56 spherical harmonic model ($l=m \leq 6$), also contribute to residual sphere anomalies. An anomaly of degree 6 in spherical harmonic expansion has a lateral length of over 50°, certainly not small for residual sphere analysis. The comparison between computed and observed residual spheres for the deeper earthquakes is a direct test of the reliability of the deep mantle model, and our results can be compared with similar tests performed in the above mentioned studies.

Dziewonski [1984] also showed that the lower mantle was responsible for a large part of the character of the residual sphere. The source region does not generally dominate the large-scale patterns of observed travel time residuals. We agree that large scale structure of the lower mantle is important in the residual sphere at long wavelength. A basic premise of some previous studies is that the long wavelength pattern is due to near source structure, in particular,

deep slabs. Creager and Jordan explicitly correct for the effects of Dziewonski's lower mantle and conclude that the correction is minor, but helps in the variance reduction. In contrast, we conclude that the lower mantle and near receiver effects are more likely to be dominant, particularly for the deeper events. My computed deep mantle patterns using the Clayton-Comer velocity model have long wavelength components that are much larger in amplitude than in the Dziewonski model. Dziewonski also points out that his model underestimates the residual sphere variations by about a factor of two, even in non-slab regions. His method of smoothing and damping is expected to underestimate the total variation, particularly since he uses a minimum-norm inversion algorithm. He also subtracts out the azimuthal parts of the station residuals. These are expected to contain much of the information about lower mantle structure. Thus, it is perhaps not surprising that correcting for the Dziewonski lower mantle does not affect Creager and Jordan's conclusion about near source heterogeneity and deep slab penetration.

Fitting for Near Source Fast Velocity Trend. The fitting for the fast bands in residual spheres does not need *a priori* assumptions about the size, location or orientation of the fast slab-like anomalies. It can also detect shallow dipping slab-like anomalies which would not be detectable in previous studies. The reliability of a fast band obtained by this method depends on both the coverage of data, as indicated by the residual vs. colatitude graph, and the correlation coefficient of the fitting. The best fitting fast trend for every event fitted are plotted, although some fits are not very successful

because of limited coverage.

The orientation of the detectable fast bands after the two teleseismic corrections resemble each other well for events under Mariana, Izu-Bonin and Japan trenches. The resemblance indicates the similarity of the two corrections. The fast bands in these areas are quite consistent and generally agree with the seismic trends. Particularly, the predominant fast band for most deep earthquakes under Japan is subhorizontal; and the results for events under the Izu-Bonin trench are consistent with a previous finding [Zhou and Clayton, 1989] that the slab in this area subducts steeply and flattens to subhorizontal around 500-550 km in a "fingering" process. Under the Mariana trench where the slab descends near vertically, the amplitude of the fast bands decreases with depth. The fast bands for the Kuril events are very inconsistent after two types of corrections and different from the seismic trend.

The subducting lithospheric slab in the northwest Pacific, as indicated by the fitting results of some residual sphere data in this chapter, may extend below the deepest earthquakes. In the best case here for events in the Mariana area where the slab dips nearly vertical and fast bands in residual sphere follow the seismicity trend well, shallow to deep events show a general decrease in slab signature. Unfortunately, the depth extent of the slab cannot be uniquely determined by the residual sphere method without assuming the velocity anomalies. For example, the amplitude of the slab signature (the C_2 term) for the deepest event, event 3, ISC depth 624 km, is about 0.5-0.7 sec. This value means a 100-120 km depth extension of a 5% fast velocity slab in a background velocity of 10 km/sec.

4.9 Conclusions

I have analyzed P wave travel time residual spheres of 145 best observed subduction zone earthquakes along the northwest edge of the Pacific. The observed residual spheres are compared to predictions of a composite upper mantle-lower mantle velocity model, constructed by embedding a regional model into a global mantle model, both from previous travel time inversions. The composite model explains much of the residual sphere data in pattern, including some short wavelength features, and in amplitude. This modeling approach is suggestive as to the locations of the mantle heterogeneities that cause the residual sphere anomalies.

The predicted residual spheres for the upper mantle model alone do not, in general, explain the pattern or amplitude of the observed residual spheres, particularly for the deeper events. The region immediately below the deepest earthquakes, depths from 650 km to 1500 km, usually does not control the residual sphere pattern, having an effect comparable to or smaller than the effect of the remaining mantle regions. Many residual sphere anomalies, similar to the expected signature of a fast subducting slab, are actually caused by diffuse deep mantle and near receiver heterogeneities that have no clear connection with a deep slab near the source. Without correcting for these teleseismic effects, it is impossible to determine even the orientation, not to say the depth extent, of the subducting slab based on the residual spheres.

Two types of teleseismic corrections are suggested, either by using a reliable mantle model or by using teleseismic station averages based only on

events in the study region. A method to detect a slab-like fast band in residual sphere is devised by seeking the best fitting low degree harmonics. Application of this method to residual sphere data of 44 earthquakes in the Northwest Pacific indicates consistent fast bands under the Mariana, Izu-Bonin and Japan trenches, but rather variable fast trend under the Kuril trench. The orientation of the fast bands generally agrees with the seismic trend under the Mariana and Japan trenches, and for regions shallower than 500 km under the Izu-Bonin trench. The amplitude of the fast bands decreases with depth under the Mariana trench where the slab descends near vertically, while no such decreasing trend is found under Japan where the slab is in a subhorizontal dipping. The fast bands for deep Kuril events are quite different from the seismic trend, and they are flat after correction for the teleseismic station averages.

Finally, the static gravitational potential from the upper mantle velocity models of Chapter 2 are computed. The prediction potential has a similar pattern with the degree 6-9 components of the geoid observed over the region, indicating that the velocity model probably satisfies the weak constraint of gravitational patterns.

References to Chapter 4

Anderson, Don. L., A seismic equation of state, *Geophys. J. R. astr. Soc.*, **13**, 9-30, 1967.

Clayton, R. W., and R. P. Comer, A tomographic analysis of mantle heterogeneities from body wave travel times, *Eos Trans. AGU*, **64**, 776, 1983.

Creager, K. C., and T. H. Jordan, Slab penetration into the lower mantle, *J. Geophys. Res.*, **89**, 3031-3049, 1984.

Creager, K. C., and T. H. Jordan, Slab penetration into the lower mantle beneath the Mariana and other island arcs of the northwest Pacific, *J. Geophys. Res.*, **91**, 3573-3580, 1986.

Davies, D., and D. P. McKenzie, Seismic travel-time residuals and plates, *Geophys. J. R. astr. Soc.*, **18**, 51-63, 1969.

Dziewonski, A. M., Mapping the lower mantle: determination of lateral heterogeneity in P velocity up to degree and order 6, *J. Geophys. Res.*, **89**, 5929-5952, 1984.

Dziewonski, A. M., B. H. Hager, and R. J. O'Connell, Large-scale heterogeneities in the lower mantle, *J. Geophys. Res.*, **82**, 239-255, 1977.

Dziewonski, A. M., and Don L. Anderson, Preliminary reference earth model, *Phys. Earth Planet. Inter.*, **25**, 297-356, 1981.

Dziewonski, A. M., and F. Gilbert, The effects of small, aspherical perturbations on travel times and a re-examination of the corrections for ellipticity, *Geophys. J. R. astr. Soc.*, **44**, 7-17, 1976.

Dziewonski, A. M., and J. H. Woodhouse, Global images of the earth's interior, *Science*, **236**, 37-48, 1987.

Grow, J. A., and C. Bowin, Evidence for high density crust and mantle beneath the Chile trench due to the descending lithosphere, *J. Geophys. Res.*, **80**, 1449-1458, 1975.

Gudmundsson, O., J. H. Davies, and R. W. Clayton, Stochastic analysis of global travel time data: mantle heterogeneity and random errors in the ISC data, *submitted to Geophys. J.*, 1989.

Hager, B. H., Subducted slabs and the geoid: constraints on mantle rheology and flow, *J. Geophys. Res.*, **89**, 6003-6015, 1984.

Hager, B. H., and R. W. Clayton, Constraints on the structure of mantle convection using seismic observations, flow models, and the geoid, in W. R. Peltier, ed., *Mantle Convection*, Gordon & Breach, in press, 1989.

Hager, B. H., R. W. Clayton, M. A. Richards, R. P. Comer, and A. M. Dziewonski, Lower mantle heterogeneity, dynamic topography and the geoid, *Nature*, **313**, 541-545, 1985.

Hatherton, T., Gravity and seismicity of asymmetric active regions, *Nature*,

221, 353-355, 1969.

Jordan, T. H., Lithospheric slab penetration into the lower mantle beneath the Sea of Okhotsk, *J. Geophys.*, **43**, 473-496, 1977.

O'Connell, R. J., Pleistocene glaciation and the viscosity of the lower mantle, *Geophys. J. R. astr. Soc.*, **23**, 299-327, 1971.

Stacey, F. D., Physics of the earth, *2nd ed., New York: Wiley*, 414 p., 1977.

Tanimoto, T., Long wavelength S-wave velocity structure throughout the mantle, submitted to *Geophys. J. R. astr. Soc.*, 1988.

Watts, A. B., and M. Talwani, Gravity effect of downgoing lithospheric slab beneath island arcs, *Geol. Soc. Am. Bull.*, **86**, 1-4, 1975.

Zhou, H., Prismatic method in solving the gravitational potential, with applications at Cerro Prieto geothermal field, Northern Mexico, *Masters thesis*, California State University at Long Beach, 1984.

Zhou, H., How well can we resolve the deep seismic slab with seismic tomography? *Geophys. Res. Lett.*, **15**, 1425-1428, 1988.

Zhou, H. W., and R. W. Clayton, Travel-time inversion for P and S velocities beneath the northwest edge of the Pacific: slab fingering? *Eos Trans. AGU*, **68**, 1379, 1987.

Zhou, H., and R. W. Clayton, P and S Wave Travel-Time Inversions for Subducting Slab under the Island Arcs of the Northwest Pacific prepare to submit to *J. Geophys. Res.*, 1988.

CHAPTER 5

SEISMIC STRESS IN THE SLAB
as inferred from focal mechanisms

Abstract

Focal mechanism solutions from CMT and other previous studies in the NW Pacific and Tonga-Kermadec regions are analyzed. These regions include most of the subducting slabs in the world where earthquakes occur nearly continuously throughout the depth range of the upper mantle. Abnormal stress patterns are seen at major junctions of the arcs. The depth boundary between tension and compression in the central parts of these arcs appears to depend on the dip and topology of the slab. The boundary is generally smooth and shallower than 150-200 km according to the available data, although it is much deeper at certain places such as the Mariana arc. P and T axes from the focal mechanisms are presented in comparison with tomographically derived velocity structures of Chapter 2 and Chapter 3 for these regions. Deep compression axes and fast velocity slab anomalies are in consistent alignment, even when the slab is contorted or flattened.

5.1 Introduction

In this chapter the seismic stress regime in the slab, as inferred from available earthquake source mechanism solutions, is examined. From a seismological point of view, two important aspects of observations about the slab are its seismic morphology and state of stress. Our knowledge about the

morphology of the slab has relied primarily on the geometry of Wadati-Benioff zone earthquakes and seismic high-velocity, low-attenuation slab anomalies. These anomalies, which are interpreted as being primarily due to cold subducting lithosphere (e.g., Toksöz *et al.*, 1971), have been observed beneath Japan and other arcs to depths of at least several hundred kilometers (e.g., Utsu, 1971; Hirahara, 1981). Slab-like fast anomalies in the upper mantle depth range are evident in recent three-dimensional tomographic inversions (e.g., studies described in previous chapters of this thesis, and published results by Zhou and Clayton, 1987, 1988; Kamiya *et al.*, 1988; and Zhou, 1988).

The state of stress in slabs is inferred primarily from stress axes of focal mechanism solutions for mantle earthquakes. Analyses by Isacks *et al.* (1968) and Isacks and Molnar (1969) suggested that earthquakes deeper than about 70 km occur within the descending lithosphere in response to stresses in the slabs. The primary support for their suggestion is that the down-dip direction of subduction is usually parallel with the compressional or tensional stress axes. In examining the relationship of earthquake stress axes to the orientation of Wadati-Benioff zones (in two-dimensions), Isacks and Molnar (1971) found consistent down-dip compression in the slabs below about 300 km depth, and down-dip tension or mixed stress at depths shallower than about 300 km. Actually, about half the focal mechanisms between 200 and 300 km indicate down-dip compression, and most of the mechanisms below 215 km are compressional (Anderson, 1979). Recent global reviews of intermediate-depth earthquake mechanisms in association with subduction process can be found in Astiz *et al.* (1988) and Lay *et al.* (1989).

The research described in this chapter extends the analysis of earthquake stress axes in subduction zones into three-dimensions to explore the variation of state of stress in slabs along their strike, and to reveal the relationship between the stress axes and seismic morphology of the slabs based on seismicity and high velocity anomalies. This analysis is enabled by the availability of a large quantity of reliable focal mechanism solutions and detailed tomographic velocity images around some major subduction zones.

This chapter concentrates on two West Pacific regions: from Kuril via Japan to Mariana and from Tonga to Kermadec. These include most of the subducting slabs in which earthquakes occur nearly continuously throughout the depth range of the upper mantle. The particularly dense earthquake mechanism solutions in these two regions allow mapping of the boundary which divides the deep down-dip compression regime from the shallower down-dip tension or mixed stress regime (PT boundary). The relationship between earthquake stress axes and seismic morphology of deep slabs in three-dimensions furnishes new insight into the physical state of slabs.

5.2 Earthquake Stress Axes

As described in the previous section, earthquake stress axes in this thesis are referred to principal stress axes in a focal mechanism solution, specifically, a double-couple mechanism solution.

5.2.1 Earthquake focal mechanisms

Observations of first-motion and radiation patterns of most earthquakes as well as theoretical considerations show that a double-couple mechanism solution is the most appropriate model for forces involved in an event (e.g., Sykes, 1967; Kanamori, 1970; Dziewonski *et al.*, 1981). It is therefore common practice to obtain a double-couple fault-plane solution of each earthquake to match the first-motion and radiation data. The principal axes of a double-couple mechanism solution, i.e., the P (compressional), T (tensional) and B (null) axes, are also principal stress axes if the fault plane is a plane of maximum shear. Following previous studies (e.g., Isacks *et al.*, 1968) the principal axes from the double-couple solutions are assumed to be coincident with the principal stress axes in the slab. As shown in earlier studies, the inferred stress axes tend to be parallel or perpendicular to the down-dip direction of subduction, thus justifying the above assumption, at least for events deeper than 70 km.

Most shallow earthquakes ($<$70 km) in subduction zones occur in response to either relative motions between lithospheric plates, or bending and faulting of the plates near trenches (e.g., Christensen and Ruff, 1983, 1988). They are excluded from the analysis in this chapter.

5.2.2 Compilation of the data

Compared to ten years ago, an order of magnitude more earthquake source mechanisms is now available. This is due to the development (Dziewonski *et al.*, 1981; Kanamori and Given, 1981) and routine determination of source parameters by moment tensor inversions using new digital data. Valuable products are the centroid-moment tensor (CMT) solutions of medium to large magnitude events since 1977 by the Harvard group (Dziewonski and Woodhouse [1983], Giardini [1984], and Dziewonski *et al.* [1983a-c, 1984a-c, 1985a-d, 1986a-c, 1987a-g, and 1988a-f]).

As shown in Table 5.1 the focal mechanism data in this study consists of over 800 solutions from published seismic first-motion and radiation pattern studies in the two west Pacific regions. The solutions are grouped into many area slices (cross sections), whose locations can be found in Figures 5.4 and 5.5. The solutions in each slice are in the ascending order of focal depths.

About 80% of the solutions are from CMT catalogs of the Harvard group (up to the end of September, 1987). The compilation also includes events from the original collection of Isacks and Molnar (1971), and solution sets by Chandra (1971), Oike (1971), Stauder and Maulchin (1976), Sengupta and Toksöz, (1977), Billington (1978), Richter (1979), Fujita and Kanamori (1981) and Astiz *et al.* (1988). The solutions are generally well constrained. No attempt is made here to discard or modify any of the mechanism solutions. Although there are several dozen solutions for events occurred before 1960, most of the data covers the time period from 1960 to 1987. As shown in Figure 5.1 and Figure 5.2, the observed P and T axes are projected onto map

Table 5.1 Compilation of deep and intermediate-depth focal mechanisms.

Slice	No.	Date	Lat. (°)	Lon. (°)	Depth (km)	m_b	T Axis δ (°)	T Axis θ (°)	P Axis δ (°)	P Axis θ (°)	Ref.
N1											
	1	11/ 6/77	53.34N	159.97E	94.0	5.2	62	98	27	292	CMT
	2	7/25/60	54.00N	159.00E	100.0	6.9	26	182	46	301	FK
	3	11/24/71	52.90N	159.19E	106.0	7.3	49	300	41	120	ALK
	4	11/14/82	52.77N	158.74E	110.0	5.9	37	142	53	318	CMT
	5	6/ 1/84	53.60N	159.52E	114.8	5.3	40	111	43	330	CMT
	6	8/25/85	53.61N	159.29E	134.7	5.3	49	102	39	302	CMT
	7	7/ 6/87	53.09N	158.45E	157.5	-	33	138	57	320	CMT
	8	7/24/83	53.81N	158.46E	177.4	6.1	45	139	43	298	CMT
	9	4/16/87	54.83N	157.84E	333.1	5.0	21	34	51	277	CMT
N2											
	1	4/25/83	51.13N	157.07E	100.6	5.2	58	98	32	270	CMT
	2	10/13/81	51.39N	156.92E	112.2	5.3	20	248	66	102	CMT
	3	1/ 7/80	50.73N	157.51E	121.5	5.6	21	182	40	292	CMT
	4	3/ 2/86	51.54N	157.26E	126.3	5.6	23	105	64	314	CMT
	5	8/22/79	51.89N	158.01E	126.7	5.6	44	67	30	303	CMT
	6	12/26/64	51.90N	156.70E	145.0	-	45	120	45	300	IM
	7	3/31/87	53.05N	156.62E	191.2	5.2	28	195	17	294	CMT
	8	3/18/64	52.60N	153.70E	424.0	-	45	140	45	320	BJ
	9	8/ 1/65	52.73N	153.48E	446.0	-	24	215	23	316	OI
N3											
	1	9/19/87	50.37N	155.79E	72.4	-	32	300	58	114	CMT
	2	8/14/78	49.66N	156.32E	77.8	5.8	30	340	58	137	CMT
	3	9/ 8/87	49.46N	156.79E	105.1	-	28	283	52	150	CMT
	4	2/ 5/66	50.00N	155.40E	121.0	-	54	280	28	141	IM
	5	5/12/77	49.73N	155.19E	128.3	5.3	31	148	55	298	CMT
	6	8/ 8/82	50.91N	156.07E	136.9	-	47	281	40	127	CMT
	7	10/28/78	50.00N	156.28E	139.5	5.5	56	317	33	129	CMT
	8	1/29/63	49.70N	155.00E	143.0	-	48	328	40	122	IM
	9	9/21/77	51.04N	155.82E	212.7	5.6	33	129	54	334	CMT
	10	5/15/84	51.00N	154.32E	308.5	5.0	1	121	72	28	CMT
	11	10/12/67	52.20N	152.50E	476.0	-	20	93	46	331	IM
	12	8/ 5/86	52.91N	152.85E	511.5	4.7	30	90	60	271	CMT
	13	8/15/87	52.19N	152.35E	518.8	-	25	196	41	310	CMT
	14	12/30/79	52.38N	151.90E	548.7	5.4	33	115	54	270	CMT
	15	8/30/70	52.36N	151.73E	625.0	-	5	130	85	310	ST
N4											
	1	3/28/86	48.39N	154.58E	74.7	5.2	14	312	31	214	CMT
	2	9/ 3/78	48.94N	154.76E	117.6	5.5	47	150	41	311	CMT
	3	2/19/86	48.43N	153.17E	119.2	5.3	38	114	45	331	CMT
	4	3/22/72	49.06N	153.57E	134.0	6.8	30	114	58	311	SM
	5	12/ 1/67	49.50N	154.40E	136.0	-	51	325	36	117	IM
	6	5/30/85	48.76N	153.96E	150.7	5.5	31	316	57	159	CMT
	7	8/22/84	49.23N	153.08E	153.8	5.2	21	108	63	327	CMT
	8	9/ 1/65	51.29N	150.70E	501.0	-	7	252	35	347	OI
	9	6/ 4/84	51.20N	150.61E	505.6	5.2	30	76	29	327	CMT
	10	6/10/80	51.49N	150.27E	569.1	5.2	30	61	60	242	CMT

Table 5.1 (continued)

Slice	No.	Date	Lat. (°)	Lon. (°)	Depth (km)	m_b	T Axis δ (°)	T Axis θ (°)	P Axis δ (°)	P Axis θ (°)	Ref.
N5											
	1	4/20/78	46.51N	151.92E	78.7	5.5	40	74	35	308	CMT
	2	8/ 4/64	46.60N	151.40E	86.0	-	51	133	39	313	IM
	3	3/ 3/87	46.16N	152.40E	96.8	5.9	25	295	60	151	CMT
	4	8/28/83	46.21N	151.72E	97.5	5.5	38	112	40	243	CMT
	5	10/ 4/78	46.06N	151.52E	98.9	5.7	23	302	1	211	CMT
	6	12/10/77	47.29N	153.12E	119.0	5.2	15	219	26	121	CMT
	7	7/20/79	47.15N	152.72E	132.1	5.2	30	37	37	154	CMT
	8	10/30/83	47.57N	153.01E	133.7	-	49	309	41	132	CMT
	9	7/19/86	47.05N	151.32E	153.4	5.9	34	114	53	322	CMT
	10	6/19/77	46.38N	151.19E	157.4	5.6	37	94	44	317	CMT
	11	12/20/77	47.81N	153.12E	159.1	5.8	37	116	53	305	CMT
	12	7/10/78	48.27N	150.18E	343.7	5.1	25	123	64	291	CMT
	13	6/21/78	47.98N	149.01E	402.0	5.9	44	121	35	253	CMT
	14	1/ 4/87	49.53N	149.51E	505.4	5.1	28	96	58	308	CMT
	15	5/18/87	49.12N	147.39E	551.7	6.0	38	140	52	320	CMT
	16	1/29/82	49.15N	147.85E	553.8	5.2	21	73	44	321	CMT
	17	1/25/79	50.38N	148.63E	587.6	5.4	41	106	47	306	CMT
	18	7/14/87	49.59N	147.67E	588.6	-	51	142	30	279	CMT
	19	4/20/84	50.19N	148.77E	592.8	6.0	29	154	60	323	CMT
	20	11/27/82	50.22N	147.01E	628.0	5.6	68	82	22	261	CMT
N6											
	1	9/23/87	45.70N	149.57E	130.9	-	3	192	31	283	CMT
	2	1/29/78	45.65N	149.57E	159.0	5.5	46	358	14	103	CMT
	3	7/ 8/87	46.23N	149.53E	159.4	-	30	117	59	290	CMT
	4	8/17/61	46.40N	149.30E	160.0	6.7	35	130	50	275	FK
	5	6/10/79	46.48N	148.15E	271.0	4.9	46	348	21	234	CMT
	6	4/23/84	47.49N	146.56E	417.0	6.0	80	52	7	281	CMT
	7	2/23/85	47.31N	145.57E	429.3	5.4	44	137	36	272	CMT
	8	11/22/66	48.00N	146.80E	452.0	-	75	102	15	280	IM
	9	12/22/80	48.14N	145.95E	485.1	5.4	69	102	21	269	CMT
	10	2/ 6/81	48.24N	146.48E	517.1	5.3	55	134	21	258	CMT
	11	2/ 1/84	49.10N	146.31E	581.3	6.0	50	133	39	328	CMT
N7											
	1	3/14/86	43.79N	147.34E	78.3	5.8	28	336	54	115	CMT
	2	7/ 4/79	43.64N	146.53E	80.5	6.0	59	170	21	300	CMT
	3	4/ 5/86	43.99N	147.88E	83.0	5.3	0	150	27	240	CMT
	4	6/20/83	45.00N	147.54E	93.1	-	8	357	18	90	CMT
	5	4/11/83	44.03N	147.86E	101.5	5.7	38	10	40	140	CMT
	6	5/14/79	44.43N	147.05E	108.5	5.6	58	19	19	256	CMT
	7	12/10/85	43.76N	146.90E	120.0	5.3	26	7	46	127	CMT
	8	3/27/85	44.28N	146.78E	142.3	6.0	37	19	18	123	CMT
	9	5/18/87	44.84N	146.91E	145.1	5.3	61	19	26	228	CMT
	10	1/26/85	44.84N	146.60E	172.7	5.4	32	23	7	117	CMT
	11	12/ 6/78	44.74N	145.82E	181.0	6.7	18	22	28	282	CMT
	12	10/25/65	44.20N	145.30E	181.0	-	50	346	36	139	OI
	13	10/25/65	44.20N	145.30E	181.0	-	50	346	36	139	IM

Table 5.1 (continued).

Slice	No.	Date	Lat. (°)	Lon. (°)	Depth (km)	m_b	T Axis δ (°)	T Axis θ (°)	P Axis δ (°)	P Axis θ (°)	Ref.
	14	10/18/85	46.05N	146.10E	277.1	6.0	39	357	49	156	CMT
	15	6/30/64	46.60N	144.60E	383.0	-	43	18	36	151	IM
	16	8/ 1/65	46.82N	143.84E	384.0	-	27	207	17	306	OI
N8											
	1	5/31/86	43.12N	145.50E	70.7	5.4	28	4	59	157	CMT
	2	12/14/79	42.57N	144.73E	72.6	5.5	25	15	65	202	CMT
	3	6/23/64	43.20N	146.20E	76.0	-	48	356	36	142	IM
	4	10/28/78	42.68N	143.87E	82.0	5.1	55	22	24	251	CMT
	5	9/19/67	43.00N	145.20E	84.0	-	50	6	35	148	IM
	6	3/16/84	43.09N	146.42E	84.0	5.6	84	269	4	139	CMT
	7	5/23/78	42.57N	144.62E	87.8	5.6	36	25	32	142	CMT
	8	3/10/85	43.20N	145.81E	101.2	5.3	49	340	37	129	CMT
	9	2/18/80	43.42N	145.72E	124.3	5.4	28	350	62	163	CMT
	10	1/19/69	45.00N	143.20E	204.0	6.5	28	16	22	274	Cn
	11	7/14/82	45.62N	142.57E	328.7	-	43	28	11	287	CMT
	12	1/ 6/85	45.56N	143.06E	332.5	5.3	38	14	14	273	CMT
	13	5/ 7/87	46.67N	139.01E	442.2	6.1	53	38	18	283	CMT
N9											
	1	2/24/77	42.27N	142.31E	73.0	5.3	10	137	17	230	CMT
	2	3/19/72	40.83N	141.90E	76.0	6.0	2	46	24	315	SM
	3	12/ 2/81	40.75N	142.15E	83.3	5.8	3	176	27	84	CMT
	4	6/ 1/85	41.60N	141.94E	84.6	5.2	59	328	24	108	CMT
	5	1/14/87	42.73N	142.73E	89.4	6.5	38	349	52	177	CMT
	6	5/29/83	42.68N	142.98E	93.1	5.3	45	90	40	237	CMT
	7	9/12/81	42.70N	143.31E	105.3	4.9	12	167	3	258	CMT
	8	3/ 6/84	42.53N	142.83E	106.2	5.5	37	5	48	153	CMT
	9	6/21/84	42.46N	142.48E	106.5	5.5	37	38	24	148	CMT
	10	5/29/82	42.46N	143.20E	118.1	5.7	49	345	41	164	CMT
	11	1/23/81	42.20N	142.07E	120.9	6.3	35	335	55	146	CMT
	12	3/17/83	41.80N	139.97E	124.6	5.3	63	85	22	301	CMT
	13	5/21/64	42.90N	141.90E	129.0	-	64	120	22	333	OI
	14	12/ 6/85	43.10N	140.86E	152.1	5.1	50	170	40	355	CMT
	15	7/ 4/67	43.20N	142.50E	160.0	-	45	356	43	193	IM
	16	8/20/66	43.10N	140.60E	163.0	-	53	120	33	328	IM
	17	7/28/81	41.68N	139.97E	177.8	5.4	10	340	78	133	CMT
	18	6/21/79	43.63N	139.63E	241.5	5.4	65	125	20	344	CMT
	19	5/ 8/81	42.85N	138.37E	248.0	6.0	16	26	44	132	CMT
	20	5/31/81	44.72N	137.77E	280.8	5.4	22	7	19	104	CMT
	21	2/20/31	44.90N	135.80E	350.0	-	27	207	27	311	HIM
N10											
	1	6/ 8/77	38.40N	141.75E	81.6	5.5	32	21	11	284	CMT
	2	11/26/80	40.35N	141.12E	91.9	5.8	37	78	43	303	CMT
	3	11/27/80	40.14N	141.27E	108.7	5.4	45	34	33	264	CMT
	4	3/28/85	40.42N	140.17E	168.8	6.1	24	219	63	65	CMT
	5	6/ 9/80	40.68N	139.92E	172.1	5.6	55	83	19	324	CMT
	6	7/27/65	40.21N	139.36E	195.0	-	60	125	30	306	OI
	7	10/21/78	41.31N	135.41E	380.9	5.1	69	96	20	297	CMT

Table 5.1 (continued)

Slice	No.	Date	Lat. (°)	Lon. (°)	Depth (km)	m_b	T Axis δ (°)	T Axis θ (°)	P Axis δ (°)	P Axis θ (°)	Ref.
	8	6/15/78	43.37N	135.43E	381.6	5.2	37	57	29	301	CMT
	9	2/11/87	43.13N	132.16E	504.2	5.4	6	177	21	269	CMT
	10	2/ 3/77	42.59N	130.49E	504.7	5.0	30	16	21	274	CMT
	11	9/28/83	41.42N	131.78E	519.9	5.1	18	21	24	283	CMT
	12	12/25/79	42.93N	131.33E	543.0	5.0	52	97	36	299	CMT
	13	11/27/81	42.88N	131.12E	546.2	5.7	42	48	38	274	CMT
	14	8/ 6/65	41.39N	131.34E	554.0	-	14	20	26	283	OI
	15	4/10/69	42.02N	131.07E	564.0	-	17	10	32	268	ST
	16	4/15/84	42.73N	131.24E	566.8	5.0	39	79	32	319	CMT
	17	9/ 9/77	42.59N	131.86E	567.7	4.9	7	15	22	282	CMT
	18	10/ 8/83	44.18N	130.39E	572.8	5.7	70	80	20	261	CMT
	19	1/31/79	42.92N	130.95E	575.2	5.7	38	49	21	301	CMT
	20	3/ 9/77	41.48N	131.55E	578.6	5.9	58	86	29	295	CMT
	21	1/ 3/57	43.80N	130.60E	593.0	-	55	86	33	287	Hi
	22	8/16/79	41.97N	131.74E	604.4	6.1	59	76	26	294	CMT
N11											
	1	8/23/82	37.55N	141.35E	89.1	-	38	316	47	169	CMT
	2	7/28/85	37.20N	140.52E	109.0	5.3	41	145	36	275	CMT
	3	10/ 7/85	38.02N	140.41E	114.8	5.1	54	101	25	330	CMT
	4	3/ 4/59	37.60N	138.70E	219.0	-	7	246	23	350	Ic
	5	5/28/79	37.33N	136.82E	279.3	5.1	37	48	31	292	CMT
	6	2/ 3/82	36.83N	134.28E	341.6	5.4	1	184	9	274	CMT
	7	3/11/84	38.54N	135.09E	353.8	5.3	57	132	33	301	CMT
	8	3/ 6/78	38.34N	134.12E	430.1	5.1	42	145	22	256	CMT
	9	1/18/80	37.64N	133.52E	432.5	5.5	52	115	31	255	CMT
	10	5/31/35	38.60N	134.20E	450.0	-	7	27	41	291	Hi
	11	12/11/64	38.90N	130.22E	551.0	-	18	73	34	330	OI
	12	1/24/64	38.75N	129.54E	557.0	-	61	149	27	308	OI
	13	1/24/64	38.80N	129.50E	557.0	-	56	157	26	294	IM
	14	10/ 8/60	40.20N	130.00E	605.0	-	56	118	34	298	Hi
N12											
	1	2/27/83	35.83N	140.09E	73.4	5.9	74	286	15	85	CMT
	2	3/15/83	35.44N	136.57E	74.0	5.4	8	236	70	124	CMT
	3	9/23/80	35.83N	139.91E	75.3	5.4	16	66	74	239	CMT
	4	3/12/80	34.87N	140.29E	80.5	5.5	47	246	43	63	CMT
	5	8/12/82	34.25N	139.03E	113.0	5.3	23	50	16	313	CMT
	6	10/ 4/85	35.52N	139.74E	113.7	5.8	37	57	44	281	CMT
	7	5/14/54	36.00N	137.40E	225.0	-	29	198	49	71	RA
	8	10/ 8/78	35.95N	137.35E	257.6	5.3	39	234	51	55	CMT
	9	11/14/86	35.98N	136.72E	261.7	5.1	37	213	46	70	CMT
	10	10/26/52	34.30N	137.50E	290.0	-	8	178	24	272	Hi
	11	6/ 2/29	34.50N	137.20E	350.0	-	58	98	32	278	HIM
	12	8/13/67	35.30N	135.30E	357.0	-	28	330	59	124	IM
	13	5/ 5/32	34.60N	135.30E	360.0	-	45	55	45	235	HIM
	14	6/23/65	35.51N	135.56E	363.0	-	2	192	60	98	OI
	15	3/31/80	35.33N	135.59E	367.1	5.8	19	162	48	50	CMT
	16	-/-/29	35.00N	137.00E	386.0	-	15	150	50	265	OI

Table 5.1 (continued)

Slice	No.	Date	Lat. (°)	Lon. (°)	Depth (km)	m_b	T Axis δ (°)	T Axis θ (°)	P Axis δ (°)	P Axis θ (°)	Ref.
N13											
	1	10/20/80	32.93N	140.54E	81.0	5.6	28	79	54	303	CMT
	2	11/17/77	33.64N	140.40E	103.6	5.5	42	59	14	315	CMT
	3	11/29/83	32.48N	139.71E	126.1	5.7	31	79	40	318	CMT
	4	4/26/87	31.97N	139.49E	147.3	5.2	35	80	16	181	CMT
	5	5/ 1/65	33.48N	138.97E	230.0	-	27	72	52	302	OI
	6	6/25/36	32.40N	138.00E	300.0	-	43	76	43	282	HIM
	7	7/16/87	33.04N	137.97E	301.4	-	53	52	25	283	CMT
	8	1/ 6/81	32.81N	138.11E	304.5	5.4	27	50	34	299	CMT
	9	6/11/64	33.10N	137.89E	341.0	-	3	10	43	277	OI
	10	4/20/42	33.00N	137.80E	350.0	-	45	100	45	280	HIM
	11	3/ 5/81	32.05N	137.85E	357.4	5.1	58	116	30	275	CMT
	12	1/ 1/84	33.38N	136.81E	383.6	6.5	57	50	28	265	CMT
	13	4/22/80	32.10N	137.37E	388.1	5.7	38	57	44	278	CMT
	14	3/10/66	32.20N	137.70E	390.0	-	53	101	33	255	KS
	15	10/ 7/86	31.85N	137.37E	395.6	5.0	53	86	37	276	CMT
	16	3/ 7/78	31.90N	137.44E	434.4	6.9	57	46	30	254	CMT
N14											
	1	1/15/64	29.20N	141.10E	80.0	-	66	34	12	154	KS
	2	12/19/80	30.49N	141.03E	90.3	6.2	57	91	31	293	CMT
	3	9/ 6/82	29.18N	140.65E	155.6	6.6	11	51	39	312	CMT
	4	9/14/87	30.36N	139.77E	167.1	-	35	90	43	319	CMT
	5	1/14/79	29.08N	139.60E	363.9	4.9	29	111	59	311	CMT
	6	4/24/84	30.81N	138.46E	394.8	6.2	24	44	50	282	CMT
	7	4/10/85	29.92N	138.86E	398.1	5.8	26	52	58	270	CMT
	8	1/11/78	30.07N	138.74E	412.2	5.3	30	41	58	202	CMT
	9	5/19/87	29.90N	139.30E	421.5	5.5	68	53	17	271	CMT
	10	4/12/65	30.21N	138.68E	425.0	-	24	36	46	265	OI
	11	4/12/65	30.20N	138.70E	428.0	-	51	48	32	263	KS
	12	8/19/65	30.29N	138.58E	443.0	-	14	10	27	273	OI
	13	4/ 4/32	30.60N	139.50E	445.0	-	43	53	43	263	HIM
	14	3/ 6/84	29.60N	139.11E	446.0	6.3	39	44	44	261	CMT
	15	6/12/82	30.47N	138.10E	447.5	5.5	50	64	39	240	CMT
	16	3/ 5/84	28.86N	139.34E	455.6	5.1	35	38	54	236	CMT
	17	1/16/86	29.65N	139.39E	455.7	5.2	32	37	37	280	CMT
	18	6/23/82	29.03N	138.59E	466.8	-	19	57	60	290	CMT
	19	2/18/56	30.20N	138.10E	475.0	-	4	338	35	246	RA
	20	1/ 1/77	30.62N	136.80E	476.5	5.2	29	354	45	230	CMT
	21	5/31/81	30.71N	137.54E	482.9	5.1	14	349	53	239	CMT
	22	5/ 7/64	30.59N	137.84E	485.0	-	5	181	65	282	OI
	23	4/20/77	30.34N	137.70E	495.4	5.5	12	142	70	15	CMT
	24	7/18/78	30.39N	137.34E	497.8	4.9	14	336	45	231	CMT
	25	3/19/87	29.26N	137.80E	524.0	5.3	24	342	7	249	CMT
	26	12/29/77	28.50N	138.34E	538.4	5.2	24	358	58	220	CMT
	27	7/ 4/82	27.92N	136.48E	551.8	6.3	32	189	50	326	CMT
N15											
	1	6/ 5/85	28.84N	141.36E	79.7	5.1	66	199	24	13	CMT

Table 5.1 (continued)

Slice	No.	Date	Lat. (°)	Lon. (°)	Depth (km)	m_b	T Axis δ (°)	T Axis θ (°)	P Axis δ (°)	P Axis θ (°)	Ref.
	2	12/11/79	28.81N	140.83E	124.7	6.1	44	74	25	317	CMT
	3	4/16/80	27.90N	140.07E	231.8	5.4	30	221	38	338	CMT
	4	5/21/77	27.28N	139.72E	345.2	5.1	15	64	62	302	CMT
	5	12/16/80	28.34N	139.48E	384.2	5.3	11	77	56	331	CMT
	6	9/ 7/79	27.84N	139.40E	422.9	4.9	0	89	81	180	CMT
	7	12/ 3/85	26.90N	140.44E	425.4	6.1	16	129	68	356	CMT
	8	11/17/84	28.35N	139.72E	439.7	5.3	6	175	84	324	CMT
	9	5/13/77	28.12N	139.73E	439.7	5.8	25	60	60	275	CMT
	10	9/ 8/82	26.76N	140.49E	441.4	5.4	11	252	52	357	CMT
	11	4/ 3/85	28.40N	139.61E	455.1	5.9	24	36	55	265	CMT
	12	3/17/86	27.37N	139.81E	457.7	5.5	7	61	60	318	CMT
	13	10/ 4/85	27.56N	139.82E	467.7	5.6	16	49	61	287	CMT
	14	7/11/51	28.10N	139.90E	475.0	-	26	37	53	268	RA
	15	5/10/78	27.77N	139.68E	493.8	5.0	18	19	60	255	CMT
	16	9/10/85	27.14N	139.91E	496.9	5.8	21	35	60	263	CMT
	17	5/21/84	26.80N	140.07E	504.9	5.0	35	42	55	223	CMT
	18	1/17/80	28.24N	138.62E	507.0	5.3	84	38	5	241	CMT
	19	3/ 3/65	28.12N	139.51E	507.0	-	20	18	48	255	OI
	20	9/ 5/85	28.00N	139.40E	515.5	4.9	2	324	76	228	CMT
	21	2/ 3/86	27.84N	139.34E	516.0	5.7	28	1	38	247	CMT
	22	10/14/82	27.15N	140.23E	517.1	5.1	20	8	70	196	CMT
N16											
	1	3/15/78	26.22N	140.65E	270.1	6.1	23	70	30	326	CMT
	2	12/11/80	26.33N	140.23E	475.9	5.3	1	256	77	350	CMT
N17											
	1	2/28/86	23.93N	142.32E	87.7	5.1	23	148	19	50	CMT
	2	5/29/87	22.69N	143.31E	133.7	5.2	46	198	37	340	CMT
	3	7/ 7/85	22.41N	141.80E	252.6	5.4	7	103	73	218	CMT
	4	2/ 8/80	22.35N	141.74E	278.9	5.3	40	43	40	179	CMT
	5	5/25/79	24.01N	142.08E	578.7	5.5	29	193	56	46	CMT
	6	5/18/79	23.94N	142.66E	580.9	5.8	2	149	87	285	CMT
N18											
	1	12/ 4/84	22.46N	143.39E	100.0	5.8	27	174	59	322	CMT
	2	2/27/82	22.42N	143.45E	103.6	5.9	25	52	14	315	CMT
	3	11/29/79	22.45N	143.65E	113.3	5.3	32	199	19	301	CMT
	4	3/12/84	22.19N	143.63E	191.7	5.3	62	91	14	332	CMT
	5	7/27/77	21.61N	142.73E	296.0	5.1	77	266	5	18	CMT
N19											
	1	1/21/87	20.55N	144.78E	113.3	5.6	43	88	46	255	CMT
	2	7/24/77	19.30N	144.62E	409.1	5.4	5	230	74	338	CMT
	3	12/27/86	20.08N	144.17E	425.9	5.1	20	201	47	314	CMT
	4	8/15/78	19.74N	144.31E	488.9	5.4	17	134	73	317	CMT
	5	12/27/82	19.64N	145.07E	608.8	5.3	16	32	70	249	CMT
	6	3/ 7/62	19.10N	145.20E	683.0	-	0	49	90	49	KS
N20											
	1	6/17/77	18.78N	145.39E	82.7	5.6	21	189	15	93	CMT
	2	10/19/78	16.95N	146.14E	99.1	5.3	37	194	46	54	CMT

Table 5.1 (continued)

Slice	No.	Date	Lat. (°)	Lon. (°)	Depth (km)	m_b	T Axis δ (°)	T Axis θ (°)	P Axis δ (°)	P Axis θ (°)	Ref.
	3	5/ 2/85	19.05N	145.97E	113.4	5.1	21	179	52	60	CMT
	4	1/ 2/65	19.10N	145.80E	136.0	-	22	177	60	43	KS
	5	5/ 9/87	19.06N	145.42E	144.4	5.2	2	158	28	67	CMT
	6	9/14/83	18.07N	145.96E	148.4	6.0	12	187	42	85	CMT
	7	4/ 7/82	18.93N	145.42E	157.0	-	28	194	48	68	CMT
	8	9/ 9/78	18.42N	145.47E	193.0	5.2	56	202	19	82	CMT
	9	12/18/78	18.45N	145.42E	200.9	5.2	46	174	13	69	CMT
	10	10/14/81	18.24N	145.35E	202.5	5.0	55	207	29	65	CMT
	11	5/25/85	17.40N	145.60E	205.6	5.3	47	144	33	9	CMT
	12	5/24/77	18.36N	145.51E	206.1	5.7	47	161	6	64	CMT
	13	4/14/85	18.90N	145.10E	214.4	5.0	41	151	9	54	CMT
	14	5/13/79	18.79N	145.42E	215.6	5.9	48	152	4	58	CMT
	15	4/13/86	17.18N	145.57E	296.7	5.1	71	230	9	111	CMT
	16	12/25/79	18.44N	145.16E	576.0	5.4	15	58	41	314	CMT
	17	10/30/79	18.68N	145.27E	578.7	5.6	17	89	64	322	CMT
	18	10/17/79	18.54N	145.30E	583.8	6.1	0	260	55	350	CMT
	19	5/10/70	18.62N	145.41E	587.0	-	4	261	66	4	ST
	20	2/27/77	18.21N	145.30E	592.6	5.0	4	75	60	337	CMT
	21	1/ 4/82	17.92N	145.46E	595.2	6.1	13	256	77	78	CMT
N21											
	1	4/17/87	15.19N	145.71E	94.9	5.3	37	303	47	87	CMT
	2	11/ 7/77	15.09N	144.87E	263.8	5.4	18	133	54	17	CMT
	3	6/ 7/81	16.64N	145.15E	311.8	5.7	73	247	10	15	CMT
S1											
	1	4/13/86	15.35S	173.00W	73.4	5.3	29	185	32	75	CMT
	2	8/20/86	16.85S	173.18W	75.9	5.5	27	241	60	90	CMT
	3	11/14/78	15.87S	173.26W	76.2	5.4	53	230	37	51	CMT
	4	9/15/80	15.55S	173.57W	80.6	5.3	41	203	23	315	CMT
	5	4/15/86	15.63S	173.75W	84.4	5.3	53	113	35	274	CMT
	6	4/27/85	15.67S	173.35W	90.4	5.7	48	259	25	136	CMT
	7	4/27/82	16.54S	174.17W	91.3	-	47	57	30	288	CMT
	8	3/23/79	15.43S	173.95W	97.9	5.2	27	151	48	274	CMT
	9	11/29/86	16.06S	173.77W	100.5	5.3	70	114	16	330	CMT
	10	3/11/68	16.20S	173.90W	112.0	6.2	19	49	63	184	IM
	11	10/15/84	15.81S	173.40W	119.7	6.5	42	265	44	56	CMT
	12	10/19/84	15.93S	173.58W	124.5	5.7	51	270	39	91	CMT
	13	10/26/69	16.20S	173.90W	127.0	-	55	243	26	110	Ri
	14	10/17/86	16.47S	173.14W	129.8	5.3	39	237	38	108	CMT
	15	4/18/84	16.10S	174.02W	158.0	5.9	24	97	65	264	CMT
	16	1/22/80	15.92S	173.99W	173.1	5.3	55	264	34	69	CMT
	17	11/30/85	16.34S	174.19W	179.1	5.6	52	201	22	81	CMT
	18	4/26/80	15.38S	174.32W	185.2	5.5	29	256	58	103	CMT
	19	6/ 1/83	16.93S	174.39W	185.7	6.1	21	126	68	313	CMT
	20	8/13/81	15.91S	174.22W	188.0	5.4	64	190	26	358	CMT
	21	5/ 1/69	16.70S	174.60W	205.0	6.1	13	16	59	131	Ri
	22	6/ 4/74	15.89S	175.04W	256.0	6.3	39	286	50	106	Ri
	23	10/28/79	16.76S	174.74W	265.3	5.0	39	12	50	206	CMT

Table 5.1 (continued)

Slice	No.	Date	Lat. (°)	Lon. (°)	Depth (km)	m_b	T Axis δ (°)	T Axis θ (°)	P Axis δ (°)	P Axis θ (°)	Ref.
	24	2/25/84	16.78S	174.70W	269.0	5.7	36	351	52	195	CMT
	25	6/15/84	15.90S	174.66W	269.6	6.2	17	105	66	240	CMT
	26	5/29/83	15.82S	174.73W	275.6	5.5	17	111	72	305	CMT
	27	7/ 3/80	15.65S	174.66W	283.6	5.0	16	84	71	297	CMT
	28	7/12/80	15.89S	175.04W	287.5	5.3	23	97	59	321	CMT
	29	6/10/84	16.06S	174.93W	308.1	4.9	29	317	57	170	CMT
	30	6/ 5/85	15.47S	177.83W	380.3	5.1	5	298	85	118	CMT
	31	12/15/86	15.94S	177.30W	429.1	5.0	49	121	17	233	CMT
	32	9/ 6/86	15.60S	177.85W	435.8	5.0	79	27	10	187	CMT
	33	6/19/85	15.74S	178.01W	473.1	4.9	42	141	7	237	CMT
S2											
	1	7/30/82	18.45S	173.74W	70.3	5.5	36	258	47	116	CMT
	2	3/26/77	18.53S	174.15W	105.2	5.6	47	304	28	69	CMT
	3	8/11/77	17.77S	174.14W	106.0	6.3	39	71	49	270	CMT
	4	6/11/82	17.40S	174.09W	113.2	6.3	34	105	53	259	CMT
	5	2/ 1/85	17.67S	174.01W	127.3	5.6	37	110	52	277	CMT
	6	5/28/81	17.24S	174.19W	131.2	5.4	27	332	39	86	CMT
	7	4/25/86	17.17S	173.85W	139.6	5.3	52	269	38	90	CMT
	8	7/28/84	17.11S	173.93W	144.2	5.5	55	230	35	59	CMT
	9	10/30/84	17.07S	173.75W	150.3	6.0	53	273	36	103	CMT
	10	1/17/75	17.90S	174.60W	153.0	5.8	11	124	67	241	Ri
	11	1/15/72	18.30S	174.60W	155.0	-	43	123	37	257	Bi
	12	6/25/78	17.02S	174.22W	163.7	5.5	18	175	61	300	CMT
	13	8/15/83	17.23S	174.62W	180.7	5.5	16	117	73	320	CMT
	14	7/30/86	17.93S	175.21W	196.8	4.8	22	21	36	129	CMT
	15	3/21/82	18.49S	175.26W	217.3	5.8	27	115	60	267	CMT
	16	5/22/72	17.70S	175.20W	227.0	6.1	9	210	80	3	Ri
	17	3/ 4/67	18.40S	175.40W	228.0	-	32	144	32	258	Bi
	18	9/17/87	18.48S	175.30W	246.1	-	37	141	48	286	CMT
	19	10/13/84	17.93S	174.85W	250.9	5.2	30	118	60	288	CMT
	20	11/ 5/85	16.53S	177.59W	266.7	5.3	33	302	39	180	CMT
	21	6/15/84	18.15S	175.01W	271.7	5.1	30	335	20	78	CMT
	22	12/14/86	18.42S	174.94W	273.3	5.0	60	18	0	108	CMT
	23	4/26/87	17.05S	174.74W	277.4	5.4	1	0	72	268	CMT
	24	5/28/79	18.06S	175.31W	286.0	5.3	35	106	50	254	CMT
	25	7/31/84	16.92S	176.16W	297.8	5.1	39	68	50	263	CMT
	26	11/18/78	16.73S	176.90W	410.2	5.3	54	110	9	213	CMT
	27	4/25/84	17.31S	177.26W	418.4	5.7	42	116	44	265	CMT
	28	12/25/80	16.84S	178.76W	502.1	5.0	30	202	30	92	CMT
	29	4/13/87	16.85S	178.84W	530.6	5.0	10	127	26	32	CMT
	30	8/ 1/86	17.03S	178.91W	531.3	4.9	18	137	1	46	CMT
	31	7/ 3/84	17.51S	179.05W	533.4	5.7	60	334	6	232	CMT
	32	1/20/84	17.60S	178.77W	545.2	5.3	71	181	8	295	CMT
	33	7/29/86	17.56S	178.61W	559.7	5.1	5	57	49	321	CMT
	34	8/25/63	17.50S	178.70W	563.0	-	33	118	42	244	ISO
	35	11/26/77	17.30S	178.26W	568.6	5.5	23	117	41	229	CMT
	36	11/16/85	17.00S	178.69W	568.6	5.1	9	128	51	229	CMT

Table 5.1 (continued)

Slice	No.	Date	Lat. (°)	Lon. (°)	Depth (km)	m_b	T Axis δ (°)	T Axis θ (°)	P Axis δ (°)	P Axis θ (°)	Ref.
	37	8/23/79	17.42S	179.22W	576.5	5.3	48	357	21	241	CMT
	38	3/15/86	17.55S	178.84W	577.6	5.2	5	326	4	236	CMT
	39	11/ 9/79	17.13S	179.20W	588.0	5.5	49	43	37	252	CMT
	40	1/10/84	17.36S	178.71W	603.8	5.1	22	102	38	354	CMT
	41	11/22/84	17.72S	178.05W	663.0	5.8	2	222	14	312	CMT
S3											
	1	4/17/87	19.82S	174.18W	87.4	5.3	59	150	13	263	CMT
	2	11/14/69	19.70S	175.80W	209.0	-	34	91	54	251	Bi
	3	4/18/83	19.70S	175.70W	214.6	-	23	113	17	210	CMT
	4	3/18/65	19.90S	175.90W	219.0	6.0	37	140	32	79	ISO
	5	6/28/86	19.96S	175.71W	222.1	6.1	40	114	44	258	CMT
	6	12/27/71	19.90S	175.80W	224.0	-	22	162	32	267	Bi
	7	4/15/83	18.97S	175.60W	226.0	5.7	19	142	55	262	CMT
	8	7/10/86	19.58S	175.69W	226.2	5.2	46	139	38	283	CMT
	9	4/29/84	19.49S	175.62W	229.5	5.4	19	144	35	248	CMT
	10	4/28/79	19.35S	175.66W	229.7	5.3	39	88	46	301	CMT
	11	11/18/84	18.81S	175.21W	229.7	5.6	19	135	44	245	CMT
	12	11/30/80	19.23S	176.06W	238.0	6.0	43	123	46	292	CMT
	13	1/18/87	19.33S	175.60W	245.6	5.1	47	136	30	266	CMT
	14	11/ 6/84	18.58S	175.37W	246.7	5.4	34	124	53	279	CMT
	15	6/ 6/77	19.61S	175.57W	247.2	5.1	51	87	26	320	CMT
	16	9/15/85	19.19S	175.58W	258.0	5.7	27	130	58	272	CMT
	17	2/ 4/86	19.92S	175.39W	268.1	5.2	26	146	57	286	CMT
	18	1/22/87	18.91S	175.60W	278.4	5.1	65	116	25	282	CMT
	19	7/ 7/83	19.00S	177.47W	378.6	-	23	245	11	339	CMT
	20	4/29/87	19.06S	177.84W	410.6	5.9	54	195	22	318	CMT
	21	2/10/87	19.47S	177.38W	418.5	6.1	27	94	61	294	CMT
	22	11/18/65	18.80S	177.80W	424.0	6.2	37	173	37	300	ISO
	23	11/17/84	18.84S	177.96W	471.5	6.0	64	163	26	339	CMT
	24	9/ 1/84	18.08S	178.30W	485.7	5.4	18	225	34	328	CMT
	25	10/10/85	18.88S	178.01W	495.4	4.9	49	141	41	309	CMT
	26	5/15/77	19.37S	177.83W	506.4	5.5	19	93	71	278	CMT
	27	1/16/86	17.95S	178.18W	509.7	5.1	37	331	19	226	CMT
	28	2/23/85	18.97S	177.85W	526.1	5.1	26	147	63	338	CMT
	29	2/25/80	17.88S	178.63W	529.4	5.5	35	177	5	84	CMT
	30	4/14/77	17.79S	178.94W	533.4	5.2	14	177	75	11	CMT
	31	4/10/65	17.80S	178.80W	535.0	-	33	348	28	236	ISO
	32	7/17/87	17.90S	179.27W	537.9	-	19	25	37	280	CMT
	33	11/29/83	19.19S	177.97W	540.0	5.8	14	273	71	49	CMT
	34	11/27/86	18.02S	178.38W	547.5	5.1	27	160	25	264	CMT
	35	8/29/79	17.61S	179.09W	551.2	5.3	39	347	4	254	CMT
	36	4/22/77	18.54S	178.10W	554.3	5.5	24	150	54	277	CMT
	37	7/24/79	17.59S	179.02W	556.2	5.2	2	337	32	245	CMT
	38	9/25/82	17.58S	179.08W	556.8	-	7	213	69	322	CMT
	39	12/27/77	17.90S	178.85W	557.0	5.3	83	40	5	180	CMT
	40	9/30/84	17.85S	178.90W	560.5	4.8	53	349	17	235	CMT
	41	1/17/82	17.76S	179.04W	560.9	-	64	310	1	218	CMT

Table 5.1 (continued)

Slice	No.	Date	Lat. (°)	Lon. (°)	Depth (km)	m_b	T Axis δ (°)	T Axis θ (°)	P Axis δ (°)	P Axis θ (°)	Ref.
	42	6/14/80	18.34S	178.17W	561.0	5.6	47	145	43	323	CMT
	43	4/ 1/86	17.87S	178.57W	562.4	5.7	23	244	63	97	CMT
	44	12/30/86	19.13S	177.87W	563.2	5.2	6	315	53	54	CMT
	45	6/ 3/77	18.83S	178.02W	565.5	5.3	27	216	55	352	CMT
	46	7/29/79	17.91S	178.69W	566.5	5.4	49	108	41	274	CMT
	47	4/ 6/85	18.07S	178.45W	567.6	5.2	15	18	42	274	CMT
	48	10/16/78	17.70S	178.99W	568.8	5.4	69	323	0	233	CMT
	49	3/ 8/77	17.83S	178.78W	574.4	5.3	32	1	39	240	CMT
	50	10/ 5/77	18.66S	177.92W	575.2	5.6	21	108	69	285	CMT
	51	10/27/85	17.96S	178.78W	577.0	5.2	60	123	18	246	CMT
	52	2/14/87	17.76S	178.90W	577.9	5.7	53	0	9	258	CMT
	53	12/12/86	18.36S	179.13W	579.1	5.2	5	42	69	299	CMT
	54	5/25/83	18.66S	177.60W	581.5	-	4	58	74	314	CMT
	55	5/ 1/78	19.25S	177.64W	584.7	5.5	15	127	63	249	CMT
	56	7/21/66	17.80S	178.60W	590.0	5.8	6	189	27	95	ISO
	57	9/12/64	17.60S	179.70W	592.0	-	41	44	48	243	ISO
	58	1/31/87	17.58S	178.95W	592.2	5.2	52	353	13	246	CMT
	59	8/13/78	17.90S	178.42W	593.5	5.5	8	88	63	342	CMT
	60	4/27/86	17.89S	178.41W	594.4	5.2	26	108	64	277	CMT
	61	4/22/80	18.53S	178.37W	595.9	5.6	37	154	52	345	CMT
	62	11/ 6/86	17.79S	178.53W	597.1	5.4	17	9	59	249	CMT
	63	3/ 3/83	17.84S	178.37W	597.4	-	2	79	68	344	CMT
	64	5/25/77	17.68S	178.96W	598.3	5.4	19	0	28	259	CMT
	65	8/ 7/86	18.02S	178.27W	603.4	5.0	14	18	40	276	CMT
	66	5/17/78	18.11S	178.64W	604.7	5.1	63	335	5	75	CMT
	67	11/23/83	17.98S	178.52W	605.8	-	49	309	41	132	CMT
	68	1/21/77	18.30S	178.40W	607.0	5.8	27	67	63	255	CMT
	69	7/20/80	18.03S	178.75W	608.0	6.0	27	22	35	271	CMT
	70	1/ 1/82	17.96S	178.52W	609.8	5.5	33	25	32	272	CMT
	71	5/15/87	18.05S	179.05W	610.0	4.9	47	329	20	216	CMT
	72	3/29/86	17.84S	178.65W	618.3	5.3	32	342	18	240	CMT
	73	8/30/81	17.99S	178.35W	618.4	5.4	60	351	2	257	CMT
	74	5/17/87	17.89S	178.44W	619.3	5.3	48	13	6	277	CMT
	75	12/ 4/80	17.62S	179.90W	619.4	5.1	22	344	52	222	CMT
	76	8/11/87	17.94S	178.60W	621.5	-	45	45	13	302	CMT
	77	4/12/79	18.02S	178.26W	622.8	5.4	27	114	61	315	CMT
	78	8/ 6/87	18.30S	178.51W	623.8	-	44	97	46	290	CMT
	79	12/25/65	18.20S	179.10W	624.0	-	3	2	67	264	ISO
	80	10/18/77	18.30S	178.47W	629.4	5.3	40	23	35	257	CMT
	81	1/25/86	18.29S	177.76W	634.9	4.9	59	149	31	329	CMT
	82	1/28/82	18.02S	179.54W	639.2	5.4	48	45	40	246	CMT
	83	7/29/87	18.20S	178.35W	645.3	-	11	343	59	233	CMT
	84	12/ 9/65	18.12S	178.12W	649.0	5.7	3	8	46	94	ISO
	85	12/ 8/83	18.98S	178.27W	649.3	5.4	3	186	33	278	CMT
	86	7/29/87	18.05S	178.33W	654.0	-	5	343	53	246	CMT
	87	10/20/81	18.12S	179.57W	656.0	5.6	58	54	32	241	CMT

Table 5.1 (continued)

Slice	No.	Date	Lat. (°)	Lon. (°)	Depth (km)	m_b	T Axis δ (°)	T Axis θ (°)	P Axis δ (°)	P Axis θ (°)	Ref.
S4											
	1	8/10/66	20.20S	175.30W	95.0	-	29	62	54	282	ISO
	2	7/29/86	20.67S	175.71W	137.1	5.4	18	103	71	265	CMT
	3	8/26/87	21.14S	175.53W	141.7	-	59	258	25	115	CMT
	4	6/16/81	20.26S	175.42W	164.3	5.4	29	341	39	97	CMT
	5	4/10/82	21.11S	176.29W	198.1	-	50	114	40	283	CMT
	6	3/19/87	20.30S	175.96W	215.3	5.8	38	126	47	273	CMT
	7	10/14/79	20.08S	175.78W	216.5	5.4	23	120	42	233	CMT
	8	11/11/79	20.44S	176.20W	218.0	5.5	35	118	54	282	CMT
	9	3/ 2/84	21.18S	176.43W	231.3	5.4	21	120	67	274	CMT
	10	6/21/81	20.65S	176.44W	235.2	5.3	52	105	16	217	CMT
	11	12/19/73	20.60S	176.50W	246.0	-	43	138	42	288	Ri
	12	9/26/68	20.90S	176.70W	251.0	6.0	13	341	71	118	Ri
	13	2/18/70	20.80S	176.90W	259.0	-	41	112	38	342	Ri
	14	4/27/85	21.23S	176.81W	261.8	5.7	40	105	14	3	CMT
	15	1/ 6/83	19.93S	176.20W	280.1	-	4	250	33	343	CMT
	16	5/ 3/78	21.05S	177.68W	302.8	5.4	29	84	30	335	CMT
	17	11/15/84	19.81S	177.93W	305.3	5.7	23	260	38	9	CMT
	18	5/22/77	19.71S	177.31W	346.9	5.2	8	71	24	338	CMT
	19	5/21/62	19.90S	177.20W	351.0	-	38	98	50	294	IM
	20	1/14/77	19.72S	177.82W	358.2	5.2	29	250	39	8	CMT
	21	11/ 6/83	20.02S	177.86W	393.8	5.5	45	99	27	339	CMT
	22	6/16/81	20.37S	177.93W	408.3	5.0	29	91	47	324	CMT
	23	4/14/86	20.70S	177.61W	509.0	5.3	14	0	66	236	CMT
	24	11/13/81	20.76S	178.01W	512.9	5.5	27	94	60	302	CMT
	25	5/ 3/78	20.78S	178.05W	515.8	5.2	41	24	17	278	CMT
	26	10/ 7/78	19.99S	177.88W	522.7	5.1	4	159	61	256	CMT
	27	11/21/85	20.77S	178.17W	528.6	5.4	39	136	49	296	CMT
	28	2/ 5/85	20.96S	177.95W	533.2	5.3	13	12	53	263	CMT
	29	11/30/82	20.37S	178.31W	539.1	5.2	9	121	76	354	CMT
	30	3/15/85	20.57S	178.31W	539.9	5.5	8	61	51	321	CMT
	31	7/27/80	19.57S	179.64E	553.5	5.3	13	265	11	358	CMT
	32	10/ 3/80	20.08S	178.22W	558.8	5.4	12	18	45	276	CMT
	33	11/30/77	20.58S	178.62W	559.8	5.5	30	167	57	320	CMT
	34	3/22/80	20.80S	178.18W	560.3	5.0	10	201	53	304	CMT
	35	12/ 5/85	20.62S	178.46W	561.5	4.9	15	65	71	281	CMT
	36	8/11/79	20.45S	178.44W	561.7	5.3	18	161	70	8	CMT
	37	1/ 5/77	20.74S	178.59W	561.8	5.2	25	169	58	310	CMT
	38	5/11/87	20.51S	178.61W	568.6	5.3	40	149	50	318	CMT
	39	7/20/79	20.56S	178.53W	570.2	5.4	38	87	47	299	CMT
	40	7/20/84	20.67S	178.76W	574.6	5.2	1	20	74	288	CMT
	41	11/27/77	20.68S	178.49W	575.4	5.6	39	159	49	315	CMT
	42	3/14/84	20.16S	178.08W	576.1	5.7	45	129	43	326	CMT
	43	8/10/77	20.56S	178.72W	577.0	5.4	26	126	62	324	CMT
	44	6/28/79	20.68S	178.32W	578.6	5.3	24	132	61	277	CMT
	45	5/ 3/87	20.66S	178.73W	591.4	5.3	5	214	53	311	CMT
	46	5/ 3/83	20.21S	178.49W	592.1	-	3	220	57	315	CMT

Table 5.1 (continued)

Slice	No.	Date	Lat. (°)	Lon. (°)	Depth (km)	m_b	T Axis δ (°)	T Axis θ (°)	P Axis δ (°)	P Axis θ (°)	Ref.
	47	9/15/84	20.71S	178.71W	592.6	5.5	7	249	54	348	CMT
	48	9/ 6/86	20.43S	178.70W	593.2	5.2	35	111	55	301	CMT
	49	10/20/84	20.75S	178.39W	593.7	5.4	46	144	42	302	CMT
	50	10/30/77	20.72S	178.67W	595.4	5.6	26	197	46	316	CMT
	51	2/ 7/78	20.05S	178.60W	599.8	5.4	40	151	50	323	CMT
	52	2/19/78	20.57S	179.05W	600.0	5.4	40	170	48	334	CMT
	53	6/17/80	20.13S	178.55W	601.7	5.6	23	192	52	315	CMT
	54	5/ 2/83	20.52S	178.67W	604.9	-	25	125	65	314	CMT
	55	12/24/83	20.00S	178.48W	607.0	5.3	46	159	44	327	CMT
	56	8/ 1/77	20.50S	178.25W	611.3	5.3	27	104	37	351	CMT
	57	7/ 5/82	20.33S	179.20W	612.0	5.5	24	136	65	332	CMT
	58	8/ 6/85	20.10S	178.48W	613.8	5.4	55	165	33	323	CMT
	59	1/28/70	20.70S	178.80W	614.0	-	18	193	68	337	Bi
	60	2/18/80	20.39S	178.47W	614.8	5.3	5	228	24	320	CMT
	61	2/24/81	20.63S	178.88W	618.1	5.3	19	178	71	4	CMT
	62	5/28/82	20.10S	179.30W	621.7	5.3	9	143	75	17	CMT
	63	10/ 7/81	20.52S	179.00W	624.6	5.9	22	166	59	298	CMT
	64	10/29/79	20.28S	178.62W	625.4	5.3	13	195	35	294	CMT
	65	9/16/80	20.30S	179.46W	631.3	5.3	31	124	50	350	CMT
	66	2/ 6/81	20.59S	179.11W	637.0	5.6	13	183	71	313	CMT
	67	4/ 2/85	20.43S	179.28W	637.5	5.4	28	151	62	330	CMT
	68	8/ 7/85	19.44S	177.86W	643.4	5.3	6	198	16	289	CMT
	69	5/14/86	20.36S	178.99W	645.6	5.0	24	209	63	0	CMT
	70	9/ 8/85	20.42S	179.07W	651.1	5.0	29	141	58	292	CMT
	71	1/26/72	20.20S	178.90W	660.0	-	34	153	56	335	Bi
	72	10/22/85	20.49S	179.31W	684.5	5.0	59	105	30	302	CMT
	73	10/10/84	20.34S	179.29W	691.3	5.6	46	49	33	276	CMT
	74	6/17/77	19.86S	179.23W	693.9	5.7	18	61	42	314	CMT
S5											
	1	7/28/80	22.28S	175.36W	75.1	5.4	65	133	22	283	CMT
	2	3/23/71	22.90S	176.10W	77.0	-	44	108	44	268	Bi
	3	8/20/65	22.90S	176.10W	79.0	-	50	93	40	263	ISO
	4	8/25/81	22.47S	175.70W	108.0	5.8	7	248	27	155	CMT
	5	2/19/85	22.88S	176.35W	122.6	5.3	38	98	52	282	CMT
	6	6/ 6/81	22.29S	175.97W	130.8	5.4	30	116	29	225	CMT
	7	10/12/85	21.79S	176.08W	170.1	5.8	31	118	54	263	CMT
	8	3/25/86	22.15S	176.78W	189.0	5.1	48	115	42	300	CMT
	9	10/30/86	21.68S	176.45W	196.3	6.4	40	111	50	288	CMT
	10	12/17/85	21.86S	176.63W	201.3	5.1	34	107	49	324	CMT
	11	8/ 5/79	22.95S	177.10W	229.2	6.4	32	124	57	315	CMT
	12	4/29/79	22.38S	177.71W	236.9	5.4	4	83	59	347	CMT
	13	6/25/83	21.86S	177.34W	273.5	5.5	22	84	52	322	CMT
	14	4/28/69	22.40S	177.70W	296.0	-	24	246	11	342	Ri
	15	8/24/85	22.32S	177.72W	361.2	5.6	10	92	79	294	CMT
	16	2/18/79	21.00S	178.08W	378.1	5.1	43	252	17	358	CMT
	17	9/28/84	21.67S	177.73W	384.6	5.8	29	119	61	288	CMT
	18	10/26/85	22.04S	177.87W	396.1	5.0	23	140	62	282	CMT

Table 5.1 (continued)

Slice	No.	Date	Lat. (°)	Lon. (°)	Depth (km)	m_b	T Axis δ (°)	T Axis θ (°)	P Axis δ (°)	P Axis θ (°)	Ref.
	19	10/19/78	21.55S	177.81W	396.8	5.3	5	111	81	350	CMT
	20	12/25/85	21.68S	178.55W	461.8	5.6	30	138	44	15	CMT
	21	6/ 3/86	21.00S	178.04W	504.7	5.4	21	68	60	296	CMT
	22	1/ 7/86	21.26S	178.43W	531.5	5.2	2	199	87	336	CMT
	23	4/10/71	21.20S	178.80W	533.0	-	12	216	76	12	Bi
	24	5/22/65	21.10S	178.60W	540.0	-	14	208	71	347	ISO
	25	7/ 1/83	20.78S	178.60W	544.1	-	30	130	56	317	CMT
	26	10/17/78	20.90S	178.36W	547.0	5.4	14	55	44	312	CMT
	27	11/ 9/82	21.08S	179.02W	554.4	5.2	29	135	60	334	CMT
	28	7/16/82	20.99S	179.14W	562.0	5.6	16	216	56	331	CMT
	29	6/16/86	21.86S	178.87W	564.8	6.1	27	135	62	300	CMT
	30	5/26/86	20.24S	179.03E	567.5	6.8	40	174	43	34	CMT
	31	6/ 5/86	19.79S	178.46E	574.2	5.1	4	345	9	254	CMT
	32	3/27/79	21.74S	179.12W	574.5	5.3	17	292	48	42	CMT
	33	3/14/77	20.74S	178.80W	579.0	5.4	1	197	51	288	CMT
	34	7/18/79	21.31S	179.00W	581.5	5.3	28	136	62	308	CMT
	35	4/16/77	21.13S	179.35W	581.8	5.2	31	203	59	17	CMT
	36	8/26/87	20.80S	178.60W	588.3	-	39	103	45	316	CMT
	37	3/31/81	20.93S	179.43W	591.7	5.2	3	185	62	280	CMT
	38	10/ 2/80	20.65S	179.08W	592.3	5.3	19	61	55	302	CMT
	39	4/10/83	21.89S	179.77W	593.6	5.3	29	65	21	322	CMT
	40	1/24/69	21.90S	179.50W	595.0	-	38	94	43	314	Bi
	41	11/ 6/79	21.08S	178.88W	596.1	5.7	21	140	68	303	CMT
	42	7/ 6/77	21.18S	178.81W	596.2	5.8	17	94	52	341	CMT
	43	7/ 2/86	22.04S	179.49W	598.3	5.5	38	96	47	309	CMT
	44	7/17/86	22.06S	179.07W	599.0	4.8	37	160	35	283	CMT
	45	3/25/78	21.26S	178.82W	599.6	5.7	12	192	55	300	CMT
	46	12/ 2/81	21.60S	179.83W	599.7	5.6	37	94	48	304	CMT
	47	4/20/87	21.65S	179.17W	600.6	5.3	42	71	44	280	CMT
	48	10/27/78	20.65S	178.97W	601.6	5.3	28	150	60	304	CMT
	49	10/12/68	20.80S	178.70W	603.0	-	9	201	58	306	Bi
	50	7/10/77	21.80S	179.47W	603.3	5.3	48	135	40	292	CMT
	51	5/26/86	21.57S	179.30W	603.4	5.9	3	7	43	274	CMT
	52	10/ 2/67	21.00S	178.80W	604.0	-	34	186	53	339	IM
	53	4/24/79	20.81S	178.90W	604.2	6.0	23	158	66	350	CMT
	54	2/13/80	20.75S	179.20W	605.0	5.4	34	152	56	328	CMT
	55	2/20/86	22.01S	179.60W	607.0	5.6	45	109	42	313	CMT
	56	9/25/77	22.14S	179.24W	607.3	5.4	38	80	28	325	CMT
	57	1/15/80	22.01S	179.79W	607.9	5.5	20	86	70	255	CMT
	58	11/ 9/72	21.00S	179.00W	609.0	-	33	168	51	312	Bi
	59	1/30/80	21.63S	179.55W	609.4	5.4	39	95	41	320	CMT
	60	9/ 1/87	21.81S	179.44W	612.5	-	45	87	41	298	CMT
	61	12/21/78	21.98S	179.45W	612.8	5.6	48	108	40	311	CMT
	62	9/24/87	21.69S	179.68W	613.9	-	55	85	34	274	CMT
	63	1/30/85	20.69S	179.11W	613.9	5.2	20	38	21	299	CMT
	64	11/25/81	20.68S	179.07W	614.6	5.9	24	119	64	320	CMT
	65	12/17/77	20.91S	178.98W	615.5	5.1	30	164	59	326	CMT

Table 5.1 (continued)

Slice	No.	Date	Lat. (°)	Lon. (°)	Depth (km)	m_b	T Axis δ (°)	T Axis θ (°)	P Axis δ (°)	P Axis θ (°)	Ref.
	66	5/27/82	20.74S	178.96W	615.7	-	32	158	57	319	CMT
	67	4/22/84	22.05S	179.24W	616.6	5.7	59	163	25	303	CMT
	68	4/15/73	20.70S	178.80E	617.0	-	34	186	53	339	Bi
	69	2/19/80	22.17S	179.42W	617.2	5.4	69	130	21	294	CMT
	70	9/10/62	21.30S	179.10W	618.0	-	10	87	60	341	IM
	71	7/10/77	21.14S	179.14W	623.5	5.4	23	165	37	274	CMT
	72	8/23/79	21.26S	179.42W	624.5	5.1	69	215	6	322	CMT
	73	8/27/85	21.01S	179.00W	627.3	5.1	39	53	21	305	CMT
	74	11/27/85	21.01S	179.18W	627.4	5.2	42	145	48	339	CMT
	75	12/17/83	20.93S	178.94W	628.2	-	50	105	38	310	CMT
	76	3/17/66	21.10S	179.20W	630.0	6.2	24	300	64	132	ISO
	77	9/12/68	21.60S	179.30W	632.0	-	9	107	66	0	Bi
	78	11/16/84	21.55S	179.20W	633.3	5.2	54	114	34	272	CMT
	79	9/ 5/84	20.86S	179.29W	633.3	5.3	35	91	51	302	CMT
	80	6/25/77	20.98S	179.63W	633.7	5.4	44	108	45	269	CMT
	81	10/12/67	21.10S	179.20W	636.0	-	32	109	43	341	IM
	82	2/14/86	20.85S	179.14W	637.4	5.3	34	118	50	336	CMT
	83	8/28/85	20.89S	179.00W	640.4	5.9	22	126	68	315	CMT
	84	6/ 6/75	20.60S	179.10W	650.0	-	37	126	47	269	Bi
	85	2/22/80	21.75S	179.93E	652.3	5.3	50	56	25	293	CMT
	86	1/ 2/83	21.14S	178.32W	652.3	-	18	196	31	297	CMT
	87	10/ 9/67	21.10S	179.30W	654.0	-	40	138	48	330	IM
	88	12/14/77	21.01S	179.35W	657.6	5.6	22	100	53	337	CMT
	89	1/ 9/85	20.83S	179.11W	660.4	5.3	53	46	24	279	CMT
	90	11/30/85	20.83S	178.64W	662.1	4.9	9	233	74	354	CMT
	91	1/10/77	20.75S	179.70W	666.2	5.5	21	28	36	282	CMT
	92	11/28/79	20.85S	179.27W	678.0	5.4	46	101	42	298	CMT
	93	3/ 9/78	21.52S	179.41E	679.5	5.2	63	227	6	329	CMT
S6											
	1	6/29/85	24.51S	176.04W	70.8	5.2	74	260	14	114	CMT
	2	4/29/82	24.73S	177.37W	114.0	-	38	119	46	335	CMT
	3	9/ 6/86	23.15S	176.86W	128.8	5.6	21	101	68	273	CMT
	4	8/12/67	24.70S	177.50W	134.0	6.5	58	205	24	161	IM
	5	8/21/83	23.38S	176.72W	138.6	5.5	25	128	55	260	CMT
	6	5/12/80	23.58S	177.41W	151.9	5.5	60	175	27	326	CMT
	7	12/25/82	23.12S	177.24W	158.5	-	41	118	46	271	CMT
	8	5/31/84	23.41S	177.22W	159.4	4.8	62	115	9	8	CMT
	9	4/13/80	23.74S	176.70W	166.2	6.7	31	101	51	325	CMT
	10	1/27/86	23.72S	177.17W	169.4	5.1	27	61	42	303	CMT
	11	8/15/68	23.90S	177.20W	186.0	-	56	268	32	72	Bi
	12	1/ 4/82	23.21S	177.19W	190.5	6.0	31	115	58	312	CMT
	13	1/25/85	22.97S	177.39W	202.3	5.5	44	134	46	308	CMT
	14	11/10/81	23.13S	177.67W	232.7	5.2	29	85	59	291	CMT
	15	7/17/83	23.32S	177.39W	306.4	5.2	21	114	60	342	CMT
	16	1/19/84	23.65S	178.18W	335.7	5.9	50	104	38	262	CMT
	17	3/28/86	23.01S	178.79W	398.4	5.4	19	101	52	345	CMT
	18	8/ 8/77	23.44S	179.53W	445.1	5.2	6	18	33	112	CMT

Table 5.1 (continued)

Slice	No.	Date	Lat. (°)	Lon. (°)	Depth (km)	m_b	T Axis δ (°)	T Axis θ (°)	P Axis δ (°)	P Axis θ (°)	Ref.
	19	9/ 8/79	22.74S	179.11W	448.9	5.1	16	206	45	314	CMT
	20	9/30/78	22.91S	179.15W	467.3	5.4	30	143	56	291	CMT
	21	1/14/79	22.49S	179.39W	488.0	5.2	36	324	31	80	CMT
	22	3/21/84	23.49S	179.47W	499.5	5.1	46	44	42	243	CMT
	23	1/31/82	22.77S	179.15W	503.6	5.6	1	211	87	325	CMT
	24	9/16/83	23.61S	179.78W	517.3	5.9	39	55	36	289	CMT
	25	6/17/78	22.83S	179.83W	520.5	5.6	52	334	10	231	CMT
	26	2/11/87	22.44S	179.97E	524.1	5.1	47	43	43	211	CMT
	27	11/22/81	23.62S	179.67E	527.8	5.4	27	50	61	254	CMT
	28	6/27/83	23.71S	179.98W	528.9	-	29	81	46	316	CMT
	29	3/23/74	23.90S	179.80W	535.0	-	60	90	19	324	Ri
	30	2/ 8/81	22.82S	179.40E	535.7	5.3	31	61	53	279	CMT
	31	12/28/73	23.90S	179.90W	539.0	-	60	60	24	284	Ri
	32	11/20/71	23.40S	179.90W	543.0	-	55	74	35	245	Bi
	33	3/14/85	23.44S	179.98W	545.9	5.0	62	88	11	337	CMT
	34	2/ 7/82	23.34S	179.13E	546.3	-	3	73	55	168	CMT
	35	7/17/78	23.51S	179.87W	547.4	5.4	50	65	17	313	CMT
	36	10/ 7/63	23.60S	180.00E	548.0	-	51	73	33	284	ISO
	37	2/20/86	23.18S	179.86E	552.1	5.2	19	62	56	301	CMT
	38	4/28/81	23.62S	179.93W	553.3	6.0	47	63	31	291	CMT
	39	3/12/84	23.51S	179.79W	555.9	5.5	53	93	31	309	CMT
	40	5/18/78	23.08S	179.95E	558.1	5.3	17	81	58	323	CMT
	41	9/ 8/63	23.60S	180.00E	559.0	-	62	75	27	278	ISO
	42	9/17/82	23.15S	179.83E	561.5	5.9	53	81	34	284	CMT
	43	8/ 2/84	23.56S	179.93E	561.7	5.4	0	213	68	303	CMT
	44	9/29/85	23.28S	179.18E	566.2	4.9	8	49	66	157	CMT
	45	7/20/79	23.69S	179.89E	566.4	5.4	49	98	24	336	CMT
	46	9/14/86	23.16S	178.85E	571.3	5.2	2	238	62	144	CMT
	47	8/26/84	23.27S	178.67E	571.8	6.0	22	176	50	295	CMT
	48	7/10/85	23.45S	178.66E	572.2	5.1	11	215	78	57	CMT
	49	12/28/84	23.46S	179.05E	576.7	5.3	6	203	53	301	CMT
	50	12/28/64	22.20S	179.60W	579.0	-	46	162	38	305	ISO
	51	9/11/81	23.32S	179.16E	580.6	5.2	2	236	63	141	CMT
	52	4/ 4/87	22.65S	179.48W	585.7	5.3	42	83	48	270	CMT
	53	4/25/81	22.25S	179.41E	588.0	5.7	4	238	32	330	CMT
	54	5/20/84	22.65S	179.25E	591.4	5.2	26	276	64	102	CMT
	55	12/26/80	22.06S	179.87W	591.6	5.5	22	42	67	241	CMT
	56	11/25/79	22.16S	179.54W	593.4	5.4	49	63	39	266	CMT
	57	9/25/84	22.06S	179.87W	594.9	5.1	59	5	12	115	CMT
	58	7/23/87	23.35S	179.73E	594.9	-	25	345	65	169	CMT
	59	1/17/84	22.15S	179.98W	596.8	5.6	33	36	24	289	CMT
	60	12/22/82	23.59S	179.41E	597.0	-	4	28	22	297	CMT
	61	4/ 8/71	22.20S	179.50W	598.0	-	64	341	6	92	Bi
	62	12/ 8/83	22.20S	179.60W	598.6	5.4	65	89	24	287	CMT
	63	7/ 8/79	22.20S	179.73W	600.4	5.5	32	79	52	295	CMT
	64	10/23/77	22.32S	179.15W	600.9	5.0	45	98	29	334	CMT
	65	8/17/78	22.06S	179.76W	607.5	5.6	10	151	65	264	CMT

Table 5.1 (continued)

Slice	No.	Date	Lat. (°)	Lon. (°)	Depth (km)	m_b	T Axis δ (°)	T Axis θ (°)	P Axis δ (°)	P Axis θ (°)	Ref.
	66	12/22/86	23.02S	179.23E	618.1	5.2	19	220	34	323	CMT
	67	8/ 3/84	22.64S	179.02E	621.6	5.1	5	28	64	129	CMT
	68	11/24/80	22.36S	178.66E	636.3	5.3	7	164	56	264	CMT
	69	2/10/69	22.70S	178.80W	670.0	-	35	207	45	343	Bi
S7											
	1	1/20/70	25.80S	177.30W	80.0	-	53	159	37	331	Ri
	2	2/ 6/79	25.41S	177.03W	82.6	5.4	24	65	51	302	CMT
	3	1/28/78	25.95S	177.35W	97.6	6.0	51	105	29	334	CMT
	4	4/12/71	26.70S	177.10W	101.0	-	65	102	10	349	Ri
	5	7/27/86	25.98S	177.42W	109.2	5.8	29	106	35	353	CMT
	6	8/ 1/68	26.60S	177.50W	123.0	5.6	44	210	3	305	Ri
	7	1/ 4/85	25.73S	177.61W	138.6	5.3	56	156	34	348	CMT
	8	2/ 7/83	26.54S	177.80W	157.4	-	33	91	50	311	CMT
	9	7/ 4/63	26.30S	177.80W	190.0	-	1	71	39	339	ISO
	10	11/23/78	26.55S	177.95W	190.5	5.5	37	224	38	350	CMT
	11	7/21/64	26.00S	177.90W	200.0	-	47	107	42	308	ISO
	12	9/16/78	25.47S	178.22W	235.2	5.7	28	72	27	327	CMT
	13	9/ 7/81	25.65S	178.01W	262.5	5.2	17	266	5	358	CMT
	14	2/22/75	24.98S	178.88W	333.0	6.6	32	79	51	115	Ri
	15	2/ 7/84	25.41S	178.88W	355.1	5.4	30	36	38	279	CMT
	16	4/19/82	25.97S	178.81W	357.9	-	43	97	43	249	CMT
	17	7/21/73	24.83S	179.19W	373.0	6.1	39	284	49	124	Ri
	18	8/17/81	25.40S	179.44W	396.9	5.5	38	94	51	258	CMT
	19	10/24/81	24.74S	179.46W	398.2	5.2	35	100	27	349	CMT
	20	3/17/72	24.80S	179.60W	415.0	-	50	344	8	243	Bi
	21	5/ 7/77	25.79S	179.83E	462.3	5.4	23	52	28	309	CMT
	22	11/ 3/82	24.83S	179.75E	467.7	5.3	37	76	48	289	CMT
	23	2/ 3/76	25.14S	179.70W	477.0	6.0	58	103	30	276	Ri
	24	4/ 3/87	24.93S	179.42E	477.8	5.2	33	101	56	300	CMT
	25	3/23/78	24.73S	180.00W	481.5	5.5	61	19	26	227	CMT
	26	7/ 3/79	24.14S	179.75W	494.3	5.1	6	138	82	281	CMT
	27	5/27/81	25.23S	179.37E	499.6	5.3	34	95	48	233	CMT
	28	9/20/84	24.46S	179.97E	505.1	5.3	35	97	48	236	CMT
	29	10/13/85	25.02S	179.73E	506.7	5.0	39	88	51	260	CMT
	30	1/29/79	24.24S	179.81E	509.4	5.5	36	86	54	261	CMT
	31	11/12/84	24.90S	179.66E	512.2	5.1	47	92	34	315	CMT
	32	4/ 5/81	25.03S	179.63E	521.4	5.3	57	98	21	332	CMT
	33	2/21/85	24.19S	179.96E	521.4	5.0	13	75	62	320	CMT
	34	8/ 2/85	25.31S	179.69E	523.4	5.1	18	94	60	330	CMT
	35	2/16/83	25.23S	179.49E	526.6	5.4	47	88	36	307	CMT
	36	7/26/81	24.06S	179.71E	531.1	5.2	58	76	28	290	CMT
	37	3/30/72	25.70S	179.40W	532.0	-	46	61	28	295	Ri
	38	9/26/84	24.17S	179.89E	534.0	5.0	58	79	19	317	CMT
	39	12/ 3/86	23.93S	179.92E	539.1	5.2	45	81	39	296	CMT
	40	12/26/86	24.39S	179.75E	539.7	4.9	53	48	26	277	CMT
	41	11/18/86	24.37S	179.92W	540.9	5.3	61	90	25	300	CMT
	42	8/20/87	24.16S	178.89E	542.3	-	33	58	33	303	CMT

Table 5.1 (continued)

Slice	No.	Date	Lat. (°)	Lon. (°)	Depth (km)	m_b	T Axis δ (°)	T Axis θ (°)	P Axis δ (°)	P Axis θ (°)	Ref.
	43	2/ 9/80	23.78S	179.26E	556.3	5.3	4	41	82	158	CMT
	44	1/17/65	24.60S	178.40E	557.0	-	34	228	54	69	ISO
	45	7/17/80	23.58S	178.83E	558.1	5.0	19	30	55	149	CMT
	46	8/ 6/86	24.09S	179.98E	558.4	5.0	66	116	21	321	CMT
	47	5/12/82	24.64S	179.08E	559.8	5.6	42	105	36	334	CMT
	48	6/20/83	23.68S	179.23E	561.9	5.6	21	12	66	160	CMT
	49	3/29/79	24.09S	178.19E	568.6	5.4	31	253	56	104	CMT
	50	7/18/84	24.01S	179.91W	575.3	5.5	4	20	27	288	CMT
	51	2/15/71	25.20S	178.40E	589.0	-	6	177	73	289	Bi
	52	4/18/78	25.13S	178.29E	598.4	5.6	52	76	33	292	CMT
	53	5/ 3/87	24.80S	178.15E	630.6	5.2	19	100	69	305	CMT
S8											
	1	2/25/87	28.10S	177.15W	74.6	5.0	69	305	16	83	CMT
	2	1/24/76	28.60S	177.60W	78.0	5.8	48	327	8	61	Ri
	3	3/ 7/72	28.20S	178.30W	192.0	6.1	12	245	42	348	Ri
	4	9/19/77	27.60S	177.90W	202.8	5.1	9	98	47	358	CMT
	5	8/31/87	26.74S	178.65W	315.5	-	20	102	35	357	CMT
	6	5/11/72	27.70S	178.90W	355.0	-	59	129	31	309	Ri
	7	8/23/84	26.86S	179.90E	462.9	5.1	27	208	31	100	CMT
	8	3/ 5/86	26.44S	178.16E	634.9	5.1	58	73	14	320	CMT
	9	2/27/80	26.97S	178.14E	637.4	5.5	28	178	13	81	CMT
	10	2/19/85	25.33S	177.76E	649.3	5.1	24	207	61	349	CMT
	11	7/ 7/87	25.52S	177.84E	655.3	-	28	180	60	339	CMT
S9											
	1	10/19/84	30.42S	178.48W	92.0	5.5	45	112	45	284	CMT
	2	6/25/84	30.71S	179.33W	139.3	5.2	38	100	52	286	CMT
	3	10/ 5/82	29.86S	178.28W	162.6	5.5	27	79	10	344	CMT
	4	6/26/81	29.98S	178.80W	163.8	5.7	29	102	59	302	CMT
	5	7/ 4/81	30.36S	179.06W	184.6	5.3	19	96	52	341	CMT
	6	1/26/83	30.52S	179.21W	224.1	6.1	38	177	52	354	CMT
	7	4/20/87	30.39S	179.49W	231.3	5.2	36	98	49	310	CMT
	8	10/20/85	29.01S	178.73W	262.0	5.3	13	111	36	11	CMT
	9	3/ 6/84	29.32S	179.21W	298.5	5.2	11	280	52	25	CMT
	10	9/28/81	29.27S	178.65W	309.1	5.9	28	103	45	341	CMT
	11	1/31/81	30.39S	179.84W	319.3	5.1	21	284	47	39	CMT
	12	3/28/72	30.70S	178.80W	337.0	5.6	1	87	42	356	Ri
	13	2/13/78	30.03S	179.73W	340.1	5.3	7	114	47	17	CMT
	14	1/20/68	29.90S	179.50W	349.0	6.0	11	87	76	115	IM
	15	5/ 3/81	30.43S	179.78W	440.6	5.0	9	258	76	29	CMT
	16	4/ 2/85	29.77S	178.97E	539.4	5.0	17	203	72	41	CMT
S10											
	1	8/19/81	32.76S	179.07E	211.8	5.1	2	231	65	325	CMT
	2	8/ 5/64	32.20S	179.80E	216.0	-	58	254	32	74	ISO
	3	9/13/86	31.73S	179.94W	231.0	5.8	2	282	55	15	CMT
	4	9/ 4/67	31.40S	179.40W	231.0	6.2	55	263	32	241	IM
	5	3/ 5/82	31.57S	179.73E	232.1	-	21	122	59	351	CMT

Table 5.1 (continued)

Slice	No.	Date	Lat. (°)	Lon. (°)	Depth (km)	m_b	T Axis δ (°)	T Axis θ (°)	P Axis δ (°)	P Axis θ (°)	Ref.
	6	7/23/84	30.86S	180.00W	336.7	5.3	3	120	45	27	CMT
	7	11/21/77	31.09S	179.94W	341.1	5.2	17	290	38	33	CMT
	8	3/14/77	31.65S	179.78E	352.4	5.0	9	96	52	355	CMT
	9	1/ 7/82	31.52S	179.30E	425.3	-	6	104	46	7	CMT
	10	12/ 5/86	31.07S	179.71E	432.8	5.4	15	81	68	309	CMT
	11	11/ 8/79	32.07S	179.43E	455.1	5.7	12	262	55	10	CMT

Events in each slice are in ascending order of focal depths. If a T or a P axis is along the down-dip direction of the slab, the corresponding plunge (δ) and azimuth (θ) angles are underlined.

The references are: ALK — Astiz et al., 1988; CMT — Dziewonski and Woodhouse, 1983, Giardini, 1984, and Dziewonski *et al.*, 1983a-c, 1984a-c, 1985a-d, 1986a-c, 1987a-g, and 1988a-f; Bi — Billington, 1978; BJ — Berckhemer and Jacob, 1968; Cn — Chandra, 1971; FK — Fujita and Kanamori, 1981; HIM — works by Honda and Masatsuka [1952] and Honda *et al.* [1967] as compiled by Isacks and Molnar, 1971; Hi — Hirasawa, 1966; Ic — Ichikawa, 1966; IM — Isacks and Molnar, 1971; ISO — Isacks *et al.*, 1969; KS — Katsumata and Sykes, 1969; OI — Oike, 1971; RA — Ritsema, 1965; Ri — Richtrer, 1979; SM — Stauder and Maulchin, 1976; ST — Sengupta and Toksöz, 1977.

Figure 5.1. Earthquake stress axes in the NW Pacific. Heavy dashed line contours deep seismicity at 100 km intervals, and light contour line shows 2-km isobath. Open circles are compressional events, filled squares are tensional events and filled triangles are ambiguous events. Compressional and tensional axes for each event are shown as solid and dashed bars, respectively, projected onto this map view.

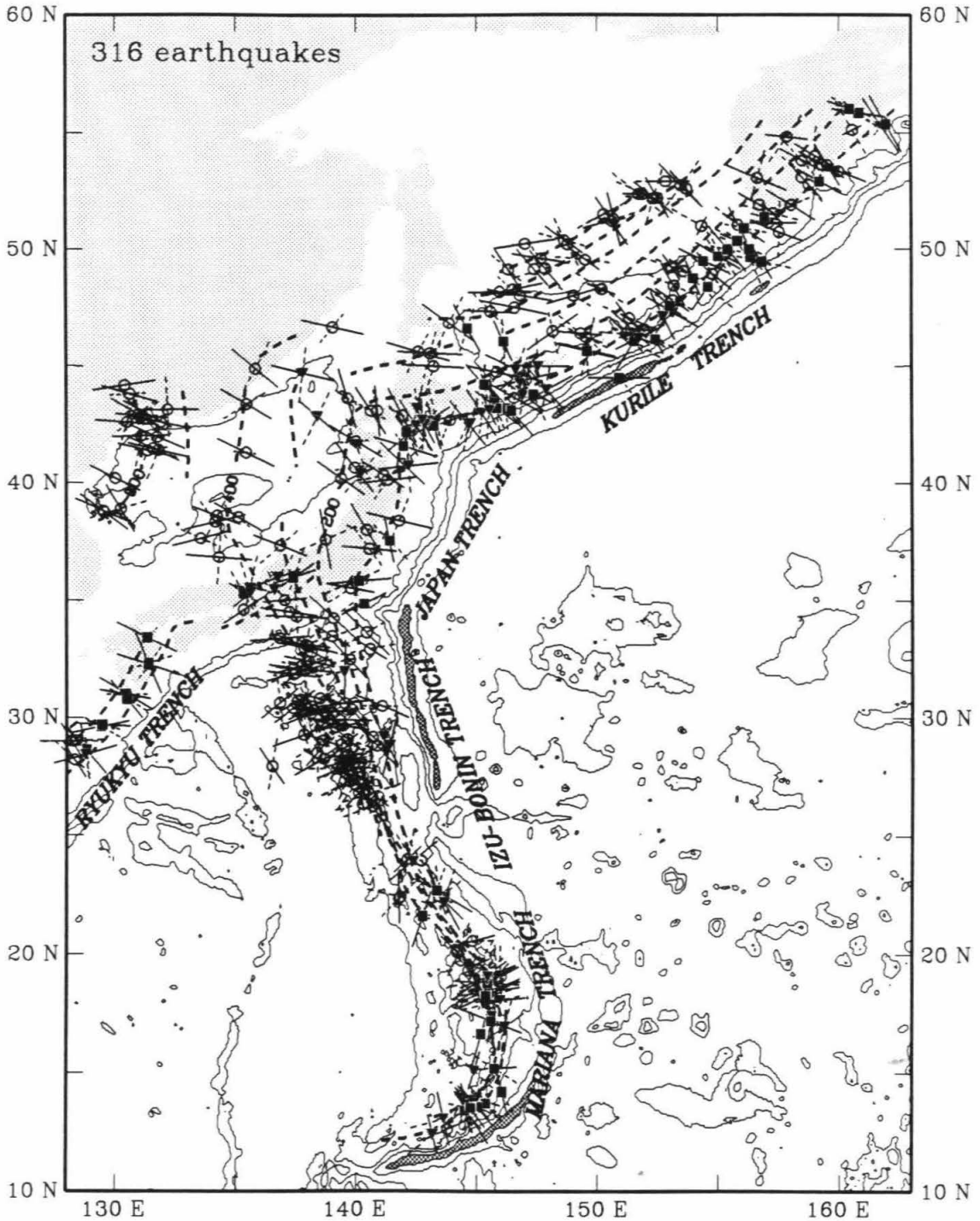
316 earthquakes
60 N
50 N
40 N
30 N
20 N
10 N
130 E
140 E
150 E
160 E
KURILE TRENCH
JAPAN TRENCH
IZU-BONIN TRENCH
MARIANA TRENCH
RYUKYU TRENCH
100
200

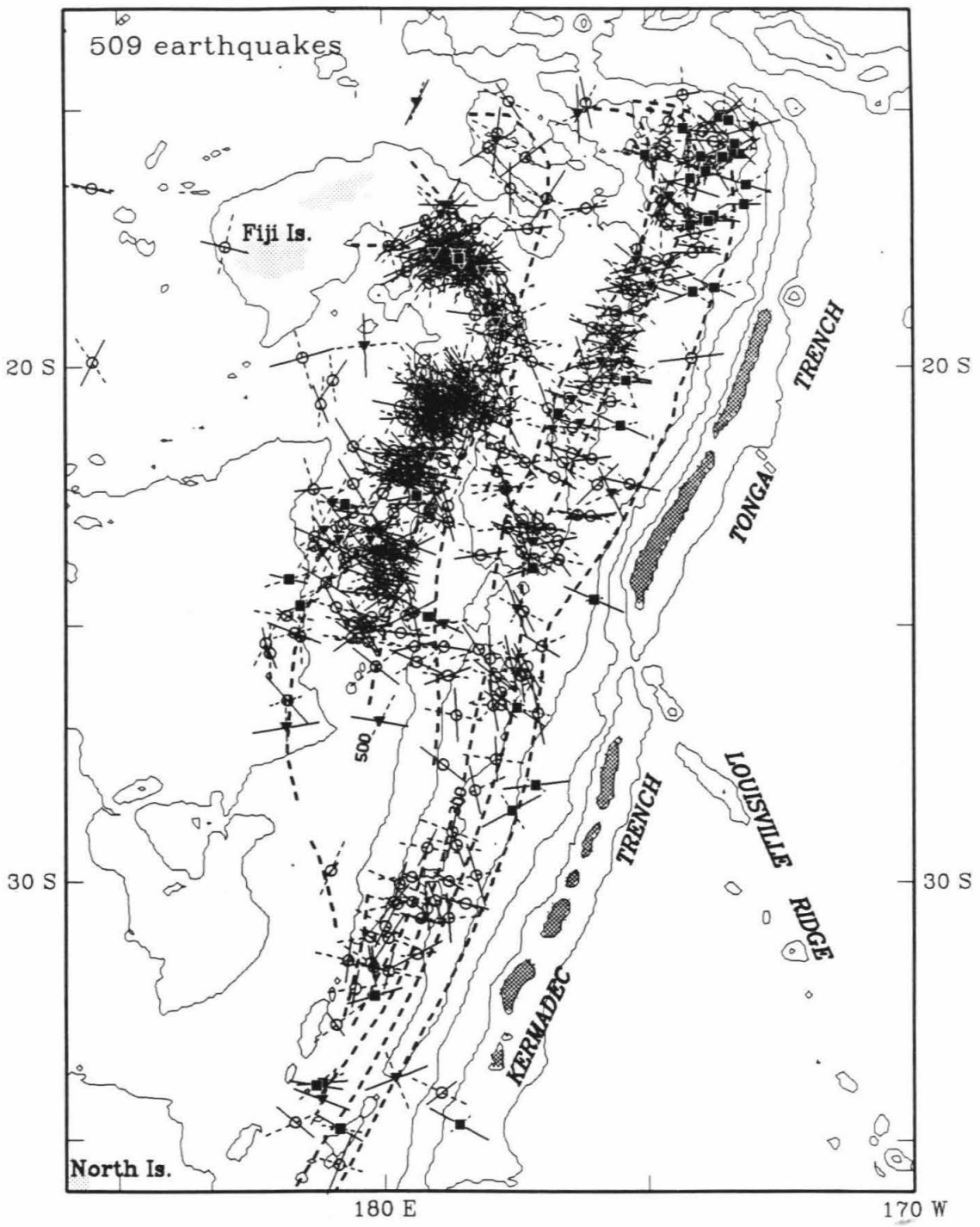

Figure 5.2. Earthquake stress axes in the Tonga-Kermadec region. The plotting convention follows that of Figure 5.1.

views in the NW Pacific and Tonga-Kermadec regions, respectively.

5.3 Seismic Stress in Slabs

5.3.1 Determining the down-dip stress regime

The down-dip direction is defined as the local direction of subduction in the slab (Isacks *et al.*, 1968; Isacks and Molnar, 1969). A similar term, "in plate," has also been recommended (Fujita and Kanamori, 1981). Nevertheless, the term "down-dip" is well understood, and the key issue then is to find the local down-dip direction for each earthquake.

In this study the down-dip direction is inferred both from seismicity pattern and reliable and coherent fast velocity slab anomalies in the tomographic images. Since slab dip usually varies with depth and the slabs are often contorted, a rather qualitative approach is taken in determining down-dip stress for each earthquake. The P and T axes for earthquakes in the two regions are plotted in stereo pairs for three-dimensional viewing (Figure 5.3). The stereo views of the principal axes in conjunction with views of the seismicity and the velocity structure (particularly in places of sparse seismicity) allow each earthquake to be identified as "down-dip compression," "down-dip tension" or "ambiguous." An "ambiguous" event refers to one with down-dip B axes, or none of the principal axes is close to the down-dip direction. For some of the deepest earthquakes under the Tonga arc, the

Figure 5.3. Stereo views of principal stress axes. a). NW Pacific; b). Tonga-Kermadec arcs. There are two pairs of stereo view plots for each region; the top pair shows all mechanism solutions and the bottom pair excludes all solutions which are down-dip compressional.

a) NW PACIFIC all events n=316

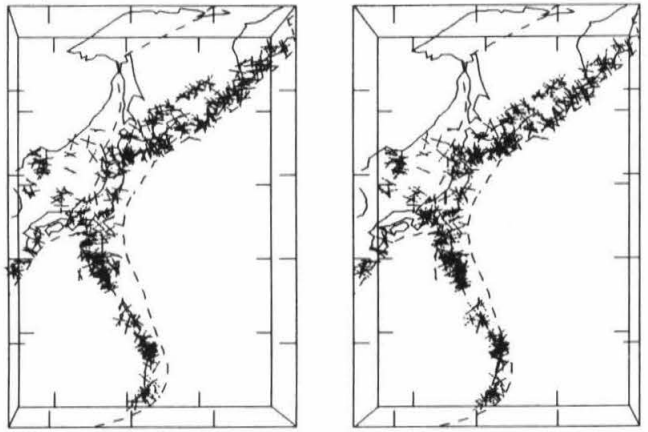

excluding down-dip P events n=112

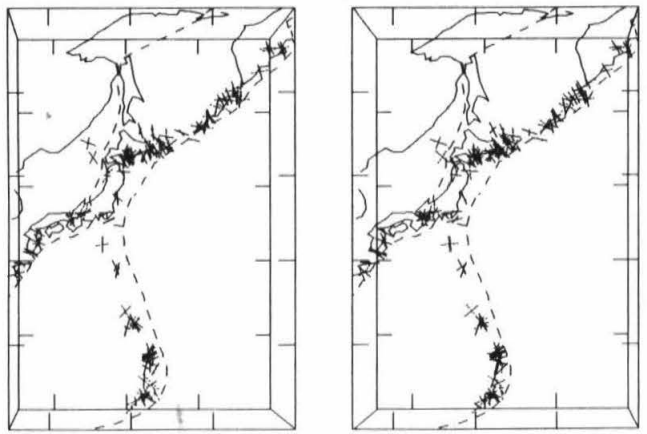

b) TONGA-KERMADEC all events n=509

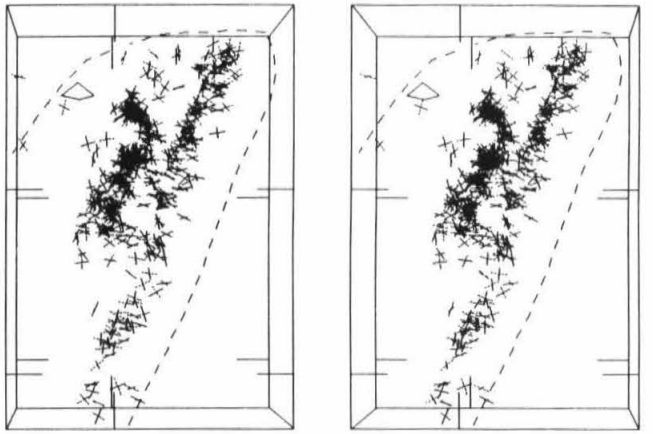

excluding down-dip P events n=79

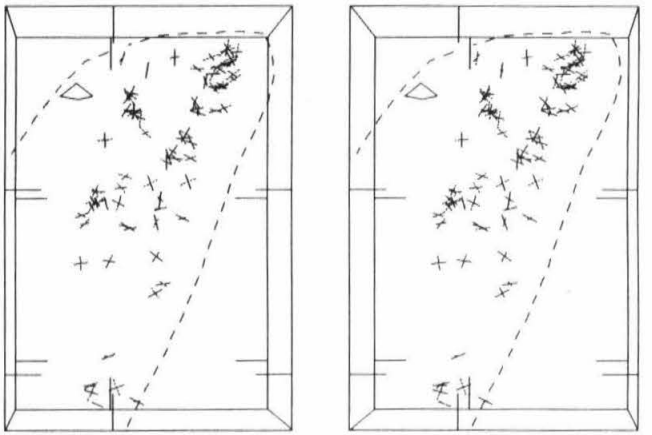

assignment of the down-dip stress regime is rather difficult due to extensive contortions both in the deep Wadati-Benioff zones and in the seismic slab anomalies.

5.3.2 Observations of down-dip stress in slabs

Figures 5.4 and 5.5 summarize the observations on down-dip stress regimes of slabs in the NW Pacific and Tonga-Kermadec regions. These show the interpreted PT boundary between compression and tension or mixed regimes, and the abnormal stress pattern underneath some junctions of arcs. Down-dip tensional or ambiguous mechanisms take about one third of the data in the NW Pacific region, and only about 15% of the data in the Tonga-Kermadec region (Figure 5.3). Once again, the general pattern of down-dip compression overlain by down-dip tension or mixed stress is confirmed for these two regions. This pattern is particularly consistent in the NW Pacific region. In the Tonga-Kermadec region a considerable number of tensional or ambiguous earthquakes appear to occur within deepest clusters of compressional events. The above pattern is also clearly visible in Table 5.1, in which values for a P or a T axis are underlined if it is found to be in down-dip direction.

The most striking feature shown in Figures 5.4 and 5.5 is the deep occurrence of tensional or ambiguous earthquakes underneath several major junctions of arcs. The P axes of most of these tensional or ambiguous events are perpendicular to the slab surface, while the corresponding T axes varies,

Figure 5.4. Interpretation of stress regime in the NW Pacific. The plotting convention follows that of Figure 5.1. Heavy solid lines are the interpreted PT boundaries. The boxes indicate the locations of cross sections N1 to N21.

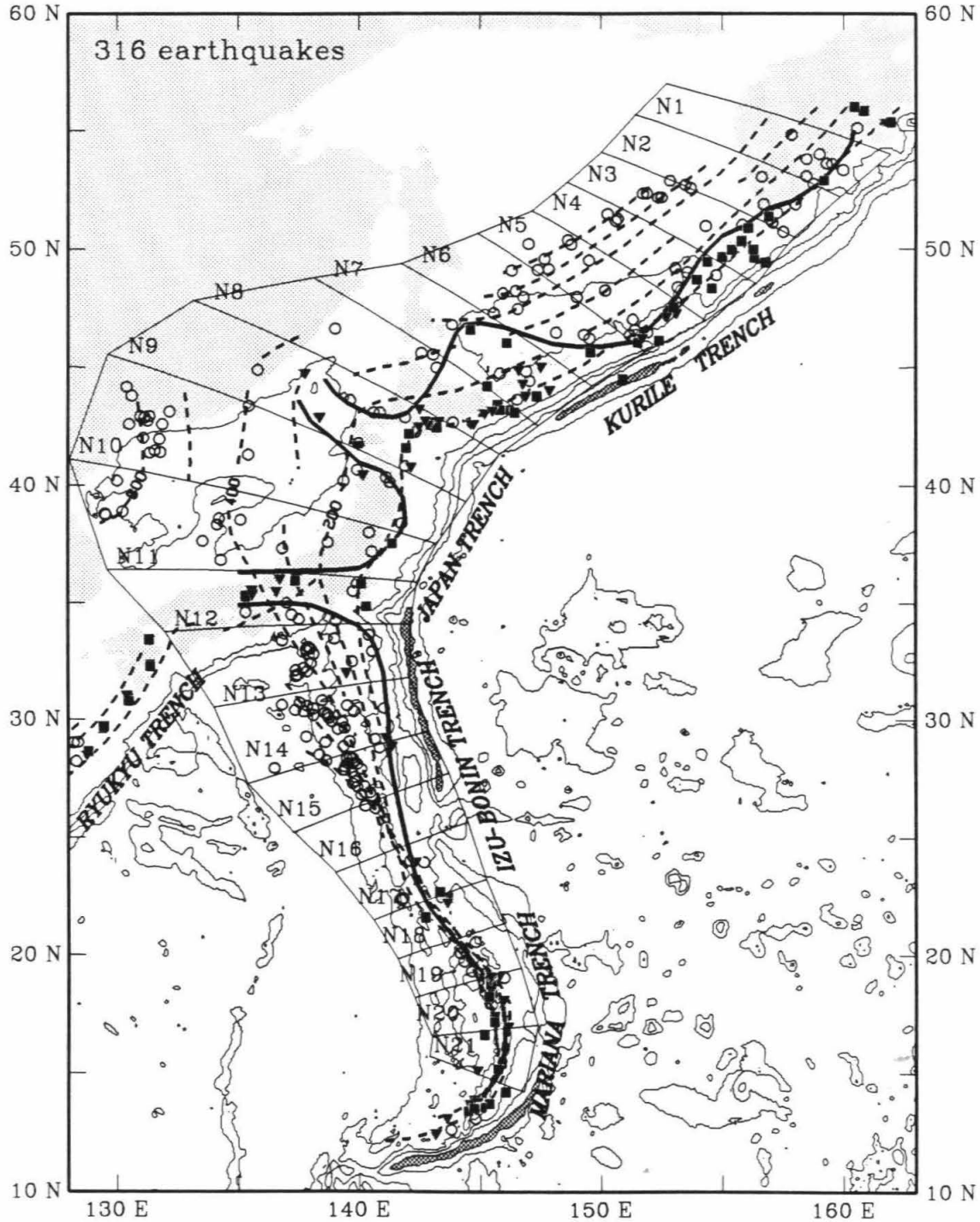
316 earthquakes
60 N
50 N
40 N
30 N
20 N
10 N
130 E
140 E
150 E
160 E
N1
N2
N3
N4
N5
N6
N7
N8
N9
N10
N11
N12
N13
N14
N15
N16
N17
N18
N19
N20
N21
KURILE TRENCH
JAPAN TRENCH
IZU-BONIN TRENCH
MARIANA TRENCH
RYUKYU TRENCH

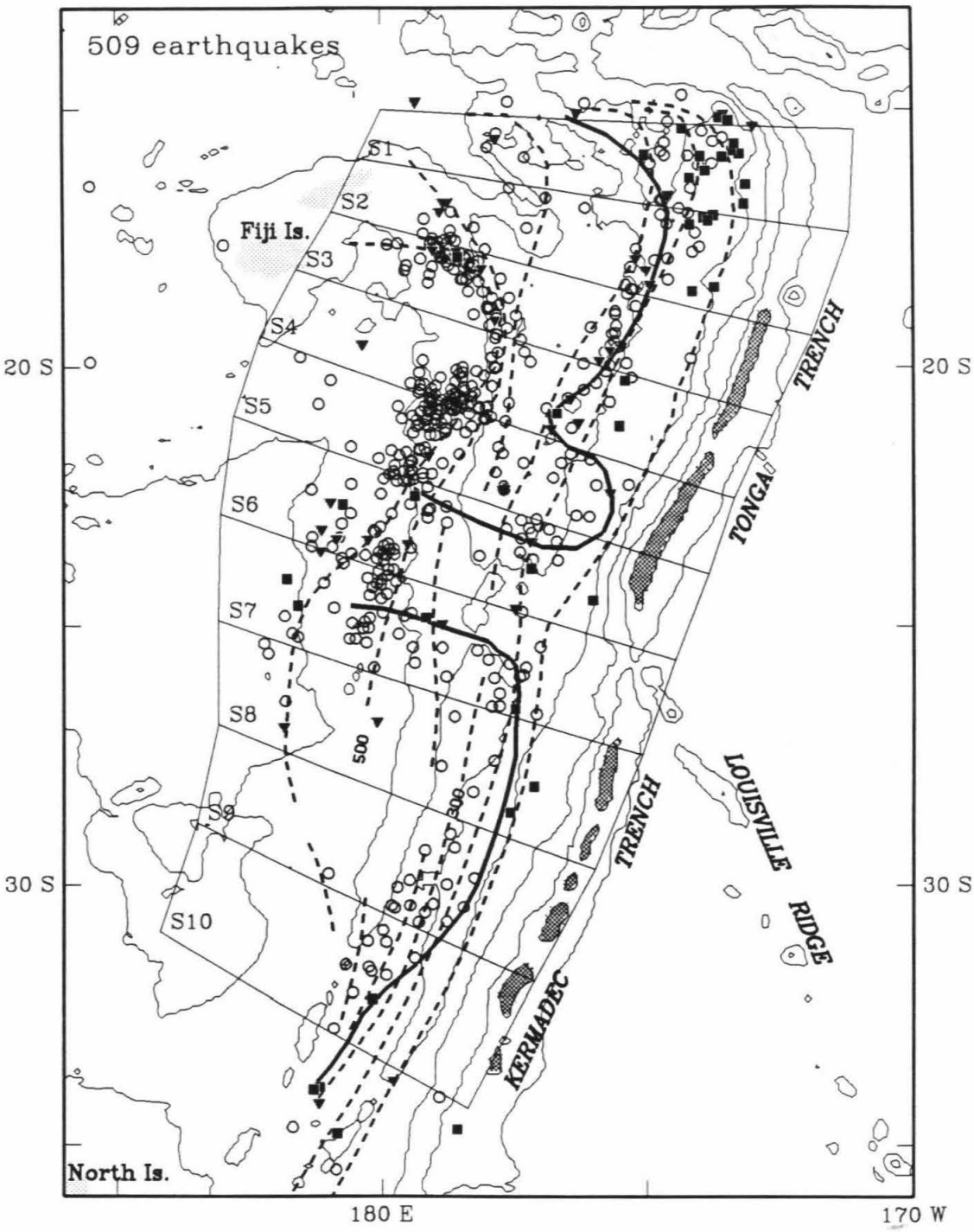

Figure 5.5. Interpretation of stress regime in the Tonga-Kermadec region. The plotting convention follows that of Figures 5.1. Heavy solid lines are the interpreted PT boundaries. The boxes locate cross sections S1 to S10.

but is consistent, within each area. Some of these events are deeper than 350 km, contrasting with compressional events as shallow as 150 km under adjacent arcs. These abnormal stress patterns clearly define distortions or cuts on the PT boundary, suggesting an important influence from lateral stress within the slab, or between slabs, at these localities. The most obvious cuts are underneath the junctions between Hokkaido and Honshu and between the Japan and Izu-Bonin arcs; both locations are underlain by deep seismicity gaps. The cut between the Tonga and Kermadec arcs is mixed with many down-dip compressional earthquakes; however, it corresponds to the regional seismicity gap at intermediate depths as well as the location at which the Louisville Ridge joins the Tonga-Kermadec trench from the southeast (Figure 5.5).

Away from regions underneath junctions of arcs, the PT boundary goes from about 100 km to 350 km depths. Under the Kuril, Japan, Izu-Bonin, Tonga and Kermadec arcs, the PT boundary is generally above 150-200 km depth (Figures 5.4 and 5.5). In the Mariana arc the boundary is between 310 km and 410 km. The boundary is quite smooth beneath the central parts of arcs, although it fluctuates in some areas, such as that in N7 of Figure 5.4 and in S4 of Figure 5.5. In their 1969 paper Isacks and Molnar proposed very shallow PT boundary depth under the Tonga, Northern Honshu and Izu-Bonin trenches, based on less than one tenth of the amount of focal mechanism data utilized in the current study. For these regions, it appears that the previous view of mixed stress regime above 300 km depth is perhaps a result of combining events under central parts of arcs and junctions of arcs.

In the central parts of arcs, at least in the two study regions, the depth of the PT boundary appears to correlate with dip and, perhaps, also with the topology of the slab (Figure 5.6). The boundary is about 350 km deep in the Mariana slab, which dips nearly vertically, and less than 100 km deep in the shallowly dipping Honshu slab. The Tonga, Kermadec, Kuril and Izu-Bonin slabs have intermediate characteristics. The Izu-Bonin slab possesses a particularly shallow PT boundary as well as an obvious topological change, flattening around 500 km depth.

As shown in Figure 5.6 the PT boundary is interpreted around the deepest intermediate-depth tensional events. The stress patterns above the PT boundary in the Tonga-Kermadec region, however, usually contain more down-dip compression than down-dip tension. For those earthquakes which are deeper than the PT boundary, although they are in dominant down-dip compression, their P axes sometimes may be in a slightly, but systematically, different direction from that normal to the arc. For instance, most deep and intermediate depth earthquakes under the northeasterly striking Kuril arc seem to have their P axes shifted slightly to the west (Figure 5.3a) from the surface plate motion direction which is approximately perpendicular to the arc.

5.4 Comparison with Seismic Morphology of Deep Slabs

The seismicity distributions, i.e., the Wadati-Benioff zones, in most parts of the two study regions are continuous from the surface down to about 650

Figure 5.6. Compilations of stress axes in cross sections. a). beneath the central portions of arcs; b). beneath the junction or edges of arcs. The cross sections in each panel are ordered by generally increasing dip angle of subduction zones. The plot is exaggerated vertically by a factor of 2.5, but the P and T axes remain in their true orientation. Filled squares and triangles are tensional and ambiguous events, respectively. Some of them, such as a tensional and an ambiguous event in the 400-500 km depth range under N. Kermadec (S7) as well as an ambiguous events under Honshu (N10), can be attributed to the nearby cuts on the PT boundary (see Figures 5.4 and 5.5). The range of interpreted PT boundary for each area is enclosed by a dashed box. Notice that the PT boundary beneath the central parts of arcs (panel a) is generally deeper when the dip of a subduction zone is steeper.

a).
Depth
[km]
600
400
200
0
Distance [degree]
0
5
10
15
20
25
30
Honshu
(N10-N11)
Hokkaido
(N8)
N. Kermadec
(S7-S8)
N. Tonga
(S2-S3)
Kurile
(N1-N6)
S. Tonga
(S4-S5)
Izu-Bonin
(N13-N16)
S. Kermadec
(S9-S10)
Mariana
(N17-N21)

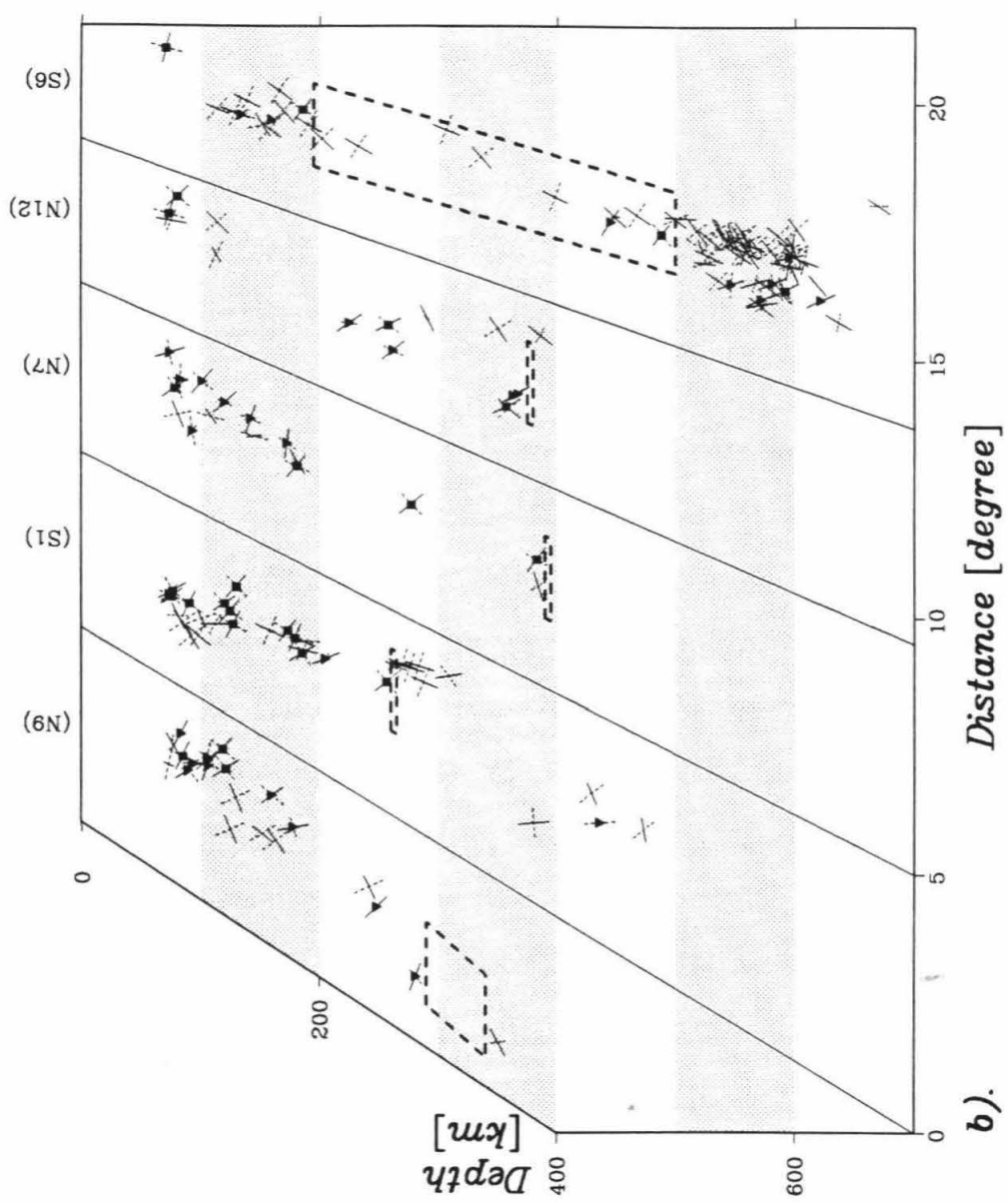
(N9)
(S1)
(N7)
(N12)
(S6)
0
200
400
600
Depth [km]
0
5
10
15
20
Distance [degree]

b).

km. The dip of these zones, however, varies considerably, especially in the NW Pacific region (Figure 5.1). It ranges from about 30° under Honshu to near vertical under the Mariana arc. The cuts on the PT boundary are in places of maximum change in slab dip and are associated with spatial gaps in seismic activity. In the down-dip direction, the Wadati-Benioff zone is relatively smooth in many places, but it is heavily contorted under the Izu-Bonin and Tonga arcs, and flattens to subhorizontal at its deepest extent. The contortion and flattening, perhaps unsurprisingly, produce some of the most distinguishable deep seismicity peaks at these places (Vassiliou and Hager, 1988) right above abrupt cutoffs in seismic activity. This kind of contortion pattern in the Tonga region has been taken as evidence for major shear deformation and lateral displacement of the deep slab (Giardini and Woodhouse, 1984, 1986).

A series of cross sections of seismic velocity images around subduction zones in the two regions in conjunction with stress axes data are displayed in Figure 5.7. The velocity images, with an inversion block size of $1° \times 1° \times 50$km, are obtained in Chapter 2 and Chapter 3, using hundreds of thousands of P wave travel times compiled by the International Seismic Centre. Tests on resolution and noise for the inversion, as discussed in the previous chapters, suggest that most patterns in these images are well resolved; however, anomalies near the edge of the covered region are noisier, and resolution for amplitude becomes poorer with depth.

P and T axes from focal mechanism data are projected onto the velocity cross sections in Figure 5.7. In the lower part of the upper mantle, the down-

Figure 5.7. Cross sections of P wave velocity images in comparison with stress axes. The velocity anomalies are contoured with 1% interval. White and cross-hatched areas are fast and slow velocities, respectively. Grey areas have less than a half percent variation from the reference velocity; black denote poorly sampled areas. P and T axes of available focal mechanism solutions in each cross section are also projected onto each panel. Other earthquake foci are shown with small open triangles. Notice that most of the compressional axes consistently follow the down-dip directions of the fast slab-like anomalies.

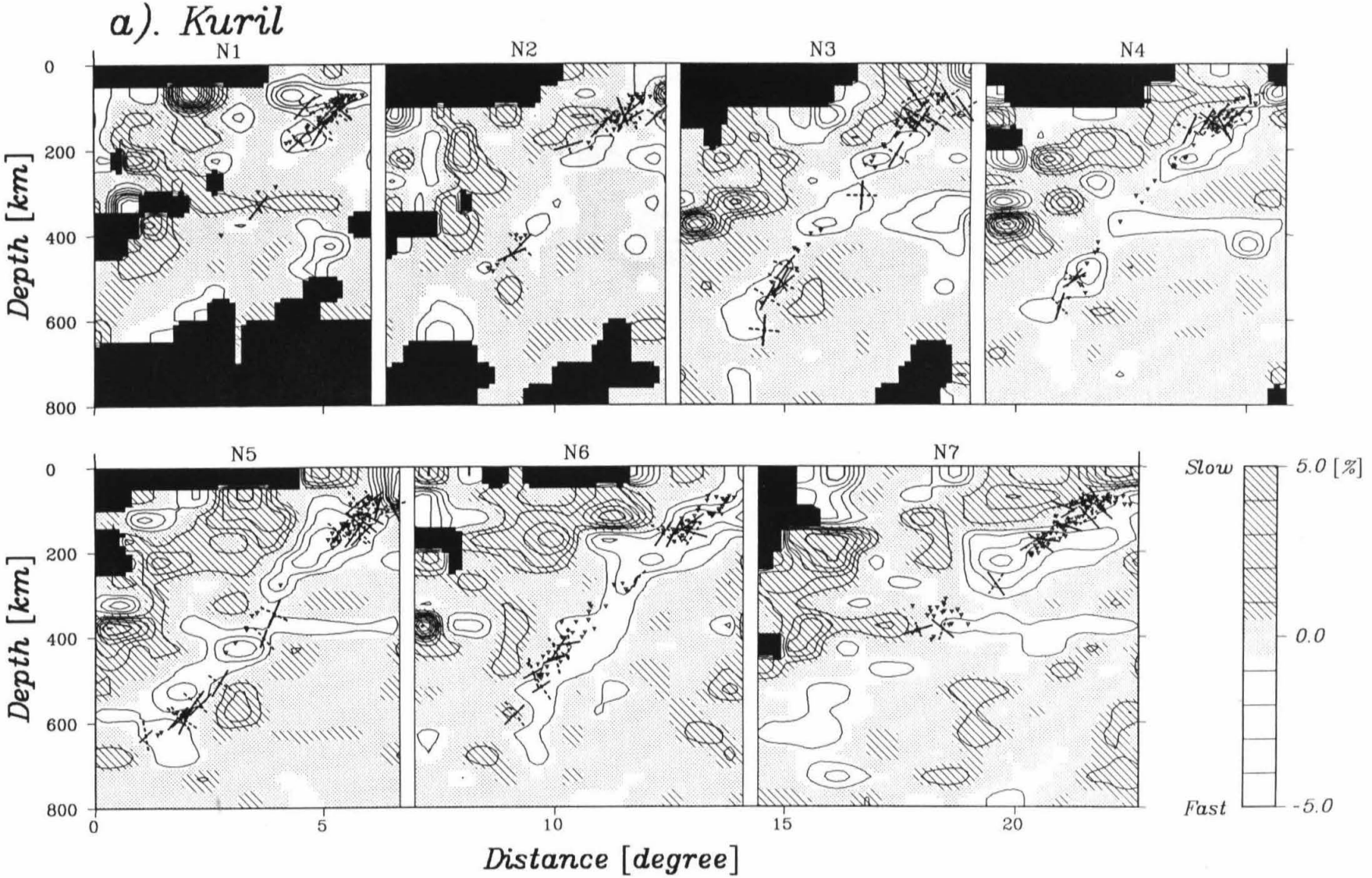
a). Kuril
N1
N2
N3
N4
N5
N6
N7
Depth [km]
0
200
400
600
800
0
5
10
15
20
Distance [degree]
Slow
Fast
5.0 [%]
0.0
-5.0

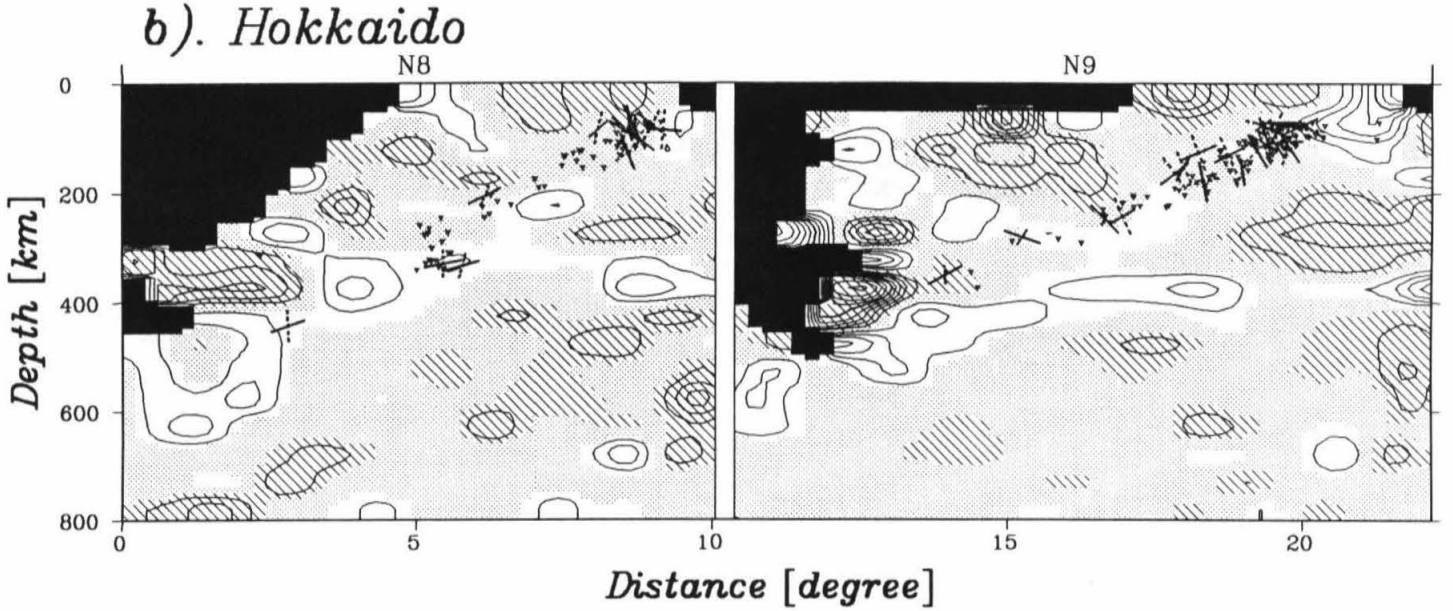
b). Hokkaido
N8
N9
0
200
400
600
800
Depth [km]
0
5
10
15
20
Distance [degree]

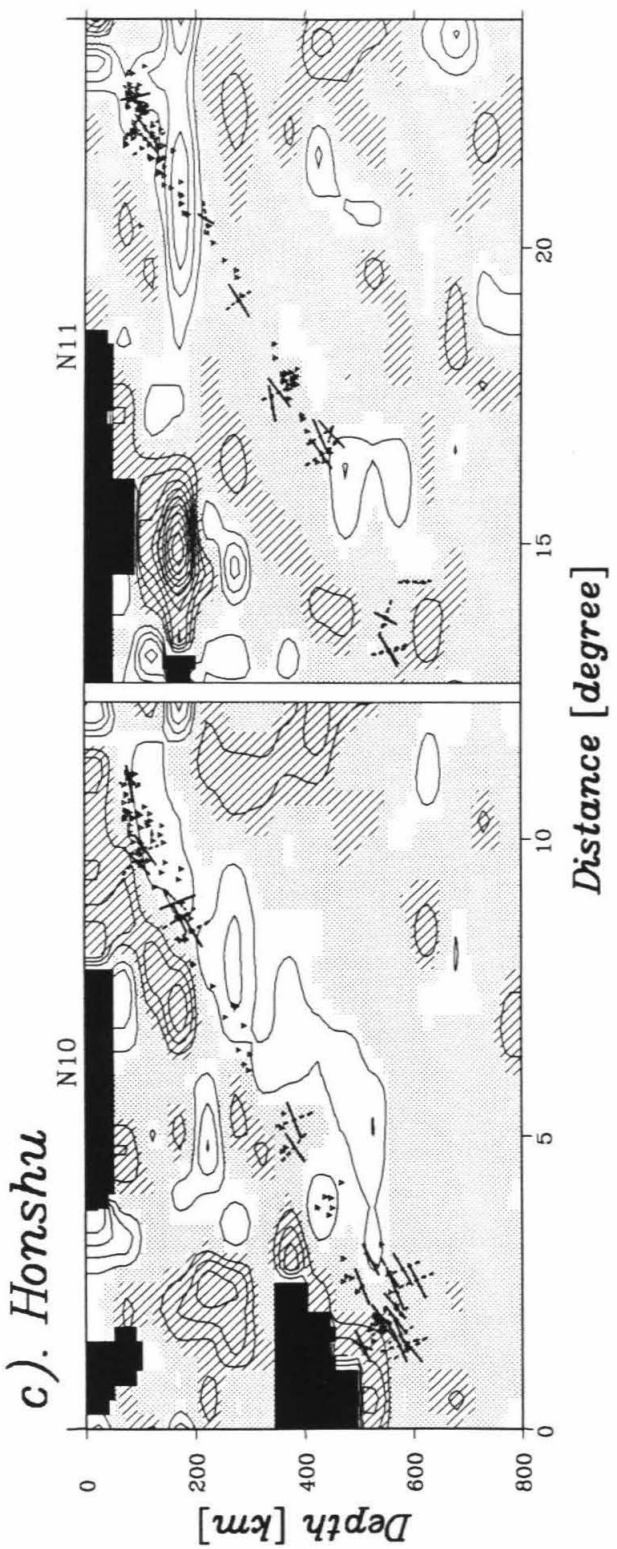
c). Honshu
N10
N11
Depth [km]
0
200
400
600
800
0
5
10
15
20
Distance [degree]

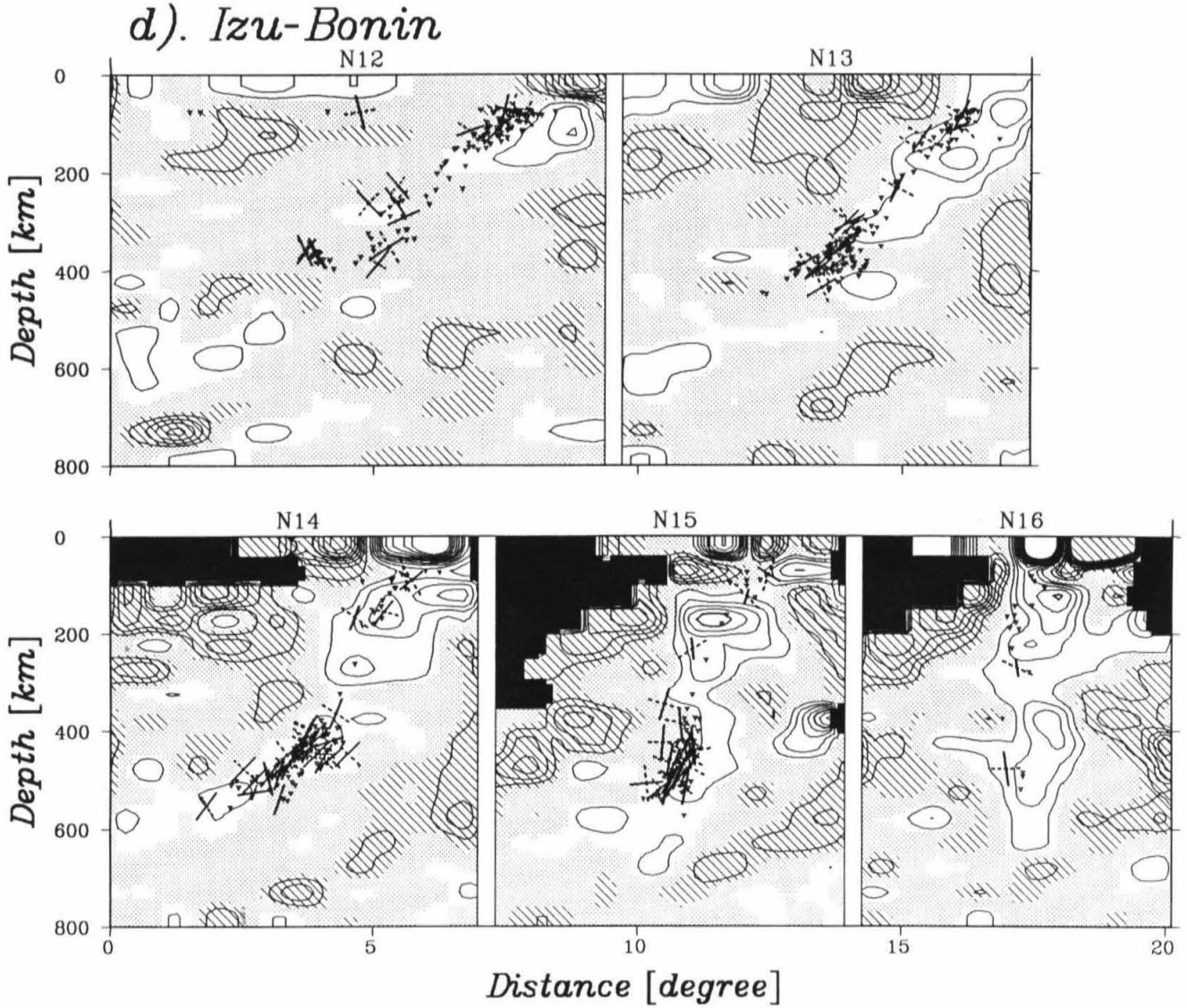
d). Izu-Bonin
N12
N13
N14
N15
N16
Depth [km]
0
200
400
600
800
0
5
10
15
20
Distance [degree]

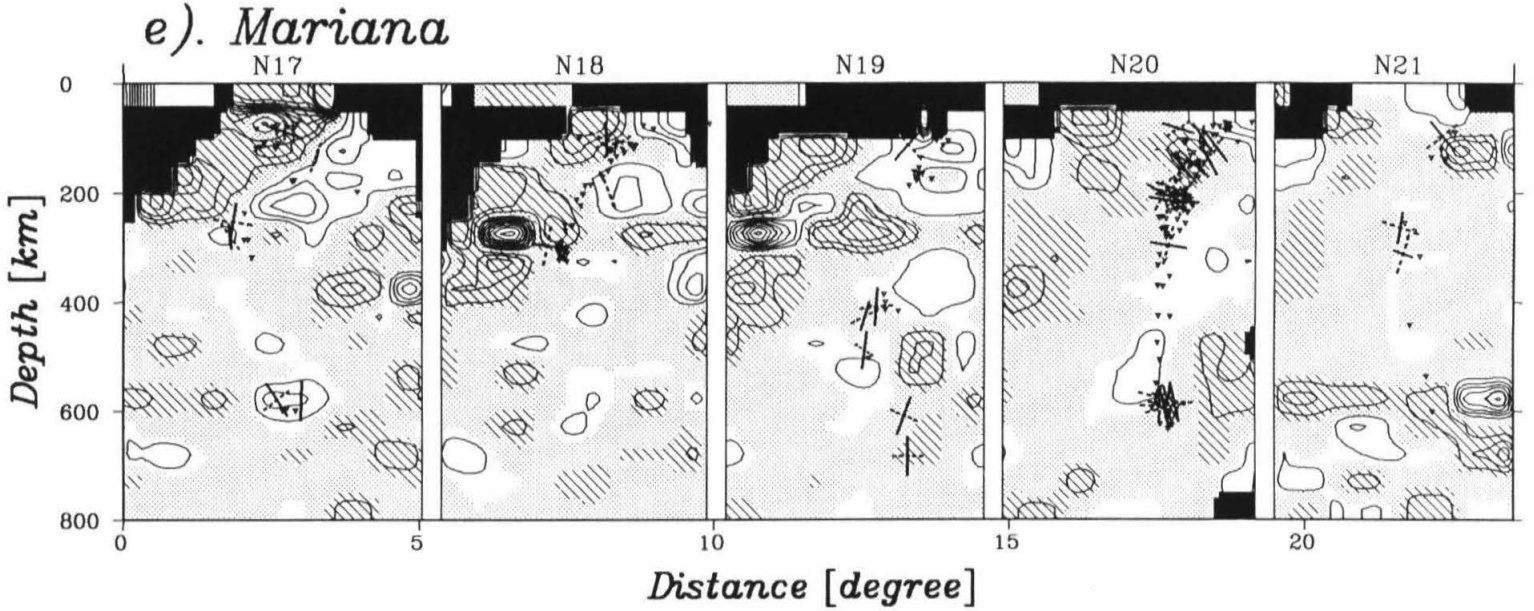
e). Mariana
N17
N18
N19
N20
N21
0
200
400
600
800
Depth [km]
0
5
10
15
20
Distance [degree]

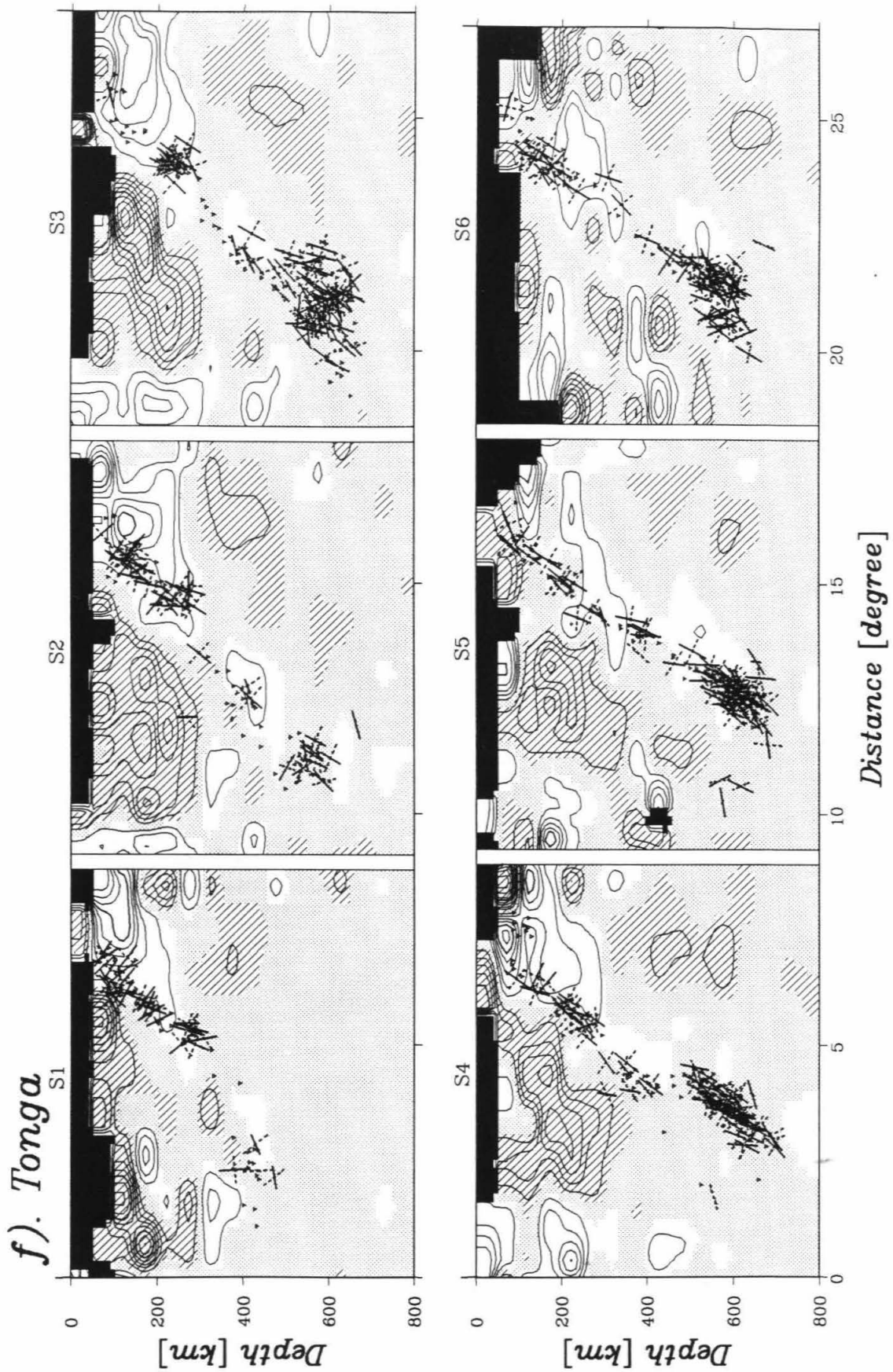
f). Tonga
S1
S2
S3
S4
S5
S6
Depth [km]
Depth [km]
0
200
400
600
800
0
5
10
15
20
25
Distance [degree]

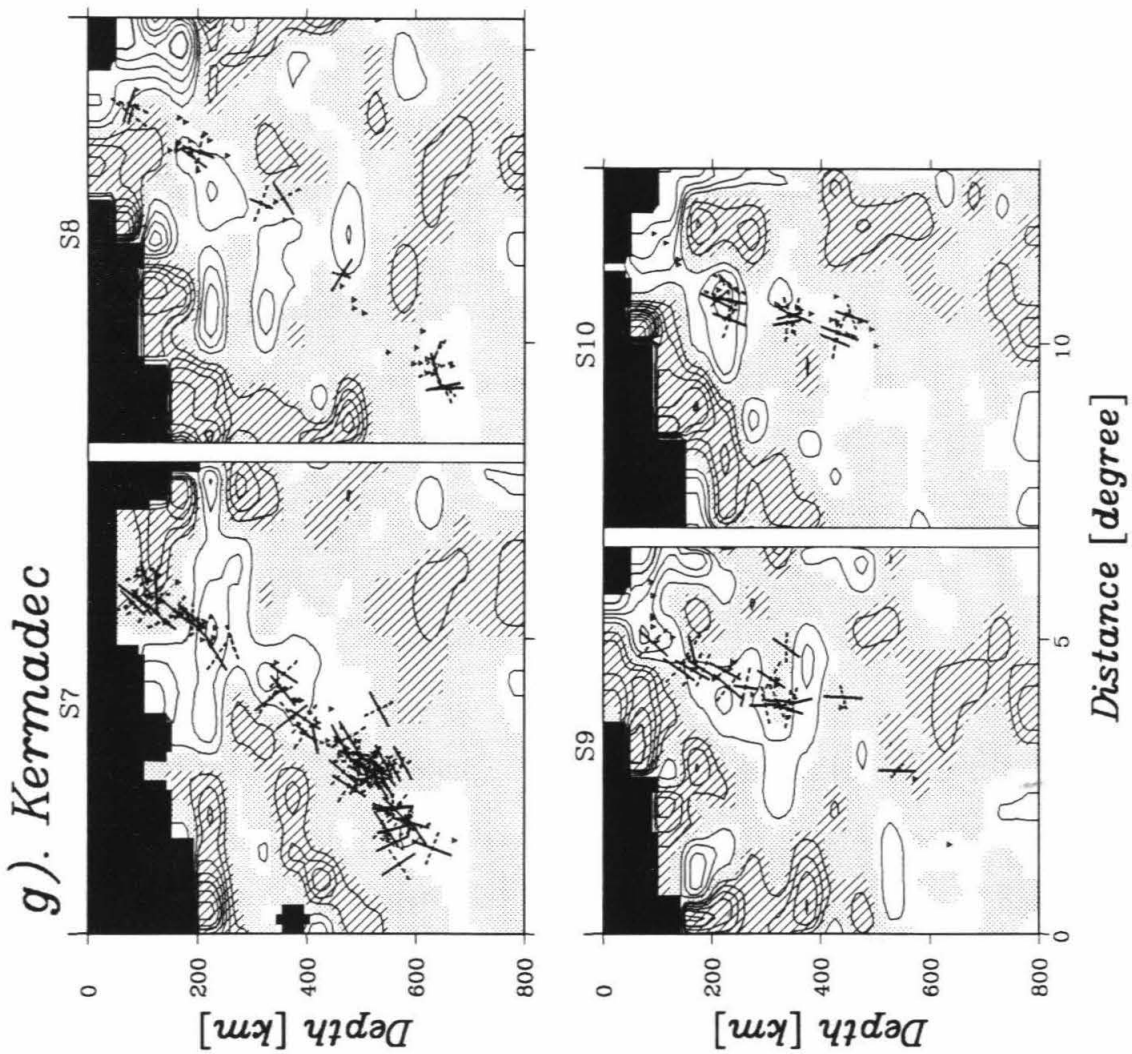
g). Kermadec
S7
S8
S9
S10
Depth [km]
0
200
400
600
800
0
5
10
Distance [degree]

dip compression axes consistently follow the trend of fast velocity anomalies associated with Wadati-Benioff zones, even in cases where the anomalies are contorted or flattened to subhorizontal around the largest earthquake clusters at the bottom of the upper mantle beneath the Izu-Bonin arc (N14 and N15) and the Tonga arc (S5, S6 and S7). The down-dip compression pattern at depth therefore may be taken as an useful reference in inferring subducting slabs from seismic velocity structures. For instance, our tomographic images in Figure 5.7 show that a fast slab under Japan (Honshu) slid with a small dip angle to regions beneath continental Asia, and a slab under the Izu-Bonin trench bends to sub-horizontal; these anomalies are consistent with the directions of the observed compressional axes.

For some of the deepest earthquakes (e.g., N14, N17, S7 and S8), however, the fast velocity trend is parallel to one of the nodal planes, which, by definition, bisect the P and T directions. Hence, a possibility arises that earthquakes at the tip of the Wadati-Benioff zone may not necessarily be in down-dip compression, as also evident from a rather complex situation in the deepest stress axes under the Tonga arc (S2-S7).

5.5 Discussion

A major result of this research is the pattern found for the PT boundary based on reliable focal mechanism data in the NW Pacific and the Tonga-Kermadec regions. It is understood that the boundary is a loosely defined one,

i.e., the down-dip tensional mechanisms above the boundary could be mixed with down-dip compressional events. Previously, the available CMT moment tensor solutions have been analyzed in a global context (Vassiliou, 1984; Apperson and Frohlich, 1987), and interpreted with viscous fluid models of subducting slabs (Vassiliou and Hager, 1988). These works confirmed down-dip compression in the slab at depths below 300 km. For the two regions examined in this study, however, it appears that the previous view of mixed stress regime above 300 km depth is perhaps the combination of events under central parts of arcs and junctions of arcs.

New mechanism data will certainly improve the detail of the boundary, but the pattern and general location of the boundary seem unlikely to be changed much by source relocation. At depths greater than about 200 km, different types of mechanism solutions in the two regions are spatially separated well (Figures 5.4 and 5.5), especially in the NW Pacific, during the time span of the data for more than 28 years. At shallower depths, however, the mixed stress patterns seen in this chapter could be attributed to temporal variation in focal mechanisms in response to earthquake cycles of large interplate subduction events (Astiz and Kanamori, 1986; Dmowska *et al.*, 1988; Astiz *et al.*, 1988; and Lay *et al.*, 1989) and/or existence of double seismic zones in certain places (e.g., Hasegawa and Umino, 1978; and Stauder and Maulchin, 1976). In fact, the presence of mixtures of down-dip compressional and tensional events above the PT boundary beneath the Kuril and Tonga arcs (Figure 5.6), as the most strongly coupled subduction zones in the two regions, is consistent with the presence of temporal variations in

mechanisms in strongly coupled slabs (e.g., Christensen and Ruff, 1988).

The cuts on the PT boundaries in the two regions generally agree with segment boundaries previously proposed by Burbach and Frohlich (1986) in their extensive review of lateral changes in Wadati-Benioff zone structure. The anomalous focal mechanisms, i.e., P axes normal to the slab surface, under the two arc junctions in the NW Pacific were observed by these authors with the CMT data available then; they also pointed out the lack of deep seismicity below these places. The state of stress in the slab at these corner locations is apparently highly controlled by the lateral geometry of the slab. Hence, a (down-dip) two-dimensional representation of the stress regime in slabs should exclude these places as well as the edge of an arc such as the northern end of the Tonga arc.

Christensen and Lay (1988) proposed that the Louisville Ridge as a possibly buoyant feature perturbs the regional stress regime at both intermediate and shallow depths in the slab. Viewed on the stress patterns around the cut of the PT boundary at the location (Figure 5.5) and the possibility of southward horizontal shear of deep material (Giardini and Woodhouse, 1986), it seems that perturbation from the subducted Louisville Ridge also contributes to the deep stress anomaly. As mentioned at the end of the previous section, some mixtures of tensional events with compressional events near the bottom of the Tonga seismic zone are probably due to complexity in slab morphology and plate motions. The complexity may be associated with the fact that the Tonga seismic zone possesses the highest level of seismic activity in the world.

Beneath the central parts of arcs in the NW Pacific and Tonga-Kermadec regions, the stress patterns in slabs (Figure 5.6), except for the Mariana arc, are consistent with model c of Isacks and Molnar (1969), i.e., nearly the entire gravitational load of the slab is supported from below and, perhaps, from the edges. The slab goes into compression at a shallow depth and the PT boundary depth apparently depends on slab dip and topology. The stress patterns in these regions with continuous seismicity over 600 km depth differ considerably from other regions which either lack deep seismicity and with dominant tension (Aleutians and Ryukyus), or have a seismicity truncation at intermediate depth between tensional shallow events and compressional deep events (Peru and Chile). The dominance of tensional events under the central parts of most arcs considered here terminates around 100-150 km depth. This implies an increase in the stress guide effect (Isacks *et al.*, 1968) of slabs in response to encountering resistance at depth. The slab pull force for these oldest slabs is proposed to be large (Spence, 1987), making the shallow PT boundary even more interesting.

The nature of the descending oceanic lithospheric slab in subduction zones is an important issue due to its bearing on models of mantle convection and the chemical evolution of the Earth (Isacks *et al.*, 1968; Toksöz *et al.*, 1973; Richter, 1979; and Hager *et al.*, 1983). The comparison between the earthquake focal mechanisms and detailed tomographic velocity images as examined in this study furnishes new information on the morphology of deep slabs. Consistent alignment between slab anomalies and deep compressional axes of earthquakes gives greater confidence in interpreting images of

subducting slabs from seismic tomographic structures.

The penetrating or trapping of the slab with respect to the upper and lower mantle boundary is sensitive to the density differences between slab and ambient mantle, slab and lower mantle, and dip (Kincaid and Olson, 1987). Morphology of the slab and the boundary between the upper and lower mantle depend on the viscosity contrast at the boundary (Gurnis and Hager, 1988). There may also be a chemical contrast at the boundary (Anderson, 1989). Down-dip compression is usually interpreted as resistance to subduction due to resisting forces on the edges and/or at the tip of the slab. Flattening in seismicity, P axes and the fast velocity slab anomalies near the bottom of the upper mantle beneath the Izu-Bonin and Tonga arcs, indicates the flattening behavior of the deep subducted slab at these locations.

5.5 Conclusions

A compilation of published focal mechanism solutions in the NW Pacific and Tonga-Kermadec regions confirms the general pattern of down-dip compression overlain by down-dip tension or mixed stress in slabs as it was originally found by Isacks and Molnar. Anomalous focal mechanisms are seen beneath the junctions and edges of the arcs. The PT boundary under the central parts of these arcs appears to depend on the dip and topology of the slab. Except certain places such as the Mariana arc, the boundary is generally shallower than 150-200 km in these regions. The previous view of a deeper

boundary around 300 km depth is perhaps a stacked result of events under central parts of arcs and junctions of arcs.

The observed deep compression axes are in consistent alignment with fast slab anomalies in tomographically derived velocity structures of these regions, even when the slab is contorted or flattened. The results of the current study support that the negative gravitational buoyancy associated with slabs is a dominant driving force, which is resisted by a barrier below. Based solely on the appearance of fast slab-like anomalies in relation to the deep earthquake zone and compressional stress axes, it seems that in many regions, such as that beneath the Japan, Izu-Bonin, Kermadec arcs and parts of the Tonga arc, the slab flattens to subhorizontal at the base of the upper mantle. In other regions, such as under the Kuril and parts of the Mariana and Tonga arcs, a fast region extends several hundred km below the deepest earthquakes.

References to Chapter 5

Anderson, Don L., The deep structure of continents, *J. Geophys. Res.*, **84**, 7555-7560, 1979.

Anderson, Don L., Composition of the Earth, *Science*, **243**, 367-370, 1989.

Apperson, K. D., and C. Frohlich, The relationship between Wadati-Benioff zone geometry and P, T and B axes of intermediate and deep focus earthquakes, *J. Geophys. Res.*, **92**, 13821-13831, 1987.

Astiz, L., and H. Kanamori, Interplate coupling and temporal variation of mechanisms of intermediate-depth earthquakes in Chile, *Bull. Seism. Soc. Am.*, **76**, 1614-1622, 1986.

Astiz, L., T. Lay, and H. Kanamori, Large intermediate-depth earthquakes and the subduction process, *Phys. Earth Planet. Inter.*, **53**, 80-166, 1988.

Billington, S., The morphology and tectonics of subducted lithosphere in the Tonga-Fiji-Kermadec region from seismicity and focal mechanism solutions, *Ph.D. Thesis*, Cornell Univ., Ithaca, N.Y, 1978.

Berckhemer, H., and K. H. Jacob, Investigation of the dynamical process in earthquake foci by analyzing the pulse shape of body waves, *Final Rep., Contract AF61(052)-801*, Inst. of Meteorology and Geophysics, Univ. of Frankfurt, 1968,

Burbach, G. V., and C. Frohlich, Intermediate and deep seismicity and lateral structure of subducted lithosphere in the Circum-Pacific region, *Rev. of Geophys.*, **24**, 833-874, 1986.

Chandra, U., Combination of P and S data for determination of earthquake focal mechanism, *Bull. Seism. Soc. Am.*, **61**, 1655-1673, 1971.

Christensen, D. H., and T. Lay, Large earthquakes in the Tonga region associated with subduction of the Louisville Ridge, *J. Geophys. Res.*, **93**, 13367-13389, 1988.

Christensen, D. H., and L. J. Ruff, Outer-rise earthquakes and seismic coupling, *Geophys. Res. Lett.*, **10**, 697-700, 1983.

Christensen, D. H., and L. J. Ruff, Seismic coupling and outer-rise earthquakes, *J. Geophys. Res.*, **93**, 13421-13444, 1988.

Dmowska, R., J. R. Rice, L. C. Lovison, and D. Josell, Stress transfer and seismic phenomena in coupled subduction zones during the earthquake cycle, *J. Geophys. Res.*, **93**, 7869-7884, 1988.

Dziewonski, A. M., T. A. Chou, and J. H. Woodhouse, Determination of earthquake source parameters from waveform data for studies of global and regional seismicity, *J. Geophys. Res.*, **86**, 2825-2852, 1981.

Dziewonski, A. M., A. Friedman, D. Giardini, and J. H. Woodhouse, Global seismicity of 1982: centroid-moment tensor solutions for 308 earthquakes, *Phys. Earth Planet. Int.*, **33**, 76-90, 1983a.

Dziewonski, A. M., A. Friedman, and J. H. Woodhouse, Centroid-moment tensor solutions for January - March 1983, *Phys. Earth Planet. Int.*, **33**, 71-75, 1983b.

Dziewonski, A. M., J. E. Franzen, and J. H. Woodhouse, Centroid-moment tensor solutions for April - June 1983, *Phys. Earth Planet. Int.*, **33**, 243-249, 1983c.

Dziewonski, A. M., J. E. Franzen, and J. H. Woodhouse, Centroid-moment tensor solutions for July - September 1983, *Phys. Earth Planet. Int.*, **34**, 1-8, 1984a.

Dziewonski, A. M., J. E. Franzen, and J. H. Woodhouse, Centroid-moment tensor solutions for October - December 1983, *Phys. Earth Planet. Int.*, **34**, 129-136, 1984b.

Dziewonski, A. M., J. E. Franzen, and J. H. Woodhouse, Centroid-moment tensor solutions for January - March 1984, *Phys. Earth Planet. Int.*, **34**, 209-219, 1984c.

Dziewonski, A. M., J. E. Franzen, and J. H. Woodhouse, Centroid-moment tensor solutions for April - June 1984, *Phys. Earth Planet. Int.*, **37**, 87-96, 1985a.

Dziewonski, A. M., J. E. Franzen, and J. H. Woodhouse, Centroid-moment tensor solutions for July - September 1984, *Phys. Earth Planet. Int.*, **38**, 203-213, 1985b.

Dziewonski, A. M., J. E. Franzen, and J. H. Woodhouse, Centroid-moment tensor solutions for October - December 1984, *Phys. Earth Planet. Int.*, **39**, 147-156, 1985c.

Dziewonski, A. M., J. E. Franzen, and J. H. Woodhouse, Centroid-moment tensor solutions for January - March 1985, *Phys. Earth Planet. Int.*, **40**, 249-258, 1985d.

Dziewonski, A. M., J. E. Franzen, and J. H. Woodhouse, Centroid-moment tensor solutions for April - June 1985, *Phys. Earth Planet. Int.*, **41**, 215-224, 1986a.

Dziewonski, A. M., J. E. Franzen, and J. H. Woodhouse, Centroid-moment tensor solutions for July - September 1985, *Phys. Earth Planet. Int.*, **42**, 205-214, 1986b.

Dziewonski, A. M., J. E. Franzen, and J. H. Woodhouse, Centroid-moment tensor solutions for October - December 1985, *Phys. Earth Planet. Int.*, **43**, 185-195, 1986c.

Dziewonski, A. M., G. Ekström, J. E. Franzen, and J. H. Woodhouse, Global seismicity of 1977: centroid-moment tensor solutions for 471 earthquakes, *Phys. Earth Planet. Int.*, **45**, 11-36, 1987a.

Dziewonski, A. M., G. Ekström, J. E. Franzen, and J. H. Woodhouse, Global seismicity of 1978: centroid-moment tensor solutions for 512 earthquakes, *Phys. Earth Planet. Int.*, **46**, 316-342, 1987b.

Dziewonski, A. M., G. Ekström, J. E. Franzen, and J. H. Woodhouse, Global seismicity of 1979: centroid-moment tensor solutions for 524 earthquakes, *Phys. Earth Planet. Int.*, **48**, 18-46, 1987c.

Dziewonski, A. M., G. Ekström, J. E. Franzen, and J. H. Woodhouse, Centroid-moment tensor solutions for January - March 1986, *Phys. Earth Planet. Int.*, **45**, 1-10, 1987d.

Dziewonski, A. M., G. Ekström, J. E. Franzen, and J. H. Woodhouse, Centroid-moment tensor solutions for April - June 1986, *Phys. Earth Planet. Int.*, **45**, 229-239, 1987e.

Dziewonski, A. M., G. Ekström, J. E. Franzen, and J. H. Woodhouse, Centroid-moment tensor solutions for July - September 1986, *Phys. Earth Planet. Int.*, **46**, 305-315, 1987f.

Dziewonski, A. M., G. Ekström, J. H. Woodhouse, and G. Zwart, Centroid-moment tensor solutions for October - December 1986, *Phys. Earth Planet. Int.*, **48**, 5-17, 1987g.

Dziewonski, A. M., G. Ekström, J. E. Franzen, and J. H. Woodhouse, Global seismicity of 1980: centroid-moment tensor solutions for 515 earthquakes, *Phys. Earth Planet. Int.*, **50**, 127-154, 1988a.

Dziewonski, A. M., G. Ekström, J. E. Franzen, and J. H. Woodhouse, Global seismicity of 1981: centroid-moment tensor solutions for 542 earthquakes, *Phys. Earth Planet. Int.*, **50**, 155-182, 1988b.

Dziewonski, A. M., G. Ekström, J. H. Woodhouse, and G. Zwart, Centroid-moment tensor solutions for January - March 1987, *Phys. Earth Planet. Int.*, **50**, 116-126, 1988c.

Dziewonski, A. M., G. Ekström, J. H. Woodhouse, and G. Zwart, Centroid-moment tensor solutions for April - June 1987, *Phys. Earth Planet. Int.*, **50**, 215-225, 1988d.

Dziewonski, A. M., G. Ekström, J. H. Woodhouse, and G. Zwart, Centroid-moment tensor solutions for July - September 1987, *Phys. Earth Planet. Int.*, **53**, 1-11, 1988e.

Dziewonski, A. M., G. Ekström, J. E. Franzen, and J. H. Woodhouse, Global seismicity of 1982 and 1983: centroid-moment tensor solutions for 553 earthquakes, *Phys. Earth Planet. Int.*, **53**, 17-45, 1988f.

Dziewonski, A. M., and J. H. Woodhouse, An experiment in the systematic study of global seismicity: centroid-moment tensor solutions for 201 moderate and large earthquakes of 1981, *J. Geophys. Res.*, **88**, 3247-3271, 1983.

Fujita, K., and H. Kanamori, Double seismic zone and stresses of intermediate depth earthquakes, *Geophys. J. R. astr. Soc.*, **66**, 131-156, 1981.

Giardini, D., Systematic analysis of deep seismicity: 200 centroid-moment tensor solutions for earthquakes between 1977 and 1980, *Geophys. J. R. astr. Soc.*, **77**, 883-914, 1984.

Giardini, D., and J. H. Woodhouse, Deep seismicity and modes of deformation in Tonga subduction zone, *Nature*, **307**, 505-509, 1984.

Giardini, D., and J. H. Woodhouse, Horizontal shear flow in the mantle beneath the Tonga arc, *Nature*, **319**, 551-555, 1986.

Gurnis, M., and B. H. Hager, Controls on the structure of subducted slabs and the viscosity of the lower mantle, *Nature*, **335**, 317-321, 1988.

Hager, B. H., R. J. O'Connell, and A. Raefsky, Subduction, back-arc spreading and global mantle flow, *Tectonophys.*, **99**, 165-189, 1983.

Hirahara, K., Three-dimensional seismic structure beneath southwest Japan: The subducting Philippine Sea plate, *Tectonophys.*, **79**, 1-41, 1981.

Hasegawa, A., and N. Umino, Focal mechanisms and the distribution of seismicity in northeastern Japan, *Progr. Abstr. Seism. Soc. Japan.*, **1**, 34, 1978 (in Japanese).

Honda, H., and A. Masatsuka, On the mechanisms of earthquakes and the stresses producing them in Japan and its vicinity, *Sci. Rep., Tokoku Univ., Ser. 5, Geophys.*, **4**, 42-60, 1952.

Honda, H., A. Masatsuka, and M. Ichikawa, On the mechanism of earthquakes and stresses producing them in Japan and its vicinity, 3, *Geophys. Mag.*, **33**, 271-279, 1967.

Hirasawa, T., A least squares method for the focal mechanism determinations from S wave data (2), *Bull. Earthquake Res. Inst. Tokyo Univ.*, **44**, 919-938, 1966.

Ichikawa, M., Mechanism of earthquakes in and near Japan, 1950-1962, *Pap. Meteorol. Geophys.* (Tokyo), **16**, 201-229, 1966.

Isacks, B., and P. Molnar, Mantle earthquake mechanisms and sinking of the lithosphere, *Nature*, **223**, 1121-1124, 1969.

Isacks, B., and P. Molnar, Distribution of stresses in the descending lithosphere from a global survey of focal mechanism solution of mantle earthquakes, *Rev. Geophys. Space Phys.*, **9**, 103-174, 1971.

Isacks, B., J. Oliver, and L. R. Sykes, Seismology and the new global tectonics, *J. Geophys. Res.*, **73**, 5855-5899, 1968.

Isacks, B., L. R. Sykes, and J. Oliver, Focal mechanisms of deep and shallow earthquakes in the Tonga-Kermadec region and the tectonics of island arcs, *Bull. Geol. Soc. Amer.*, **80**, 1443-1470, 1969.

Katsumata, M., and L. R. Sykes, Seismicity and tectonics of the western Pacific: Izu-Mariana-Caroline and Ryukyu-Taiwan regions, *J. Geophys. Res.*, **74**, 5923-5948, 1969.

Kamiya, S., T. Miyatake, and K. Hirahara, How deep can we see the high velocity anomalies beneath the Japan Island? *Geophys. Res. Lett.*, **15**, 828-831, 1988.

Kanamori, H., Synthesis of long-period surface waves and its application to earthquake source studies—Kurile islands earthquakes of October 13,

1963, *J. Geophys. Res.*, **75**, 5011-5027, 1970.

Kanamori, H., and J. W. Given, Use of long period surface waves for rapid determination of earthquake source parameters, *Phys. Earth Planet. Inter.*, **27**, 8-31, 1981.

Kincaid, C., and P. Olson, An experimental study of subduction and slab migration, *J. Geophys. Res.*, **92**, 13832-13840, 1987.

Lay, T., L. Astiz, H. Kanamori, and D. H. Christensen, Temporal variation of large intraplate earthquakes in coupled subduction zones, *Phys. Earth Planet. Inter.*, in press, 1989.

Oike, K., On the nature of the occurrence of intermediate and deep earthquakes. 1. the world wide distribution of the earthquake generating stress, *Bull. Disas. Prev. Res. Inst.*, Kyoto Univ., **20**, 145-182, 1971.

Ritsema, A. R., The mechanism of some deep and intermediate earthquakes in the region of Japan, *Bull. Earthquake Res. Inst. Tokyo Univ.*, **43**, 39-52, 1965.

Richter, F. M., Focal mechanisms and seismic energy release of deep and intermediate earthquakes in the Tonga-Kermadec region and their bearing on the depth extent of mantle flow, *J. Geophys. Res.*, **84**, 6783-6795, 1979.

Sengupta, M. K., and M. Nafi Toksöz, The amplitudes of P waves and magnitude corrections for deep focus earthquakes, *J. Geophys. Res.*, **82**, 2971-2980, 1977.

Spence, W., Slab pull and the seismotectonics of subducting lithosphere, *Rev. Geophys.*, **25**, 55-69, 1987.

Stauder, W., and L. Maulchin, Fault motion in the larger earthquakes of the Kurile-Kamchatka arc and the Kurile-Hokkaido corner, *J. Geophys. Res.*, **81**, 2297-2308, 1976.

Sykes, L. R., Mechanism of earthquakes and nature of faulting on the mid-oceanic ridge, *J. Geophys. Res.*, **72**, 2131-2153, 1967.

Toksöz, M. Nafi, J. W. Minear, and B. R. Julian, Temperature field and geophysical effects of a down-going slab, *J. Geophys. Res.*, **76**, 1113-1138, 1971.

Toksöz, M. Nafi, N. H. Sleep, and A. T. Smith, Evolution of the downgoing lithosphere and the mechanisms of deep focus earthquakes, *Geophys. J. R. astr. Soc.*, **35**, 285-310, 1973.

Utsu, T., Seismological evidence for anomalous structure of island arcs with special reference to the Japanese region, *Rev. Geophys. Space Phys.*, **9**, 839-890, 1971.

Vassiliou, M. S., The state of stress in subducting slabs as revealed by earthquakes analyzed by moment tensor inversion, *Earth Planet. Sci. Lett.*, **69**, 195-202, 1984.

Vassiliou, M. S., and B. H. Hager, Subduction zone earthquakes and stress in slabs, *PAGEOPH*, **128**, 547-624, 1988.

Zhou, H., How well can we resolve the deep seismic slab with seismic tomography? *Geophys. Res. Lett.*, **15**, 1425-1428, 1988.

Zhou, H. W., and R. W. Clayton, Travel-time inversion for P and S velocities beneath the northwest edge of the Pacific: slab fingering? *Eos Trans. AGU*, **68**, 1379, 1987.

Zhou, H., and R. W. Clayton, P wave velocities around subduction zones in the southwest Pacific, *Eos Trans. AGU*, **69**, 398, 1988.